ISSN 0288-4534
CODEN: KONAE7

KONA Powder and Particle Journal

No. 26 (2008)

Published by Hosokawa Powder Technology Foundation

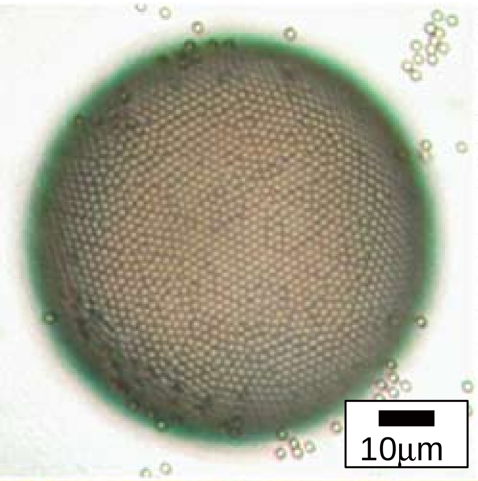

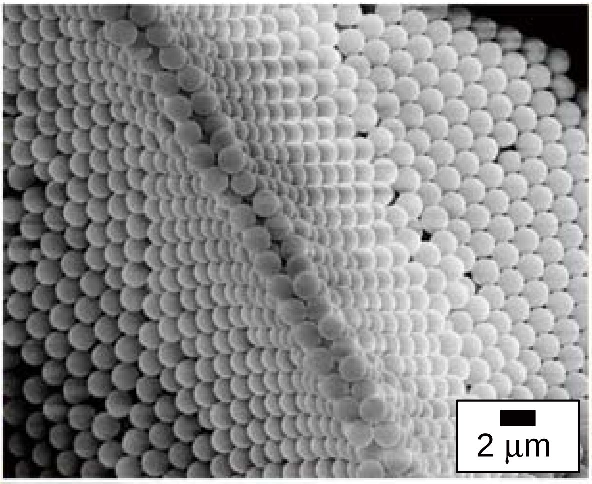

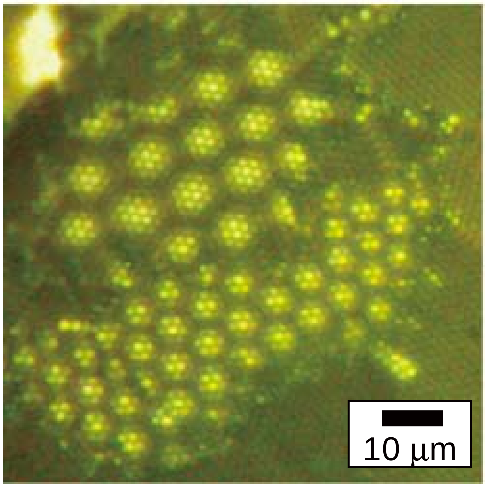

available online – www.kona.or.jp

KONA Powder and Particle Journal

http://www.kona.or.jp

KONA is a refereed scientific journal that publishes articles on powder and particle sciences and technology. KONA has been published annually since 1983 in Japan. KONA is distributed to researchers, members of the scientific community, universities and research libraries throughout the world.

About the Cover of Journal“ KONA”

The Chinese character “粉” is pronounced “KONA” in Japanese, and means “Powder” . The hand written “粉” is after the late Mr. Eiichi Hosokawa, founder of the Hosokawa Micron Corporation.

Headquarters of Hosokawa Micron Corporation

Editorial Board

Y. Tsuji	Editor-in-Chief (Professor Emeritus of Osaka Univ., JAPAN)

Asia / Oceania Editorial Board

H. Emi	(Professor Emeritus of Kanazawa Univ., JAPAN)
Y. Fukumori	(Kobe Gakuin Univ., JAPAN)
J. Hidaka	(Doshisha Univ., JAPAN)
K. Higashitani	(Kyoto Univ., JAPAN)
Y. Kang	(Chungnam National Univ., KOREA)
Y. Kousaka	(Professor Emeritus of Osaka Prefecture Univ., JAPAN)
J. Li	(Chinese Academy of Science)
H. Masuda	(Professor Emeritus of Kyoto Univ., JAPAN)
M. Naito	(Osaka Univ., JAPAN)
K. Nogi	(Osaka Univ., JAPAN)
Pradip	(Tata Research Development and Design Centre)
M. Rhodes	(Monash Univ., AUSTRALIA)
M. Takahashi	(Nagoya Institute of Technology, JAPAN)
W. Tanthapanichakoon	(National Science and Technology Development Agency, THAILAND)
T. Yokoyama	(Hosokawa Powder Technology Research Institute, JAPAN)
Secretariat	
T. Kawamura	(Hosokawa Powder Technology Foundation, JAPAN)

Europe / Africa Editorial Board

M. Ghadiri	Chairman (Univ. of Leeds, UNITED KINGDOM)
B. Biscans	(Univ. de Toulouse, FRANCE)
N.Z. Lyakhov	(Institute of Solid State Chemistry, RUSSIA)
J. Marijnissen	(Univ. of Delft, NETHERLANDS)
W. Peukert	(Univ. Erlangen, GERMANY)
S.E. Pratsinis	(ETH Züich, SWITZERLAND)
Secretariat	
P. Krubeck	(Hosokawa Micron GmbH, GERMANY)
J. Stein	(Hosokawa Alpine AG)

American Editorial Board

B.M. Moudgil	Chairman (Univ. of Florida., U.S.A.)
D.W. Fuerstenau	Vice Chairman (Univ. of California, U.S.A.)
F. Concha	(Univ. of Concepció, CHILE)
R. Flagan	(California Institute of Technology, U.S.A.)
A.I. Hickey	(Univ. of North Carolina, U.S.A.)
R. Hogg	(Pennsylvania State Univ., U.S.A.)
V. Marble	(Univ. of Minnesota, USA)
S.B. Savage	(McGill Univ., CANADA)
Secretariat	
C.C. Huang	(Hosokawa Micron Powder Systems, U.S.A.)

■Publication Office
Hosokawa Powder Technology Foundation (Japan) in Hosokawa Micron Corporation
No. 9, 1-chome, Shoudai Tajika, Hirakata-shi, Osaka 573-1132, Japan
e-mail : info@kona.or.jp

KONA Powder and Particie Journal No. 26 (2008)

CONTENTS

<Review Papers>

< Original Research Papers >

＜Translated Research Papers＞

＜Tutorial＞

＜Information Articles＞

＜Academic publication concerning powder technology in Japan(2008)＞

The Letter from the Editor

Yutaka Tsuji
Editor-in-Chief

I am pleased to announce a good news of KONA. At long last, KONA has been accepted as a journal registered in the web-of-science. It might be a little surprising that KONA had not been registered and thus did not have "impact factor" though it has been regularly published and distributed in the world more than a quarter century. The reason of the delay is that we did not take any action for a long time for such a database. In a sense we were satisfied with good reputation of KONA among a number of readers in the world related to powder technology. However the word "impact factor" is very influential regardless our likes or dislikes. We know that there are many good journals without the impact factor, especially in the countries where English is not common. However, journals without the impact factor are sometimes regarded as being not international. Since a few years ago, strong voices saying "the impact factor is mandatory" arose from editorial members of KONA. Therefore, three years ago we applied for registration in the web-of-science. The Thomson-Reuter company has been investigating the quality of a journal based on three samples submitted after the action of application. KONA is an annual journal and so it has taken three years to be put on the table of decision.

The hurdle for acceptance in web-of-science is getting higher and higher. I hear that the ratio of acceptance is about 10% nowadays. This means that only one out of ten journals is accepted. This situation is quite hard in general, but I had confidence kept in my mind because KONA satisfies all the necessary conditions to be accepted; quality of papers, regular publication and international diversity.

KONA has some unique aspects as an international journal. First, its editorial system should be pointed out. We have three regional editorial boards in the world. The one is Asia and Oceania board, the second is the American board and the third is the European and African. All members are well known as experts in the field of powder and particle technology. Our editing policy is to take a good balance in these three regions. Each board reviews the articles submitted independently. About one third of articles come from each region. In this sense, international diversity of articles is automatically satisfied.

Second, I would like to point out another uniqueness. KONA is issued by a public foundation. The name of the foundation is Hosokawa Powder Technology Foundation. This foundation is a public service corporation approved by the Japanese government. The word "Hosokawa" is the name of the president of Hosokawa Micron Co. The foundation was established by his donation. The foundation conducts various activities besides issuing KONA, for example, providing research grants, organizing a conference and a symposium. All the costs of KONA are covered by the income of the foundation. Though the foundation has the name of Hosokawa, the foundation is completely independent of the company. Management of the foundation is not influenced by the company business at all. In this sense, basic structure of the foundation is strong. We do not care at all about the number of subscription. We need not consider profit because the foundation should not make profit under the law of Japanese government,.

Next, I will write about timeliness of printing. If you see KONA, you will find contents of three Japanese journals in the last part of KONA. The purpose of listing these contents is to provide information of articles written in Japanese to our readers outside Japan. Originally the contents are in Japanese and these contents shown in KONA are translated ones. The date of issue of KONA is December 25th. It is not easy to include the contents of the whole year of other journals in December. KONA is published in the printed version and the electric version. We keep this date of issue, December 25th, for the electric version. The printed version is distributed in the first week of January. The reason of this small delay is that even if KONA is printed on December 25th, it is very difficult to dispatch it to our readers by post because most offices are closed from the end of December to the beginning of January.

We have found a problem of KONA in the process of application. The problem is its name. KONA means "powder" in Japanese, but this is understood only by Japanese. If you search the word "KONA" in the web site, you will reach the KONA coast in Hawaii. Taking the opportunity of web-of-science acceptance, it is declared that the official name of the journal is "KONA Powder and Particle Journal." When you cite papers in our journal, do not use only "KONA" nor "KONA Journal" , but precisely write "KONA Powder and Particle Journal."

Y. Tsuji

Comment of the Cover Photograph
Smart particles as a foam stabilizer

Syuji Fujii, Anthony J. Ryan and Steven P. Armes
Department of Applied Chemistry,
Osaka Institute of Technology

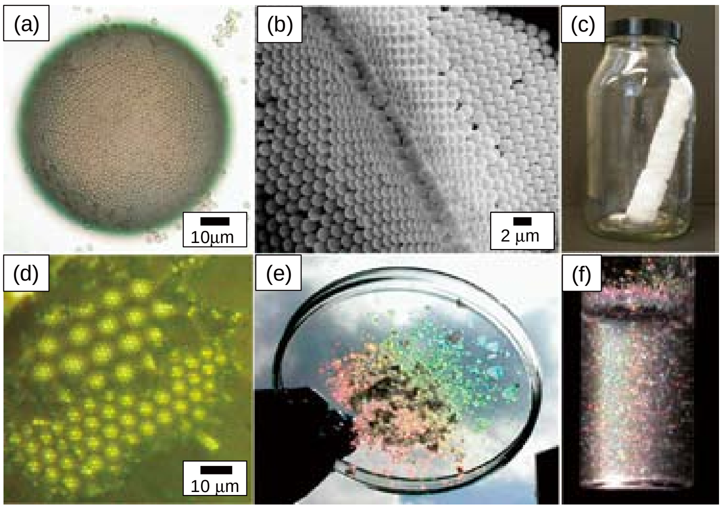

Foams of various types are widely used in many products and formulations, in various industrial processes, and also for the synthesis of advanced materials of controlled porosity. Long-term foam stability is desirable in many cases, however achieving this is rather difficult in fluid systems. Foams are typically stabilized with small molecule surfactants or surface-active polymers or globular proteins; there are relatively few reports of foams stabilized solely by solid particles.

Although solid particles were first used by Ramsden and Pickering to stabilize emulsions and foams approximately one hundred years ago[1], there is considerable renewed interest in this area.[2] There are a number of studies of foams that are stabilized by a combination of solid particles with surfactants and/or surface-active polymers, but relatively few reports of foams stabilized solely by solid particles. Foam stabilized solely by solid particles should be of particular interest for applications where the use of surfactants should be avoided or minimized, such as cosmetic formulations and food manufacturing and perhaps also for the synthesis of new materials.

We have serendipitously found that near-monodisperse, sterically-stabilized latex particles can be used to prepare highly stable foams in the absence of any surfactants or surface-active polymers.[3] Figure 1a and 1b show optical and scanning electron micrographs of the latex foam prepared using near-monodisperse micrometer-sized sterically stabilized polystyrene latex particles. The particulate foam was stable even after drying (Figure 1c). Moreover, using the latexes leads to particulate foams with interesting optical effects such as moiré pattern (Figure 1d) and structural color (Figure 1e and 1f) due to the exquisite long-range structural order of the latex particles within the bilayers formed after drainage of the aqueous phase. [Copyright, American Chemical Society.]

1. (a) Ramsden, W. *Proc. Roy. Soc.,* **1903,** 72, 156.; (b) Pickering, S. U. *J. Chem. Soc.,* **1907***,* 91, 2001.
2. B. P. Binks, T. S. Horozov Edn., “Colloidal particles at liquid interfaces”, Cambridge University Press, **2006**
3. (a) S. Fujii, A. J. Ryan, S. P. Armes *J. Am. Chem. Soc.* **2006**, 128, 7882.; (b) S. Fujii, P. D. Iddon, A. J. Ryan, S. P. Armes *Langmuir,* **2006**, 22, 7512.

Synthesis of Ultradispersed Powders from Products of Polytetrafluoroethylene Pyrolisis[†]

V.M. Bouznik
Institute of Metallurgy and Material Science RAS[1]
L.N. Ignatieva[*]**, V.G. Kuryavyi, A.K. Tsvetnikov**
Institute of Chemistry FEDRAS[2]

Abstract

The method of obtaining ultradispersed powders from the gas phase of PTFE pyrolysis products is presented in this review. The fact that nanoaerosols form in the gas medium was stated. The monoparticles with various structures are formed from nanoaerosols. The monoparticles in their turn organize composite formations. The ultradispersed powder consists of two PTFE fractions (low- and high-molecular). The differences of fraction structures are revealed by various physical methods. The industrial-scale production of the obtained powder was demonstrated.

Keywords: polytetrafluoroethylene powder, nanomaterials, structure, properties

Introduction

Powdered materials occupy several specific segments of international production and markets, while in some cases they form the whole sector, in particular, powder metallurgy. In the case of polymers, powders are used to produce bulk half-finished and finished goods whose quality is to a great extent determined not only by chemical composition but also by the size and shape of powder particles. In view of this, the tendency to produce specific types of powders, initially of minimum particle size, is quite understandable. One of the directions of using powdered polymer materials is concerned with their application as components during the development of composite materials. In this case, their properties will depend significantly on the powder material used. All the above can also be applied to fluoropolymers.

Modern industrial technologies provide polytetrafluoroethylene (PTFE) in a powder form which is then sold as a commodity or used to produce granules of bulk Fluoroplast half-finished goods for subsequent processing into finished ones. Most of the respective industrial technologies apply the reaction of polymerization of the gaseous monomer of tetrafluoroethylene (TFE) in aqueous medium under specific technological conditions with adding initiators 1). The powders thus obtained have particle sizes of 50-500 micrometers. Although when further processed in a jet-type mill, it is possible to attain particle sizes of 10-50 micrometers 1), the practical needs sometimes require even finer particles.

The technology of synthesis in a gas phase has been widely used in the production of inorganic powders, in particular, metallic ones 2). For PTFE, this technology was not applied for a number of reasons. First, it was thought by some that the polymer heating results in chemical decomposition with the emission of a gaseous monomer C_2F_4 (more than 90%) that does not have the tendency for simple polymerization 1, 3). Second, since polymers can be characterized as "weak" objects tending to significantly change their properties under slight external impact, it appears complicated to find an optimal technological regime for the synthesis. Third, polymers are also characterized by complex mechanisms of thermal decomposition of initial polymer and formation of aerosols and particles in a gas phase. As a result, the processes of product formation from the gas phase and their structure are difficult for understanding and theoretical interpretation.

It was shown by a number of authors' studies that the process of PTFE production from pyrolysis

---

[†] Accepted:

[1] Leninskiy prospect, 49, Moscow 119361, Russia
[2] Prosp. 100-letia Vladivostoka, 159, Vladivostok, 690022, Russia
[*] Corresponding author
ignatieva@ich.dvo.ru

products is principally possible and, moreover, is economically and technologically sound to be applied on an industrial scale [4-8]. The achievements made include: patents on the method of powder production, the product itself, respective equipment for its production [4-6], and FORUM product trademark [7]. A pilot-plant-scale production of ultradispersed powder has been established at the facilities of an academic institute. One of the main advantages of the method consists in the possibility of using PTFE waste as raw materials. Since there is no efficient technology of secondary processing of PTFE products at present, besides an economic problem, an ecological problem arises – the necessity of processing waste accumulated at industrial facilities.

The present work discusses the processes of producing PTFE powder from the gas phase of the products of pyrolysis of bulk polymers.

1. The Nature of Formation of Nanoaerosols in Gaseous Products of PTFE Pyrolysis

As was mentioned earlier, it had been an established opinion that upon heating, PTFE decomposes with a predominant emission of the monomer tetrafluoroethylene (TFE) that does not tend to polymerize in a gas phase without initiators or radiation effect. However, under specific conditions a mist forms in the gaseous products of PTFE pyrolysis while a white powder emerges on the reactor walls. The mist observation reflects the light dispersion on the formed particles that is possible only in the case when the particles have sizes comparable to a quarter of the visible light range wavelength. Aerosols form as a result of the interaction of molecular radicals – the products of PTFE pyrolysis and monomer molecules. The conditions of the emerging radicals are related to the pyrolysis temperature conditions while the possibility of their interaction in a gaseous medium is determined by pressure and the reactor design.

Different aspects of PTFE thermal decomposition were studied in a number of works, for example, in [3, 9, 10]. The polymer is stable up to the temperature 300℃, however, at higher values it softens due to melting. At higher temperatures and prolonged exposure one can observe a marked destruction, in particular at a temperature of around 800℃, decomposition results in 97% output of monomer – C_2F_4 [9]. Mass-spectrometry studies [8] have shown that in the temperature range 357-410℃, the main products in the Fluoroplast gas phase include C_2F_4, C_3F_6 and C_3F_5 with the ratio of evaporated components during the whole experiment 1:0.04:0.02, respectively. The pyrolysis product composition and the components ratio depend on the temperature conditions, but it is evident that multiple components in the gas phase are characteristic for any temperature conditions. The product's diversity in the gas phase is expressed also in IR-spectra presented in **Fig. 1**.

The study of aerosol formation in PTFE pyrolysis products was conducted in [11]. Measurements of the aerosol disperse composition were performed with the nanoaerosol diffusion spectrometer[12]. The dependence of the average particle size on technological conditions was established – these conditions include the time and temperature of initial product pyrolysis and the difference between the pyrolysis and nucle-

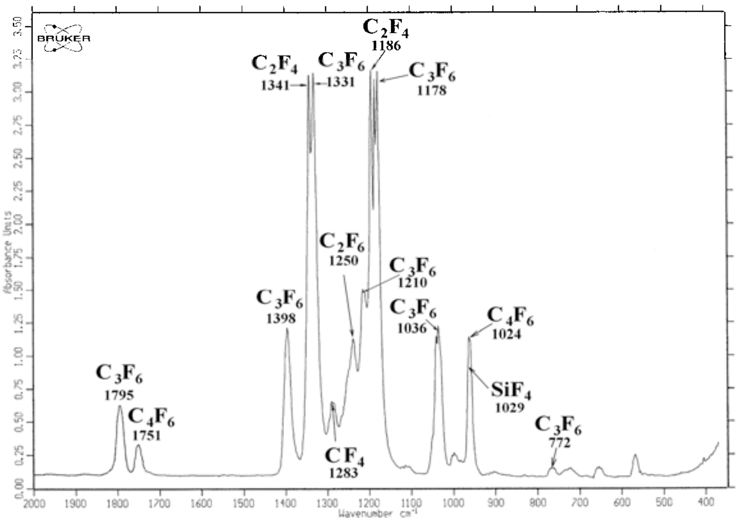

Fig. 1. IR-spectrum of PTFE thermal destruction products.

ation temperatures (**Fig. 2**). Increase of the pyrolysis time results not only in the average aerosol particle size growth, but also in the radial distribution dispersion that is clearly seen from the figure. Since the the particles sizes of the observed aerosols are tens of nanometers, they can be called nanoaerosols.

The dependence of the aerosol particle sizes on the initial PTFE pyrolysis time has been stated in [11]. The 15-fold change of the particle median diameter was observed when varying the decomposition temperature in the range 400-580℃ while the nucleation temperature was constant (60℃).

The overall nucleation rate in all channels available in PTFE thermal decomposition products has the tendency to grow with increasing decomposition temperature at constant nucleation temperature. This appears to be natural, since with increasing decomposition temperature, one can observe a growth of the component's partial contents at invariable nucleation temperature which results in an increase of the nuclei formation intensity.

One can assume the following picture of nanoaerosol formation in the gas phase of PTFE pyrolysis products: The fluorocarbon medium of pyrolysis products contains a set of molecular radicals and molecules, and a variety of them stipulates the possibility of multi-channel nucleation process. Nucleation formations emerge due to density fluctuations of gaseous radicals, and this is accompanied by a polymerization process. Under these temperatures, destruction of the monomer (C_2F_4) molecules is possible which results in the formation of polymerization-active elements, and this in turn leads to the emergence of an additional nucleation channel. Since the monomer share is high, this channel can be efficient and can improve the formation of nanoaerosols. In the fluorocarbon molecules medium nanoaerosols would increase their particle sizes due to condensation of gas-medium molecular formations on them. The condensation process is just as possible on nanoaerosol surfaces as on reactor walls.

It is evident from the presented results that variation of the technical parameters (temperature, pyrolysis time, initial product particle shape and size, gaseous fluorocarbon product pressure, etc.) can contribute to controlling the nanoaerosol particle sizes and, therefore, the ultradispersed PTFE particle structure.

2. Morphological Structure and Self-organization of Ultradispersed Powders

The particle shapes of the obtained powder were studied by the electronic microscopy method (**Fig. 3**). The particle surface metallization distorted the particle true shape to a spherical one. Besides particles that we should call monoparticles, one can observe aggregates built from monoparticles and larger agglomerates formed from aggregates and molecules. The respective terminology was taken from [2].

The presence of the above-mentioned formations was confirmed by particle size measurements (**Fig. 3**) with the Sympatec HELOS – H1084, whose measurement principle is based on the analysis of powder particles subjected to laser irradiation scattering [15].

A dry powder was introduced into the measurement chamber by the air flow at a controlled rate that enabled one to study the effect of air flow on the powder particles' aggregation. One could observe several peaks of the size distribution function (**Fig. 3**) corresponding to monoparticles, aggregate and agglomerate formations. Monoparticles have diameters

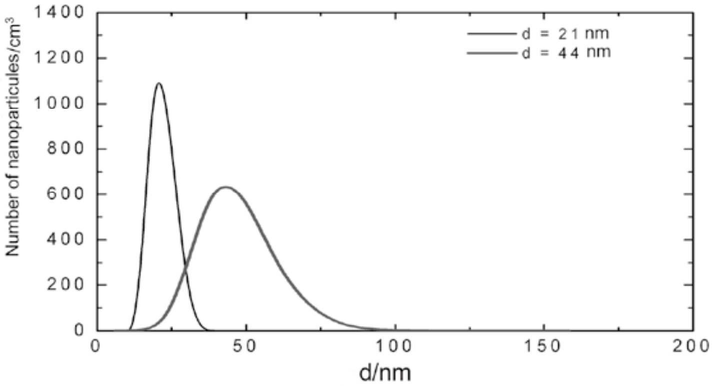

Fig. 2. The radial distribution of nanoaerosol particles as a function of the technological conditions and pyrolysis time. Distribution with the average diameter value 21 corresponds to the thermolysis time of 70 minutes; distribution with the value of 44 nm to the time of 365 minutes. The thermolysis temperature was 496℃, the nucleation temperature 60℃ [11].

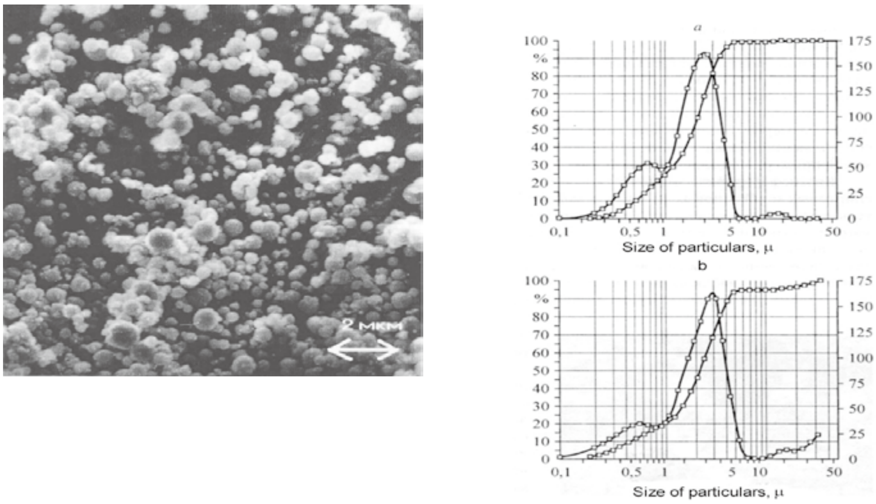

Fig. 3. Micrograph of UPTFE particles (left) and particle size distribution as a function of the air jet pressure (right), the photograph mark length is 2 micrometers [15].

from 0.1 up to 1.0 micrometers – an accurate upper limit cannot be determined due to aggregate distribution function superimposition. The average statistical value of monoparticle size is 0.55 micrometers. Aggregates have sizes within the range 1-5 micrometers with the maximum function value at 2.5 μ; agglomerates are larger than 10 μ.

The size distribution function depends on the air flow pressure which reflects the destructibility of agglomerates and associates by air flow. In [15], the kinetics of aggregate formation was studied – turbulent air flows resulting in destruction of aggregates and agglomerates were created in a closed space. The particle sizes were determined by scattering the laser irradiation throughout the powder particles. The absence of monoparticle aggregates in the beginning of an experiment was revealed in a single-mode function of monoparticle size distribution. After excluding the turbulence, the emergence of a peak corresponding to the formation of agglomerates was detected, and the radial distribution function became similar to that presented in **Fig. 3**.

Use of atomic force spectroscopy (AFM) enabled us to study the monoparticles' shapes (**Fig. 4**) in

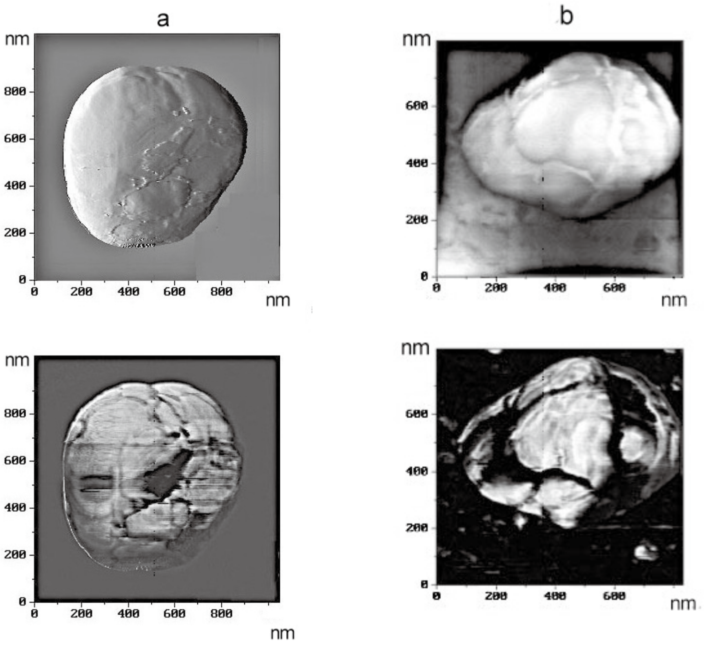

Fig. 4. AFM-image of UPTFE monoparticles. Block-type monoparticles on left; solid monoparticles on right [6]; amplitude image representation at top; phase representation at bottom; picture size: (a) – 1.05 × 1.05 μ, (b) – 0.85 × 0.85 μ.

more detail. As seen from the figure, the particles do not have ideal spherical shapes, and that is very clearly seen for the left-hand particle – it consists of interlocked blocks of sizes from tens to hundreds of nanometers. The phase AFM-images represent areas of different color/shade (dark and light) that corresponds to the presence of fluoropolymers of different structure. As was shown in our studies, monoparticles consisted of high- and low-molecular fractions. The monoparticle-forming blocks are of a high-molecular nature while the binding and coating mass is of a low-molecular one. Besides the block-type monoparticles, one can observe particles of a solid structure (**Fig. 8**, left-hand picture). The presence of monoparticles of two types – block and solid – was also confirmed by the method of transmission electronic microscopy [6]. One should mention that solid particles have the coating (possibly film-like) from a low-molecular polymer, their thickness is around 10 nm.

One can suggest the following scheme of nanoparticle formation: Molecular radicals serve as starting material to form dimers and larger oligomer formations, in other words, the macromolecule formation process is underway.

Macromolecules then form nanoparticles observed in a gaseous medium that transform into monoparticles in two ways: first, nanoparticles grow to the sizes of monoparticles, and second, nanoparticles coalesce to form block-type monoparticles. Coalescence can be accompanied by the formation of molecular (covalent) and supramolecular bonds which provides the block-type monoparticles' stability. The method of monoparticle formation depends on the respective thermodynamic conditions.

One can develop a multi-level hierarchical scheme of the powders' self-organization. The first level includes molecular radicals of angstrom size. The second level describes nanoblocks (nanoaerosols) with sizes of several dozens of nanometers. The third level is related to block-type solid monoparticles (100-700 nm). The fourth level includes monoparticle aggregates with weak bonds and, as a result, low mechanical stability (500-5000 nm). The fifth level is made up of agglomerates of monoparticles and aggregates (10000-30000 nm) with even weaker bonds between elements.

3. Peculiarities of Structure and Properties of Ultradispersed PTFE Powders

The X-ray diffraction studies conducted on PTFE samples of Fluoroplast-4^{TM} and FORUM^{TM} [16] have shown the difference in the polymers' crystalline fraction structures. At room temperature, an ultradispersed sample has the crystal phase disordered along the axis of the hexagonal atomic packing of fluorocarbon chain molecules. One should mention that in industrial PTFE samples, this is observed only above +30℃. The high-temperature phase hardening takes place. Disordering is the result of CF_2 groups rotating around the macromolecule axis.

Spectroscopic studies performed using the IR- and ^{19}F NMR methods [17] have also shown the difference in chemical composition of the ultradispersed macromolecule sample . Additional lines are expressed in the spectra which can be explained by the presence of side trifluoromethyl (CF_3) and end olefin ($CF=CF_2$) groups, along with CF_2-fragments, in fluororcarbon chains. The groups are characteristic for macromolecules of the low-molecular fraction of an ultradispersed fluoropolymer.

The difference in the ultradispersed PTFE structure results in the corresponding difference of properties as compared to fluoropolymer industrial samples, in particular, thermal samples. Derivatograph studies have revealed that the temperature of weight loss for an industrial sample of Fluoroplast-4 starts above 475℃ , while the whole temperature range is within one hundred centigrade [10, 18]. The DTA curve shows an endothermic effect around 315℃ that is attributed to sample melting. The exothermic peaks (525 and 575℃) emerge as a result of oxidation processes [10, 18]. The thermal behavior of the FORUM^{TM} – powder is markedly different: the weight loss temperature starts in the range 60-70℃; the polymer decomposition range is 60-550℃; one can also distinguish the areas of slow (60-290℃) and fast (290-550 ℃) thermal decomposition. Such a behavior is explained by the presence of phases of different thermal stability and different molecular weight.

Mass spectrometry data on the analysis of PTFE gaseous products strongly depend on the pyrolysis conditions. Pyrolysis of a sample of F-4 at temperatures above 400℃ produces just a few main components (C_2F_4, C_3F_6 and C_3F_5), while for FORUM^{TM} –, more than 45 gaseous components were found at a pyrolysis temperature of 144℃ [18]. The main components on concentration include C_3F_5 (peak intensity 100), CF_3 (97.4), while the concentration of the C_2F_4 monomer is not high and corresponds to the intensity of 30. One can also observe small concentrations of relatively large formations (for example, $C_{18}F_{35}$) with mass number 881.

Another difference in the FORUM® temperature behavior, as compared to industrial PTFE samples, is the absence of phase transitions at temperatures 19℃ и 30℃, while at the same time, the heat capacity temperature dependence shows a wide peak at a temperature of 21℃[16]. Phase transitions are concerned with restructuring of the PTFE crystalline component, while the FORUM™ has a crystalline structure at room temperature corresponding to the PTFE high-temperature phase. The low-temperature anomaly is most probably related to restructuring in the amorphous phase of the ultradispersed product.

4. Production of PTFE Low-temperature Fractions

A wide temperature range of the thermal destruction and sublimation of phases with different molecular weights of the product FORUM® makes it technologically possible to separate fractions by a repeated thermal treatment. Indeed, by heating the product at the low-molecular fraction destruction temperature, one can obtain the residue which would contain the high-molecular fraction exclusively. On the other hand, pyrolysis of the FORUM® product is accompanied with the emergence of large amounts of different fluorocarbon fragments capable of forming different structural and morphological forms of polymers.

We have analysed the FORUM® product at temperatures 70, 140 and 300℃, and it was stated that the samples of fluoropolymer groups differed significantly in morphological structure [19]. The first-group samples comprise films of micron-size area and nanosize thickness (**Fig. 10**). In the second-group samples, one can observe multilayer tubes of lengths from 10 up to 300 micrometers and diameters from 2 to 20 μ obtained through flat fragments rolling and other formations. As regards the third-group samples, they are represented by calibrated balls of around 1 μ in size (**Fig. 5**).

The investigations of FORUM® pyrolysis products by the mass-spectrometric method showed the availability of a wide range of molecular and radical components, for example, CF_3, C_2F_4, C_2F_6, C_3F_5 C_4F_9 and others[16]. The ratio of these components depends on the pyrolysis temperature of the initial powder. It is possible that each component forms particles of a powder with various morphological structures. The difference in the particle's morphology must therefore be related to the fact that gaseous products were obtained at different temperatures of FORUM® pyrolysis.

The difference is also revealed by the fact that while the X-ray diffractograms of the powder obtained at high temperatures is identical to that of industrially produced PTFE, quite a different picture characterizes the low-temperature fraction (**Fig. 6**)[20]: crystal peaks are absent at high values of Bragg angles, two clearly expressed diffuse halos and a set of sharp reflections in the small angles area are observed. Such a picture can be attributed to the presence of layered formations.

A significant difference is also characteristic for the sample's thermal parameters (**Fig. 7**). The weight loss of the low-temperature fraction starts at 50℃ and finishes at around 150℃, it proceeds in a single phase, and its rate is different at the initial and final stages, which is reflected by asymmetry of the minimum on the DTG-curve. It is possibly related to increasing decomposition intensity after melting. The DTA-curve shows an anomaly with extremum at 83℃ that is attributed to the polymer melting. The weight loss of the high-temperature fraction occurs in the temperature range 120-300℃, where one can separate two stages with a boundary region in the area above 200℃. The same area is characterized by an anomaly of the DTA-curve that could be connected to the polymer melting.

The difference in temperature behavior can be related with that of the molecular weights of the macromolecules: low-temperature-fraction molecules correspond to lower weight values. The NMR- and IR-spectroscopy studies have confirmed the latter

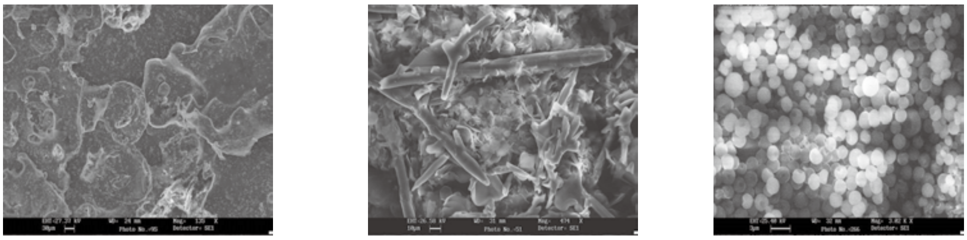

Fig. 5. Micrographs of FORUM™ powder pyrolysis products at different temperatures (from left to right: 70, 150 and 300℃) [19]. Marks correspond to 30, 10, and 3 micrometers, respectively.

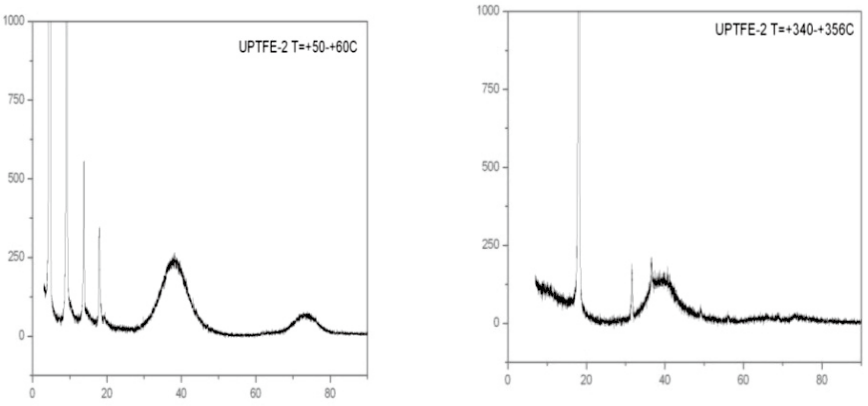

Fig. 6. X-ray diffractograms of powders of low-temperature (70℃) and high-temperature (300℃) fractions [20].

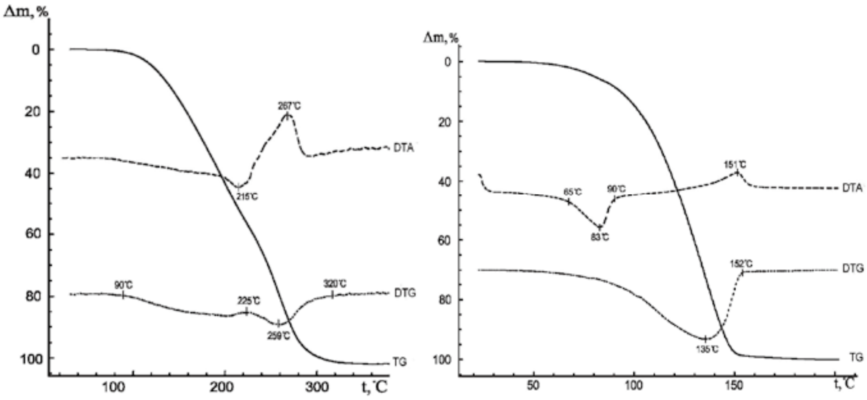

Fig. 7. Data of derivatograph studies of low- and high-temperature fractions [20].

fact – the low-temperature-fraction macromolecules contain end olefin and center trifluoromethyl groups[21]. A marked intensity of respective signals reflects their significant quantity and small sizes of molecular chains. In high-temperature fractions, these signals are absent.

The advantage of the low-molecular fraction is its solubility in supercritical CO_2 that allows using the solution technology to apply thin fluoropolymer coatings of thickness 2-4 nm[22]. Such coatings enable one to make the surface hydrophobic without disrupting its micro- and nano-profile, thus fulfilling the superhydrophobicity conditions and making the surface self-cleaning. We managed to develop surfaces with the water drop wetting angle of 160° [23]. Use of the solution technology in supercritical CO_2 also enabled us to encapsulate hydrocarbon paraffins into the fluoropolymer shell with formation of colloidosomes of a size 300 micrometers and the coating thickness up to 10 micrometers [23-35].

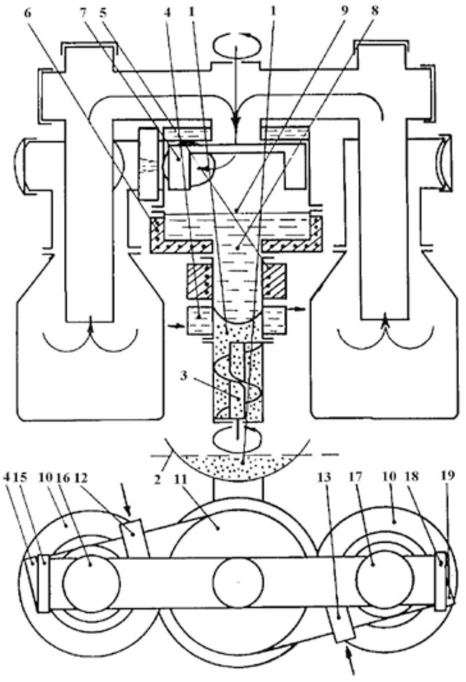

Fig. 8. Schematic of the installation for highly dispersed PTFE FORUM® production.

1 - PTFE chips; 2 - bunker; 3 - worm feeder; 4, 11, 12, 13 – coolers; 5 - preheating zone; 6 - reactor; 7 - centrifugal fan; 8, 9 - gages; 10 - cyclones; 14, 15, 16, 17, 18, 19 - working holes

5. Production and Application of Ultradispersed powders

The technological set-up of the installation is presented in **Fig. 8**. The technological process of producing highly-dispersed PTFE FORUM® proceeds as follows: The bulk PTFE chips (1) are loaded into bunker (2) and fed by a worm feeder (3) to a pre-heating zone (5) and further into a reactor (6). Due to the water cooler (4), the PTFE melt hardens as a moving plug, thus preventing the intake of air into the reactor and the escape of PTFE destruction products into the room. The temperature and melt level are controlled by two gages (8, 9).

The centrifugal fan (7) creates gas-dynamic conditions when a cooled monomer is fed to the PTFE melt surface, prevents further polymer decomposition into low-molecular fragments, facilitates its fast condensation into microparticles and carries the powder thus formed to cyclones (10) which separate the solid product from the gas phase. The monomer is then returned to the reactor. The monomer is continuously cooled by water coolers (12, 13). The excess of monomer and other gaseous pyrolysis products is removed through one of the working holes (4, 15, 16, 17, 18, 19) for further disposal [25].

Fast destruction product cooling and conducting the process at temperatures above 520° enable one to completely exclude the formation of highly toxic perfluoroisobuthylene and to reduce down to minimum values the formation of toxic hexafluoropropylene. The installation design (raw materials fed from below through a liquid gate of PTFE melt) excludes the input of air into reactor and, therefore, eliminates the danger of toxic carbon fluoroxide formation. The safety interlocking systems automatically shut down the installation at critical operation conditions.

The suggested method is not energy-consuming and enables one to use any PTFE waste, including composites, with a high degree of productivity that substantially reduces the product cost. Small particle sizes (0.1-1 micrometers), low molecular weight and the presence of active sites on the surface ensure high PTFE adhesion to metals, glass and other solid materials, thus enabling one to apply thin polymer layers.

The fields of practical application of the highly dispersed PTFE are extensive: protective coatings for metallic parts destined for use in aggressive and sterile media, anti-scale and anti-friction coatings, neutral fillers for cosmetics and medical preparations, dry lubricants and fire-prevention components, additives for oils to reduce the vibroactivity of mechanisms, etc.

In order to extend the fields of application of the sub-micron PTFE FORUM® powder, the bulk PTFE thermal destruction was performed in a reduction atmosphere. In this case, low molecular weight and the presence of hydrogen in the PTFE polymer chain intensify the PTFE molecules' lyophilic behavior and reactivity, which enables one to use the obtained powder as an initial cathode material for lithium chemical batteries (CB).

The application of cathode materials on the basis of modified PTFE in lithium chemical batteries can result in a 35% increase of CB energy capacity as compared to graphite monofluoride and a 4-fold decrease of its cost, since the technology of producing graphite monofluoride is based on using gaseous fluorine and is associated with strict requirements relating to the production safety.

In order to increase the adhesive ability of the PTFE particles to metal and to stabilize PTFE suspensions in the case of the FORUM® powder application in oil mixtures for anti-wear additives to oils and lubricants, the PTFE thermal destruction was performed in the presence of oxygen [6].

Conclusion

The possibility of obtaining nano- and microsize fluoropolymer particles from the gas phase of PTFE pyrolysis products has been stated. The process of nanoaerosol formation and its dependence on the temperature and pyrolysis time was studied and it was established that it is possible to control the fluoropolymer nanoaerosol sizes by changing the technological conditions.

The powder monoparticles' structural features were revealed: two structural forms – solid and block-type – are generated from nanoaerosols. A multistage hierarchical scheme of organization of the powder obtained by using the gas-phase method was suggested. The presence of two types of polymers corresponding to low-molecular and high-molecular fractions was stated. Suggestions on the formation mechanisms of fluoropolymer particles in gas-phase products from PTFE pyrolysis were presented.

The possibility of separating low- and high-molecular fractions of fluoropolymers by secondary thermal processing of the FORUM® was shown, and the structure and properties of fractions obtained at different pyrolysis temperatures were investigated.

The possibility of industrial-scale production of ultradispersed powder was demonstrated, and the fields of its practical application were analysed. The powder production not only resolves commercial tasks but also provides solutions for the ecological processing of PTFE waste into commercial products.

Acknowledgements

The authors are thankful to colleagues who participated in studies on the subject discussed here: O.M. Gorbenko (Institute of Chemistry FEDRAS), M.P. Anisimov, I.N. Mikhalin (Institute of Catalysis SD RAS), P.P. Semyannikov (Institute of Inorganic Chemistry SD RAS), L.N. Nikitin, A.R. Khokhlova (A.N. Nesmeyanov's Institute of Elementoorganic Compounds RAS), M.O. Gallyamov (Moscow State University). This work is supported by *RFBR Grant* № 06-03-32185a *and Grant FEBRAS, I issue*, № 06-I-П8-008.

References

1) Panshin, Yu. A., Malkevich, S. G.; Dunayevskaya, Ts.S. (1978): "Fluoroplasty", Khimia, Leningrad, in Russia.
2) Gutsch, A., Kramer, M., Michael, G., Muhlenweg, H., Pridohl, M. and Zimmermann, G. (2002): Gas-phase production of nanoparticles, KONA Powder and Particle Journal, 20, P.24.
3) Madorsky, S. (1967): Thermal decomposition of organic polymers,. M. Mir, P. 328. In Russia.
4) Tsvetnikov, A.K. and Uminsky, A.A.: RU Patent 1775419.
5) Tsvetnikov, A. K.: RU Patent 20353085.
6) Tsvetnikov, A. K., Bouznik, V. M. and Matveenko,. L.A.: RU Patent 2100376.
7) Trademark FORUM № 140123.
8) Bouznik, V. M., Fomin, V. M., Alkhimov, A.P. and Ignatieva, L. N., et el. (2005): "Metal-polymer nanocomposites",. Novosibirsk: SO RAN, 260. p. in Russia.
9) Currie, J.A. and Pathmanand, N. (1974): Anal. Calorim. 3, 629.
10) Vnutskih, Zh.A., Fyodorov, A. A., Chekryshkin, Yu.S., Ismagilov, Z.P. and Kerzhentsev, M. A. (2001): J. Chem. for Sustainable Development, 9, 621, in Russia.
11) Anisimov, M.P., Baklanov, A.M., Onishchuk, A.A., Semyannikov, P.P. and Bouznik, V.M. (2005): Generation of aerosols from polytetrafluoroethylene thermal decomposition products, Bull. Russ. Acad. Sci., 405, 6, 768.
12) Mavliev, R. A., Ankilov, A.N., Baklanov, A.M., Gorbunov, B. Z., Kakutkina, N. A., Kutsenogy, K.P., Pashchenko, S. E. and Makarov, V.I. (1984): Colloid J., 46, 6, 1136, in Russia.
13) Bouznik, V. M., Tsvetnikov, A. K., Shikunov, B.Yu. and Polkin, V.V. (2002): Size and shape of particles of ultradispersed polytetrafluoroethylene produced by the thermal gas dynamic method, J. Prospective Materials, 2, 89, in Russia.
14) Bouznik, V. M., Kirik, S.D., Solovyov, L. A. and Tsvetnikov, A. K. (2004): A crystal structure of ultra – dispersed form of polytetrafluoroethylene based on X-ray powder diffraction data, Powder Diffraction, 19 (2), 135.
15) Ignatieva, L. N., Tsvetnikov, A.K., Livshitz, A. N., Saldin, V.I. and Bouznik, V. M. (2002): J. Struct. Chem., 43, 1, 69, in Russia.
16) Bouznik, V.M., Mikhalin, I.N., Semyannikov, P. P., et al. (2004): Peculiarities of thermal destruction and calorimetry of ultradispersed polytetrafluoroethylene. J. Chem. for Sustainable Development, 12, 605, in Russia.
17) Kuryavyi, V. G., Tsvetnikov, A.K. and Bouznik, V. M. (2002): Morphological structure of ultradispersed polytetrafluoroethylene pyrolysis products, J. Prospective Materials, 6, 71, in Russia.
18) Bouznik, V. M., Gorbenko, O.M., Ignatieva, L. N., Tsvetnikov, A.K. and Mashtalyar, D. V. (2007): Thermal properties of sublimation products of ultardispersed polytetrafluoroethylene, J. Prospective Materials, 6, 56, Russia.
19) Ignatieva, L. N., Tsvetnikov, A. K., Gorbenko, O.M., Kaidalova, T. A. and Bouznik, V. M. (2004): J. Struct. Chem., 45, 830, in Russia.
20) Gallyamov, M.O., Bouznik, V.M., Tsvetnikov, A.K., Vinokur, R. A., Nikitin, L.N., Said-GAliev, S. E., Lebedeva, O.V., Khokhlov, A. R. and Schaumburg, K. (2003): Bull. Russ. Acad. Sci., 392, 1, 77.
21) Gallyamov, M. O., Nikitin, L. N., Nikolaev, A. Yu., Obraztsov, A. N., Bouznik, V. M. and Khokhlov, A. R. (2007): Formation of Superhydrophobic Surfaces by the Deposition of Coatings from Supercritical Carbon Dioxide, Colloid Journal, 69(4), 411, in Russia.
22) Gallyamov, M.O., Bouznik, V.M., Tsvetnikov, A.K., Vinokur, R.A., Nikitin, L. N., Said-Galiev, S. E., Khokhlov, A.R. and Schaumburg, K. J. (2004): Chem. Phys., 23, 6, 76, in Russia.
23) Gallyamov, M.O., Bouznik, V.M., Tsvetnikov, A.K., Vinokur, R. A., Nikitin, L. N., Said-Galiev, S.E., Lebedeva, O.V., Khokhlov, A.R. and Schaumburg, K. (2004): Polymer Preprints, 45(1), 504.
24) Tsvetnikov, A. K., Uminsky, A. A. and Tsarev, V. A.: RU Patent 1763210.
25) Tsvetnikov, A. K. and Uminsky, A. A.: RU Patent 1808194.

Author's short biography

V.M. Bouznik

Bouznik Vuacheslav Mikhailovich was born in 1945. In 1967, he graduated from the State University in Tomsk. He received his PhD in physics and mathematics in 1972; his doctor of sciences in chemistry in 1985; he became a corresponding member of RAS in 1994 and a full member of RAS in 1997. He worked in scientific organizations of the Siberian branch, was director of the Institute of Chemistry of the Far Eastern Branch of RAS from 1990-1995 in Vladivostok. From 1996, he was chairman of the Presidium of Khabarovsk Scientific Center FEBRAS and head of the fluoride materials laboratory in the Institute of Chemistry FBRAS. He is now a main scientific employee of the A.A. Baikov Institute of Metallurgy and Material Science RAS and Institute of Chemistry, FEBRAS.

He is a specialist in the physical chemistry of crystal, glass and polymer materials and nuclear-spectral methods of research. Scientific interests: structure, physico-chemical properties, creation of new materials, sustainable development, small forms of production in scientific organizations. His research has been reported in more than 300 articles in international and Russian magazines, among them are 5 monographs and 15 inventions.

L.N. Ignatieva

Ignatieva Lidia Nikolaevna was born in 1947 in Ulan-Ude. She graduated from the Far East State University, Vladivostok. She became an employee of the Institute of Chemistry FEBRAS in 1971 and received her PhD in physical chemistry in 1980 at the Institute of Chemisrtry FEBRAS; her doctor of sciences in 2000. She is head of the Fluoride Materials Laboratory of Institute of Chemistry, FEBRAS. Her main research interests include structure materials, inorganic compounds, fluoride and oxyfluoride glass, fluorocarbon materials, among them nanomaterials. Her research has been reported in more then 100 articles in international and Russian scientific journals and book chapters, and has been presented at scientific conferences.

V.G. Kuryavyi

Valery Georgievich Kuryavyi was born in 1952 in Kavalerovo. In 1974 he graduated from the Far East State University, Vladivostok. He became an employee of the Institute of Chemistry FEBRAS in 1976. He received his PhD in physical chemistry in 2000 at the Institute of Chemistry FEBRAS, Vladivostok, Russia. Valery Georgievich Kuryavyi is the author of more than 50 articles in scientific journals and book chapters and 3 inventions. His scientific interest: microscopic measurements.

A.K. Tsvetnikov

Alexander K. Tsvetnikov was born in 1950 in Khabarovsk, USSR. He has been an employee of the Institute of Chemistry FEBRAS since 1974, and graduated from the Far East State University in Vladivostok as a chemist in 1976 and received his PhD at the Institute of Chemistry FEBRAS, Vladivostok, Russia, on: "Synthesis, structure and application layered and linear fluorinecarbon substances" in 1998. He is head of Fluorine of Carbon Materials Group at the Institute of Chemistry, FEBRAS. Alexander K. Tsvetnikov is the author of more than 40 articles in scientific journals and book chapters and 30 inventions. He also is the author of technological articles and the head of the pilot production of nanofluoropolymers FORUM® .

Generation and Sizing of Particles for Aerosol-Based Nanotechnology[†]

George Biskos [1,2*],
Faculty of Applied Sciences, Delft University of Technology[1]
Department of Environmental Studies, University of the Aegean[2]

Vincent Vons, Caner U. Yurteri and Andreas Schmidt-Ott
Faculty of Applied Sciences, Delft University of Technology[1]

Abstract

Traditionally, the generation of nanoparticles for technological applications has been mostly performed by classical wet chemistry or lithographic methods, and their size has been commonly determined in situ by electron microscopy techniques. Advances in aerosol technology over the past 30 years have provided methods that enable the generation and measurement of nanosize building blocks, and have opened up new opportunities in the assembly of nanostructured materials and nanodevices. This article provides a brief review on state-of-the-art techniques for generating nanoparticles of well-defined size and chemical composition in view of applications in nanotechnology. Covering atomization techniques from the liquid phase and nanoparticle synthesis from the gas phase, we discuss the advantages and limitations of each method. Considering the advantages of on-line methods that aerosols instruments offer, we describe the most efficient techniques for measuring the size distributions of airborne nanosize particles. Finally, we provide a brief discussion on existing and emerging applications of aerosol-based nanotechnology.

Keywords: gas plase, nanoparticle synthesis, nanostructure, nanomaterials

1. Introduction

Developing methods to manipulate matter and to assemble structures on the nanometer scale is of great interest in many technological applications. Nanostructured materials exhibit novel and enhanced properties compared to their bulk counterparts. Having characteristic scales below 100 nm, the behavior of these materials is primarily determined by the physical and chemical properties of their building blocks, i.e. the nanoparticles, which in turn depend on their chemical composition and size. By controlling the size and composition of these building-block nanoparticles, one can tailor nanostructured materials for specific applications in a relatively simple manner.

Traditionally, the term nanoparticle is used for solid or liquid particles of sizes below 100 nm (cf. Hinds 1999; Baron and Willeke 2001). For particles containing 2 and up to approx. 10^3 atoms or molecules, the term cluster is often used. In most of the synthesis methods discussed in this paper, the sizes of the particles range from a few nm up to 50 nm.

Nanoparticles can be synthesized in the liquid or the gas phase. Liquid routes such as incipient wetness impregnation, coprecipitation and grafting, and sol-gel, are batch processes that often involve large amounts of solvents. A great drawback of these methods is the introduction of impurities. These are always more abundant in liquids than in gases, and even the most advanced methods apply surfactants that contaminate the particles produced. Nanoparticle formation in the gas phase (i.e. aerosol formation) on the other hand, offers high purity and the ability to synthesize nanostructures in a continuous process (Pratsinis and Mastrangelo 1989; Mädler et al. 2002). In addition, aerosol techniques reduce waste formation thereby making them more attractive for large-

---

[†] Accepted: August 23, 2008

[1] Delft 2628-BL, The Netherlands
[2] Mytilene 81100, Greece
[*] Correspondence author
E-mail: g.biskos@tudelft.nl, biskos@aegean.gr

scale manufacturing.

Aerosol-based nanotechnology includes the mechanisms for generating nanoparticles, the techniques for measuring their physical and chemical properties, as well as the processes used for their deposition to form films or specific structures. Aerosol nanoparticles can be generated by a range of methods depending on the desired composition and size. Advances in the field of aerosol instrumentation over the past decades have allowed for high accuracy and precision measurements of the physical and chemical properties of suspended nanoparticles. In addition, the simplicity of the methods for manipulating and depositing gas-suspended nanoparticles to form specific structures makes aerosol science and technology one of the enabling disciplines in the broader field of nanotechnology.

As a result of the growing advances in aerosol technology, nanostructured materials with unique properties are already being fabricated via synthesis in the gas phase. For example, aerosol-based methods are being used in the fabrication of opto- and nano-electronic devices. In addition, nanoparticles synthesized in the gas phase have been shown to have enhanced catalytic (e.g., Stark et al. 2002) and gas sensing properties (e.g., Kennedy et al. 2000). Finally, aerosol techniques are believed to have great potential for medical applications (e.g., Tartaj et al. 2003).

Early reviews on aerosol nanoparticle synthesis have been given by Gurav et al. (1993) and by Kruis et al. (1998), whereas Heidenreich et al. (2003) provided a broader overview on the technical aspects of aerosol science and technology. Other reviews have focused on specific particle generation methods and their applications. For example, Grace and Marijnissen (1994) and recently Jaworek (2008) have provided overviews of particle generation from electrospray atomization. Gutsch et al. (2002) and Swihart (2003) have described the available methods for synthesizing particles from the gas phase, whereas Strobel et al. (2006) and Strobel and Pratsinis (2007) have reviewed particle synthesis techniques using flame reactors for specific applications. A comprehensive description on the available aerosol instruments with emphasis on the measurements of atmospheric particles is given by McMurry (2000). In this paper, we review various methods for generating and sizing aerosol nanoparticles, and highlight some technological applications where aerosol techniques are employed.

2. Aerosol Nanoparticle Generation

Nanoparticle generation via the aerosol route provides a powerful way of manufacturing nanostructured materials of well-defined morphology and chemical composition. Aerosol nanoparticles can be produced by either atomizing a solution of specific composition to form droplets that crystallize to solid particles upon subsequent evaporation of the solvent, or from gas-to-particle conversion via nucleation and growth by condensation and coagulation.

Atomization of solutions can be achieved by mechanical methods (i.e. nebulization) or by applying an electrostatic potential between the solution and a counter electrode (i.e. electrohydrodynamic atomization). Gas-to-particle synthesis can be achieved by using furnace, flame, plasma, or laser reactors, glowing wires and spark discharges. In the following paragraphs, we provide a brief overview of the techniques for generating aerosol nanosized particles as well as those that in our opinion have the largest potential for applications in nanotechnology.

2.1 Atomization of liquid solutions

One way of generating aerosol particles is by atomizing liquid solutions of a specified chemical composition. Atomizers can be categorized depending on the forces applied to break up the liquid into small airborne droplets (Hinds 1999). For aerosol-based applications in nanotechnology, the most appropriate methods are pneumatic, ultrasonic, and electrospray atomization because they produce relatively small primary droplets (1-10 μm in diameter). Other methods, e.g. spinning-disk atomizers, produce much larger primary droplets (> 100 μm) and in much lower concentrations, making them inappropriate for use in aerosol-based applications in nanotechnology.

Upon evaporation of the solvent of the atomized droplet, the solute crystallizes to form solid particles. Depending on the solute concentration of the primary droplets, solid nanoparticles of different diameters can be generated. Nanosize solid particles of well-defined composition can be generated by the atomization of solutions of less than 0.1 wt% and subsequent evaporation of the solvent. Fracturing and chemical treatment of the particles can be applied by pyrolysis of the atomized droplets. This technique is in many cases much more favorable because it leads to higher particle number concentrations. Compared to synthesis methods from the gas phase, one limitation of all atomization techniques is the presence of impurities in the solvent. Unless these impurities are volatile, they remain on the crystallized solid particles thereby affecting their physical and chemical properties in an uncontrollable manner. The relatively low particle concentration of the generated aerosols restricts these methods for applications that require only small amounts of particles.

2.1.1 Pneumatic atomization (nebulization)

In pneumatic atomizers, pressurized air is introduced via an orifice in such a way that the expanding air stream moves perpendicularly to the end of a tube connected to the liquid reservoir. Due to the Bernoulli effect, the low pressure created at the tube end draws the liquid from the reservoir into the air stream. The high forces occurring at the air-liquid interface cause the solution to break up into small liquid droplets which become airborne and are carried away by the air flow. The spray stream is then directed onto an impactor plate where the larger droplets are deposited and are either directed back to the liquid reservoir or break up into smaller droplets and exit the atomizer in the outlet stream.

Depending on the geometric characteristics and the operating conditions, pneumatic atomizers produce primary droplets in the size range of 1-10 μm and concentrations from 5 to 50 gm^{-3}. The particles generated by pneumatic atomization are polydisperse (σ_g of 1.4 or greater) with a moderate charging level that depends on particle diameter and solute concentration (Forsyth et al. 1998; Tsai et al. 2006). If their size has to be controlled within a narrower range, a classifier (commonly a differential mobility analyzer, cf. § 3.1) has to be employed downstream of the particle generator.

Many designs of pneumatic aerosol atomizers are described in the literature and are commercially available (e.g. May 1973; Liu and Lee 1975). Most of them have been developed for producing particles for inhalation therapy or for calibrating aerosol instruments. Despite this, pneumatic atomization has been successfully used for synthesizing aerosol nanoparticles from colloid solutions for technological application (e.g. Hampsey et al. 2005).

2.1.2 Ultrasonic atomization

Another way of breaking up a solution to micronsized droplets is by ultrasonically vibrating its air-liquid interface (Wood and Loomis 1927). The mechanical energy applied from a piezoelectric crystal to the system agitates the surface of the solution, thereby creating capillary waves that break up into micronsized droplets (Faraday 1831; Kelvin 1871; Rayleigh 1883; Lang 1962). A particle-free air stream is passed over the solution to take away the generated airborne particles. The diameter of the primary droplets produced is a function of the frequency of vibration and the physical properties of the solution, i.e. surface tension and density.

Two mechanisms are responsible for the formation of droplets from ultrasonic atomization: the formation of capillary waves and the break-up of cavitation bubbles. Boguslavskii and Eknadiosyants (1969) combined both mechanisms theoretically and suggested that drop formation is initiated by capillary waves initiated and driven by cavitation bubbles. Cavitation is obviously accountable for at least a large proportion of the disintegration from thick and viscous films, in particular at high ultrasonic intensities, but atomization cannot be explained by cavitation effects alone. As the power supplied to the atomizer and the throughput of the atomizer is increased, cavitation effects become more predominant. However, the interaction between them and the limits to which one mechanism could predominate over the other are still under debate and require both experimental and theoretical investigation. The most recent reviews of mechanisms related to ultrasonic droplet formation as well as alternative mechanisms for droplet ejection are provided by Barreras et al. (2002) and Yule and Al-Suleimani (2000).

Due to resonance modes and the limitations of the piezoelectric material, ultrasonic atomizers are limited by a maximum frequency of around 3 MHz. Frequencies greater than that are required to generate droplets of less then 2 μm in diameter. Although frequencies up to the GHz range can be applied using surface acoustic wave devices, the performance of ultrasonic atomizers mainly depends on selection of the driving method and vibration mode (Kurosawa et al. 1995; Ju et al. 2008). As one might expect, the dimensions of transducers for operation at high frequencies are small to limit the possibility of multimode operation. This makes it necessary for throughputs to be particularly low.

A form of ultrasonic nozzle used for generating standard size droplets is the Vibrating Orifice Aerosol Generator (VOAG) (Berglund and Liu 1973). The principle of the VOAG is based on the instability and break-up of a cylindrical liquid jet and dispersion in a proper manner. the size range of droplets can be controlled between 0.25 and 50 μm.

Compared to pneumatic atomizers, ultrasonic atomizers can generate highly monodisperse particles (σ_g of less than 1.02). Although the performance of ultrasonic atomizers remains inherently stable, their greatest drawback is that the particle number concentrations are significantly lower compared to other techniques.

2.1.3 Electrohydrodynamic atomization

Electrohydrodynamic atomization (EHDA), or electrospraying, is a method for producing very fine monodisperse droplets from a liquid under the influence of electrical forces. By controlling the liquid flow rate and the electrostatic potential between the liquid and the counter electrode, droplets within a narrow size range with mean diameters from nanometers up to several micrometers can be generated. Besides generating monodisperse droplets, electrosprays are also distinguished by their self-dispersing nature due to columbic repulsion, the possibility of trajectory control of the produced charged droplets, and the reduced risk of nozzle clogging due to large size of the orifice compared to the size of the droplets.

Different spraying modes can be obtained depending on the strength of the electric stresses relative to the surface tension stress on the liquid surface and on the inertia of the liquid leaving the nozzle (Zeleny 1914; Zeleny 1917; Cloupeau and Prunetfoch 1994; Grace and Marijnissen 1994). For the production of monodisperse nanoparticles, the so called cone-jet mode is desirable. In this mode, the liquid is typically pumped through a nozzle at a flow rate of the order of μl hr^{-1} to ml hr^{-1}, and an electric field is applied between the nozzle and a counter electrode. This electric field induces a surface charge in the growing meniscus created at the nozzle. Due to this surface charge and the electric field, an electric stress is created on the liquid-air interface. Depending on the electric field strength and the liquid flow rate, the electric stress can overcome the surface tension stress and transform the shape of the liquid surface from a dome to a cone, i.e. the Taylor cone (Taylor 1964). The tangential component of the electric field accelerates the charge carriers at the liquid surface toward the cone apex. These ions collide with liquid molecules, thereby accelerating the surrounding liquid. As a result, a thin liquid jet emerges at the cone apex (Zeleny 1914; Zeleny 1917). Depending on the ratio of the normal electric stress to the surface tension stress on the jet surface, the jet either breaks up due to axisymmetric instabilities, also called varicose instabilities, or due to varicose and lateral instabilities, called kink instabilities (Fernandez de la Mora and Loscertales 1994; Rosell-Lompart and Fernandez de la Mora 1994; Tang and Gomez 1995; Hartman et al. 2000). Monodisperse droplets are produced at a low stress ratio in the varicose break-up mode.

The droplets produced by EHDA carry a high electric charge in the range of the Rayleigh charge limit (Hartman et al. 2000). Upon evaporation, the droplets exceed the Rayleigh charge limit, resulting in their shattering into smaller droplets. To avoid Rayleigh disintegration and to control particle size distribution, the droplets have to be completely or partially neutralized (Davis and Bridges 1994; Smith et al. 2002).

Scaling laws can be used to estimate the operational conditions for producing nanodroplets of a certain size. Fernandez de la Mora and Loscertales (1994), and Gañán-Calvo et al. (1997) have provided scaling laws for estimating the size of the droplets produced (or jet diameter) and the electric current required for a given liquid to be sprayed in the cone-jet mode as a function of liquid properties and flow rate. Hartman and co-workers refined the scaling laws for EHDA in the cone-jet mode using theoretically derived models for the cone, jet and droplet size (Hartman et al. 1999; Hartman et al. 2000). Recent studies on EHDA have focused on the quantitative understanding of the transport and evaporation of the droplets as they leave the nozzle (cf. Wilhelm et al. 2003) in order to provide controlled film morphology in applications such as electroceramics (Wilhelm et al. 2005) and bone prosthetics (Leeuwenburgh et al. 2006).

Several authors have already reported on the production of nanoparticles using the EHDA route (Fernandez de la Mora et al. 1990; Rulison and Flagan 1994; Hull et al. 1997; Lenggoro et al. 2000; Ciach et al. 2002; van Erven et al. 2005). A recent review on the subject is provided by Jaworek and Sobczyk (2008). If the right solvent properties are achieved, EHDA can be seen as a generic way to produce well-defined nanoparticles of various compositions on demand (Marijnissen et al. 2008).

Industrial implementation of EHDA, however, is limited by the low production rates. In order to generate fairly small-sized particles, extremely low flow rates are required. For example, flow rates of less than 0.1 ml h^{-1} for a single nozzle are needed to obtain droplets in a micrometer diameter range. It is impossible to increase the throughput of material production from a single nozzle by simply increasing the flow rate. Thus an out-scaling rather than up-scaling is needed for boosting the number of injection ports.

There have been many efforts reported on the out-scaling of EHDA including the use of an array of capillaries, an array of holes in combination with non-wetting material, serrations, grooves, multijet mode operation, and MEMS-based manufacturing as summarized by Deng and Gomez (2007). Increasing the number of capillary nozzles seems to be a simple and effective way of increasing the number of droplets. However, out-scaling mainly suffers from electric field intensity variations and thus droplet size changes from nozzle to nozzle.

2.1.4 Spray pyrolysis

Suspended solution droplets produced by atomization need drying in order to produce solid particles upon crystallization of the solute in most applications. Depending on the temperature used for conditioning the droplets, the processes can be classified as freeze drying, spray drying and spray pyrolysis. Although all three processes are very similar, the lower temperature associated with the freeze and spray drying prohibit any reactions from taking place within the particles (cf. Baron and Willeke 2001). In spray pyrolysis on the other hand, the high temperatures not only rapidly evaporate the solvent and initiate reactions within the solution droplets, but can also cause fragmentation of the particles. As a result, solid particles smaller than 100 nm can be easily produced by spray pyrolysis, making the process very favorable for applications in nanotechnology. Solid particles produced by the low-temperature drying of atomized solution droplets (i.e. freeze and spray drying) are typically larger.

In spray pyrolysis, the atomized particles are heated in a furnace (e.g. Messing et al. 1993), a flame (e.g. Mädler et al. 2002), or a laser beam (e.g. Cauchetier et al. 1994). The high temperatures cause rapid evaporation of the solvent of the droplets and the initiation of inter-particle reactions that lead to the final product. The physical (size, morphology, and density) and chemical properties of the particles generated by spray pyrolysis depend on the composition of the liquid precursors, the atomization method, and the operating conditions of the apparatus. Solid particles are formed with proper choice of the precursor solution and careful control of the temperature history of the particles, but morphology control is still largely an empirical process (Sproson et al. 1986; Lenggoro et al. 2000). Often, hollow or fragmented particles are obtained when the solvent evaporation rate is too high compared to the rate of crystallization.

Particles of a uniform composition and size can be produced via spray pyrolysis. A great advantage compared to particle synthesis from the gas phase (cf. § 2.2) is that multicomponent materials can be easily produced by controlling the stoichiometry of the precursor solution. Particle synthesis techniques from the gas phase introduce a higher difficulty in manufacturing multicomponent particles because of the differences in the pressures and the nucleation/condensation rates of the involved vapors (Gurav et al. 1993). In addition, the capability of producing unagglomerated and high-purity particles makes spray pyrolysis a favorable process for many applications.

Spray pyrolysis at low pressures has been shown to produce particles of a much smaller diameter compared to higher pressure systems (e.g. Kang and Park 1996). In low-pressure spray pyrolysis, the solvent evaporation rate is much higher than the solute crystallization rate. As a result, larger particles are fragmented into smaller pieces that undergo simultaneous solvent evaporation to produce nanoparticles or weakly agglomerated particles, thereby avoiding the formation of hollow particles. In the case of low-pressure spray pyrolysis, particle morphology is highly dependent on the temperature of the heating section, whereas the solubility of the precursor solutions can greatly influence the degree of agglomeration of the particles (Lenggoro et al. 2003).

Apart from reaction furnaces, lasers (e.g. Cauchetier et al. 1994) and flames (e.g. Mädler et al. 2002) have also been used to pyrolyse atomized aerosol droplets. In laser spray pyrolysis systems, the droplets generated by atomization are passed through a laser beam allowing highly localized heating and subsequent rapid cooling. Heating is generally done using lasers whose energy is either absorbed by one of the precursors or by an inert photosensitizer such as sulfur hexafluoride. In flame spray pyrolysis, atomized particles are directed into a flame. Two types of flame spray pyrolysis are identified: in the first case the atomized droplets sustain the flame that is made by evaporating and burning droplets, and in the second case a supporting fuel is supplied separately from the precursor-atomized droplets. Particles with sizes from 1 to 200 nm at production rates that reach up to 250 g h^{-1} have been produced using flame spray pyrolysis (e.g. Laine et al. 1999).

2.2 Particle synthesis from the gas phase

Material evaporation followed by subsequent nucleation and condensation in an inert gas is a widely used approach for generating aerosol particles of uniform chemical composition. The great advantage of particle synthesis from the gas phase is the high purity and the high production rates (Pratsinis and Mastrangelo 1989). In addition, when the cooling of the gas-vapor system is well controlled, the morphology and size of the particles can be precisely adjusted.

Various energy sources can be used to evaporate materials for particle synthesis in the gas phase. Furnace reactors, glowing wires, and spark discharges use electrical energy to heat and vaporize the desired materials. Flame reactors utilize the heat from combustion to oxidize the vapors which then form clusters and nanoparticles in the cooler regions of the reactor. Plasma and laser reactors utilize the high energy of an ionized gas (plasma), whereas laser reactors employ the high energy and precision of a laser beam.

Particle synthesis from the gas phase is most appropriate for generating single-component particles. One of the great advantages of gas-phase routes for particle synthesis is that small high-purity particles within a very narrow size range can be generated in great quantities. Although several studies have shown that synthesis of binary and ternary mixed particles can be achieved via the gas-phase route, these methods are not as convenient for producing multicomponent particles because differences in the vapor pressures and subsequently in the nucleation and growth rates of the various species can easily lead to internally and externally mixed aerosols. Other drawbacks include the formation of agglomerates and problems in handling hazardous gases.

The following paragraphs outline some of the most commonly used methods for evaporating bulk materials for aerosol nanoparticle synthesis in the gas phase.

2.2.1 Furnace generators

Applying heat to evaporate materials is the most straightforward technique for synthesizing high-purity nanoparticles in the gas phase. In practice, the materials of interest are evaporated by heating in a tubular flow reactor, typically at atmospheric pressure. A gas stream is passed over the evaporating material to carry the vapors away from the heating section of the generator. As the vapors cool downstream of the heating section, they nucleate into clusters containing a few thousands of atoms or molecules which subsequently grow to nanoparticles by coagulation and condensation. The residence times and cooling rates can be adjusted to allow good control over particle size and morphology.

Furnace generators have been successfully used to generate nanoparticles of a range of compositions (Scheibel and Porstendörfer 1983; Gurav et al. 1994). Employing a differential mobility analyzer (cf. § 3.1) downstream of the generator, many research groups have produced monodisperse nanometer-sized particles made of noble metals (e.g. Magnusson et al. 1999; Lehtinen et al. 2004) and semiconductors (e.g. Kruis et al. 2000). One drawback of this technique is that for sizes larger than a few tens of nanometers, the particle morphology becomes irregular since agglomeration occurs as a result of the high particle concentrations. Although for some applications the agglomerated shape of the particles may not be a great problem, generation of uniformly shaped particles is desired in many cases.

Restructuring of the particles can be accomplished by after-treating the agglomerated particles. Depending on the chemical composition, different treatment techniques can be used for particle restructuring. Metal particles for example, can be sintered by heating them up to moderate temperatures (e.g. Schmidt-Ott 1988; Shimada et al. 1994; Ku and Maynard 2006). Salt particles, on the other hand, can restructure upon interaction with water vapor (cf. Mikhailov et al. 2004; Biskos et al. 2006).

Another limitation of the furnace generators is that the material to be evaporated needs to have a much lower melting point than that of the material used for the inner walls of the furnace. If this is not the case, then vapors emanating from the inner walls of the furnace can contaminate the particles. As a result, the production of particles from metals with a high melting point is difficult using furnace reactors. In an attempt to minimize particle impurities from the heated walls and the required heating energy of furnace reactors, Jung et al. (2006) proposed the use of a small ceramic heater for the evaporation of various metals to form aerosol particles, and demonstrated that high-purity silver particles can be generated in this way.

2.2.2 Glowing-wire aerosol generator

There is a need for clean particle production for all applications where surface contamination has an impact on basic properties. This is generally the case for particles smaller than some tens of nanometers and to a larger extent in the range of atomic clusters, where every single atom matters. The glowing wire method fulfils the condition of extreme purity, and very recently it has been demonstrated that atomic cluster production with this method is feasible (Peineke et al. 2008). Material is evaporated from a resistively heated wire and subsequently quenched by a gas stream. The high purity achieved by the glowing wire method arises from the fact that only the particle-forming material is heated, which avoids hot surfaces as sources of contaminants. The amount of material produced hardly reaches 1 μg hr^{-1}, so that possible applications are restricted to those that require only small amounts such as gas sensors (e.g. Favier et al. 2001).

The method was introduced by Schmidt-Ott et al. (1980) and has been applied for the production of metallic particles for research purposes since then (e.g. Burtscher et al. 1982; Müller et al. 1987; Schmidt-Ott et al. 1997; Fernandez de la Mora et al. 2003; Nasibulin et al. 2005). The fact that a significant fraction of the particles formed is charged is of special interest because the aerosol is directly applicable for mobility classification, avoiding additional charging which usually introduces contaminants, as shown by de la Mora et al. (2003). The self-charging effect has been studied and explained in a recent publication by Peineke and Schmidt-Ott (2008). The extreme purity achieved by this method was demonstrated by the group of Burtscher and Schmidt-Ott (Muller et al. 1987). More recently, Peineke et al. (2006) have examined the glowing wire method more systematically, and in a very recent unpublished study of the group, it was demonstrated that a glowing wire can be applied as a source of atomic clusters. Together with the newest developments in mobility analyzers for the ionic range, this technique introduces aerosol technology into the domain of atomic cluster research.

Nanoparticles are formed by condensation from a supersaturated vapor. The material is evaporated by passing a high current through a conducting wire suspended in a flowing inert gas. By mixing with the gas, the vapor is drastically quenched, reaching supersaturations higher than 10^6. A minimum evaporation rate is required for particles to be formed by this process. Most metals reach this minimum value below the melting point. A list of metals for which the method is applicable is given by Peineke et al. (2006). Glowing wire generators are usually composed of standard stainless steel UHV parts, making them easy and cost-effective to build. Water cooling may be added to avoid the housing heating up. The wire is resistively heated close to its melting temperature by a DC low-voltage/high-current supply. The output remains most stable when operated under constant voltage U because the heating power P reduces if the resistance R of the wire increases according to, $P = {U^2}/{R}$, and wire breakage due to temperature variations and decreasing wire diameter is avoided. The wire diameter changes very slowly, resulting in a change of some 10 mA (<0.1%) during one hour. The constant voltage mode delivers a sufficiently constant aerosol output for most purposes. Electric mobility measurements show that the size distributions of the particles generated by glowing wires is log-normal. The self-charging phenomenon allows the production of high concentrations (10^5-10^6cm^{-3}) of monodisperse particles by means of a differential mobility analyzer, if the charged particle concentration is enhanced by biasing the wire potential with respect to the surrounding metal housing (Peineke and Schmidt-Ott 2008).

2.2.3 Spark-discharge generator

Spark discharge is one of the most versatile techniques for generating nanoparticles in the gas phase. The method was introduced by Schwyn et al. (1988) and has been applied by a number of research groups since then (e.g. Evans et al. 2003; Evans et al. 2003; Horvath and Gangl 2003; Roth et al. 2004). The technique has already been used for the production of carbon (Helsper et al. 1993), metals (Schwyn et al. 1988; Tabrizi et al. 2008b), and metal oxide nanoparticles (Kim and Chang 2005; Oh et al. 2007). The particles produced by this method are very similar to those obtained by laser ablation (Ullmann et al. 2002). With respect to this frequently used technique, spark discharge has the advantage of not requiring a laser, applying only inexpensive components and having a potential for scaling-up by operating many sparks in parallel. The method has been characterized in detail in a very recent publication by Tabrizi et al. (2008a). The method has the same advantage of extremely high purity as the glowing wire method, since only the material that forms the nanoparticles is heated. It can be applied to any conductive material including semiconductors. Due to the extremely fast quenching of the vapor, it is unique for mixing materials (Evans et al. 2003). Substantial progress in mixing on an atomic scale as well as a nanoscale on metals that are miscible (Tabrizi et al. 2008b) and immiscible (Tabrizi et al. 2008c) has recently been made and will be published shortly. These new possibilities of mixing on a nanoscale are of great interest, for example in preparing advanced catalysts.

The process of spark discharge is initiated by gas breakdown and formation of a conducting plasma channel. The rapid discharge consists of a current associated with a high temperature (typically 20000 K). As a result, electrode material is evaporated in the vicinity of the spark. This is followed by rapid cooling, initially governed by adiabatic expansion and radiation. Below the evaporation temperature, cooling is dominated by thermal conduction. Because the vapor cloud is small compared to other evaporation-condensation processes, the cooling period at temperatures below the boiling point is relatively small, thereby leading to the formation of high concentrations of very small particles. Spark generators typically consist of a chamber of the order of a few hundred cm^3 in volume, in which two opposing cylindrical electrodes are mounted at an adjustable distance. The electrodes which are several mm in diameter and up to a few millimeters apart are connected to a high-voltage power supply, and in parallel to a capacitor with a capacitance of some tens of nF. The power supply delivers a constant current, periodically recharging the capacitor after discharge has occurred at the breakdown voltage. The electric circuit including the spark contains an inductive component, which leads to a damped oscillatory discharge process of a few microseconds in duration (Tabrizi et al. 2008a). Because the current is temporarily reversed during this oscillation, both electrodes are ablated. This would not be the case in a unipolar discharge, because the positive ions in the plasma ablate the cathode more strongly than the electrons ablate the anode. The spark frequency can typically be adjusted up to 1 kHz. Above this frequency a continuous discharge tends to occur. Such a process produces much larger particles (tens of nm in diameter), while fast sparks lead to nanoparticles smaller than 10 nm in diameter.

The mean particle size can be controlled via the energy per spark, which is in turn determined by the capacitance and the distance between the electrodes. The particle mass produced per unit time is proportional to the spark frequency. Separated, unagglomerated particles a few nanometers in size can be obtained if the inert gas flow through the generator is high enough with respect to the spark repetition frequency. In principle, this enables the coating of individual particles when a vapor deposition step is added. The nanoparticulate mass produced is typically a few g kWh^{-1}. Using the example of gold it was shown that with gases purified at the spot, the method produces particles which are so clean that sintering of the agglomerated particles occurs at room temperature, leading to branched solid structures (Tabrizi et al. 2008b). Different electrode materials lead to different mean primary particle sizes and mass production rates, where thermal conductivity, evaporation enthalpy and the boiling point have a major influence. Knowing these properties, an estimate for the mass production rate can be obtained (Tabrizi et al. 2008b). In the latter publication, it is also shown that if the spark generation of nanoparticles is performed in a standing or almost standing gas in the presence of an electric field, an aerogel is formed. It has a web-like structure that bridges the space between surfaces of different electric potential.

2.2.4 Flame synthesis

Using flames has been another popular way of generating particles in the gas phase. Due to the high production rates, flames have been widely employed in industry to produce carbon black and ceramic particles (e.g. titanium dioxide, silica, etc.) for use as material reinforcing agents, and for the manufacture of catalysts and optical fibers (Ulrich 1984; Pratsinis 1998).

Flame reactors for aerosol generation can be classified as vapor- or liquid-fed depending on the state of the reactants used to form the desired particles. Particle formation is initiated by the combustion of vapor- or liquid-phase precursors during the fast temperature increase in the flames, which can reach up to approx. 2500°K. Initially, oxidized vapors form clusters that grow to nanoparticles through further vapor condensation and coagulation with other particles. Depending on the target application, a range of particle compositions can be manufactured by carefully selecting the gas or liquid precursors. The physical properties of the produced particles (i.e. size and morphology) can be tailored by empirically controlling the operating parameters of the flame (i.e. flow rates and temperature gradients). The crystalline structure of the particles can be also adjusted by adding dopants to the feed stream (Vemury and Pratsinis 1995) and by controlling the temperature history of the particles, as has been demonstrated by Jiang et al. (2007) and shown computationally by Johannessen et al. (2000; 2001) and Tsantilis et al. (2002). The application of external electric fields has also been shown to provide good control of the physical and chemical characteristics of the produced particles (Vemury and Pratsinis 1995; Kammler and Pratsinis 2000; Kammler et al. 2003).

Although the most common application of particle flame synthesis has been the manufacturing of carbon blacks in fuel-rich flames using aromatic hydrocarbons as precursors (cf. Donnet et al. 1993), recent efforts have focused on the oxidation of the metal halide vapors in hydrocarbon-supported flames for generating metal oxide (e.g. Jensen et al. 2000; Arabi-Katbi et al. 2002; Jensen et al. 2003), and alloy nanoparticles (e.g. Stark et al. 2001; Keskinen et al.

2004; Chakraborty et al. 2005) for a range of applications. The most characteristic example of nanoparticle generation by flame reactors is titanium dioxide, which as a rutile is commonly used in pigments, and as an anatase is preferred in photocatalysis and as an effective UV absorber (Strobel and Pratsinis 2007).

Aggregate formation has been a disadvantage associated with flame particle synthesis as it can lead to problems in consolidation and sintering during the fabrication of large ceramic parts. Recent studies, however, have shown that non-agglomerated (Mueller et al. 2004) or weakly agglomerated particles (Mueller et al. 2004) can be generated in diffusion flames depending on the operating conditions. Another disadvantage is that flames may present difficulties in synthesizing multicomponent particles due to differences in nucleation and growth rates of the various species involved. Despite this difficulty, however, multicomponent particles have been successfully manufactured using aerosol flame reactors (cf. Strobel et al. 2006; Strobel and Pratsinis 2007 and references therein).

The great advantage of flame synthesis is that high particle production rates (up to a few hundreds of g h^{-1}) can be easily achieved at a very low cost. Considering also the flexibility of these methods to control the physical and chemical properties of the particles, flame synthesis is one of the most prominent methods for fabricating particles for applications in nanotechnology.

2.2.5 Plasma synthesis

The number of different types of plasma is very large, and quite a few have been explored for nanoparticle production. Plasmas can be broadly divided into two types: thermal or hot and cold. Hot plasmas are in or close to the local thermodynamic equilibrium, the gas molecules and the free electrons have approximately the same temperature (several thousand K). In cold, non-thermal plasmas, the free electrons have temperatures of several eV, whereas the overall gas temperature is close to ambient.

Particle production with cold plasmas usually starts with a volatile precursor which is introduced into the plasma as a vapor in a carrier gas. The precursor can be hydrocarbons, metal halides, metal organics or volatile silicon compounds. Once introduced into the plasma, the molecules of the precursor are dissociated by the energetic species in the plasma, resulting in a cloud of metal or silicon atoms. Due to the low overall gas temperature, these atoms rapidly nucleate to clusters which then grow to nanoparticles through further condensation of the vapors. Hydrocarbons tend to polymerize under the influence of the active species, eventually they form particles. Vollath and Sickafus (1992) used a cold microwave plasma at reduced pressure to produce metal-oxide nanoparticles. The process takes place between 400 and 750 K, and particles leave the reaction zone carrying charges of the same (positive) sign. This greatly reduces agglomeration, as identically charged particles will repel each other (Vollath and Szabo 2005). This process therefore results in very monodisperse particles. Vollath and co-workers also investigated the subsequent in-situ coating of the nanoparticles using monomethylmetacrylate (MMA) vapor (Vollath and Szabo 1999), which in a second microwave plasma results in polymerization to form a coating of PMMA (Perspex). The only disadvantage of the process is that it requires a vacuum system, as it takes place between 5-100 mbar, also limiting the production rate. The vacuum is required to prevent the plasma from turning into a hot plasma.

At atmospheric pressure, cold plasmas can be generated by using a dielectric barrier discharge (DBD). A non-conductive material such as alumina or borosilicate glass (the dielectric barrier) is placed between two electrodes, between which an oscillating electric field is applied. The dielectric barrier prevents the transition into a hot arc plasma since the charges produced by the discharge are deposited on it (Kunhardt 2000). Using such configurations, simple atmospheric plasma systems using nitrogen, argon or helium as a carrier gas can produce high particle concentrations without requiring a complicated vacuum system. Particles have been successfully produced from ferrocene, acetylene and hexamethyldisiloxane (Vons et al. 2006), and from titaniumisopropoxide for the production of titania particles (Bai et al. 2004; Chen et al. 2007). Furthermore, this type of plasma can also be used for gas-phase particle coating, both for particles from another DBD plasma or particles produced using other methods (e.g. Lei et al. 2006; Marino et al. 2007). Under certain conditions, particles can be generated by sputtering of the dielectric barrier (Jidenko and Borra 2004). DBD plasmas are used on a large scale for the generation of ozone from air and for water purification, which proves that up-scaling of the process is possible.

Other cold plasma systems have been used for the production of iron and carbon nanoparticle production (Barankin et al. 2006). These systems use a commercial atmospheric pressure plasma jet system described by Nowling et al. in 2002. In these systems, a radiofrequency plasma is kept in a non-equilibrium state by using a high-helium gas flow which removes the charged species before an arc breakdown can occur.

Particle synthesis in hot plasmas is performed by dissociation of volatile precursors. However, the highly reactive and extremely hot environment of thermal plasmas allows the use of many other feedstocks in the gas, liquid or solid phase. The extreme heat of a thermal plasma can be used to evaporate micron-sized solid particles of nearly any material introduced as an aerosol into the plasma, which can subsequently recondense to nanoparticles under the right conditions. This has been done mostly in inductively coupled (ICP) radiofrequency (RF) plasma torches (Gutsch et al. 2002; Goortani et al. 2006; Ye et al. 2007), and also in thermal microwave plasmas (Weigle et al. 2004). ICP plasmas are generated by applying RF power to a coil wrapped around a quartz tube through which the plasma flows. The coil induces currents on the boundaries of the plasma, thus transferring the energy to sustain it. A separate electrode and ignition system are required to initiate the plasma. The advantage of the ICP is that no electrodes are in contact with the plasma, thereby reducing contamination from electrode wear. To obtain the high cooling rates required to reach the supersaturations sufficient for nanoparticle formation, quench gas is often injected behind the plasma. Liquid-fed ICP processes have been developed with both solutions containing the desired element (Suzuki et al. 1992), or pure liquids (Ishigaki et al. 2005). Using normal spray techniques, the liquid is atomized and the resultant spray is fed to the plasma.

In a direct current (DC) arc, a discharge between two electrodes draws high currents (1-250 A), while the voltage drop over the plasma is rather low, i.e. in the order of a few tens of volts. The high current densities cause the extremely high temperatures. Two different arc configurations have been applied for nanoparticle production: normal arcs and arc jets or plasma torches. Normal DC arcs are used to evaporate the electrode or material contained in a basket or boat-shaped electrode (Mahoney and Andres 1995; Chen et al. 2007), and the vapors are subsequently condensed to form nanoparticles using a high quench gas flow. DC arc jets operate in a similar way to the ICP torches, but the plasma is made by striking a DC arc between an axial cathode and a coaxial anode with a conical gap. A high gas flow between the cathode and the anode forms a high-temperature arc jet downstream of the gap. Nanoparticles are generated by introducing gaseous precursors such as $SiCl_4$ and CH_4 into the plasma (Rao et al. 1995; Hafiz et al. 2006). Although the electrical circuitry for DC arc jet plasmas is simpler than for ICP plasmas, the fact that the cathode and anode are in contact with the plasma increases the chance of wear of the electrodes and contamination of the product.

Both hot and cold plasmas have their advantages. The hot plasmas all have high production rates, and can operate with many different materials, especially the ICP plasmas. This makes them very interesting for industrial application. They do, however, require very high gas flows and have high power consumption (in the case of ICPs, only 20-40% of the input power actually goes to the plasma, the remainder is lost in associated circuitry; cf. Reece Roth (1995)). High-temperature plasmas usually result in larger particles compared to cold plasmas, mainly due to sintering.

Cold plasmas require the right vapor precursors, which can be quite expensive for some elements, and usually have lower production rates. However, the cold gas temperature is beneficial for energy consumption and getting energy exactly where is needed (i.e. into the dissociation of the precursor and not the heating of the plasma gas). Furthermore, the low temperature reduces sintering, which is reflected by the fact that the primary particle size for cold plasmas is usually smaller. Cold plasmas are also suitable for the coating of already formed particles in the aerosol phase, as the low temperatures prevent further sintering of the particles.

2.2.6 Laser ablation

Laser ablation is another way of generating nanoparticles from the gas phase. In this method, solid targets are typically rotated in a cylindrical ablation chamber. The beam from an excimer laser enters the ablation chamber through a quartz window onto the target material. Upon interaction of the laser beam with the target material, the surface is heated beyond its boiling point and forms vapors. By increasing the irradiance even more, the vapor becomes superheated and ionized, forming plasma. Carrier gas flowing over the heated surface takes the vapors out of the ablation chamber. As the vapors move away from the ablation region, they cool down and form clusters, which then grow to nanoparticles by further condensation of the vapors and coagulation with other particles. Particles of a range of compositions can be easily generated by changing the target material. Typical mass production rates are of the order of 100 ng per pulse. Control over the ablated mass is achieved by varying pulse energy and frequency of the laser.

Laser ablation techniques have been employed to produce a range of metal oxide nanoparticles (cf. Kato 1976). Metal oxide particles can be generated by ablating metal oxide targets in an inert gas or pure metals in an oxidizing gas. For example, ablation of aluminum in the presence of oxygen can produce alumina nanoparticles of very high purity (Johnston et al. 1992). Several studies have focused on the operating parameters that control particle size and morphology in laser ablation systems (Sasaki et al. 1998; Camata et al. 2000; Ogawa et al. 2000). An increase in flow rate produces smaller aggregates and smaller primary particles. Increasing pulse energy and pulse frequency causes an increase in the aggregate size, primary particle size, and number concentration. Nevertheless, the size of the primary particles has been shown to range within a narrow size range up to approx. 15 nm, independent of the materials used (Ullmann et al. 2002).

The purity of the aerosol product depends primarily on the purity of the carrier gas and the target material. Since the laser beam is focused on the target, contamination by materials released from other surfaces in the ablation chamber is less likely.

3. Sizing and Counting Aerosol Nanoparticles

There are numerous methods for sizing aerosol particles in the nanometer range. These methods can be classified depending on whether the particles are deposited on a surface or suspended in a gas. The size and morphology of deposited particles can be estimated by microscopy techniques. Scanning and transmission electron microscopes (SEM and TEM, respectively) can be applied for direct size and morphology measurements of deposited nanoparticles. Advanced image analysis software has been developed and used for the rapid estimation of particle size and morphology distributions.

The great advantage of electron microscopy techniques is that they can be applied for a relatively wide range of particle sizes. TEMs for example, allow sizing of particles from the nanometer up to the micrometer range. SEMs typically have a lower size resolution but are also suitable for a similarly wide range of particle sizes. SEM and TEM imaging requires the collection of particles on substrates before examination. One drawback of the microscopic techniques is that particle deposition has to be carefully planned so that the substrates have a good coverage of sample particles. Depending on the composition and size of the particles, evaporation by the high energy beams can also affect the measurements. In this case, special coatings can be applied to the particles prior to imaging in order to overcome this limitation.

Sizing nanoparticles on-line when they are suspended in the gas is in many cases much more favorable due to the ability of probing their dynamic behavior. Although a wide range of techniques is commercially available (e.g. aerodynamic particle sizing, optical particle sizing, etc.), their application depends on the particle size range to be measured. By far the most efficient and widely used method for sizing particles in the nanometer range is by measuring their electrical mobility. Electrical mobility techniques were initially developed to measure ions in gases (Zeleny 1900; Erikson 1921; Zeleny 1929). Around the 1920s and 30s when the technique was widely accepted, researchers started realizing that heavier ions (what we now call nanoparticles) exist in the atmosphere (Erikson 1922; Chapman 1937). Rohmann (1923) was one of the first investigators to employ the method for measuring airborne particles. However, it was not until the 1960s that the technique was seen to be useful for measuring aerosol size distributions and the first mobility analyzers, i.e. the Whitby Aerosol Analyser (Whitby and Clark 1966), became commercially available. A thorough review of the available designs at that time is given by Tammet (1970). A historical retrospect of the developments in electrical mobility measurements is provided by Flagan (1998).

Available instruments for electrical mobility particle measurements are the Scanning Mobility Particle Sizer (SMPS) (Wang and Flagan 1990), the Electrical Aerosol Analyser (EAA) (Whitby and Clark 1966), the Electrical Aerosol Spectrometer of Tartu University (Tammet et al. 1998; Tammet et al. 2002) and the recently announced Differential Mobility Spectrometer (DMS) (Biskos et al. 2002; Biskos et al. 2005) and Engine Exhaust Particle Sizer (EEPS) (Johnson et al. 2004). Although these instruments are all designed to measure aerosol size distributions using the same principles, one might prove better than the others for special applications depending on the concentration of particles, the response, and the spectral resolution required.

The most commonly used electrical mobility spectrometer for measuring nanoparticles is by far the SMPS. Compared to the other instruments that use the same operating principles, the SMPS exhibits very high size resolution, enabling detection of particle size differences of the order of less than one nanometer. SMPS systems consist of two main parts: the electrostatic classifier and the particle counter. Charged aerosol particles are classified according to their electrical mobility by the classifier (typically a differential mobility analyzer; cf. § 3.1) and their concentration is subsequently measured by the particle counter (a Faraday cup electrometer or a condensation particle counter; cf. § 3.2 and 3.3, respectively). By varying the operating conditions of the classifier, particles having a range of electrical mobilities can be classified in different size bins. The entire particle size distribution can be estimated by measuring the particle number concentrations that correspond to the different size bins. Finally, the measured electrical mobility distributions are converted to particle size distributions using inversion algorithms.

The classifier-counter arrangements can be operated in a scanning (SMPS) or a stepping (DMPS: Differential Mobility Particle Sizer) mode. The next paragraphs give a description of the most widely used electrical mobility classifier (i.e. the Differential Mobility Analyzer, DMA) and particle counters (i.e. the Faraday cup electrometer, and the Condensation Particle Counter, CPC) used in SMPS and DMPS systems.

3.1 The differential mobility analyzer

The DMA consists of two concentric electrodes with the inner rod maintained at a controlled potential and the outer tube electrically grounded. The polydisperse aerosol enters the DMA in a perimetric flow close to the outer electrode surrounding a particle-free sheath flow. The sheath flow is introduced into the DMA from the same end of the column around the central rod and both streams flow in the same direction. A narrow aerosol inlet annulus is designed to uniformly distribute the particles in the main flow of the instrument, which, maintained laminar, facilitates high-resolution classification.

Depending on their polarity, charged particles move towards or away from the high-voltage central rod, whereas uncharged particles are unaffected by the electric field in the column. Most commonly, a negative voltage is applied to the central rod so that positively charged particles are drawn towards it. The landing location of the particles on the central rod is a function of their electrical mobility and the operating conditions of the DMA (flow rate and central rod voltage). Particles of high electrical mobility precipitate close to the aerosol inlet, whereas particles of lower mobility precipitate further down the column. Particles within a narrow range of mobilities exit the DMA through the monodisperse sample flow, i.e. a circumferential slit on the central rod located downstream of the aerosol inlet. The monodisperse flow is then transferred to the detector where particle number concentrations are measured. All the remaining particles exit the DMA via the excess flow.

Most DMAs are based on the improved version of the Hewitt mobility analyzer proposed by Knutson and Whitby (1975). This original design is associated with high diffusional losses in the aerosol inlet and outlet thereby restricting the performance of the DMA for particles smaller than approx. 10 nm. Many research groups have focused on improving the penetration efficiency of sub-10 nm particles through the DMA by proposing different designs. Winklmayr et al. (1991) developed a cylindrical DMA (the Vienna DMA) with a novel tangential flow aerosol inlet that minimizes diffusional losses. Reducing the residence time of the particles in the DMA by shortening the total length and increasing the flow, they achieved higher transmission efficiencies and managed to classify particles with diameters as small as 1 nm. In the same direction, Chen et al. (1998) developed and tested a new cylindrical DMA (the Nano DMA) that uses a modified aerosol inlet and a much shorter column compared to the original design. A more innovative design was proposed by Zhang et al. (1995) and later by Mesbah et al. (1997), who independently developed the Radial DMA (R-DMA). The R-DMA classifies particles in a radial flow towards the center of two parallel disk electrodes. Although the high transmission efficiencies of ultrafine particles through the R-DMA made it more favorable compared to the cylindrical DMA, its low resolution for the larger range of particle sizes limited its wide use in SMPS and DMPS systems. More recent developments have led to high-flow DMAs capable of size-separating small ions and molecules. It has been applied to protein and polymer molecules, and recent work to be published soon involving one of the authors (A.S.), showed that it is a useful instrument for atomic cluster separation down to 2 atoms.

Originally, the DMA was designed to generate monodisperse particle samples from polydisperse aerosols for calibration purposes (Liu and Pui 1974). A year later, Knutson and Whitby (1975) proposed using the instrument for measuring aerosol size distributions. Further work by Hoppel (1978) and Haaf (1980), who proposed algorithms to determine size distributions from mobility measurements by the DMA, showed that the technique can be very powerful. Using the DMAs both as a way of generating monodisperse particles and as a classifier for measuring particle size distributions has been very useful in aerosol science and technology. The feature of the DMA for producing monodisperse particles is in many cases important in nanoparticle synthesis via aerosol methods, because most aerosol generation methods produce polydisperse particles from which only a very narrow size range is desired.

Highly concentrated aerosols produced by most generation methods outlined in the previous section require dilution before they can be efficiently classified in a DMA. This can be a serious limitation when DMAs are used in the generation process to select particles of a narrow size range, as it can significantly reduce the production rates. Another limitation of these classifiers is that particles are classified according to their electrical mobility and not directly based on their size. As a result, particles of different size and shape can be included in the monodisperse samples depending on the charge and the morphology distribution of the particles, respectively.

3.2 Faraday cup electrometers

The number concentration of an aerosol flow carrying charged particles can be determined using a Faraday cup electrometer. In this type of detectors, particles from the sample flow are collected in a high-efficiency filter housed in a metal enclosure, i.e. a Faraday cup. This filter is isolated from the metal housing which is connected to the ground through the electrometer. The metal housing shields the electrometer from any external disturbances. Charges that are trapped in the Faraday cup induce a current which is proportional to the amount of charge collection rate on the filter. The particle number concentration can then be estimated from the current if the number of charges on each particle and the aerosol flow rate are known.

Typically, Faraday cup electrometers have sensitivities of the order of a few fA (He et al. 2007). Considering that the sampled particles are moderately charged, the minimum particle number concentration that Faraday cup electrometers can measure is of the order of 10^2-10^3 particles cm^{-3} for typical flow rates.

3.3 The condensation particle counter

Another method of measuring the particle number concentrations of an aerosol sample is by using optical instruments. Because particles smaller than approx. 100 nm are difficult to detect optically since their size is smaller compared to the wavelength of most light sources, growth of the particles to a detectable size is required. Particle growth is achieved by condensation prior to detection in CPCs.

The CPC consists of three main parts: the saturation tube, the condensation tube, and the optical detection system. The incoming sample passes first through the saturator where the aerosol becomes saturated with a working fluid (typically butanol). Upon cooling of the aerosol, the vapors supersaturate and condense on the particles which grow into larger droplets. Finally, the grown droplets pass through the optical detector where their total number in a unit volume is measured. The commercial CPCs are based on the design originally proposed by Agarwal and Sem (1980). Single-particle counters such as the CPC are much more powerful devices than multiple-particle counters that measure extinction of light through the aerosol (Sinclair and Hoopes 1975; Davies and Egilmez 1985). In principle, their ability to detect single particles makes them capable of measuring particle concentrations down to any level. However, for highly concentrated aerosols typically produced by the methods described in the previous section, Faraday cup electrometers may be more appropriate.

4. Applications of Aerosol-Based Nanotechnology

Nanoparticle building blocks of a well-defined size and chemical composition are necessary in many technological applications. Some aerosol techniques for synthesizing such nanoparticles are already being used in industry, whereas recent advances in aerosol science and technology indicate that several other techniques have a great potential for up- and outscaling. This section gives a brief outline of existing applications of aerosol-based nanotechnology and provides an outlook of the potential that these techniques can have.

Perhaps the most widespread use of aerosol-based methods in industry has been for the synthesis of carbon black nanoparticles. Carbon black nanoparticles have been used as strengthening or reinforcing agents for rubber in automobile tires (Medalia 1978). Other applications of carbon black particles include the manufacture of pigments, coatings, and various polymers with enhanced electrical and mechanical properties (Donnet et al. 1993). Despite the fact that synthesis techniques and applications of carbon black nanoparticles have been well established, recent research has shown that particle mixtures of carbon black and silica are opening up a new generation of reinforcing agents for rubber (Wang et al. 2000). Internally mixed carbon black/silica particles have also been manufactured in premixed flame aerosol reactors by the combustion of acetylene and $SiCl_4$ (Spicer et al. 1998; Kammler et al. 2001). The combination of carbon black and silica is more effective in reinforcing rubber because compared to carbon black alone, it provides the capability for monufacturing the so-called "green tires".

The synthesis of ceramic particles has been another widespread application of aerosol methods in the industry. Flame-synthesized fumed silica particles are used as fillers in silicone rubber, as strengthening and reinforcing agents, catalyst carriers, polishing materials in microelectronics, and in the manufacture of optical fibers (cf. Pratsinis 1998). Titanium dioxide nanoparticles also find many applications depending on their crystallinity. For example, rutile titanium dioxide particles with a diameter of approx. 250 nm are commonly used in pigments to provide maximum whiteness and opacity. This is by far the largest application of titanium dioxide particles typically generated by flame synthesis techniques. Titanium dioxide particles can also be used in photocatalysts for water and gas purification, in gas sensors, and as supports in the manufacturing of catalysts (cf. Pratsinis 1998 and references therein). Alumina particles produced via the aerosol route have also been used for the fabrication of integrated circuit substrates, high-pressure sodium-vapor lamps, catalyst supports and high-performance materials (cf. Kaya et al. 2002; Ye et al. 2007).

Nanoparticle building block synthesis methods via the aerosol route exhibit great potential for applications in the fabrication of electronic components (e.g. Prost et al. 1998). Alloy particles synthesized by spray pyrolysis have been used for the formation of conductive films in electronic devices such as hybrid integrated circuits and multilayer ceramic capacitors (e.g. Nagashima et al. 1991). Due to their dielectric and ferroelectric properties, barium titanate nanoparticles have been synthesized via the same technique for the fabrication of multilayer ceramic capacitors, transducers, and thermistors (Lee et al. 2005), whereas γ-Fe_2O_3 nanoparticles synthesized in the same way have shown great potential for use in magnetic recording media (Gonzalez-Carreno et al. 1993).

Nanoparticle building blocks with sizes below a few nanometers have various potential applications in electronics where quantum confinement effects may be advantageous (Flagan et al. 1991; Wiedensohler et al. 1992). These nanosized systems, commonly referred to as quantum dots or zero-dimensional structures, have altered electrical properties compared to their large-particle counterparts, because the electronic state space in these structures is discrete as a result of the three-dimensional confinement. Silicon nanocrystals for example, are widely considered a material with great potential for a wide spectrum of applications and novel devices (e.g. single-electron transistors, vertical transistors, and floating gate memory devices), as well as for applications in solid-state lighting (e.g. Kang et al. 2006).

Nanoparticles synthesized via the aerosol route can also have great potential in the manufacture of materials for efficient energy storage. For instance, solid-state batteries that use electrodes made of nanoparticles of transition-metal oxides exhibit higher electrochemical capacities and lifetimes (Poizot et al. 2000). Nanostrucutred metal hydrate materials can also exhibit higher hydrogen storage capacities and rapid kinetics (Zaluska et al. 2001). Such materials can have a strong impact on energy storage systems in transportation (e.g. Schlapbach and Zuttel 2001).

Nanoparticle building blocks can also be used in the fabrication of simple and cost-effective gas sensors (e.g. Favier et al. 2001). The underlying operating principle of these sensors is that the electrical properties of films or wires made of metallic or semiconducting particles can change as a result of adsorption of gaseous species onto their surfaces. The high specific surface of these nanostructures significantly enhances gas transfer rates to the structure and thus the sensing capabilities of the sensors.

Thin films made of tin oxide particles were shown to have gas sensing properties almost three decades ago (Ogawa et al. 1981; Ogawa et al. 1981). Adachi et al. (1988) showed that such films can selectively detect hydrogen, nitrogen, and oxygen gases. Doping the tin dioxide films with metal particles was shown to enhance the gas selectivity of the sensors (Gautheron et al. 1993; Labeau et al. 1993; Labeau et al. 1994; Tadeev et al. 1998; Renault et al. 1999). The conductivity of nanostructured films and wires made of palladium nanoparticles have been shown to be very sensitive on the concentration of hydrogen in the overlying gas (Volkening et al. 1995; Kovacik et al. 2008). Recently, Teleki et al. (2008) showed that Nb- and Cu-doped TiO_2 structures can also be used for sensing carbon monoxide and ethanol.

Nanoparticle building blocks produced by aerosol methods have been also used in catalysis. Flame synthesis has been extensively used to produce nanoparticles for catalysts. For example, Stark et al. (2001) demonstrated that flame-synthesized vanadia–titania nanoparticles exhibit high activity for the selective catalytic reduction of nitrogen monoxide by ammonia. Chakraborty et al. (2005) produced mixed platinum-ruthenium nanoparticles by flame aerosol synthesis to catalyse the methanol oxidation reaction in direct methanol fuel cells. A thorough review on nanoparticle formation using flame synthesis techniques for fabricating catalytic materials is given by Strobel et al. (2006). Using spray pyrolysis, Backman et al. (2004) demonstrated the enhanced photocatalytic activity of silver-doped titanium dioxide particles. Finally, the catalytic activity of airborne versus deposited Ni nanoparticles has been suggested as a way to increase the transport rate of the gaseous species to the surface of the particles (Weber et al. 2006).

Nanoparticles synthesized via the aerosol route can also have therapeutic or diagnostic applications in medicine. Drugs in the form of aerosol nanoparticles can be delivered efficiently to certain parts of the human body (Dames et al. 2007). Magnetic nanoparticles (commonly referred to as magneto-pharmaceuticals) can also be administered to the human body to aid nuclear magnetic resonance imaging for diagnostic reasons (Tartaj et al. 2003). Other medical applications of nanoparticles include the biodetection of pathogens, tumor destruction via heating, tissue engineering, and localized treatment such as hyperthermia (Salata 2004). Considering the great advantages of aerosol synthesis techniques for high purity and great control over the size of the nanoparticle, one can envisage their potential future applications for advanced diagnostics and treatment methods.

5. Conclusions

In this paper we provide a brief review on state-of-the-art techniques for generating and sizing aerosol nanoparticles of well-defined size and chemical composition for applications in nanotechnology. Compared to nanoparticle synthesis via the liquid route, aerosol processes are attractive for their high purity and simplicity as they do not involve large volumes of liquid by-products. In addition, their ability to operate in a continuous rather than in a batch mode makes them favorable in many industrial and technological applications.

Aerosol particles can be synthesized from the liquid or the gas phase. Techniques that fall into these two categories have been described, and their advantages and drawbacks in view of the different application are discussed. The most efficient technique for sizing nanoparticles suspended in a gas is by measuring their electrical mobility. The operating principles of the individual components (i.e. the classifier and detectors) of the most widely used electrical mobility spectrometer are briefly described. This paper closes with a discussion on the existing applications of aerosol-based nanotechnology and an outlook of their potentials.

References

Adachi, M., Okuyama, K., Kousaka, Y., and Tanaka, H. (1988): Preparation of gas sensitive film by deposition of ultrafine tin dioxide particles, Journal of Aerosol Science, 19, pp.253-263.

Agarwal, J. K., and Sem, G. J. (1980): Continuous flow, single-particle-counting condensation nucleus counter, Journal of Aerosol Science, 11, pp.343-357.

Arabi-Katbi, O. I., Wegner, K., and Pratsinis, S. E. (2002): Aerosol synthesis of titania nanoparticles – Effect of flame orientation and configuration, Annales De Chimie-Science Des Materiaux, 27, pp.37-46.

Backman, U., Tapper, U., and Jokiniemi, J. K. (2004): An aerosol method to synthesize supported metal catalyst nanoparticles." Synthetic Metals, 142, pp.169-176.

Bai, H. L., Chen, C. C., Lin, C. S., Den, W., and Chang, C. L. (2004): Monodisperse nanoparticle synthesis by an atmospheric pressure plasma process – An example of a visible light photocatalyst, Industrial & Engineering Chemistry Research, 43, pp.7200-7203.

Barankin, M. D., Creyghton, Y., and Schmidt-Ott, A. (2006): Synthesis of nanoparticles in an atmospheric pressure glow discharge, Journal of Nanoparticle Research, 8, pp.511-517.

Baron, P. A., and Willeke, K. (2001): "Aerosol Measurement - Principles, Techniques, and Applications", Wiley.

Barreras, F., Amaveda, H., and Lozano, A. (2002): Transient high-frequency ultrasonic water atomization, Experiments in Fluids, 33, pp.405-413.

Berglund, R. N., and Liu, B. Y. H. (1973): Generation of monodisperse aerosol standards, Environmental Science & Technology, 7, pp.147-153.

Biskos, G., Malinowski, A., Russell, L. M., Buseck, P. R., and Martin, S. T. (2006): Nanosize effect on the deliquescence and the efflorescence of sodium chloride particles, Aerosol Sci. Technol., 40, pp.97-106.

Biskos, G., Reavell, K., and Collings, N. (2005): Description and theoretical analysis of a differential mobility spectrometer, Aerosol Sci. Technol., 39, pp.527-541.

Biskos, G., Reavell, K., Hands, T., and Collings, N. (2002): Fast measurements of aerosol spectra, Journal of Aerosol Science, S67-S68.

Boguslavskii, Y. Y., and Eknadiosyants, O. K. (1969): Physical mechanism of the acoustic atomization of a liquid, Soviet Phys. Acoust., 15, pp.14-21.

Burtscher, H., Scherrer, L., Siegmann, H. C., Schmidt-Ott, A., and Federer, B. (1982): Probing aerosols by photoelectric charging, Journal of Applied Physics, 53, pp.3787-3791.

Camata, R. P., Hirasawa, M., Okuyama, K., and Takeuchi, K. (2000): Observation of aerosol formation during laser ablation using a low-pressure differential mobility analyzer, Journal of Aerosol Science, 31, pp.391-401.

Cauchetier, M., Croix, O., Herlin, N., and Luce, M. (1994): Nanocomposite Si/C/N powder production by laser-aerosol interaction, Journal of the American Ceramic Society, 77, pp.993-998.

Chakraborty, D., Bischoff, H., Chorkendorff, I., and Johannessen, T. (2005): Mixed phase Pt-Ru catalyst for direct methanol fuel cell anode by flame aerosol synthesis, Journal of the Electrochemical Society, 152, A2357-A2363.

Chapman, S. (1937): Carrier mobility spectra of spray electrified liquids, Physical Review, 52, pp.184-190.

Chen, C. C., Bai, H. L., Chein, H. M., and Chen, T. M. (2007): Continuous generation of TiO_2 nanoparticles by an atmospheric pressure plasma-enhanced process, Aerosol Science and Technology, 41, pp.1018-1028.

Chen, D. R., Pui, D. Y. H., Hummes, D., Fissan, H., Quant, F. R., and Sem, G. J. (1998): Design and evaluation of a nanometer aerosol differential mobility analyzer (Nano-DMA), Journal of Aerosol Science, 29, pp.497-509.

Chen, J. H., Lu, G. H., Zhu, L. Y., and Flagan, R. C. (2007): A simple and versatile mini-arc plasma source for nanocrystal synthesis, Journal of Nanoparticle Research, 9, pp.203-213.

Ciach, T., Geerse, K. B., and Marijnissen, J. C. M. (2002): EHDA in particle production in nanostructured materials, "Optimization of Aerosol Druh Delivery", G. L. a. J. Marijnissen, ed., Kluwer Academic, Boston.

Cloupeau, M., and Prunetfoch, B. (1994): Electrohydrodynamic spraying functioning modes - A critical review, Journal of Aerosol Science, 25, pp.1021-1036.

Dames, P., Gleich, B., Flemmer, A., Hajek, K., Seidl, N., Wiekhorst, F., Eberbeck, D., Bittmann, I., Bergemann, C., Weyh, T., Trahms, L., Rosenecker, J., and Rudolph, C. (2007): Targeted delivery of magnetic aerosol droplets to the lung, Nature Nanotechnology, 2, pp.495-499.

Davies, C. N., and Egilmez, N. (1985):.The Nolan-Pollak condensation nucleus counter, Journal of Aerosol Science, 16, pp.245-259.

Davis, E. J., and Bridges, M. A. (1994): The Rayleigh limit of charge revisited - Light-scattering from exploding droplets, Journal of Aerosol Science, 25, pp.1179-1199.

Deng, W., and Gomez, A. (2007): Influence of space charge on the scale-up of multiplexed electrosprays, Journal of Aerosol Science, 38, pp.1062-1078.

Donnet, J.-B., Bansal, R. C., and Wang, M. J. (1993): "Carbon Black", Marcel Decker, New York.

Erikson, H. A. (1921): Size and aging of ions produced in air, Physical Review, 17, p.400.

Erikson, H. A. (1922): On the nature of the negative and positive ions in air, oxygen and nitrogen, Physical Review, 20, pp.117-126.

Evans, D. E., Harrison, R. M., and Ayres, J. G. (2003): The generation and characterisation of elemental carbon aerosols for human challenge studies, Aerosol Science & Technology, 37, pp.975-987.

Evans, D. E., Harrison, R. M., and Ayres, J. G. (2003): The generation and characterisation of elemental carbon aerosols for human challenge studies, Journal of Aerosol Science, 34, p.1023.

Faraday, M. (1831): On a peculiar class of acoustical figures; and on certain forms assumed by groups of particles upon vibrating elastic surfaces, Philos. Trans. R. Soc. London, 121, pp.299-340.

Favier, F., Walter, E. C., Zach, M. P., Benter, T., and Penner, R. M. (2001): Hydrogen sensors and switches from electrodeposited palladium mesowire arrays, Science, 293, pp.2227-2231.

Fernandez de la Mora, J. F., de Juan, L., Liedtke, K., and Schmidt-Ott, A. (2003): Mass and size determination of nanometer particles by means of mobility analysis and focused impaction, Journal of Aerosol Science, 34, pp.79-98.

Fernandez de la Mora, J. F., and Loscertales, I. G. (1994): The current emitted by highly conducting Taylor cones, Journal of Fluid Mechanics, 260, pp.155-184.

Fernandez de la Mora, J. F., Navascues, J., Fernandez, F., and Rosellllompart, J. (1990): Generation of submicron monodisperse aerosols in electrosprays, Journal of Aerosol Science, 21, S673-S676.

Flagan, R. C. (1998): History of electrical aerosol measurements, Aerosol Science and Technology, 28, pp.301-380.

Flagan, R. C., Atwater, H. A., and Vahala, K. J. (1991): Fabrication of semiconductor quantum dots, Journal of Aerosol Science, 22, S31-S33.

Forsyth, B., Liu, B. Y. H., and Romay, F. J. (1998): Particle charge distribution measurement for commonly generated laboratory aerosols, Aerosol Science And Technology, 28, pp.489-501.

Gañán-Calvo, A. M., Davila, J., and Barrero, A. (1997): Current and droplet size in the electrospraying of liquids. Scaling laws, Journal of Aerosol Science, 28, pp.249-275.

Gautheron, B., Labeau, M., Delabouglise, G., and Schmatz, U. (1993): Undoped and Pd-doped SnO_2 thin-films for gas sensors, Sensors and Actuators B-Chemical, 16, pp.357-362.

Gonzalez-Carreno, T., Morales, M. P., Gracia, M., and Serna, C. J. (1993): Preparation of Uniform gamma-Fe_2O_3 Particles with Nanometer-size by Spray-pyrolysis, Materials Letters, 18, pp.151-155.

Goortani, B. M., Mendoza, N., and Proulx, P. (2006): Synthesis of SiO_2 nanoparticles in RF plasma reactors: Effect of feed rate and quench gas injection, International Journal of Chemical Reactor Engineering, 4, A33.

Grace, J. M., and Marijnissen, J. C. M. (1994): A review of liquid atomization by electrical means, Journal of Aerosol Science, 25, pp.1005-1019.

Gurav, A., Kodas, T., Pluym, T., and Xiong, Y. (1993): Aerosol processing of materials, Aerosol Science and Technology, 19, pp.411-452.

Gurav, A. S., Kodas, T. T., Wang, L. M., Kauppinen, E. I., and Joutsensaari, J. (1994): Generation of nanometer-size fullerene particles via vapor condensation, Chemical Physics Letters, 218, pp.304-308.

Gutsch, A., Kramer, M., Michael, G., Muhlenweg, H., Pridohl, M., and Zimmerman, G. (2002): Gas phase production of nanoparticles, KONA Powder and Particle Journal, 20, pp.24-37.

Haaf, W. (1980): Accurate measurements of aerosol size distribution - II. Construction of a new plate condenser electric mobility analyzer and first results, Journal of Aerosol Science, 11, pp.201-212.

Hafiz, J., Mukherjee, R., Wang, X., Heberlein, J. V. R., McMurry, P. H., and Girshick, S. L. (2006): Analysis of nanostructured coatings synthesized by ballistic impaction of nanoparticles, Thin Solid Films, 515, pp.1147-1151.

Hampsey, J. E., Arsenault, S., Hu, Q. Y., and Lu, Y. F. (2005): One-step synthesis of mesoporous metal-SiO_2 particles by an aerosol-assisted self-assembly process, Chemistry Of Materials, 17, pp.2475-2480.

Hartman, R. P. A., Brunner, D. J., Camelot, D. M. A., Marijnissen, J. C. M., and Scarlett, B. (1999): Electrohydrodynamic atomization in the cone-jet mode physical modeling of the liquid cone and jet, Journal of Aerosol Science, 30, pp.823-849.

Hartman, R. P. A., Brunner, D. J., Camelot, D. M. A., Marijnissen, J. C. M., and Scarlett, B. (2000): Jet break-up in electrohydrodynamic atomization in the cone-jet mode, Journal of Aerosol Science, 31, pp.65-95.

He, M. L., Marzocca, P., and Dhaniyala, S. (2007): A new high performance battery-operated electrometer, Review of Scientific Instruments, 78.

Heidenreich, S., Buttner, H., and Ebert, F. (2003): Aerosols and their technical significance, Chemie Ingenieur Technik, 75, pp.1787-1809.

Helsper, C., Molter, W., Loffler, F., Wadenpohl, C., Kaufmann, S., and Wenninger, G. (1993): Investigations of a new aerosol generator for the production of carbon aggregate particles, Atmospheric Environment, 27, pp.1271-1275.

Hinds, W. C. (1999): “Aerosol Technology: Properties, Behavior, and Measurements of Airborne Particles”, Wiley.

Hoppel, W. A. (1978): Determination of the aerosol size distribution from the mobility distribution of the charged fraction of aerosols, Journal of Aerosol Science, 9, pp.41-54.

Horvath, H., and Gangl, M. (2003): A low-voltage spark generator for production of carbon particles, Journal of Aerosol Science, 34, pp.1581-1588.

Hull, P. J., Hutchison, J. L., Salata, O. V., and Dobson, P. J. (1997): Synthesis of nanometer-scale silver crystallites via a room-temperature electrostatic spraying process, Advanced Materials, 9, pp.413&.

Ishigaki, T., Oh, S.-M., Li, J.-G., and Park, D.-W. (2005): Controlling the synthesis of TaC nanopowders by injecting liquid precursor into RF induction plasma, Science and Technology of Advanced Materials, 6, pp.111-118.

Jaworek, A., and Sobczyk, A. T. (2008): Electrospraying route to nanotechnology – An overview, Journal of Electrostatics, 66, pp.197-219.

Jensen, J. R., Johannessen, T., Wedel, S., and Livbjerg, H. (2000): Preparation of ZnO-Al_2O_3 particles in a premixed flame, Journal of Nanoparticle Research, 2, pp.363-373.

Jensen, J. R., Johannessen, T., Wedel, S., and Livbjerg, H. (2003): A study of $Cu/ZnO/Al_2O_3$ methanol catalysts prepared by flame combustion synthesis, Journal of Catalysis, 218, pp.67-77.

Jiang, J., Chen, D. R., and Biswas, P. (2007): Synthesis of nanoparticles in a flame aerosol reactor with independent and strict control of their size, crystal phase and morphology, Nanotechnology, 18.

Jidenko, N., and Borra, J. P. (2004): Nanoparticles production by filamentary discharges in air at atmospheric pressure, Journal of Aerosol Science, 35, pp.29-40.

Johannessen, T., Pratsinis, S. E., and Livbjerg, H. (2000): Computational fluid-particle dynamics for the flame synthesis of alumina particles, Chemical Engineering Science, 55, pp.177-191.

Johannessen, T., Pratsinis, S. E., and Livbjerg, H. (2001): Computational analysis of coagulation and coalescence in the flame synthesis of titania particles, Powder Technology, 118, pp.242-250.

Johnson, T., Caldow, R., Pöcher, A., Mirme, A., and Kittelson, D. B. (2004): A new electrical mobility particle sizer spectrometer for engine exhaust particle measurements, SAE-2004-01-1341.

Johnston, G. P., Muenchausen, R., Smith, D. M., Fahrenholtz, W., and Foltyn, S. (1992): Reactive Laser Ablation Synthesis of Nanosize Alumina Powder, Journal of The American Ceramic Society, 75, pp.3293-3298.

Ju, J., Yamagata, Y., Ohmori, H., and Higuchi, T. (2008): High-frequency surface acoustic wave atomizer, Sensors and Actuators, A: Physical, 145-146, pp.437-441.

Jung, J. H., Cheol Oh, H., Soo Noh, H., Ji, J. H., and Soo Kim, S. (2006): Metal nanoparticle generation using a small ceramic heater with a local heating area, 37, p.1662.

Kammler, H. K., Jossen, R., Morrison, P. W., Pratsinis, S. E., and Beaucage, G. (2003): The effect of external electric fields during flame synthesis of titania, Powder Technology, 135, pp.310-320.

Kammler, H. K., Mueller, R., Senn, O., and Pratsinis, S. E. (2001): Synthesis of silica-carbon particles in a turbulent H-2-air flame aerosol reactor, AICHE Journal, 47, pp.1533-1543.

Kammler, H. K., and Pratsinis, S. E. (2000): Electrically-assisted flame aerosol synthesis of fumed silica at high production rates, Chemical Engineering And Processing, 39, pp.219-227.

Kang, Y. C., and Park, S. B. (1996): Preparation of nanometre size oxide particles using filter expansion aerosol generator, Journal of Materials Science, 31, pp.2409-2416.

Kang, Z. T., Arnold, B., Summers, C. J., and Wagner, B. K. (2006): Synthesis of silicon quantum dot buried SiO_x films with controlled luminescent properties for solid-state lighting, Nanotechnology, 17, pp.4477-4482.

Kato, M. (1976): Preparation of ultrafine particles of refractory oxides by gas evaporation method, Japanese Journal of Applied Physics, 15, pp.757-760.

Kaya, C., He, J. Y., Gu, X., and Butler, E. G. (2002): Nanostructured ceramic powders by hydrothermal synthesis and their applications, Microporous Mesoporous Mat., 54, pp.37-49.

Kelvin, L. (1871): Hydrokinetic solutions and observations, Philos. Mag., 42, pp.362-377.

Kennedy, M. K., Kruis, F. E., and Fissan, H. (2000): Gas phase synthesis of size selected SnO_2 nanoparticles for gas sensor applications, Metastable, Mechanically Alloyed And Nanocrystalline Materials, Pts 1 And 2, pp.949-954.

Keskinen, H., Makela, J. M., Vippola, M., Nurminen, M., Liimatainen, J., Lepisto, T., and Keskinen, J. (2004): Generation of silver/palladium nanoparticles by liquid flame spray, Journal of Materials Research, 19, pp.1544-1550.

Kim, J. T., and Chang, J. S. (2005): Generation of metal oxide aerosol particles by a pulsed spark discharge technique, Journal of Electrostatics, 63, pp.911-916.

Knutson, E. O., and Whitby, K. T. (1975): Aerosol classification by electric mobility: Apparatus, theory, and applications, Journal of Aerosol Science, 6, pp.443-451.

Kovacik, P., Biskos, G., and Schmidt-Ott, A. (2008): Hydrogen sensor based on palladium nanoparticles, European Aerosol Conference.

Kruis, F. E., Fissan, H., and Peled, A. (1998): Synthesis of nanoparticles in the gas phase for electronic, optical and magnetic applications - A review, Journal of Aerosol Science, 29, pp.511-535.

Kruis, F. E., Fissan, H., and Rellinghaus, B. (2000): Sintering and evaporation characteristics of gas-phase synthesis of size-selected PbS nanoparticles, Materials Science And Engineering B-Solid State Materials For Advanced Technology, 69, pp.329-334.

Ku, B. K., and Maynard, A. D. (2006): Generation and investigation of airborne silver nanoparticles with specific size and morphology by homogeneous nucleation, coagulation and sintering, 37, p.452.

Kunhardt, E. E. (2000): Generation of large volume, atmospheric pressure, non-equilibrium plasmas, IEEE Transactions on Plasma Science, 28, pp.189-200.

Kurosawa, M., Watanabe, T., Futami, A., and Higuchi, T. (1995): Surface acoustic wave atomizer, Sensors and Actuators, A: Physical, 50, pp.69-74.

Labeau, M., Gaskov, A. M., Gauthero, B., and Senateur, J. P. (1994): Synthesis of Pd-doped SnO_2 films on silicon and interaction with ethanol and CO, Thin Solid Films, 248, pp.6-11.

Labeau, M., Gautheron, B., Cellier, F., Valletregi, M., Garcia, E., and Calbet, J. M. G. (1993): Pt nanoparticles dispersed on SnO_2 thin-films - A microstructural study, Journal of Solid State Chemistry, 102, pp.434-439.

Laine, R. M., Baranwal, R., Hinklin, T., Treadwell, D., Sutorik, A., Bickmore, C., Waldner, K., and Neo, S. S. (1999): Making nanosized oxide powders from precursors by flame spray pyrolysis, Novel Synthesis And Processing Of Ceramics, pp.17-24.

Lang, R. J. (1962): Ultrasonic atomization of liquids, Journal of the Acoustical Society of America, 34, pp.6-&.

Lee, K. K., Kang, Y. C., Jung, K. Y., and Kim, J. H. (2005): Preparation of nano-sized $BaTiO_3$ particle by citric acid-assisted spray pyrolysis, Journal of Alloys And Compounds, 395, pp.280-285.

Leeuwenburgh, S. C. G., Heine, M. C., Wolke, J. G. C., Pratsinis, S. E., Schoonman, J., and Jansen, J. A. (2006): Morphology of calcium phosphate coatings for biomedical applications deposited using electrostatic spray deposition, Thin Solid Films, 503, pp.69-78.

Lehtinen, K. E. J., Backman, U., Jokiniemi, J. K., and Kulmala, M. (2004): Three-body collisions as a particle formation mechanism in silver nanoparticle synthesis, Journal of Colloid And Interface Science, 274, pp.526-530.

Lei, H., Tang, Y., Li, J., Luo, J., and Li, X.（2006）： In situ organic coating of metal nanoparticles.” Applied Physics Letters, 88, 083111.

Lenggoro, I. W., Hata, T., Iskandar, F., Lunden, M. M., and Okuyama, K. (2000): An experimental and modeling investigation of particle production by spray pyrolysis using a laminar flow aerosol reactor, Journal of Materials Research, 15, pp.733-743.

Lenggoro, I. W., Itoh, Y., Iida, N., and Okuyama, K. (2003): Control of size and morphology in NiO particles prepared by a low-pressure spray pyrolysis, Materials Research Bulletin, 38, pp.1819-1827.

Lenggoro, I. W., Okuyama, K., Fernandez de la Mora, J. F., and Tohge, N. (2000): Preparation of ZnS nanoparticles by electrospray pyrolysis, Journal of Aerosol Science, 31, pp.121-136.

Liu, B. Y. H., and Lee, K. W. (1975): Aerosol generator of high stability, American Industrial Hygiene Association Journal, 36, pp.861-865.

Liu, B. Y. H., and Pui, D. Y. H. (1974): A submicron aerosol standard and the primary, absolute calibration of the condensation nuclei counter, Journal of Colloid & Interface Science, 47, pp.155-171.

Mädler, L., Kammler, H. K., Mueller, R., and Pratsinis, S. E. (2002): Controlled synthesis of nanostructured particles by flame spray pyrolysis, Journal of Aerosol Science, 33, pp.369-389.

Mädler, L., Stark, W. J., and Pratsinis, S. E. (2002): Rapid synthesis of stable ZnO quantum dots, Journal of Applied Physics, 92, pp.6537-6540.

Magnusson, M. H., Deppert, K., Malm, J. O., Bovin, J. O., and Samuelson, L. (1999): Size-selected gold nanoparticles by aerosol technology, Nanostructured Materials, 12, pp.45-48.

Mahoney, W., and Andres, A. P. (1995): Aerosol synthesis of nanoscale clusters using atmospheric arc evaporation, Materials Science and Engineering A, 204, pp.160-164.

Marijnissen, J. C. M., Yurteri, C. U., van Erven, J., and

Ciach, T. (2008): Medicine Nanoparticle Production by EHDA, Proceedings of Workshop on Environmental and Medical Aerosol Nanoparticles and their Interaction with the Respiratory System, L. Gradon J. Marijnissen, ed., Springer, Warshaw (in print).

Marino, E., Huijser, T., Creyghton, Y., and van der Heijden, A. (2007): Synthesis and coating of copper oxide nanoparticles using atmospheric pressure plasmas, Surface & Coatings Technology, 201, pp.9205-9208.

May, K. R. (1973): The collison nebulizer: Description performance and application, Journal Of Aerosol Science, 4, pp.235-243.

McMurry, P. H. (2000): A review of atmospheric aerosol measurements, Atmospheric Environment, 34, pp.1959-1999.

Medalia, A. I. (1978): Effect of carbon-black on dynamic properties of rubber vulcanizates, Rubber Chem. Technol., 51, pp.437-523.

Mesbah, B., Fitzgerald, B., Hopke, P. K., and Pourprix, M. (1997): A new technique to measure the mobility size of ultrafine radioactive particles, Aerosol Science and Technology, 27, pp.381-393.

Messing, G. L., Zhang, S. C., and Jayanthi, G. V. (1993): Ceramic powder synthesis by spray-pyrolysis, Journal of the American Ceramic Society, 76, pp.2707-2726.

Mikhailov, E., Vlasenko, S., Niessner, R., and Poschl, U. (2004): Interaction of aerosol particles composed of protein and salts with water vapor: Hygroscopic growth and microstructural rearrangement, Atmospheric Chemistry and Physics, 4, pp.323-350.

Mueller, R., Jossen, R., Pratsinis, S. E., Watson, M., and Akhtar, M. K. (2004): Zirconia nanoparticles made in spray flames at high production rates, Journal Of The American Ceramic Society, 87, pp.197-202.

Mueller, R., Kammler, H. K., Pratsinis, S. E., Vital, A., Beaucage, G., and Burtscher, P. (2004): Non-agglomerated dry silica nanoparticles, Powder Technology, 140, pp.40-48.

Müller, U., Schmidt-Ott, A., and Burtscher, H. (1987): 1st Measurement Of Gas-Adsorption To Free Ultrafine Particles - O_2 On Ag, Physical Review Letters, 58, pp.1684-1686.

Müller, U., Schmidt-Ott, A., and Burtscher, H. (1987): First measurement of gas-adsorption to free ultrafine particles - O_2 on Ag, Physical Review Letters, 58, pp.1684-1686.

Nagashima, K., Himeda, T., and Kato, A. (1991): Properties of conductive films made from fine spherical silver palladium alloy particles, Journal of Materials Science, 26, pp.2477-2482.

Nasibulin, A. G., Moisala, A., Brown, D. P., Jiang, H., and Kauppinen, E. I. (2005): A novel aerosol method for single walled carbon nanotube synthesis, Chemical Physics Letters, 402, pp.227-232.

Nowling, G. R., Babayan, S. E., V., J., and R.F., H. (2002): Remote plasma-enhanced chemical vapour deposition of silicon nitride at atmospheric pressure, Plasma Sources Science and Technology, 11, pp.97-103.

Ogawa, H., Abe, A., Nishikawa, M., and Hayakawa, S. (1981): Electrical properties of tin oxide ultrafine particle films, Journal of the Electrochemical Society, 128, pp.2020-2025.

Ogawa, H., Abe, A., Nishikawa, M., and Hayakawa, S. (1981): Preparation of tin oxide-films from ultrafine particles, Journal of The Electrochemical Society, 128, pp.685-689.

Ogawa, K., Vogt, T., Ullmann, M., Johnson, S., and Friedlander, S. K. (2000): Elastic properties of nanoparticle chain aggregates of TiO_2, Al_2O_3, and Fe_2O_3 generated by laser ablation, Journal of Applied Physics, 87, pp.63-73.

Oh, H., Ji, J., Jung, J., and Kim, S. (2007): Synthesis of titania nanoparticles via spark discharge method using air as a carrier, Eco-Materials Processing and Design Viii, pp.544-545, pp.143-146.

Peineke, C., Attoui, M., Robles, R., Reber, A. C., Khanna, S. N., and Schmidt-Ott, A. (2008), A step towards chemistry with atomic clusters, submitted.

Peineke, C., Attoui, M. B., and Schmidt-Ott, A. (2006): Using a glowing wire generator for production of charged, uniformly sized nanoparticles at high concentrations, Journal of Aerosol Science, 37, pp.1651-1661.

Peineke, C., and Schmidt-Ott, A. (2008): Explanation of charged nanoparticle production from hot surfaces, Journal of Aerosol Science, 39, pp.244-252.

Poizot, P., Laruelle, S., Grugeon, S., Dupont, L., and Tarascon, J. M. (2000): Nano-sized transition-metaloxides as negative-electrode materials for lithium-ion batteries, Nature, 407, pp.496-499.

Pratsinis, S. E. (1998): Flame aerosol synthesis of ceramic powders, Progress In Energy And Combustion Science, 24, pp.197-219.

Pratsinis, S. E., and Mastrangelo, S. V. R. (1989): Material synthesis in aerosol reactors, Chemical Engineering Progress, 85, pp.62-66.

Prost, W., Kruis, F. E., Otten, F., Nielsch, K., Rellinghaus, B., Auer, U., Peled, A., Wassermann, E. F., Fissan, H., and Tegude, F. J. (1998): Monodisperse aerosol particle deposition: Prospects for nanoelectronics, Microelectronic Engineering, 42, pp.535-538.

Rao, N., Girshick, S., Heberlein, J., McMurry, P., Jones, S., Hansen, D., and Micheel, B. (1995): Nanoparticle formation using a plasma expansion process, Plasma Chemistry and Plasma Processing, 15, pp.581-606.

Rayleigh, L. (1883): On the crispations of fluid resting upon a vibrating support, Phil. Mag., 16, pp.50-58.

Reece Roth, J. (1995): "Industrial plasma engineering. Volume 1- Principles", Institute of Physics Publishing, Bristol.

Renault, O., Tadeev, A. V., Delabouglise, G., and Labeau, M. (1999): Integrated solid-state gas sensors based on SnO_2(Pd) for CO detection, Sensors and Actuators B-Chemical, 59, pp.260-264.

Rohmann, H. (1923): Methode zur Messung der Grösse von Schwebeteilchen, Zeitschrift für Physik, 17, pp.253-265 (In German).

Rosell-Lompart, J., and Fernandez de la Mora, J. F. (1994): Generation of monodisperse droplets 0.3 to 4 μm in diameter from electrified cone-jets of highly conducting and viscous-liquids, Journal of Aerosol Science, 25, pp.1093-1119.

Roth, C., Ferron, G. A., Karg, E., Lentner, B., Schumann, G., Takenaka, S., and Heyder, J. (2004): Generation of ultrafine particles by spark discharging, Aerosol Science and Technology, 38, pp.228-235.

Rulison, A. J., and Flagan, R. C. (1994): Synthesis of yttria powders by electrospray pyrolysis, Journal of the American Ceramic Society, 77, pp.3244-3250.

Salata, O. V. (2004): Applications of nanoparticles in biology and medicine, Journal of Nanobiotechnology, 2, p.3.

Sasaki, T., Terauchi, S., Koshizaki, N., and Umehara, H. (1998): The preparation of iron complex oxide nanoparticles by pulsed-laser ablation, Applied Surface Science, 129, pp.398-402.

Scheibel, H. G., and Porstendörfer, J. (1983): Generation of monodisperse Ag- and NaCl-aerosols with particle diameters between 2 and 300 nm, J. Aerosol Sci., 14, pp.113-126.

Schlapbach, L., and Zuttel, A. (2001): Hydrogen-storage materials for mobile applications, Nature, 414, pp.353-358.

Schmidt-Ott, A. (1988): New approaches to in situ characterization of ultrafine agglomerates, 19, p.553.

Schmidt-Ott, A., Marsen, B., and Sattler, K. (1997): Characterizing nanoparticles by scanning tunneling microscopy and scanning tunnelling spectroscopy, Journal of Aerosol Science, 28, S729-S730.

Schmidt-Ott, A., Schurtenberger, P., and Siegmann, H. C. (1980): Enormous yield of photoelectrons from small particles, Physical Review Letters, 45, pp.1284-1287.

Schwyn, S., Garwin, E., and Schmidt-Ott, A. (1988): Aerosol generation by spark discharge, 19, p.639.

Shimada, M., Seto, T., and Okuyama, K. (1994): Size change of very fine silver agglomerates by sintering in a heated flow, Journal of Chemical Engineering of Japan, 27, pp.795-802.

Sinclair, D., and Hoopes, G. S. (1975): A continuous flow condensation nucleus counter, Journal of Aerosol Science, 6, pp.1-7.

Smith, J. N., Flagan, R. C., and Beauchamp, J. L. (2002): Droplet evaporation and discharge dynamics in electrospray ionization, Journal of Physical Chemistry A, 106, pp.9957-9967.

Spicer, P. T., Artelt, C., Sanders, S., and Pratsinis, S. E. (1998): Flame synthesis of composite carbon black-fumed silica nanostructured particles, Journal Of Aerosol Science, 29, pp.647-659.

Sproson, D. W., Messing, G. L., and Gardner, T. J. (1986): Powder synthesis for electronic ceramics by evaporative decomposition of solutions, Ceramics International, 12, pp.3-7.

Stark, W. J., Pratsinis, S. E., and Baiker, A. (2002): Heterogeneous catalysis by flame-made nanoparticles, Chimia, 56, pp.485-489.

Stark, W. J., Wegner, K., Pratsinis, S. E., and Baiker, A. (2001): Flame aerosol synthesis of vanadia-titania nanoparticles: Structural and catalytic properties in the selective catalytic reduction of NO by NH_3, Journal of Catalysis, 197, pp.182-191.

Strobel, R., Baiker, A., and Pratsinis, S. E. (2006): Aerosol flame synthesis of catalysts, Advanced Powder Technology, 17, pp.457-480.

Strobel, R., and Pratsinis, S. E. (2007): Flame aerosol synthesis of smart nanostructured materials, Journal of Materials Chemistry, 17, pp.4743-4756.

Suzuki, M., Kagawa, M., Syono, Y., and Hirai, T. (1992): Synthesis of ultrafine single-component oxide particles by the spray-ICP technique, Journal of Materials Science, 27, pp.679-684.

Swihart, M. T. (2003): Vapor-phase synthesis of nanoparticles, Current Opinion in Colloid & Interface Science, 8, pp.127-133.

Tabrizi, N. S., Ullmann, M., Vons, V. A., and Schmidt-Ott, A. (2008a), Generation of nanoparticles by spark discharge, Journal of Nanoparticle Research, in press.

Tabrizi, N. S., Xu, Q., VanderPers, N., Lafont, U., and Schmidt-Ott, A. (2008b): Synthesis of mixed metallic nanoparticles by spark discharge, to be submitted (J. Nanoparticle Research).

Tabrizi, N. S., Xu, Q., VanderPers, N., and Schmidt-Ott, A. (2008c): Generation of mixed metallic nanoparticles from immiscible metals by spark discharge, to be submitted (J. Nanoparticle Research).

Tadeev, A. V., Delabouglise, G., and Labeau, M. (1998): Influence of Pd and Pt additives on the microstructural and electrical properties of SnO_2-based sensors, Materials Science And Engineering B-Solid State Materials For Advanced Technology, 57, pp.76-83.

Tammet, H., Mire, A., and Tamm, E. (1998): Electrical aerosol spectrometer of Tartu University, Journal of Aerosol Science. VOL29, S427-S428.

Tammet, H., Mire, A., and Tamm, E. (2002): Electrical aerosol spectrometer of Tartu University, Atmospheric Research, 62, pp.315-324.

Tammet, H. F. (1970): The aspiration method for the determination of atmospheric-ion spectra, Keter Press.

Tang, K. Q., and Gomez, A. (1995): Generation of monodisperse water droplets from electrosprays in a corona-assisted cone-jet mode, Journal of Colloid and Interface Science, 175, pp.326-332.

Tartaj, P., Morales, M. D., Veintemillas-Verdaguer, S., Gonzalez-Carreno, T., and Serna, C. J. (2003): The preparation of magnetic nanoparticles for applications in biomedicine, Journal of Physics D-Applied Physics, 36, R182-R197.

Taylor, G. (1964): Disintegration of water drops in electric field, Proceedings of the Royal Society of London series A-Mathematical and physical sciences, 280, p.383.

Teleki, A., Bjelobrk, N., and Pratsinis, S. E. (2008): Flame-made Nb- and Cu-doped TiO_2 sensors for CO and ethanol, Sensors And Actuators B-Chemical, 130, pp.449-457.

Tsai, C. J., Lin, J. S., Deshpande, C. G., and Liu, L. C. (2006): Electrostatic charge measurement and charge neutralization of fine aerosol particles during the generation process, Particle & Particle Systems Characterization, 22, pp.293-298.

Tsantilis, S., Kammler, H. K., and Pratsinis, S. E. (2002): Population balance modeling of flame synthesis of titania nanoparticles, Chemical Engineering Science, 57, pp.2139-2156.

Ullmann, M., Friedlander, S. K., and Schmidt-Ott, A. (2002): Nanoparticle formation by laser ablation, Journal of Nanoparticle Research, 4, pp.499-509.

Ulrich, G. D. (1984): Flame Synthesis of Fine Particles, Chemical & Engineering News, 62, pp.22-29.

van Erven, J., Moerman, R., and Marijnissen, J. C. M. (2005): Platinum nanoparticle production by EHDA, Aerosol Science and Technology, 39, pp.941-946.

Vemury, S., and Pratsinis, S. E. (1995): Corona-assisted flame synthesis of ultrafine titania particles, Applied Physics Letters, 66, pp.3275-3277.

Vemury, S., and Pratsinis, S. E. (1995): Dopants in flame synthesis of titania, Journal of the American Ceramic Society, 78, pp.2984-2992.

Volkening, F. A., Naidoo, M. N., Candela, G. A., Holtz, R. L., and Provenzano, V. (1995): Characterization of nanocrystalline palladium for solid state gas sensor applications, 5, p.373.

Vollath, D., and Sickafus, K. (1992): Synthesis of nanosized ceramic oxide powders by microwave plasma reactions, Nanostructured Materials, 1, pp.427-437.

Vollath, D., and Szabo, D. V. (1999): Coated nanoparticles: A new way to improved nanocomposites, Journal of Nanoparticle Research, 1, pp.235-242.

Vollath, D., and Szabo, D. V. (2005): The microwave plasma process - a versatile process to synthesise nanoparticulate materials, Journal of Nanoparticle Research, 8, pp.417-428.

Vons, V., Creyghton, Y., and Schmidt-Ott, A. (2006): Nanoparticle production using atmospheric pressure cold plasma, Journal of Nanoparticle Research, 8, pp.721-728.

Wang, M. J., Lu, S. X., and Mahmud, K. (2000): Carbon-silica dual-phase filler, a new-generation reinforcing agent for rubber. Part VI. Time-temperature superposition of dynamic properties of carbon-silica-dual-phase-filler-filled vulcanizates, Journal of Polymer Science Part B-Polymer Physics, 38, pp.1240-1249.

Wang, S. C., and Flagan, R. C. (1990): Scanning electrical mobility spectrometer, Aerosol Science and Technology, 13, pp.230-240.

Weber, A. P., Davoodi, P., Seipenbusch, M., and Kasper, G. (2006): Catalytic behavior of nickel nanoparticles: gasborne vs. supported state, Journal of Nanoparticle Research, 8, pp.445-453.

Weigle, J. C., Luhrs, C. C., Chen, C. K., Perry, W. L., Mang, J. T., Nemer, M. B., Lopez, G. P., and Phillips, J. (2004): Generation of aluminum nanoparticles using an atmospheric pressure plasma torch, Journal of Physical Chemistry B, 108, pp.18601-18607.

Whitby, K. T., and Clark, W. E. (1966): Electric aerosol particle counting and size distribution measuring system for the 0.015 to 1 μ size range, Tellus, 18, pp.573-586.

Wiedensohler, A., Hansson, H. C., Maximov, I., and Samuelson, L. (1992): Nanometer patterning of InP using aerosol and plasma-etching techniques, Applied Physics Letters, 61, pp.837-839.

Wilhelm, O., Mädler, L., and Pratsinis, S. E. (2003): Electrospray evaporation and deposition, Journal Of Aerosol Science, 34, pp.815-836.

Wilhelm, O., Pratsinis, S. E., Perednis, D., and Gauckler, L. J. (2005): Electrospray and pressurized spray deposition of yttria-stabilized zirconia films, Thin Solid Films, 479, pp.121-129.

Winklmayr, W., Reischl, G. P., Lindner, A. O., and Berner, A. (1991): A New Electromobility Spectrometer for the Measurement of Aerosol Size Distributions in the Size Range from 1 to 1000 nm, Journal of Aerosol Science, 22, pp.289-296.

Wood, R. W., and Loomis, A. L. (1927): The physical and biological effects of high frequency sound waves of great intensity, Philos. Mag., 4, pp.417-436.

Ye, R., Li, J.-G., and Ishigaki, T.（2007）: Controlled synthesis of alumina nanoparticles using inductively coupled thermal plasma with enhanced quenching, Thin Solid Films, 515, pp.4251-4257.

Yule, A. J., and Al-Suleimani, Y. (2000): On droplet formation from capillary waves on a vibrating surface, Proceedings of the Royal Society A: Mathematical, Physical and Engineering Sciences, 456, pp.1069-1085.

Zaluska, A., Zaluski, L., and Strom-Olsen, J. O. (2001): Structure, catalysis and atomic reactions on the nanoscale: a systematic approach to metal hydrides for hydrogen storage, Applied Physics A-Materials Science & Processing, 72, pp.157-165.

Zeleny, J. (1900): The velocity of the ions produced in gases by Röntgen rays, Philosophical Transactions, 195, pp.193-234.

Zeleny, J. (1914): The electrical discharge from liquid points, and a hydrostatic method of measuring the electric intensity at their surfaces, Physical Review, 3, pp.69-91.

Zeleny, J. (1917): Instability of electrified liquid surfaces, Physical Review, 10, pp.1-6.

Zeleny, J. (1929): The distribution of mobilities of ions in moist air, Physical Review, 34, pp.310-334.

Zhang, S.-H., Aksutsu, Y., Russel, L. M., Flagan, R. C., and Seinfeld, J. H. (1995): Radial differential mobility analyzer, Aerosol Science and Technology, 23, pp.357-372.

Author's short biography

George Biskos

George Biskos is an Assistant Professor at the Department of Environmental Studies at the University of the Aegean, and a Visiting Assistant Professor at the Department of Chemical Technology at Delft University of Technology. Previously he was a Research Associate at the School of Engineering and Applied Sciences at Harvard University. He holds a Ph.D. (2004) in Engineering from Cambridge University, and an M.Sc. (2000) in Environmental Engineering from Imperial College, UK. His research interests are in the broader area of aerosol science and technology, ranging from development of instrumentation for measuring airborne particles, to atmospheric aerosol chemistry and aerosol based nanotechnology.

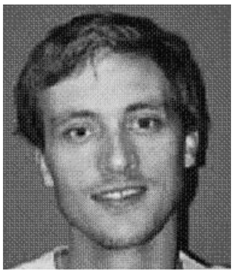

Vincent Vons

Vincent Vons is a Ph.D. student at the Department of Chemical Technology at Delft University of Technology. He holds a Bachelor's degree in Chemical Technology and Bioprocestechnology, and a Master's degree (with honours) in Chemical Technology, also from Delft University of Technology. He has worked on atmospheric pressure cold plasma nanoparticle formation, using a dielectric barrier discharge. Currently he is in the final year of his Ph.D. degree on nanoparticulate metal hydride hydrogen storage using (amongst other techniques) spark discharge nanoparticle formation.

Caner U Yurteri

Caner U. Yurteri is a visiting Assistant Professor at Delft University of Technology. He received a B.S. (1987) in Mechanical Engineering from Istanbul Technical University, Istanbul, Turkey and an M.S. (1992) and PhD (1997) degrees in Mechanical Engineering from Case Western Reserve University, Cleveland, Ohio. He then joined the Chemical Engineering Department of Purdue University as a post-doctoral researcher, the Applied Science Department of the University of Arkansas at Little Rock as a research associate, Terronics Development Corporation as a research scientist, and Particle Engineering Research Center as an assistant scientist, respectively. His work extensively involved Laser Doppler and Phase Doppler Anemometry and their applications to particle-laden flows. His research interests include particle and powder technology, medical aerosols, electrostatic coating, electrospraying and out scaling of electrospraying process.

Author's short biography

Andrease Schmidt-Ott

Andreas Schmidt-Ott, born in 1952, completed his Ph.D. thesis at the Faculty of Mathematics and Physics of the Swiss Federal Institute of Technology (ETH) in Zurich, Switzerland in 1979. He was then Research Fellow at the Atmospheric Physics Department and later Senior Research Scientist at the Solid State Physics Laboratory of the same institute. In 1988 he spent a term at the Chemical Engineering Department of the University of California, Los Angeles (S.K. Friedlander) as a Visiting Assistant Professor before joining Duisburg University (Germany). Here he was first Assistant Professor at the Faculty of Electrical Engineering and then became professor in the Mechanical Engineering Dept. of the same University. Between 1996 and 1997 he spent a 5-month sabbatical with K. Sattler at the Physics Dept. (Nanophysics Group) of the University of Hawaii at Manoa. He was Deputy Chair of the Mechanical Engineering Faculty at Duisburg University 1998 - 2001. Since March 2001 he is a Professor of Particle Technology in the Nanostructured Materials Section at Delft University of Technology, Netherlands. He served as Secretary General of the German Aerosol Association (GAeF) and Board Member of the American Association for Aerosol Research (AAAR). He is or was a member of several Editorial Boards of journals. His most prestigious award was the Smoluchowski Award, which he obtained in 1989.

Update on The Science and Technology of Diesel Particulate Filters[†]

Athanasios G. Konstandopoulos[1,2*] **and Eleni Papaioannou**[1]
Aerosol & Particle Technology Laboratory[1]
Department of Chemical Engineering, Aristotle University of Thessaloniki[2]

Abstract

As diesel emission regulations become more stringent, diesel particulate filters (DPFs) have become possibly the most important and complex diesel emission control device. This paper provides an update on the science and technology of diesel particulate emission control, drawing from the results of many research projects carried out by the authors in collaboration with the automotive industry and its suppliers. Both fundamental as well as application-oriented approaches are presented to study the physicochemical characteristics of diesel soot particles and soot deposits formed in DPFs, which are viewed as multifunctional separators/reactors. Theroretical and experimental aspects of filtration efficiency, pressure drop, ash accumulation and soot reactivity (with emphasis on catalyst-assisted soot oxidation) are addressed, employing systems ranging from small-scale filter samples to full-scale devices installed in the exhaust system of diesel engines. Properly combined, the current state of knowledge, experimental methods and simulation approaches all provide a rational and systematic route for enhancing the design and reliability of future diesel particulate emission control systems.

Keywords: diesel particulate filter, emission control, filtration, soot, catalytic oxidation, simulation

1. Introduction

Advanced fuel injection technology in conjunction with an inherent high thermal efficiency have led to an increased market share of diesel-powered vehicles especially in Europe, and the trend is expected to continue assuming the diesel engine is able to meet ever more stringent emission limits in the future. This is dependent on the employment of cost-efficient, advanced emission control systems for particulate and NO_x emissions. However, the adverse health effects of combustion-generated nanoparticles such as diesel soot generate a highly visible public debate where the role of aerosol scientists and technologists becomes very important both in terms of measurement and assessment technologies as well as technological solution developers/providers.

Particulate emission control entails measures to reduce both the solid (soot) particle emissions and the liquid particle (droplet) emissions formed due to condensation of the exhaust as it cools down. The latter can be easily reduced by regulating their precursors (reducing the fuel sulfur level and installing advanced diesel oxidation catalysts to oxidize the complete spectrum of hydrocarbon (HC) emissions). The solid soot emissions, however, remain intimately connected with the nature of the diesel combustion process, and their reduction can be achieved either by in-cylinder measures improving the combustion process itself, or by employing aftertreatment systems such as diesel particulate filters (DPFs). As diesel emission regulations become more stringent, the use of DPFs increases progressively in both light-duty/passenger car and heavy-duty/commercial vehicle applications. DPFs represent an important and highly complex type of multifunctional chemical reactor combining multiphase, separation, chemical reactions and material transformations over many disparate temporal and spatial scales (**Fig. 1**).

Modern DPFs exhibit very high filtration efficien-

[†] Accepted: August 23, 2008

[1] CERTH/CPERI, PO Box 361, Thermi, 57001 Thessaloniki, Greece.
[2] Thessaloniki, Greece
[*] Corresponding author
E-mail: agk@cperi.certh.gr

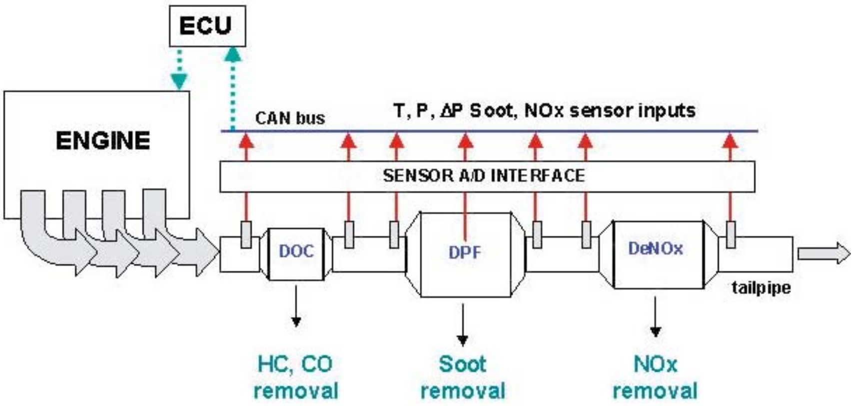

Fig. 1 Example of integrated soot-NO_x emission control system. DPF stands for diesel particulate filter. Sensory inputs of temperature (T), pressure (P), pressure drop (ΔP), soot and NO_x concentration will be required along the exhaust pipe.

cies, however, they need to be periodically cleaned (regenerated) in order to achieve efficient and safe operation of the vehicle. As typical diesel exhaust conditions are not hot enough to initiate and maintain particulate (soot) oxidation, active (engine) means are employed to raise the exhaust gas temperature up to the point that particulate oxidation can be self-sustained in the filter at fast enough rates (>650 C). To achieve the oxidation of soot particles at lower temperatures (250 – 550 C), a number of direct and indirect catalytic measures can be employed ranging from fuel additives, generation of reactive species, catalytic combustion of post-injected fuel and filter coatings promoting soot oxidation.

Modern trends[1, 2, 3, 4] in passenger car emission control systems are now focusing on so-called "fit-for-life" solutions, thus overcoming the need for servicing (ash removal) of the DPF during the vehicle lifetime. Robustness and durability of the engine and emission control system is also clearly a first priority in heavy-duty surface transportation. These trends pose specific challenges and create new opportunities in the area of diesel emission control technology.

State-of-the-art diesel emission control systems are complex assemblies of chemical reactors and separators, sometimes integrating different functionalities on the same monolithic support to achieve demanding requirements in space and cost, especially in passenger cars[5, 6, 7]. Such complex emission control systems require advanced simulation tools for their cost-effective design, development, system-level integration and optimization. In addition, requirements for robust on-board monitoring and control generate the need for efficient algorithms which are implementable in computationally limited engine control units (ECUs) and which will provide accurate knowledge of the state of the emission control system during vehicle operation, and which can be used in control loops for management of the integrated powertrain-emission control system.

In the present paper, we provide an overview of our work in the area of diesel particulate emission control technologies, drawing from an over ten-year participation in several research projects in collaboration with the automotive industry and its suppliers.

The structure of the paper is as follows: Initially, we discuss the physicochemical characteristics of diesel soot and then descibe the operation of a DPF as a separator, addressing its filtration efficiency and pressure drop behavior. We then discuss the operation of the DPF as a reactor and address the regeneration process (the oxidation of accumulated soot by various techniques, with emphasis on catalyst-assisted soot oxidation). Subsequently, we discuss the application of advanced simulation methods to DPF systems and provide the conclusions of this study.

2. Diesel Soot

The characterization of soot particles emitted from modern diesel engines is a prerequisite for any particulate emission control approach, and has attracted enormous interest in the literature, with some representative recent studies being those in reference[8, 9].

From a control technology point of view, we are interested in the state of the soot particles in the raw exhaust upstream of the DPF. Depending on the exhaust temperature, organic components from the lubrication oil and/or the fuel could condense on the soot particles and form the so-called soluble organic fraction (SOF) of diesel particulate. However, this is typically a phenomenon occurring upon dilution of the exhaust, sometimes leading to the formation of additional particles, the so-called nucleation mode [9]. A high-SOF-content soot is sometimes referred to as "wet soot", and a low-SOF-content soot as "dry soot". It should be noted though, that reference to the SOF content of diesel particulate matter almost always implies particulate matter sampled on a Teflon–coated filter after a relatively long residence time and a dilution process in a dilution tunnel at a temperature of 52℃ , just as the legislated sampling protocols stipulate.

It must be borne in mind that sampling lines and flame ionization analyzers for hydrocarbon emissions measurements from the exhaust typically operate at 190℃ to avoid condensation-induced sampling artifacts. In studies of diesel particulates under raw exhaust conditions using gravimetric raw exhaust sampling techniques[10], it was observed that at an exhaust temperature of 350℃ no particle-bound SOF was present.

Most modern DPF systems are preceded by a diesel oxidation catalyst (DOC), which is employed to oxidize exhaust hydrocarbons (injected in the engine cylinder or in the exhaust) and thus raise the exhaust temperature to the levels needed for DPF regeneration. The DOC almost eliminates any SOF that might be present on the soot particles, hence for the remainder of this paper, the term soot particle will imply the *predominantly solid aggregates* that exist in diesel exhaust (also known as the accumulation mode particles[9]).

The available measurements indicate that the majority of emitted solid diesel aggregate particles have electrical mobility and aerodynamic diameters in the range of 10-300 nm. Primary particle diameters are found to lie in the range of 8 to 40 nm[8, 9, 11].

The composition and morphology of diesel soot particles in the raw exhaust is very important, as this is the aerosol that challenges the DPF. The morphology of the soot particles affects the structure of deposits[12] that are formed in the DPF (hence the engine backpressure), while their composition (which is predominantly carbonaceous) affects their oxidation potential and hence the ease of DPF regeneration[13, 14, 15, 16, 17]. The substructure of soot primary particles obtained by different combustion sources and fuels has been studied by high-resolution transmission electron microscopy (TEM)[13, 14, 15, 18, 19], and it is connected to the soot reactivity.

Harris and Maricq[20] have shown that soot particle size distributions from various types of diesel engines (model years from 1995-1998), running on different fuels under a wide range of operating conditions, can be approximated by a "signature distribution" when the number-based particle size distribution (PSD) is normalized with respect to the total particle number concentration and the particle size is scaled with respect to the mean particle size. We refer to this way of presentation as Harris-Maricq (HM) coordinates. More recently[21, 22], we have measured soot size distributions from the exhaust of 5 turbo-charged, direct-injection diesel engines (model years 1997-2003) with displacements in the 1.9-2.4L range and advanced fuel-injection systems (3 common-rail, one pump unit injector, and one rotary-pump-based fuel-injection system). Particles were measured employing a Scanning Mobility Particle Sizer (SMPS) and a Long Path Multi-wavelength Extinction (LPME) analyser as described in[11], and the obtained size distributions are plotted in **Fig. 2**, in HM coordinates. The average value of σ_g for each engine (operating at several steady state points) is also given in **Fig. 2**. A remarkable constancy of σ_g is observed, $\sigma_g = 1.89 \pm 0.08$. When the Harris and Maricq[20] data are included, all data are consistent to within 4% with a constant shape for the particle size distribution with an average $\sigma_g = 1.84$. The constant shape for the size distribution arises as the steady state solution of the soot aggregate population balance that accounts for coagulation and oxidative fragmentation processes [21].

The oxidative fragmentation of soot particles has been observed in flame studies by[23] and limits further aggregate growth. The resulting soot fragments re-collide with the soot aggregates, leading to the establishment of a steady state at which point coagulation balances fragmentation and therefore the emergence of a size distribution with a "constant shape". Naturally the simultaneous occurrence of these two processes will lead to a distribution of soot aggregate morphologies. It is well known that diffusion limited cluster-cluster aggregation, (DLCCA), a much-studied growth mechanism[24, 25, 26], leads to aggregate structures with a $D_f = 1.8$, while diffusion limited aggregation (DLA) (a growth mechanism where monomers collide with clusters) leads to aggregate structures with a $D_f = 2.5$. Employing a simultaneous measurement of electrical-mobility-based and aerodynamic-diameter-based distributions, we plot in **Fig. 3** how the fractal dimension of diesel soot aggregates is distributed according to their electrical mobility diameter, as presented in[27].

We observe a very robust pattern over the different engines and operation conditions tested, namely that small soot particles have a nearly spherical/

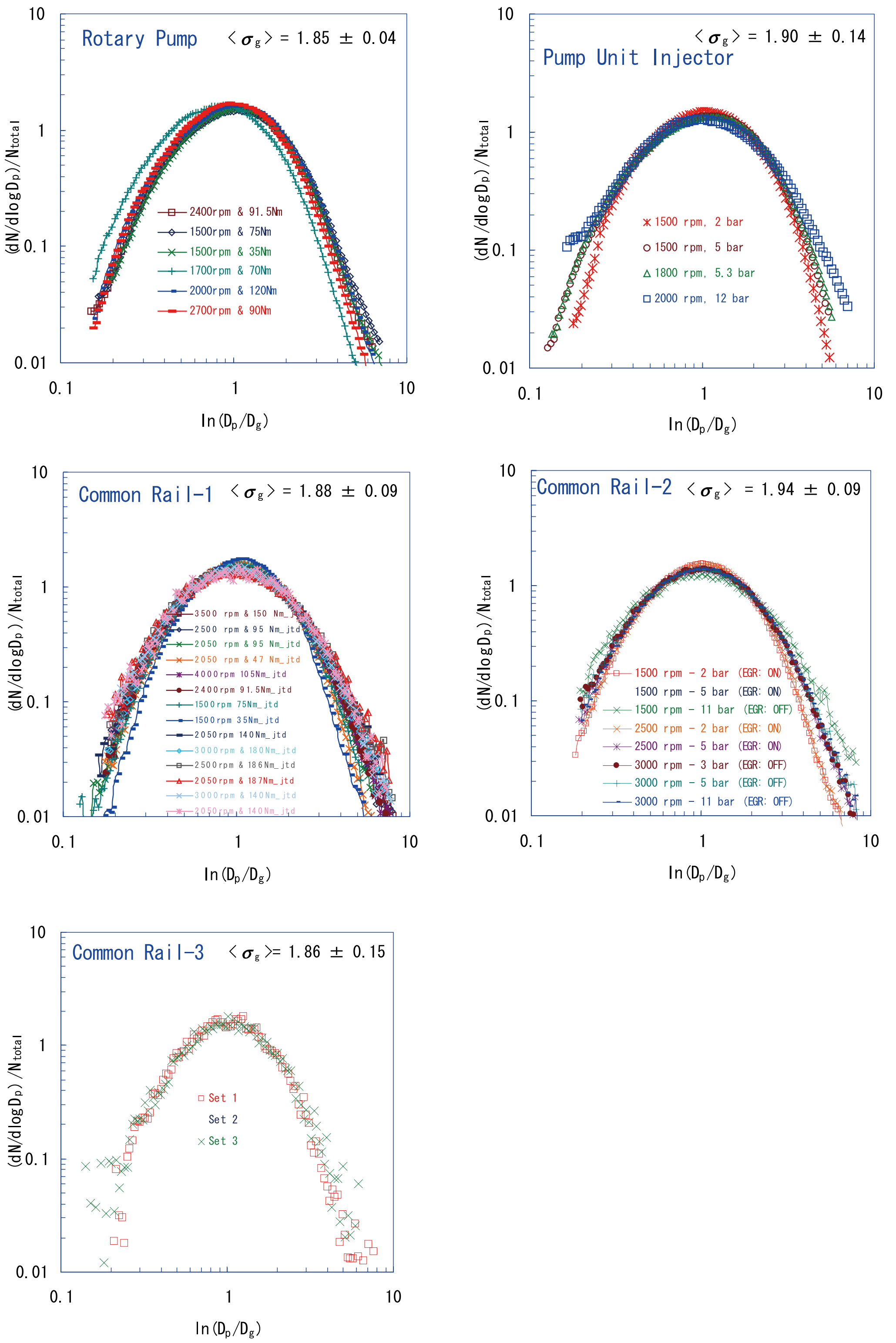

Fig. 2 Measured soot PSDs for five different engines at several operation points. N is the particle number concentration, D_p the particle diameter, D_g the geometric mean particle diameter and σ_g the geometric standard deviation of the PSD.

compact morphology (D_f = 3) which rapidly evolves toward the value D_f= 1.8 (the DLCCA limit) as the soot aggregate size increases up to about 100 nm. Then further increase of the aggregate size leads

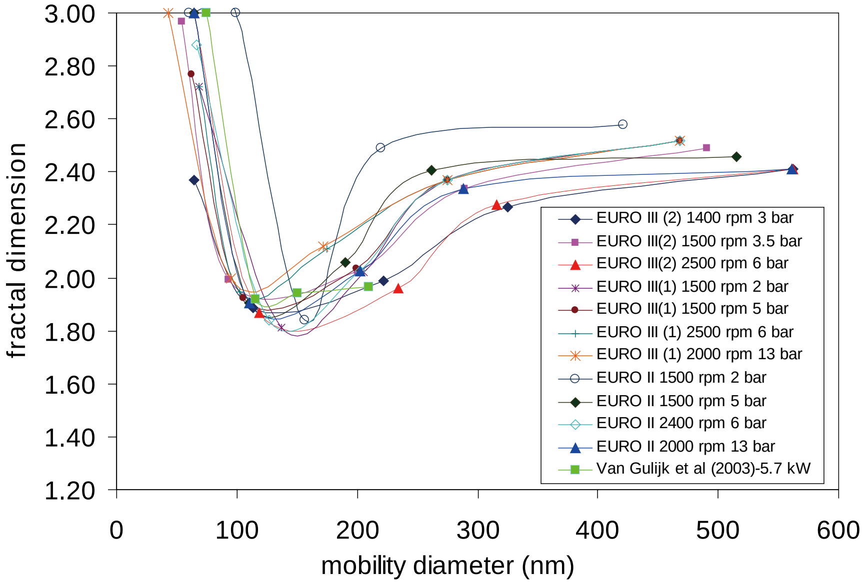

Fig. 3 Fractal dimension of soot aggregates with different mobility diameters obtained with different engines and operating conditions. Measurements from one Euro II and two Euro III diesel engines and a diesel generator [29] as presented in [27].

to an increase of D_f to a range of around 2.4-2.5. As mentioned above, such a fractal dimension is consistent with a mechanism of addition of monomers to a cluster, and we rationalize it by considering the removal by oxidative fragmentation of smaller units from a large soot aggregate and their subsequent re-collision with the same or other aggregates, through a type of DLA process. The data are consistent with an overall average $D_f = 2.4$, and a similar average D_f has been obtained by[28], among others.

In[21] it is shown that in principle, σ_g does not have a universal value but rather depends on the soot aggregate morphology (as described by the soot aggregate fractal dimension, D_f) and the mode of the oxidative fragmentation process (e.g. attrition, random fragmentation, equal size fragmentation, etc). An average fractal dimension $D_f= 2.4$ for the diesel soot aggregates [28] and a physically realistic random fragmentation mode are shown to be consistent in [21] with the experimentally observed values of σ_g. An explicit connection between the combustion process, the aggregate morphology and the easily measured σ_g can therefore be made.

3. The DPF as a Separator: Filtration and Pressure Drop

Filters separate the diesel soot aggregates from the exhaust by means of a variety of transport mechanisms. The main deposition mechanisms are those of Brownian diffusion and direct interception, while thermophoresis can be important in the presence of temperature gradients[30]. Over the last 20 years, many DPF system concepts have appeared which incorporate different filter media and geometric configurations, regeneration technologies and control/monitoring options. The interested reader should consult the literature[31, 32, 33] as well as on-line databases[34].

1) Filter media and configurations

The filter media and geometric configuration is a key element in the DPF system, and the selection process calls for a careful balancing of different criteria including pressure drop performance, particulate collection efficiency, regeneration, durability and cost. Geometric configurations of filters are listed in **Table 1**[35, 36].

The wall-flow monolith honeycomb design originally introduced in 1981[37] still remains the most popular configuration, since it is a very compact arrangement, thus exhibiting a low pressure drop without having to make sacrifices in filtration rate or available space.

Representative material properties are given in[36].

Since the majority of filter configurations use some sort of wall-flow arrangement, we will focus our investigation for the remaining of the paper on the wall-flow geometry and honeycomb structures. It should be noted though that the developments/results can be extended direct to the other geometries[38]. In the following text, we examine the factors that affect the

Table 1 Diesel Particulate Filter Materials and Configurations

Ceramic	
Oxide ceramics	
• Cordierite	• Extruded honeycomb wall-flow monoliths
• Mullite	• Extruded honeycomb wall-flow monoliths
• Aluminum titanate (tialite)	• Foam monolithic blocks and plates
	• Extruded honeycomb wall-flow monoliths
Non-oxide ceramics	
• Recrystallized silicon carbide	• Extruded honeycomb wall-flow monoliths
• Silicon-bonded silicon carbide	• Fibrous felts
• Silicon nitride	• Extruded honeycomb wall-flow monoliths
	• Extruded honeycomb wall-flow monoliths
Metallic	
• Sintered metal powder	• Pleated wall-flow sheets
• Metal fiber	• Fibrous felt elements and cartridges
• Metal foam	• Sheets and cartridges

pressure drop and filtration efficiency of DPFs.

2) Filtration theory

The first applications and validations of filtration theory to diesel particulate filters were made in[39] for fibrous structures and in[30] for wall-flow extruded filters. As flow in porous media represents a challenging area of fluid mechanics, initial approaches[39, 40, 41] have employed so-called unit-cell models where the porous filter wall is approximated as a collection of "cells", each hosting an object of simple geometry (a sphere for granular filters and a cylinder for fibrous filters). In these studies, it was shown that the classic filtration theory employing the concept of the "unit collector" (spheres for extruded filters and cylinders for fibrous and foamy structures) can give a good estimate of the size-specific collection efficiency of "clean" DPFs with respect to solid particles.

Fig. 4 demonstrates that application of the unit-cell filtration theory can successfully describe the emitted size distribution of diesel aggregates at the DPF outlet for widely varying pore sizes of prototype SiC-based extruded wall-flow monoliths with a porosity of 42%.

To account for the effect of particle accumulation on the filtration process, the unit-cell-based filtration theory was extended to include a local re-computation of the evolving unit-cell geometry (**Fig. 5**) caused by deposition of particles[35]. The transient filtration model derived was tested with very good agreement against experimental data with ceramic, metallic and fibrous filters, see for example[42]

3) Flow resistance and pressure drop of filters

Based on the fundamental principles of fluid mechanics and flow through porous media, Konstandopoulos and Johnson[30] published the first analytical solutions for the flow fields and pressure drop of wall-flow monoliths in terms of the filter media microstructure and geometric configuration that were validated experimentally for a particular extruded monolith design. The analytical model (extended for non-Darcian flow effects) was later shown to be in excellent agreement with 3-D computational fluid dynamics (CFD) simulations and was further validated against a larger variety of filter media[42, 43, 44]. The Konstandopoulos and Johnson[30] model has been extensively tested against a variety of filter samples, and it is reported to give excellent *a-priori* predictions of the pressure drop, opening up new development possibilities[41, 45, 46].

The approach was later extended to include the influence of the accumulated soot accounting explicitly for the soot layer microstructure and its dependence on the operating conditions of the DPF[12, 47]. In the present section, we outline the dominant factors that are responsible for the pressure drop of clean and soot-loaded DPFs[48].

3.1 Clean filters

Based on previous work in the area[30, 35, 40, 43, 49, 50], the flow resistance of a clean DPF as expressed by its pressure drop can be very accurately described by totalling the individual pressure drop contributions, shown in **Fig. 6**. Each contribution to the pressure drop requires the specification of one or more parameters, which collectively define the required set of what we term "flow resistance descriptors".

Flow resistance descriptors of DPF walls, experimental protocols for their determination and useful correlations have already been presented in[48]. The thin porous wall contributes a pressure drop that is described by the sum of a Darcy term and a so-called Forchheimer term[30, 35, 40, 47, 49]

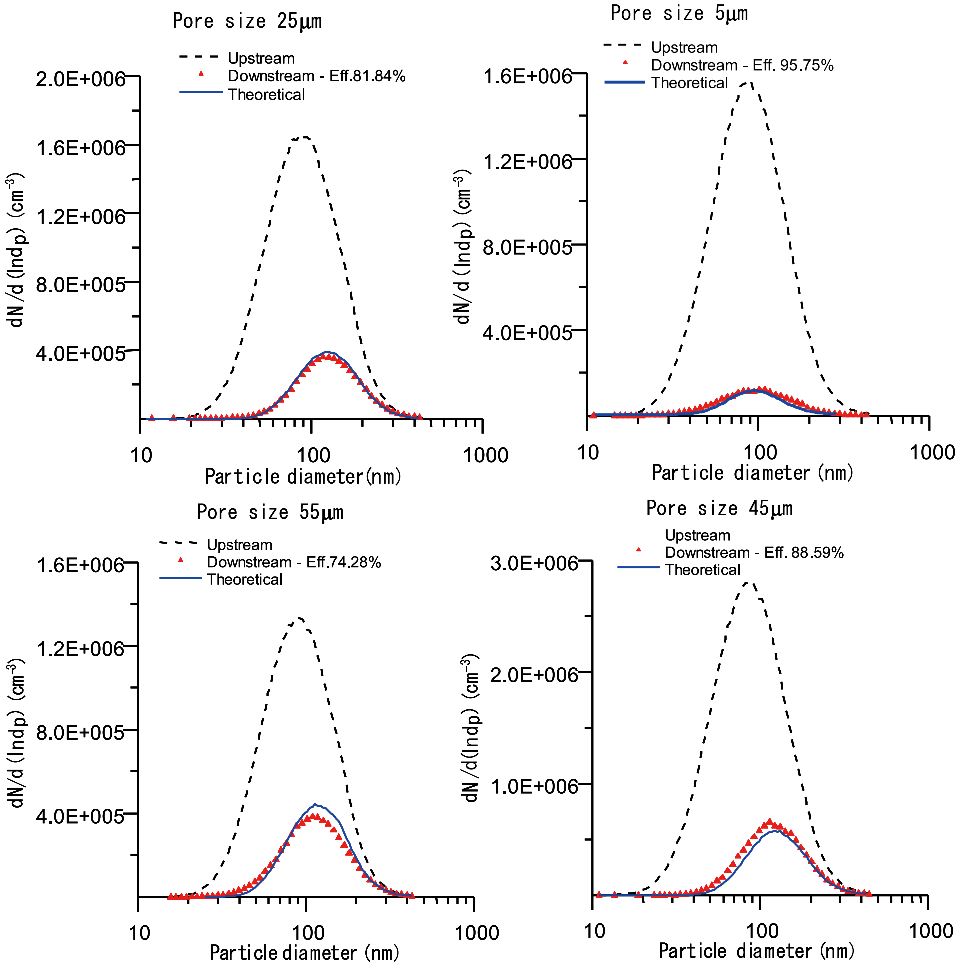

Fig. 4 Effect of pore size on the size distribution of emitted soot aggregates. The DPFs tested are prototype SiC-based extruded wall-flow monoliths with a porosity of 42%. The theoretical lines are the predictions of the unit-cell-based filtration theory [30, 35]

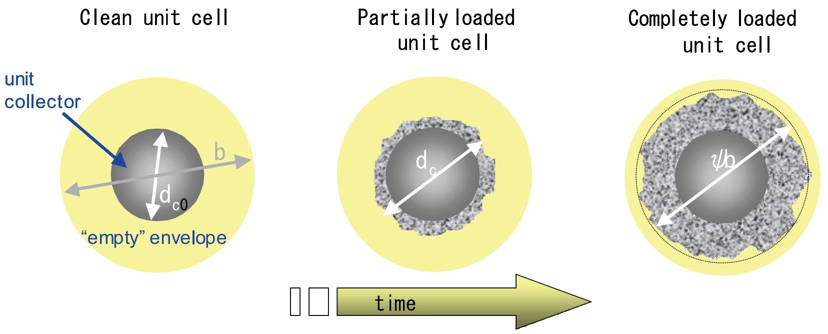

Fig. 5 Unit-cell filtration model. The collector size dc and the empty envelope b are matched to the macroscopic porosity of the filter. The unit-cell blocks when the size of the collector becomes a fraction ψ of b [35, 42]

$$\Delta P_{wall} = \underbrace{\frac{\mu}{k} u_w w_s}_{Darcy} + \underbrace{\beta \rho u_w^2 w_s}_{Forchheimer} \qquad \text{Eq. 1}$$

The parameters appearing in Eq. 1 that need to be specified to permit estimations of the pressure drop are the Darcy permeability k and the Forchheimer coefficient β. The permeability has dimensions of length squared, and $k^{1/2}$ represents a pore level length scale, characteristic of the porous medium. It should be emphasized that the permeability and the

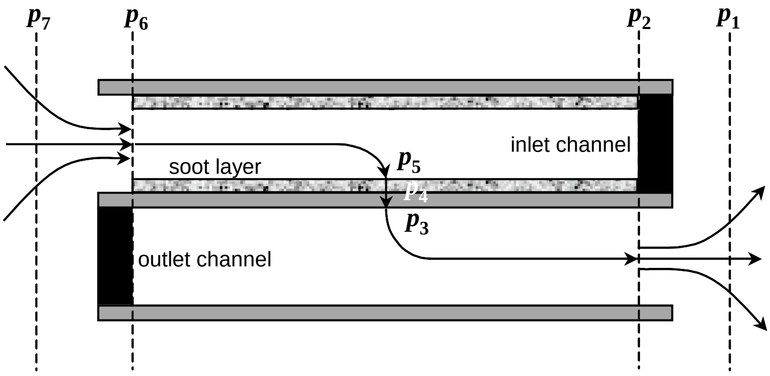

Fig. 6 Schematic of channels adjacent to filter inlet and outlet depicting local pressure values for the derivation of the effects of compressibility on pressure drop.

Forchheimer coefficient are *intensive* properties of the porous medium and for a homogeneous medium, will not depend on the size of the sample measured.

In our past work[30, 35, 47)], we have introduced and validated a generalized representation for the permeability of DPFs, which can be stated as:

$$k_{wall} = f_w(\varepsilon) \cdot d_c^2 \cdot SCF(d_c) \qquad \text{Eq. 2}$$

where $SCF = 1 + Kn\left(1.257 + 0.4e^{-1.1/Kn}\right)$ is the Stokes-Cunnigham factor[51)] accounting for slip-flow effects that are dependent on the local value of the Knudsen number of the flow through the porous filter wall, $Kn = 2\lambda/d_c$ (based on the prevailing mean free path λ and the typical grain diameter dc of the filter media), and the hydrodynamic interaction function $f_w(\varepsilon)$ for sintered granular media was derived in several interchangeable forms[48)].

$$f_w(\varepsilon) = \begin{cases} 0.09 \times f(\varepsilon) = 0.09 \times \dfrac{2}{9} \cdot \dfrac{\left[2 - \frac{9}{5} \cdot (1-\varepsilon)^{1/3} - \varepsilon - \frac{1}{5} \cdot (1-\varepsilon)^2\right]}{(1-\varepsilon)} \\ \\ \dfrac{\varepsilon^3}{585 \times (1-\varepsilon)^2} \\ \\ 0\{.018 \times \varepsilon^{4.34} \end{cases} \qquad \text{Eq. 3}$$

Slip-flow phenomena are not usually observed in bare (uncoated) DPFs since the pore/grain size of these filters is sufficiently greater than the gas mean free path. For some catalyst-coated filters, however, temperature-dependent slip-flow effects may cause the pressure drop to become smaller than that predicted from continuum flow. In this case, and as shown in[35)], one can employ a slip-flow-corrected permeability of the coating, $k_{coating}$. that depends on the local value of the Knudsen number of the flow through the coating, $Kn = 2\lambda/d_{grain}$ where d_{grain} is a characteristic length scale of the coating (which usually has a granular character). $k_{coating} = f(\varepsilon) \times d_{grain}^2 \times SCF$

The Forchheimer coefficient has dimensions of inverse length. Both k and β can then be related to a "pore size" (which is operationally defined by the employed measurement technique) and porosity of the porous medium. In[48)] it was shown that the Forchheimer coefficient β and the Darcy permeability k were interrelated according to:

$$\beta = \frac{const.}{\varepsilon^{1.5}\sqrt{k}} \qquad \text{Eq. (4)}$$

The value of the constant in Eq. (4) will depend on the actual morphology of the elements making up the porous medium. Based on the known structural properties of commercially available wall-flow DPFs (porosity in the order of 50% and pore size in the 10-30 μm range) and ranges of DPF operating flow rates, it can be assumed that the Forchheimer contribution to the pressure drop will be negligible, unless filters are operated at relatively high filtration velocities. This can occur for some newer filter designs based on sheets of sintered metal, fibrous materials or foam structures. From experiments with granular sintered metal filter media[38)] the value of the constant was found to be equal to 0.34, while from experiments with high-porosity fibrous filter media, the constant was evaluated to be 16.6[47)].

Additional pressure drop occurs in a wall-flow filter due to frictional losses of the flow along the square channels of the filter. This pressure loss has a linear dependence on channel velocity for laminar flow, in a square channel of inlet opening a and length L, according to:

$$\Delta P_{friction} = \frac{\mu U L}{a^2} 2 c_f \mathrm{Re} \xi \qquad \text{Eq. 5}$$

where c_f Re, for fully developed laminar flow in a square cross-sectional channel, has a constant value of 14.227, and in our notation we designate:

$$F=2c_f\text{Re} \qquad \text{Eq. 6}$$

The assumption of fully developed laminar flow is usually satisfied in a wall-flow filter since the Re number based on the channel opening is typically less than 1000 for a DPF measuring 5.66 inches ×6 inches and with 200 cells/in^2(cpsi). The factor ξ is a correction accounting for the effect of strong suction or injection on c_f Re. For typical wall-flow filter applications, ξ can be taken as equal to 1 since local wall-flow velocities u_w are small enough to keep the wall Re number ($u_w a\,\rho/\mu$) less than 2 [30].

Finally, there are inertial losses due to contraction and expansion of the flow as it enters and leaves the filter channels. This component increases with the axial channel inlet velocity U according to:

$$\Delta P_{contr./expan.}=\zeta\frac{\rho U^2}{2} \qquad \text{Eq. 7}$$

where ζ is the so-called contraction/expansion inertial loss coefficient, which in general depends on the filter fractional open cross sectional flow area and on the Reynolds number[47]. All these contributions are included in the following equation that gives the total pressure drop of a clean wall-flow filter:

$$\Delta P=\frac{\mu Q}{2V_{DPF}}(a+w_s)^2\left[\frac{w_s}{ka}+\frac{8FL^2}{3a^4}\right]+\frac{\rho Q^2(a+w_s)^4}{V_{DPF}^2a^2}\left[\frac{\beta w_s}{4}+2\zeta\left(\frac{L}{a}\right)^2\right] \qquad \text{Eq. 8}$$

Eq. 8 has been shown to be a predictive and validated macroscopic model for the pressure drop of wall-flow filters[30, 35, 40, 43, 49, 50], and requires as input the flow rate Q, the filter geometrical characteristics (V_{DPF}, a, ws. L), the wall permeability k and the filter inertial loss coefficient, ζ. Eq. 8 can then be employed in conjunction with experimental data to determine the relevant flow resistance coefficients k and ζ, provided that all other parameters entered in Eq. 8 are known or can be independently measured.

The estimation of k can also be attempted from the filter microstructure, employing any of a number of idealized geometrical descriptions of the porous medium structure, an approach that was used in the past[48]. In that case, the required input data are the “porosity” and “pore size”, parameters that are themselves operationally defined based on the measurement technique. Such estimations, however, based as they are on idealized geometrical representations of the filter microstructure, provide only order-of-magnitude estimates of the wall permeability. True-to-the-geometry representations based on statistical computer reconstruction of the porous filter wall from microscope pictures and subsequent computational analysis of the flow through the wall have been introduced in[47, 48, 52] and provide more accurate estimates.

Experiments for direct measurements of wall permeability can be performed using either filter disks of the same material formulation[35] or pieces from the filter wall, after the orthogonal walls have been removed carefully[53]. Such experiments are quite time-consuming and are not easy to employ for the routine analysis of samples. An easier, non-destructive alternative for determination of the permeability of a wall-flow filter sample is to rely on careful experimental measurements made on complete honeycombs and the application of predictive, continuum-level mathematical models, such as Eq. 8. This is now standard industrial practice[54].

For the determination from first principles of the inertial losses coefficient, ζ, the use of three-dimensional CFD simulation has already proved to be promising[47]. However, the computational effort required for an extensive parametric study of a multi-channel configuration[47] makes experimental testing a more flexible alternative.

3.2 Soot-loaded filters

Depending on their microstructure, filters can exhibit more a so-called deep bed filtration mode or a so-called cake (or surface) filtration mode[55]. With reference to **Fig. 7**, the deep-bed filtration mode occurs initially (i.e. all filter structures will exhibit it) and is characterized by a non-linear increase of the filter pressure drop as a function of the accumulated soot mass in the filter. This is due to the initial deposition of soot particles inside the porous structure of the filter wall, which block the flow paths locally. Depending on the microstructure of the porous filter, even a small amount of deposited soot may have a huge effect on the pressure drop, since it may block a disproportionately large part of the pore structure, hence the non-linear character of the pressure drop evolution. As the porous wall becomes more and more blocked by the deposited soot, there is a smooth transition to the cake filtration mode, where a macroscopic soot layer grows on top of the filter wall, characterized by a linear dependence of the pressure drop on the accumulated particulate mass in the filter.

It is obvious that more porous wall structures will exhibit a more pronounced deep-bed mode of filtration, however, in all filter structures that are currently commercially employed for DPFs, a cake

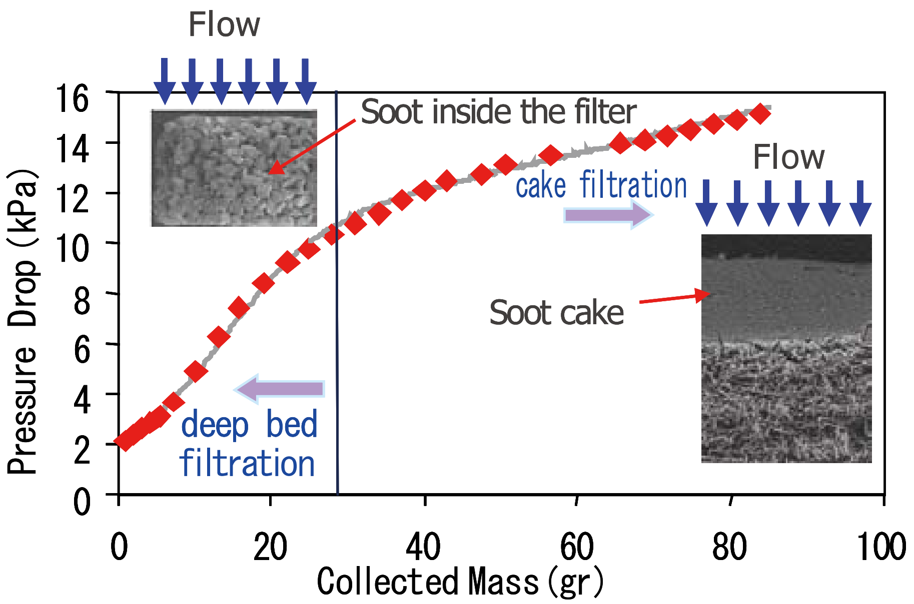

Fig. 7 Filtration modes: from deep-bed to cake (surface) filtration.

mode of filtration eventually sets in, since the amount of soot one might want to be stored in the DPF before its regeneration is initiated is higher by far than the amount that the porous wall can accommodate. Typically, the porous wall will store between 0.5-2 g/m^2 of soot mass per filtration area (depending on the filter structure), while the total amount of soot stored before regeneration is on the order of 10 g/m^2 (depending on the employed DPF material and configuration).

For predominantly cake-mode-type DPFs, a closed-form expression has been derived for the pressure drop as a function of soot loading[35].

The soot-loaded DPF pressure drop is expressed in terms of a uniform, effective soot deposit thickness, w on the filter wall[35], which with reference to **Fig. 8** is computed as follows:

$$w = \frac{\alpha - \sqrt{\alpha^2 - \frac{m_{soot}}{N_{cells} L \rho_{soot}}}}{2} \qquad \text{Eq. 9}$$

$$\Delta P = \frac{\mu Q}{2V_{DPF}}(a+w_s)^2\left[\frac{w_s}{k_o\alpha} + \frac{1}{2k_{soot}}\ln\left(\frac{\alpha}{\alpha-2w}\right) + \frac{4FL^2}{3}\left(\frac{1}{(\alpha-2w)^4} + \frac{1}{\alpha^4}\right)\right] + \frac{\rho Q^2(\alpha+w_s)^4}{V_{DPF}^2\alpha^2}\left[\frac{\beta w_s}{4} + 2\zeta\left(\frac{L}{\alpha}\right)^2\right] \qquad \text{Eq. 10}$$

The analytical expression for the DPF pressure drop has been extensively validated (**Fig. 9**) against 3-D CFD and experimental results [35].

Fig. 10 depicts the experimental transient loading behavior of different DPFs and their simulation using the transient filtration model of Konstandopoulos et al.[35].

Whenever the DPF pressure drop is significant when compared to the atmospheric pressure, compressibility effects need to be taken into account. The DPF pressure drop in the case of compressible flow has been analyzed in[48] as explained in the Appendix.

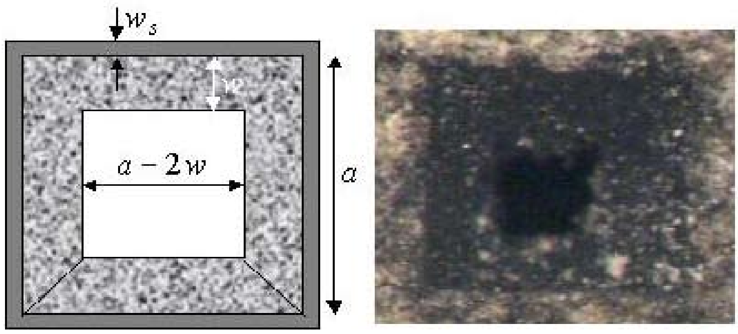

Fig. 8 Schematic and nomenclature of soot cake accumulation inside the cross-section of a channel (left) and image of soot accumulated in a DPF channel (right).

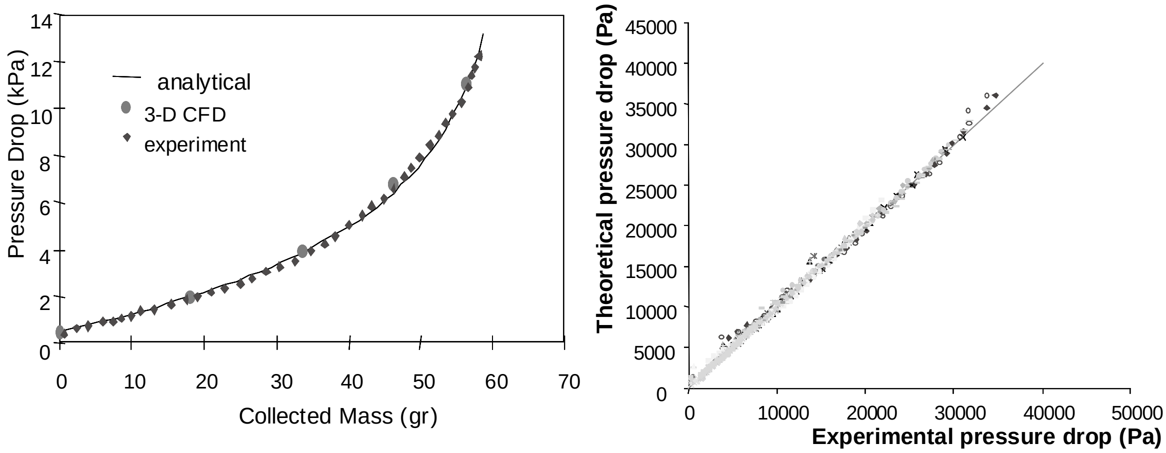

Fig. 9 Validation of an analytical pressure drop model with 3-D CFD (left) from [35], and experiments (right) with 10 filters in 31 experimental runs with light- and heavy-duty diesel engines from [43].

3.3 Soot deposit microstructure

Konstandopoulos et al. [12] demonstrated for the first time that during filter loading, the microstructure of the soot cake is determined by the relative strength of convective vs. diffusive transport of the soot aggregates towards the deposit **Fig. 11**. The soot cake packing density (ρ_{soot}) and permeability (k_{soot}) were therefore shown to be not just "static" intrinsic physical properties of the soot cake, as it was commonly assumed in the literature. They were instead shown to be "dynamic" material properties of the soot porous cake that depend on the deposit growth mechanism and its history, and that they are determined by the prevailing value of the dimensionless mass transfer Peclet number, $Pe = u_w d_{pr}/D_p$, where d_{pr} is the primary particle size of the soot aggregates and D_p is the soot aggregate diffusion coefficient.

The soot cake packing density (ρ_{soot}) and permeability (k_{soot}) can be related to the porosity ε and primary particle size (d_{pr}) of the soot aggregates as follows[12]:

$$\rho_{soot} = \tilde{\rho} \cdot (1-\varepsilon) \qquad \text{Eq. 11}$$

$$k_{soot} = f(\varepsilon) \cdot d_{pr}^2 \cdot SCF \qquad \text{Eq. 12}$$

where *SCF* is the Stokes-Cunningham factor calculated with a Knudsen number (K_n) based on the primary soot particle size (d_{pr}) from:

$$SCF = 1 + Kn \cdot (1.257 + 0.4e^{-1.1/Kn}) \qquad \text{Eq. 13}$$

and $f(\varepsilon)$ is the Kuwabara hydrodynamic function which depends on the porosity ε, through[30, 55]:

$$f(\varepsilon) = \frac{2}{9} \cdot \left[\frac{2 - \frac{9}{5}(1-\varepsilon)^{1/3} - \varepsilon - \frac{1}{5}(1-\varepsilon)^2}{(1-\varepsilon)} \right] \qquad \text{Eq. 14}$$

Further insight into soot cake properties has been obtained by model experiments with soot aggregates generated by a Combustion Aerosol Standard (CAST) burner (Matter Engineering, Switzerland). The CAST is a quenched diffusion flame gas (propane) burner that allows the stable and controlled generation of soot aggregates over a much larger size range than that found in diesel exhaust. **Fig. 12** depicts the hydrodynamic resistance factor $(\rho \times k)_{soot}$ of CAST soot-deposited cakes on flat disk-shaped glass-fiber filters as a function of the Peclet number and aggregate mobility diameter d_{ag}.

The values of the aggregate mobility diameters shown in **Fig. 12** are values measured by the Scanning Mobility Particle Sizer (SMPS). The data are consistent with a scaling relation of the form:

$$(\rho \times k)_{soot} = \tilde{\rho} \cdot (1-\varepsilon) \cdot f(\varepsilon) \cdot d_{pr}^2 \cdot SCF \qquad \text{Eq. 15}$$

where the porosity of the deposits follows a power law in terms of the Peclet number[12, 56)

$$\varepsilon(Pe) = 1 - (1-\varepsilon_\infty) \cdot \left(1 + \frac{Pe_0}{Pe}\right)^{-n} \qquad \text{Eq. 16}$$

Eq. 16 generalizes earlier porosity-Peclet number power-law correlations[12] obtained at $Pe > 0.3$ down to the diffusion-limited deposition limit. Pe_0 is a characteristic cross-over P_e number defining the scale beyond which the convective mechanism will take over the diffusive mechanism of deposition, and ε_∞ the large Peclet number asymptote of the porosity. Using Eq. 16, the experimental data of **Fig. 12** can be collapsed on a single curve as shown in **Fig. 13**.

At sufficiently high values of the pressure drop,

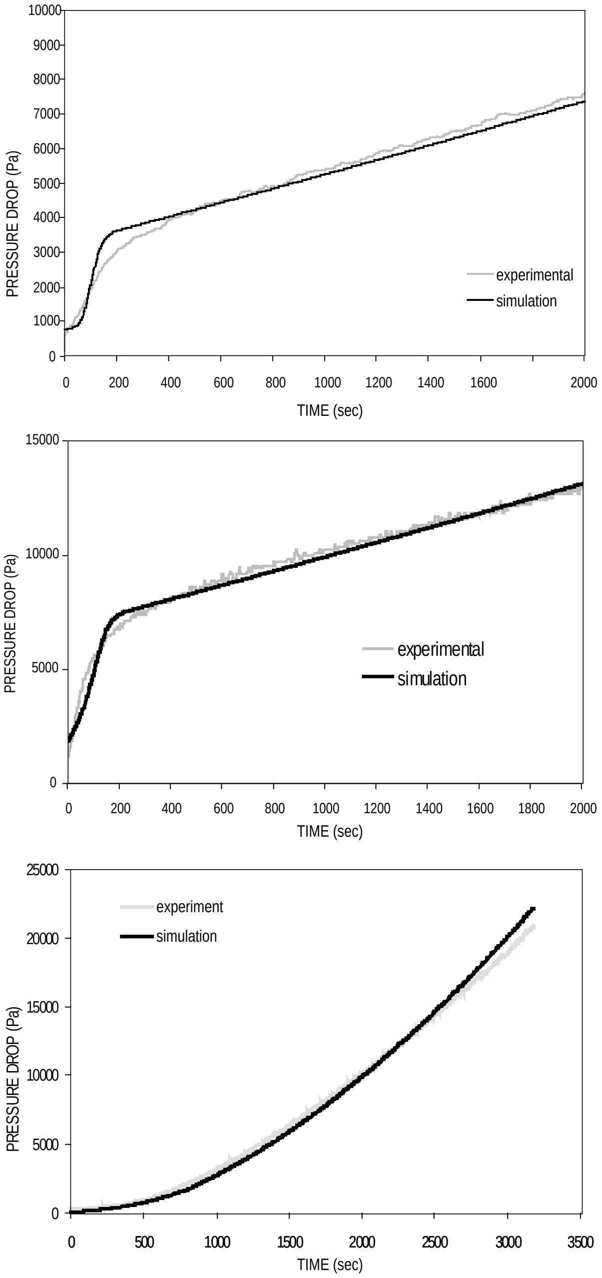

Fig. 10 Transient loading of a SiC (top), cordierite (middle) and fibrous metal (bottom) filter in the exhaust of a diesel engine. Experimental data and simulation results [42].

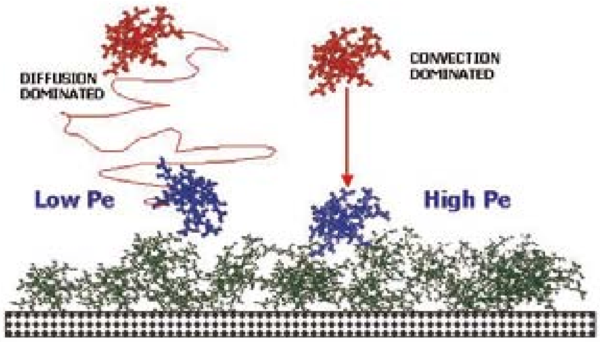

Fig. 11 Soot deposit growth mechanism: competition between diffusion- and convection-dominated growth, as determined by the Peclet number, leads to more porous deposits in the case of diffusion-limited deposition [12].

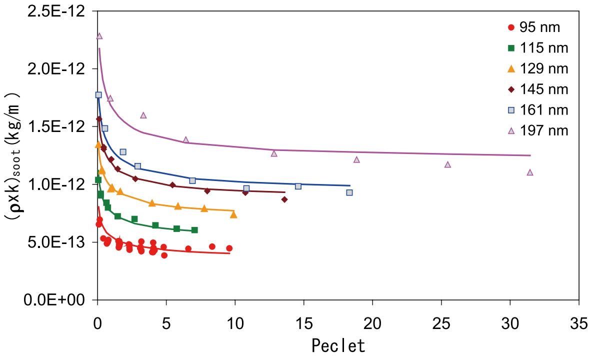

Fig. 12 Experimental measurements of CAST soot hydrodynamic resistance factor as a function of the Peclet number and aggregate mobility diameter. The continuous lines are plotted using the scaling relation form Eq. 15, Eq. 16 [47].

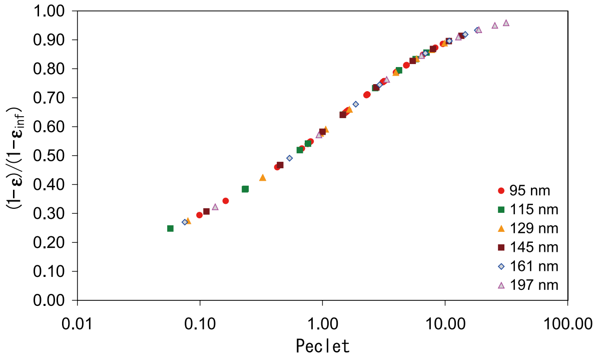

Fig. 13 Dependence of the soot cake porosity for different soot aggregate sizes at the prevailing Peclet number.

soot deposit compaction starts to set in. Konstandopoulos et al.[47] accounted for deposit compaction in the pressure drop model, treating the soot deposit as a Bingham-type of material that remains undeformed below a yield pressure and that deforms with a power law in the post-yield region:

$$\frac{\phi}{\phi_0}=\left(\frac{\Delta P-\Delta P_{cr}}{\Delta P^{*}}\right)^{\delta} \qquad \text{Eq. 17}$$

with ϕ denoting the solid fraction (1- ε) and ϕ the solid fraction of the deposit in the uncompacted stage. ΔPcr is the critical or yield pressure drop for the onset of deposit compaction, and ΔP* is a scaling constant to make the equation dimensionally correct. The extended pressure drop model that accounts for deposit compaction was applied in[47] to obtain for the first time the evolution of the soot deposit microstructure under compaction. As shown in **Fig. 14**, critical pressure drops for the onset of compaction of soot

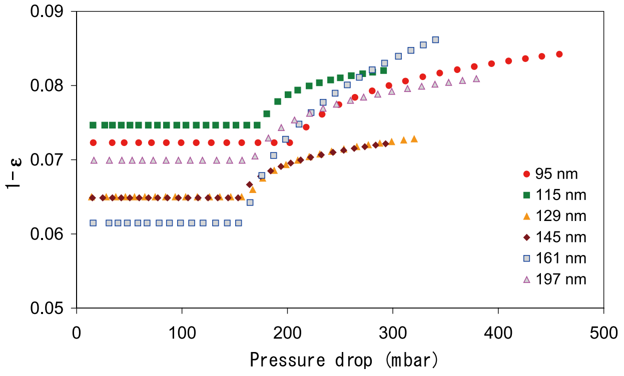

Fig. 14 Pressure-drop-induced compaction of soot cake deposits as a function of soot aggregate size.

cakes created by CAST-generated soot aggregates of different size are in the vicinity of 200 mbar and cause a gradual increase of the solid fraction (1- ε) of the compacted soot deposit, which can reach 25-30% for some aggregate sizes at high enough values of the pressure drop (> 400 mbar). These high pressure drops are non-typical for appropriately sized DPFs and under regular DPF operation, but it is possible to quantitatively take into account such phenomena if the need arises with the simple deposit compaction model mentioned above.

3.4 Effect of ash accumulation

The DPF pressure drop model has been extended to account for the presence of ashes in the channels of the DPF in[27, 47]. Ash deposit growth dynamics was described with a mechanistic model that exhibits different ash deposition profiles: deposition along the filter channel walls as well as deposition at the end of the filter channel. A comparison to experimental data available in the literature (**Fig. 15**) showed good quantitative agreement, and the model can be used to describe the dynamic ash transport and deposition phenomena inside the DPF.

Considering two idealized modes of ash accumulation, namely (i) ash only on the wall (forming a layer in series with the porous wall and the soot cake) and (ii) ash only at the end of the DPF channel (forming a plug that reduces the DPF length), it was possible to derive in[57] analytic approximations for the optimum cell density of wall-flow filters that minimizes the DPF pressure drop, under the combined constraints of a prescribed filter volume, exhaust flow, temperature, as well as different soot and ash loadings inside the filter, and thus to facilitate the task of selection and reliable employment of diesel particulate filters over the vehicle life-cycle.

4. The DPF as a Reactor

As already mentioned, modern DPFs need to be periodically cleaned (regenerated) in order to achieve efficient and safe operation of the vehicle. As typical diesel exhaust conditions are not hot enough to initiate and maintain particulate (soot) oxidation, active (engine) means are employed to raise the exhaust gas temperature up to the point that particulate oxidation can be self-sustained in the filter, and therefore the filter acts as a soot oxidation reactor. DPF regeneration can be achieved by employing a number of different approaches including direct and indirect catalytic measures ranging from fuel-borne catalysts (also known as fuel additives), generation of reactive species, catalytic combustion of post-injected fuel and filter coatings promoting soot oxidation, as discussed in the subsequent sections.

1) Regeneration measures

It is convenient to classify regeneration measures [31, 32, 33, 34] as active (employing external or engine means, see **Table 2**) or passive (usually employing catalytic means, although catalytic means can also be applied in active systems, see **Table 3**). Combinations of measures are also common.

2) Soot oxidation rate during regeneration

During regeneration tests with an increasing temperature, the pressure drop of the soot-loaded filters decreases and at the same time CO and CO_2 gases are emitted as the soot collected inside the filters oxidizes. In order to evaluate the regeneration behavior of different DPF technologies, the soot oxidation rate has to be calculated as a function of temperature. The normalized soot oxidation rate (s^{-1}) is defined as:

$$\dot{r}_{soot} = \frac{1}{m_0}\frac{dm}{dt} \qquad \text{Eq. 18}$$

where m_0 is the initial amount of soot mass collected. The soot consumption rate dm/dt is typically computed by adding the CO and CO_2 produced during the oxidation in a synthetic exhaust gas stream which does not contain CO or CO_2 in order to detect the soot-derived CO/CO_2. The evolution of the normalized soot oxidation rate as a function of temperature, an example of which is given in **Fig. 16**, provides a means to compare and evaluate different DPF technologies with respect to their soot oxidation activity. In addition, the CO selectivity which is defined as:

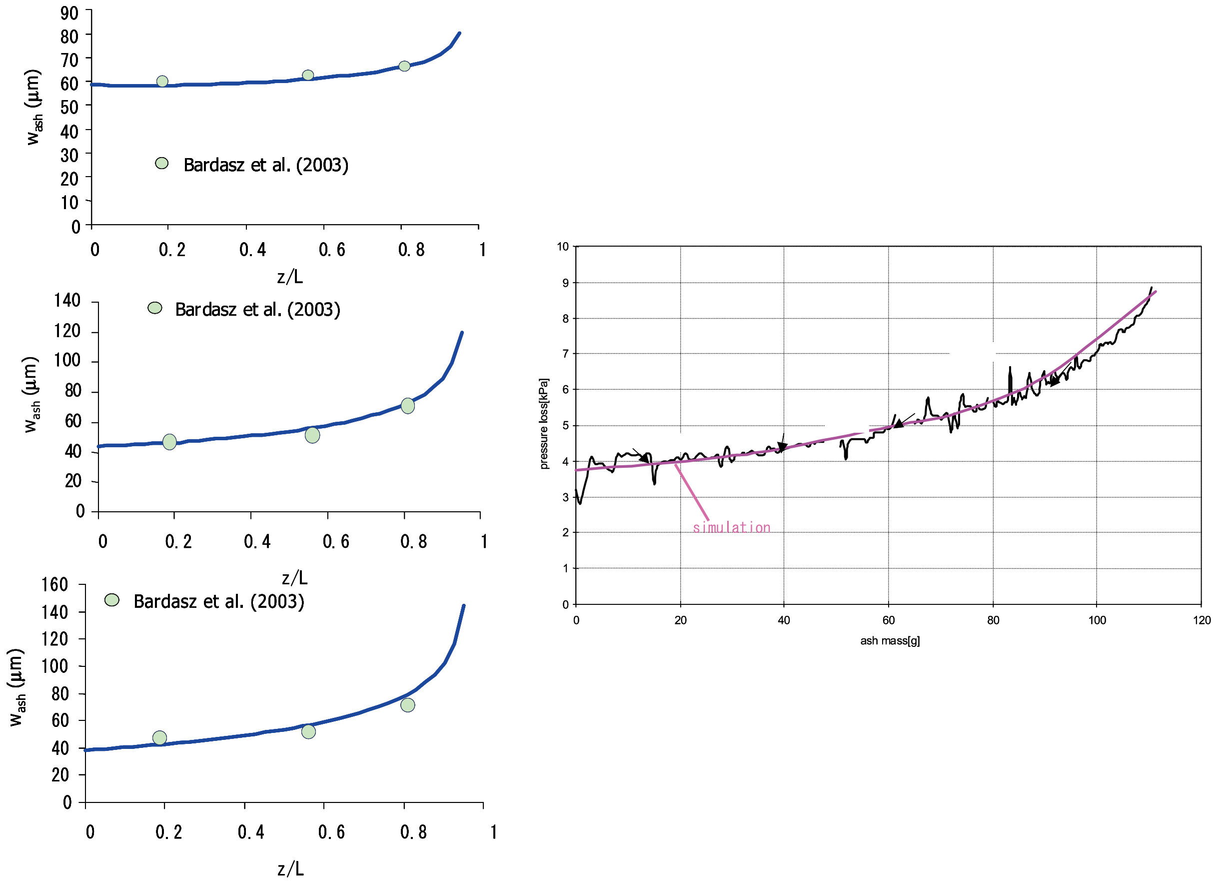

Fig. 15 Left: Simulated ash profile along the normalized filter length (z/L) vs. experimental data of Bardasz et al. with ash of different qualities, generated by high-sulfur oil doped into fuel (top), low-sulfur oil doped into fuel (middle), high-sulfur oil, regular use undoped into fuel (bottom). Right: Effect of ash accumulation on the DPF pressure drop. Experimental data courtesy of Ibiden Co. Ltd. and simulation results[47].

Table 2 Active Regeneration Measures

External means
- Fuel burners (full and partial flow)
- Electric heating (upstream or embedded in the filter)
- Microwave heating
- Injection of combustibles (e.g. fuel) in the exhaust
- Injection of catalytic and/or reactive species in the exhaust (e.g. H_2O_2[59])
- Generation of reactive species (e.g. non-thermal plasma [60])
- Electrochemical filter reactor [61]

Engine means
- Exhaust gas recirculation
- Post-injection of fuel
- Decrease of boost pressure
- Intercooler bypass
- Injection timing retard

Table 3 Passive Regeneration Measures

- Catalytic means
- Fuel-borne catalysts
- Catalytic filter coatings
- Reactive species generation (e.g. NO_2 [62])

$$f_{CO} = \frac{CO}{CO + CO_2} \qquad \text{Eq. 19}$$

can be also calculated. The CO selectivity is an important parameter because it affects the total heat release during regeneration.

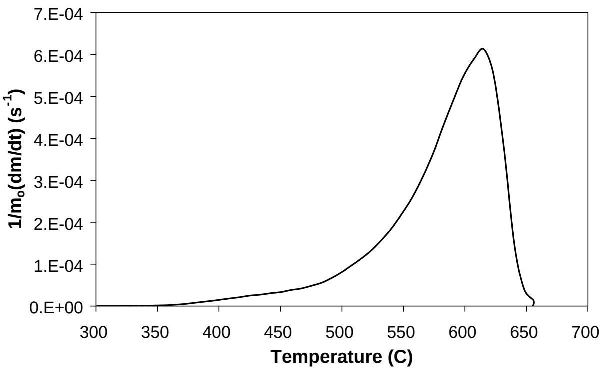

Fig. 16 Soot oxidation rate as a function of temperature.

3) Catalytic DPFs

The development of catalytic DPFs (CDPFs) aims at achieving:

(i) some soot oxidation activity under moderate exhaust temperature to prolong as much as possible the intervals between fixed regenerations, exploiting direct (i.e. through oxygen transfer) as well as indirect (through NO$_2$ generation) soot oxidation;

(ii) reduced soot ignition temperatures compared to uncatalyzed filters to allow for energy savings during regeneration;

(iii) tolerance to ash accumulation.

To achieve these goals, it is important to understand the different soot oxidation mechanisms and the significance of the soot-catalyst geometric proximity.

3.1 Catalytic oxidation mechanisms

Catalytic soot oxidation has a long history[63], while some recent reviews appear in[64, 65]. Catalyst chemistry is an important factor affecting the performance of a CDPF. Currently available CDPFs in the market feature predominantly catalytic coatings based on Pt-group metal (PGM) formulations aimed at oxidizing NO into NO$_2$ in order to achieve soot combustion at a lower temperature, motivated by the success of the CRT™ NO$_2$-assisted system[62]. The influence of NO$_2$ on soot oxidation, in conjunction with a highly selective NO to NO$_2$ oxidation promoting catalytic coating on a DPF, was studied experimentally and theoretically for the first time in[35]. At that time, NO$_2$-regenerative technologies were practiced with uncatalyzed filters[60, 62], and it was suggested that combinations of NO$_2$-regenerative technologies with catalytic filters could lower the dependence of NO$_2$-regenerative technologies on high engine-out NO$_x$ concentrations, as NO$_x$ emission standards become tighter. This has now become standard practice[60].

PGM-based CDPFs do not have a strong direct soot oxidation activity[11] and their operation depends on the balance between NO$_2$ and soot in the exhaust. It has nevertheless become clear from these developments that a noble metal such as Pt could have a beneficial role if used in conjunction with a direct soot oxidation catalyst, since Pt can also deliver "active oxygen" to the soot-catalyst interface in addition to oxidizing NO into NO$_2$.

Soot oxidation catalysts based on base metal oxides are thought to act through two mechanisms[64, 65].

(i) Redox mechanism: carbon oxidation is caused by lattice oxygen from the catalyst (reduction step) and re-oxidation of the catalyst by oxygen from the gas phase (oxidation step)

(ii) Spill-over mechanism: dissociation of adsorbed gas-phase oxygen over the catalyst surface occurs, followed by surface diffusion to the soot surface where carbon oxidation occurs.

The above mechanisms are not mutually exclusive and a soot oxidation catalyst can exhibit both.

Direct catalytic soot oxidation requires soot-catalyst proximity, a fact that has been known for almost half a century[66]. The problem of soot-catalyst contact in diesel emission control systems was recognized in the 1980s[63] as a barrier for active catalytic filter development, and it has become popularized in more recent laboratory studies of powdered carbon black-catalyst mixtures, with the introduction of so-called "loose" and "tight" contact[64, 65] samples. Direct demonstration of soot-catalyst contact effects on diesel soot oxidation in filters has been published in[67].

A mathematical description of the incomplete soot-catalyst contact, the so-called "Two-Layer Model" was introduced a decade ago, and it has since been incorporated into state-of-the-art DPF simulators[68, 69, 70, 71]. This forms the basic analysis tool that we employ in analysing soot oxidation rates in CDPFs as discussed in the next section.

3.2 The two-layer model of CDPF

Soot particle-catalyst contact is determined by the details of catalyst distribution in the filter (a type of "frozen" randomness) and the details of soot particle deposition and resulting deposit microstructure as well as soot deposit restructuring (a type of evolving randomness), it is therefore important to study it under realistic conditions, i.e. depositing fractal diesel soot aggregates from an engine under similar conditions of Peclet number, Pe[12]. The effect of Pe on the soot deposit microstructure, soot-catalyst contact and reactivity is addressed in[72].

CDPF development has to address two key areas[67]: Chemistry and geometry and their interaction through the catalyst deposition process. The works in the literature dealing with chemistry at the powder synthesis level are too numerous to be cited here, while quantitative analyses of geometric effects have not been published as extensively. In the present work, in the geometric aspects of soot oxidation, we emphasize the kinetics in CDPFs by applying the two-layer formalism to analyze well-controlled direct catalytic soot oxidation experiments. **Fig. 17** depicts a schematic of the two-layer model[68]. Soot and catalyst coexist in a region (Layer I), on top of which a soot-only layer exists (Layer II).

Layer I: Catalyst-affected layer

As the catalyst coating can interpenetrate or overlap partially with the top part of the wall, we can define Layer I to be the region over which a spatial "field of catalyst activity" exists. Particles that oxidize when found within the "field of activity" are considered in contact with the catalyst. The fraction $\beta \in [0\text{-}1]$ of the soot surface in contact with the catalyst generally depends on the filter and coating structure and the deposition mode of soot in the filter. In general, β can vary dynamically due to reaction (oxidative fragmentation) and/or restructuring of soot microstructure. This layer can "store" a certain amount of soot (which depends on coating structure and filtration velocity) until it is filled up.

Layer II: Soot cake layer

This layer is formed by soot particles which form a "queue" on top of the filled-up catalyst-affected Layer I. These particles can locally migrate into the catalyst-affected layer depending on an interaction parameter $\xi \in [0\text{-}1]$. This also depends on the filter and coating structure and can vary dynamically for the same reasons as β.

The interested reader can consult the original references for the mathematical formulation of the two-layer model[68]. A simple way, however, to understand the two-layer model dynamics is to consider the following system of kinetics in Eq. 20 and Eq. 21. In Eq. 20, m_1 is the mass of soot in Layer I, a fraction β of which reacts with a catalytic rate and the rest of it reacts non-catalytically (thermal oxidation). In Eq. (2), m_2 is the mass of soot in Layer II which is consumed by thermal oxidation, but which also migrates in proportion to the parameter ξ into any "open" space that becomes available in Layer I after some of the m_1 soot reacts.

$$\frac{dm_1}{dt} = (-k_{cat}\beta m_1 - k_{th}(1-\beta)m_1)(1-\xi) \qquad \text{Eq. 20}$$

$$\frac{dm_2}{dt} = -(k_{th}m_2 + \xi(\beta k_{cat} + (1-\beta)k_{th}m_1)) \qquad \text{Eq. 21}$$

In the simplest applications of the two-layer model, the parameters β and ξ are taken to be constant. The reaction constants are assumed to follow global modified Arrhenius forms[68], and for well-controlled experiments with negligible oxygen variation across the filter, they can be assumed to incorporate into their pre-exponentials the oxygen concentration as well as the surface area of the soot. The two-layer formulation can also describe a fuel-borne catalyst system considering only Layer I and setting m_2 and ξ equal to zero.

A number of filter structures have been catalyzed in-house with base-metal catalysts with a variety of coating technologies, aimed at direct catalytic soot oxidation. All filter structures had a disk form of 60 mm in diameter and they were loaded with soot under identical exhaust conditions in side-stream reactors, already described in the past[33, 73], and they were subsequently subjected to a slow temperature ramp (3℃/min) under a 10% O_2-in-N_2 atmosphere in order to study soot oxidation in them by following the evolution of CO and CO_2 and effecting overall carbon

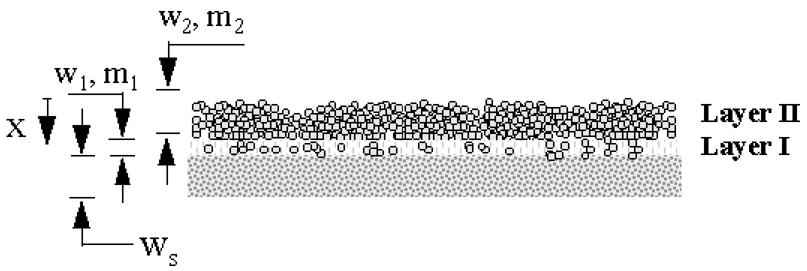

Fig. 17 Schematic illustrating the DPF wall, catalytic-coating-influenced Layer I and the top Layer II that is not in the sphere of influence of the catalyst.

balance.

For all the catalyzed materials there was a similar soot oxidation pattern. In **Fig. 18**, a typical soot oxidation rate curve for the aforementioned materials is depicted, where two regions of soot oxidation are observed. The first peak (in the region of 400-500℃), at lower temperature, originates mainly from the soot oxidized due to the soot-catalyst contact in Layer I, and the second peak, at a higher temperature, originates from the rest of the soot that is oxidized in Layer II. The first peak depends on the level of the contact that exists between the soot and the catalyst, whereas the second one occurs at the typical temperature range of thermal soot oxidation.

Fig. 19 demonstrates how the two modes of soot oxidation (catalytic and non-catalytic) add up to give the total soot oxidation behavior according to the two-layer model.

It is clear that the first peak results from the soot that already exists in contact with the catalyst in Layer I as well as from contributions of soot which migrates from Layer II into Layer I. The double peak is therefore a direct manifestation of the importance that catalyst layer geometry plays in establishing different modes of contact between the deposited soot particles and the catalytic coating. It is not possible to explain this double peak structure of the soot oxidation curves with a model based only on chemistry, since uncatalyzed soot oxidation exhibits a single peak and the same is true for mixtures of soot-catalyst powders[67].

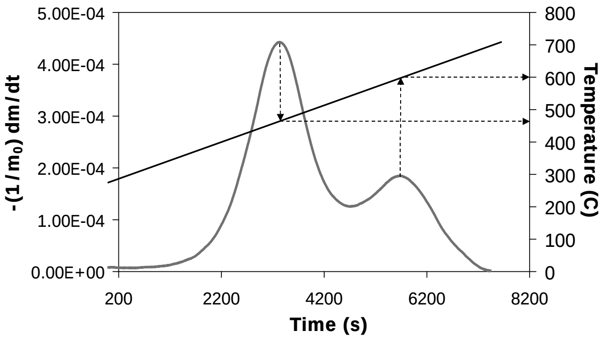

Fig. 18 Soot oxidation rate on catalyzed filter.

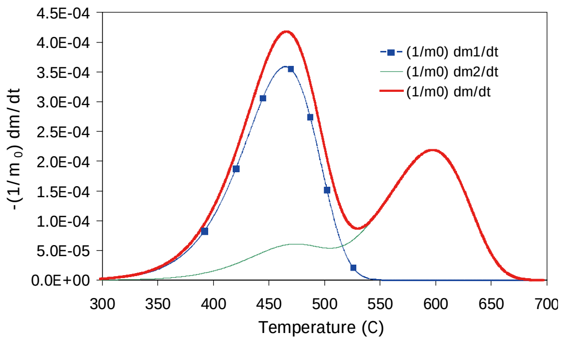

Fig. 19 Soot oxidation based on the two-layer model.

An example of application of the two-layer model to analyze the soot conversion on a catalytic filter is shown in **Fig. 20**, while **Fig. 21** demonstrates the ability of the two-layer model to describe the soot oxidation of several catalytic filter samples to within +/-5%[74].

The reduced activation energy (E/R) for the thermal oxidation for these samples is in the range of 21000 – 22000 (K)[74], and it is within the values usually reported in the literature, e.g.[63, 64, 65, 66, 67]. Catalytic oxidation activation energies are almost the same or up to 15% lower, and depend on the type of catalyst and coating technology employed[74]. Depending on the catalyst coating technology, the state of soot-catalyst contact expressed by β can span a large range

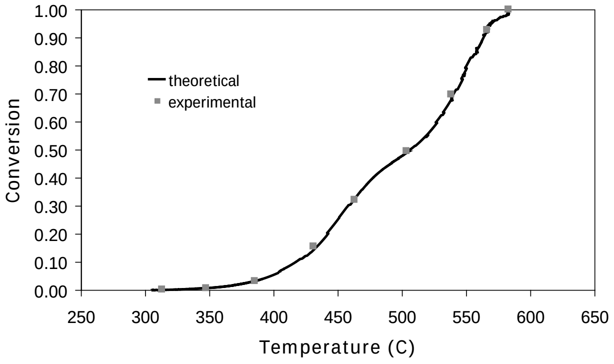

Fig. 20 Application of the two-layer model to experimental data for a catalyzed filter sample [74].

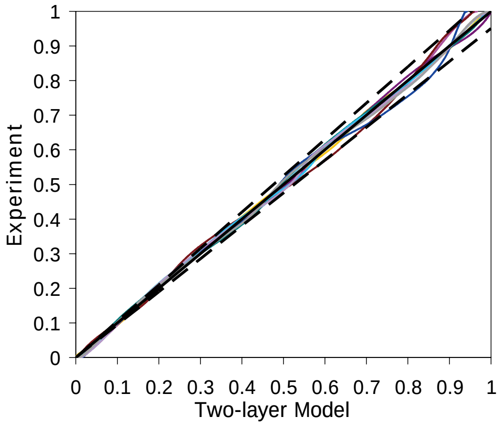

Fig. 21 Comparison of experimental data on soot conversion with the two-layer model. The dotted lines correspond to the +/- 5% spread from the line of perfect agreement.

(values of β from 0.0006 up to 0.214 have been measured in[74]), while migration of soot from Layer II into the catalyst-affected Layer I can occur with a varying degree of intensity as measured by the ξ parameter, which is measured to range from 0 (no migration) up to 0.642[74]. These findings demonstrate the important effect that the filter/catalyst micro-structural environment can have on the global oxidation kinetics. Essentially, it is possible to oxidize a small amount of soot in the catalyst-affected Layer I and still obtain a sufficiently high macroscopic reaction rate provided that the migration of soot from the top Layer II can proceed at an appropriate rate[74].

3.3 Catalyst formulations

Following the results of basic research on catalysts, e.g.[64, 65, 75, 76, 77, 78, 79, 80], we have embarked on a program of synthesis and screening soot oxidation catalysts with the goal of depositing them on filters. Numerous catalyst formulations with different characteristics have been studied[67] in order to arrive at a family of mixed oxide catalysts with high intrinsic soot oxidation activity, designated as E37. Although these catalyst formulations are proprietary and will not be listed here, the basic ingredient is cerium oxide doped with different rare earth and transition metals.

3.4 Catalyst deposition techniques

Catalyst deposition on the porous filter substrates can be performed either with a pre-formed catalyst powder slurry filtration procedure or by dipping the substrates into catalyst precursor solutions and subsequent firing. The coated filters are then thermally treated in a furnace. Permeability changes on the order of 15% can be noticed for filter samples coated by wet chemistry techniques[67].

We have introduced[81, 82] the aerosol spray pyrolysis technique (ASP), which combines catalyst synthesis and deposition on a porous substrate in one step, as an alternative to wet chemistry multi-step techniques (which include powder synthesis, slurry deposition and firing steps). The ASP procedure also has the advantages of precise control of the catalyst particle composition and of the quantity deposited, as well as its spatial deposition profile along the porous filter wall. An added benefit is the fact that the catalyst is deposited with the same mechanism as the soot particles, a feature which is expected to maximize the contact of the soot particles with the pre-deposited catalyst sites during filter operation.

In the aerosol spray pyrolysis technique, catalyst nanoparticles of controlled size are synthesized from the thermal decomposition/evaporation of precursor solution droplets introduced in a hot-tube aerosol reactor. Subsequently, these are deposited in-situ on porous substrates introduced in the reactor. Factors affecting the particle formation are the type of solution precursor, the temperature and the residence time in the reactor prior to deposition on the filter wall. Aerosol/vapor-phase techniques lead to nanostructured catalysts with controlled deposition profiles on the porous filter wall[67].

4) DPF Assessment in the exhaust

The assessment of CDPF technologies is ultimately performed by exposing full-size CDPFs on the engine exhaust and evaluating their regeneration behavior according to a certain methodology. In the present section, we provide an example of such an assessment, employing prototype in-house catalyzed full-scale DPFs, as well as a description of our testing methodology.

4.1 Engine and DPF characteristics

Full-scale DPFs were tested in the exhaust of a Euro III passenger car diesel engine (displacement 1.9 L, rated power 60 kW) with common-rail fuel injection, coupled to a servo-controlled dynamometer. The engine was operated under steady-state conditions as well as under transient conditions. Transient operation was achieved by simulating the speed and torque profiles of the New European Driving Cycle (NEDC) for the specific engine in the dynamometer, in collaboration with the engine manufacturer.

The characteristics of the DPFs (SiC wall-flow filters, 5.66 inches diameter × 6 inches long, 200 cells/in^2) in terms of their catalyst loading are shown in **Table 4**, and are denoted as DPF A-D. Overall, 4 catalyzed DPFs (at different loadings of the E37 catalyst in combination with a noble metal) were tested. An uncatalyzed DPF was also used as a reference. In **Table 4**, x is the amount of catalyst load (referred to as E37) and y is the amount of noble metal (NM) added in the filter. The noble metal is from the platinum group.

4.2 Regeneration method and control

Modifications of the engine tuning in conjunction with fuel post injection through the common rail system, EGR rate variation, boost pressure variation or throttling offers great opportunities to increase the exhaust temperature without adversely affecting fuel penalty and driveability conditions. Specific strategies

Table 4 Characteristics of the DPFs tested

DPF	Catalyst loading
A	No catalyst
B	E37: 2.7 × / NM: 0y
C	E37: 1 × / NM: 1y
D	E37: 2 × / NM: 1y

that focus on a combination of boost pressure, EGR rate increase, and fuel injection modification have therefore been implemented by engine manufacturers[4, 11].

In some cases[83], the exhaust temperature is (in addition to engine measures) raised by exhaust-port fuel injection in front of a diesel oxidation catalyst (DOC). The same technique is also applied for some retrofit applications[84]. The applicability of the technique relies on having the DOC above the hydrocarbon light-off temperature (about 150 C), a condition,which is met with our test engine running over the NEDC, consisting of four city cycles and one extra urban (EU) cycle. **Fig. 22** shows the exhaust gas temperature of our engine over the cycle. As our Euro III test diesel engine has a “closed ECU” (i.e. a production ECU), we have selected exhaust port injection in front of a DOC as the means to raise the exhaust gas temperature, and in turn to effect regeneration of the DPF.

The exhaust port fuel injection set-up was constructed from standard automotive spare parts and consists of an air-assisted nozzle and auxiliary fuel and air pumps. Fuel flow to the nozzle is controlled by a custom electronic circuit defining the nozzle opening time and the period between injections. The fuel injection system has been optimized with the aid of a phase-Doppler analyzer in terms of droplet size. The fuel injection location was selected with the aid of CFD calculations so as to allow the fuel droplets to evaporate and the resulting diesel vapor to reach the DOC inlet with an even distribution. Fuel dosing and calibration of the system has been performed at representative engine operating conditions, and its effect on the increase of exhaust temperature has been studied providing an operational map.

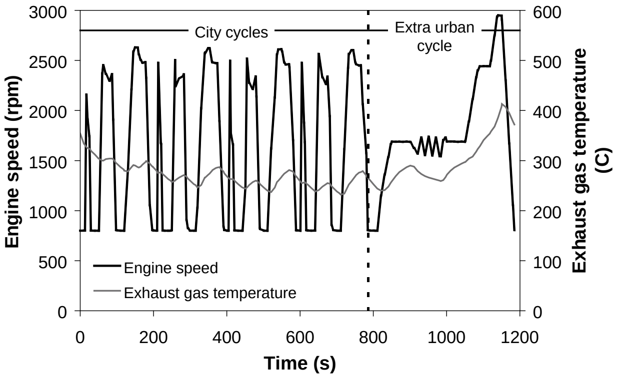

Fig. 22 Exhaust gas temperature and engine speed over the NEDC cycle.

Proprietary improvements in the virtual soot sensor include a detailed account of the effects of soot deposit microstructure under reactive and non-reactive conditions[12, 47] and emergency procedures in the case of virtual sensor failure (caused either by a hardware malfunction or by deviations from pre-programmed specific criteria and error bounds). When this occurs, regeneration would be initiated based on estimating the soot mass load from stored emission data.

4.3 Screening of DPF systems

The DPFs were tested in series with a DOC (Cordierite, 5.66 inches × 4 inches, 400 cells/in^2) in an exhaust set-up in order to study the influence of NO_2 in conjunction with the catalytic coating on soot oxidation.

Initial tests employed the DPFs A-D and an engine operating point where direct NO_2-soot oxidation was very low (due to a NO_x/soot ratio of 4) in order to test the ability of the catalytic coatings to deliver NO_2 to the soot collected inside the filter. The results of the DPF loadings at 2400 rpm and 6 bar brake mean effective pressure are shown in **Fig. 23**, while the soot mass load obtained from the virtual sensor is shown in **Fig. 24**.

As seen in **Fig. 24**, the presence of a DOC (hence NO_2 in the DPF inlet) causes an acceleration of soot oxidation with respect to the uncoated filter. Interestingly enough, DPF B - despite its zero noble metal content - exhibits continuous regeneration behavior very quickly, and this is maintained up to a challenge mass load of 8 g/m^2. This is attributed to the higher catalyst load (2.7 ×) it had with respect to the other filters. The thick porous coating creates an effective filter medium with soot and catalyst in close proximity, and at the same time provides the extra residence time for increased NO_2 turnover. DPFs C and D exhibit similar loading behavior with a progressively lower rate than the uncatalyzed DPF A.

The soot loading curves shown in **Fig. 23** indicate that the catalyzed DPFs B, C and D would reach a continuous regeneration state if they were exposed to the exhaust gas for sufficiently long periods, as a simple first-order reaction-deposition dynamic model would indicate[38]. These results demonstrate that the soot oxidation catalyst content as well as the noble

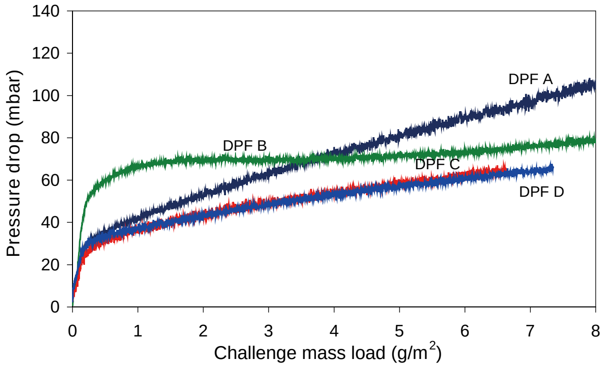

Fig. 23 Pressure drop of DPFs A, B, C and D as a function of challenge soot mass at steady state. DPF inlet temperature: 370 C, exhaust mass flow rate: 50 g/s, NO_x/soot ratio: 4.

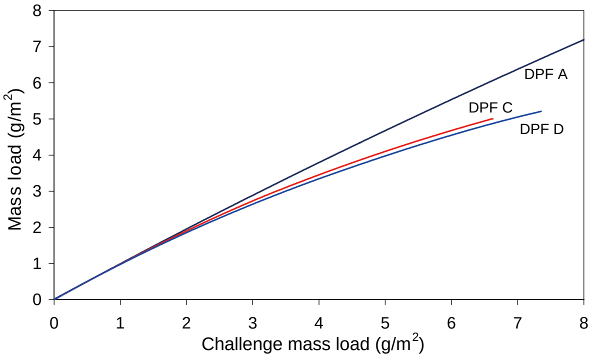

Fig. 24 Soot mass load of DPFs A, C and D at steady state. DPF B soot mass load is estimated to be close to zero. DPF inlet temperature: 370 C, exhaust mass flow rate: 50 g/s, NO_x/soot ratio: 4.

metal presence affect the DPF soot accumulation rate and need to be optimized, taking into account tradeoffs between pressure drop, activity and cost.

The same DPF samples were also tested under a stepped temperature increase procedure to study their catalytic activity at higher temperatures. To this end, increasing quantities of engine fuel were injected upstream of the DOC in order to increase the exhaust gas temperature at the entrance of the DPFs, in steps of about 50 C. A representative result for DPF B is shown in **Fig. 25** in terms of DPF pressure drop and in **Fig. 26** in terms of soot mass load estimated by the virtual sensor.

The comparative assessment of the DPFs A-D in terms of the soot mass oxidation rate is shown in **Fig. 27**. It is evident that all DPFs exhibit significant and similar high temperature catalytic activity with respect to the uncatalyzed DPF A.

Based on these results, DPF C was chosen for subsequent study as an optimum compromise between catalyst load (directly affecting the cost and base system pressure drop), direct and indirect reactivity with NO_2 and a good catalytic reactivity at higher temperature with soot.

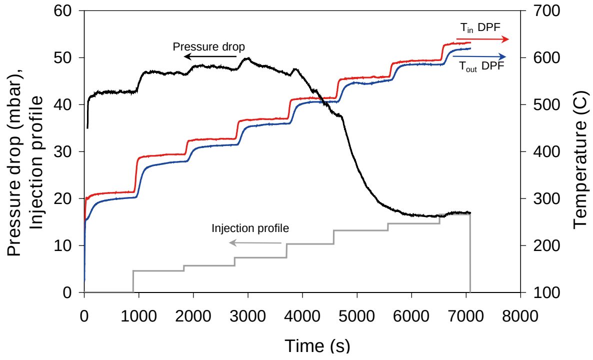

Fig. 25 Pressure drop and injection profile at stepped temperature soot oxidation for DPF B.

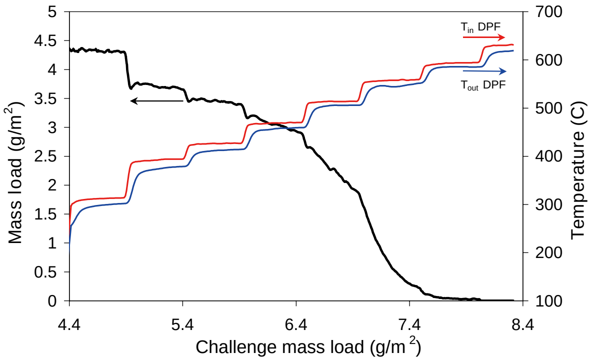

Fig. 26 Mass load calculated by the virtual soot sensor as a function of challenge mass load at stepped temperature soot oxidation for DPF B.

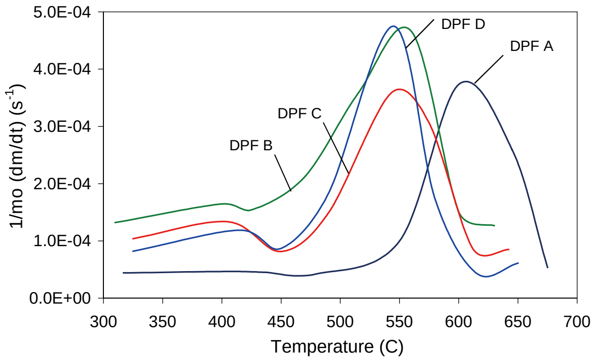

Fig. 27 Comparison of DPFs A-D over stepped temperature soot oxidation.

4.4 Transient Testing

The DOC-DPF C system was tested over a number of new European driving cycles in order to evaluate its behavior under transient conditions. With reference to **Fig. 28**, it is evident that the DPF exhibits

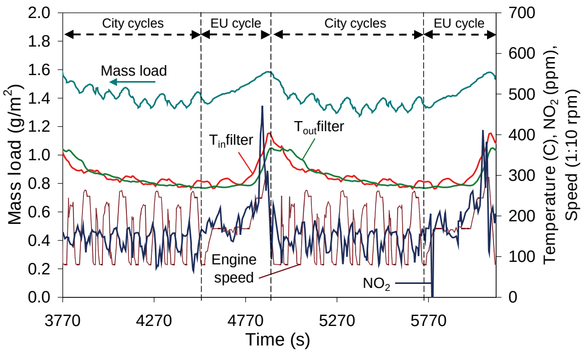

Fig. 28 Mass load variation under transient conditions during successive NEDCs.

good reactivity under NEDC conditions since the soot mass deposited in the DPF is oxidized when the exhaust temperature exceeds about 300℃ over the extra urban (EU) part of the cycle. The result is a very low rate of net soot mass loading of the system, which makes studies of soot accumulation extremely time-consuming.

To accelerate the loading process, DPF C was initially loaded without a DOC placed upstream up to soot mass loads of 8–10 g/m^2. Then the DOC was installed upstream of the DPF C and the system was subjected to exhaust-port injection schedules. By controlling the exhaust-port fuel injection rate and duration, it was possible to reach DPF temperatures in excess of 650-700 C and thus to apply varying amounts of external energy to the DPF at different points of the transient cycle. Examples of such tests are shown in **Fig. 29** and **Fig. 30**.

Fig. 29 depicts two successive fuel injections (each one with a duration of 2 min) performed at different soot mass load levels in the DPF, leading to partial regenerations. **Fig. 30** depicts a complete regeneration achieved by extending the duration of fuel injection to 33 min. Prolonged operation of the system would result in an increase of the “clean” DPF mass load due to the ash accumulation. The virtual sensor is programmed to take this into account by containing information on the flow resistance of ash-loaded filter materials[38].

Using such tests in conjunction with a state-of-the-art real-time DPF simulator [70, 71], it is possible to calibrate and to fully integrate model-based regeneration strategies with the soot virtual sensor module (see[86] for an early description of such strategies). Our current implementation relies on maintaining a target soot mass load in the DPF by injecting a quantity of fuel upstream of the DOC at appropriate instants. Since an exponential trade-off between the soot mass load in the DPF and fuel injection duration exists as shown in **Fig. 31**, it is evident that maintaining a target (constant) soot load in the DPF permits a priori optimization of the DPF size and cell density as well as significant fuel penalty savings.

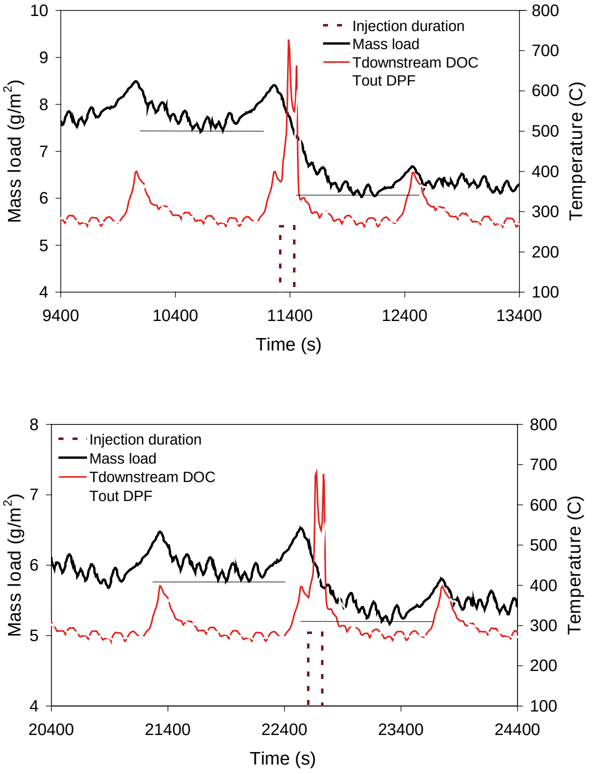

Fig. 29 Controlled regeneration over the NEDC by exhaust-port fuel injection initiated at different soot loadings of the DPF. Top: at 8 g/m^2. Bottom: at 6 g/m^2.

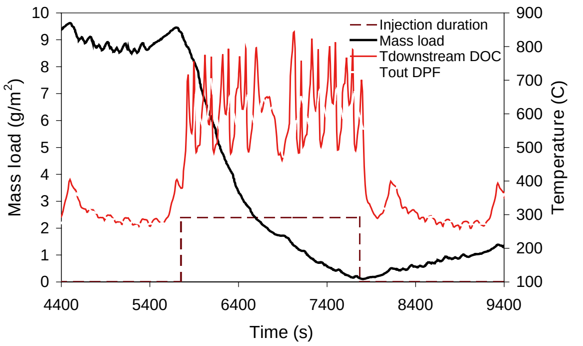

Fig. 30 Complete regeneration over the NEDC by exhaust-port fuel injection initiated at a soot loading of 9 g/m^2.

As an example and based on our data with DPF C, we estimate that over the EUDC cycle, it is possible to maintain a target soot load of 5 g/m^2 with a fuel penalty of about 0.23% (a model-based controlled regeneration to bring the soot load whenever it reaches 6 g/m^2 down to 4 g/m^2). In comparison, a regeneration strategy that aims at a periodically completely

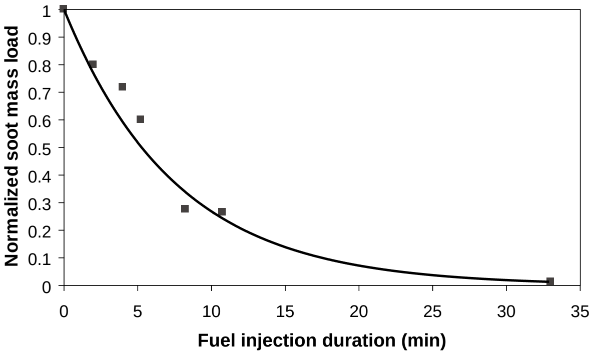

Fig. 31 Normalized soot mass load in the DPF vs. fuel injection duration.

cleaned DPF whenever the soot load reaches 10g/m^2 would result in a fuel penalty of 0.52%.

Even though state-of-the art actively managed DPF systems[4] employing various aspects of the early virtual sensor models [50, 85] achieve impressively minimum amounts of fuel penalty (about 0.7%), it is clear that significant gains could be made by bringing novel and computationally fast simulation algorithms (also known as virtual sensors) into the developments of future ECUs.

5. Simulation Approaches to DPFs

Based on a traditional design of experiments approach, diesel particulate filter design, system integration and control becomes very time-consuming and costly due to the high number of tests required. This provides a privileged window of opportunity for the application of simulation. A recent review of advances in DPF simulation technology is given in [47, 87]. While the interested reader is encouraged to consult these references and their cited literature for more detailed information on the underlying assumptions regarding the treatment of the various physicochemical phenomena (including soot particle transport, deposition and oxidation), in the present paragraph we provide an overview of the mode of use of the different simulation models in practice.

The multiscale nature of the problem lends itself to a hierarchical organization of the different models. The models at each spatial scale are classified according to their complexity and detail in the representation of the actual situation. Three sub-models corresponding to the three size scales (wall, channel, entire filter) must be combined to give an overall simulation model of the DPF. Ideally, we would like to employ the most detailed treatment from each scale. Such an approach would thus entail a true-to-the-geometry description of the porous filter wall, along with a 3-D CFD simulation of each channel, coupled through conjugate heat transfer to the other numerous (on the order of a few thousand) channels of the DPF. As this is for obvious reasons impossible even with computing resources of the foreseeable future, the employed strategy is to use the most detailed models at each spatial scale in order to validate and extract parameters for simpler (lower-degrees-of-freedom) models applicable to the next scale. These relatively simple lower-order models are then connected with the hierarchically superior models in the next spatial scale, and the procedure is repeated over the entire DPF scale.

At the wall-scale algorithmic as well as process-based reconstruction techniques are employed to generate 3-D "digital materials" that are realistic representations of DPF microstructures. This is especially important for the development of new filter materials, the optimization of catalyst deposition inside the porous wall and for the design of gradient-functional filter microstructures where multiple functionalities in terms of particle separation and catalyst distribution (for combined gas and particle emission control) can be exploited. We refer to this approach as microflow simulation. Examples of computer-reconstructed DPF porous media are given in **Fig. 32** and encompass all currently available filtration media: extruded ceramic filters (including reaction-formed media as cordierite and grain-sintered media as SiC), fibrous filters, foams and sintered metal powder/wire mesh. Using the reconstructed porous material and Lattice Boltzmann-based methods (see e.g.[88]), the flow field inside the filter porous wall can be obtained. The computation of soot deposition in the filter wall can then be carried out based on iterations between convective-diffusion soot deposition and flow field updates (as the porous wall structure is being progressively blocked by the deposited soot)[47, 52]. An example of soot deposition in a granular-structured DPF "digital material" is shown in **Fig. 33**.

In practice, the detailed microflow simulation is employed when one is interested in developing new filter wall structures that need to meet specific requirements of flow resistance, filtration efficiency and catalyst coating accommodation. The models at this scale are therefore of the highest interest to the manufacturers of filter media. In this case, the majority of the experimental development revolves around small-scale filter samples, frequently in disk form, that are quite convenient for use in laboratory-scale experiments[35]. Depending on the outcome of this de-

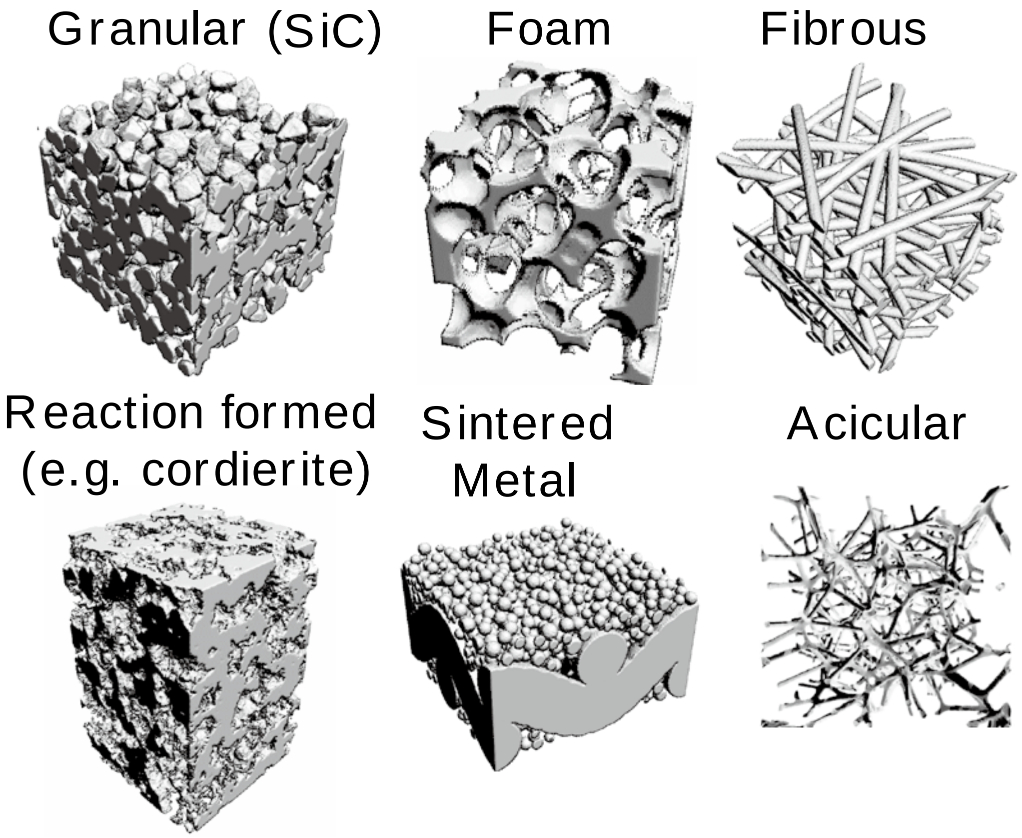

Fig. 32 Computer reconstruction of various porous filters.

velopment, interesting filter structures can be scaled-up into monolithic honeycomb samples. The use of a unit-cell structural description of the filter wall can be very advantageous at this stage, since with a minimal number of physically relevant parameters[35, 42] and well-characterized experiments, a description of the filtration and pressure drop behavior of the DPF can be achieved in a very computationally efficient manner. However, this information cannot be embedded directly into a filter channel simulation without significant computational resources, since the number of state variables needed for this is an order of magnitude higher. The already presented two-layer model in this case offers a compact description that can be embedded into a channel-scale simulation.

Channel-scale simulation is appropriate for the initial design and sizing of the DPF for an application. In this case, 3-D CFD is typically employed to assess the applicability of the classic perimeter-averaged approach[89], e.g. for filter channels of other shapes[44]. Otherwise, the single-channel perimeter-averaged formalism[30, 44, 89] represents a fast and accurate approach which can be employed in conjunction with well-defined experimental campaigns to obtain needed physicochemical parameters of the DPF in consideration. Single-channel simulation accounts for the majority of the simulation activities of the industry (DPF suppliers, catalyst coaters, emission control system integrators, engine manufacturers), and can provide useful estimates of axial soot loading distributions, pressure drop behavior and magnitude and location of temperature exotherms and thermal gradients during regeneration.

After the initial design phase, a DPF becomes part of an exhaust emission control system where its behavior also depends on the other components of the system. DPF models coupled with simulations of other emission control devices are then the appropriate tools to employ for system optimization and control. An example of a coupled simulation of a diesel oxidation catalyst (DOC) and a DPF in series is shown in **Fig. 34**. We observe how a hydrocarbon pulse injection upstream of the DOC raises the exhaust temperature and causes regeneration of the DPF. Such simulation tools are very useful for the development and optimization of post-injection strategies for DPF regeneration.

Important issues for the DPF performance at this

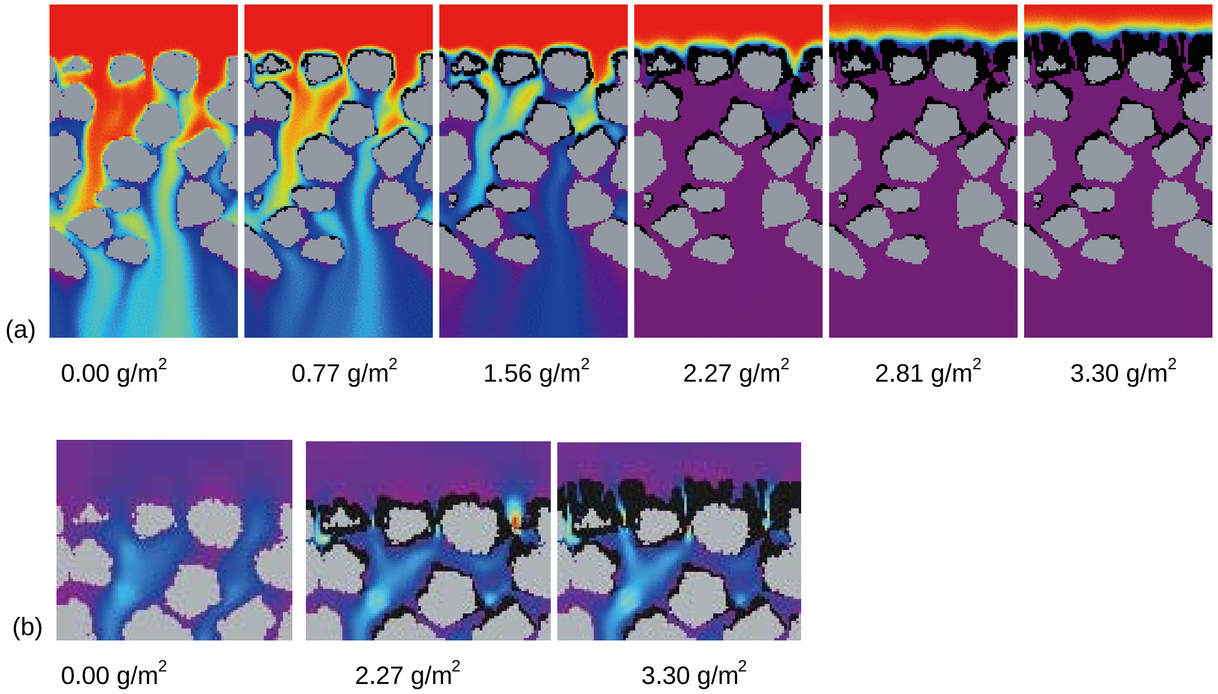

Fig. 33 Visualisation of soot deposition at different surface mass loads in an extruded ceramic (granular) filter wall. (a) Development of soot deposits (black) and soot mass fraction in the wall (solid material is gray) to the onset of cake formation. Soot mass fraction scale is from 0 (violet) to the inflow value (red). In (b), the velocity on a section through the filter wall is shown, with overlay of the soot deposit shapes.

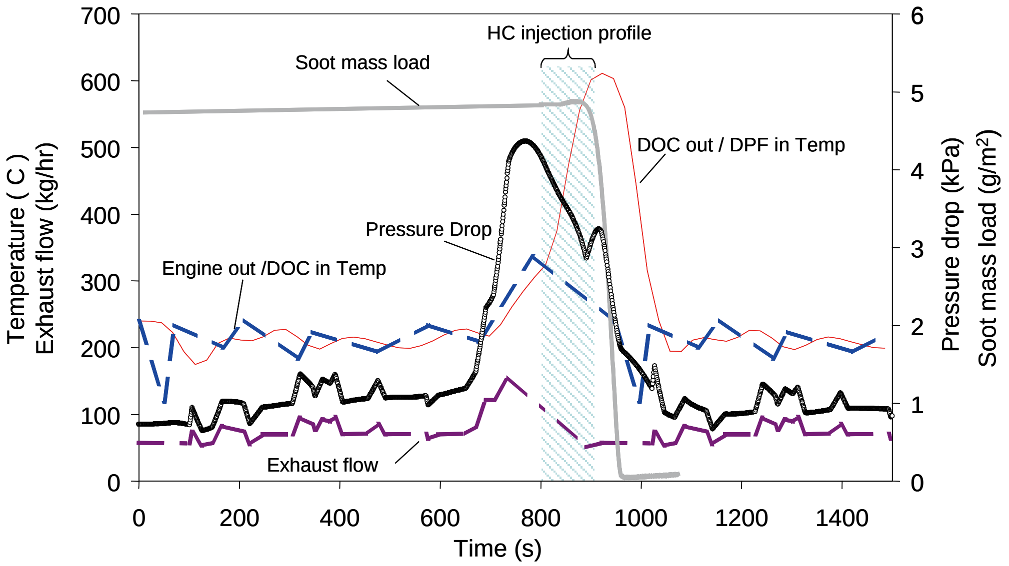

Fig. 34 Coupled DOC-DPF simulation. The 142mm × 152 mm, 200 cpsi SiC DPF regeneration is effected by hydrocarbon injection upstream of a 142mm × 152 mm 400 cpsi DOC over transient engine operation.

level are the development of transversal soot loading non-uniformities, induced by inlet cone flow and temperature maldistributions and/or by heat losses to the environment from the DPF external can surface. In addition, incomplete regenerations of the DPF need to be described. The continuum multichannel approach[69, 70, 71] represents a computationally tractable and accurate tool to address the previously mentioned issues. The development of highly integrated simulators of multi-functional exhaust emission control systems requires the interfacing of multichannel models of DPFs as well as other honeycomb-type converters to standard 3-D computational fluid dynamics solvers. Recent advances in this area include the rigorous integration into the continuum multichannel framework of segmented filter designs, computationally efficient discretizations of non-axisymmetric filter geometries (e.g. oval and trapezoidal shapes), and intelligent coupling to general-purpose CFD solvers to account for spatial distributions of inlet conditions brought about by specific upstream exhaust piping layouts as well as to temporal variations caused by engine operation. An example of a 3-D simulation of a DPF is shown in **Fig. 35**.

While computing limitations still remain the barrier for the routine employment of detailed simulations of coupled emission control components over the entire exhaust system scale, we anticipate that in the near future such simulations will be widely employed by the industry, exploiting grid-computing environments. This means that from a research point of view, DPF simulation will focus on providing a deeper understanding and more detailed description of the coupled transport, structural and reaction phenomena occurring at the wall and pore scales, to permit materialization of the vision for an a-priori design of advanced microstructures, hosting multifunctional catalysts for the highly compact and efficient emission control devices of the future.

6. Conclusions

The diesel particulate filter (DPF) has evolved into the most complex emission control device, due to its multiscale and multitemporal operational nature in combination with the different functionalities (particle separation/gas and particle catalytic reactions) embedded in it. Despite the challenges offered by this state of affairs, it has been possible to develop a systematic understanding of the science and technology of DPFs. Our starting point has been fundamental studies of diesel soot particle size, composition and morphology, and the mechanisms that determine the microstructural properties of soot deposits in DPFs. Filtration efficiency, pressure drop, ash accumulation and soot reactivity (with emphasis on catalyst-assisted soot oxidation) were then addressed, employing experimental methodologies ranging from small-scale filter set-ups to full-scale devices installed in the exhaust of diesel engines. The experimental methods are complemented by computational approaches that range from true-to-geometry representations of porous DPF microstructures up to entire emission control system simulations. Properly combined, the current state of knowledge, experimental methods and simulation approaches provide a rational and systematic route for enhancing the design

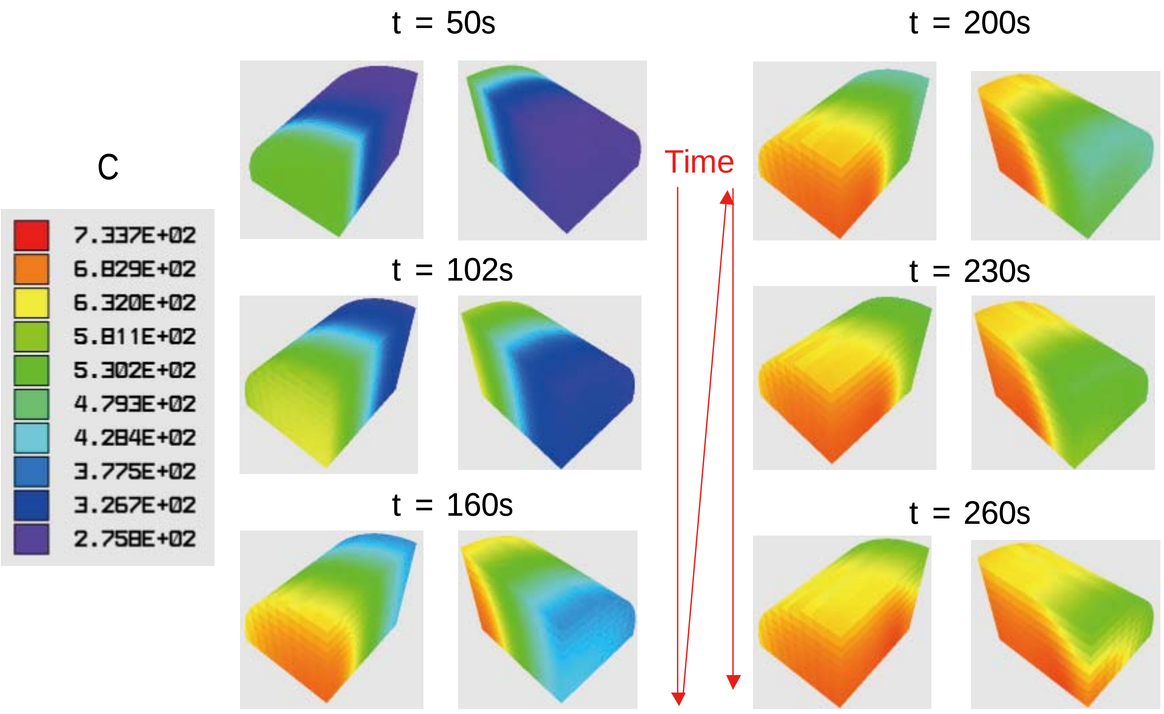

Fig. 35 3-D -DPF simulation. Example of of temperature field evolution in a 11.25 in × 12 in DPF during regeneration.

and reliability of future diesel particulate emission control systems.

Acknowledgements

Our work in the diesel emissions area has been supported in part by the European Commission framework programs through industrial collaborative projects DIDTREAT, CERFIL, MULTISENS, ART-DEXA, PSICO-DEXA, SYLOC-DEXA, STYFF-DEXA, FLOWGRID, IMITEC, COMET, MAAPHRI, IPSY, PAGODE, TOP-EXPERT, ATLANTIS, the Hellenic General Secretariat for Research and Technology through collaborative projects EPET-II, PAVE, EPAN and by a number of automotive industries and their suppliers. We are very grateful to them as well as to our colleagues at the APT Laboratory for all their hard work and support during these years. This paper is dedicated to the memory of our dear colleague Dr. Michael Claussen of CUTEC GmbH /University of Clausthal, Germany.

References

1) Ogyu, K., Ohno, K., Hong S. and Komori, T. (2004): Ash Storage Capacity Enhancement of Diesel Particulate Filter, SAE Tech. Paper No. 2004-01-0949.

2) Young, D.M., Hickman, D.L., Bhatia, G. and Gunasekaran, N. (2004): Ash Storage Concept for Diesel Particulate Filters, SAE Tech. Paper No. 2004-01-0948.

3) Bardon, S., Bouteiller, B., Bonnail, N., Girot, P., Gleize, V., Oxarango, L., Higelin, P., Michelin, J., Schuerholz, S. and Terres, F. (2004): Asymmetrical Channels to Increase DPF Lifetime, SAE Tech. Paper No. 2004-01-0950.

4) Boretto, G., Imarisio, R., Rellecati, P., Barucchi, E. and Sanguedolce, A. (2004): Serial Application of a Catalyzed Particulate Filter on Common Rail DI Diesel Engines For Passenger Cars, F2004V068, FISITA World Automotive Congress, Barcelona, Spain, May 23-27, 2004.

5) Nakatani, K., Hirota, S., Takeshima, S., Itoh, K., Tanaka, T. and Dohmae, K. (2002): Simultaneous PM and NOx Reduction System for Diesel Engines, SAE Tech. Paper No. 2002-01-0957.

6) http://www.greencarcongress.com/2006/01/mercedes_to_int.html

7) http://world.honda.com/news/2006/c060925DieselEngine/

8) Burtscher, H. (2005): Physical characterization of particulate emissions from diesel engines: a review, J. Aerosol Science, 36 (7), pp.896-932.

9) Kittelson, David B. (1998): Engines and nanoparticles: a review, J. Aerosol Science, 29 (5-6), pp.575-588.

10) Konstandopoulos, A.G., Gratz, L.D., Johnson, J.H., Bagley, S.T.and Leddy, D.G. (1988): Ceramic Particulate Traps for Diesel Emissions Control-Effects of a Manganese-Copper Fuel Additive, SAE Tech Paper No. 880009, SAE Trans. 97 sec. 6 (J. Engines) pp.37-53.

11) Konstandopoulos, A.G., Zarvalis, D., Papaioannou, E., Vlachos, N.D., Boretto, G., Pidria, M.F., Faraldi, P., Piacenza, O., Prenninger, P., Cartus, T., Schreier, H., Brandstatter, W., Wassermayr, C., Lepperhof, G., Scholz, V., Luers, B., Schnitzler, J., Claussen, M., Wollmann, A., Maly, M., Tsotridis, G., Vaglieco, B.M., Merola, S.S., Webster, D., Bergeal, D., Gorsmann, C., Obernosterer, H., Fino, D., Russo, N., Saracco, G., Specchia, V., Moral, N., D'Anna, A., D'Alessio, A., Zahoransky, R., Laile, E., Schmidt, S. and Ranalli, M. (2004): The Diesel Exhaust Aftertreatment (DEXA) Cluster: A Systematic Approach to Diesel Particulate Emission Control in Europe, SAE Tech. Paper No. 2004-01-0694 (SP-1861).

12) Konstandopoulos, A.G., Skaperdas, E. and Masoudi, M. (2002): Microstructural Properties of Soot Deposits in Diesel Particulate Traps, SAE Tech. Paper No. 2002-01-1015, SAE Trans. 111 (J. Fuels & Lubricants), pp. 434-442. Also in SAE SP, 1673, Diesel Exhausts Emission Control, pp. 181-190.

13) Van der Wal, Yezerets Aleksey, Currier, N.L., Kim, D., and Wang, C.M. (2007): Study of diesel soot collected from diesel particulate filters, Carbon, 45 (1), pp.70-77.

14) Van der Wal, R.L. and Tomasek, A. J. (2003): Soot oxidation: dependence upon initial nanostructure, Combustion and Flame, 134 (1-2), pp.1-9.

15) Van der Wal, R.L. and Tomasek, A.J. (2004): Soot nanostructure: dependence upon synthesis conditions, Combustion and Flame, 136 (1-2), pp.129-140.

16) Higgins, K.J., Jung, H., Kittelson, D.B., Roberts, J.T., and Zachariah, M.R. (2002): Size-Selected Nanoparticle Chemistry: Kinetics of Soot Oxidation, J. Phys. Chem. A, 106 (1), pp.96 -103.

17) Jung, H., Kittelson, D. and Zachariah, M.R. (2004): Kinetics and visualization of soot oxidation using transmission electron microscopy, Combustion and Flame, 136, pp.445–456.

18) Ishiguro, T., Takatori, Y. and Akihama, K. (1997): Microstructure of diesel soot particles probed by electron microscopy - First observation of inner core and outer shell, Combustion and Flame, 108 (1-2), pp.231-234.

19) Ishiguro, T., Suzuki, N, Fujitani, Y. and Morimoto, H. (1991): Microstructural changes of diesel soot during oxidation, Combustion and Flame, 85 (1-2), pp.1-6.

20) Harris, S.J. and Maricq, M.M. (2002): The Role of Fragmentation in Defining the Signature Size Distribution of Diesel Soot, J. Aerosol Science, 33, pp.935–942.

21) Kostoglou, M. and Konstandopoulos, A.G. (2006): On the Size Distribution of Diesel Soot Aggregates Undergoing Coagulation and Fragmentation, IAC.

22) Konstandopoulos, A.G. and Kostoglou, M. (2003): Modeling of diesel particulate size distributions with

oxidative fragmentation and coagulation, ETH-Conference on Combustion Generated Particles.

23) Merrill, C.J., Lighty, J.S., Eddings, E.G. and Sarofim, A.F. (2004): Investigation of the Oxidation and Fragmentation of Soot in a Two-Stage Flat Flame Burner System Utilizing a Scanning Mobility Particle Sizer, Western States Section of the Combustion Institute, Davis, CA, March 29-30.

24) Meakin, P.(1998): "Fractals, Scaling and Growth Far From Equilibrium", Cambridge University Press; 1st edition (January 15, 1998).

25) Viscek, Tamas (1992): "Fractal Growth Phenomena", World Scientific Publishing Co Pte Ltd.

26) Julien, R. and Botet, R. (1987): "Aggregation and Fractal Aggregates" , World Scientific.

27) Kostoglou, M. and Konstandopoulos, A.G. (2004): Oxidative Fragmentation and Coagulation of Diesel Soot Aggregates, ETH-Conference on Combustion Generated Particles.

28) Park, K., Cao, F., Kittelson, D.B. and McMurry, P.H. (2003): Relationship Between Particle Mass and Mobility for Diesel Exhaust Particles, Environmental Science and Technology, 37, pp.577-583.

29) Van Gulijk, C., Marijnissen, J.C.M., Makkee, M., Moulijn, J.A. and Schmidt-Ott, A. (2004): Measuring diesel soot with a scanning mobility particle sizer and an electrical low-pressure impactor: performance assessment with a model for fractal-like agglomerates, J. of Aerosol Science, 35 (5), pp.633-655.

30) Konstandopoulos, A.G., and Johnson, J.H. (1989): Wall-Flow Diesel Particulate Filters - Their Pressure Drop and Collection Efficiency, SAE Transactions 1998, Sec. 3 (J. Engines), SAE Technical Paper 890405, pp.625-647.

31) Diesel Exhaust Aftertreatment(1999): SAE Special Publication, SP-1414.

32) Diesel Exhaust Aftertreatment(1998): SAE Special Publication, SP-1313.

33) Diesel Exhaust Aftertreatment(1997): SAE Special Publication, SP-1227.

34) http://www.dieselnet.com

35) Konstandopoulos, A.G., Kostoglou, M., Skaperdas, E., Papaioannou, E., Zarvalis, D. and Kladopoulou, E. (2000): Fundamental Studies of Diesel Particulate Filters - Transient Loading, Regeneration and Aging, SAE Tech. Paper No. 2000-01-1016, SAE Trans. 109 (J. Fuels & Lubricants), pp. 683-705. Also in SAE SP, 1497, Diesel Exhaust Aftertreatment, pp. 189-211.

36) Adler Joerg(2005): Ceramic Diesel Particulate Filters" Int. J. of Applied Ceramic Techn. 2 (6), pp.429–439.

37) Howitt, J. and Montierth, M. (1981): Cellular ceramic diesel particulate filter, SAE Paper No. 81104.

38) Konstandopoulos, A.G., Vlachos, N. , Stavropoulos, I, Skopa S., Schumacher, U.,Woiki, D. and Frey, M. (2005): Study of a Sintered Metal Diesel Particulate Trap, SAE Technical Paper No. 2005-01-0968, SAE SP, 1940, Diesel Exhaust Emission Control Modeling, pp.217-228. Also in SAE Trans. 114 (J. Fuels & Lubricants), pp.465-475.

39) Oh, S., McDonald, J., Vaneman, G., Hegedus, L. (1981): Mathematical modeling of fibrous filters for diesel particulate - Theory and experiments, SAE Paper No 810113.

40) Konstandopoulos, A., Skaperdas, E., Warren, J. and Allansson, R. (1999): Optimized filter design and selection criteria for continuously regenerating diesel particulate traps, SAE Paper No 1999-01-0468.

41) Auto Emissions Magazine(1999): Corning Inc., No. 14.

42) Vlachos, N., Housiada, P., Zarvalis, D. and Konstandopoulos, A.G. (2002): Transient Filtration and Pressure-Drop Behavior of Diesel Particulate Filters, in Particle Loading & Filtration Kinetics in Fibrous Filters, U. Karlsruhe, June 27-30, (2002).

43) Masoudi, M., Konstandopoulos, A.G., Nikitidis, M. S., Skaperdas, E., Zarvalis, D., Kladopoulou, E. and Altiparmakis, C. (2001): Validation of a Model and Development of a Simulator for Predicting the Pressure Drop of Diesel Particulate Filters, SAE Tech. Paper No. 2001-01-911, SAE Trans. 110 (J. Fuels & Lubricants), pp.650-656. Also in SAE SP, 1582, Diesel Emission Control, pp.153-160.

44) Konstandopoulos, A.G., Vlachos, N., Housiada, P. and Kostoglou, M. (2003): Simulation of Triangular-Cell-Shaped, Fibrous Wall-Flow Filters, SAE Tech. Paper No. 2003-01-0844, SAE Trans. 112 (J. Fuels & Lubricants), pp.680-690. Also in SAE SP, 1755, Diesel Emission Measurement and Modelling, pp.227-238.

45) Masoudi, M., Heibel, A. and Then, P.M. (2000): Predicting Pressure Drop of Diesel Particulate Filters - Theory and Experiment, SAE Technical Paper 2000-01-0184.

46) Floerchinger, P., Anderson, M., Hou, Z., Taubert, T., Steinbrueck, E. and Angelo, T. (2003): Prediction and Validation of Pressure Drop for Catalyzed Diesel Particulate Filters, SAE Technical Paper 2003-01-0843 (SP-1755).

47) Konstandopoulos, A.G., Kostoglou, M., Vlachos, N. and Kladopoulou, E. (2005): Progress in Diesel Particulate Filter Simulation, SAE Technical Paper No. 2005-01-0946, SAE SP, 1940, Diesel Exhaust Emission Control Modeling, pp.11-40.

48) Konstandopoulos, A.G. (2003): Flow Resistance Descriptors for Diesel Particulate Filters: Definitions, Measurements and Testing, SAE Tech. Paper No. 2003-01-0846 (SP-1755).

49) Konstandopoulos, A.G., Skaperdas, E. and Masoudi, M. (2001): Inertial Contributions to the Pressure Drop of Diesel Particulate Filters, SAE Technical Paper 2001-01-0909.

50) Skaperdas, E. and Konstandopoulos, A.G. (2001): Prediction of Diesel Particulate Filter Loading Behavior for System Control Applications, CD AUTO 2001, 3rd International Conference on Control and Diagnostics in Automotive Applications, 4-6 July 2001, Sestri-Levante, Italy.

51) Friedlander, S.K. (1977): "Smoke, Dust and Haze.

Fundamentals of Aerosol Behavior", Wiley-Interscience.

52) Vlachos, N.D. and Konstandopoulos, A. G. (2003): Digital Materials Methods for DPF Development, SAE Tech. Paper No. 2006-01-0260.

53) Merkel, G., Beall, D. M., Hickman, D.L., and Vernacotola, M.J. (2001): Effects of Microstructure and Cell Geometry on Performance of Cordierite Diesel Particulate Filters, SAE Technical Paper 2001-01-0193.

54) Ido, T., Ogyu, K., Ohira, A., Hayashi, M. and Ohno, K. and Konstandopoulos, A.G. (2005): Study on the Filter Structure of SiC-DPF with Gas Permeability for Emission Control, SAE Technical Paper 2005-01-0578.

55) Chi, T.(1989): "Granular Filtration of Aerosols and Hydrosols", Butterworths series in chemical engineering (Butterworth, Stoneham, MA, 1989).

56) Rodriguez-Perez, D., Castillo, J.L., Antoranz, J.C., Konstandopoulos, A.G. and Vlachos, N. (2004): Mixed ODE-MC Model for the Soot Cake Formation in a Square Section Filter, European Aerosol Conference EAC 2004, Budapest, Hungary, 6-10 Sep.

57) Konstandopoulos, A. G. and Kladopoulou, E. (2004): The Optimum Cell Density for Wall-Flow Monolithic Filters: Effects of Filter Permeability, Soot Cake Structure and Ash Loading, SAE Tech. Paper No. 2004-01-1133 (SP-1861).

58) Bardasz, E., Mackney, D., Britton, N., Kleinschek, G., Olofsson, K., Murray, I and Walker, A.P. (2003): Investigations of the Interactions between Lubricant-Derived Species and Aftertreatment Systems on a State-of-the-Art Heavy Duty Diesel Engine, SAE Tech. Paper No. 2003-01-1963.

59) Roth, P., Eckhardt, T., Franz, B. and Patschull, J. (1998): H2O2-assisted regeneration of diesel particulate traps at typical exhaust gas temperatures, Combust. Flame 115, p.28.

60) Lueders, H., Stommel, P. and Geckler, S. (1999): Diesel exhaust treatment-new approaches to ultra low emission diesel vehicles, SAE Paper No. 1999-01-0108.

61) Christensen, H., Dinesen, J., Engell, H. and Hansen, K. (1999): Electrochemical reactor for exhaust gas purification, SAE Paper No 1999-01-0472.

62) Hawker, P., Myers, N., Huthwohl, G., Vogel, H., Bates, B., Magnusson, L. and Bronneberg, P. (1997): Experience with a new particulate trap technology in Europe, SAE Paper No. 970182.

63) Murphy, M.J., Hillenbrand, L.J., Trayser, D.A. and Wasser, J.H. (1981): Assessment of Diesel Particulate Control - Direct and Catalytic Oxidation, SAE Tech. Paper No. 810112.

64) Van Setten, B. (2001): "Development of a Liquid Catalyst for Diesel Soot Oxidation", Ph.D Thesis, Technical University of Delft, Netherlands.

65) Neeft, J.P. (1995): "Catalytic Oxidation of Soot; Potential for the Reduction of Diesel Particulate Emissions" , Ph.D. Thesis, Technical University of Delft, Netherlands.

66) Hennig, G.R. (1962): Catalytic Oxidation of Graphite, J. Inorg. Nucl. Chem., 24, pp.1129-1137.

67) Konstandopoulos, A.G., Papaioannou, E., Zarvalis, D., Skopa, S., Baltzopoulou, P., Kladopoulou, E., Kostoglou, M. and Lorentzou, S. (2005): Catalytic Filter Systems with Direct and Indirect Soot Oxidation Activity, SAE Tech. Paper No. 2005-01-0670 (SP-1942).

68) Konstandopoulos, A.G. and Kostoglou, M. (1999): Periodically Reversed Flow Regeneration of Diesel Particulate Traps, SAE Tech. Paper No. 1999-01-0469.

69) Kostoglou, M., Housiada, P. and Konstandopoulos, A.G. (2003): Multi-channel Simulation of Regeneration in Honeycomb Monolithic Diesel Particulate Filters, Chem. Eng. Sci., 58, pp.3273-3283.

70) Konstandopoulos, A. G., Kostoglou, M. and Housiada, P. (2001): Spatial Non-Uniformities in Diesel Particulate Trap Regeneration, SAE Tech. Paper No. 2000-01-0908.

71) Konstandopoulos, A.G., Kostoglou, M., Housiada, P., Vlachos, N. and Zarvalis, D. (2003): Multichannel Simulation of Soot Oxidation in Diesel Particulate Filters, SAE Tech. Paper No. 2003-01-0839.

72) Konstandopoulos, A.G., Lorentzou, S. and Kladopoulou, E.: Convective-Diffusive Deposition and Diesel Soot Reactivity in Catalyzed Particulate Filters, to be submitted.

73) Konstandopoulos, A.G., Zarvalis, D., Kladopoulou, E. and Dolios, I. (2006): A Multi-Reactor Assembly for Screening of Diesel Particulate Filters, SAE Tech. Paper No. 2006-01-0874.

74) Konstandopoulos, A.G., Kostoglou, M., Lorentzou, S., Pagkoura, C., Papaioannou, E., Ohno, K., Ogyu, K. and Oya, T.(2007): Soot Oxidation Kinetics in Diesel Particulate Filters, SAE Tech. Paper No. 2007 01-1129.

75) Neeft, J. P., Van Pruissen, O.P., Makkee, M. and. Moulijn, J. A. (1997): Catalysts For The Oxidation Of Soot From Diesel Exhaust Gases II. Contact Between Soot And Catalyst Under Practical Conditions, Applied Catalysis B: Environmental, 12 (1), pp.21-31.

76) Badini, C., Saracco, G. and Serra, V. (1997): Combustion of carbonaceous materials by Cu–K–V based catalysts I. Role of copper and potassium vanadates, Applied Catalysis B: Environmental, 11 (3-4), pp.307-328.

77) McKee, D.W., Spiro, C. L., Kosky, P. G. and Lamby, E.J. (1985): Eutectic Salt Catalysts for Graphite and Coal Char Gasification, Fuel, 64 (6), pp.805-809.

78) Fino, D. (2003): "Diesel-Soot Catalytic Combustion" , Ph.D. Thesis, Politechnico di Torino, Italy.

79) Ciambelli, P., Palma, V., Russo, P. and Vaccaro, S. (2002): Deep Filtration and Catalytic Oxidation: An Effective Way for Soot Removal, Catalysis Today, 73 (3-4), pp.363-370.

80) Ciambelli, P., Palma, V., Russo, P. and Vaccaro, S. (2003): Redox Properties of a TiO2 Supported Cu-V-K-Cl Catalyst in Low Temperature Soot Oxidation, Journal of Molecular Catalysis A: Chemical, 204-205, pp.673-681.

81) Karadimitra, K., Papaioannou, E., Macheridou, G. and Konstandopoulos, A. G. (2001): Ceria Nanoparticle

Coated Filters for Soot Emission Control, PARTEC 2001, International Congress for Particle Technology, Nuremberg, Germany, 27-29 March.

82) Karadimitra, K., Lorentzou, S., Agrafiotis, C. and Konstandopoulos, A.G. (2004): Modelling of Catalytic Particle Synthesis via Spray Pyrolysis & In-Situ Deposition on Porous Materials, PARTEC 2004, International Conference for Particle Technology, Nuremberg, Germany, March 16 -18.

83) Hiratsuka, Y., Ishihara, M., Tanaka, M., Suzuki, J. and Takagi, N. (2004): The Latest Technology of Controlling Micro-Pore in Cordierite Diesel Particulate Filter for DPNR System, SAE Tech. Paper No. 2004-01-2028.

84) Edgar, B. (2004): Emission Control Systems and Components for Retrofit, and First-fit Applications, 10th Annual Diesel Emissions Reduction (DEER) Conference, Coronado, California, August 29–September 2.

85) Konstandopoulos, A. G. and Kladopoulou, E. (2003): A Virtual Sensor for On-Board Diagnostics and Control of Diesel Particulate Filters, CDAuto03A2028, CD AUTO 03, 4th International Conference on Control and Diagnostics in Automotive Applications, Sestri-Levante, Italy, 18-20 June.

86) Kladopoulou, E., Yang, S. L., Johnson, J.H., Parker, G.G., Konstandopoulos, A.G. (2003): A Study Describing the Performance of Diesel Particulate Filters During Loading and Regeneration - A Lumped Parameter Model for Control Applications, SAE Tech. Paper No. 2003-01-0842 (SP-1755).

87) Konstandopoulos, A.G, Kostoglou, M. and Vlachos, N. (2006): The multiscale nature of diesel particulate filters, International Journal of Vehicle Design, 41, pp.256-284.

88) Chen, S. and Doolen, G. (1998): Lattice Boltzmann Method for Fluid Flows, Ann. Rev. Fluid Mech., 30, pp.329-????.

89) Bisset, E.J. (1984): Mathematical Model of the Thermal Regeneration of a Wall-Flow Monolith Diesel Particulate Filter, Chem. Eng. Sci., 39, pp.1233-1244.

Appendix

With reference to **Fig. 36**, the DPF pressure drop is written as the sum of various components, each of which can be determined in closed form as shown below:

$$\Delta P = p_7 - p_1 = \underbrace{(p_7 - p_6)}_{contraction} + \underbrace{(p_6 - p_5)}_{inlet\ channel} + \underbrace{(p_5 - p_4)}_{soot\ layer} + \underbrace{(p_4 - p_3)}_{filter\ wall} + \underbrace{(p_3 - p_2)}_{outlet\ channel} + \underbrace{(p_2 - p_1)}_{\text{exp}ansion} \tag{A.1}$$

$$\Delta P = \Delta P_{contraction} + \Delta P_{inlet\ channel} + \Delta P_{soot\ layer} + \Delta P_{filter\ wall} + \Delta P_{outlet\ channel} + \Delta P_{\text{exp}ansion} \tag{A.2}$$

$$\Delta P_{expansion} = p_2 - p_1 = \sqrt{p_1^2 + \frac{8}{3}\frac{\zeta \dot{m}^2 RT}{MW}\frac{(a+w_s)^4}{V_{DPF}^2 a^2}\left(\frac{L}{a}\right)^2} - p_1 \tag{A.3}$$

$$\Delta P_{filterwall} = p_4 - p_3 = \sqrt{p_3^2 + \frac{\mu}{k_w}\frac{\dot{m}RT}{MW}\frac{(a+w_s)^2}{V_{DPF}a}w_s + \beta\frac{\dot{m}^2 RT}{MW}\frac{(a+w_s)^4}{2V_{DPF}^2 a^2}w_s} - p_3 \tag{A.4}$$

$$\Delta P_{outlet\ channel} = p_3 - p_2 = \sqrt{p_2^2 + \frac{\mu \dot{m}RT}{MW}\frac{(a+w_s)^2}{V_{DPF}}\frac{4FL^2}{3a^4}} - p_2 \tag{A.5}$$

$$\Delta P_{soot\ layer} = p_5 - p_4 = \sqrt{p_4^2 + \frac{\mu}{k_{soot}}\frac{\dot{m}RT}{MW}\frac{(a+w_s)^2}{2V_{DPF}}\ln\left(\frac{a}{a-2w}\right)} - p_4 \tag{A.6}$$

$$\Delta P_{inlet\ channel} = p_6 - p_5 = \sqrt{p_5^2 + \frac{\mu \dot{m}RT}{MW}\frac{(a+w_s)^2}{V_{DPF}}\frac{4FL^2}{3(a-2w)^4}} - p_5 \tag{A.7}$$

$$\Delta P_{contraction} = p_7 - p_6 = \sqrt{p_6^2 + \frac{4}{3}\frac{\zeta \dot{m}^2 RT}{MW}\frac{(a+w_s)^4}{V_{DPF}^2 a^2}\left(\frac{L}{a}\right)^2} - p_6 \tag{A.8}$$

$$\Delta P = \Delta P_{contraction} + \Delta P_{inlet\ channel} + \Delta P_{soot\ layer} + \Delta P_{filter\ wall} + \Delta P_{outlet\ channel} + \Delta P_{\text{exp}ansion} \tag{A.9}$$

The total pressure drop computation accounting for compressibility effects is performed easily in a spreadsheet by a back-substitution scheme, employing Eqs. (A.1-A.9) in dreereverse order, i.e. starting the calculation from the downstream side, where the pressure p_1 is known, and continuing upstream for the calculation of the remaining components. In the above equations, $\dot{m}$ the exhaust mass flow rate, while MW is the exhaust molecular weight. The effect of compressibility is illustrated in **Fig. 36**, where the pressure drop for a DPF, calculated with the incompressible and the compressible approach, is shown.

A deviation is observed at values of pressure drop which exceed 15 kPa with the incompressible model resulting in an overestimation of the pressure drop by about 7%. A maximum pressure drop of 12-14 kPa is usually prescribed by vehicle manufacturers when sizing a DPF for a series application, therefore in most practically relevant situations, the analytic incompressible model can be applied with very good accuracy.

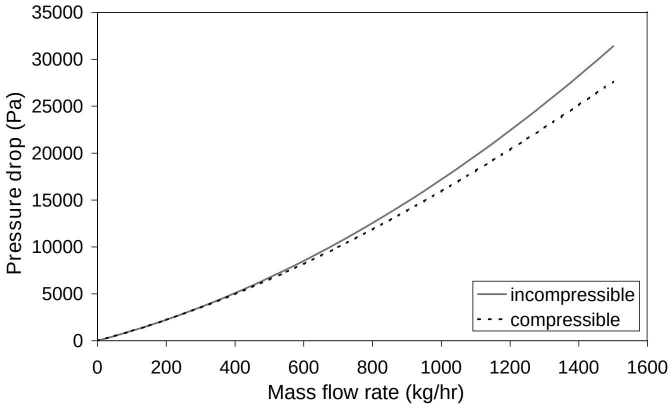

Fig. 36 Incompressible and compressible pressure drop model for a 5.66 in × 6 in, 181cpsi/14mil DPF, with $k=1\times10^{-13}$ m^2 and $\zeta=5$.

Author's short biography

Athanasios G. Konstandopoulos

Dr. Athanasios G. Konstandopoulos, Descartes Laureate (2006), is a specialist in combustion aerosols and nanoparticles. He is the Founder and Director of the Aerosol & Particle Technology (APT) Laboratory (http://apt.cperi.certh.gr) at CPERI/CERTH and a member of the faculty of Chemical Engineering at Aristotle University. He is the author of more than 100 scientific and technical papers and a Fellow of the Society of Automotive Engineers (SAE). He has a hybrid background in Mechanical (DiplME, Aristotle University, MSc Michigan Tech) and Chemical Engineering (MSc, MPhil, PhD, Yale University).

Eleni Papaioannou

Ms. Eleni Papaioannou is the Chief Operating Officer of the Aerosol & Particle Technology (APT) Laboratory (http://apt.cperi.certh.gr) at CPERI/CERTH. She has more than 12 years of professional engineering experience in nanoparticle emission control technologies and biological effects of nanoparticles. She has managed and technically supervised numerous collaborative projects of the APT Laboratory with the automotive industry and its suppliers. She is the author of 20 scientific and technical papers and she holds a Diploma in Chemical Engineering (Aristotle University).

The Numerical Modelling of the Flow in Hydrocyclones[†]

Andrzej F.Nowakowski[*],
Department of Mechanical Engineering,
University of Sheffield[1]
Michael J.Doby
Experimental Station E304/A213
DuPont[2]

Abstract

Over the last decade, the progress in numerical modelling of hydrocyclones has advanced at a rapid pace. A summary of the recent advancements is undertaken in the paper to summarize the major directions and developments in hydrocyclone modelling. The important aspects that contribute to the accurate simulation of general internal swirling flows and other characteristic features occurring in hydrocyclones modelling are covered. The relevant issues are: the formulation of the governing equations (classical versus stress divergence form), the imposition of boundary conditions especially regarding the open part of the outlet boundary conditions and the problem of proper representation of the computational domain. The complex flow pattern that occurs in hydrocyclones invalidates several assumptions in the standard turbulence models. Challenges still remain in predicting accurately the effects of turbulence anisotropy. A performance review of selected equations closures is presented with insight on their potential and limitations. The flow predictions obtained using the Reynolds Stress Model (RSM) and Large Eddy Simulation (LES) turbulence models are examined. The predictions of the free surface flow and air core dimensions have yet to be fully resolved. The same concerns the problem of simulating large number of particles. The recent important developments related to the solid/gas and sold/liquid interaction problems are presented together with intriguing challenges one need to overcome in order to numerically handle multi-component flows. The Lagrangian and multi-continuum Eulerian techniques are considered. The attempt to systemize various approaches for multi-component flows according to their accurateness and relevance to the various flow regimes in hydrocyclones is undertaken. The issue of experimental validation is crucial to provide confidence in hydrocyclone flow-field models and the current state of experimental data is examined. Finally, suggestions for the future direction of hydrocyclone modelling are highlighted.

Keywords: hydrocyclone, computational fluid dynamics, numerical methods, swirling flow, multicomponent flow

1. Introduction

Hydrocyclones are primarily used for the separation of particulate slurries as well as liquid-liquid systems. A wide variety of industries, including petrochemical, mineral processing, and pharmaceutical, have recognized the advantages of hydrocyclones in separation. The effectiveness of the hydrocyclone in diverse applications signifies the economic and operational value as a separational unit. The foremost advantage is the versatility of the hydrocyclone in a variety of applications — concentrating, dewatering, and separation. The economic cost of a hydrocyclone is significantly less compared with other common unit of operations. Due to absence of moving parts, a hydrocyclone has an extended operational life and low maintenance costs versus other separation technologies. These characteristic traits allow continuous operation without severely affecting the performance of the process. A significant drawback to hydrocyclones is the amount of waste that is produced from the separation. Another disadvantage is the large

---

[†] Accepted : July 2, 2008
[1] Mappin Street, Sheffield S1 3JD, United Kingdom
[2] Wilmington, DE 19809, United States
[*] Corresponding author.
TEL.: +44 114 222 7812
E-mail: a.f.nowakowski@sheffield.ac.uk

dependence of the separational efficiency on the mass flow rate, which is a difficult parameter to control. Although the affect can be reduced by certain measures, the efficiency of separation will vary with time in a process. Despite the disadvantages, hydrocyclones are still a widely used unit of separation.

A hydrocyclne operates by tangentially inserting a feed that causes a high centrifugal force to occur. The slurry is injected into the hydrocyclone via one or several tangential inlets. The confinement of the feed in the conical/cylindrical section of a hydrocyclone produces a high swirl flow, which is the primary mechanism of separation for particles or droplets from liquid—solid or liquid-liquid mixtures. The combined axial and tangential components of velocity field characterize a flow streamline that rotates around the central axis. Bank and Gauvin (1977) revealed that the radial velocity has a minor contribution in the separation of the particles. The wall curvature directs the flow into a spiral path that travels downwards towards the apex, as shown in **Fig.1**. While the wall friction reduces the tangential velocity, the radial contraction in the conical section maintains the magnitude of the velocity. The centrifugal force acting on the particles is directly proportional to the mass of the particle. Larger particles tend to be driven towards the wall, while smaller particles tend to accumulate in the center. The heavy particles in the suspension travel towards the hydrocyclone wall and then down to the apex. In the conical contraction section, an axial reversal flow is formed and moves upwards carrying the smaller particles through the vortex finder. According to Rietema (1961), the total pressure drop across the hydrocyclone consists of the inlet velocity head, friction losses and the centrifugal head. The pressure drop determines the maximum volumetric throughput that can be processed.

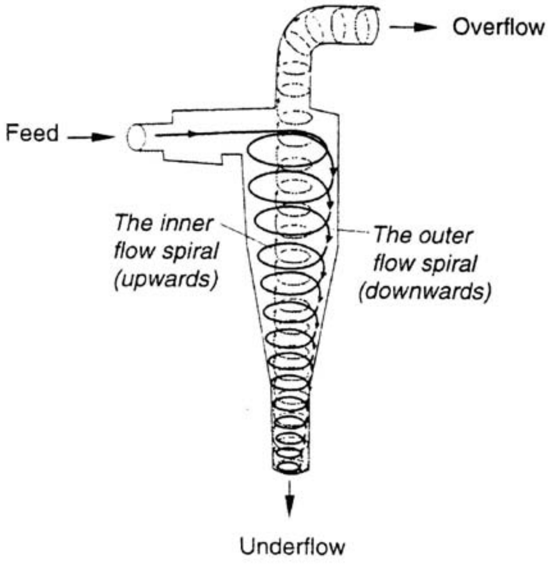

Fig.1 Schematic diagram of a hydrocyclone explaining the principle of operation.

Although hydrocyclones have been used in industry since the 1950s, the details of the flow behavior are still not well understood. Modelling and experimental investigation of the complexity and range of phenomena of fluid flow in a slurry separator has been attempted for many years and is presented in numerous scientific contributions. The nature of fluid flow and in particular the swirling flow characteristic has been studied experimentally by Fisher and Flack (2002), theoretically using computational methods by Nowakowski et al. (2004), or simplified analytical approaches with the most extensive presented by Bloor and Ingham (1987). All these strands of the research confirm that a vortex constituting a swirl flow is composed of two separate vortices, a free and forced. A forced vortex resembles a solid body rotation. Near the wall, the swirling components become less dominant and the device geometry exerts more influence. The relationship between the tangential velocity and the radius is inversely proportional in the free vortex and proportional in the forced vortex. Although this phenomenon seems to be obvious, it is intuitively understood and is observed in prevalent studies, there are some uncertainties related to how the swirl flow could be controlled. Detailed investigation of the velocity patterns in various flow regimes may provide a fruitful avenue for understanding a number of open issues regarding internal swirling flow and the implications on separational efficiency in a hydrocyclone. Detailed knowledge of the flow structure is required if one is to consider such issues as energy saving, cost or product quality. Several benefits could arise from this knowledge, for instance: areas of high erosion may be identified and potentially minimized or accounted for in design; design modifications for improved separation or reverse engineering of a hydrocyclone's geometry could be obtained.

Along the hydrocyclone axis, an area of low pressure is created by high angular momentum. This may cause the formation of a rotating free liquid surface at the centre. If the hydrocyclone is open to the atmosphere, air is inhaled through the outlet orifices and forms a central air core. If the air core exists, the pressure at the air-liquid interface is equivalent to atmospheric pressure if we neglect both the surface tension and viscous forces. Air core formation in a hydrocyclone is not currently known. The prevalent thought, however, is that the air enters from both outlets and eventually reaches a critical point, which combines the two air vortices, Cullivan *et al.* (2004). A majority of the current hydrocyclone modeling work has largely ignored the complex features of air-core development, by making several simplified assumptions.

The operational states of hydrocyclones have been defined by the type of discharge at the hydrocyclone apex. The three different operational states can be distinguished, which are spray, roping, and transitional discharge. Spray discharge is the occurrence of unobstructed flow through the apex and exits the apex in the form of an "umbrella" . The roping discharge states occurs when the apex has been impeded. The roping state reduces the separation efficiency by affecting the split ratio of the device. Neesse *et al.* (2004) show that the optimal hydrocyclone operation conditions occur in the transitional discharge state between roping and spray. Datta and Som (2000) present the effects of changing different operating parameters on the discharge angle.

A popular method of hydrocyclone design consists of varying operational parameters, such as pressure drop, cut size, and volumetric throughput to determine the effects of the changes. For example Kelsall (1952) developed a design process that uses an empirical model to produce a classification curve at different flow rates. Using the classification curve, the hydrocyclone's geometrical parameters could be defined for different process streams. A classification curve is normally used to determine the d_{50} parameter, which is the particle size that has an equal chance of exiting either the overflow or underflow.

The emergence of high performance computing has allowed the numerical simulation of partial differential equations become a viable alternative to physical experiments and empirical methods. The problem associated with mathematical modelling of the flow patterns involves the solution of strongly coupled, non-linear partial differential equations of the conservation of mass and momentum and lies well beyond any analytical approach. Additionally in the context of modelling a flow in hydrocyclones the challenges are related to the complex flow behaviour arising from the three-dimensional flow entry; multi-phase interactions; and the mechanisms governing the formation of an air-core (when the hydrocyclone is open to the atmosphere). Consequently, computational studies have been in general, limited to low particle-concentration flows and to simplified geometries of the hydrocyclone entry region.

Even with current limitations, computational methods of design have significant advantages over the empirical data, such as for example freedom to change the geometry quickly for verification of possible changes in separational efficiency.

The paper reviews the existing theoretical models and addresses how the computational algorithms could be extended to include complex interactions between continuous and dispersed phases. Specifically, the paper considers methodologies for velocity field prediction and modeling of the particle distribution. A strategy for future developments in these areas is outlined. The paper also briefly discusses essential measurement techniques for the validation of hydrocyclone flow field.

2. The Formulation of the Governing Equations and the Velocity Field Prediction

Nowakowski *et al.* (2004) provided a compilation of many of the major contributions to the study of hydrocyclone fluid dynamics between the years: 1982-2003. The application of full three-dimensional modelling to the hydrocyclone has been attempted only during the last decade with early attempts being made by Concha et al. (1998). Authors such as He et al. (1999) demonstrated that full three-dimensional modelling is essential in order to accurately model the hydrocyclone flow field, as a result of its inherent axial asymmetry. The present authors have endeavoured to compute hydrocyclone performance using their own finite element code and the commercial computational fluid dynamics package Fluent. Some aspects of the numerical algorithm development have previously been described in detail in Nowakowski and Dyakowski (2003). The present review is focused on fully three-dimensional approach and introduces a summary of numerical studies from the year 2000 onwards.

The objective is to compute the flow problem in a hydrocyclone modelled by the Navier-Stokes equations in three-dimensional domain Ω with boundary

$\partial\Omega = \Gamma_{Dw} + \Gamma_{De} + \Gamma_N$. The Γ_{Dw} stands for solid walls and Γ_{De} for inlet boundary, while Γ_N indicates the outflow parts of boundary. The underlying equations written in primitive variables and stress-divergence form are:

$$\frac{\partial \boldsymbol{u}}{\partial t} + (\boldsymbol{u}\cdot\nabla)\,\boldsymbol{u} - \frac{1}{\rho}\nabla\cdot\tau = 0 \qquad (1)$$

$$\mathrm{div}\boldsymbol{u} = 0 \qquad (2)$$

where constitutive relations for incompressible fluids are given by

$$\tau = -p\boldsymbol{I} + 2\mu\boldsymbol{D}(\boldsymbol{u}) \;\; \boldsymbol{D}(\boldsymbol{u}) = \frac{1}{2}\left[\nabla\boldsymbol{u} + (\nabla\boldsymbol{u})^T\right] \qquad (3)$$

The standard notation for velocity $\boldsymbol{u}$ and pressure p is used and ρ is constant density; μ dynamic viscosity; τ is the total stress and $\boldsymbol{I}$ is the identity tensor. The initial velocity field is assumed to satisfy incompressibility constraint (2). The advantage of stress-divergence form is that it can readily treat problems with fluid constitutive equations in a more general way than the classical form where the stress tensor is decomposed. Therefore, the extensions of the application of numerical techniques to Non-Newtonian fluid can be considered. Secondly the stress-divergence form leads to the physical Neumann boundary conditions that represent force $\boldsymbol{f}$

$$\boldsymbol{f} = \tau\cdot\boldsymbol{n} = -p\boldsymbol{n} + 2\mu\boldsymbol{D}(\boldsymbol{u})\cdot\boldsymbol{n} = \hat{\boldsymbol{f}} \text{ on } \Gamma_{\mathrm{N}} \qquad (4)$$

and Dirichlet boundary condition for velocity field $\boldsymbol{u}$ at the inlet and solid walls

$$\boldsymbol{u} = 0 \quad \text{on } \Gamma_{\mathrm{Dw}} \quad \text{and} \quad \boldsymbol{u} = \hat{\boldsymbol{u}} \text{ on } \Gamma_{\mathrm{De}} \qquad (5)$$

where $\boldsymbol{n}$ is unit outer vector normal to $\partial\Omega$, $\hat{\boldsymbol{f}}$ is applied vector valued force on the boundary, while $\hat{\boldsymbol{u}}$ is specified velocity profile at the inlet.

The velocity $\mathbf{u}_b$ must satisfy the global condition.

$$\oint_{\Gamma} \boldsymbol{n}\cdot\hat{\boldsymbol{u}} = 0 \qquad (6)$$

that follows from integrating the continuity equation (2) over the domain Ω and using the divergence theorem. A serious difficulty encountered is the determination of the pressure field and the fulfilment of the incompressibility constraint. While the continuity equation represents a constraint for the velocity field, the pressure variable, which appears in the momentum equation through the term ∇p, provides a degree of freedom necessary to satisfy such a constraint. It is important to note that no boundary condition is prescribed for the pressure. On inflow and outflow boundaries, the pressure can only be supplemented as a part of the Neumann type of boundary condition.

The specific form of the governing equations depends on the choice of dependent variables. The primitive variable formulation (the equations written in terms of $\boldsymbol{u}$ and p) has been preferred by the authors and other hydrocyclone investigators. The primitive variable formulation expressed in the "stress-divergence" form (Gresho, 1991) is commonly used in the finite element numerical framework. A numerical solution of the equations of motion in a hydrocyclone has also been obtained using a stream-function-vorticity formulation by Ovalle *et al.* (2005).

The numerical treatment of even the simplest turbulent flows generates enormous difficulties. Primarily, this is due to the complicated hydrocyclone geometry generating swirling flow and the fact that the non-linearity in the Navier-Stokes equations, gives rise to a very broad range of spatial and temporal turbulent scales.

The Reynolds Averaged Navier-Stokes equations (RANS) modelling approach enables the approximation of the turbulence effects on the mean flow. The Reynolds equations have the same form as the instantaneous equation 1, with the exception of the second-moment or correlation tensor, R = $<\overline{\boldsymbol{u}'\otimes\boldsymbol{u}'}>$.

$$\frac{\partial\bar{\boldsymbol{u}}}{\partial t} + (\bar{\boldsymbol{u}}\cdot\nabla)\bar{\boldsymbol{u}} + \frac{1}{\rho}\nabla\bar{p} - \nu\,\nabla\cdot[\nabla\bar{\boldsymbol{u}} + (\nabla\bar{\boldsymbol{u}})^T]$$
$$+\nabla\cdot <\overline{\boldsymbol{u}'\otimes\boldsymbol{u}'}> = 0 \qquad (7)$$

The equations were solved using a finite element code introduced by Nowakowski and Dyakowski (2003) for laminar and turbulent regime. In order to clarify the three-dimensional structure of the flow and show its swirling features the particle trajectories were plotted in **Fig.2**. The simulation results demonstrated that the short-circuit flow moves from the feed inlet and along the outer wall of the vortex finder tube until joining the rest of fluid in the overflow. The results also revealed the development of the double helical flows, the inner-upward and outer-downward helical flows (**Fig.2**), and the change of the processing vortex core as it moves about the hydrocyclone axis as well as the characteristic pattern of the developing flow at the underflow and overflow outlets. The numerical simulations were able to reproduce the swirling character of the flow in both vertical and horizontal directions and confirmed the existence of asymmetry as observed in labora-

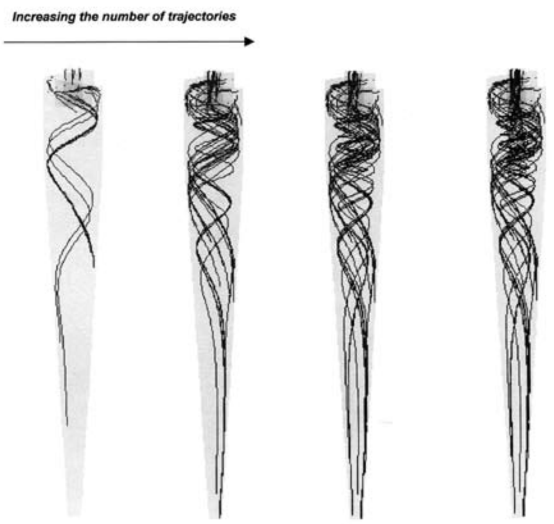

Fig.2 Simulation results obtained from the developed finite element software. Trajectories of mass less particles released from the hydrocyclone inlet (Nowakowski and Dyakowski, 2003).

tory experiments. At the outlets, the mathematical description of the problem (stress-divergence form) enabled imposition of natural boundary conditions in terms of forces, provided that the necessary data can be determined experimentally. In the simulations performed, zero stress boundary conditions were prescribed at the hydrocyclone outlets. This boundary choice is neutral in character, does not restrict the profile of velocity field, and is dictated by the need to truncate computational domain. Such an imposition of boundary conditions avoids any *a priori* assumptions concerning the velocity field at the outlets and most importantly, does not define the mass split-ratio. The postulated descriptions of outflow boundary conditions enable simulation of a characteristic spray profile velocity field at the spigot. Doby *et al.* (2005) investigated the interaction between the swirling flow and velocity profile at the outlet. The studies were carried out for fluids with different properties and it was shown that with the proper imposition of boundary conditions the flow develops naturally.

Owing to the complex hydrocyclone geometry an unstructured mesh generation technique has been used by a majority of researches studying the numerical flow in hydrocyclones. The key advantage of the unstructured grid methodology is the ability to handle not only the hydrocyclones of the same class but also with different geometry configuration.

3. Turbulence Modelling

All models, discussed below, are based on the time-averaged equations and the turbulence effects are incorporated through the Reynolds stress tensor. To obtain a quantitative solution several assumptions concerning the physics of the turbulent flow have to be made.

In RANS, the right choice of turbulence closure that addresses the unknown correlation terms of the velocity fluctuations (Reynolds stresses) is vital for correct separation prediction. The highly rotational fluid flow in the hydrocyclone makes otherwise successful RANS turbulence models fail to produce practically reasonable results. It is well known, for example, that for swirl flows the k-ε model (Harlow and Nakayama, 1968) predicts a too rapid decay of the swirl because it assumes isotropic viscosity, when in fact Reynolds stresses in hydrocyclone are highly anisotropic (Petty and Parks, 2001). The k-ε turbulence model is a two-equation model in which transport equations are solved for the turbulent kinetic energy, k, and its dissipation rate, ε. There are many forms of the k-ε model, which have been used for several decades, and is currently the most widely utilized model for industrial applications. The k-ε model provides accurate solutions for fully turbulent flows. Although Dai *et al.*, (1999) modified the k-ε model to calculate the anisotropic character of turbulence flow within a hydrocyclone by developing the model constants $C_{\varepsilon 1}$, $C_{\varepsilon 2}$ and $C\mu$.. These constants in the standard k-ε model were determined from experimental measuremrnts in a wind tunnel with almost uniform velocity fields. It is apparent that these constants, determined in this way, are not applicable to hydrocyclone flow field.

Many research groups used the computational fluid dynamics package Fluent, with its finite volume platform, to investigate the capability of different turbulence models for hydrocyclone simulation. Cullivan *et al.* (2003) highlighted that modelling of hydrocyclone flow-field requires comprehensive modelling of turbulence to account for significant anisotropy and turbulence generation mechanisms. The Fluent full differential stress model (DSM) with high-order treatment of the pressure-strain term has been shown to be a good compromise between accuracy and computational cost. The DSM does not represent an entirely accurate description of the turbulence, in particular sub-grid scale modeling and equilibrium turbulence is assumed. The equilibrium assumption presumes that the rate of transfer of turbulence energy down through the energy containing length-scales is constant, which is not expected to hold for the rapidly developing and short residence time hydrocyclone flow-field. Even so, the DSM turbulence model offers practicality in terms of computational resource.

Earlier turbulence models were purely dissipative and did not account for Reynolds-stress relaxation effects. In present practice of modelling turbulence in hydrocyclones Reynolds stresses are calculated from a set of partial differential equations. Each Reynolds stress component can be viewed as a 'property' of fluid. Its progress is determined by its rate of production, destruction, diffusive spread and redistribution between components. The redistribution mechanism is governed by the "pressure–strain" tensor which is zero for an isotropic turbulence. The RSM model consists of a set of six partial differential equations for each component and one partial differential equation for the dissipation rate (Appendix A). Reynolds Stress Model (RSM) has been applied as turbulence closure in the study presented by Kraipech-Evans *et al.* (2008). The simulations using RSM model and supporting validation studies in the context of hydrocyclones were also presented in recent papers of Bhaskar *et al.* (2007) and Wang and Yu (2006). The RSM model was found to predict well anisotropic turbulence. The RSM provides information about all the stress components and contains exact terms for swirling effects in the stress transport equations.

The Algebraic Stress Model (ASM) model was developed to account for anisotropy without solving for Reynolds stress transport equations. The ASM is based on the assumption that the convective and diffusive transport terms are removed or modelled, thus reducing the equations of Reynolds stress transport to algebraic equations. Chu and Chen (1999) introduced the algebraic stress turbulence model in simulation of a hydrocyclone flow, which is computationally less expensive than the Reynolds stress model, but still possesses a few of the RSM characteristics.

Alternatives such as large-eddy simulation (LES) and proper-orthogonal decomposition are still subject to active research and these require considerable additional computational cost. Slack *et al.* (2000) have demonstrated the DSM to perform remarkably well in comparison to LES without such prohibitively high computational costs.

The direct numerical simulation (DNS) and large eddy simulation (LES) are becoming more important and viable options for the solution of transitional and turbulent flows governed by the system of equations (1) and (7). The number of grid points required for a DNS is determined by the ratio of the respective length scales of the energy carrying dissipative eddies. This ratio is a very rapidly growing function of the Reynolds number and consequently the application of direct simulation is at present limited to flows at moderate Reynolds numbers and rather simple geometries. In the LES simulation approach, the severe Reynolds number restrictions are bypassed by directly simulating the large scales only and modelling the effects of missng small scales by using a subgrid model. Unlike the Reynolds averaged Navier-Stokes equations approach (RANS), large-eddy simulations retain the full three-dimensionality and time dependence of the fluctuating turbulent field. As a result of recent progress the LES technique has been used for cyclone (Slack *et al.*, 2000) or hydrocyclone (Delgadillo and Rajamani, 2005) simulation. It seems that the computationally more expensive LES provides the best solution for capture of time dependent vortex oscillations and non-equilibrium turbulence, which will potentially impact the separation efficiency. Challenging tasks associated with LES are the implementation of a sub-grid scale model accounting for the effects of particles and the correlation of different time scales related to collisions and aggregation of particles.

Although many of simpler turbulence models are often incapable of handling the strong vortical features that are present in hydrocyclones, the emphasis on simplicity, computational speed and robustness in an industrial context does not always allow the adoption of more advanced models. Using the averaged Navier-Stokes equations for modelling requires empirical or semiempirical information on the structure of the turbulence and the relationship to the mean flow. The information needed for the modelling is not easily obtained in hydrocyclones.

4. Air-core Modelling

The air core is an interesting and not well-understood phenomenon that occurs in hydrocyclones and drastically influences the efficiency of separation. Predictions of the air-core diameter have been provided through: application of Bernoulli's equation applied with a minimisation procedure (Davidson, 1988); through the use of an effective air-core interface viscosity (Dyakowski and Williams, 1995); as

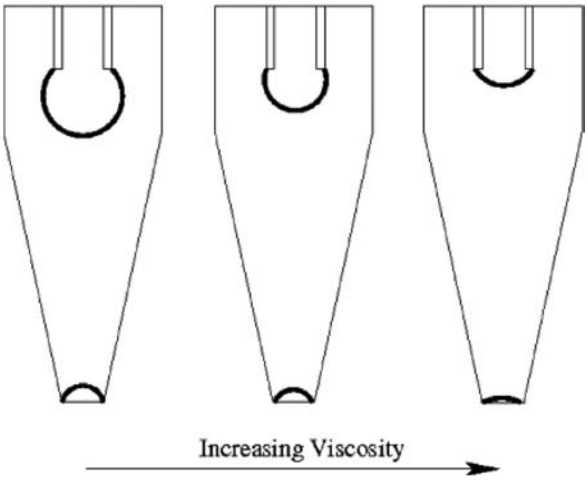

Fig.3 The effect of viscosity on the formation of the air core (Doby *et al.*, 2008).

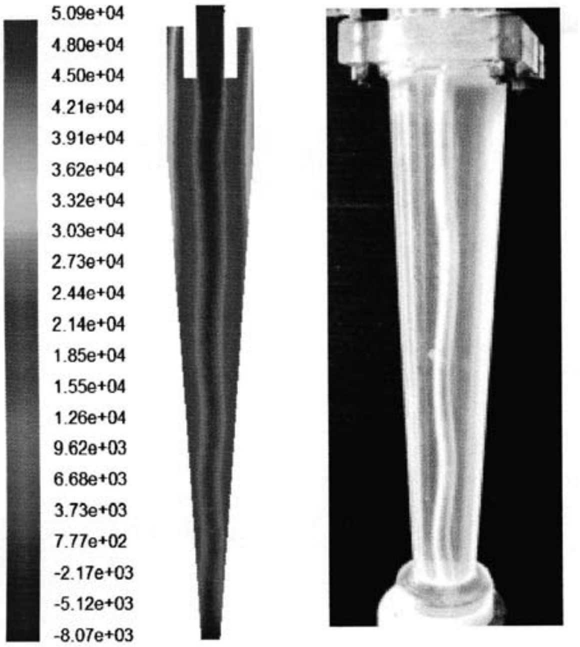

Fig.4 The obtained pressure (Pascal) of fluid projected on a vertical plane of the hydrocyclone: a) operating with an air core, b) experimental observation (Kraipech *et al.*, 2008).

well as through application of Young-Laplace's relation (Concha *et al.*, 1998). The later two approaches offer the potential to account for asymmetric air-core geometry. Dyakowski and Williams (1993) showed that the air core is not stationary, but has an oscillatory nature. The oscillations could be caused either by fluctuations in the feed or induced inertial waves (Ovalle and Concha, 2005). Delgadillo and Rajamani (2005) investigated the dynamics of the air core using a LES turbulence model. Doby *et al.* (2008) numerically examined different flows at varying viscosities and revealed that low viscosity feeds tend to develop a larger low-pressure area in the center region of the hydrocyclone than feeds at high viscosity (**Fig.3**). As shown in **Fig.3**, air from the atmosphere pushes the fluid due to the low pressure formation in the center area and upper section in the vicinity of the vortex finder. The total area of the low pressure reduces with increasing viscosity. Based on the contours of the apex and upper section, the air core formation appears to begin in both the upper and at the apex. The air core starts from each of the outlets and combines together in the central part of the cyclone. The numerical and experimentally observed trends for hydrocyclones operating with an air core and with an inserted metal-rod were comparatively discussed in Kraipech *et al.* (2008) (**Fig.4**). The air-core characteristics obtained in this work are similar to the experimental observation as can be seen in **Fig.4**. The air core was found to be unstable and its size, shape and position are unfixed because of the instability of the gas–liquid interface.

Calculation of the position of the air-core can be done using the interface-tracking algorithm, which is based on the volume of fluid method (VOF) of Hirt and Nichols (1981). The equation of motion (1) and (2) are solved for the mixture to obtain the velocity field which is shared between the two phases. The volume fraction averaged density ρ is given by

$$\rho = \sum_k \alpha_k \rho_k \tag{8}$$

The fraction of fluid in each cell is defined as α_k, which varies between 0 and 1. An additional transport equation for the volume fraction has to be solved in order to track the air-core. It has the following form:

$$\frac{\partial \alpha}{\partial t} + u_j \frac{\partial \alpha}{\partial x_i} = 0 \tag{9}$$

Delgadillo and Rajamani (2005) used the interface tracking algorithm based on the volume of fluid method (VOF) for calculating the position of the air-core. It was found however that the RSM model predicts an air-core, which is irregular and does not agree with experiment. Alternatively, if VOF or other multi-continuum approaches are not used in numerical simulations, where the air core is considered, the interfacial boundary conditions are required. Natural boundary conditions, as postulated by Nowakowski and Dyakowski (2003), relating forces could be advantageous for such simulations.

The other approach that could be proposed to tackle air-core is the capture of the liquid-gas interface by means of the level set method of Osher and Sethian (1988). This is relatively simple and versatile approach for computing and analyzing the motion of an interface in three dimensions. Caiden et al. (2001) further developed this approach for the two-phase flow regime addressing the boundary conditions and coupling at the compressible/incompressible interface.

The accurate modelling of the air core still remains a challenging task and it is expected that various new approaches will be adapted to hydrocylone simulation as a result of the recent progress in the development of numerical methods for tackling free surface flows. The important issue is to address an air-core creation phenomenon as a strongly coupled problem to the slurry concentration and swirling flow pattern, which governs the flow split between the outlets.

5. Numerical Approach to Multi-component Flows

In modelling the hydrocyclone performance, the influence of the particles on the flow is significant, particularly in the dense slurry flow, when the exchange of momentum from the particle–fluid, particle–particle and particle–wall interactions affect the velocity of the fluid. This may cause inefficiency in separation performance. The frequently reported but anomalous 'fish-hook' effect, which results in an excess of fines reporting to the underflow, has not been categorically explained. The presence of the vortex-ring behind particles seems to be worthy of consideration in terms of hydrocyclone performance. It may be responsible an additional mechanism for finer particles reporting to the underflow in the wake behind the larger particles. Such a mechanism may explain the shape of the selectivity curve, and the fact that the bypass value is higher than the water recovery to the underflow. This selectivity curve does not have a sigmoidal shape, but exhibits a dip in regions of finer particle size. This dip is known as the fish–hook effect.

Kraipech *et al.* (2005) studied three important particle interactions, which are the liquid-solid (drag) interaction, particle-particle lubrication, and particle-particle collisions interactions. The study of the importance of these particle interactions was conducted by applying the time scale analysis. This method is based on the force balance equation and can determine the predominant interaction of the flow within a hydrocyclone. The result shows that the particle-particle interactions due to the lubrication and collision mechanisms only play an important role in the area near the hydrocyclone wall, and near the air core. The majority of the hydrocyclone's area is dominated by the particle-fluid interaction. Therefore such a estimation can only be used to obtain a rough information of the predominant particle interaction and the concentration map. The idea behind this study is to reduce the complexity of modelling the particle motion in a hydrocyclone, since the particle-particle interaction can be ignored in most areas of a hydrocyclone.

Solid-liquid interaction problems are still difficult to solve with existing computational methods. The most popular numerical techniques for simulation of fluid-solid two-phase flows can be classified into several different categories.

5.1. A multi-continuum model

The most natural approach is to use a continuum theory that treats the solid and the fluid as interpenetrating continua, each governed by conservation laws, either postulated or derived by averaging. The work of Drew and Passman (1999) focuses on the fundamental aspects of such systems of equations. This Eulerian-Eulerian approach results in field equations for the flow properties for all phases in the system, but leads to unknown terms representing the interactions between the phases. These terms must be modelled to close the description of the system (constitutive relationships). The nature of the detailed interactions between the solids and the fluid is not the consequence of mixture theories alone and hence the derivation of such constitutive equations is an active research area (see Marchioro *et al.*, 2001). Experimental data, recently published in the literature, showed that during the sedimentation process smaller particles move at almost identical velocities to the larger particles, from which it can be concluded that the smaller particles appear to be influenced by larger particles wake. Such observations are crucial for construction of the set of constitutive equations required for the multi-continuum model. Thus, many *ad hoc* approaches, based on phenomenological considerations and physical intuition, have been applied but with only limited success. The Eulerian-Eulerian approach has been used in practical engineering multiphase flow simulations. The two-dimensional multi-continuum approach of Pericleous and Rhodes (1986; 1987) was well advanced for its time and represents to some degree the direction that modern day multiphase hydrocyclone modelling could take. However, modelling a distribution of types and sizes of particles complicates the continuum formulation because separate continuity and momentum equations have to be solved for each particle size and type. Nowakowski *et al* (2000) introduces the concepts and principles of multi-continuum framework for studying of the hydrodynamics of the flow in a hydrocyclone. In this model the carrying liquid is described as one continuum, and each particle fraction, with its characteristic size is described as a separate continuum. Particle-particle and particle-liquid interactions derived from a lubrication theory and a collision theory are described.

5.2. Particle tracking technique

A second approach to multiphase flow simulations is the Eulerian-Lagrangian model for fluid-solid simulation (see e.g. Patankar *et al.*, 2001). The approach provides a direct description of the particulate flow by tracking the motion of individual particles. Newton's second law, with empirical or semi-empirical forms for the hydrodynamic forces, governs particle motion. The particles do not perturb the flow field (unless computationally expensive coupling is undertaken) and the fluid satisfies the continuum equations that are solved on a fixed field in the usual Eulerian way. In hydrocyclones (see e.g. Ma *et al.*, 2000) this *one-way* coupling between the phases has been employed mainly for dilute systems with a maximum solids volume fraction of 5%. For such cases the volume occupied by the particles in a computational cell may be neglected. However, the accumulation of solid particles in regions of high fluid strain rate and low vorticity can result in high values of the local particle concentration, indicating the presence of a significant (local) coupling of the two phases. When solids concentration exceeds 5% by volume, the presence of particles changes the viscosity stresses and results in the generation of extra inertial stresses. The latter, known as the Bagnold dispersive stresses, result from particle-particle collisions, which are important when particle concentration exceeds 10% by volume. In case of shearing particles of mixed size, the larger particles drift towards the zone of least shear strain, e.g. towards the hydrocyclone axis, and the smaller particles towards that of greater shear strain, e.g. to the wall. Consideration of the Bagnold stresses might prove useful for explaining the 'fish-hook' effect (see e.g. Kraipech *et al.* 2002).

The equation of motion of a spherical particle in a fluid neglecting the interactions with other particles can be written as:

$$\frac{d}{dt}\boldsymbol{x}_p = \boldsymbol{u}_p \tag{10}$$

$$m_p \frac{d}{dt}\boldsymbol{u}_p = m_p \left(1 - \frac{\rho}{\rho_p}\right) \boldsymbol{g} + \boldsymbol{F}_p \tag{11}$$

where $\boldsymbol{x}_p$ is the particle position, m_p is the mass and ρ_p is the density of the particle, $\boldsymbol{u}_p$ the instantaneous velocity of the particle and g the body acceleration. The term $\boldsymbol{F}_p$ on the right hand side of the equation represent the force caused by particle-fluid interaction. In the most general case it could constitute of the following contributors modelled using empirical formulas (see e.g. Kraipech *et al.*, 2005):

$$\boldsymbol{F}_p = \boldsymbol{F}_D + \boldsymbol{F}_{AM} + \boldsymbol{F}_{LS} + \boldsymbol{F}_{LM} + \boldsymbol{F}_{BF} + \boldsymbol{F}_{PG} \tag{12}$$

The term $\boldsymbol{F}_D$ is the Stokes drag law that was derived with the assumption of uniform velocity and pressure field

$$\boldsymbol{F}_D = \frac{1}{2}\rho C_D \frac{\pi d^2}{4} \left|\boldsymbol{u} - \boldsymbol{u}_p\right| (\boldsymbol{u} - \boldsymbol{u}_p) \tag{13}$$

The drag coefficient C_D depends on variety parameters such as the particle size and shape, local Reynolds number, and local fluid density. It is assumed that particle density is sufficiently low that the collective effects on particle drag are unimportant, and the common assumption is made that the particles are spherical. Therefore these assumptions do not allow simulation of dragging mechanism of fine particles by large particles. Such an important mechanism may explain the shape of the selectivity curve in hydrocyclones, and the fact that the bypass value is higher than the water recovery to the underflow. The selectivity curve does not have a sigmoidal shape, but exhibits a dip in regions of finer particle size. The force $\boldsymbol{F}_{AM}$ is due to the apparent mass, which is the force to accelerate the apparent mass of the particle relative to the fluid.

$$\boldsymbol{F}_{AM} = \frac{1}{2}\frac{m_p\rho}{\rho_p}\frac{d\left(\boldsymbol{u}-\boldsymbol{u}_p\right)}{dt} \tag{14}$$

The force $\boldsymbol{F}_{BF}$ is due to the temporal delay in the boundary layer around the particle as the relative velocity changes with time. This force represents viscous effects due to the acceleration of the relative velocity.

$$\boldsymbol{F}_{BF} = \frac{3}{2}d^2\sqrt{\pi\rho\mu}\int_{t_0}^{t}\frac{1}{\sqrt{t-\tau}}\frac{d\left(\boldsymbol{u}-\boldsymbol{u}_p\right)}{d\tau}d\tau \tag{15}$$

The $\boldsymbol{F}_{LS}$ is the Saffman lift force produced by the pressure distribution developed on the particle due to the rotation induced by a fluid velocity gradient ($\dot{\gamma}$ is the rate of fluid deformation).

$$\boldsymbol{F}_{LS} = 1.615d^2\sqrt{\mu\rho\dot{\gamma}}\left(\boldsymbol{u}-\boldsymbol{u}_p\right) \tag{16}$$

The Magnus lift force $\boldsymbol{F}_{LM}$ is due to the rotation of the particle. This force is caused by a pressure difference between both sides of the particle resulting from the velocity difference due to the rotation.

$$\boldsymbol{F}_{LM} = \frac{1}{2}\rho\left(\boldsymbol{u}-\boldsymbol{u}_p\right)^2 C_L\frac{\pi d^2}{4} \tag{17}$$

The force $\boldsymbol{F}_{PG}$ is due to the pressure gradient in the fluid surrounding the particle.

$$\boldsymbol{F}_{PG} = -\boldsymbol{u}_p\nabla p \tag{18}$$

The dense flow is characterized by high collision frequencies between particles, and hence their motion is dominantly influenced by particle-particle collisions. Interactions between the fluid and particles are of minor importance (Sommerfeld, 2001).

5.3. Other approaches

The third approach for simulating the motion of both the fluid and the solid particles is termed direct numerical simulation (DNS). To extract information implicit in the equations of motion for solid-liquid flows, it is necessary to numerically solve the coupled system of differential equations consisting of the equations of fluid motion, and the equations of rigid-body motion (governing the particle motions), together with suitable initial and boundary conditions. These equations are coupled through the no-slip boundary condition on the particle surfaces and through the hydrodynamic forces and torques exerted by the fluid on particles (see e.g. Glowinski *et al.*, 2001). Two classes of methods have been developed in DNS simulations: *Arbitrary Lagrange-Euler (ALE)* methods on body fitted moving unstructured grids and *Fictitious Domain Methods*, which allow the flow calculation on a fixed grid. The first approach (Hu *et al.*, 2001) is enormously computationally expensive and at present it is not feasible to model 3D particulate flows with large number of particles of different sizes, shapes and densities. Computing acceleration based on Newton's second law with forces given by the local fluid forces on the particle would require a very fine, moving and deforming mesh for each particle. This is the obvious disadvantage of the approach, which on the other hand may be the only theoretical tool capable of studying the nonlinear and geometrically complicated phenomena of particle-particle and particle-wall interactions. Glowinski *et al.* (2001) developed the fictitious domain approach called the Distributed-Lagrange-Multiplier (DLM) method. The key idea is that fluid fills the whole computational domain inside as well as outside the particles boundaries, which eliminates the need for repeated remeshing. The Lagrange multiplier (physically a pseudo body force) is introduced to enforce the interior (fictitious) fluids to satisfy the constraint of rigid body motion, much like the pressure in incompressible fluid flow whose gradient is the force required to maintain the constraint of incompressibility. The method was used to investigate the sedimentation of 6400 disks settling down in a rectangular cavity and the fluidization of 1204 nylon spheres in a slit bed (Pan *et al.*, 2002).

Other recent computational approaches to solid-liquid flows, inspired by molecular dynamics, are cellular automata and the Lattice Boltzmann Method (LBM). Originating from discrete kinetic theory, the latter approach has shown considerable promise and is being pursued by a number of investigators. Fully resolved simulations of colliding spheres were presented by Ten Cate *et al.* (2004) with a lubrication force used to account for subgrid hydrodynamic interaction between approaching particles. An interesting combination of the LBM and immersed boundary approaches is presented in Feng and Michealides (2005). There are still challenges to overcome in order to demonstrate the LBE schemes as a competitive methodology, compared to the direct solution of the conservation equations of continuum mechanics. These, apart from a limitation on admissible time and length scales, include a consistent modelling of energy transport and elimination of excessive numerical discretization errors (Nourgaliev *et al.*, 2003). The interesting results produced by the LBM methods are not yet sufficiently practicable, for implementation for industrial scale hydrocyclones.

Experimental studies recently published on the influence of the fluid on the solid-solid collisions, investigated the mechanism of the rebound of a particle colliding with a fully immersed wall in a viscous fluid. This has been analysed using a high-speed video camera by Gondret *et al.* (2002) and Joseph and Hunt (2004). As a result the parameter such as a minimum particle Stokes number, below that no rebound occurs, normal and tangential coefficients of restitutions have been defined. This knowledge could prove to be useful for numerical simulations since it accounts for the combined effects of the interstitial fluid and the inelasticity of contact. Currently, several simulation methods do not allow for particle-wall collisions, because contact would break the lattice modelling of the fluid.

Although many theoretical and computational studies have helped to increase our physical understanding of solid-liquid flows, accurate and reliable predictions of such flows are still limited. The race to create state of the art numerical technique for solid-liquid flows has just acquired “momentum” and will have no shortage of intellectual stimulus due to the wide range of applications. The commercial CFD codes have reached a reasonable level of maturity and are accepted as an analysis tool for one-phase simulations. Despite the enormous advances in the development of numerical techniques a similar potential for solid-liquid flows, and multiphase flows generally, has yet to be fully exploited.

6. Experimental Validation

The confidence in hydrocyclone flow-field predictions can only be obtained by experimental validation. The validation study should concern the internal flow field. Doby *et al.* (2007) investigated the swirl flow mechanism in a cylindrical container. They constructed apparatus to enable the lids of a cylinder to be rotated. Due to shear forces, the rotation of the lid induces a flow field on the fluid. The test environment both numerical and experimental was created to conduct a flow pattern analysis. The study allowed validation of the numerical results and verification of experimental LDA technique before replacing the cylindrical container with specially constructed hydrocyclone. The container geometry was used as a benchmark to identify errors in measurements and data analysis. This simple swirl flow generator led to good predictions of a complicated flow. The study provided confidence in using the established tools for examining the flow field in hydrocyclones. The setup enabled incremental changes in the vortex structure to be studied and helped understanding when the fluid develops into unsteady 3D flow. Such an experimental setup could be used to study the performance of second-order closures in order to establish their potential and limitations in the context of swirling flows and possibly to contribute to numerical model improvement.

Laser doppler velocimetry (LDV) technique has been widely used to measure the velocity patterns in a hydrocyclone. Chine and Concha (2000) used LDV techniques to measure the velocity profile in conical and cylindrical hydrocyclones. The majority of work has been done to measure the 2D flow. Fisher and Flack (2002) have provided an extensive amount of 3D LDA measurements, which could be used for numerical validation of velocity pattern.

Equally important is validation of the hydrocyclone separation performance. The discussion of low-solid flow and high-solid flow field measurements techniques is presented in Nowakowski *et al.* (2004). The high-solids flow measurement precludes non-intrusive application of laser methods due to light extinction. There exist a wide range of applicable techniques, such as electrical impedance tomography, X-ray, Positron-emission, radioactive particle-tracking, ultrasound and nuclear magnetic resonance to mention a few. In case of electrical impedence tomography knowledge of the inter-relation between the conductivity and concentration fields permits reconstruction of the solids concentration. The challenge however is to form constitutive relations between the particle concentration and size distribution and the bulk conductivity. For example, during the hydrocyclone start-up phase or when operating with air-core instability, temporal conductivity changes are induced by air-core motion.

7. Conclusions

Advanced computational and experimental techniques are still needed to obtain a more in depth understanding of the complex physical phenomena affecting hydrocyclone performance. The knowledge of the different phenomena, such as particle–particle, particle–fluid, and particle–wall interactions would open the way to describe the particle effects on the suppression or generation of turbulence and on non-Newtonian slurry flows.

The appropriate use of turbulence models in numerical simulations is necessary for a correct prediction of both the fluid flow field, and the separation performance in a hydrocyclone. This becomes particularly important due to the existence of highly rotational fluid flow of the anisotropic nature with the turbulence not fully developed. Such a situation often makes some of the otherwise very successful turbulence models fail to produce a practical result for the fluid flow in hydrocyclones. Nevertheless the standard computational methods used for hydrocyclone design have significant advantages over the empirical approaches, such as the possibility of changing the geometry quickly to evaluate possible changes in the separation efficiency. Numerical methods should not be used without experimental verification and the understanding of their limitations. Future work should investigate an appropriate method to model turbulent flow within a hydrocyclone. Large Eddy Simulation (LES) is suggested technique that could be used as this approach solves for the largest scale motions of the flow while approximating or modelling only the small scale motions. It can be considered as a compromise between the Reynolds-Averaged Navier-Stokes equations (RANS) approach and the Direct Numerical Simulation (DNS) approach. LES approach, although still very costly computationally, is becoming more viable option for the solution of transitional and turbulent flow.

Apart from a fully 3D flow, the complex flow behaviour in a hydrocyclone arises from multiphase interactions and the mechanisms governing the formation of an air core. Further investigation on advance modelling, which allows simulation of an air core and multi-phase flow, will be required. For modelling multi-phase flow, an application of a multi-continuum model is particularly attractive because complex interactions between phases can be implemented. The complementary time scale analysis can provide a quantitative discussion concerning the importance of various types of forces affecting the particle motion. The accuracy of the prediction of the particle flow could be improved by taking into account the time dependency of fluid flow.

During the last decade, many papers related to the numerical simulation of a hydrocyclone flow were published. As a result, a framework for a 3D flow simulation of complex flow within a hydrocyclone has been laid out, which hopefully will allow the computational techniques to be improved as more research is performed and computing power increases. The primary purpose of the future research should be focused on providing a numerical approach for simulation of the flow in hydrocyclones, which should be flexible enough to be used for multi-objective design purposes. To develop automatic design methods, the numerical simulations need to be combined with automatic search and optimisation procedures (Nowakowski *et al.*, 2004; Slack, *et al.*, 2004).

Appendix A

The Reynolds Stress Model (RSM) is a second-order closure model. The model represents the solution of the transport equations of the six Reynolds stress components together with the equations for the three mean velocities and the dissipation equation for the dissipation rate, ε, of the turbulent kinetic energy. The variables ρ, p and μ below represent density, pressure and molecular viscosity respectively. The velocity u_i is decomposed into its mean and fluctuating components:

$$u_i = \bar{u}_i + u'_i$$

The Reynolds stress term $-\rho\,\overline{u_i u_j}$ includes the turbulence closure, which is modelled in order to close momentum and continuity equations. Reynolds stresses are modelled by the following equation:

$$\frac{D\left(\rho\overline{u'_i u'_j}\right)}{Dt} = \frac{\partial\left(\rho\overline{u'_i u'_j}\right)}{\partial t} + \frac{\partial \rho u_k \overline{u'_i u'_j}}{\partial x_k} \qquad \text{(A1)}$$
$$= P_{ij} + D_{T,ij} + D_{L,ij} + \Phi_{ij} + F_{ij} - \varepsilon_{ij}$$

The right hand side terms are:

$$P_{ij} = -\rho\left(\overline{u'_i u'_k}\frac{\partial u_j}{\partial x_k} + \overline{u'_j u'_k}\frac{\partial u_i}{\partial x_k}\right) \qquad \text{(A2)}$$

$$D_{T,ij} = -\frac{\partial}{\partial x_k}\left(\overline{p\left(\delta_{ik}u'_j + \delta_{kj}u'_i\right)} + \rho\overline{u'_i u'_j u'_k}\right)$$

$$D_{L,ij} = -\frac{\partial}{\partial x_k}\left(\mu\frac{\partial\overline{u'_i u'_j}}{\partial x_k}\right) \qquad \text{(A3)}$$

$$\Phi_{ij} = \overline{p\left(\frac{\partial u'_i}{\partial x_j} + \frac{\partial u'_j}{\partial x_i}\right)} \qquad \text{(A4)}$$

$$F_{ij} = -\rho\Omega_k\left(\overline{u'_j u'_m}e_{ikm} + \overline{u'_i u'_m}e_{jkm}\right) \qquad \text{(A5)}$$

$$\varepsilon_{ij} = 2\mu\overline{\frac{\partial u'_i}{\partial x_k}\frac{\partial u'_j}{\partial x_k}} \qquad \text{(A6)}$$

The P_{ij} term represents the stress production, $D_{T,ij}$ is the turbulent diffusion term, $D_{L,ij}$ is the molecular diffusion term, Φ_{ij} is the pressure-strain term, F_{ij} is the rotation production term and ε_{ij} is the dissipation term. Here Ω_k is the rotation vector, δ is the Kronecker delta and e_{ijk} = 1 if *i, j,* k are different and in cyclic order; e_{ijk} = -1. if *i, j,* k are different and in anti-cyclic order, and e_{ijk} = 0 if any two indices are the same.

The dissipation, pressure-strain, and turbulent diffusion terms cannot be computed exactly in terms of the other terms in the equations and therefore are modeled. The pressure-strain term is obtained from a linear-strain model:

$$\Phi_{ij} = \Phi_{ij,1} + \Phi_{ij,2} \ . \tag{A7}$$

The slow pressure-strain, $\Phi_{ij,1}$ is modelled as

$$\Phi_{ij,1} = -\rho C_1 \frac{\varepsilon}{k}\left(\overline{u_i' u_j'} - \frac{1}{3}\overline{u_k' u_k'}\delta_{ij}\right) . \tag{A8}$$

Here, variable *k* represents the turbulent kinetic energy:

$$k = \frac{1}{2}\rho\overline{u_i' u_i'} \tag{A9}$$

The rapid pressure-strain term, $\Phi_{ij,2}$ is modelled as

$$\Phi_{ij,2} = -\rho C_2 \left(P_{ij} - \frac{1}{3}P_{kk}\delta_{ij}\right) . \tag{A10}$$

The adjustable constants $C_1, C_2,$ have the standard values and are equal to 1.8, 0.6, respectively.

The close relation postulated for viscous dissipation term:

$$\varepsilon_{ij} = \frac{\partial}{\partial x_m}\left(C_\mu \frac{k^2}{\varepsilon\sigma_\varepsilon}\frac{\partial \varepsilon_{ij}}{\partial x_m}\right) + C_{1\varepsilon}C_\mu E_{ij}E_{ij} - C_{2\varepsilon}\frac{\varepsilon^2}{k}. \tag{A11}$$

The adjustable constants C_μ, $C_{1\varepsilon}$, $C_{2\varepsilon}$ σ_k, σ_ε are 0.09, 1.44, 1.92, 1.0 and 1.3 respectively. The mean strain rate is E_{ij} expressed as

$$E_{ij} = \frac{1}{2}\left(\frac{\partial u_i}{\partial x_j} + \frac{\partial u_j}{\partial x_i}\right). \tag{A12}$$

In the near-wall region of hydrocyclones the solution variables change with large gradients. The popular near wall models (wall functions) do not resolve accurately the near-wall region for strongly swirling flows. Due to the significant stream-wise pressure gradients, body forces and strong secondary flows the assumption of local equilibrium does not hold. Therefore the Fluent two-layer zonal model was found to be more suitable. The two-layer near wall models divide the whole domain into two regions, a viscosity affected region and a fully turbulent region. The demarcation of the two region is determined by a wall distance-based, turbulent Reynolds number

$$\mathrm{Re}_y = \rho y \frac{\sqrt{k}}{\mu} \ , \tag{A13}$$

where *y* is the normal distance from the wall at the cell centres. In the near-wall region when $Re_y < 200$, the one-equation model of Wolfstein (1969) is employed. For the values $Re_y > 200$ the RSM model is used.

References

Bank, N. and Gauvin, W. H. (1977): Measurement of flow characteristics in a confined vortex flow.Canadian Journal of Chemical Engineering, 55, pp.397-402.

Bhaskar, K. U., Murthy, Y. R., Raju, M. R., Tivari, S, Srivastava, J. K. and Ramakrishnan, N. (2007): CFD simulation and experimental validation studies on hydrocyclone, Miner. Eng. 20, pp.60-71.

Bloor, M.I.G. and Ingham, D.B. (1987). The flow in industrial cyclones, J Fluid Mech, 178, pp.507-519.

Caiden, R., Fedkiw, R.P. and Anderson, C. (2001): A numerical method for two-phase flow consisting of separate compressible and incompressible regions. Journal of Computational Physics 166 1, pp.1-27.

Chine, B. and Concha, F. (2000): Flow patterns in conical and cylindrical hydrocyclones. Chemical Engineering Journal, 80, pp.267-273.

Chu, L-Y. and Chen, W. (1999): Numerical Simulation of Turbulence and Its Structure, 9, pp 128-136.

Concha, F., Castro, B., Ovalle, E. and Romero, J. (1998): Numerical simulation of the flow pattern in a hydrocyclone. In Innovation in physical separation technology, pp.35-60.

Cullivan, J.C., Williams, R.A. and Cross, C.R. (2003): Understanding the hydrocyclone separator through computational fluid dynamics. Transactions of the IChemE, Part A, Chemical Engineering, Research and Design, 81 (A4), pp.455-466.

Cullivan, J.C., Williams, R.A., Dyakowski T. and Cross, C.R.(2004): New understanding of a hydrocyclone flow field and separation mechanism from computational fluid dynamics. Mineral Engineering, 17(5), pp.651-660.

Dai, G.Q., Li, J.M. and Chen, W.M. (1999): Numerical prediction of liquid flow within a hydrocyclone, Chemical Engineering Journal, 74, pp.211-216.

Datta, A. and Som, S.K. (2000): Numerical prediction of air core diameter, coefficient of discharge and spray cone angle of a swirl spray pressure nozzle. International Journal of Heat and Fluid Flow, 21, pp.412-419.

Davidson, M.R. (1988): Numerical calculations of flow in a hydrocyclone operating without an air core. Applied Mathematical Modelling, 12, pp.119-128.

Delgadillo, J.A. and Rajamani, R.K. (2005): A comparative study of three turbulence-closure models for the hydrocyclone problem, Int. J. Mineral Process. 77, pp.217-230.

Doby, M.J., Kraipech, W. and Nowakowski, A.F. (2005): Numerical prediction of outlet velocity patterns in solid-liquid separators. Chemical Engineering Journal, 111 (2-3), pp.173-180.

Doby, M.J., Nowakowski, A.F., Nowak, E. and Dyakowski, T. (2007): Numerical and experimental examination of swirl flow in a cylindrical container with rotating lids, Minerals Engineering, 20-4, pp.361-367.

Doby, M.J., Nowakowski, A.F. and Dyakowski, T. (2008): Understanding air core formation in hydrocyclones by studying pressure distribution as a function of viscosity. International Journal of Mineral Processing, In Press.

Drew, D.A. and Passman, S.L., (1999): "Theory of Multicomponent Fluids" , Springer-verlag, New York.

Dyakowski, T., Williams, R.A. (1993): Modeling turbulent flow within a small-diameter hydrocyclone. Chemical Engineering Science 6, pp.1143-1152.

Dyakowski, T. and Williams, R.A. (1995): Prediction of aircore size and shape in a hydrocyclone. International Journal of Mineral Processing, 43 (1-2), pp.1-14.

Fisher, M.J. and Flack, R.D. (2002): Velocity distributions in a hydrocyclone separator. Experiments in Fluids 32, pp.302-312.

Feng, Z-G. and Michaelides, E.E., 2005. Proteus: a direct forcing method in the simulations of particulate flows, J. Comput. Physics, 202, pp.20-51.

Glowinski, R., Pan, T.W., Hesla, T.I., Joseph, D.D. and Periaux, J. (2001): A fictious domain approach to the direct numerical simulation of incompressible viscous flow past moving rigid bodies: Application to particulate flow. Journal of Computational Physics 169 2, pp.363-426.

Gondret P., Lance M. and Petit L. (2002): Bouncing motion of spherical particles in fluids, Phys. Fluids, 14, pp:643-652.

Gresho, P.M. (1991): Incompressible fluid dynamics-some fundamental issues, Annual Review of Fluid Mechanics 23 (1991), pp.413-453.

Harlow, F. H. and Nakayama, P. I., 1968. Transport of turbulence energy decay rate, Los Alamos Sci. Lab., LA-3854.

He, P., Salcudean, M. and Gartshore, I.S., 1999. A numerical simulation of hydrocyclones. Chemical Engineering Research and Design, 77 (A5), 429-441.

Hirt, C. W. and Nichols, B. D., 1981. Volume of fluid (VOF) method for the dynamics of free boundaries, J. Comput. Phys. 39, 201-225.

Hu, H., Saga, T., Kobayashi, T., Taniguchi, N. and Yasuki, M. (2001): Dual-plane stereoscopic particle image velocimetry: system set-up and its application on a lobed jet mixing flow. Experiments in Fluids 31, pp.277-293.

Joseph G.G. and Hunt M.L. (2004.): Oblique particle-wall collisions in a liquid, J. Fluid Mechanics, 510, pp.71-93.

Kelsall, D.F. (1952): A study of the motion of solid particles in a hydraulic cyclone. Transactions of IChemE, 30, pp.87-108.

Kraipech, W., Chen, W., Parma, F. and Dyakowski, T. (2002): Modelling the fish-hook effect of the flow within hydrocyclones, Int. J. Miner. Process. 66, pp.49-65.

Kraipech, W., Nowakowski, A. F., Dyakowski, T. and Suksangpanomrung, A. (2005): An investigation of the effect of the particle-fluid and particle-particle interactions on the flow within a hydrocyclone, Chem. Eng. J. 111, pp.189-197.

Kraipech-Evans, W, Suksangpanomrung, A. and Nowakowski, A. F. (2008): The simulation of the flow within a hydrocyclone operating with an air core and with an inserted metal rod, Chemical Engineering Journal, 143 (1-3) pp.51-61.

Ma, L., Ingham, D.B. and Wen, X. (2000): Numerical modelling of the fluid and particle penetration through small sampling cyclones. Journal of Aerosol Science 31-9, pp.1097-1119.

Marchioro, M., Tanksley, M., Wang, W. and Prosperetti, A. (2001): Flow of spatially non-uniform suspensions, Part II. Systematic derivation of closure relations. International Journal of Multiphase Flow 27-2, pp.237-276.

Neesse, T., Schneider, M., Dueck, J., Golyk, V., Butenbach, S. and Tiefel, H. (2004): Hydrocyclone operation at the transition point rope/spray discharge. Minerals Engineering, 17(5), pp.733-737.

Nowakowski, A.F., Kraipech, W., Williams, R.A. and Dyakowski, T. (2000): The hydrodynamics of a hydrocyclone based on a three-dimensional multi-continuum model. Chemical Engineering Journal 80 1-3, pp.275-282.

Nowakowski, A.F. and Dyakowski, T. (2003): Investigation of swirling flow structure in hydrocyclones. Chemical Engineering Research and Design 81(A), pp.862-873.

Nowakowski, A.F. Cullivan, J.C., Williams, R.A and Dyakowski, T. (2004): Application of CFD to modeling the flow in hydrocyclones. Is this a realizable option or still a research challenge? Minerals Engineering 17 (5), pp.661-669.

Nourgaliev R.R., Dinh T.N., Theofanous T.G. and Joseph D. (2003): The lattice Boltzmann equation method: theoretical interpretation, numerics and implications, Int. J. Multiphase Flow, 29, pp.117-169.

Osher, S. and Sethian, J.A. (1988): Fronts Propagating with Curvature-Dependent Speed: Algorithms Based on Hamilton-Jacobi Formulations, Journal of Computational Physics, 79, pp.12-49.

Ovalle, E., Araya, R. and Concha, F. (2005): The role of wave propagation in hydrocyclone operations I: An axisymmetric streamfunction formulation for a conical hydrocyclone Chemical Engineering Journal, 111 (2-3), pp.205-211.

Ovalle, E. and Concha, F. (2005). Role of wave propagation in hydrocyclone operations II. Wave propagation in the air-water interface of a conical hydrocyclone, Chemical Engineering Journal, 111, pp.213-223.

Pan T-W., Joseph, D.D., Bai, R., Glowinski, R. and Sarin, V. (2002): Fluidization of 1204 spheres: simulation and experiment, Journal of Fluid Mechanics, 451, pp.169-191.

Patankar, N.A. and Joseph, D.D. (2001): Modelling and numerical simulation of particulate flows by the Eulerian-Lagrangian approach. International Journal of Multiphase Flow 27-10, pp.1659-1684.

Pericleous, K.A. and Rhodes, N. (1986): The hydrocyclone classifier - a numerical approach. International Journal of Mineral Processing 17 1-2, pp.23-43.

Pericleous, K.A. (1987): Mathematical simulation of hydrocyclones. Applied Mathematical Modelling 11-4, pp.242-255.

Petty, C.A. and Parks, S.M. (2001): Flow predictions within hydrocyclones. Filtration and separation, 38, pp.28-34.

Rietema, K. (1961): Performance and design of hydrocyclones-II:Pressure drop in the hydrocyclones. Chemical Engineering Science, 15, pp.303-309.

Slack, M.D., Prasad, R.O., Bakker, A. and Boysan, F. (2000): Advances in cyclone modelling using unstructured grids. Trans IchemE., 78, pp.1098-1104.

Slack, M. D., Del Porte, S. and Engelman, M. S. (2004): Designing automated computational fluid dynamics modelling tools for hydrocyclone design. Minerals Engineering, 17, pp.705-711.

Sommerfeld, M. (2001): Validation of a stochastic Lagrangian modelling approach for inter-particle collisions in homogeneous isotropic turbulence, Int. J. Multiphase Flow 27, pp.1829-1858.

Ten Cate A, Derksen J.J., Portela L.M. and van den Akker H.E.A. (2004): Fully resolved simulations of colliding monodisperse spheres in forced isotropic turbulence, J. Fluid Mechanics, 519, pp.233-271.

Wang, B. and Yu, A.B. (2006): Numerical study of particle-fluid flow in hydrocyclones with different body dimensions, Miner. Eng. 19, pp.1022-1033.

Wolfstein, M. (1969): The Velocity and Temperature Distribution of One-Dimensional Flow with Turbulence Augmentation and Pressure Gradient. Int. J. Heat Mass Transfer, 12, pp.301-318.

Author’s short biography

Dr A.F. Nowakowski

Dr A.F. Nowakowski is a Lecturer at the University Sheffield, Sheffield, U.K. He joined the Department of Mechanical Engineering in 2004 having previously spent five years as a Research Fellow at UMIST (University of Manchester Institute of Science and Technology). He obtained his Ph.D. from Warsaw University of Technology in the area of computational fluid mechanics in 1997. His academic background is in applied and computational mechanics and his scientific interests are in the field of computational fluid mechanics. His research activity has been concentrated in the general area of aerodynamics and multicomponent and multiphase flows. In all of these categories, he has developed the algorithms to simulate relevant flow phenomena. His numerical applications have been used to solve the problems of practical interest, including the flow in hydrocyclones or for predicting the optimal configuration of newly designed flow meters.

Michael Doby

Michael Doby received a B.S. degree from Georgia Institute of Technology in 2003 and a Ph.D. from University of Manchester in 2007, both in Chemical Engineering. After graduation, Dr. Doby was employed at DuPont Experimental Station in Wilmington, DE in 2007 as a Research Engineer in the Particle Technologies Group. Currently, he is an active participant in AFS and AICHE with research interests in solid-liquid separations and bulk solids handling.

Issues in Particle Size Analysis[†]

R. Hogg
Department of Energy and Mineral Engineering,
The Pennsylvania State University[1]

Abstract

Important issues that arise in the acquisition, presentation and interpretation of particle size data are discussed. Presentation of size distributions as relative quantity versus size, representation of quantity by number, mass, etc., and procedures for inter-conversion of the different forms are described. Definitions of various kinds of average sizes are presented. Limitations on their use and the importance of precise definition are emphasized. Definitions of size for irregular particles, the role of particle shape and implications with regard to comparability of analytical results based on different principles and procedures are evaluated. Different types of measurement procedures are classified according to whether they involve measurements on individual particles, on separated classes of particles or on complete assemblages. The restrictions and constraints, such as size limitations and resolution which apply to these types, are discussed.

Keywords: particle size distribution, average size, surface area, size definition, size measurement, limitations and constraints on sizing procedures

Introduction

The size distribution in particulate materials is of major importance in determining system behavior and is a primary focus of most characterization efforts. Various procedures can be applied for size analysis and instruments are available based on a range of different principles. The choice of a suitable analytical method for a specific application depends on the nature of the material and the reason(s) for performing the analysis.

This paper is not intended to be a comprehensive review of procedures for particle size analysis. Details of specific procedures and their relative strengths and weaknesses have been given by Allen [1]. The primary objective here is to highlight some important issues related to the acquisition, presentation and interpretation of particle size data. Emphasis is on powders and liquid suspensions, but some reference to aerosol measurements is included for completeness.

Size Distribution

Particle systems normally involve a collection of sizes – complete uniformity is extremely rare. Consequently, it is generally necessary to express the results of an analysis in the form of a distribution: relative quantity versus particle size. The latter is usually represented by a characteristic linear dimension. Quantity is most commonly given as the fraction of the total number, mass or volume of particles that fall into some size range. Alternatively, but less frequently used, quantity can also be represented by fractional area or length. A useful generalization [2,3] is to present the distribution by a *particle size density function* $q_r(x)$ defined such that:

$q_r(x)$ = fractional quantity that has size between x and $x + dx$ (1)

where x is size and $r = 0, 1, 2,$ or 3 corresponding to number, length, area or volume respectively. The different forms are the same only for sets of identical particles; the differences between forms increases with distribution width. The mass and volume distributions are identical unless density varies systematically with size.

Distributions can also be expressed in cumulative form by the *particle size distribution function* $Q_r(x)$ where

$Q_r(x)$ = fractional quantity finer than size x (2)

and

[†] Accepted on July 2, 2008

[1] 213 Hosler Building , University Park, PA 16802, USA
TEL: (814) 865-3802, FAX: (814) 865-3248
E-mail: rxh19@psu.edu

$$Q_r(x) = \int_0^x q_r(x)dx \tag{3}$$

The above represent the distribution in continuous form, which is appropriate since size is generally a continuous variable. However, size data often appear in discrete form as the relative quantity in finite size intervals, such that

$(q_r)_i$ = fractional quantity in size interval i (4)

and

$$Q_r(x_i) = \sum_{j=1}^{i-1} (q_r)_j \tag{5}$$

where size 1 represents the smallest size present. Alternatively, the cumulative form may be defined as

$$Q_r(x_i) = \sum_{j=i+1}^{m} (q_r)_j \tag{6}$$

where size m is the minimum size and size 1 corresponds to the maximum. In both cases, $Q_r(x_i)$ represents the fraction finer than the lower limit of interval i. The choice of whether size 1 should represent the smallest or largest may depend on the application. In applications to size reduction processes size 1 is usually designated as the largest and m as an arbitrary minimum, while the reverse is more convenient for crystallization or agglomeration.

In practice, distributions are normally presented in either the discrete, incremental form $(q_r)_i$ or the cumulative $Q_r(x)$. The cumulative form offers some advantage in that size x is uniquely defined whereas the incremental form refers to a finite range. Furthermore, because $Q_r(x)$ is by definition a monotonic function, it is typically easier to fit to an algebraic form than the more complex $(q_r)_i$. On the other hand, the cumulative form tends to obscure fine detail in the distribution, while graphical presentation of the incremental form offers a clearer picture of the distribution of sizes. It should be noted that the incremental distribution $(q_r)_i$ is not a direct estimate of the density function $q_r(x)$, which can be approximated by

$$q_r(x_i) \approx \frac{(q_r)_i}{\Delta x_i} \tag{7}$$

in which Δx_i is the size interval width, which typically is arranged to vary with size. Direct experimental determination of the density function is rarely practical.

Quantity representation by number, mass/volume etc. is usually dictated by the procedure used to acquire the data. Transformation from one representation to another, e.g. $Q_0(x)$ to $Q_3(x)$ can be accomplished using [2,3]:

$$q_t(x) = \frac{x^{t-r} q_r(x)}{\int_0^\infty x^{t-r} q_r(x)dx} \tag{8}$$

with

$$q_r(x) = \frac{dQ_r(x)}{dx} \tag{9}$$

Alternatively

$$(q_t)_i = \frac{(\bar{x}_i)^{t-r}(q_r)_i}{\sum_{i=1}^{m} (\bar{x}_i)^{t-r}(q_r)_i} \tag{10}$$

where $\bar{x}_i$ is the average size in interval i. While such transformations are mathematically straightforward, their application requires accurate knowledge of the complete distribution, especially the “tails” . For example, in transforming from the volume (r = 3) to the number (r = 0) distribution, the integral in Equation 8 includes the term $1/x^3$ and is therefore dominated by the finest sizes for which information on the quantity present is typically subject to the largest errors. Conversely, the reverse transformation, number to volume, is dominated by the largest sizes, for which serious statistical errors in particle counting are common. Examples of such transformations are given in the appendix.

Average sizes

If average sizes are to be used, it is critical that they be clearly defined because of the essentially infinite number of possibilities that exist for any distribution. Median sizes $x_{50,r}$ are defined such that

$$Q_r(x_{50,r}) = 1/2 \tag{11}$$

Typically, median sizes are estimated directly from plots of the cumulative distribution Qr(x) or by numerical interpolation of the data. Modes are given by maxima in the size density function. Mean sizes can be defined by the moments of the distribution:

$$M_{s,r} = \int_0^\infty x^s q_r(x)dx \tag{12}$$

where $M_{s,r}$ is s^{th} moment of the distribution $q_r(x)$ and s can take on any value. Each moment defines a mean size:

$$\bar{x}_{s,r} = M_{s,r}^{1/s} \tag{13}$$

The value of the median, mode or any particular mean increases as r increases.

Surface Area

The surface area of a collection of particles is an important characteristic in its own right and can also be used as a measure of average size. Different measures of the surface area of a particle can result in quite different values. The *geometric* area is defined on the basis of an assumed macroscopic shape (sphere, cube, etc.,), neglecting small-scale surface irregularities and roughness, and is directly related to size. The *external* area includes any such microscopic features. Cracks and pores within particles provide additional *internal* area, which may be independent of particle size. The *total* area is the sum of the external and internal contributions; its relation to size will generally depend on the relative magnitude of the two contributions.

The geometric surface area, commonly expressed as the volume or mass specific surface, S_v *or* S_m (surface area per unit volume or mass) can be estimated from the particle size distribution. For a sphere of diameter x, $S_v = 6/x$ which, for a collection of particles, can be used to define a specific surface mean diameter, $\bar{x}_{sv}$ such that

$$\bar{x}_{sv} = 6/S_v \tag{14}$$

The specific surface area can be estimated from moments of either the number or volume distribution using [2, 3]

$$S_v = k_{2,3}\frac{M_{2,0}}{M_{3,0}} = k_{2,3}M_{-1,3} \tag{15}$$

where $k_{2,3}$ is the area to volume shape factor (= 6 for spheres). Because of the inverse relationship to size, accurate estimates require precise knowledge of the fine “tail” of the size distribution.

Some examples of the estimation of surface area and various average sizes are given in the appendix.

Surface area can be determined directly by adsorption measurements (usually gas) which normally yield the total area. The permeability of a bed of particles to fluid flow can be used to estimate the external area. Comparisons of the different measurements can provide information on shape factors, surface roughness and internal porosity.

Definition of Size

In order to express the size of a particle as a single, linear dimension, it is strictly necessary to define its shape and to indicate which characteristic dimension is being used, e.g. diameter of a sphere, side of a cube etc. In practice, most particles are irregular in shape and simple definitions are not available. Probably the nearest thing to a unique size definition would be particle volume. Unfortunately, procedures for measuring particle volume are quite limited, especially for very small particles. The usual approach is to define size as an *equivalent sphere diameter* i.e. the diameter of a sphere that would be the same in some respect as the particle. Definitions and applications of some commonly used equivalent-sphere diameters are presented in **Table 1**.

In the case of isometric particles, for which three mutually perpendicular dimensions have the same magnitude, variations among equivalent-sphere diameters determined by different procedures can be expected to be small. However, for elongated or flattened particles variations may be quite large. Furthermore, there may appear to be variations within a set of identical particles due to orientation effects. For sizing procedures that involve gravity or inertial forces, differences in density will also lead to variations in equivalent-sphere diameter.

Particle Size Determination

Sampling

As in any characterization procedure, sampling is a critical step in the determination of particle size distributions. Procedures for avoiding physical bias in sampling particulate materials have been discussed at length by Gy [4,5] and, with particular reference to size analysis, by Allen [1]. Statistical errors can be minimized through the use of a sufficiently large sample. A formula for estimating the required sample size can be obtained by consideration of the statistics of random mixtures [6]. A simplified version is given by:

$$M \approx \frac{2\rho x_m^3}{\varepsilon^2 q_m}(grams) \tag{16}$$

where M is the required sample weight, ρ is the solid density (g/cm^3), x_m is the maximum size present (cm), q_m is the smallest relative amount of that size that would be considered significant and ε is the acceptable relative error. Examples of required sample sizes are shown in **Table 2**.

It is clear from the table that sample size can be critical in analyses of materials containing particles larger than 1mm, but is typically satisfied automatically (by instrument requirements) in sub-sieve analyses.

Types of Measurement Procedures

While it is common to speak of particle size measurement, it should be recognized that procedures for determining size distribution involve measurement of both size and relative quantity. For many procedures, the actual measurement is of quantity while size is inferred from the response to external forces

Table 1 Equivalent Sphere Diameters

Diameter	Definition	Formula*	Application
Volume	Diameter of a sphere with the same volume as the particle	$d_v = \left(\frac{6V}{\pi}\right)^{1/3}$	Baseline standard; Coulter counter
Surface	Diameter of a sphere with the same surface area as the particle	$d_s = \left(\frac{S}{\pi}\right)^{1/2}$	
Specific Surface	Diameter of a sphere with the same specific surface area as the particle	$d_{sv} = \frac{d_v^3}{d_s^2}$	Surface area, Permeametry, Gas Adsorption
Projected Area (random)	Diameter of a sphere with the same projected area as the particle in a given orientation	$d_a = 2\left(\frac{A_a}{\pi}\right)^{1/2}$	Light Scattering; Optical Counters
Projected Area (stable)	Diameter of a sphere with the same projected area as the particle in a stable rest position	$d_{as} = 2\left(\frac{A_{as}}{\pi}\right)^{1/2}$	Microscopy
Stokes	Diameter of a sphere with the same density and settling velocity as the particle, under laminar flow conditions	$d_{st} = \left(\frac{18\mu v}{\Delta\rho g}\right)^{1/2}$ $d_{st} \approx \left(\frac{d_v^3}{d_s}\right)^{1/2}$	Sedimentation
Aerodynamic	Diameter of a sphere of density 1g/cm^3 that has the same aerodynamic behavior as the particle	$d_{ae} \approx d_{st}\sqrt{\rho}$	Cascade Impactors

*Symbols:

A_a:	particle projected area (random orientation)	(L^2)
A_{as}:	particle projected area (stable rest plane)	(L^2)
d_a:	projected area diameter (random orientation)	(L)
d_{ae}:	aerodynamic diameter	(L)
d_{as}:	projected area diameter (stable rest plane)	(L)
d_s:	surface diameter	(L)
d_{st}:	Stokes diameter	(L)
d_{sv}:	Specific surface mean diameter	(L)
d_v:	volume diameter	(L)
g:	acceleration due to gravity	(L/T^2)
S:	particle surface area	(L^2)
v:	settling velocity	(L/T)
V:	particle volume	(L^3)
μ:	fluid viscosity	(M/LT)
ρ:	solid density	(M/L^3)
$\Delta\rho$:	density difference	(M/L^3)

Table 2 Required sample size for determination of the size distribution of powder with relative error less than 5%. Particle density 2.5 g/cm^3; 1% by weight in the top size fraction.

Maximum Particle Size	Required Sample Size
1cm	200kg
1mm	200g
100 μm	0.2 g
10 μm	0.2mg
1 μm	0.2 μg

or other stimuli. Experimental procedures generally fall into one of three groups depending on whether measurements are made on:

1. individual particles
2. classes of particles separated according to size
3. all sizes simultaneously

In the first type, individual particles are examined one at a time and their size is determined either by direct measurement as in microscopy/image analysis or through their response to some kind of sensing system as in automatic particle counters. Quantity is typically determined by simple counting, leading to a direct measure of the number size distribution. In the case of electrical sensing methods, which estimate particle volume through the reduction of electrical conductivity by electrolyte displacement, an alternative to counting is to determine the volume distribution directly by accumulating individual particle volumes.

The second group includes sieving, sedimentation and cascade impactors and involves size classification based on ability to pass through an aperture, differential settling in a fluid or particle inertia in a flow stream. Size is not measured directly but is assigned on the basis of aperture size, settling time or flow velocity (by calibration). Relative quantity is commonly determined by direct weighing of the classified material. Concentration measurement by attenuation of radiation is often used for quantity determination in sedimentation systems. Sieving and impaction give a direct measure of the incremental mass distribution; sedimentation normally yields the cumulative form.

Methods based on radiation scattering (light or sound) generally fall into the third group. The complete distribution is estimated by comparing scattering intensities for a range of angles, frequencies etc., with predictions from scattering theory. In effect, iterative procedures are used to find the distribution that gives the closest fit to the scattering data. Results are generally reported as a volume distribution. Dynamic light scattering, sometimes referred to as quasi-elastic light scattering (QELS) or photon correlation spectroscopy (PCS), uses autocorrelation procedures to evaluate fluctuations in scattering intensity at a fixed angle, typically 90°. Characteristic time-scales for the fluctuations are used to estimate diffusion coefficients due to Brownian motion which are related to size through the Stokes-Einstein relationship. Estimates of the size distribution are obtained by curve-fitting to standard forms.

Restrictions and Constraints

All experimental test procedures have relative advantages and disadvantages. Besides differences between systems operating on the same basic principle, there are inherent problems associated with each of the general approaches.

Size Limitations: Most of the available techniques have an optimum range of applicability. While this range can be quite broad – imaging techniques such as microscopy, for example, can cover the entire range from molecular to astronomic – the practical limits for any specific application are usually much narrower. At any particular scale, image analysis is generally limited to a size range of not much more than 10:1. The lower end is limited by resolution and the upper by counting statistics. Similar constraints apply to other analytical procedures.

An important distinction can be made between two basic types of size limits:

- Measurement limits
- Detection limits

Measurement limits arise when a procedure recognizes the existence of particles outside of the range of applicability and provides a measure of their quantity. Sieving procedures provide a good example of measurement limits. Size information is provided only over the range of sieve sizes used but the quantities coarser than the coarsest sieve and finer than the finest are readily determined. Detection limits occur when particles outside of the range are invisible to the system and are assumed to be absent. This type is normally associated with the lower end of the range. Apparent size distributions obtaining using systems subject to measurement and detection limits are compared in **Fig. 1**.

Procedures based on individual particle counting are especially prone to detection limits. For imaging methods, the problem can be addressed by the use of progressively higher magnification. However, since observations at a particular magnification are essentially subject to detection limits, construction of the overall size distribution requires matching of the separate data sets obtained at the different magnifications. Problems associated with the matching procedures can be a major source of errors in the application of image analysis to systems with broad size distributions.

Automatic counters based on light scattering or electrical sensing are usually subject to an absolute limit. Such instruments are inappropriate for use with materials containing undersize particles. The results of measurements for which substantial quantities are reported at sizes adjacent to the lower limit should be regarded as questionable.

Methods that involve size separation are generally

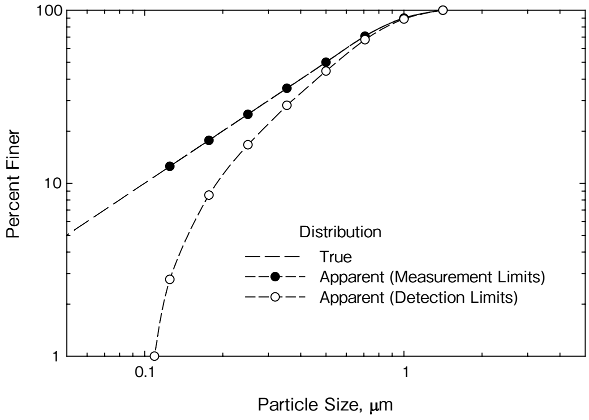

Fig. 1 The effect of lower size limits on size distribution measurements.

subject only to measurement limits. Grossly oversize particles can present problems in sedimentation because of their very high settling rate which leads to difficulty in preparing uniform initial dispersions. Oversize particles can lead to blockage of orifices in cascade impactors applied to airborne particles. However, high settling velocities tend to eliminate such particles prior to entering the device.

Lower detection limits are typical also for radiation scattering systems. Scattering by particles smaller than the wavelength of the incident beam is relatively weak and insensitive to scattering angle. Since information on how scattering from such particles is handled in the algorithms used to estimate size distribution is not generally available to the user, the exact nature of these limits is unclear. Again, reported distributions showing large quantities close to the lower limit should be treated with caution. Modern, commercial scattering systems often claim “full-range” capability, from < 1µm to about 1 mm. This is certainly advantageous for samples whose size range is not known *a priori*. However, its value is limited by the need to minimize settling of coarse particles so as to maintain a homogeneous suspension in the field of view. For low-density materials, this can be achieved by dispersion in liquids of similar density but this is impractical for higher density solids such as most minerals.

The existence of a finite range of applicability for most sizing procedures can present problems in the analysis of materials containing a broad range of sizes – soil samples, for example, may include particles ranging from pebbles 1 cm or larger down to submicron clay particles. Particle modification processes such as comminution often involve progressive reduction in size from as large as tens of centimeters to micron and sub-micron sizes. In such cases, it is usually necessary to employ more than one procedure for complete characterization of the material or evaluation of the process.

The first step in implementation of a two-stage size analysis is to separate the material into a coarse and a fine fraction at some intermediate size. Since sieving generally provides the sharpest separation, this is usually the preferred method for making the separation and, by extension, for analysis of the coarse fraction. The fine fraction can be analyzed by an appropriate method such as light scattering or sedimentation. Because the two measurement procedures involve different definitions of size, there remains the question of matching the two parts of the complete distribution. A simple, and usually effective, solution is to provide significant overlap between the two sets of measurements, for example by sieving down to 400 US mesh (37 µm) and performing the sub-sieve analysis on a -200 mesh (74 µm) fraction. The complete distribution is obtained by adjusting one of the sets of sizes so as to produce a smooth, continuous cumulative curve. An example of the evaluation of the complete distribution from a two-stage analysis is given in **Fig. 2**.

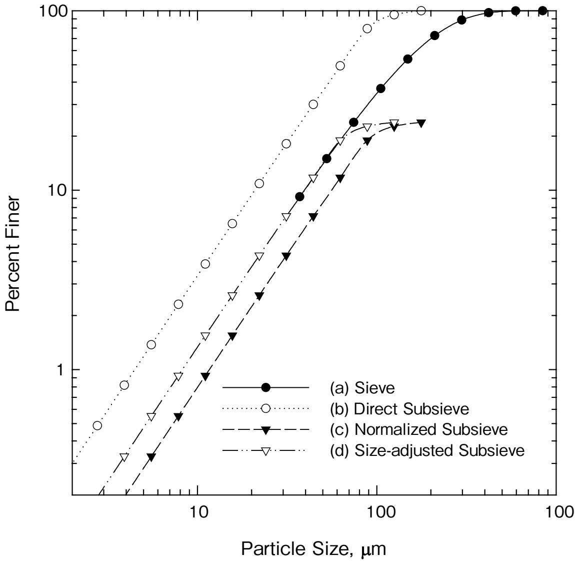

Fig. 2 Example of the combination of sieve and subsieve data to obtain an overall size distribution. Procedure:

1. Perform sieve analysis down to 400 US mesh (37 μm) – curve (a)
2. Subsieve size analysis on -200 US mesh (74 μm) fraction from sieving – curve (b)
3. Normalize subsieve data with respect to fraction finer than 200 US mesh in sieve analysis – curve (c)
4. Adjust size scale for normalized subsieve data to form a smooth curve with sieve data – curve (d)

Curves (a) and (d) represent the complete (sieve equivalent) size distribution.

Applications to processes such as comminution are also sensitive to detection limits at the finest sizes. Evaluation of ultrafine grinding processes often requires analysis of sets of size distributions starting from a relatively coarse feed to final products that may extend well into the submicron range, thus necessitating the two-stage approach. The use of sedimentation methods for the sub-sieve stage, while tedious, generally provides the greatest accuracy. Because of their operational simplicity, light scattering procedures present an attractive alternative. However, uncertainty with regard to their lower size limit means that these methods should be used with caution. Standard light scattering systems can be extended into the submicron range but claims of further extension to still finer sizes are of dubious valid-

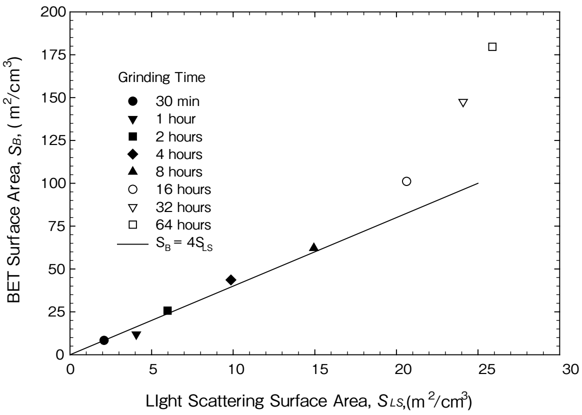

Fig. 3 Correlation between specific surface areas of ground quartz measured by BET gas adsorption and laser scattering/diffraction.

ity. Angular scattering patterns for such particles are relatively insensitive to size, while scattered intensity at any angle decreases so drastically with size that contributions from fine particles are overwhelmed by those from coarser material.

The validity of light scattering data for ultrafine material can be assessed using supplementary measurements of surface area by gas adsorption whose accuracy actually increases with decreasing size. An example of this approach is shown in **Fig. 3** based on data for the grinding of quartz from a feed size of about 50μm to a final product with a maximum size of about 0.3μm. It can be seen from the figure that the measured areas are in direct proportion for the coarser products with an approximately 4:1 ratio of the gas adsorption area to that from light scattering, reflecting the role of irregular shape and surface roughness. For the finer products, obtained after grinding for more than 8 hours, the BET area shows a steady increase relative to that derived from light scattering. This deviation is attributed to the failure of the light scattering system to account fully for particles smaller than about 0.2μm.

Resolution: Different procedures for size analysis vary in their ability to discriminate between sizes. Methods such as microscopy and automatic particle counters that involve measurements on individual particles generally provide the highest resolution. Those such as light scattering that estimate the size distribution from the collective response of the whole system are typically less able to discriminate and tend to smooth over fine detail in the distribution. Dynamic light scattering, for which the distribution is typically estimated by fitting to a standard form, tends to have quite low resolution. Procedures such as sieving, impaction and sedimentation, which include separation by size, fall somewhere between the other two groups. Sieving provides excellent discrimination at the actual aperture sizes but gives no information on intermediate sizes. The situation is similar for cascade impactors, although the sharpness of separation is lower. Sedimentation methods can give information at any size but resolution is also limited by low separation sharpness.

Resolution is particularly important in the analysis of narrow size distributions, low resolution invariably leading to an apparent broadening of the distribution [7]. Precise description of the "tails" of the distribution is critical to some applications. For example, a single oversize particle in an abrasive powder used for surface polishing can lead to catastrophic results [8]. High resolution is a necessity for the analysis of such materials.

Operational Constraints: In addition to factors such as precision, resolution, reproducibility, etc., there are other requirements that influence the appropriateness of the different procedures for specific applications. These include response time, versatility, requirements for operator skill and experience, equipment cost and availability and on-line capability. Response time is critically important in quality control and, especially, direct process control applications. Laser scattering/diffraction systems are particularly attractive for such applications. Instrument response times are typically a few minutes so that dispersion stability is not critical. As a consequence, sample preparation is usually fairly straightforward. Automatic particle counters also offer very rapid instrument response. However, problems with aperture blockage and/or sensing zone contamination tend to reduce reliability and render sample preparation more critical. Microscopy and the separation-type procedures such as sieving, sedimentation and impaction for which response times can be several hours are obviously unsuitable for such applications.

Versatility in terms of applicability to a variety of materials and physical conditions can be important where access to a broad range of equipment may be limited. Light scattering systems can be applied to most materials, cover a broad range of sizes and can be applied to particles suspended in liquid or gas, but require relatively expensive, dedicated equipment. Sieving requires fairly low-cost equipment but is generally limited to particles coarser than about 20 μm. Sedimentation methods are mostly restricted to particles in liquid suspension while impactors are only applicable to aerosols.

Some procedures require considerable skill and experience on the part of the operator in order to ensure reliable, accurate results, while others need only a basic knowledge of the operating procedure. Modern light scattering systems and, to some extent, automatic counters generally fall into the latter category while sieving, sedimentation and especially microscopy/image analysis and cascade impactors are more demanding. In all cases, however, sufficient experience and understanding of the process, to identify suspect results etc., is desirable.

Of the standard, laboratory procedures, light scattering offers the greatest potential for on-line applications. Problems include the substantial dilution often needed for slurry systems and deposition on cell windows in aerosol measurements. Acoustic measurements on slurries can be made at high concentrations, but resolution is generally low for these methods and the presence of air bubbles can lead to serious errors.

Errors occur in all measurements. In size analysis, errors can be associated with size and/or quantity. As noted previously, with the exception of imaging methods, size is generally assigned, by theory or calibration, rather than by actual measurement. Consequently, most of the error typically occurs in the quantity measurement. Even with image analysis, size estimation can be made reasonably accurate and errors usually arise from counting statistics, especially in determination of the volume distribution – a single particle of size 10 units is equivalent to 1000 of size one unit. At the same time, while the image size may be accurately determined, the actual particle size is typically overestimated due to preferred orientation.

Errors in analysis by sieving can generally be attributed to failure to ensure that all particles small enough to pass through each opening actually do so. Blinding of fine sieves by adhesion and/or bridging over openings can seriously exacerbate this problem. The result is that sieving tends to overestimate size and, if blinding occurs, to narrow the apparent distribution.

Errors in analysis by automatic counters commonly result from failure to recognize the detection limit and from the problem of coincidence – simultaneous passage of more than one particle through the sensing zone. The latter can be minimized by choosing a sufficiently low concentration. However, if the concentration is too low, background noise can become significant, leading to false counts. Complete dispersion of the particles is obviously a requirement but, because of the low concentrations used and the rapid response time, reagglomeration is not usually a problem. Bias in sampling can also lead to errors, particularly in the use of electrical sensing methods. Typical procedures involve pre-dispersion of the particles in an appropriate (usually aqueous) solution followed by addition to the electrolyte used in the measurement. A common approach is to add the dispersion dropwise from a pipette or eyedropper until the desired concentration is reached. Preferential settling of the larger particles in the pipette can produce significant bias. The recommended procedure is to transfer and rinse out the entire amount of a small quantity in the pipette and repeat as needed.

Most sedimentation systems for particle size analysis involve measurement of the relative concentration of particles remaining in suspension at some depth after some time of settling. The depth and time define the settling velocity and, through the use of Stokes law, the size of the largest particles remaining, while the relative concentration is equal to the fraction finer than that size. Stokes law is strictly valid only for small particles, typically finer than about 50μm for gravity settling of minerals in water. This is often considered to establish an upper size limit to the procedure. However, this problem is easily surmounted through the use the Haywood correlations [9] or the expressions presented by Concha and Almendra [10]. In practice, the upper limit is dictated by problems in making measurements at very short times. Similarly, the lower size limit is often ascribed to the effects of Brownian motion. It seems more likely, however, that this limitation is due primarily to other factors such as sampling errors and thermal gradients, etc. [1,11]. The lower size limit can be reduced through the use of centrifuges, at the cost of increased complexity of the experimental procedure and data analysis [1]. It should be noted that reduction of the lower size limit is accompanied by an equivalent reduction in the upper limit.

Errors in sedimentation size analysis are normally associated with the concentration measurement. In the case of sampling types such as the classical Andreasen pipette, errors can occur due to disturbance during sampling, cross-contamination between samples and inaccurate concentration measurement. X-ray attenuation is often used for *in situ* concentration measurement thus avoiding problems associated with sample extraction. Absorption of X-rays by suspended solids depends on the atomic weight of the elements involved. When only light elements are included, as in silicate minerals and especially organics, relatively high solids concentrations are required to ensure reliable concentration estimates. This can lead to hindered settling effects that slow down the overall settling process leading to apparently finer distributions. Particle interactions can also affect the relative settling rates among different sizes thus invalidating the size-separation basis of the technique and can cause an apparent narrowing of the distribution. Stabilization of the suspension to eliminate reagglomeration of the particles during the rather long settling times normally required is critically important. Unexpectedly narrow apparent distributions, especially those showing a sharp cut-off in the fine sizes, are often an indication of inadequate stabilization of the suspension.

Errors in size analysis by light scattering can be attributed to the resolution problems noted previously and to orientation effects for non-spherical particles. Such particles are assigned a size based on the cross-sectional area presented to the incident light. The size assigned is interpreted as a volume diameter and is usually larger than the true value, especially for flattened particles. The result is that light scattering systems typically report size distributions that are coarser than those obtained by other methods [7].

The restrictions and constraints associated with widely-used analytical procedures are summarized in **Table 3**.

Nanoparticles

Since most of the analytical procedures described above have lower size limits close to one micrometer, determination of nanoparticle size distributions presents particular problems. Imaging methods, by electron microscopy for example, can give quite accurate measures of individual particle sizes and reasonable descriptions of narrow size distributions. However, for relatively broad distributions these methods are subject to serious problems associated with the need to use several magnifications to ensure adequate coverage of the size range and the subsequent uncertainties in matching the different sets of data. Production of suitable, well-dispersed images may also be difficult.

Dynamic light scattering is specifically applicable to particles in the nano-size range. However, procedures for the direct determination of the distribution of sizes remain to be developed. Generally, distributions are estimated by curve-fitting to standard forms. Problems associated with the extension of standard light scattering procedures into the nano-size range were discussed in a previous section of this article.

Centrifugal sedimentation is probably the most appropriate method for determining nanoparticle size distributions. However, procedures generally involve a high degree of operator skill and equipment availability is rather limited.

Conclusions

The distribution of sizes present is a principal characteristic of any particulate system. Presentation of size analyses should always include specification of the basis of the distribution (number, volume etc.) and some indication of the definition of size used. Average sizes can be useful characteristic parameters if clearly defined. Analytical procedures generally express size as an equivalent sphere diameter defined as the diameter of a sphere that would give the same response as the particle. It follows that different methods often give different results. Procedures based on different principles are all subject to inherent restrictions and constraints; further restrictions, applicable to commercial equipment, are generally

Table 3 Performance characteristics of experimental procedures for particle size analysis

Method	Limitations	Resolution	Operational Constraints			
			Response Time	Versatility	Operator Skill	Errors
Image Analysis	Upper & Lower Detection*	High	Long	High	High	Matching
Sieving	Measurement	High	Long	+ 20 μm	Medium High	Blinding
Sedimentation	Measurement	Medium	Long	Liquid Suspension	High	Dispersion Stability
Light Scattering	Lower Detection	Medium Low	Short	High	Medium	Orientation Effects
Dynamic Light Scattering		Low	Medium-Short	Sub-Micron	Medium	
Automatic Counters	Lower Detection	High	Short		Medium	Coincidence
Cascade Impactors	Measurement	Medium High	Long	Airborne Particles	High	Collection Efficiency, Dispersion

* At any given magnification

beyond the scope of this paper.

It is recommended that the following be kept in mind in selecting the appropriate analytical procedure for a specific application:

- The definition of size used – e.g. “sieve diameter”, “area diameter”, “Stokes diameter”, etc.
- The basis for representing quantity in size ranges – number, volume, mass
- The range of applicability – since most methods can only be used over a limited range of sizes it may be necessary to use more than one method to cover a broad range of sizes and combine the data to obtain the complete distribution
- The nature of the size limits:
  - *Measurement limits*: information is obtained only in the range of applicability of the method but the relative amounts falling outside of the range are measured
  - *Detection limits*: particles outside of the range are not detected and *assumed* to be absent

  Measurement limits are preferred; lower detection limits are especially troublesome. Upper limits can usually be avoided by pre-classification of the particles – commonly by sieving. This approach is generally impractical for lower limits due to the difficulty of precise classification at very fine sizes
- Resolution – the ability to discriminate among the sizes present and to indicate fine detail in the size distribution
- Reproducibility/repeatability – replicate analyses should agree closely
- Ease of use – the need for special operator skills
- Response time – applicability for on-stream analysis or quality control
- Special considerations – reaction with suspending liquids (e.g. water); dispersion/deaggregation problems etc.
- Sample size constraints – some procedures require relatively large samples
- Appropriateness to the particular application – e.g. the use of aerodynamic methods for airborne particulates.

Nomenclature

A_a :	particle projected area (random orientation)	[L^2]
A_{as} :	particle projected area (stable rest plane)	[L^2]
d_a :	projected area diameter (random orientation)	[L]
d_{ae} :	aerodynamic diameter	[L]
d_{as} :	projected area diameter (stable rest plane)	[L]
d_s :	surface diameter	[L]
d_{st} :	Stokes diameter	[L]
d_{sv} :	Specific surface mean diameter	[L]
d_v :	volume diameter	[L]
g :	acceleration due to gravity	[L/T^2]
$k_{2,3}$:	surface/volume shape factor	[–]
M :	sample weight	[M]
$M_{s,r}$:	s^{th} moment of size distribution $q_r(x)$	[L^s]
q_m :	specified minimum detection level	[–]
$q_r(x)$:	particle size density function	[L^{-1}]
$(q_r)_i$:	incremental size distribution	[–]
$Q_r(x)$:	cumulative size distribution	[–]
S :	particle surface area	[L^2]
S_B :	BET (gas adsorption) surface area	[L^{-1}]
S_{LS} :	surface area by light scattering	[L^{-1}]
S_m :	mass specific surface area	[L^2/M]
S_v :	volume specific surface area	[L^{-1}]
v :	settling velocity	[L/T]
V :	particle volume	[L^3]
x :	particle size	[L]
x_i :	lower limit of size interval i	[L]
$\bar{x}_i$:	mean size in interval i	[L]
Δx_i :	width of size interval i	[L]
x_m :	maximum size	[L]
$x_{50,r}$:	median size of distribution $q_r(x)$	[L]
$\bar{x}_{s,r}$:	x^s-based mean size of distribution $q_r(x)$	[L]
$\bar{x}_{sv}$:	specific surface mean diameter	[L]
ε :	specified sampling error	[–]
μ :	fluid viscosity	[M/LT]
ρ :	solid density	[M/L^3]
$\Delta\rho$:	density difference	[M/L^3]

References

1) Allen, T. (1997): “Particle Size Measurement”, 5th Edition, Chapman and Hall, London.
2) Rumpf, H. and Ebert, K.F. (1964): Darstellung von Korngrossenverteilungen und Berechnung der Spezifischen Oberflache, Chem. Ing. Tech., 36. pp.523-537.
3) Leschonski, K. (1984): Representation and Evaluation of Particle Size Analysis Data, Particle Characterization, 1. pp.89-95.
4) Gy, P. (1982): “Sampling of Particulate Materials, Theory and Practice”, 2nd Revised Edition. Elsevier, Amsterdam.
5) Gy, P. (1998): “Sampling for Analytical Purposes”, Wiley, New York
6) Hogg, R. (1988): Characterization Problems in Comminution – an Overview, Intl. J. Miner. Process., 22,

pp.25-40.

7) Hogg, R., Turek, M.L. and Kaya, E. (2004): The Role of Particle Shape in Size Analysis and the Evaluation of Comminution Processes, Particulate Science and Technology, 22, pp.355-366.

8) Dumm, T.F. (2005): Characterization of Low-Level, Oversize Particles in Abrasive Powders, KONA Powder and Particle Journal, 23, pp.129-137.

9) Heywood, H. (1962): Uniform and Nonuniform Motion of Particles in Fluids, In: Proceeding of the Symposium on the Interaction between Fluids and Particles. Institution of Chemical Engineers, pp.1–8.

10) Concha, F. and Almendra, E.R. (1979): Settling Velocities of Particulate Systems, I. Settling Velocities of Individual Spherical Particles, Intl. J. Miner. Process., 5. pp.349-367.

11) Chung, H.S. and Hogg, R. (1985): The Effect of Brownian Motion on Particle Size Analysis by Sedimentation, Powder Technology, 41. pp.211-216.

Appendix: Manipulation of Particle Size Data

Examples of size distribution transformations are given in **Table A1** and **Fig. A1**. The procedure for transforming a measured number distribution to the corresponding volume distribution is shown in **Table A1**. The results of transformations from number to volume and *vice versa*, based on reasonable estimates from the same actual distribution, are illustrated in **Fig. A1**. Specifically, the "measured" distributions are simulated assuming a 100g sample for the volume distribution and a count of 1000 particles for the number distribution. The figure clearly demonstrates the pitfalls typically encountered in making such estimates. In each case the "calculated" distribution differs substantially from its "measured" equivalent with the major discrepancies in the tails. In principle, the estimates can be improved by increasing the amount of sample used in the analysis. However, the required increase may be very large indeed as illustrated in **Fig. A2** in which it can be seen that increasing the total number of particles counted from 1,000 to as much as 100,000 still leaves considerable error in the estimated volume distribution.

Illustration of graphical estimation of median sizes is included in **Fig. A1**. Examples of the calculation of specific surface area and some average sizes are given in **Table A2**. The dominant contribution of the fine sizes in the estimation of quantities such as surface area that are inversely related to size is readily apparent from the third column of the table.

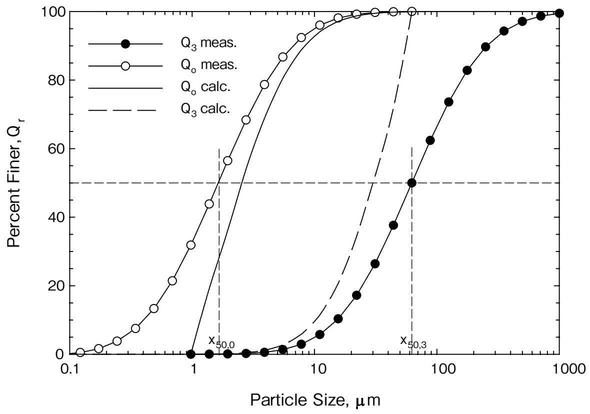

Fig. A1 Examples of size distribution transformations: number to volume and volume to number.

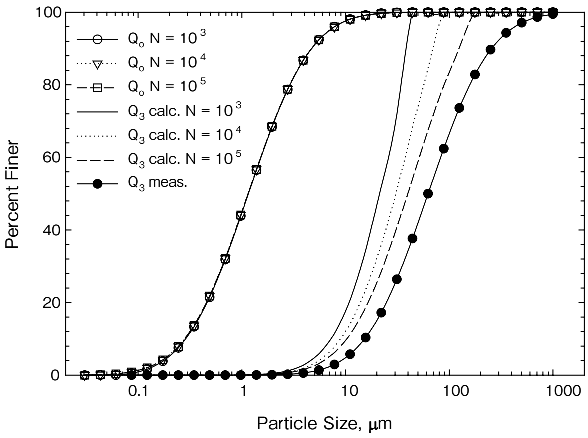

Fig. A2 Effect of total number of particles counted N on transformation of number to volume distribution.

Table A1 Estimation of volume distribution by transformation from measured number distribution

Interval Boundary, μm	Interval Mean size, x, μm	Measured Number Distribution, (r = 0)		x^3q_o	Calculated Volume Distribution, (r = 3)	
		Cum. Q_o	Incr. q_o		Incr. q_3	Cum. Q_3
125.0		1.00				1.0000
	105.1		0.000	0.00	0.000	
88.4		1.00				1.0000
	74.3		0.001	410.59	0.338	
62.5		1.00				0.6620
	52.6		0.002	290.33	0.239	
44.2		1.00				0.4230
	37.2		0.004	205.3	0.169	
31.3		0.99				0.2540
	26.3		0.007	127.02	0.105	
22.1		0.99				0.1494
	18.6		0.011	70.57	0.058	
15.6		0.98				0.0913
	13.1		0.02	45.36	0.037	
11.0		0.96				0.054
	9.29		0.033	26.46	0.022	
7.81		0.92				0.0322
	6.57		0.057	16.16	0.013	
5.52		0.87				0.0189
	4.65		0.095	9.52	0.008	
3.91		0.77				0.0111
	3.28		0.259	9.18	0.008	
2.76		0.51				0.0035
	2.32		0.291	3.65	0.003	
1.95		0.22				0.0005
	1.64		0.120	0.53	0.000	
1.38		0.10				0.0001
	1.16		0.050	0.08	0.000	
0.98		0.05				0.000
	0.82		0.030	0.02	0.000	
0.69		0.02				0.000
			0.020	0.00	0	
		Sum:	**1**	**1214.78**	**1**	

Table A2 Estimation of average sizes from volume distribution

Interval mean Size, x (μm)	Incremental Volume Distribution, $q_3(x)$	$q_3(x)/x$ (mm^{-1})	$xq_3(x)$ (μm)
840.90	0.001	0.00	0.457
594.60	0.001	0.00	0.867
420.45	0.004	0.01	1.490
297.30	0.008	0.03	2.321
210.22	0.016	0.07	3.275
148.65	0.028	0.19	4.187
105.11	0.046	0.44	4.850
74.33	0.068	0.92	5.089
52.56	0.092	1.75	4.839
37.16	0.112	3.02	4.168
26.28	0.124	4.71	3.253
18.58	0.124	6.66	2.300
13.14	0.112	8.54	1.474
9.29	0.092	9.91	0.855
6.57	0.068	10.42	0.450
4.65	0.046	9.93	0.214
3.28	0.028	8.58	0.093
2.32	0.016	6.71	0.036
1.64	0.008	4.75	0.013
1.16	0.004	3.05	0.004
0.82	0.002	2.75	0.002
0.58	0.001	1.38	0.000
0.41	0.000	0.63	0.000
Sum:	**1.000**	**82.45**	**40.238**

Estimates:

Specific Surface Area:

$$S_v = 6\sum q_3(x)/x = 0.495\ \mu\text{m}^{-1}\ (\text{m}^2/\text{cm}^3)$$

Specific Surface Mean Diameter:

$$\bar{x}_{sv} = 6/S_v = 1/\sum q_3(x)/x = 12.13\ \mu\text{m}$$

Volume Mean Diameter:

$$\bar{x}_{13} = \sum x q_3(x) = 40.24\ \mu\text{m}$$

Author's short biography

Richard Hogg

Richard Hogg is Professor Emeritus of Mineral Processing and GeoEnvironmental Engineering at the Pennsylvania State University. He received a B.Sc. from the University of Leeds and the M.S. and PhD degrees from the University of California at Berkeley. Dr Hogg's research interests include fine particle processing, particle characterization, and colloid and surface chemistry.

Particulate Science and Technology in the Engineering of Slurries for Chemical Mechanical Planarization[†]

S. Raghavan[*]
Department of Materials Science and Engineering, The University of Arizona[1]
M. Keswani
Department of Chemical Engineering, The University of Arizona[2]
R. Jia
Department of Materials Science and Mineral Engineering, University of California[3]
(Currently with Applied Materials, Santa Clara, CA)

Abstract

Chemical Mechanical Planarization (CMP) is a process that is now routinely used to planarize metal as well dielectric films during the fabrication of integrated circuits. This process uses slurries comprised of fine abrasive particles, such as silica, ceria or alumina. The stability and performance of the slurries are influenced by the size and properties of these particles, which in turn are influenced by their synthesis route. Stability is important to improve slurry lifetime and minimize defects such as microscratching caused by particle agglomerates or large particle counts (LPC) during polishing. The rheological behavior of slurry affects the friction at the pad-particle-wafer interface and alters the material removal rate. It is, thus, necessary to carefully engineer the slurry characteristics to achieve good removal rate and planarity without causing defects. This paper reviews the published literature on the synthesis of abrasive particles used in the preparation of CMP slurries as well as stability and rheological characteristics of slurries made from these particles. A brief account of particle-film interactions and importance of LPC in wafer scratching is also provided.

Keywords: chemical mechanical planarization, CMP, fumed silica, colloidal silica, ceria, alumina, slurry stability, coefficient of friction, COF, large particle count, LPC

1. Introduction

The fabrication of integrated circuits involves many steps in which topography in deposited dielectric and metal films is removed in order to create complex patterns of interconnects. The removal of topography is often referred to as planarization and a process known as Chemical Mechanical Planarization or CMP is routinely used to achieve this. In a CMP process, a wafer is held in a rotating carrier, which is pressed against a rotating polymeric pad on to which an aqueous slurry is dispensed [1)]. A schematic of first generation CMP tool is shown in **Fig. 1**.

The abrasive particles in the slurry along with the applied load (force) on the wafer and rotation provides the mechanical action for the removal of mate-

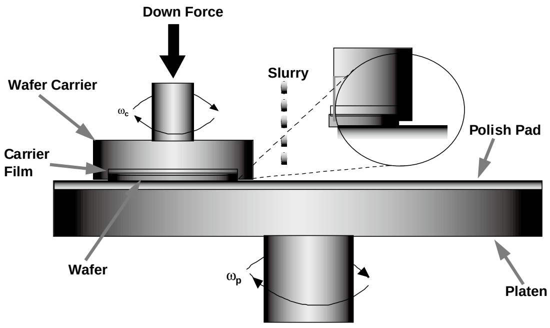

Fig. 1 Schematic diagram of a CMP process.

[†] Accepted : July 2, 2008
[1] Tucson, AZ 85721, USA
[2] Tucson, AZ 85721, USA
[3] Santa clara, CA95054, USA
[*] Corresponding author
TEL: 520-979-2348, FAX: 520-621-8059
E-mail: srini@u.arizona.edu

rial. The chemicals in the slurry provide the synergistic chemical action to improve selectivity between different types of films. The removal rate of a film is proportional to the applied pressure on the wafer and the relative velocity between the pad and the wafer.

Slurry is one of the most important consumables in CMP. It consists of fine abrasive particles that are dispersed in an aqueous solution containing one or more of various chemicals such as oxidizers, pH stabilizers, metal ion complexants and corrosion inhibitors [2)]. Silica, alumina or ceria particles in the size range of 50 to 150 nm are most commonly used for making the slurries. The pH of the slurry affects the surface charge on the particles, which in turn influences slurry stability. Agglomeration of slurry particles results in large particles, which tend to create defects such as scratches on films that are planarized. Choosing slurry which provides good removal rates without causing defects is of utmost importance in CMP.

A comparison of the characteristics of typical slurries used in CMP of metal and dielectric films is given in **Table 1**. Slurries used to planarize dielectric films such as SiO_2 or fluorinated silicon dioxide (FSG) typically contain 10% by weight of silica particles at alkaline pH values, as the removal is mostly mechanical in nature. These slurries typically provide a removal rate of the order of 2500 Å/min. Slurries for copper CMP contain a smaller amount of abrasives (~ 3% by weight) and are maintained at slightly acidic pH (4-6) values. These slurries contain an oxidant such as hydrogen peroxide and a copper complexant to enhance the chemical component of CMP. The removal rates of copper in these slurries can be tuned to a value between 500 to 6000 Å/min by controlling oxidizer, complexant and inhibitor concentrations.

This paper reviews the published literature on the synthesis of abrasive particles used in the preparation of CMP slurries as well as stability and rheological characteristics of slurries made from these particles. A brief account of particle-film interactions and importance of particle agglomerates in wafer scratching is also provided.

2. Abrasives in CMP Slurries

Colloidal sized SiO_2, CeO_2 and Al_2O_3 particles are used in the manufacturing of CMP slurries. Today, silica particles are predominantly used in the preparation of slurries for dielectric as well as metal CMP. Alumina particles find limited used in the manufacturing of slurries for tungsten CMP; however, because of their hardness, they are slowly falling out of vogue. Ceria slurries find use in the removal of oxide dielectric during the formation of shallow trench isolation (STI) structures.

2.1. Silica particles and slurries

Two types of silica particles, fumed and colloidal silica, are used in the preparation of slurries for dielectric and metal CMP.

2.1.1. Fumed silica

2.1.1.1. Synthesis of fumed silica

Fumed silica is produced by the oxidation of chlorosilane in a flame at temperatures greater than 1000℃

Table 1 Comparison of the characteristics of typical slurries used in CMP

	Solid Content (weight %)	pH	Additives
SLURRIES FOR CMP OF SiO_2 AND FLUORINATED SiO_2 (aka FSG) FILMS			
Fumed silica slurries	~10	11-11.2	Biocide, surfactant
Colloidal Silica Slurries	~30	10	Biocide, surfactant
Ceria Slurries	0.1 to 4	4-6	Inorganic acids, amino acids to provide selectivity between nitride and oxide films
SLURRIES FOR TUNGSTEN CMP			
Fumed silica slurries	2-4	1.5-3.0	Oxidant (hydrogen peroxide, ferric nitrate), catalyst (metal ions), complexant
Fumed alumina slurries	2-4	2-4	Oxidant (potassium iodate, hydrogen peroxide), complexant, slurry stabilizer
SLURRIES FOR COPPER CMP			
Colloidal Silica slurries	2-4	4-6	Oxidant (hydrogen peroxide), complexant, corrosion inhibitor
SLURRIES FOR TANTALUM CMP			
Colloidal Silica slurries	8 -10	9-10	Oxidant (hydrogen peroxide)

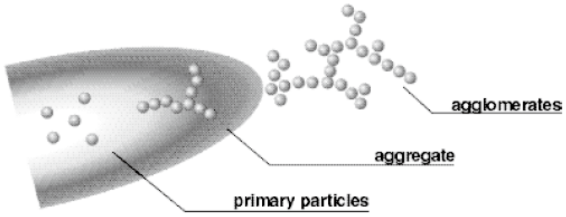

Fig.2 Synthesis of Fumed Silica particles using Flame Process [4].

according to the following reaction [3].

$$SiCl_4(v) + 2H_2(g) + O_2(g) \rightarrow SiO_2(s) + 4HCl(v) \qquad (R1)$$

The primary silica particles that are formed during the reaction are about 30 nm in diameter. However, they aggregate due to high temperatures that exist in the flame during synthesis, as illustrated in **Fig.2** [4]. Zones of different temperatures in the flame are represented by different colors in this Fig. The temperature zone, where primary particles are formed, is close to the fusion point of silica (1710 ^{0}C). As the particles move outside this zone, they cool below the fusion point and form aggregates. The aggregates are roughly 140-160 nm in size and have a very irregular shape. These aggregates tend to agglomerate during the cooling of the particles and need to be dispersed during the preparation of slurries. The aggregate size is technically the primary particle size in these slurries.

Silica slurries used for planarization of SiO_2 as well as fluorinated SiO_2 (FSG) films are typically made from fumed silica particles. The weight percent of silica particles in these slurries is about 10 %, with pH adjusted to 11.0 using potassium hydroxide (**Table 1**). Because of the high pH, there is a significant amount of dissolved silica in the slurries. It is believed that these soluble silicates provide electrosteric stabilization to the slurries. Additionally, these slurries often contain a biocide such as isothiazolin to prevent the growth of bacteria during storage. One of the advantages of fumed silica slurries is that it does not contain any sodium ions as impurity. However, because of the use of chlorosilane as a starting material in the manufacturing, chloride ions are invariably present in fumed silica slurries. Chloride ions are undesirable since they can cause metal corrosion.

2.1.2. Colloidal silica

The use of colloidal silica particles in CMP slurries has increased significantly over the last decade since it is possible to synthesize particles that are very uniform in shape and size using solution techniques. Unlike fumed silica, these particles are present in their primary size and not as aggregates. The size of these particles can be controlled anywhere between 5 nm and 200 nm by optimization of concentration of reactants and process conditions.

2.1.2.1. Synthesis of colloidal silica

There are many methods available to prepare colloidal silica particles, which include peptization, acid neutralization, dialysis, electrodialysis, ion exchange and hydrolysis and condensation of organosiloxanes (Stober method). The ion exchange and Stober method are the dominant methods used in the production of colloidal silica particles for CMP slurries.

In the ion exchange process, a solution of sodium silicate is passed through a strong acid cation exchange resin producing silicic acid, which is then converted to silica using an alkali such as ammonium hydroxide [5]. Alternatively, the sodium silicate solution and steam can be passed through a weak acid ion exchange resin at temperatures to produce finer particles of silica that can be subsequently enlarged [6]. The colloidal dispersion is then concentrated by ultrafiltration. Sodium ions greatly deteriorate integrated circuit device performance, and hence semiconductor industries are constantly looking for slurries that contain lower than 1 ppm of total sodium (solid + solution). Since, the ion exchange process uses sodium silicate as a starting material, it is important to purify the synthesized silica slurry to remove sodium ions. This is typically done by a deionization process.

One method to produce colloidal silica with very low sodium content is the Stober method that was patented in 1972. In this method, an organosiloxane, such as tertra ethoxyorthosilicate, dissolved in alcohol is hydrolyzed using ammonium hydroxide as a catalyst [7]. The particle size depends on the catalyst and water concentration. Similar to the ion-exchange method, Stober method also yields particles which are spherical and uniform in size but with negligible sodium content. However, production of silica using this method is quite expensive compared to the ion exchange methodology. Integrated Circuit manufacturing industries have to decide between high purity and high cost of Stober silica versus lower cost and less pure ion exchange silica. A compromise product made from potassium silicate with low levels of sodium can perhaps bridge the gap.

2.1.3. Stability of aqueous silica dispersions

Agglomeration of abrasive particles is inevitable

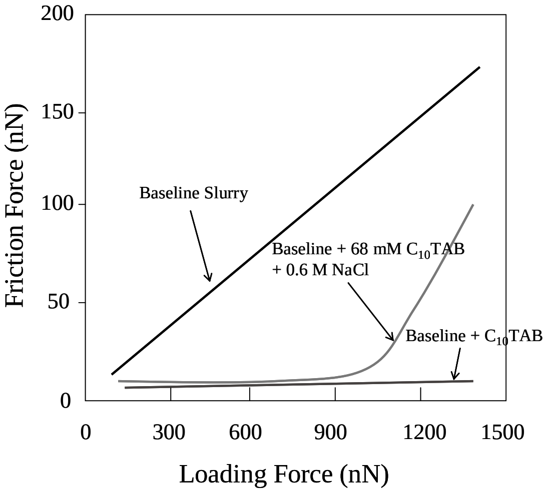

Fig.3 AFM friction force measurements on silica wafer for silica slurry containing C_{10}TAB and NaCl as additives (**Fig.9** from [8]; Redrawn with permission from Elsevier).

in slurries but the kinetics of the process is of relevance. Unstable slurries with a wide particle size distribution can lead to wafer scratching and defects. In order to achieve effective planarization, with very few defects, it is essential to ensure long term stability.

Surfactants have been used in silica slurries to prevent particle agglomeration. Basim et al. evaluated the stability of slurries containing 12 weight percent of 0.2 μm sol-gel silica particles in the presence of cationic surfactants (C_nTAB). They found that stability of silica particles increased with the carbon chain length of the C_nTAB surfactant [8]. However, the disadvantage with use of surfactants in slurries is that they reduce the friction between the wafer and the pad during polishing which lowers the material removal rate. **Fig.3** shows that frictional force, measured by AFM, increases linearly with normal force for baseline silica slurry in the absence of surfactant and a salt. Addition of 68 mM of C_{10}TAB to baseline slurry drastically reduces the frictional force which begins to increase slowly beyond a critical loading force in the presence of 0.6 M NaCl. This increase of friction force in NaCl has been attributed to partial desorption of cationic surfactant from negatively charged silica.

An interesting approach to preventing scratches on the wafer surface while maintaining the stability and activity of abrasives is the use of porous particles in CMP slurries [9]. The effective Hamaker constant of silica particles has been found to decrease from 0.67 $\times 10^{-20}$ J to 0.23 $\times 10^{-20}$ J with increase in porosity from 2 % to 60 %. Lower Hamaker constant is likely to reduce interaction between the particles and therefore expected to improve their stability.

The dependence of stability of silica slurries on pH and electrolyte concentration is 'anomalous' and does not follow the pattern predicted by conventional DLVO theory [10]. Iler found that silica sols were colloidally stable at isoelectric point pH and at high electrolyte concentration near neutral pH [11]. Allen and Matijevic noted an increased stability of silica sols with decrease in pH from 11.0 to 6.0 for 0.15 M of Na^+ in solution [12]. It was proposed that protective silicate ologomeric and polymeric barrier layer is formed on the silica surface at pH lower than 10.5, and extends upto 2 nm at pH of 8.0 in 0.15 M of salt. This polymer layer usually comes from soluble silicates, such as sodium silicates, that are universal dispersants of many electrostatic colloids. The barrier layer can be viewed as M^+-polysilicic coating that increases in thickness as Na^+ (or salt) is added to dispersion providing greater stability. Similarly, decreasing pH 11.0 to 6.0 reduces the –SiOH ionization and reduces the binding of cation-silanol groups according to reaction R2.

$$M^{n+} + x\,(\equiv SiOH) \longleftrightarrow M\,(\equiv SiO)_x^{(n-x)+} + xH^+ \qquad \text{(R2)}$$

The reduced cation-silanol binding allows more sites to be available for binding of cation-polymer species to the silanol group, which improves the silica sols stability. However, since the desired levels of sodium in CMP slurries are very low, stabilization by this mechanism is not very useful. Hydration stabilization mechanism has provided insight on differences in stability observed with different types of ions [13].

2.1.4. Rheology of aqueous silica dispersions

Viscosity of CMP slurries is an important parameter that influences the slurry film thickness between the pad and the wafer and affects the drag force due to three body (pad-abrasives-wafer) interactions. The removal rate of material in CMP can vary depending on the friction between the pad and the wafer. The coefficient of friction (COF), defined as the ratio of shear force to the normal force, is a good indicator of frictional forces that exist during polishing. A plot of COF versus the Sommerfeld number (*So*), known as Stribeck-Gumbel curve, is often used to determine the extent of wafer-slurry-pad contact [14]. The *So* is a dimensionless grouping of CMP specific parameters defined according to equation 1.

$$So = \frac{V\mu}{P\delta} \qquad (1)$$

In the above equation, V is the relative velocity between the pad and the wafer, μ is viscosity of the slurry, P is the applied downforce divided by the actual contact area between the pad and the wafer, δ is the effective slurry film thickness. The contact area depends on the groove pattern in a polishing pad.

As can be discerned from equation 1, *So* increases with slurry viscosity for specified values of V, P and δ. Since COF depends on *So*, variation in slurry viscosity can significantly affect frictional forces between the wafer and the pad during polishing.

The different modes of lubrication exhibited during polishing are represented by the Stribeck-Gumbel curve as presented in **Fig.4**. In boundary lubrication, where abrasives, pad and wafer are in intimate contact, the COF is constant and independent of *So*. The lubricant film thickness between the pad and the wafer is approximately zero and excessive wear can occur in this mode of polishing. The second mode of lubrication is partial lubrication where partial contact occurs between the wafer, pad and abrasives. Under this condition, the slurry film thickness between the wafer and the pad is approximately equal to mean surface rougness of the pad. Finally, at large values of *So*, hydrodynamic lubrication occurs where the liquid film totally separates the pad and the wafer and the COF becomes a weak function of *So*. The film thickness, in this case, is much larger than the mean surface rougness of the pad.

Assuming values of V, P and μ to be 0.5 m/s, 2 psi and 2 mPa-s during polishing, the effective lubricant film thickness, δ, is approximately 50 µm for concave shape of the wafer [15]. The Sommerfeld number for these conditions can be computed as 0.0015. The Stribeck-Gumbel curve suggests the existence of boundary lubrication mechanism, in which case the COF should be constant and stable.

Comparison of frictional characteristics of fumed (12.5 weight % of 110 nm particles at pH of ~ 11) and colloidal silica slurries (30 weight % of 50 nm particles at pH of ~ 10) used for oxide CMP shows that fumed silica slurries exhibit higher COF than colloidal silica slurries. As indicated in **Fig.5**, the average values of COF for fumed silica and colloidal silica slurries are 0.3 and 0.22 respectively. Both slurries display boundary lubrication, in the Sommerfeld number range of 10^{-4} to 10^{-3}.

In a CMP process, shearing of the slurry can occur during various stages of polishing such as pumping, mixing of ingredients or sedimentation of abrasives. The shear rates during these processes are lower than 1000 s^{-1} and hence viscosity of slurries under these conditions can be easily measured using conventional viscometers based on rotating concentric cylinders or plates.

Much higher shearing occurs during the actual polishing process when the wafer, pad and abrasives are in contact. The resulting shear rate between the wafer and the pad can be calculated by determining

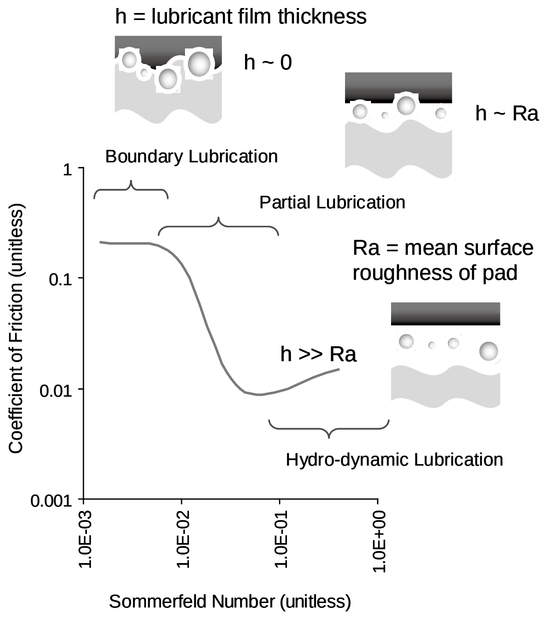

Fig.4 Stribeck – Gumbel curve for CMP Applications (Courtesy of Prof. Philipossian, The University of Arizona).

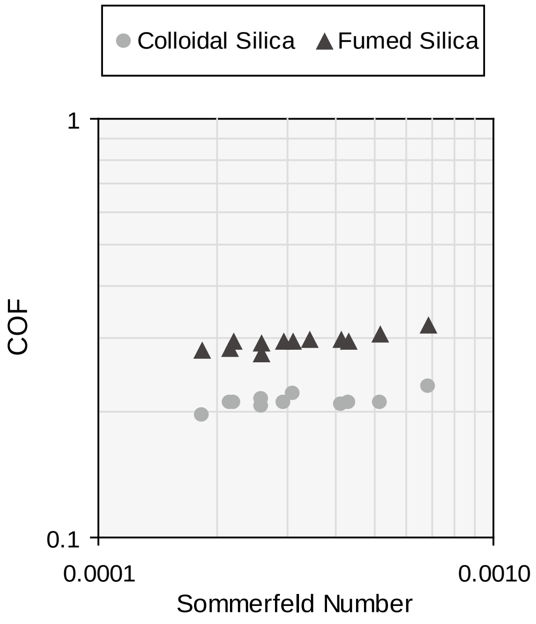

Fig.5 Comparison of COF values of Colloidal and Fumed silica slurries (Courtesy of Prof. Philipossian, The University of Arizona).

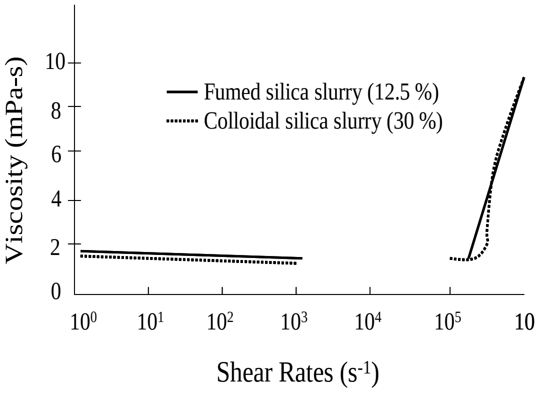

Fig.6 Rhelogical behavior of commercial fumed and colloidal silica slurries at different shear rates (Redrawn from **Fig.3** in [16)] with permission from Material Research Society).

the relative pad wafer velocity and the lubricant film thickness. Typical values of average relative velocity between the wafer and the pad range from 0.5 m/s to 1.0 m/s. Assuming a slurry film thickness between 35 μm and 60 μm at a downforce of 2 to 6 psi [15)], shear rates of 8000 s^{-1} to 30000 s^{-1} can be calculated to exist during actual polishing conditions. High pressure capillary or slit viscometers are typically used to measure viscosity at such shear rates.

Lortz et al. studied the rheology of commercially available colloidal and fumed silica CMP slurries containing 30 % and 12.5 % abrasives respectively [16)]. It was found that at shear rates lower than 1000 s^{-1}, the slurries behaved as Newtonian fluids with nearly constant viscosities of 2 mPa-s, as shown in **Fig.6**. When the shear rates were increased from 100,000 to 1000,000 s^{-1}, the viscosity for both slurries increased from approximately 2 to 10 mPa-s.

The rheological properties of aqueous silica dispersions, synthesized by Stober process, have been investigated as a function of particle size (0.1 – 1 μm) at pH values of about 9 and 3 (IEP). Measurements were carried out for particle volume fractions of 0.05 to 0.5 at shear rates of 0.1-1000 s^{-1} [17)]. The suspension, at pH value close to 9.0, behaved as newtonian fluid when the volume fraction of particles was equal to or less than 0.3. At higher volume fraction, shear thinning behavior was observed. These results are displayed in **Fig.7**.

The shear thinning effect was attributed to breaking of agglomerates formed at higher volume fraction, causing reduction in viscosity as the particles become free. The effect was more pronounced for smaller particles (0.1 μm) and at smaller shear rates (1-10 s^{-1}). The viscosity for dispersions made from 0.1 μm particles at a volume fraction of 0.45 reduced from about 10 mPa-s to 0.2 mPa-s with increase in shear rates from 1 to 1000 s^{-1}. In the case of slurries made from larger paricles of 1 μm in size, similar increase in shear rates reduced the viscosity from 0.05 mPa-s to 0.02 mPa-s. At a given volume fraction, higher viscosity observed for smaller particles was attributed to lower interparticle distance resulting in stronger inteactions between particles. Depending on the particle size, the viscosity of the silica suspension started to increase significantly at volume fraction of about 0.4. The transition from viscoelastic liquid like properties to elastic solid like behavior was observed at this volume fraction.

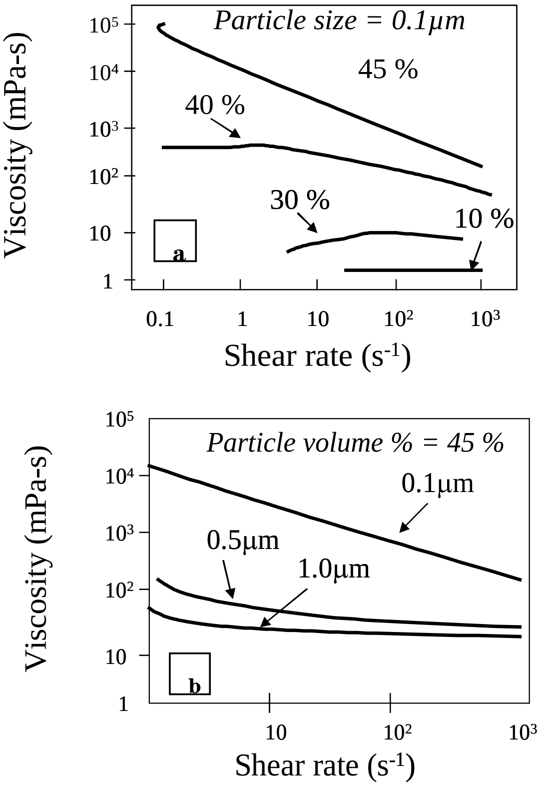

Fig.7 Viscosity as a function of shear rates for silica dispersion a) 0.1 μm abrasives at different volume percent and b) 45 % (vol) abrasives of different sizes (Redrawn from **Fig.3** and **4** in [17)] requested permission from Taylor and Francis).

Mooney's correlation, expressed in equation 2, is often used to obtain the relationship between relative viscosity (viscosity of suspension to that of suspending fluid) and particle volume fraction for silica dispersion [17), 18)].

$$\eta = \eta_0 Exp\left(\frac{\alpha\phi}{1-\left(\frac{\phi}{\phi_m}\right)}\right) \tag{2}$$

where η and η_0 are the viscosity of suspension and suspending fluid respectively, α is the fitting parameter, ϕ and ϕ_m are the particle volume fraction and maximum packing fraction respectively. The values of α and ϕ_m have been estimated to vary between 2.78 and 4.9 and 0.7 and 0.74 respectively for colloidal silica dispersions.

2.2. Ceria particles and slurries

2.2.1. Synthesis of ceria

Two most common routes for the synthesis of CeO_2 particles are solid-state displacement and wet chemical precipitation [19)-21)]. In the solid-state displacement method, cerium salt such as cerium chloride or cerium carbonate in its anhydrous form is milled with a base such as NaOH to induce a chemical displacement reaction to form cerium (+3) hydroxide. This mechanochemical reaction is followed by calcination in air at temperatures in excess of 500 ^{0}C. In the wet chemical precipitation method, an aqueous solution containing a cerium salt, typically cerium nitrate is hydrolyzed with a base and then calcined. There is at least one report in the literature which describes the formation of cerium (+3) hydroxyl carbonate by aqueous phase precipitation followed by calcination to produce CeO_2. More recently, vapor phase techniques have been used to synthesize fine ceria particles. In a technique known as Physical Vapor Synthesis (PVS), a solid precursor of Ce is vaporized, reacted with a gas and cooled at a controlled rate to form nano particles. A modified version of this process known as Nano-Arc Synthesis (NAS) is capable of working with a wide variety of precursors to form nano-particles. It is claimed that the NAS process is capable of providing in situ surface modification to create very stable dispersions in water, which can be used for CMP.

Literature values of iso-electric point (IEP) of ceria particles fall in the range 6 to 10.3. There is at least one commercial product (AdNanco Ceria) that has a thin carbonate coating to increase the IEP to 10 [22)]. The dependence of IEP value on synthesis method and calcination temperature is yet to be established.

The use of ceria particles in slurries for dielectric polishing is due to the strong chemical interaction between ceria and silica. In this context, a detailed understanding of surface chemistry of ceria and silica is essential. The acid-base behavior of surface hydroxyls in aqueous dispersions of ceria particles has been predicted based on multi-site complexation or 'MUSIC' model developed by Van Riemsdijk [23), 24)]. Ceria crystallites are expected to exhibit three types of surface hydroxyls, monodentate, bidentate and tridentate, depending on site coordination. The estimated values of equilibrium constant for deprotonation reactions, corresponding to ceria surface sites Ce_2-OH, Ce_1-OH and Ce_3-OH, are summarized in **Table 2**. The calculated point of zero charge (PZC) of ceria from these pKa values occurs at a pH of 7.9.

Table 2 Equilibrium constants for deprotonation reactions for aqueous dispersions of ceria particles [24)]

Deprotonation Reaction	pKa Value
$-Ce_1-OH_2^{+0.5} \leftrightarrow -Ce_1-OH^{-0.5}+H^+$	10.4
$-Ce_1-OH^{-0.5} \leftrightarrow -Ce_1-O^{-1.5}+H^+$	24.2
$-Ce_2-OH_2^{+1} \leftrightarrow -Ce_2-OH^0+H^+$	1.0
$-Ce_2-OH^0 \leftrightarrow -Ce_2-O^{-1}+H^+$	14.8
$-Ce_3-OH_2^{+1.5} \leftrightarrow -Ce_3-OH^{+0.5}+H^+$	-8.3
$-Ce_3-OH^{+0.5} \leftrightarrow -Ce_3-O^{-0.5}+H^+$	5.5

2.2.2. Stability of aqueous ceria dispersions

Ceria slurries have been increasingly used for STI CMP as they offer better selectivity of removal rates between SiO_2 and Si_3N_4 compared to slurries with other abrasives. However, ceria slurries have the major disadvantage of inducing defects on the wafer surface due to agglomeration of abrasives [25)]. Further, ceria particles due to higher density (~ 7000 Kg/m^3) than alumina (~ 4000 Kg/m^3) or silica (~ 2000 Kg/m^3) particles are prone to faster sedimentation. Thus, stabilization of ceria slurries is critical for its successful implementation in STI CMP.

Ceria slurries are commonly stabilized by water soluble polymers such as poly methylacrylate acid (PMMA) and poly acrylic acid (PAA) for dielectric CMP [26)]. The adsorption of these polymers is believed to increase the zeta potential of ceria abrasives in neutral and alkaline pH range from 6 to 9 [27)]. This increase in the zeta potential of ceria abrasives is understood to be due to ionization of the polymeric molecules to form negatively charged macromolecules with increase in pH of the solution. Kim et al. found that ceria slurries, containing 1 % abrasives and 1 % PMMA, were very well dispersed in neutral and alkaline conditions with narrow particle size distribution from 0.01 to 1 µm [27)]. By contrast, the same dispersion in acidic pH condition was observed to be unstable with a large agglomeration of particles and a wide size distribution ranging from 0.02 to 100 µm. Lower zeta potential of ceria abrasives in acidic pH regions was considered to be the cause for decrease in the slurry stability. The IEP of ceria shifted from pH of 7 to 2.5 with addition of PMMA.

2.2.3. Rheology of aqueous ceria dispersions

The rheological properties of aqueous ceria dispersions were investigated by Hsu and Nacu [28)]. For ceria volume fractions less than 2%, the slurries exhibited Newtonian behavior and at higher volume fractions shear-thinning behavior was observed. In the absence of any added electrolyte, a maximum in viscosity was measured at the IEP (~ 6.0) of the ceria particles. Interestingly, they found the IEP to increase with increase in NaCl concentration.

In another study by Kim et al., the rheological behavior of ceria slurries with 1 % solid content was examined as a function of pH for shear rates between 10 and 1000 s^{-1} [27)]. These slurries contained polymethylacrylate acid as an additive, which shifted the IEP of ceria particles from 7 to 2.5. In the basic and neutral pH regions, the slurry showed newtonian behavior with a constant viscosity of less than 1 mPa-s. In the acidic pH region, the particles were found to agglomerate and the viscosity dropped from 2.5 mPa-s to 0.5 mPa-s with increase in shear rate from 10 to 1000 s^{-1}. The shear thinning behavior in acidic pH suggested breaking of agglomerated particle structure with increasing shear rates.

2.3. Alumina particles and slurries

2.3.1. Synthesis of alumina

Sol-gel method is the most common method for synthesis of alumina particles in aqueous solution [29)]. In sol gel process, aluminium alkoxide is used as a precursor which undergoes hydrolysis reaction in excess water under vigorous stirring followed by peptization of the hydroxide to a sol and eventually a gel. Peptization requires that a critical concentration (0.03 to 0.1 mole of acid per mole of alkoxide) of certain acids (nitric acid, perchloric acid and hydrochloric acid) be introduced in the slurry, which must be maintained at 80 ^{0}C for sufficient time [30)]. The pyrolysis of dried gel forms alumina particles [31)]. Since the reactivity of aluminium alkoxide is very high, a chelating agent is normally used to control the hydrolysis rate. The sol gel route for synthesis of alumina provides advantages such as high surface area, better purity, narrow size and pore distribution, [32)].

Fumed alumina is manufactured by hydrolysis of gas precursors such as aluminum chloride in hydrogen/oxygen flame at about 1800 ^{0}C [33)]. The high pressure gas precursor is mixed with oxygen or air and introduced in the reaction chamber along with a fuel such as methane. The water vapor that is formed as an intermediate reacts with vapors of $AlCl_3$ to produces fumed alumina (Al_2O_3). The overall reaction for the formation of oxide can be represented as:

$$2AlCl_3 + 6H_2 + 3O_2 \rightarrow Al_2O_3 + 3H_2O + 6HCl \tag{R3}$$

Reaction R3 is exothermic and therefore super-saturation of gaseous oxide occurs rapidly in the reaction chamber. The oxide molecules start to condense into small liquid droplets after they leave the flame or reaction zone. The mixture of gaseous and liquid Al_2O_3 is then passed through a series of tubes or the coagulation zone, where temperature gradients exist that result in formation of primary alumina particles. Aggregation of primary particles occurs in the aggregation zone and is controlled by temperature, concentration of primary particles and time spent by the particles in the aggregation zone. Hot steam may be used to remove hydrochloric acid from the surface of particles. The primary particles of fumed alumina synthesized by this process are about 13 nm with a specific area of 100 m^2/gram.

2.3.2. Stability of aqueous alumina dispersions

Alumina dispersions are commonly stabilized under acidic conditions for use in CMP [34), 35)]. In contrast to the commercially available silica slurries that are normally stable, alumina slurries have been found to require continuous stirring to maintain the particles in suspension [36)]. Alumina slurries are often stabilized by additives including amphiphilic polymeric surfactants such as DAPRAL (a maleic anhydride α-olefin copolymer) or polyacrylic acid [37), 38)].

A commercial alumina slurry for metal CMP would contain an oxidant such as hydrogen peroxide, ferric nitrate or potassium iodate. Luo et al. investigated the effect of Fe^{3+} ions and BTA, a corrosion inhibitor, on the stability of two weight percent alumina (0.3 μm) slurry [36)]. They found that at pH values less than 2.0, ferric ion concentrations higher than 0.01 M decreased slurry stability. At pH values higher than 2.2, Fe^{3+} precipitated out as $Fe(OH)_3$, which increased coagulation of alumina particles causing instability. In the case of BTA, the stability of alumina particles, at pH of 1.3, was affected only for BTA concentrations greater than 0.01 M. The settling rate of alumina particles increased by about eight times when BTA concentration was increased from 0.01 M to 0.1 M. The adsorption of BTA anion on positive alumina surface was concluded to be responsible for slurry instability.

2.3.3. Rheology of aqueous alumina dispersions

The rheological properties of colloidal alumina (0.2 µm) dispersions of 1-40 volume percent solid in the pH range 2.0 – 10.0 were studied by Wang et al. [39)]. Dispersions containing 20 % solids in the pH range from 2.0 to 6.8 behaved as Newtonian fluid whereas under conditions of similar concentration but higher pH values between 8.2 and 10.0, they exhibited pseudoplastic behavior. In addition, basic dispersions were characterized by a higher viscosity than acidic dispersions. The apparent viscosity in the pH range of 2.0 – 7.0 for particle concentration equal to or lower than 20 % was found to be between 10^{-3} and 10^{-2} Pa-s. This viscosity range increased to 10^{-3} – 1.0 Pa-s for dispersions with higher pH between 7.0 and 10.0.

2.4. Particle—film interactions in CMP

2.4.1. CeO_2 particle - SiO_2 film interactions

Ceria based slurries have been used in glass polishing for many decades and are finding increased use in the formation of shallow trench isolation (STI) structures by the polishing of silicon dioxide films with a high selectivity over nitride. A mechanism commonly known as “Chemical Tooth Model” has been proposed to explain the interaction of ceria particles with silica surface during CMP [40)]. This model proposes that ceria particles temporarily bind to silica surface during polishing via condensation reactions of the form.

$$\text{-Si-O}^- + \text{-Ce-OH} \rightarrow \text{-Si-O}^- \cdots \text{Ce-OH} \rightarrow \text{-Si-O-Ce-} + \text{OH}^- \qquad \text{(R4)}$$

During shearing actions that prevail during polishing, the –Si-O-Si – bonds that are bound to the surface –Si-O-Ce- bonds are strained and removed as shown in R5. The net result is the removal of a certain amount of SiO_2 film.

$$\text{-Si-O-Si-O-Ce-} \rightarrow \text{-Si-O} \cdots \text{Si-O-Ce-} \rightarrow \text{-Si-O (film)} + \text{-Si-O-Ce- (particle)} \qquad \text{(R5)}$$

Under slightly acidic (~ pH 4) and near neutral conditions, high removal (polishing) rate of silica films can be achieved at solid contents lower than a few weight percent. This is in contrast to silica slurries which have to be used at much higher percent (~ 10%) solids for providing the same rate.

Ceria slurries that provide very high selectivity between oxide and nitride contain additives that interact with nitride surface. Various amino and carboxylic acids have been found to be useful for improving selectivity [41), 42)].

2.4.2. SiO_2 particle - SiO_2 film interactions

The hydration of silica films as well as attack of Si-O bond by OH^- ions play a key role in SiO_2 CMP. At alkaline pH of about 11, even though both silica particle and silica films are characterized by negative zeta potential, removal rates as high as 2000 Å/min can be achieved. This precludes any type of interactions similar to those between ceria and silica. Dissolution and softening of silica by OH^- most likely contributes to removal mechanism.

2.4.3. SiO_2 particle - ta film interactions

In the case of tantalum polishing, rapid oxidation of tantalum films to tantalum oxide (Ta_2O_5) is observed. The binding of silica particle to Ta_2O_5 is similar to binding of ceria particles and has been postulated to be responsible for high removal rates. The tantalum removal rate is known to increases with increase in weight percent of silica in slurries.

Vijayakumar et al. investigated the removal of tantalum in silica slurry at pH of 6.0 [43)]. Formation and mechanical tearing of Ti-O-Si bonds was considered as the primary removal mechanism. The Ta-O-H and Si-O-H react to form Ti-O-Si bonds according to reaction R6.

$$Ta-O-H+Si-O-H \rightarrow Ta-O-Si+H_2O \qquad \text{(R6)}$$

It was proposed that first multiple contact points are formed between silica particles and Ta_2O_5 on tantalum surface. The movement of silica particles away from the surface causes straining and removal of Ta_2O_5 lump.

2.5. Large particle counts (LPC) in CMP slurries

Filtration of slurries is done to remove large defect generating agglomerates, commonly referred to as large particle counts or LPC. Scratching of films due to a small number of large particles present in CMP slurries has been recognized as a critical problem in CMP. Large particles can be traced to two different sources; particle synthesis / milling procedure and slurry distribution loop in a fabrication plant. In fumed and colloidal silica slurries, particles with diameter of 0.5 µm or greater are considered to be large particles. Fumed silica slurries are more sensitive to shear agglomeration compared to colloidal silica slurries. Alumina and ceria slurries, on the other hand, are least sensitive to shearing conditions.

Proper choice of slurry handling and dispense systems can reduce the formation of LPC in CMP slurries. In a study by Johl et al., it was found that recirculation of slurries using diaphragm pump generated much lower LPC than that using bellows pump [44)]. The effect was attributed to difference in the shearing action in these two pumps. Similarly, centrifugal pumps cause less flocculation of particles than bellows type pump [45)].

Large particles in slurries can be characterized using several techniques including static light scattering (SLS), capillary hydrodynamic fractionation (CHDF), acoustic spectroscopy (AS), and single particle optical sensing (SPOS). Ramsen et al. obtained a correlation between LPC, measured by SPOS method, and surface defects generated during dielectric polishing by CMP slurries containing 9 % fumed silica abrasives at pH of 3.0 [46)]. The surface defects were characterized by measuring the number of scratches on wafers using dark field optical microscopy. As shown in **Fig.8**, the scratch counts on wafer increased approximately linearly with fraction of LPC (corresponding to particles with diameters ranging from 0.469 to 1.887 μm) in slurries. This suggested that scratch formation was predominantly due to large particles in the slurry that get trapped between the wafer and the pad during polishing. A size of 0.68 μm was estimated as the minimum particle diameter that contributed effectively to wafer scratching at the experimental polishing conditions.

2.6. Conclusions

The synthesis route for abrasives influences the primary particle size, their tendency to agglomerate and the type of ionic contamination they introduce into slurries. In order to ensure slurry stability and minimize surface defectivity, additives such as surfactants or polymers can be used. However, these stabilizers also tend to lubricate or reduce the friction between wafer and abrasive particles and lower the material removal rate. Use of functionalized particles with tailored surfaces is a viable option and needs to be explored. The rheological behavior of slurries should be ideally determined at shear rates of the order of 30,000 s^{-1}, which typically exists in CMP. Chemical interaction or binding between abrasives and the film followed by shearing action during polishing is critical to achieve selectivity and high material removal rates. Control of Large Particle Counts in CMP slurries is important to reduce scratching of films during polishing.

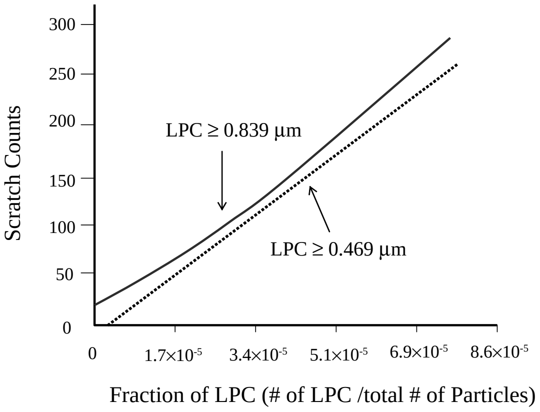

Fig.8 Correlation between wafer scratch counts and LPC for particles with diameters ranging from 0.469 to 1.887 μm (**Fig.9** in [46)]; Redrawn with permission from The Electrochemical Society).

References

1) Zantye, P., Kumar, A. and Sikder, A. (2004): Chemical Mechanical Planarization for Microelectronics Applications, Materials Science and Engineering, R 45, pp.89-220.
2) Muthukumaran, A. (2008): Chemical Systems for Electrochemical Mechanical Planarization of Copper and Tantalum Films, Doctoral Dissertation, The University of Arizona.
3) Bergna, H. and Roberts, W. (2006): Colloidal Silica: Fundamentals and Applications, CRC Press.
4) Cabot Microelectronics Corporation, Available from Internet website:. http://www.cabot-corp.com/cws/businesses.nsf/CWSID/cws BUS200310021538PM6651?OpenDocument.
5) Bergna, H. (1990): The Colloid Chemistry of Silica, Advances in Chemistry Series, 23, pp.54-55.
6) Precision Colloids, LLC Presentation on Colloidal Silica in CMP: The Challenge of Price versus Purity, Nanometer Precision in Particle Sizing (2004).
7) Stober, W. (1972): Method of Producing Monodisperse Silica Spheres Having a Dispersed Radioactive Tracer, Patent # 3634558, US Patent Office.
8) Basim, G., Vakarelski, I.. and Moudgil, B. (2003): Role of Interaction Forces in Controlling the Stability and Polishing Performance of CMP Slurries, Journal of Colloid and Interface Science, 263, 2, pp.506-515.
9) Choi, S. (2002): Synthesis and Characterization of Nanoporous Silicon Dioxide Particulate for Low Defectivity in Low-k Dielectric Chemical Mechanical Polishing, Doctoral Dissertation, University of Florida.
10) Healy, T. (1994): Stability of Aqueous Silica Sols, Advances in Chemistry Series, vol 234, 7, pp.147-159.
11) Iler, R. (1979): "The Chemistry of Silica" , Wiley, New York.
12) Allen, L. and Matijevic, E. (1970): Stability of Colloidal Silica – II. Ionic Exchange, Journal of Colloid Interface

Science, 33, pp.420-429.

13) Furlong, D., Freeman, P. and Lau, A. (1981): The adsorption of Soluble Silica at Solid-Aqueous Solution Interfaces: I. Leaching from Glass—an Electrokinetic Study, Journal of Colloid Interface Science, 80, pp.20-31.

14) Sorooshian, J. (2005): Tribological, Thermal and Kinetic Characterization of Dielectric and Metal Chemical Mechanical Planarization Processes, Doctoral Dissertation, The University of Arizona.

15) Lu, J., Coppeta, J., Rogers, C., Manno, V., Racz, L., Philipossian, A. Moinpour, M. and Kaufman, F. (2000): The Effect of Wafer Shape on Slurry Film Thickness and Friction Coefficients in Chemical Mechanical Planarization, Material Research Society Symposium, 613, pp.E1.2.1 – E1.2.6.

16) Lortz, W., Menzel, F. , Brandes, R., Klaessig, F., Knothe, T. and Shibasaki, T. (2003): News from the M in CMP, Viscosity of CMP Slurries, a Constant?, Material Research Society Symposium, 767, pp. F1.7.1-F1.7.10.

17) Chen, S., Oye, G. and Sjoblom, J. (2005): Rheological Properties of Aqueous Silica Particle Suspensions, Journal of Dispersion Science and Technology, 26, 4, pp.495-501.

18) Mooney, M. (1951): The Viscosity of Concentrated Suspension of Spherical Particles, The Journal of Colloidal Science, vol 6, pp.162-170.

19) Tsuzuki, T. and McCormick, P. (2001): Synthesis of Ultrafine Ceria Powders by Mechanochemical Processing, Journal of American Ceramic Society, 84, 7, pp.1453-1458.

20) Li, Y., Zhou, X., Wang, Y. and You, X. (2004): Preparation of Nano-sized CeO_2 by Mechanochemical Reaction of Cerium Carbonate with Sodium Hydroxide, Materials Letters, 58, 1, pp.245-249.

21) Janos, P. and Petrak, M. (1991): Preparation of Ceria-based polishing Powders from Carbonates, Journal of Materials Science, 26, pp.4062-4066.

22) Available from Internet website: http://www.advancednanomaterials.com.

23) Nabavi, M., Spalla, O. and Cabane, B. (1993): Surface Chemistry of Nanometric Ceria Particles in Aqueous Dispersions, Journal of Colloid and Interface Science, 160, pp.459-471.

24) Evans, D. (2004): Cerium Oxide Abrasives – Observations and Analysis, Material Research Society Symposium, 816, pp.K9.1.1-K9.1.12.

25) Kim, D., Kang, H., Kim, S. , Paik, U. and Park, J. (2006): Reduction of Large Particles in Ceria Slurry by Aging and Selective Sedimentation and Its Effect on Shallow Trench Isolation Chemical Mechanical Planarization, Japanese Journal of Applies Physics, 45, 9A, pp.6790-6794.

26) Shimono, N., Koyama, N. and Kawaguchi, M. (2006): Polymer Adsorption Effects on Stabilities and Chemical Mechanical Polishing Properties of Ceria Particles, Japanese Journal of Applied Physics, 45, 5A, pp.4196-4200.

27) Kim, S., Lee, S. and Paik, U. (2003): Influence of the Electrokinetic Behaviors of Abrasive Ceria Particles and the Deposited Plasma-Enhanced Tetraethylorthosilicate and Chemically Vapor Deposited Si_3N_4 Films in an Aqueous Medium on Chemical Mechanical Planarization for Shallow Trench Isolation, Journal of Material Research Society, 18, pp.2163-2169.

28) Hsu, J. and Nacu, A. (2004): An Experimental Study on the Rheological properties of Aqueous Ceria Dispersions, Journal of Colloid and Interface Science, 274, 1, pp.277-284.

29) Park, J., Oh, S., Paik, U. and Moon, S. (2002): Preparation of Aluminium Particles Using Ammonium Acatate as Precipitating Agent, Materials Letters, 56, 4, pp.429-434.

30) Yoldas, B. (1975): Alumina Sol Preparation from Alkoxides, American Ceramic Society Bulletin, 54, 3, pp.289-290.

31) Saha, S. (1994): Preparation of Alumina by Sol-Gel Process, Its Structures and Properties, Journal of Sol-Gel Science and Technology, 3, pp.117-126.

32) Amini, M., Sabounchei, S., Mirnajafi, F., Mirzaee, M. and Sharbatdaran, M. (2005): Preparation of γ-Alumina from Aluminium Aminoalkoxides, Ceramics – Silkaty, 49, 2, pp.138-141.

33) Hubbard, A. (2002): Encyclopedia of Surface and Colloid Science, 4, CRC Press.

34) Steigerwald, J., Zirpoli, R., Murarka, S., Price, D. and Gutmann, R. (1994): Pattern Geometry Effects in the Chemical - Mechanical Polishing of Inlaid Copper Structures, Journal of The Electrochemical Society, 141, pp.2842-2848.

35) Steigerwald, J., Duquette, D., Murarka, S. and Gutmann, R. (1995): Electrochemical Potential Measurements During the Chemical – Mechanical Polishing of Copper Thin Films, Journal of The Electrochemical Society, 142, pp. 2379-2385.

36) Luo, Q., Campbell, D. and Babu, S. (1996): Stabilization of Alumina Slurry for Chemical-Mechanical Polishing of Copper, Langmuir, 12, pp.3563-3566.

37) Yu X. and Somasundaran, P. (1994): Stabilization of Alumina Suspensions in Aqueous and Non-aqueous Media by a Hydrophobically Modified Polymer, Colloids and Surfaces, 89 A, pp.277-281.

38) Li, C., Yu, X. and Somasundaran, P. (1992): Effect of a Comb-like Amphiphilic Polymer on the Stability of Alumina Dispersions, Colloids and Surfaces, 69 A, pp.155-158.

39) Wang, X. and Hirata, Y. (2000): Electrical and Rheological Properties of Colloidal Alumina Suspensions, Journal of Ceramic Processing Research, 1, 1, pp.64-68.

40) Cook, L. (1990): Chamical Processes in Glass Polishing, Journal of Non-Crystalline Solids, 120, pp.152-171.

41) Carter, P. and Johns, T. (2005): Interfacial Reactivity Between Ceria and Silicon Dioxide and Silicon Nitride Surfaces, Electrochemical and Solid State Letters, 8,

8, pp.G 218-G221.
42) America W. and Babu, S. (2004) : Slurry Additive Effects on the Suppression of Silicon Nitride Removal during CMP, Electrochemical and Solid State Letters, 7, 12, pp.G 327-G330.
43) Vijayakumar, A., Du, T., Sundaram, K. and Desai, V. (2003): Polishing Mechanism of Tantalum Films by SiO2 Particles, Microelectronic Engineering, 70, pp.93-101.
44) Johl, B. and Singh, R. (2003): Optimum Process Performance Through Better CMP Slurry Management, Solid State Technology, Aug.
45) Singh, R. and Chang, F. (2008): Presentation on 'Why do Specific Pumps Increase Over-size Particle Size Distribution in CMP Slurries?', Levitronix CMP Users Conference (Available from Internet website:http://www.levitronix.com/ Downloads.Semiconductor.CMPUser2008.php).
46) Remsen, E., Anjur, S., Boldridge, D., Kamiti, M., Li, S., Johns, T., Dowell, C., Kasthurirangan, J. and Feeney, P. (2006): Analysis of Large Particle Count in Fumed Silica Slurries and its Correlation with Scratch Defects Generated by CMP, Journal of The Electrochemical Society, 153, 5, pp.G453-G461.

Author's short biography

Dr Srini Raghavan

Srini Raghavan is a professor of Materials Science and Engineering at the University of Arizona. He obtained his Ph.D in Materials Science and Mineral Engineering from the University of California, Berkeley, in 1976 and has been on the faculty of University of Arizona since 1978. His research interests lie in the areas of wet processing of semiconductor materials, chemical mechanical planarization, and applied colloid and electrochemistry. He has over 110 refereed publications and four patents to his credit. He is a member of Electrochemical Society, Materials Research Society and National Association of Corrosion Engineers. He can be reached at srini@u.arizona.edu.

Dr Manish Keswani

Manish Keswani is currently working as a Post-doctoral Research Associate with Professor Srini Raghavan in the Department of Materials Science and Engineering at The University of Arizona. Manish received his PhD degree in Chemical Engineering from The University of Arizona in May 2008, MS degree in chemical engineering from Texas A&M University-Kingsville in 2002 and his B. Tech degree in chemical engineering from Laxminarayan Institute of Technology, India in 1999. His current research interests include CMP and wafer and mask cleaning for microelectronics applications.. He can be reached at manishk@email.arizona.edu.

Renhe Jia

Dr. Renhe Jia is a currently a Member of Technical Staff at Applied Materials Inc, Santa Clara, CA, currently working on the reliability of photovoltaic modules. He received a BS in mineral engineering from Anhui University of Science and Technology, 1993, and MS in 1999 and PhD in 20003 in Materials Science and Mineral Engineering from University of California, Berkeley.
Since 2002, Dr. Jia has been with Applied Materials Inc. working on advanced technology development in chemical mechanical planarization (CMP), electrochemical mechanical planarization (eCMP), cleaning, advanced packaging, lithography, and solar module reliability.
Since 2004, Dr. Jia has been an industrial mentor for SRC/SEMATECH Engineering Research Center for Environmentally Benign Semiconductor Manufacturing, and has been serving as a committee member for CMP and Post-CMP Cleaning for International Semiconductor Technology Conference since 2006.
Dr. Jia has 11 published papers on surface and interface chemistry and processing of materials, and 23 granted/published patent applications in semiconductor processing. He can be reached at Renhe_ Jia@amat.com.

Applications of the Atomic Force Microscope in the Development of Propellant-based Inhalation Formulations[†]

Libo Wu and Sandro R. P. da Rocha*
Department of Chemical Engineering and Materials Science, Wayne State University[1]

Abstract

As the atomic force microscope (AFM) becomes a more accessible tool in the laboratory, researchers involved in the development of pharmaceutical formulations are taking advantage of its unique capabilities. In this work we review the uses of the AFM in the development of hydrofluoroalkane-based pressurized metered-dose inhaler formulations. Perspectives and limitations of the AFM and related techniques in this area also discussed.

Keywords: AFM, pMDIs, force measurements, propellant-based inhalation formulations, hydrofluoroalkanes, HFAs

1. Introduction

It is now accepted that aerosol inhalation therapy is not simply the preferred route for the treatment of respiratory disorders[1)], but it may also offer significant advantages in targeting the systemic circulation[1-4)]. The large surface area[5)], sluggish clearance[6)], and low proteolytic activity[7)] of the alveolar region provide for the opportunity of fast drug uptake, second only to the intravenous route[8)], and (typically) enhanced drug bioavailability[5, 9)]. The lungs are also now seen as much more resilient and robust than first thought[1)]. Another advantage of oral inhalation is that, in contrast to oral and nasal routes, therapeutic biomolecules delivered to the lungs can cross into the systemic circulation without the need of penetration enhancers[5)]. All these advantages have stirred a lot of interest in the development of novel oral inhalation formulations[7)].

One can, thus, ask why such potential has not been fully realized yet. While the pulmonary drug delivery technology market is no doubt large, and expected to grow to $9 billion by 2009, it still represents less then 20% of the overall drug delivery market[10)]. Perhaps one of the most notable challenges has been with respect to formulation of product development. For example, protein and gene delivery to the lungs hold great promise in the treatment of clinically important diseases such as cystic fibrosis[11)] and lung cancer[12)]. However, early attempts to formulate genes in nebulizers proved to be quite challenging[13)]. Difficulties in translating the CFC-based pressurized metered-dose inhaler (pMDI) formulations (strictly small molecular weight molecules) to hydrofluoroalkane (HFA) propellants[14)], as mandated by the Montreal Protocol[15)], serves as another illustration of the hurdles in the development of oral inhalation formulations.

Based in part on the typically poor performance of existing pMDI formulations, little work has been done to formulate therapeutic biomolecules in propellant-based inhalers[7)]. It is also surprising that while dry powder inhalers (DPIs) are expected to soon occupy 75% of the pulmonary drug delivery market[10)], it was not until 2006 that the first DPI product containing a large therapeutic biomolecule (insulin) was launched in the market - this is not only the first DPI, but also the first oral inhalation formulation with a therapeutic biomolecule[16)]. These problems are expected to be addressed, at least in part, by carefully considering the drug delivery devices and formulation strategies during the pre-formulation stage of product development, and by improved characterization of the physical behavior of the formulations.

The Atomic Force Microscope (AFM) is uniquely suited to probe the interaction between single particles, and particle-surface interactions in both air and liquid, and can thus provide microscopic information that can help guide the design of devices, excipients

---

[†] Accepted: July 2, 2008

[1] 5050 Anthony Wayne Dr., Detroit, MI-48202
* Corresponding author.
TEL: +1-313-577-4669, FAX: +1-313-578-5820.
E-mail: sdr@eng.wayne.edu

and novel particle technologies to develop systems of relevance to both DPIs and pMDIs. This contrasts with traditional approaches that measure dispersion stability and particle interactions from a bulk perspective as in sedimentation rate experiments[17)], centrifugal technique[18)], laser scattering[19)], and inverse gas chromatography (IGC)[20)]. In this work we focus on the application of AFM and its related techniques to systems of relevance to Hydrofluoroalkane (HFA)-based pMDIs. For detailed information on the applications of AFM for systems of interest to DPIs, the reader is directed to another recently published review[21)].

In what follows (part 2 of the manuscript), we will briefly discuss different oral inhalation devices, focusing on the formulation challenges that pMDIs are currently facing. A description of some of the recently proposed alternative propellant-based inhalation formulations is provided. This section will serve to demonstrate the relevance of AFM in the development of novel propellant-based inhalation formulations. The fundamentals of AFM and related techniques will be presented in detail in part 3. In the last part of this work (part 4), we review the studies that have focused on systems of relevance to Hydrofluoroalkane (HFA)-based pMDIs - mostly those systems where forces were measured in liquid HFAs. Current challenges and opportunities in the application of AFM and its related techniques to systems of relevance to pMDIs are also discussed.

2. pMDIs: The Formulation and Challenges in Improving their Market Share

2.1. The pMDI formulation

A typical pMDI consists of a canister sealed with a metering valve, and lodged upside down in an actuator, as schematically shown in **Fig.1**.

The compressed liquid propellant, which consists of more than 98% of the formulation[22)], is in equilibrium with its vapor (under saturation pressure) in the canister. The system is purposely kept in equilibrium with its vapor phase (vs. being in a compressed liquid phase) so that the solvent quality and the pressure inside the canister remain the same from the beginning to end of the formulation, thus helping maintain dose uniformity[22)]. Commercial pMDI formulations contain small solutes either in solution (drugs dissolved in the propellant, usually with the help of a co-solvent) or in suspension (micronized drug crystals with or without the help of other excipients)[23)]. The approximately 20 HFA-based pMDIs in the market today are somewhat evenly distributed between solution and dispersion formulations[23)]. The propellant generates a pressure of 50-80 psig inside the sealed unit[14)]. Upon pressing the actuator, the propellant and active drug (with potentially other excipients) that have been previously stored in the metering chamber are exposed to atmospheric pressure. The propellant flash evaporates to form an aerosol cloud containing the drug (along with any other excipients), which is inhaled by the patient[24)].

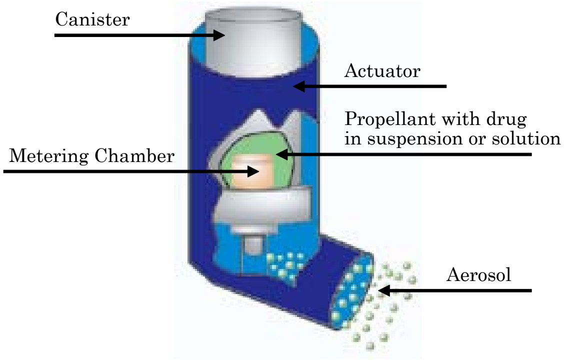

Fig.1 Schematic diagram of a pressurized metered-dose inhaler (pMDI).

2.2. Challenges in the development of pMDI formulations

The advantages and disadvantages associated with the different aerosol inhalation devices have been extensively discussed in the past[22, 25, 26)]. Nebulizers require that the aqueous medication is atomized into fine droplets that are inhaled by patients through a mouthpiece or mask. The use of nebulizers is generally limited to in-house treatment since the devices are not portable[27)]. pMDIs are the most widely used inhalation devices because they are portable, easy to use, and have high patient compliance. They also typically generate reproducible dosages, and the drugs are protected from the elements, as they remain in a sealed environment[14)]. One of the major drawbacks of pMDIs is the substantial oropharyngeal deposition typically observed, which may be somewhat mitigated by the use of spacers[28)]. Other considerations with pMDIs are the limited concentration of the delivery dosage[29)], and limited range of drugs that can at this time be formulated[22)]. DPIs are breath-activated devices. Patient coordination, therefore, is not as important, resulting in typically better deposition in the deep lungs compared to pMDIs. The deposition efficiency of DPIs is, however, still dependent on the patient's respiratory flow[30)]. While motor-driven DPIs have been introduced to overcome such deficiencies[31)], the devices are costly. It is worth pointing out, however, that the device selection depends highly on the medical indication, patient compliance, the formulation, and the characteristics of the agent being administered[27]. The ability to formulate in both DPIs and pMDIs is, therefore, of importance from the patient compliance and commercial stand points.

Besides the inherent difficulties (discussed above) in formulating with pMDIs, the development of propellant-based inhalers has also been challenged by the phase-out of CFCs, as mandated by the Montreal Protocol[15]. The more environmentally friendly and non-ozone depleting[32]* HFA propellants, more specifically, 1,1,1,2-tetrafluoroethane (HFA134a) and 1,1,1,2,3,3,3-heptafluoropropane (HFA227), are currently used in pMDIs[33]. In spite of the fact that the operation of pMDIs with HFAs is similar to those with CFCs, previous CFC formulations are generally not compatible with HFAs due to the significantly different solvent properties between these two classes of fluids[15]. For example, the excipients used in FDA-approved CFC formulations have extremely low solubility in HFAs[8]. The design of HFA-philic excipients is, therefore, of great relevance. However, the lack of fundamental understanding on the solvation forces in the semi-fluorinated HFAs is hindering the resolution of the challenges in improving existing formulations, and also from developing novel HFA-based pMDIs[34].

While the market share of HFA-based pMDIs by 2009 (out of the whole inhalation delivery market) is estimated to be only 5%, losing ground especially to DPIs, this trend may be reversed if existing reformulation issues can be overcome[10, 22]. As new technologies become available in propellant-based inhalation formulations, especially with therapeutics that target the systemic circulation and/or therapeutic biomolecules, it is expected that the market share of pMDIs will grow within the inhalation aerosol market, and may also take some of the market share currently not being targeted by oral inhalation products.

2.3. Novel HFA-based pMDI formulations

With the phase-out of CFC-based formulations, and challenges in reformulating in HFA propellants, research groups in academia and industry are taking the opportunity to innovate[23]. Efforts in the development of novel propellant-based inhalation formulations[†] can be classified with respect to the nature of the dispersed phase: aqueous- (emulsions/microemulsions) and nonaqueous(solid)-based systems[23, 35].

Aqueous-based dispersions can be stabilized in the form of emulsions (micron size and kinetically stable)[22] or microemulsions (nanometer in size - transparent, and thermodynamically stable)[36, 37] provided a suitable amphiphile is identified. Poly(lactide)-[38], poly(propylene oxide)-[39] and fluorine-based[40] nonionic amphiphiles have been shown to be effective in stabilizing reverse water-in-HFA (W/HFA) emulsions. The emulsion-based formulations can be potentially used for the local or systemic delivery of therapeutics to and through the lungs. W/HFA microemulsions have also been suggested as a potential formulation for the pulmonary delivery of therapeutics (both small molecules and large biomolecules)[36]. Fluorinated ionic and non-ionic amphiphiles can form microemulsions of water in propellant HFA[41, 42]. However, the range of suitable fluorinated surfactants is limited due to their potential toxicity[40, 43]. Water-in-HFA227 microemulsions have been recently reported in the presence of an ethoxylated triblock copolymer and ethanol[36]. The uptake of biomolecules and anticancer therapeutics, and the aerosol characteristics of the corresponding formulations have been investigated[36]. Microemulsions may serve as an alternative to traditional solution/dispersion-based formulations of high-potency systems as the active component remains solubilized within the core of the aggregate, preventing its interaction with the container walls and other parts of the device that may significantly reduce the dosage[41, 42]. Some results of the attempts associated with the formulation of aqueous emulsions and microemulsion in propellant HFAs are shown in **Fig.2**.

One of the challenges in the development of such formulations is the fact that a large concentration of surfactants and cosolvents are usually required to stabilize the aqueous domains.[36] The presence of such low-volatility excipients can reduce the vapor pressure of the aerosol mixture, thus negatively affecting the efficiency of the aerosol[36]. A significant body of work from AFM-related techniques provided the insight for the design of amphiphiles containing highly HFA-philic groups, which are required for the formation and stabilization of such aqueous aggregates[34, 35]. We will discuss (below) in detail how AFM can be used to probe solvation forces in systems of relevance to pMDIs.

Traditional non-aqueous pMDI formulations are usually composed of pharmaceutical particles in suspension or drugs in solution in a propellant HFA[23].

---

[*] Although HFAs are not ozone-depleting, they are green house gases and are also known to produce tri-fluoroacetic acid (TFA,s CF_3COOH) in the troposphere[32].

[†] Solution-based formulations are not being directly considered here.

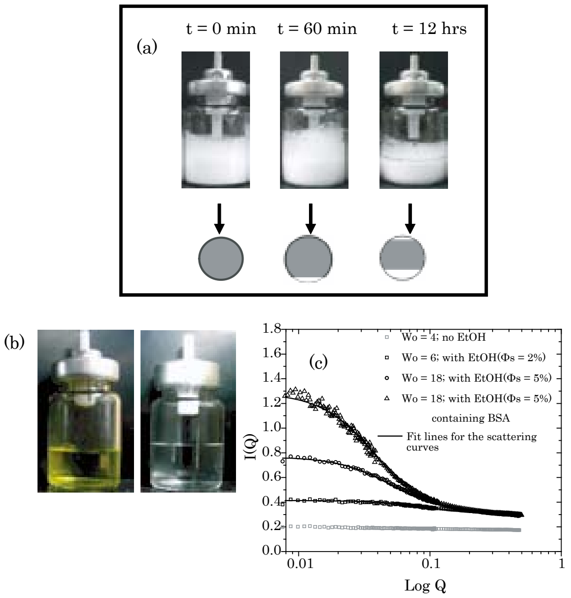

Fig.2 Results from some attempts to develop emulsion and microemulsion-based pMDI formulations. (a) Schematic diagram and digital images of the water-in-HFA227 emulsion formed at 30:70 v/v water/HFA227 and 1 w/w % $EO_{13}PO_{30}EO_{13}$; adapted from ref. [39]; (b) physical stability of pMDI formulations containing reverse aqueous microemulsions of (left) a yellow probe, and (right) 3mM irinotecan hydrochloride (anti-cancer drug) in HFA134a, in the presence of 10 % w/w ethanol, stabilized by 5.65 % w/w (21.5 mM) $PO_{22}EO_{14}PO_{22}$; adapted from ref. [37]; (c) Small angle scattering spectra of reverse aggregates of water in HFA134a in the presence and absence of alcohol. Curves as a function of the corrected water-to-surfactant molar ratio (W_o). The curve with highest scattering demonstrates the uptake of a model biomolecule within the core of the aggregate. Reprinted from ref. [36], with permission from RSC Publishing.

Cosolvents (notably ethanol) are generally required in the solution-based formulations to help solubilize the active pharmaceutical ingredients. There are several limitations associated with solution formulations. The drug of interest must be soluble in the propellant or propellant-excipient mixture, thus significantly restricting the range of therapeutics (certainly of biomolecules) that can be formulated. The presence of less volatile components (such as alcohol) may alter the aerosol performance[37], and the chemical stability of the formulation[44]. In dispersion-based formulations, colloidal stability of the pharmaceutical particles is key in controlling aerosol efficiency[23, 35, 45] Stability of colloids in HFA propellants can be achieved either through the addition of stabilizing excipients[45] or by altering the particle surface chemistry or its morphology[46-50]. There have been several studies focusing on the development of novel HFA-philic excipients capable of imparting stability to micronized drug dispersions in HFA propellants[23, 45, 51-53]. Efforts have also been made to modify the surface of particles. For example, poly(ethylene glycol) (PEG), poly(vinyl pyrrolidone) (PVP), and poly(vinyl acetate) (PVA) have been employed to coat the particles surface to reduce the cohesive forces[47-49]. Drugs have also been formulated as cores within polymeric shells designed with HFA-philic (biodegradable and biocompatible) moieties, which were used to reduce inter-particulate forces in HFA propellants[46]. The advantage of particle surface modification compared with surfactant-stabilized colloids is that no / little free stabilizers remain in solution, thus decreasing the potentially toxic effects of excipients[47]. Challenges associated with the synthesis of well-balanced amphiphiles are also circumvented. Engineering particles with certain morphological architectures can also help enhance colloidal stability[50, 54, 55]. For instance, porous particles possess excellent stability in HFAs, as the propellant can penetrate inside the particles, leading to improved density matching of the particles with the propellant, and also a reduction of the van der Waals forces between the particles[50]. Particles with a high degree of surface roughness can also be used to improve physical stability of the formulation by reducing the area of contact between particles[56]. Some results related to efforts in the development of novel (solid) suspension-based pMDI formulations are shown in **Fig.3**.

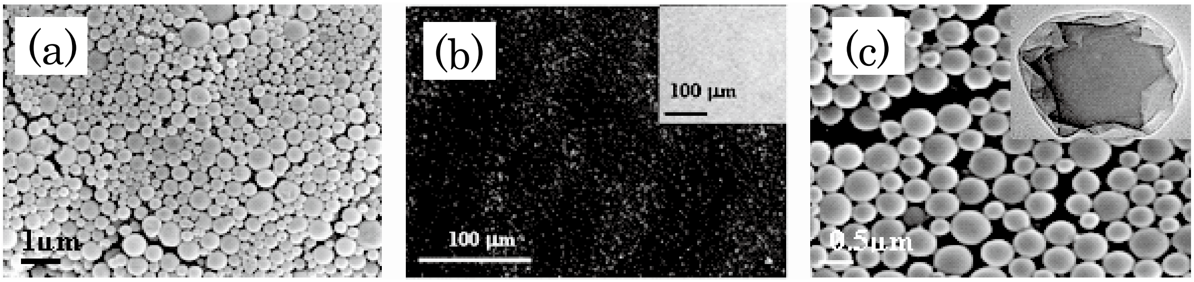

Fig.3 (a) SEM micrograph of PEG-trapped salbutamol sulfate (SS) spheres prepared by emulsification diffusion; long term stability in HFA227 was achieved; Reprinted from ref. [47] with permission from Elsevier. (b) SEM and (Inset) Optical image of salbutamol suspension with 0.1 mM $LA_{53}EO_{22}LA_{53}$ HPFP solution. Reprinted from ref. [45] with permission from American Chemical Society. (c) SEM image of core-shell particles with SS as the drug core and oligo(lactide)-*g*-chitosan as the HFA insoluble shell, (Inset) TEM image. Reprinted from ref. [46] with permission from Springer. Enhanced stability in HFA227 was achieved due to the good solvation of the outermost part of the particle shell by HFA.

Knowledge of the influence of the modification of the chemistry of the particle surface, or the particle morphology, or the presence of excipients affect particle cohesive/ adhesive interactions have contributed significantly to the development of novel excipients and particle engineering technologies relevant to pMDI formulations, some of which were discussed above. The applicability of AFM to the measurement of forces between particles and particle-surface forces of relevance to pMDIs will be discussed in detail below. First, however, it is necessary to understand the basics of AFM hardware, related theory and AFM-derived techniques.

3. The AFM and Related Techniques

3.1. The AFM and its hardware

The AFM was invented in the mid 80's[57]. It was a welcome addition to the family of scanning probe techniques as previous microscopes could not image the topography of non-conductive samples. With the resolution of nanometers (nm) or higher (lateral of order of 10 nm and vertical as high as 1 Å), and force sensitivity as low as 10^{-12} N (1 pN)[58], the AFM has key components of (i) a cantilever, usually made of Si or Si_3N_4, which can be integrated with a pyramidal sharp tip with radii of 5～50 nm; (ii) a piezoelectric scanner, which controls the movement of the AFM tip or sample precisely in the x, y and z directions; and (iii) a photo diode sensor, which is used to detect the laser reflected from the backside of the cantilever (gold plated to enhance the reflection of the laser). A schematic diagram of the main components of an AFM is shown in **Fig.4**. There are many variants to this scheme. The reader is directed to earlier reviews for more detail on this topic.[59-62]

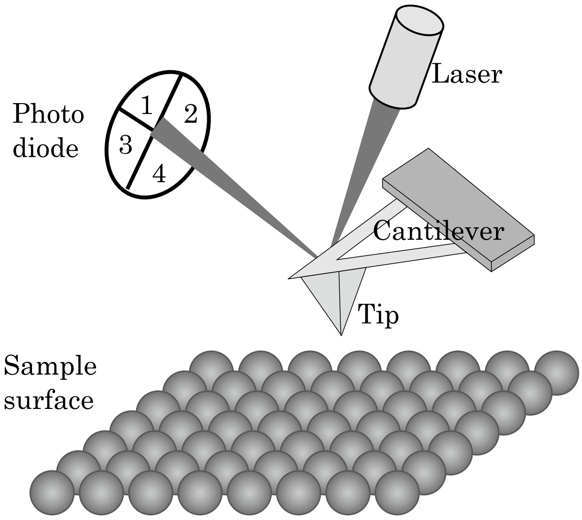

Fig.4 Schematic diagram of the main components of an AFM. Adapted from ref. [60].

3.2. Imaging with AFM

There are two basic types of operation modes for AFM imaging: contact mode and tapping mode[60]. In the contact mode regime, the system is connected, via a feedback loop, to a piezo motor, which controls the position of either the sample or AFM tip. The force between the tip and the sample surface is usually kept repulsive and constant during scanning so that any changes in the surface topography will cause a deflection on the cantilever[62]. This deflection is detected by the photodiode signal via the reflected laser, thus leading to an adjustment in the height of the piezo-electric scanner to compensate for the deflection. The force is, thus, maintained at the set point. Based on the force measurements, a topographic image of the surface is generated[63]. Tapping mode is the other commonly used imaging mode[60]. In this case, the cantilever is oscillated at or close to its resonant frequency. Since the cantilever is oscillating and tapping on the sample surface, it contacts the sample in a very short time scale so that the lateral forces applied to the cantilever during scanning are reduced significantly. Tapping mode is especially suited for soft surfaces[60]. AFM imaging is an important technique in the pharmaceutical industry[59]. The applicability of AFM imaging to pMDI related formulations includes the investigation of the effect of propellant on the aerosol canister lining[64], roughness measurements for drug crystal substrates[20], and determination of contact radii for colloidal AFM probes[65]. AFM can also be used to evaluate fluid viscosity according to the resonant frequency shift of the cantilever when immersed in a medium[66]. This may be an attractive way to determine the effect of more expensive excipients on the viscosity of systems relevant to pMDIs.

3.3. Force measurements with AFM

AFM is not only capable of generating images with high resolution[60], but also (and perhaps most importantly) to directly probe forces between surfaces[59, 62]. There have been several excellent reviews on the principles and applications of force measurements by AFM[59, 62], and the reader is directed to those references for more details on the technique. Here we provide the minimum amount of information on the basics of force measurements by AFM, which are required to appreciate the discussion that follow on solvation forces in HFAs, and colloid stability in pMDI-related systems.

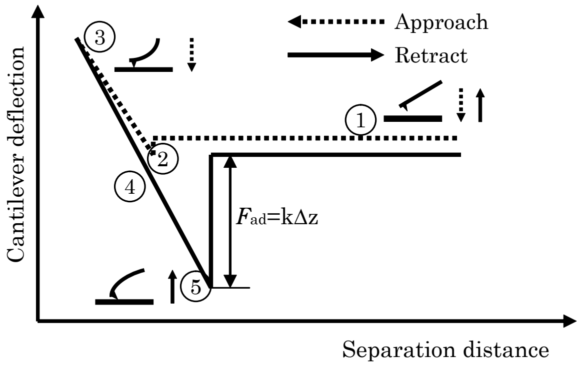

Fig.5 Schematic diagram of a typical AFM force-curve.

A typical force-distance AFM curve with the complete approach-retract cycle is shown in **Fig.5**. At large separation distances (1) there is no detectable force between tip and substrate, so that the AFM cantilever is not deflected; the difference between the approach and retract cycles in this region is usually caused by the hydrodynamic drag due to the presence of the medium[59]; (2) as the tip approaches the substrate, it jumps into contact due to Van der Waals (VDW) attractive forces; (3) after the contact, a linear cantilever deflection is observed as the tip moves further into contact with the substrate; (4) when the cantilever deflection reaches the force set point, the tip starts retracting from the substrate; in this contact regime, the discrepancy between approach and retract line is originated from the plastic or viscoelastic deformation of the sample; (5) the force needed to pull the tip off from contact with the substrate as the tip retracts from the substrate is defined as the force of adhesion (F_{ad})[‡] between the tip and substrate. F_{ad} is determined from the normal displacement (Δz) and spring constant (k) of the cantilever ($F_{ad} = k \cdot \Delta z$)[59].

There are two types of modifications to a typical AFM force measurement (modifications to the tip and/or substrate) that can be extremely valuable in the studies of colloid stability and surface science, namely: chemical force microscopy (CFM)[61], and colloidal probe microscopy (CPM)[59].

3.3.1. The chemical force microscopy (CFM) technique

CFM is an area of great interest as it can be utilized to probe forces in a variety of systems of relevance in engineering and science[61, 67]. Several excellent reviews have been published on CFM, and the reader is directed to those for more details on the technique[59, 61, 62, 67]. To perform CFM, a sample surface and AFM tip are both chemically modified with functionalities of interest[61]. The functionalities typically have terminal groups with some specific chemistry, and points of attachment to the substrate - either silanes or thiols. The functionalities can be deposited by self-assembly (vapor phase or solution)[34]. CFM can in principle be used to measure molecular interactions ranging from weak van der Waals (VDW) (< 10^{-12} N) to strong covalent bonds (10^{-7} N)[59, 62]. A schematic diagram of a chemically modified tip and substrate for a CFM experiment is shown in **Fig.6**.

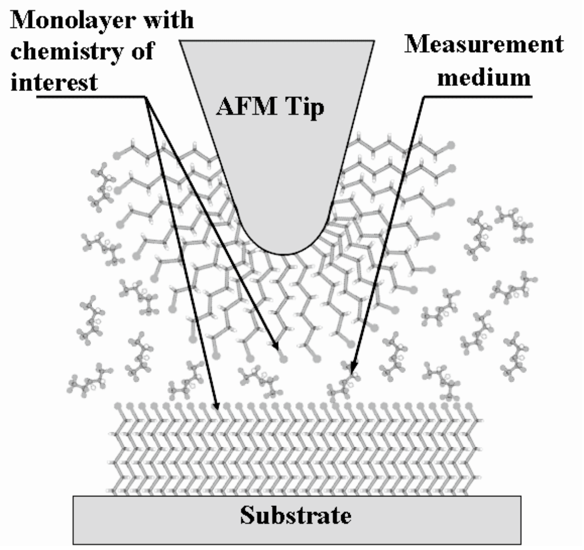

Fig.6 Schematic diagram of a CFM probe and substrate modified with a monolayer containing terminal groups having a particular chemistry, in a solvent environment.

Thiols with appropriate alkyl chain lengths have been shown to form compact monolayers when deposited onto solid substrates[68]. The reliability in depositing thiols may prove valuable, as microscopic information on the monolayer is often required to interpret the CFM results[59]. Under appropriate circumstances, compact silane monolayers can be also formed[68, 69]. This is relevant because it may circumvent the need to generate (the sometimes cumbersome step) smooth gold layers on both the substrate and the AFM tip, which are required for the deposition of thiols[70]. The use of silanes also simplifies the functionalization of colloidal probes[61]. That flexibility may prove valuable as higher sensitivity may be achieved compared to the modification of the tip alone. Colloidal probes also provide the opportunity to determine the geometry of the interacting surfaces more quantitatively[34].

Typical force curves as those shown in **Fig.5** are also observed in CFM experiments with small mole-

---

[‡] Loosely called adhesion; can represent either cohesive or adhesive forces.

cules[62]. The complexity of the force curves increases significantly, however, for systems involving polymers and/or those with specific interactions (e.g. ligand-receptor)[59]. One of the key pieces of information that can be extracted from CFM experiments is contained in the F_{ad} obtained in the retract stage of the force curve measurement[62]. Different types of interactions can be studied quantitatively by varying the moieties attached to the AFM tips, including the solvent medium effects[61, 67]. The solvent environment plays a crucial role in the force measurements[59, 61]. When the solvent is chemically similar to the functional groups on the tip and sample, the force required to pull the tip off the sample is expected to be small as the enthalpic penalty for breaking the contact (creating the functionalized tip-medium and functionalized substrate-medium interfaces) is small. On the other hand, the incompatibility of the solvent with the functional groups on the tip and sample would render a large F_{ad}.[59]

CFM can serve, therefore, to understand solvation forces, and thus to identify/design/screen chemistries that could have enhanced solubility and capable of working as stabilizers of drug dispersions[35]. Some of the limitations associated with the CFM technique include the fact that some chemistries of interest may not be commercially available in the form of a silane or thiol, thus requiring the synthesis of those moieties - which may not be trivial. In certain circumstances, degradation of the monolayers may occur[59]. Because the region of contact between the AFM probe and the substrate may not be probed directly, reproducibility in the experiments (in many independent repeats) is thus key to CFM[61, 62].

3.3.1.1. Single molecule (pair) force from CFM

CFM results are typically normalized by the radius of curvature of the AFM tip (R) to allow for comparison between different systems[61]. While such information is quantitative, and generally sufficient to understand trends in solvation forces[62], theories describing elastic deformation that exists during the contact between sample and substrate may be employed to further normalize the F_{ad}[59], and can thus be used to corroborate experimental findings or in tandem with theoretical studies[59].

The F_{ad} of an elastically deformed tip and substrate can be described by the Johnson-Kendall-Roberts (JKR)[59] or the Derjaguin-Muller-Toporov (DMT)[62] model, as shown in the equations grouped in **Fig.7**.

The difference between these two models is that the JKR model considers the interaction only within the contact region while DMT model assumes that adhesion forces are originated from interaction outside the contact region[59, 65, 71]. The area of contact between tip and substrate (as the contact ruptures during the retraction stage of the CFM) is given by equation (*f*) shown in **Fig.7**. One of the challenges related to the evaluation of single molecule (pair) force from CFM is to find out the area per molecule

(a) $$F_{ad} = 2\pi R W_{tms} \qquad \text{(DMT Model)}$$

(b) $$F_{ad} = 1.5\pi R W_{tms} \qquad \text{(JKR Model)}$$

(c) $$\varphi_0 = \left(\frac{W_{tms}^2 R}{E^{*2} z_0^3} \right)^{\frac{1}{3}}$$

(d) $$W_{tms} = \gamma_{tm} + \gamma_{sm} - \gamma_{ts}$$

(e) $$\gamma_{sm} = \gamma_s - \gamma_m \cos\theta$$

(f) $$a = \left(\frac{1.5\pi R^2 W_{tip-medium-substrate}}{K} \right)^{\frac{1}{3}}$$

(g) $$\frac{1}{K} = \frac{3}{4}\left(\frac{1-v_{tip}^2}{E_{tip}} + \frac{1-v_{substrate}^2}{E_{substrate}} \right)$$

(h) $$n = \pi a^2/A$$

(i) $$F_s = F_{ad}/n$$

Fig.7 (a) DMT Model for F_{ad}, where R is the radius of curvature of the AFM tip. W_{tms} is the work per unit area required to separate the modified tip and substrate in the solvent medium. (b) JKR Model for $F_{ad.}$ (c) This equation may be used to select which model is more appropriate (DMT, JKR), where z_0 is the equilibrium size of the atoms at contact. E^* equals to 3K/4, K is the reduced elastic modulus shown in equation (g). JKR is suggested if ϕ_0 exceeds 0.3, otherwise DMT model should be employed[71]. (d) W_{tms} *is* given by the interfacial energy, where γ_{tm} and γ_{sm} are interfacial free energy of the tip and substrate with the medium respectively, γ_{ts} is the interfacial free energy between the tip and substrate. For the same functional groups on the surface of the tip and substrate, γ_{ts} is zero, and $W_{tms} = 2\gamma_{tm} = 2\gamma_{sm}$.[59] (e) Young's equation from which γ_{sm} and γ_{tm} can be calculated, where γ_s and γ_m are the surface free energy of substrate and medium respectively and θ is the contact angle of the medium on the substrate. Note that according to the equations given above, F_{ad} can be estimated from θ measurements, provided θ is large enough. (f) Contact radius a according to the JKR Model, where K is the reduced elastic modulus for the tip-substrate combination and given by equation (g), v is the Poisson ratio, and E is the Young's modulus. The number of contact groups n at rupture can be determined as shown in equation (h), where A is the area per molecule. (i) F_{ad} can be further normalized to single molecule (pair) force $F_{s.}$

(A) on the highly curved AFM tip - less of an issue on the flat substrate, necessary to find 'n' see **Fig.7**(h). There is also some potential variability in the value selected for the Young's modulus and Poisson ratio of the modified AFM tip[59]. Moreover, both DMT and JKR models are just theoretical approximations. Therefore, a combination of repeated experiments, different approaches to surface modification, and corroboration with theoretical results all should help improve confidence on CFM results.

3.3.2. The colloidal probe microscopy (CPM) technique

The principle of operation of CPM is very similar to CFM[59]. Instead of measuring interaction forces between functional groups, however, the adhesive/cohesive interactions between a single particle attached to an AFM tip with another particle or a planar substrate are evaluated. A schematic diagram and real (optical and SEM) images of the tip and substrate assembly for a CPM experiment are shown in **Fig.8**.

The single particle is usually glued to an AFM tip using epoxy resin or another adhesive[59]. CPM can be used to understand the forces between particles, or particles with surfaces, which dominate the colloidal behavior of a variety of materials and processes of technological relevance[59]. When retracting the tip from the substrate, the total force (F_{ad}) required to detach the colloidal probe from sample surface is a sum of components, which depend on the conditions of the medium (air/solvent; polar/nonpolar) and the nature of the particle and substrate[59]. The lowest common denominator (forces that are always present) are the van der Waals forces (F_{vdw}). When F_{vdw} dominates F_{ad}, as it is expected in most systems of relevance to pMDIs, then F_{ad} can be used to estimate the Hamaker constant of drugs of interest[59]. This will be the topic of a section to be presented later on the manuscript.

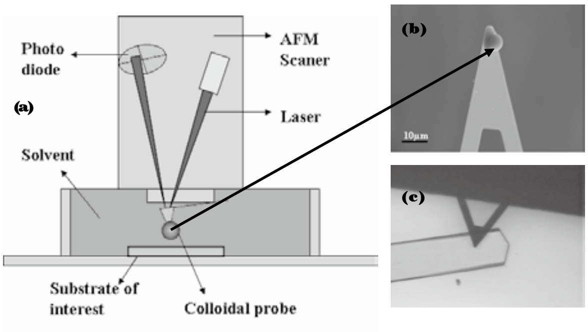

Fig.8 **(a)** Schematic diagram of the elements in CPM microscopy in a liquid solvent; (b) SEM micrograph of a CPM probe. Reprinted from ref. [47] with permission from Elsevier; (c) Optical micrograph of the modified AFM cantilever and the smooth single crystal during an F_{ad} measurement in HPFP. Reprinted from ref. [45] with permission from American Chemical Society.

F_{ad} from CPM has been successfully used to understand the effect of the solvent medium and excipients on the stability of colloidal dispersions[59], including those of relevance to pMDI formulations[45, 51, 72]. A low F_{ad} correlates with reduced inter-particulate forces (and thus enhanced physical stability), and vice versa. The variation of F_{ad} is dependent on the roughness of substrate surface. F_{ad} histograms generally have a Gaussian distribution of forces for smooth substrates[20, 73]. The size of the particles are typically not important. Even for large particles, gravitational forces can be usually neglected during CPM measurements - the gravitational forces on a 50 μm particle is ~1 pN[21].

The magnitude of the force obtained from CPM is highly dependent on the contact area, whose precise determination is especially difficult in systems where the probe is a micronized crystal, as it is typically the case in pMDI formualtions[45, 51]. Hence, normalization of forces with respect to the contact area and the subsequent comparison for different types of probes in the case of CPM is a much harder proposition when compared to CFM[59]. Despite availability of established methodologies in the literature, as for example contact area deconvolution by a tip characterization grating substrate[65] and AFM imaging of lithography indentation[74], it is still very challenging and demanding to precisely determine the contact area and geometry of an irregular drug crystal attached to an AFM tip[20, 65]. This limitation may restrict comparison of data collected between different groups, and even within the same group, when using different probes[20]. While careful experimentation using a single tip (and then repeated experiments to confirm trends) may be used to screen excipients, the comparison between different particle preparation methodologies, for example, is restricted if a precise contact is not known[20]. Readers are directed to ref. [59] (review article) for more details on the CPM technique.

3.4. The measurement medium

The magnitude of the forces between surfaces (such as those measured by AFM) is highly dependent on the measurement medium[59, 61, 62]. DPIs are composed of particles that come in contact with (humid) air upon device actuation[26]. AFM experiments for DPI-related systems are, therefore, usually conducted in air[75, 76], and preferably with rigorous control of the humidity[77)], as capillary forces (due to the presence of water in the environment) dominate particle-particle interaction[21, 76)]. On the other hand, the drugs in pMDIs are either solubilized or dispersed in the propellant[23)]. Therefore, force measurements for pMDI-related formulations are typically performed in liquid.[§] However, due to the low boiling point of HFA227 (246.88 K)[15)] and HFA134a (256.65 K)[15)], the HFA propellants are in the gaseous state under ambient conditions. HFA propellants cannot, therefore, be used directly as the force measurement medium in existing commercial AFM systems. Model propellants, which are liquid at ambient conditions and are suitable for use in conventional AFMs, have, therefore, been proposed[78)]. The model solvent should have a molecular structure and physicochemical properties similar to the propellant HFAs. Because of its physicochemical properties, the hydrofluoroalkane 2H,3H-perfluoropentane (HPFP)[**] has emerged as the model liquid propellant of choice. Some of the properties of HPFP more closely resemble those of HFA134a such as dipole moment and dielectric constant, while others more closely match those of HFA227, such as molecular size and boiling point[78)]. While the literature is still somewhat limited in terms of directly probing the ability of HPFP to mimic propellant HFAs[78)], at least in terms of the physical stability of dispersion formulations, the results in HPFP seem to better correlate to those in HFA227[78)]. Our group has recently demonstrated that the magnitude of the enthalpic interactions (dispersion+electrostatic) between propellant HFAs and polar fragments increased significantly on going from HFA134a to HFA227 due to the acidity of *H* and the larger size of the HFA227 molecule[79)]. In this aspect, we would expect HPFP to be a closer match to HFA227. Currently, the measurement medium of AFM is limited to air or liquid, and there is still no AFM available in the market that has accommodated a high-pressure environment. Although HPFP is widely accepted as being similar to HFAs, and it is commonly used as an alternative propellant for HFAs (not only for AFM experiments)[78)], these solvents have different physicochemical properties. Caution is thus suggested when extrapolating the results from AFM to propellant-based formulations.

4. The AFM and the Development of Propellant-based Inhalation Formulations

Force measurements by AFM have been widely used in the development of novel inhalation formulations, especially for DPIs[21)], and more recently for systems of relevance to pMDIs[23)]. DPI formulations usually contain micronized drug particles by themselves or drug particles mixed with a larger particle carrier (e.g. lactose particles) that work as a flowing agent[26, 80)]. CPM is especially suited to assess the adhesive/cohesive balance between the drug and carrier particles, which affects the blending and efficiency of the aerosol generated[21)]. AFM is also of great relevance in the design of alternative propellant-based pMDI formulations[23)]. CFM can be used to screen potential candidate chemistries with enhanced solubility and ability to stabilize dispersions in HFAs[34, 35)]. CPM is also well-suited for the development of suspension-based pMDI formulations, which account for approximately 50% of currently marketed pMDIs[23, 45)]. The effects of the solvent environment and additives, such as cosolvents and amphiphiles, on traditional dispersion formulations can be investigated by CPM[45]. A review[††] of all AFM, CFM and CPM work reported to date on pMDI-related systems is discussed below. A summary of the studies is given in **Table 1**. We also address other measurements that can be made with the AFM and that are of potential interest to pMDIs such as determination of particle density[81, 82)] and Hamaker constant[59, 83)].

4.1 Solvation forces by CFM

Understanding solvation in hydrofluoroalkane propellants is of great importance for the development of novel pMDI formulations. Steric stabilization is the predominant mechanism for imparting stability to colloidal particles in low dielectric media such as HFA propellants[84)]. The ability of the propellant in solvating the stabilizing moieties govern particle-particle interaction[35, 45)]. When two colloidal particles approach each other, the stabilizing tails on the particles' surfaces may interpenetrate. If the medium is a good solvent for the stabilizing moiety, the interpenetration is thermodynamically disfavored, leading to stable colloidal suspensions[84)].

CFM studies are relevant not only in the context of the traditional solution and dispersion pMDI formulations, which generally require surfactants as

---

[§] Some initial force measurements related to pMDI formulations were conducted in air[75)].

[**] Vendors for HPFP include Synquest Labs, Inc; TMC Industries, Inc; Apollo Scientific, Inc; and Dupont.

[††] An exhaustive search was performed on SciFinder®. Works published by April 2008 (which was the deadline for submission of this manuscript) have been included in this review.

Table 1 A summary of the literature work (journal articles) on AFM, CFM and CPM related to pMDI formulations

AFM	AFM probe	Substrate	Excipient	Medium	Purpose	Year
Imaging	[a] silicon tapping-mode tip	Epoxy-coated aluminum	None	Air	Characterization of the properties of the wall lining after exposure to propellants, up to 40 ℃	1997[64]
	Silicon tapping-mode tip	SS, BUD and FF crystal	None	Air	Determination of drug crystal roughness	2005[20]
	Silicon tapping-mode tip	Aluminum coated with various materials	None	Air	Determination of canister surface roughness coated with various materials	2006[73]
CFM	**AFM probe**	**Substrate**	**Excipient**	**Medium**	**Purpose**	**Year**
Solvation forces	[b]Silane-modified AFM tip	Silane-modified substrate	None	HPFP	Investigation of HFA-philicity of hydrogenated and fluorinated moieties	2007[34]
	Silane-modified AFM tip	Silane-modified substrate	None	HPFP	Investigation of HFA-philicity of an ester-based moiety	2007[85]
	Silane-modified AFM tip	Silane-modified substrate	None	HPFP	Investigation of HFA-philicity of an ether-based moiety	2007[35]
CPM	**Drug probe**	**Substrate**	**Excipient**	**Medium**	**Purpose**	**Year**
Design of pMDI hardware	[c]Single micronized Salbutamol sulfate (SS) particle	Borosilicate glass, aluminum, PTFE-coated aluminum	None	HPFP	Evaluation of forces between a single SS particle with different pMDI canister materials	2003[72]
	Formoterol fumarate (FF) particle cluster	Aluminum PEG, PVP and FF coated aluminum	PEG, PVP	HPFP	Evaluation of the effect of excipients on the interaction between drug particles and canister wall	2004[90]
	Single micronized SS, budesonide (BUD) and FF particles	Aluminum coated with various materials	None	HPFP	Evaluation of the interaction of various drugs with a series of pMDI canister lining materials	2006[73]
Formulation design without excipients	Single micronized SS particles	Pyrolytic graphite	None	HPFP	[d] Determination of the effect of particle geometry on forces	2003[65]
	Single micronized SS, BUD and FF particles	SS, BUD and FF crystals	None	HPFP	Determination of cohesive/adhesive balance for various drugs in excipient-free medium	2005[20, 89]
Excipient Design	Single micronized (SS)	SS crystal	PEG, PVP	HPFP	Investigation of the effect of polymeric excipients on inter-particulate forces for SS	2007[51]
	Single micronized Salbutamol base (SB)	SB crystal	Ethanol, PLA-PEG-PLA, Oleic acid, Pluronic® surfactant	HPFP	Evaluation of the effect of various excipients on the inter-particulate forces for SB	2007[45]
Particle Surface Engineering	Single SS sphere, Single PEG-coated SS sphere	SS spheres, PEG-coated SS spheres	PEG 300	HPFP	Evaluation of effect of PEG-coating on inter-particulates forces	2008[47]
	Single SS core-shell particle, Single BSA core-shell particle	SS core-shell particles, BSA core-shell particles	Oligo(lactide)-grafted-chitosan	HPFP	Evaluation of the effect of an HFA-philic shell on the inter-particle forces for both small drug solutes and biomolecules	2008[46]

[a] first AFM; [b] First CFM; and [c] first CPM study involving a system of relevance to pMDIs. [d] the geometrical profile of the drug probe (and area of contact) was evaluated, and the work of cohesion quantitatively determined by CPM.

excipients, but also for the development of novel HFA-based formulations that can be potentially used for the delivery of drugs (small molecule and large therapeutic biomolecules) to and through the lungs, such as reverse aqueous microemulsions and emulsions in HFAs, and other particle-based approaches that require the presence of well-solvated stabilizing moieties[23].

Our group has utilized CFM to evaluate the forces of interaction between a chemically modified AFM tip and substrate in HPFP[34, 35, 85]. The tip and substrate were modified by silane chemistry, using both solution and vapor phase approaches[34, 35, 85]. Contact angle measurements and extensive force measurements were conducted to confirm quality of the silane monolayer at each step during the surface modification procedure[34]. Several different types of chemistries were investigated, including a methyl-based (*CH*) moiety (octyltrichlorosilane, $CH_3(CH_2)_7SiCl_3$), and a more polar ether- (*COC*) (3-methoxypropyltrimethoxysilane, $CH_3O(CH_2)_3Si(OCH_3)_3$) and ester- (*C(O)OC*) (2-acetoxyethyltrichlorosilane, $CH_3COO(CH_2)_2SiCl_3$) terminated silanes[34, 35, 85]. The *CH* moiety represents the tails of surfactants in FDA-approved pMDI formulations, which have low solubility in HFAs[33]. It thus represents the baseline moiety. *COC* and *C(O)OC* contain polar sites that may provide for an opportunity for enhanced interactions with the propellant HFAs.

The CFM results, plotted as the normalized adhesion forced F_{ad} / *R* (where *R* is the radius of curvature of the AFM tip) are shown in **Fig.9**. For a methyl-modified tip and substrate in HPFP F_{ad} / *R* was found to be 68.2 mN·m^{-1}.[34] The F_{ad} / *R* for the ether and ester-based moieties is 24.8 and 4.8 mN·m^{-1}, respectively. A lower F_{ad} indicates a smaller enthalpic penalty for creating an interface between the chemical groups of interest (on the tip and substrate) and the liquid HFA; i.e., the ester-based moiety is the most HFA-philic, followed by the ether group. The moiety that is least solvated, as expected, is the *CH*. Such favorable enthalpic interactions between HFA and the ester and (to a less extend) ether groups is important for the development of novel pMDI formulations as those moieties are biodegradable and biocompatible, and have been used as excipients in several (other routes) formulations[45, 48, 49, 51]. It is worth mentioning, however, that the solvation of the ester-based moiety is still far away from ideal; i.e., there is still room for improvement in terms of an optimal candidate chemistry. The ideal solvation is represented by F_{ad} / *R*∼ 0 mN·m^{-1}, as is the adhesive force of methyl-based modified tip and substrate in an alkane (iso-octane) solvent[34].

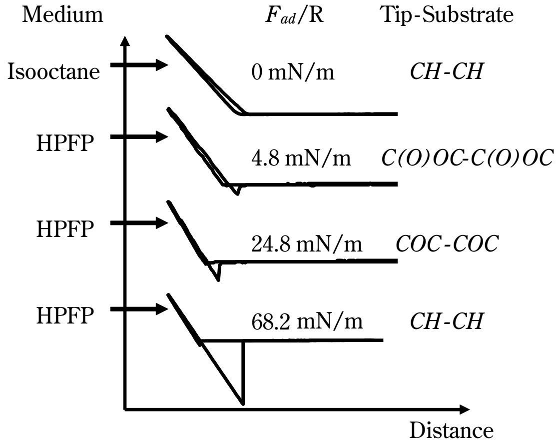

Fig.9 Normalized F_{ad} with respect to the radius (*R*) of the AFM tip. Candidate chemistries (*CH*, *COC* and *C(O)OC*) in HPFP and isooctane.

We have also evaluated the F_{ad} of a fluorinated moiety (*CF*) (1H,1H,2H,2H-perfluorooctyltrichlorosilane, $CF_3(CF_2)_5CH_2CH_2SiCl_3$) in HPFP. The F_{ad} / *R* of 6.4 mN·m^{-1} was comparable to that observed for the ester group[34], indicating that the fluorinated moiety can be solvated very well by HPFP. The application of fluorinated tail in pMDI formulations is limited owing to its potential toxicity[40, 43]. However, it is a good model system as there is detailed information on the nature and characteristics of fluorinated self-assembled monolayers[69, 86, 87] - and for methyl-based silanes as well, thus allowing a direct comparison between those two systems. Using the JKR theory, the F_{ad} was further normalized for the *CF* and *CH* systems in HPFP down to the single molecule (pair) force (F_s). F_s for the fluorinated tail in HPFP was found to be 86 pN, which is significantly less than that observed between a pair of equivalent methyl-based molecules (156 pN)[34].

The discussion above illustrates how F_{ad} results from CFM can provide an absolute scale for HFA-philicity, and are thus of great relevance for the rational design of HFA-philes that can be utilized in both traditional pMDIs and also in the development of novel pMDI formulations as will be demonstrated below. Such scale has been successfully utilized to identify and develop novel amphiphiles capable of forming stable reverse aggregates of water in HFA[36, 37], and to aid in the stabilization of solid-based dispersion in the form of traditional dispersion formulations[45, 85] and novel particle engineering technologies[46, 47]. It is also worth pointing out that the CFM results discussed above have been corroborated and complemented by computational studies where the binding energy between the HFA propellants and fragments representing the chemistries above have been determined by *ab intio* calculations[34, 35, 85]. The limitation associated with single molecule force calculation is that it is hard to obtain precise parameters regarding the properties of the silane monolayer, such as Poisson ratio, modulus and the area per molecule.

4.2. CPM in the development of pMDI formulations

There have been several studies that have highlighted the applicability of CPM to the different aspects of the formulation in pMDIs, from the hardware design, to the screening of new excipients, to the development of novel particle engineering approaches.

4.2.1. CPM and the pMDI hardware design

pMDI containers are generally manufactured with glass or aluminum, with or without an inert organic coating[14]. The interaction between drug particles and the walls of pMDI canisters should be taken into account in the pre-formulation stage of formulation development[72]. The adhesive forces between drug particles and the internal walls give rise to irreversible adsorption of the particles, thus leading to the so-called "wall loss"[72], and a subsequent reduction (and/or non-reproducibility) in the emitted dose[73]. Such losses can be detrimental to the aerosol performance of pMDIs, especially for those formulations with low drug dosages, as it is the case for high potency drugs, as the total surface area of drug may be less than that of the canister walls[72]. It is also important to observe that the internal coating of the canister should be chemically stable to the propellant-excipient mixture during the shelf life of the pMDI, so that no undesirable chemicals are extracted[64]. This (and the stability of the coating) may be a challenge in certain HFA-based pMDIs, where ethanol is typically a required excipient[33]. The adsorption of drugs onto valve gaskets and plastic valves has also been reported[88], and should thus be considered during pre-formulation as well. Several AFM studies have addressed the adhesive forces between therapeutics of interest in pMDI formulations and the walls of pMDI canisters[72, 73], and also the stability of the lining of canisters in the presence of propellant HFAs[64]. Those studies are reviewed next.

The first application of AFM in the formulation of pMDIs was in 1997, with a study on the compatibility of an epoxy lining (of aluminum cans) with propellant HFAs (HFA134a and HFA227)[64]. The effect of the propellants on the chemical stability of the lining was assessed by measuring the topography of the coating after exposure to HFAs at different temperatures (0 to 40 ℃) by contact mode AFM[64]. The results showed that the surface roughness of the lining was affected by the storage temperature and propellant type. At higher temperatures, the 'jaggedness' of the coating decreased, thus decreasing the sites for drug nucleation[64]. At the same time, it was demonstrated that alternative techniques, including contact angle, SEM and reflection-absorption FTIR, were not able to identify any changes in the morphology of the coating. These results illustrate the uniqueness of the AFM in the study of the compatibility of the coating in the presence of propellant HFAs.

CPM studies have been performed to directly probe the adhesive interactions between drugs and the walls of pMDI containers, which was previously possible only by indirect measurements[72]. The adhesion of salbutamol sulfate (SS, a short acting β_2-agonists) and various pMDI canister materials including borosilicate glass, aluminum, and poly(tetrafluoroethylene) (PTFE) coated aluminum was measured[72]. A single micronized SS particle was mounted onto the AFM tip using an epoxy resin. The force measurements were conducted in the model propellant HPFP. The separation energy was determined by integration of the area under the force-distance curve. The surface topography of each material was also measured with tapping mode AFM in air[72]. The force-distance curves and the AFM images are shown in **Fig.10**.

The CPM results showed that glass has the highest separation energy with SS particles, followed by aluminum, and PTFE coated aluminum, suggesting that low surface-energy PTFE is the best canister coating[72]. It is important to note here that the roughness of the materials in question is significantly different from each other, as indicated by the AFM micrographs. This is important as a smooth substrate is typically desired so that the contact area between probe and substrate remains approximately constant in all measurements (for the same colloidal probe tip), thus allowing the results for different substrates to be directly compared[72].

More recently, a similar CPM study from the same group extended the range of drugs and surface materials[73]. More importantly, they developed a combined

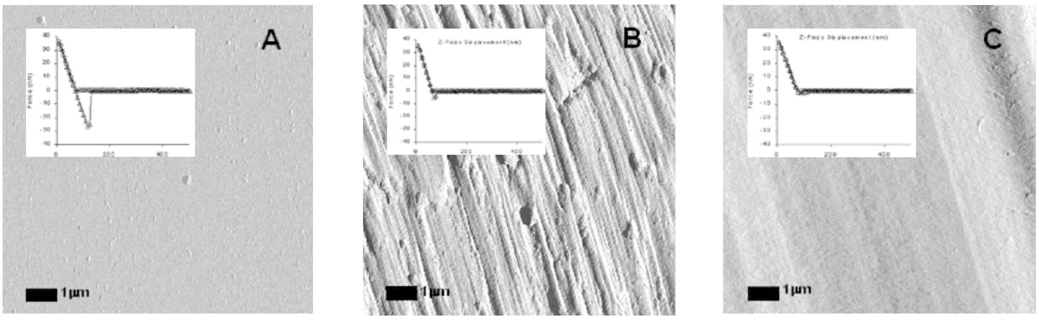

Fig.10 Representative topographical AFM images of (A) borosilicate glass, (B) aluminum, and (C) PTFE-coated aluminum canisters. Note different degrees of roughness. (Inset): Representative force–distance curves for salbutamol sulfate (drug probe) with the corresponding substrates. The order of decreasing interaction energy with SS is: glass > aluminum > PTFE-coated aluminum. Reprinted from ref. [72], with permission from Elsevier.

AFM/surface component approach (SCA) to study the nature of the drug-substrate interaction. The study helps to partially address one serious shortcoming of the CPM technique, which is the fact that the contact area between probe and substrate is typically unknown, thus preventing normalization of the force, and consequently preventing the results from different probes from being compared directly. The SCA allows one to estimate the interaction energy between drug and substrate indirectly, by using the surface tension components of both substrate and drug to determine the work of adhesion[73]. Because the work of adhesion is directly proportional to the adhesive force as measured by CPM via DMT or JKR theories - see **Fig.6**, a theory that describes well the cohesive forces is expected to correlate with the CPM results.

The adhesion of micronized SS, budesonide (BUD) and formoterol fumarate (FF) to various canister materials including aluminum, anodize aluminum and aluminum coated with perfluoroalkoxy, fluorinated ethylene propylene-polyether sulphone and PTFE was investigated[73]. The separation energy between each drug and various substrates was evaluated by CPM. The CPM results indicate that anodized aluminum has the highest adhesive force with SS, while PTFE has the lowest. The results had excellent correlation with the SCA only when the polar surface tension components of the substrate and drug particles were used, thus highlighting the relevance of polar forces on the (attractive) adhesive interactions between drug and substrate. Here again it is worth mentioning that differences in the roughness of the substrates exist. The authors point out, however, that they do not expect those to impact significantly the observed trends, as roughness less than 100 nm have been shown not to impact the interaction energy values[73]. Another important aspect of the work is that the surface tension of HPFP was assumed to be all dispersive, while HPFP is known to have a significant dipole moment[78].

For completeness, it is worth mentioning yet another CPM work where the adhesive interactions between SS and glass and PTFE (model coating for aluminum canisters) have been studied[75]. However, the CPM experiments in that work were performed in air, and are thus of little relevance to pMDIs.

Due to the challenges in the reformulation of pMDIs with HFAs, ethanol is generally used in the formulations to help solubilize excipients or active pharmaceutical ingredients[33]. The presence of ethanol may affect the physical and/or chemical stability of the canister lining and/or the interaction between the drug particles and the canister wall. CPM is uniquely suited to address those issues, and can thus be used to guide the design of pMDI hardware, including the valve stem, metering chamber, actuator orifice, and the effect of different excipients on drug-surface interactions. The studies above also indicate that AFM imaging may at times be the only tool (sensitive enough) to capture changes in the morphology of the lining in contact with the propellant-excipient mixtures. It may prove to be, therefore, an important characterization tool to investigate the effect of ethanol and new excipients as they are introduced in the market.

Perhaps one of the biggest challenges in the CPM studies lies in the inability to accurately determine the area of contact between micronized drug crystals (typically used as inhalants) and the substrates of interest, which prevents the comparison of the results between any two probes (between different labs and even within the same lab). That in turn makes it hard to compile a large body of understanding from work published in the literature. While some success has been achieved in terms of deconvoluting the contact area from a grid template[65], this is still an area where improvements would be welcome. The combination of complementary tools as CPM and SCA may prove to be very useful, as intrinsic material properties can be obtained, and thus extrapolated to other systems of interest.

4.2.2. CPM and adhesive/cohesive forces in excipient free environment

Currently there are some marketed pMDI products where no excipients are used in the formulations such as Ventolin HFA® (micronized SS in HFA134a) and Advair HFA® (combination of micronized fluticasone propionate and salmeterol xinafoate in HFA134a). The aerosol efficiency of these formulations is governed by the adhesive or cohesive interparticulate / particle-device surface forces, mediated by the propellant medium. The quantitative understanding of the interaction between drug particles is, therefore, of importance for the development of excipient-free formulations.

The effect of particle manufacturing techniques on the work of adhesion (W_{ad}) of SS was determined by CPM[65]. This is the only report attempting to quantitatively relate the F_{ad} to the work of adhesion, as determination of the area of contact (demanding proposition) is required. The F_{ad} between SS and a smooth (HOPG) substrate was related to W_{ad} by means of the JKR theory. It was observed that micronized SS is more cohesive (13 mN·μm^{-2}) than SS particles made via solution-enhanced dispersion by supercritical fluid (SEDS) (3.0 mN·μm^{-2}). The CPM results were noted to be in qualitative agreement with IGC trends. The authors rigorously characterized the area of contact between the (irregular) probes and the (atomically smooth) substrate utilizing a grid template deconvolution approach[65]. The results suggest sub-micron asperities on the SS particles. Challenges arise in such determinations as damage during the imaging processing of the particle against the calibration grating may occur. Furthermore, the contact radius is still an estimate (a fitted value) to the dimensions (X-Y) of the area believed to be in contact with the particle. The roughness at the nanoscale, which can also affect the F_{ad}[59], cannot be resolved either.

Inter-particulate forces between SS, BUD and FF have been determined by CPM[20]. The drug probes were prepared for all the three drugs on tipless cantilevers, and large crystal substrates were obtained by a sitting drop crystallization technique. The surface topography of the large drug crystals was examined by tapping mode AFM in air, and shown to be smooth, with the root-mean-squared roughness less than 2 nm over a 25 μm area, thus providing a uniform contact area for the CPM experiments. The forces of adhesion and cohesion between the drug probes and crystal substrates were measured in HPFP, and the cohesion/adhesion ratios were obtained. A single probe was utilized to measure the cohesive/adhesive forces - the results can thus be directly compared for that same probe. The experiments were done in triplicate to guarantee that consistent trends were observed. The results demonstrate that cohesive forces between SS particles are much stronger than the adhesive interactions with BUD and FF. BUD and FF are shown to be more adhesive with SS than cohesive. Finally, CPM results indicate that the cohesive and adhesive forces involving BUD and FF are very close. The experimental CPM results correlated very well with cohesive/adhesive ratios that were calculated from contact angle and IGC, only when the polar surface components were included[20]. The results again suggest that polar forces are important contributions in HFA solvents. Although the calculations based on the contact angle results correlated with the experimental CPM observations in terms of the cohesive/adhesive balance trend, there was still a significant quantitative discrepancy between the two methods[20].

A later study by the same group focused on correlating the adhesive/cohesive forces from contact angle and CPM with the physical stability of the formulations and the corresponding aerosol characteristics[89]. The results indicate that a strong cohesive force correlated well with poor physical stability and a small sedimentation volume (strong cohesion) of the flocculated micronized crystals. The emitted dose also decreased for the more cohesive particles, as did the fine particle fraction (concentration of drug expected to reach the lower airways). For systems where the determined adhesive forces were lower that cohesive, higher emitted doses were observed with the combination drugs[89].

As a microscopic characterization tool, CPM can be thus successfully used to determine the work of cohesion/adhesion and to evaluate adhesive/cohesive balance. In spite of the fact that the contact area between probe and substrate may not be known, the absolute value of the ratio of work of adhesion and cohesion can still be determined (as that is independent of the contact area for the same probe). Another important result is that there seems to be a strong correlation between the CPM results (in HPFP), physical stability (in propellant HFA) and the aerosol characteristics of the corresponding formulations.

4.2.3. Excipient design by CPM

While chlorofluorocarbons (CFCs) were employed as the propellants in pMDI formulation for decades, concerns about their ozone depletion potential prompted the search for more environmentally friendly alternatives[15]. Due to certain favorable properties, particularly low toxicity, low flammability, and zero ozone depletion potential, hydrofluoroalkanes were selected as acceptable alternatives to CFCs[8]. However, the transition from CFCs to the more environmentally friendly HFAs has been difficult due to the significantly different solvent properties between these classes of fluids[15]. For instance, the hydrogenated excipients in FDA-approved CFC-based formulations have very limited solubility in the semi-fluorinated HFA propellants[33], thus restricting their direct application in HFA-based pMDIs[33]. Such challenges have sparked significant interest on the design of HFA-philic excipients for pMDI formulations[33]. Due to its sensitivity and unique force detection capability, CPM has been successfully employed in the design of excipients for pMDI-based formulations. These results are summarized below.

The ability of polyethylene glycol (PEG) and polyvinylpyrrolidone (PVP) to screen adhesive/cohesive forces in systems containing FF was investigated by CPM.[90] These two excipients were chosen since they have been reported as acceptable excipients for use in HFA-based pMDIs[91], and are readily available. The drug particle probe was prepared by attaching a cluster of drug particles with the size of around 50 μm to an AFM tip. CPM was used to investigate the interaction between FF particles and various substrates including bare aluminum and aluminum spin-coated with FF (in that case, the drug-drug cohesive forces would be determined), PEG, PVP, or a mixture of PEG and PVP in HPFP solution.[90] The CPM results demonstrate that the presence of PEG homopolymer in solution can only slightly reduce the interaction forces between FF particles or FF with the canister aluminum wall. PVP or the mixture of PEG and PVP was shown to be more effective than PEG alone in decreasing the adhesive forces, but not greatly.[90] However, a new probe was prepared in each experiment, making direct comparison between the substrates difficult (even though several probes were measured for each system), as the forces can vary drastically from one probe to the next[20, 51, 65], and averaging is not necessarily representative.

The inability of PEG and PVP homopolymers to completely screen the cohesive/adhesive contact in the systems described above are not necessarily related to the (in)ability of HPFP to solvate the homopolymers. As a matter of fact, PEG interacts well with HFA134a and HFA227[79, 91]. Moreover, when tethered to the surface of drug particles, PEGs have been shown capable of imparting stability to dispersions in propellant HFAs[47]. Perhaps the poor performance of the homopolymers in those system can be more closely related to an inadequate balance/partition between HFA and the drug / lining surface[90]. The authors also suggest the poor performance of the excipients to bridging flocculation, as indicated by the jagged nature (snap-outs) of the force profile (retraction) in the presence of PVP. This is an important result that points out to the relevance of AFM in the design of excipients with appropriate balance and stabilizing moieties.

The influence of PEG (concentration and molecular weight) in the presence and absence of PVP homopolymers on the interaction forces between micronized SS particles and a smooth SS substrate was also studied by CPM[51]. Individual micronized SS particles were attached to AFM tips using a quick-setting epoxy resin. A large SS crystal substrate was prepared by recrystallization in ethanol[51]. The force measurements were conducted in purified HPFP. The concentration and molecular weight of PEG was shown to have a significant impact on inter-particulate forces[51]. Increased PEG concentration resulted in a reduction in inter-particulate forces, with the most pronounced effect in the concentration range between 0.05～0.1 v/w % for the PEGs investigated (MW of 200, 400 and 600).

The screening of cohesive forces was reported to be more effective with higher molecular weight PEGs. PEG 600 at the concentration of 0.5 v/w % can reduce the cohesive forces in SS by 89 %. This was attributed to the fact that higher molecular weight PEG is expected to provide a longer steric barrier, thus reducing the effect of the van der Waals forces[51]. However, the cohesive forces between the SS particles were not completely screened.[51] Similar reasons as those discussed above (for FF) can be attributed to the inability of the PEG homopolymer in completely shielding the interactions between SS particles. It is important to note, however, that in this study, the results from different probes were compared, and some variability is expected as F_{ad} may be greatly affected by changes in contact area. The effect of PEG on the F_{ad} was not correlated with the physical stability in propellant HFAs nor the aerosol characteristic of the corresponding formulations. More recently, our group investigated the ability of a series of biocompatible and biodegradable lactide-based copolymers in screening the cohesive forces of salbutamol base (SB) particles[45]. Copolymers are designed such that one of the blocks contains an 'anchor' segment that strongly interacts with the dispersed phase, and a well-solvated 'tail' segment that extends into the bulk/dispersing medium thus proving for the steric barrier required for screening cohesive forces that arise due to van der Waals interactions[45].

A series of triblock copolymers of the type poly(lactide)-poly(ethylene glycol)-poly(lactide) ($LA_mEO_nLA_m$) with varying molecular weight (MW) and % EO were synthesized. CPM was used to quantitatively examine the effectiveness of the amphiphiles to screen the cohesive forces between SB particles. The effect of cosolvent (ethanol), oleic acid (surfactant present in FDA-approved pMDI formulations), and a nonionic triblock copolymer with the propylene oxide moiety as the HFA-phile were also investigated.[45]

These results are of relevance as they are the first to directly assess the effectiveness of excipients typically used in FDA-approved pMDI formulations. While cohesive forces between SB crystals were shown to be somewhat suppressed upon the addition of ethanol and oleic acid to HPFP, the forces are only partially screened. In sharp contrast, the presence of $LA_mEO_nLA_m$ is capable of reducing the cohesive forces between the bare SB particles down to approximately zero, even in the absence of co-solvent. The results indicate that the LA moiety can be well solvated by HPFP, and is thus able to provide a steric barrier to flocculation[45]. This is in direct agreement with the CFM results discussed earlier where the $C(O)OC$ moiety was shown to be well-solvated by HPFP[85], and also to binding energy results from ab initio calculations that studied the interaction between HFA134a and HFA227 and a $C(O)OC$ fragment[85]. These results directly validate the CFM experiments and the theoretical results from ab initio calculations, indicating that those may indeed be appropriate tools for screening moieties for HFA-based pMDI formulations.

The effect of the concentration of $LA_mEO_nLA_m$ amphiphiles on drug-drug interaction was also investigated. A minimization of the surfactant concentration is important to reduce potential toxicity of the formulation, and its impact on the physical properties of the propellant-excipient mixture, which in turn may affect the aerosol characteristics[45]. CPM results also allowed the evaluation of the effect of the LA tail length on the adhesion force between SB drug particles. This is relevant as colloidal stabilization is dependent on the thickness of the barrier provided by the tail (LA moiety), which is directly related to the number of LA repeat units and the solvent environment[45]. The length of the LA is also relevant to its biodegradability[52]. The results revealed that amphiphiles with very short tails (less than about 2×4 repeat units) could not completely screen cohesive forces between SB (at least at moderate to low concentrations)[45].

In the study discussed above, the CPM results (performed in HPFP) were directly correlated to the physical stability of the formulation in a propellant HFA (HFA227). The results are shown in **Fig.11**. The physical stability of the formulations in HFA227 was in excellent agreement to the F_{ad} results from CPM; i.e., low Fad in HPFP correlate well with good suspension stability of the formulations in HFA227.

While the use of the (above mentioned) particular amphiphiles is limited to drugs where the PEO anchor is expected to interact with, the results regarding the applicability of LA as a stabilizing moiety are fairly general. It was, thus, proposed that LA-based amphiphiles could be extended to other suspension-based formulations, provided a suitable head-group could be identified. This hypothesis was demonstrated on a study with BUD (hydrophobic drug). The PEG group was replaced with the more hydrophobic

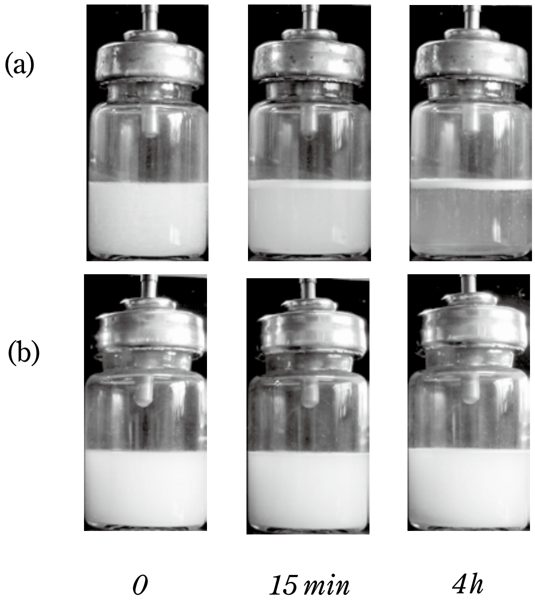

Fig.11 Dispersion stability of micronized salbutamol base particles in HFA227 (2 mg·ml^{-1}) at 298 K and saturation pressure. (a) Pure HFA227; (b) HFA227 in presence of 0.1 mM $LA_{53}EO_{22}LA_{53}$. Note the enhanced stability in the presence of the amphphiles. The enhanced stability correlates well with low F_{ad} from CPM experiments. Reprinted from ref. [45] with permission from American Chemical Society.

polycaprolactone (PCL) group. A random copolymer of PCL-PLA provided an effective steric barrier capable of imparting stability to micronized BUD in HFA227, while the PEG-based amphiphile does not[85]. With the addition of the synthesized PCL-PLA copolymer, the interaction force between BUD particles was reduced nearly 10 fold, indicating the presence of a steric barrier on the surface of the drug particles. There was also a significant improvement in terms of the physical stability of the BUD formulation in HFA227 in presence of PCL-PLA compared to that without the copolymer. The PCL-PLA copolymer is not applicable to HFA134a due to its limited solubility.

Although macroscopic information regarding the colloidal stability of suspension-based pMDI formulations can be obtained by traditional bulk sedimentation rate experiments, such techniques cannot provide quantitative microscopic information on inter-particulate forces. CPM is especially suited for that task, and in the design of excipients for pMDIs. Moreover, CPM allows decoupling of the confounding information regarding the physical stability of the dispersion and the aerosol characteristics of the corresponding formulation, which may also be affected by the device components and other formulation parameters. One important issue that is still left unresolved is the inability to directly compare the results from different groups or to use them to generate a broad knowledge on the effect of excipients on cohesive/adhesive interactions as the probes used in those studies do not have a regular geometry and the results are generally not normalized.

4.2.4. Particle surface engineering by CPM

The stabilization of solid dispersions in propellant HFAs can be also achieved via modification of the particle surface or particle morphology[23, 35]. Such approaches may offer the possibility of formulating (besides small molecular weight drugs) large therapeutic biomolecules to either target the lungs locally or for systemic delivery in the form of dispersion pMDIs[35]. Compared to surfactant-stabilized colloids, the surface and morphological modification of particles may reduce (or avoid altogether) the presence of free excipients in solution, which may serve to reduce the toxicity of the formulations. Moreover, the challenges associated with the synthesis of well-balanced amphiphiles are circumvented[47]. The study of the forces between particles with engineered surfaces and morphology is thus of relevance to the development of novel pMDIs.

One important breakthrough in particle engineering for pMDIs was the introduction of the concept of porous particles[55]. The propellant is allowed to penetrate into the pores of the particles, thus decreasing the density mismatch between the propellant and the particles. This results in an improved dispersion, as the sedimentation (creaming) velocity decreases. The van der Waals attractive interactions are also expected to be reduced, thus minimizing cohesive forces between particles[50]. The physical stability of such formulations in pMDIs and the resulting aerosol characteristics point out to the fact that indeed porous particles impart those characteristics to the dispersions[50]. An opportunity for CPM studies here would be to demonstrate how much each effect (density matching and decrease in cohesive forces) is contributing to the overall stability of the system, and how similar approaches could be used in the future to enhance the aerosol characteristics of pMDIs.

Our group has recently proposed a novel methodology for engineering polar drug particles with enhanced stability and aerosol characteristics in propellant HFAs by ‘trapping’ HFA-philic moieties (in that case PEG) onto the surface of drug particles using a modified emulsification-diffusion method[47]. The trapped moieties act as stabilizing agents, thus preventing flocculation of the otherwise unstable drug particles in propellant HFA. The interaction between single SS particles was evaluated in HPFP using CPM. A single particle was directly attached onto an AFM tip (epoxy), while the other particle was physically (and strongly) adsorbed on the substrate.

The CPM results demonstrated that the surface of SS particles can be densely covered by PEG 300 molecules, as indicated by a reduction in the cohesive force from 1.36 nN for bare SS spheres, down to approximately zero (0.07 nN) for PEG-coated SS particles. The results are summarized in **Fig.12**.

Thus, the cohesive forces between PEG-coated SS particles are almost completely screened upon trapping the HFA-philic groups (PEG) at the surface[47]. The excellent physical stability of PEG-coated SS in HFA propellant (both HFA134a and HFA227) also corroborated the CPM force results. Another important piece of information from this work was the establishment of a correlation between the CPM, the physical stability of the formulation and the corresponding aerosol characteristics. It was demonstrated that the CPM results correlate very well not only with the physical stability of the formulations, but also with the aerosol properties. A large fine particle fraction (FPF) was achieved for the PEG-coated SS formulations (65.1%) that had small F_{ad} and good

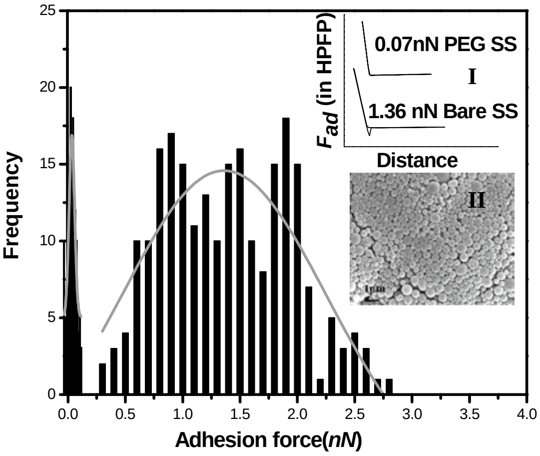

Fig.12 Adhesion force (F_{ad}) histogram between bare- (distribution to the right of the diagram) and PEG-coated SS spheres (distribution to the left of the diagram) in HPFP. The black lines represent the Gaussian fit of the histograms. (Inset I): average force curves for bare- and PEG300-modified- SS particles. (Inset II): SEM image of PEG300-coated SS spheres. As PEG is trapped onto the surface of the particles, it is capable of reducing the cohesive forces down to about zero, indicating that it can be well solvated by HPFP. Reprinted from ref. [47] with permission from Elsevier.

physical stability. These results can be contrasted with those for the unmodified SS formulation with a FPF of 39.1%, which had large F_{ad} and poor physical stability.

CPM was also used in the development of particles with a core-shell morphology$^{46)}$. In this modified emulsification-diffusion approach, particles were formed with the active component (water soluble or dispersible) in the core, and with a shell (biodegradable and biocompatible) designed so as to impart stability to the particles when dispersed in propellant HFAs$^{46)}$. Studied cores include a model small polar drug (SS) and a model biomolecule (bovine serum albumin, BSA). The particle shell consisted of oligo(lactide) (*LA*) grafts attached onto a short (degraded) chitosan (*CS*) backbone. *LA* was selected based on the CFM studies and its biocompatible and biodegradable nature. CS was utilized to impart interfacial activity to the polymer at the water-ethyl acetate interface, required in the selected particle engineering approach$^{46)}$. CPM was utilized to quantitatively evaluate the effectiveness of the shell in screening the attractive forces by measuring the F_{ad} between two single particles in HPFP$^{46)}$. The CPM results demonstrate that the cohesive forces between drug particles are significantly reduced (to nearly zero) upon the coating of the shell around the drug particle, again demonstrating the fact that HFAs are capable of solvating *LA* moieties.

The CPM results also correlated well with the bulk physical stability in HFA277. However, the core-shell particles cannot be well dispersed in HFA134a, which seems to indicate that that HPFP is a better mimic of HFA227 than HFA134a. This is an important particle engineering approach as it may create the opportunity of using pMDIs for the delivery of nanotherapeutics to and through the lungs$^{92)}$. In the studies discussed above, CPM results were shown to be to provide a novel predictor of the suspension stability of pMDI formulations and offer an opportunity to decouple the effect of particle-particle interactions from the other formulation variables on the performance of the aerosol. Because smooth spherical particles can be made using the emulsification-diffusion technique, this could perhaps be utilized as a means of normalizing the force of interaction, and thus allowing the comparison from experiments done with different CPM probes. It remains to resolve, however, whether such particles are sufficiently smooth$^{59)}$ and whether the morphology (amorphous) of the particles has a significant effect on the cohesive forces as measured by CPM$^{93)}$.

4.2.5. Particle density measurements by CPM

A novel method based on the CPM technique has been suggested to determine the density of particles$^{81, 82)}$. A single spherical particle is initially glued onto the AFM cantilever as in a typical CPM experiment. The mass of the single particle on the cantilever can be determined based on the shift in the resonant frequency of the cantilever, as is typically done in the determination of the spring constant$^{94)}$. The density is then obtained based on the particle volume, measured by a microscope. Using this technique, the effective density of spray-dried carbonhydrate particles was determined and compared to the result from nitrogen pycnometry$^{81)}$. The CPM together with various microscopic techniques revealed that the particles with an effective particle density close to the true density showed a solid appearance while hollow particles gave a lower effective particle density. The results from nitrogen pycnometry, however, could not detect the density difference for solid and highly gas permeable particles$^{81)}$. It may be concluded that AFM can provide valuable information on both particle structure and density, which is not possible to be acquired by pycnometry. The limitation of this method is the requirement for regular shaped particles so that the volume can be easily determined from microscopy$^{81)}$. There is also a limitation associated with the size of particles since the attachment of the particles to the AFM tip becomes more challenging as particle decreases to less than 10 μm.

4.2.6. Hamaker constant by CPM

Interactions between colloidal particles in the low-dielectric HFAs are dominated by the attractive van de Waals (VDW) forces as electrostatic interactions have little or no relevance in non-aqueous media. VDW forces are thus responsible for colloidal instability in HFAs. The determination of Hamaker constant is, therefore, of great relevance for the understanding of fundamental colloidal phenomena associated with pMDIs[95)].

The Hamaker constant (A_H) can be calculated from spectral or optical properties of materials through various approaches[96-97)], and also using AFM[59, 83)]. For the interaction between particles with a spherical geometry and a flat surface, the Hamaker constant can in principle be obtained by fitting the attractive part of the force-distance AFM curve to equation $F = -A_H R/6D^2$, where R is the radius of curvature of the tip and D is the separation distance.

The applicability of this method is somewhat limited due to the jump-to-contact, which occurs when the force gradient exceeds the spring constant of the cantilever, as described in section 3.3. An alternative method to determine A_H is based on the measurement of adhesion force as the AFM tip is pulled out of contact with sample surface. This approach takes into account various parameters such as surface roughness, particle geometry, and elastic properties of the interacting materials[59, 83)]. There have been several theories that have addressed the determination of A_H from CPM experiments[98-100)]. The challenges associated with this approach include difficulties in estimating the contact geometry, and in determining the surface roughness of the probe. Readers are directed to excellent reviews on this subject for more details[59, 62)].

5. Concluding Remarks

In this review we have highlighted the applicability of the AFM and related techniques to systems of relevance to pMDIs. Despite the limited number of publications in the area and the recent nature of the studies (most articles having been published in the last 5 years), it is clear that the AFM can provide valuable information to address a range of formulation issues from hardware design, to excipient screening, to particle engineering. Other areas where the AFM could be potentially used to gain relevant information to the formulation of pMDIs have been identified, including viscosity measurements, true particle density measurements, and the determination of Hamaker constants. The capability of the AFM to provide unique microscopic information with a degree of sensitivity often not achievable with alternative / bulk techniques has also been discussed. However, certain challenges, most notably the difficulty in determining the area of contact in CPM, and the structure and properties of adsorbed monolayers on the AFM probes in CFM, are clear constraints that need to be addressed. While experimental AFM results under pressure (propellant HFAs) are not available, further validation of the model solvent (HPFP) used in the AFM experiments is also granted. A combination of results from AFM and bulk techniques (e.g. contact angle) or computational studies (e.g. ab initio calculations) seem to be a powerful approach to address the many challenges in the formulation of pMDIs. It is the expectation that such fundamental information could provide for an opportunity for pMDIs to rebound on the oral inhalation market, and perhaps achieve new grounds on the overall drug delivery market, as for example in the local and systemic delivery of nanotherapeutics and (large) therapeutic biomolecules.

6. Acknowledgements

The authors would like to acknowledge financial support from the Office of the VP for Research at Wayne State University, through a Nano@Wayne grant; and from the National Science Foundation through an NSF-CBET grant no. 0553537.

References

1) Patton, J.S. and Byron, P.R. (2007): Inhaling medicines: delivering drugs to the body through the lungs, Nature Review 6, pp.67-74.
2) Okamoto, H. et al. (2002): Dry Powders for Pulmonary Delivery of Peptides and Proteins, KONA Powder and Particle Journal, 20, pp.71-83.
3) Laube, B.L. (2005): The Expanding Role of Aerosols in Systemic Drug Delivery, Gene Therapy, and Vaccination, Respiratory Care, 50, pp.1161-1176.
4) Davis, S.S. (1999): Delivery of peptide and non-peptide drugs through the respiratory tract, Pharmaceutical Science & Technology Today, 2, pp.450-456.
5) Patton, J.S. (1996): Mechanisms of Macromolecule Absorption by the Lungs, Advanced Drug Delivery Reviews, 19, pp.3-36.
6) Yu, J. and Chien, Y.W. (1997): Pulmonary drug de-

livery: physiologic and mechanistic aspects, Critical Reviews in Therapeutic Drug Carrier Systems, 14, pp.395-453.
7) Strack, T. (2007): Pulmonary administration of peptide and protein drugs, American Pharmaceutical Review, 10, pp.129-133.
8) Courrier, H.M. et al. (2002): Pulmonary Drug Delivery System: Recent Developments and Prospects, Critical Reviews in Therapeutic Drug Carrier Systems, 19, pp.425-498.
9) Groneberg, D.A. et al. (2003): Fundamentals of pulmonary drug delivery, Respiratory medicine, 97, pp.382-387.
10) U.S. Emerging Pulmonary Drug Delivery Technologies Markets. In Frost & Sullivan: 2003; Vol. Report: A375-52.
11) Suri, R. (2005): The use of human deoxyribonuclease (rhDNase) in the management of cystic fibrosis, BioDrugs, 19, pp.135-144.
12) Smyth, H.D.C. et al. (2008): Pulmonary delivery of anti-cancer agents, Drugs and the Pharmaceutical Sciences, 172, pp.81-111.
13) Birchall, J. (2007): Pulmonary delivery of nucleic acids, Expert Opinion on Drug Delivery , 4, pp.575-578.
14) Smyth, H.D.C. (2005): Propellant-driven Metered-dose Inhalers for Pulmonary Drug Delivery Expert Opinion on Drug Delivery, 2, pp.53-74.
15) McDonald, K.J. and Martin, G.P. (2000): Transition to CFC-free Metered Dose Inhalers - Into the New Millennium, International Journal of Pharmaceutics, 201, pp.89-107.
16) Schimke, K.E. and Davis, T.M.E. (2008): Inhaled human insulin (Exubera): its pharmacologic profile, efficacy and safety in the treatment of adults with diabetes mellitus, Expert Review of Clinical Pharmacology, 1, pp.13-25.
17) Ranucci, J.A. et al. (1990): Controlled flocculation in metered-dose aerosol suspensions, Pharmaceutical Technology, 14, pp.68-74.
18) Podczeck, F. and Newton, J.M. (1995): Development of an Ultracentrifuge Technique to Determine the Adhesion and Friction Properties between Particles and Surfaces, Journal of Pharmaceutical Sciences, 84, pp.1067-1071.
19) Johnson, K.A. (1990): Measurement of particle size and settling in pressurized metered dose inhalers, In AAPS, Las Vagas.
20) Traini, D. et al. (2005): Surface Energy and Interparticle Force Correlation in Model pMDI Formulations, Pharmaceutical Research, 22, pp.816-825.
21) Bunker, M.. et al. (2005): Towards screening of inhalation formulations: measuring interactions with atomic force microscopy, Expert opinion on drug delivery, 2, pp.613-624.
22) Bell, J. and Newman, S. (2007): The rejuvenated pressurized metered dose inhaler, Expert Opinion on Drug Delivery, 4, pp.215-234.
23) Rogueda, P. (2005): Novel Hydrofluoroalkane Suspension Formulations for Respiratory Drug Delivery, Expert Opinion on Drug Delivery, 2, pp.625-638.
24) Terzano, C. (2001): Pressurized Metered Dose Inhalers and Add-on Devices, Pulmonary Pharmacology and Therapeutics, 14, pp.351-366.
25) Fink, J.B. (2000): Metered-Dose Inhalers, Dry Powder Inhalers and Transitions, Respiratory Care, 45, pp.623-635.
26) Telko, M.J. and Hickey, A.J. (2005): Dry powder inhaler formulation, Respiratory Care, 50, pp.1209-1227.
27) Dalby, R. and Suman, J. (2003): Inhalation therapy: technological milestones in asthma treatment, Advanced Drug Delivery Reviews, 55, pp.779-791.
28) Feddah, M.R. et al. (2001): Influence of respiratory spacer devices on aerodynamic particle size distribution and fine particle mass of beclomethasone from metered-dose inhalers, Journal of Aerosol Medicine, 14, pp.477-485.
29) Keller, M. (1999): Innovations and Perspectives of Metered Dose Inhalers in Pulmonary Drug Delivery, International Journal of Pharmaceutics, 186, pp.81-90.
30) Frijlink, H.W. and De Boer, A.H. (2004): Dry Powder Inhalers for Pulmonary Drug Delivery, Expert Opinion on Drug Delivery, 1, pp.67-86.
31) Hickey, A.J. and Crowder, T.M. (2007): Next generation dry powder inhalation delivery systems, Lung Biology in Health and Disease, pp.445-460.
32) Tang, X. et al. (1998): Changes in tropospheric composition and air quality, Journal of Photochemistry and Photobiology, B: Biology, 46, pp.83-85.
33) Vervaet, C. and Byron, P.R. (1999): Drug-surfactant-propellant Interactions in HFA-formulations, International Journal of Pharmaceutics, 186, pp.13-30.
34) Wu, L. et al. (2007): Understanding Solvation in Hydrofluoroalkanes: Ab initio Calculations and Chemical Force Microscopy, Journal of Physical Chemistry B, 111, pp. 8096 -8104.
35) Wu, L. et al. (2007): Molecular Scale Behavior in Alternative Propellant-Based Inhaler Formulations, Inhalation Aerosols: Physical and Biological Basis for Therapy; by Hickey, A. J., 3rd Edition, pp.373-397.
36) Selvam, P. et al. (2008): Ethoxylated copolymer surfactants for the HFA134a-water interface: interfacial activity, aggregate microstructure and biomolecule uptake, Soft Matter, 4, pp.357-366.
37) Selvam, P. et al. (2008): Reverse Aqueous Aggregates in Hydrofluoroalkanes for the Non-invasive Regional Delivery of Anti-cancer Therapeutics to the Lungs, Internal Communication.
38) Selvam, P. et al. (2008): Poly(lactide)-based Non-ionic Amphiphiles for the Hydrofluoroalkane Propellant-Water Interface, Langmuir, To be submitted.
39) Chokshi, U. et al. (2008): Ethoxylated Surfactants for the HFA227-Water Interface: Interfacial Activity, Microemulsions and Emulsions, Submitted to International Journal of Pharmaceutics.
40) Courrier, H.M. et al. (2004): Reverse water-in-fluorocarbon emulsions and microemulsions obtained with

a fluorinated surfactant, Colloids and Surfaces, A, 244, pp.141-148.
41) Patel, N. et al. (2003): Fluorinated Ionic Surfactant Microemulsions in Hydrofluorocarbon 134a (HFC134a), Journal of Colloid and Interface Science, 258, pp.354-362.
42) Patel, N. et al. (2003): Formation of Fluorinated Nonionic Surfactant Microemulsions in Hydrofluorocarbon 134a (HFC134a), Journal of Colloid and Interface Science, pp.258, 345-353.
43) Courrier, H.M. et al. (2004): In vivo evaluation of a reverse water-in-fluorocarbon emulsion stabilized with a semifluorinated amphiphile as a drug delivery system through the pulmonary route, International Journal of Pharmaceutics, 282, pp.131-140.
44) Tzou, T.Z. et al. (1997): Drug from selection in Albuterol-Containing Metered-Dose inhaler formulation and its impact on chemical and physical stability, Journal of Pharmceutical Science, 86, pp.1352-1357.
45) Wu, L. and da Rocha, S.R.P. (2007): Biocompatible and Biodegradable Copolymer Stabilizers for Hydrofluoroalkane Dispersions: A Colloidal Probe Microscopy Investigation, Langmuir, 23, pp.12104-12110.
46) Wu, L. et al. (2008): Core-shell Particles for the Dispersion of Small Polar Drugs and Biomolecules in Hydrofluoroalkane Propellants, Pharmaceutical Research, 25, pp.289-301.
47) Wu, L. et al. (2008): Novel Propellant-driven Inhalation Formulations: Engineering Polar Drug Particles with Surface-trapped Hydrofluoroalkane-philes, European Journal of Pharmaceutical Sciences, 33, pp.146-158.
48) Liao, Y.H. et al. (2005): The Effects of Polyvinyl Alcohol on the In Vitro Stability and Delivery of Spray-dried Protein Particles from Surfactant-free HFA134a-based Pressurised Metered Dose Inhalers, International Journal of Pharmaceutics, 304, pp.29-39.
49) Jones, S.A. et al. (2006): Stabilization of deoxyribonuclease in hydrofluoroalkanes using miscible vinyl polymers, Journal of Controlled Release, 115, pp.1-8.
50) Dellamary, L.A. et al. (2000): Hollow Porous Particles in Metered Dose Inhalers, Pharmaceutical Research, 17, 168-174.
51) Traini, D. et al. (2006): Investigation into the Influence of Polymeric Stabilizing Excipients on Inter-particulate Forces in Pressurized Metered Dose Inhalers, International Journal of Pharmaceutics, 320, pp.58-63.
52) Stefely, J.S. et al. (2000): Biocompatible compounds for pharmaceutical drug delivery systems, US patent 6126919.
53) Stefely, J.S. et al. (2000): Design and utility of a novel class of biocompatible excipients for HFA-based MDIs, Respiratory Drug Delivery VII , pp.83-90.
54) Edwards, D.A. et al. (1998): Recent Advances in Pulmonary Drug Delivery Using Large, Porous Inhaled Particles, Journal of Applied Physiology, 85, pp.379-385.
55) Edwards, D.A. et al. (1997): Large Porous Particles for Pulmonary Drug Delivery, Science, 276, pp.1868-1871.
56) Tarara, T.E. et al. (2004): Characterization of suspension-based metered dose inhaler formulations composed of spray-dried budesonide microcrystals dispersed in HFA-134a, Pharmaceutical Research, 21, pp.1607-1614.
57) Hansma, H.G. and Pietrasanta, L. (1998): Atomic Force Microscopy and Other Scanning Probe Microscopies, Current Opinion in Chemical Biology, 2, pp.579-584.
58) Nakagawa, T. et al. (1994): Atomic Force Microscope for Chemical Sensing, Journal of Vacuum Science and Technology B, 12, pp.2215-2218.
59) Butt, H.J. et al. (2005): Force Measurements with the Atomic Force Microscope: Technique, Interpretation and Applications, Surface Science Reports, 59, pp.1-152.
60) Jandt, K.D. (2001): Atomic Force Microscopy of Biomaterials Surfaces and Interfaces, Surface Science, 491, pp.303-332.
61) Noy, A. et al. (1997): Chemical Force Microscopy, Annual Review of Materials Science, 27, pp.381-421.
62) Cappella, B. (1999): Dietler, Force-distance curves by atomic force microscopy, Surface Science Reports, 34, pp.5-104.
63) Hansma, H.G.P. (1998): Atomic force microscopy and other scanning probe microscopies, Current Opinion in Chemical Biology, 2, pp.579-584.
64) Williams, R.O. and Hu, C. (1997): A study of an epoxy aerosol can lining exposed to hydrofluoroalkane propellants, European Journal of Pharmaceutics and Biopharmaceutics , 44, pp.195-203.
65) Hooton, J.C. et al. (2003): Characterization of Particle-interactions by Atomic Force Microscopy: Effect of Contact Area, Pharmaceutical Research, 20, pp.508-514.
66) Papi, M. et al. (2006): Fluid viscosity determination by means of uncalibrated atomic force microscopy cantilevers, Applied Physics Letters, 88, pp.194102/1-194102/3.
67) Noy, A. et al. (1995): Chemical Force Microscopy: Exploiting Chemically-modified Tips to Quantify Adhesion, Friction, and Functional Group Distributions in Molecular Assemblies, Journal of the American Chemical Society, 117, pp.7943-7951.
68) Ulman, A. (1996): Formation and Structure of Self-Assembled Monolayers, Chem. Rev. 96, pp. 1533-1554.
69) Ulman, A. (1997): “An Introduction to Ultrathin Organic Films: from Langmuir-Blodgett to Self-Assembly”, Academic Press: San Diego.
70) Love, J.C. et al. (2005): Self-Assembled Monolayers of Thiolates on Metals as a Form of Nanotechnology, Chemical Review, 105, pp.1103-1169.
71) Podczeck, F. et al. (1996): The estimation of the true area of contact between microscopic particles and a flat surface in adhesion contact, Journal of Applied Physics, 79, pp.1458-1463.
72) Young, P.M. et al. (2003): Under Pressure: Predicting Pressurized Metered Dose Inhaler Interactions Using

the Atomic Force Microscope. Journal of Colloid and Interface Science, 262, pp.298-302.

73) Traini, D. et al. (2006): The Use of AFM and Surface Energy Measurements to Investigate Drug-Canister Material Interactions in a Model Pressurized Metered Dose Inhaler Formulation, Aerosol Science and Technology, 40, pp.227-236.

74) Beach, E.R. et al. (2002): Pull-off Force Measurements between Rough Surfaces by Atomic Force Microscopy, Journal of Colloid and Interface Science, 247, pp.84-99.

75) Eve, J.K. et al. (2002): A study of single drug particle adhesion interactions using atomic force microscopy, International Journal of Pharmaceutics, 238, pp.17-27.

76) Price, R. et al. (2002): The Influence of Relative Humidity on Particulate Interactions in Carrier-based Dry Powder Inhaler Formulations, International Journal of Pharmaceutics, 246, pp.47-59.

77) Young, P.M. (2004): The influence of relative humidity on the cohesion properties of micronized drugs used in inhalation therapy, Journal of Pharmaceutical Sciences, 93, pp.753-761.

78) Rogueda, P. (2003): HPFP, a Model Propellant for pMDIs, Drug Development and Industrial Pharmacy, 29, pp.39-49.

79) Peguin, R.P.S. and da Rocha, S.R.P (2008): Solvent-Solute Interactions in Hydrofluoroalkane Propellants, Journal of Physical Chemistry, C (In press).

80) Begat, P. et al. (2005): The Influence of Force Control Agents on the Cohesive-Adhesive Balance in Dry Powder Inhaler Formulations, KONA Powder and Particle Journal, 23, pp.109-121.

81) Elversson, J. et al. (2006): An atomic force microscopy approach for assessment of particle density applied to single spray-dried carbohydrate particles, Journal of Pharmaceutical Sciences, 96, pp.905 - 912.

82) Andersson, K.M. and Bergstrom, L. (2005): Density Measurements of Single Granules Using the Atomic Force Microscope, Journal of the American Ceramic Society, 88, pp.2322-2324.

83) Eichenlaub, S. et al. (2002): Hamaker Constants in Integrated Circuit Metalization, Journal of Colloid and Interface Science, 248, pp.389-397.

84) Napper, D.H. (1983): "Polymeric Stabilization of Colloidal Dispersions", Academic Press, New York, p 428.

85) Peguin, R.P.S. et al. (2007): The Ester Group: How Hydrofluoroalkane-philic Is It? Langmuir, 23, pp.8291-8294.

86) Geer, R.E. et al. (1994): X-ray and Ellipsometric Studies of Self-Assembled Monolayers of Fluorinated Chlorosilanes, Langmuir, 10, pp.1171-1176.

87) Luscombe, C.K. et al. (2003): Fluorinated Silane Self-Assembled Monolayers as Resists for Patterning Indium Tin Oxide, Langmuir, 19, pp.5273-5278.

88) Porush, I. and Shepherd, H.P. (1961): "Pressurized Metered-dose Inhalers: Science and Technology", Interscience, New York.

89) Traini, D. et al. (2007): In Vitro Investigation of Drug Particulates Interactions and Aerosol Performance of Pressurized Metered Dose Inhalers, Pharmaceutical Research., 24, pp.125-135.

90) Ashayer, R.L. (2004): Investigation of the molecular interactions in a pMDI formulation by atomic force microscopy, European Journal of Pharmaceutical Sciences, 21, pp.533-543.

91) Ridder, K.B. et al. (2005): Surfactant solubility and aggregate orientation in hydrofluoroalkanes, International Journal of Pharmaceutics, 295, pp.57-65.

92) Bharatwaj, B. et al. (2007): Towards novel inhalation formulations for the delivery of therapeutic molecules for chlamydial respiratory infections, In ENATbio Conference, Detroit, MI.

93) Roberts, C.J. (2005): What can we learn from atomic force microscopy adhesion measurements with single drug particles?, European Journal of Pharmaceutical Sciences, 24, pp.153-157.

94) Sader, J.E. et al. (1995): Method for the calibration of atomic force microscope cantilevers, Review of Scientific Instruments, 66, pp.3789-3798.

95) Johnson, K.A. (2007): Interfacial Phenomena and Phase Behavior in Metered Dose Inhaler Formulations. Inhalation Aerosols: Physical and Biological Basis for Therapy; by Hickey, A. J., 3rd Edition, pp.347-372.

96) Lifshitz, E.M. (1956): The theory of molecular attractive forces between solids. Soviet Physics. JETP, 2, pp.73-83.

97) Tabor, D. and Winterton, R.H.S. (1969): Direct measurement of normal and retarded van der Waals forces. Proceedings of the Royal Society of London, Series A: 312, pp.435-450.

98) Rumpf, H. (1990): "Particle Technology", Chapman & Hall, London.

99) Rabinovich, Y.I. et al. (2000): Adhesion between Nanoscale Rough Surfaces II. Measurement and Comparison with Theory, Journal of Colloid and Interface Science, 232, pp.17-24.

100) Cooper, K. et al. (2000): Analysis of Contact Interactions between a Rough Deformable Colloid and a Smooth Substrate, Journal of Colloid and Interface Science, 222, pp.63-74.

Author's short biography

Dr Sandro R. P. da Rocha

Sandro R. P. da Rocha received his B.S in Chemical Engineering (ChE) in 1992 from UFSM, Brazil. Soon after his graduation, he moved to Denmark where he worked for a year at the Danish Technological Institute - Taastrup, in the area of surface coatings, specializing on powder-coating technologies. He then returned to Brazil to work on his MS (1995), also in ChE, at UFSC, in the area of Supercritical Fluids. Dr. da Rocha then moved to Texas, where he obtained his PhD in ChE at the University of Texas (UT) at Austin in 2000. He continued on as a Postdoctoral Fellow also at UT – Austin, in Chemistry and Biochemistry. While in Texas he utilized a combined computational and experimental approach to investigate the properties of buried interfaces under high-pressure. Dr. da Rocha joined the Chemical Engineering and Materials Science Department at Wayne State University (Detroit, MI) in 2002, where he is now an Associate Professor. He has published nearly 40 manuscripts in peer-reviewed journals and book chapters. Dr. da Rocha's group main interests are in the development of novel oral inhalation technologies for the delivery of therapeutic biomolecules to and though the lungs for the treatment of medically relevant diseases including cancer, cystic fibrosis, diabetes and others. Experimental techniques and computational approaches are used hand-in-hand to address fundamental issues and engineering aspects required for the development of such formulations. He can be reached via e-mail at sdr@eng.wayne.edu.

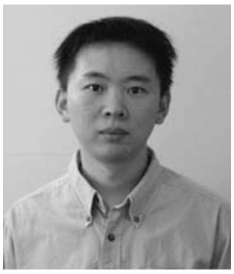

Dr Libo Wu

Libo Wu received his B.S in Polymer Engineering in 2000 from Beijing University of Chemical Technology (BUCT), China and M.S. in Polymer Engineering in 2003 from BUCT. After finishing his M.S., he joined Tsinghua Unis Insight Chemicals Inc., where he worked as Research Scientist in the area of UV-curing coatings. He joined Wayne State University (Detroit, MI, US) in 2004, and is currently pursuing his PhD in Chemical Engineering. He works under the guidance of Prof. da Rocha in the area of novel formulations for respiratory drug delivery. He has authored or co-authored approximately 20 publications in peer reviewed journals and book chapters, and has several provisional patent applications. In 2008 he received the 'Graduate Student Award', a recognition from the Engineering Alumni Association for his academic excellence, research achievements and service to the College of Engineering. He can be reached via e-mail at ap7749@wayne.edu.

Review of Adhesion Fundamentals for Micron-Scale Particles[†]

Otis R. Walton
Grainflow Dynamics Inc.[1]

Abstract

The effects of various fundamental forces on the adhesion of fine dust particles are reviewed. The particle-size and distance variation of surface-energy related (e.g., van der Waals) forces are compared to similar relations for static-electric image-forces for tribo-charged particles near (or contacting) conducting surfaces. The van der Waals force (between macroscopic spheres), a patch-charge image-force and static-electric image-forces all exhibit an inverse square variation with distance; however, these forces have dramatically different ranges-of-effect. The very short-range nature of van der Waals forces (of order 10nm) is a major reason that most real contacts, involving non-smooth surfaces, exhibit adhesion forces that are substantially lower than values predicted for smooth particles. Based on studies of Lunar and Martian regolith stimulant powders, triboelectric charges on fine particles appear to scale linearly with particle size. It is shown that below some threshold size, the adhesion (to conducting surfaces) of charged dust particles possessing such a linear charge-to-size scaling relationship, may be dominated by image-charge forces, instead of surface-energy related interactions. This is counter to what might have been expected from a cursory examination of the fundamental force relations, which would suggest van der Waals adhesion forces would dominate for small particle sizes.

Keywords: adhesion, electrostatic, van der Waals attraction, fine Powder, image-charge force, dust

1. Introduction/Background

The effects of surface-energy and image-charge forces and how their relative strength varies with particle size and with distance was a major part of a recent NASA sponsored review of the potential effects of various fundamental forces acting on lunar dust particles [Walton, 2007]. Although primarily based on that NASA report, this paper attempts to de-emphasize special lunar conditions, like an ultra-high vacuum and high incident solar UV flux and solar wind effects, and instead, describes primarily those aspects of fine particle adhesion which are applicable under terrestrial conditions. Adhesion forces acting on fine particles can arise from a variety of causes including van der Waals (*i.e.*, surface energy) interactions, electrostatic interactions, static-electric image charges in nearby conductors, and, under high humidity conditions, surface tension in menisci of adsorbed water surrounding contact points. The effects of adsorbed water was not covered in the lunar dust review, since there is virtually no in-situ atmosphere on the moon and adsorbed water would likely only be a significant contribution to adhesion inside of human habitats. A perusal of the literature on the effects of humidity on particle-scale forces, however, indicates that for many particle/surface combinations there is a dramatic increase in adhesion at high humidities. The threshold value for this dramatic increase in adhesive force appears to depend relatively strongly on the degree of surface roughness near contact points with rougher surfaces requiring higher humidity before the threshold is observed. Rabinovich [2000] and Rabinovich *et al* [2002] hypothesized that the dramatic increase in cohesion/adhesion occurs when the thickness of a layer of adsorbed water is great enough for the liquid water to 'bridge' the gap between the near surfaces (over a height comparable to the surface roughness). A number of AFM studies of the effect of humidity on adhesive forces have been

---

[†] Accepted : July 2, 2008

[1] 1141 Catalina Drive, PMB-270, Livermore, CA 94550, USA
TEL: (925) 447-4293 FAX: (925) 449-9111
E-mail: walton@grainflow.com

consistent with the ideas of Rabinovich and Moudgil. A few have found that increasing humidity decreases adhesion; however, this appears to occur most often when the initial adhesion is electrostatic in nature, so that the humidity allows the charge to leak away from the contact area. On the other hand, under very low humidity conditions, charge leak-off rates are quite low and particles can maintain charges for long periods of time. This paper does not directly examine the effects of humidity on adhesion; however analytic models exist for the distance and particle-size scaling of liquid meniscus forces for contacting spheres [Lian et al, 1993; Xue, 2007].

Fine non-conducting particles are strongly affected by surface-energy related (*i.e.*, van der Waals) interactions and by electrostatic forces. In powder handling operations conductive materials, or thin partially-conductive coatings, are often utilized to minimize charge buildup, and thus reduce problems from static-electric attraction of fine particles to surfaces. Utilization of conductive coatings or conductive materials can minimize the attraction of uncharged fine particles to charged surface regions; however the use of conducting surfaces does not eliminate static-electric forces between particles carrying charge and those conductive surfaces (even if the surface is 'grounded' so that it has no net charge). Some processes, like xerography, rely on being able to 'adjust' static-electric adhesion to be stronger than, or weaker than, van der Waals attraction between particles during different phases of the process [see box on xerography later]. In powder handling equipment, problem locations subject to charge build-up can sometimes be equipped with ion generators which flood the air at those locations with bipolar ions to neutralize the charge on the powder. Such charge cancellation processes are not evaluated in this paper.

In the most simplistic terms, two atoms 'touch' when the repulsion of the outer electron orbitals prevents the atoms from approaching closer. For atomic numbers greater than 10 this closest-approach distance is about $4\mathring{A}$, increasing slightly for higher atomic number atoms. When surface atoms in two approaching objects are separated by distances slightly greater than 'contact' or the closest-approach distance, a net attraction occurs due to induced dipole (and permanent dipole) interactions between the atoms. These dipole and other polar forces constitute surface-energy interactions which exist for all materials.

2. Surface-energy-related Attractive Forces

Van der Waals originally modified the ideal gas equation of state with two additional terms, one to account for the finite volume of the gas molecules and the other to account for an attractive force acting between molecules – which is responsible for liquid/vapor phase changes, among other macroscopic phenomena. For spherical atoms, the van der Waals forces can be thought of as arising from the instantaneous effective dipole of an orbiting electron (and its nucleus) inducing an effective instantaneous dipole in a nearby atom. The resulting dipole-dipole potential energy varies with, $1/d^6$, where d is the distance between the dipole centers of mass. A full quantum mechanical treatment of the energy of different configurations for two adjacent atoms [Feynman, 1939] confirmed that the classical electrodynamic equations were, for the most part, correctly describing these quantum-mechanical atom-atom interactions. Polar molecules (*i.e.* molecules with a permanent dipole moment) experience this interaction, and also interact with nearby molecules via permanent dipole/dipole and dipole/induced-dipole interactions. These interactions also have potential energies that vary as $1/d^6$, and are known as the Keesom and Debye energies, respectively. Collectively these three molecular-scale dipole interactions (London-dispersion [1930; 1937], Keesom [1921] and Debye [1920] energy) comprise what are currently known as van der Waals interactions (or forces) between molecules. All molecules (whether they are charged or not, have dipole moments or not, form Hydrogen bonds or not) are attracted to other nearby molecules by, at least the London-dispersion part of, the van der Waals interactions.

Surface energy (per unit area) is the work required to separate a unit area of two surfaces which are initially in intimate contact (on a molecular scale), and move them apart (doing work against the intermolecular forces of attraction) until the surfaces are infinitely far apart. Isrealachvili [1991] provides a thorough discussion of interaction energies between molecules and evaluation of the integrated effects of intermolecular interactions between all molecules in each of two spherical or planar objects separated a distance, s, apart (with particular emphasis on the case where the intermolecular potential varies with d^{-6}, where d is the distance between a pair of interacting molecules).

Planar Surfaces – Abreviating the discussion by

Isrealachvili [1991] consider a substance comprised of molecules which interact with an attractive pair potential of the form $\psi(dz) = -C_f/d^6$, where d is the distance between the molecules, and C_f is a constant. Next, consider a unit area of two planar surfaces, made of that material, which are a distance s apart. If we add all the contributions from all the $1/d^6$ pair interactions, and further integrate the resulting energy with distance, from the distance s to infinity, the result is the surface energy per unit area, as a function of the separation distance between the two planar faces, s,

$$w_p(s) = -\frac{\pi C_f \rho_a^2}{12 s^2} = -\frac{A}{12\pi s^2} \quad \text{(per unit area)} \qquad (1)$$

where ρ_a is the volume density of atoms (molecules) in the material, and $A = \pi^2 C_f \rho_a^2$, is the Hamaker constant for the material [Hamaker, 1937].

Spheres – It can be shown [Derjaguin, 1934; Krupp, 1967; Isrealachvili, 1991] that the force, F_s, between two spheres of radii, R_1 and R_2, as a function of separation, s, is related to the surface energy per unit area (as a function of separation) for two planes (*i.e.*, Eqn 1) by,

$$F_s(s) = -2\pi R^* w_p(s), \qquad (2)$$

where, $R^* = \dfrac{R_1 R_2}{R_1 + R_2}$.

If one sphere is very large, $R_2 >> R_1$ (approaching a sphere and a plane) Eqn 2 reduces to

$$F_{sp}(s) = -2\pi R w_p(s) \qquad (3)$$

or, for two equal spheres,

$$F_{ss}(s) = -\pi R w_p(s). \qquad (4)$$

Two important characteristics of van der Waals forces for spherical bodies can be deduced from these relationships (Eqns 1 – 4). First, we can substitute the expression of $w_p(s)$ from Eqn 1 into Eqn 2 to obtain the particle size and distance dependence of the attractive van der Waals force between two approaching spheres, or a sphere and a planar surface,

$$F_{vdW} = -\frac{A}{6s^2} R^*. \qquad (5)$$

Contact limit – Second, we can consider the limiting case when two bodies are in 'contact.' For two spheres in contact, where $s \approx s_o$ = molecular diameter $\approx 4\mathring{A}$, the value of $w(s_o)$ can be associated with 2γ, where γ is the conventional energy per unit area of a surface. Thus, the force of adhesion (at contact) between two (undeformed) spheres, in terms of their surface energy is [Iseralachvili, 1991],

$$F_s(s_o) = F_c = -4\pi\gamma R^*; \qquad (6)$$

which, for $R_2 >> R_1$, reduces to

$$F_{sp}(s_o) = -4\pi\gamma R \qquad (7)$$

and, for two equal size spheres becomes,

$$F_{ss}(s_o) = -2\pi\gamma R. \qquad (8)$$

This intimate relation between the planar surface energy per unit area and the cohesive force acting for sphere/plane contacts is one reason that surface energy is such a useful parameter characterizing cohesive forces of macroscopic bodies in contact. Real macroscopic bodies in contact seldom have intimate (*i.e.*, molecular-scale) planar surfaces touching. Instead, multiple surface asperities are in contact; however, each of these asperity-contacts can often be approximated as a sphere-sphere or a sphere-plane contact. The maximum difference between the attractive force for a sphere-sphere or for a sphere-plane contact is a factor of two [Krupp, 1967; Derjagiun, 1934]. Despite Isrealachvili's [1991] insistence that a sphere/plane contact can never respond like a plane/plane contact, when significant plastic deformation occurs in the contact region, the material within that region may closely resemble a plane/plane configuration wherein the cohesive force would be determined by the derivative of the energy-displacement relation, $\dfrac{-\partial w_p(s)}{\partial s}$, evaluated at contact, $s = s_o$, multiplied by the actual contact area (at the molecular level). For materials interacting with a van der Waals potential, varying with d^{-6}, this results in a force of cohesion at a planar contact (per unit area) of,

$$F_{cp} = -\frac{4\gamma}{s_o} \qquad (9)$$

The significance of surface energy to cohesive/adhesive forces is apparent from Equations (6-9).

Refinements to these relations, taking into account elastic and/or plastic deformations in the contact region have been made by many researchers, but in all cases, the cohesive force at contact is directly proportional to the surface energy per unit area of the materials involved, whether the contact consists of an undistorted sphere touching a plane, a set of nearly spherical asperities in contact, or 'flattened' nearly planar sub-regions in the contact area. Various theories differ in their interpretation of the effects of deformations in the contact region, yet all approaches show a direct relationship between the cohesive forces and the surface energy of the materials in contact. Knowledge of the surface energies of materials of interest, and estimates of the true area of contact are the key factors in being able to predict these surface-energy-related adhesive/cohesive forces acting on fine particles.

The Johnson, Kendall, Roberts (JKR) [1971] model for elastic cohesive contacts does not integrate the attractive forces over the two geometries of the contacting bodies, but instead, uses energy arguments and elastic deformation theory to account for the surface energy associated with separating elastically deformable spheres touching over a finite contact area. The model accounts for elastic deformation of the surface both in terms of the repulsive force 'flattening' the contact area (similar to a Hertzian elastic contact [Hertz, 1882]), and also a tensile region around the compressively loaded core region, increasing the size of the contact area over a purely compressive, Hertzian deformation. The JKR model predicts a pull-off force value of,

$$F_{c_{JKR}} = -3\pi\gamma R^*, \tag{10}$$

or a 25% lower value for the pull-off force over that predicted by Eqn (6) or the DMT [Derjaguin *et al.*, 1975] model. It is interesting to note that, while the JKR model is based on an analysis that includes elastic deformation of the spheres in the contact region (based on the Young's modulus and Poisson ratio of the material), the final expression for the pull-off force predicted by the JKR model is independent of the elastic constants used to obtain the force-displacement behavior.

Plastic deformation – By comparing the cohesive force between two spherical particles (Eqn 6, or 10) with the maximum load achievable for elastic spheres in contact before plastic deformation occurs, it can be shown that as particles get smaller they will eventually reach a size where the cohesive force will cause plastic deformation, even without any applied load. For example, for two equal-sized, non-cohesive, elastic spheres pressed together, the applied load at which plastic yielding begins, F_Y, varies with the square of the particle size [Johnson, 1985], *i.e.*,

$$F_Y = \frac{\pi^3 R^2 (1-\nu^2)^2}{6E^2}(1.6)^3 Y^3, \tag{11}$$

where E is Young's modulus, ν is the Poisson ratio for the material, and Y is the yield strength.

For cohesive particles in contact the pull-off force, F_c (e.g., Eqn 10) scales linearly with particle size, and it is generally accepted that at least a portion of the contact region will experience a repulsive force of the same order of magnitude as the pull-off force, F_c. For example, the force displacement relation for the JKR model is very similar in magnitude and shape to an elastic Hertzian force-displacement curve that has been shifted vertically by subtracting the cohesion force, F_c, from it (and also, perhaps, displacing it horizontally from the origin by an amount $\alpha_s/2$, see **Fig. 1**).

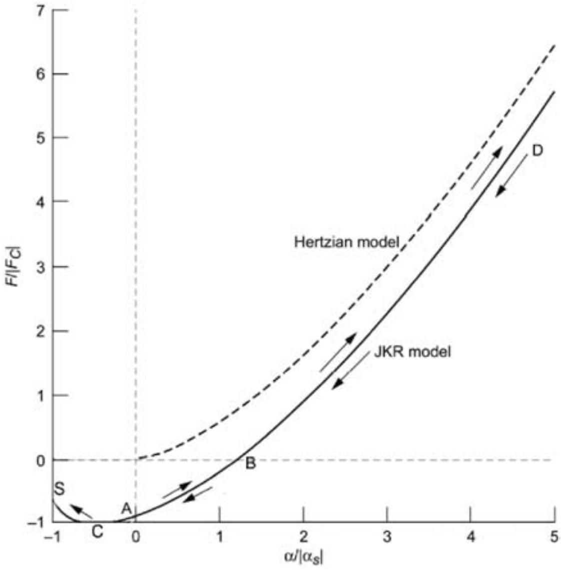

Fig. 1 Force-displacement curves for the cohesive JKR model and for a non-cohesive linear elastic Hertzian contact between two spheres. F_c is the cohesive pull-off force and α_s is the (outward) elastic displacement at final separation [Mei, 2000].

Setting F_c from Eqn 10 to F_y from Eqn 11, and further making the approximation (valid for many materials[Rabinovich, 1965]) that $Y \approx 0.003E$, and selecting $\nu = 0.3$ as a representative Poisson ratio, we obtain an estimate for the particle size, R_{cY}, below which plastic deformation would be expected for cohesive contacts, even with no applied loads,

$$R_{cY} \approx 1 \times 10^7 \frac{\gamma}{E}. \tag{12}$$

Table 1 shows the particle size (diameter) below which plastic deformation is likely due simply to the cohesional forces for two spheres in contact, without any external loads, for various values of Young's modulus, E, and surface energy, γ (assuming $\nu = 0.3$, and $Y \approx 0.003E$).

Table 1 Particle diameter below which plastic deformations occur at contacts

$E\downarrow$ and $\gamma\rightarrow$	$20\ mJ/m^2$	$200\ mJ/m^2$	$2000\ mJ/m^2$
$1GPa$	$400\mu m$	$4mm$	$40mm$
$10GPa$	$40\mu m$	$400\mu m$	$4mm$
$100GPa$	$4\mu m$	$40\mu m$	$400\mu m$

When the effects of plastic deformation, such as the broadening of the stress distribution and the widening of the contact area, are taken into account, it is observed that the plastically deformed contact region is 'flattened,' but is not truly flat. Upon unloading, the region often behaves like an elastic sphere with a larger radius. As the effective radius of the 'flattened' area increases, the effective pull-off force increases. By the time significant plastic deformation is occurring in the contact region the effective radius of the contact spot during unloading might be increased by as much as a factor of two. One approximation of the adhesive-elastic unloading from such a contact is simply a JKR model with a factor of two greater radius of curvature, $R_p \rightarrow 2R$ [Thornton & Ning, 1998]. The net effect is to increase the pull-off force, F_c by up to a factor of two,

$$F_{c-plastic} \approx -6\pi\gamma R^*. \tag{13}$$

More complex expressions describing the transition from elastic to plastic behavior have also been developed (e.g., Margus & Pollock [1974]) however, the net attraction force is within the bounds already discussed. An additional case, for extremely compliant surfaces, where total particle engulfment is possible, is described by Rimai, *et al* [1994; 1995]; however such soft surfaces are not often used in powder handling equipment.

Measurements of surface forces and energy – A variety of methods exist to measure surface energy of solid surfaces and powdered materials utilizing various 'probe' liquids or gases. Typical surface energies range from 20 to $2000mJ/m^2$, and are often in the range of 40 to $100mJ/m^2$. Evaluation of Eqn 7 with surface energies in this range, predicts a pull-off force of a few micro-Newtons for a $10\mu m$ diameter particle. AFM measurements on $8\mu m$ diameter spherical particles (of glass, polystyrene, and tin) contacting atomically flat surfaces, however, resulted in lift-off forces which were typically a factor of 50 less than 'predicted' values [Schaefer et al, 1995]. A detailed AFM mapping of the surface asperities and reinterpretation of the contacts as occurring between multiple asperities and the flat substrate, brought the theory and experiments to within a factor of 3 of each other (with the predicted pull-off force still greater than the measured values, but close enough that possible surface contamination could explain most remaining differences). Similarly, centrifuge measurements of the average adhesion forces on uncharged irregularly shaped toner particles, of nominally $10\mu m$ diameter, are as high as $50nN$ [Hays, 1994] (but nearly two orders of magnitude smaller than would be the case for perfectly smooth spheres of the same size). Also, many irregularly shaped pharmaceutical powder particles, ranging in size from $1\mu m$ to $200\mu m$, have been tested on 'functionalized' AFM tips by numerous researchers. Generally the (statistical average of the) forces measured, scale directly with the particle size – as expected from JKR (or Derjaguin) theory; and they also, usually scale directly with surface energy (when it has been separately measured). Typical pull-off forces range from 2 to $40nN$ for micron-scale particles and from 10's of nN up to ~$500nN$ for $100\mu m$ scale particles under low humidity [Nagai, 2005]. These values are considerably lower than values predicted for smooth spherical particles (e.g. Eqn 7 or 8). An evaluation of the distance dependence of van der Waals forces for particles near surfaces (e.g. Eqn 5) and a comparison with the range-of-effect of other ostensibly inverse square forces (such as electrostatic forces) can elucidate why the surface energy related forces are so sensitive to surface roughness and estimates of the area of contact, yet, electrostatic forces are relatively insensitive to surface roughness in the contact region. This range-of-effect behavior is discussed in more detail after the section below describing image-charge forces acting on particles. Walton [2007] provides a brief review of various methods utilized to measure surface energies of solids and particulate materials.

3. Image-charge Forces

When a charged particle is near a conducting surface, the charge on the particle induces a redistribution of charge in the conductor. Because the electric field at the surface of a conductor is always perpendicular to that surface (or there would be currents flowing on the surface), it follows that the potential on that surface is always a constant. That boundary condition can be satisfied by considering the field produced by an 'image' charge of opposite sign, located the same distance 'inside' the conductor that the center of charge is 'above' the surface. By uniqueness, the combined electric field from the primary charge and the image charge correctly describes the electric field in the vicinity of the charge near a conducting surface. The electrostatic Coulomb force acting on a point charge, Q, due to its image 'inside' the conductor is

$$F_I = -\frac{QQ'}{4\pi\varepsilon_0 D^2}, \tag{14}$$

where Q' is the image charge (equal in magnitude to Q), and D is the distance between the charge and its image $D = 2h$, where h is the height of the charge above the surface. For a finite-size particle, of diameter D_p, carrying a charge uniformly distributed on its surface, a similar relation holds, and $D \approx (D_p+s)$, where s is the 'gap' spacing between the sphere and the conducting surface. To correctly account for finite sized particles comprised of real dielectric materials the dipole and higher moment distributions induced by the image charge also need to be taken into account. The orientation of the dipoles are such as to increase the attraction due to the monopole terms, so that Eqn (14) represents a lower bound on the image charge force on a spherical particle (near a conducting surface) with a uniformly distributed charge Q on the particle's surface.

Approximating an irregularly shaped dielectric particle as spherical, and further approximating the additional contribution from polarization with a correction factor, β, the electrostatic image force on the particle near a planar, conductive substrate is given approximately by,

$$F_I \approx -\beta\frac{Q^2}{4\pi\varepsilon_0 (D_p+s)^2} \tag{15}$$

where Q is the particle charge, D_p is the average diameter, ε_o is the permittivity of free space and β is a correction factor which depends on the polarization of the dielectric particle. (For a dielectric constant of $\kappa = 4$, $\beta = 1.9$ [Hays, 1988]). For a typical toner particle used in xerography with a charge-to-mass ratio of 15 mC/kg and an average toner diameter of $10\mu m$, the particle charge, Q is $8fC$, and the electrostatic image charge as calculated from Eqn (15) with $s << D_p$ is ~$10nN$.

Particles can attain charge from a variety of causes; however, the most common source of charge buildup in powder handling is triboelectric charge transfer. Tribocharging is likely to result in non-uniform distributions of charge over particle surfaces. The nonuniformity in charge distribution on particles can play a significant role in the adhesive effects of the charge.

Fig. 2 shows measured average toner adhesion forces obtained from centrifuge measurements compared to the image force model calculations (*i.e.*, Eqn. 15 with $s \approx 0$) as a function of the average toner charge-to-diameter ratio [Hays, 1994]. The measured values exceed the predictions of the uniform surface charge model by factors of from 5 to 50. The dependence of the measured adhesion on charge ratio eliminates van der Waals adhesion forces as an explanation for the difference, since surface adhesion forces would be independent of charge. (Note that typical toner particles are usually 'dusted' with a small quantity of ultra-fine fumed-silica to reduce the van der Waals forces to something on the order of ~$10nN$, see box on xerography). Hays [1994] proposed that the total charged area A_t on a tribo-electrically charged toner particle represents a small part of the total toner particle's surface area. Based on Hays' model, the total charge would be $Q = \sigma A_t$, where σ is the surface charge density (in the charged regions). A small fraction, like 20%, of the charged surface area, A_c, might be in close proximity to the conducting surface. If the extent of the charged areas in close proximity, A_c, is much larger than the average distance between the charged surface and the conducting substrate, the magnitude of the electrostatic forces of adhesion can be expressed as, $F_E = -\frac{\sigma^2 A_c}{2\varepsilon_0}$, and the total adhesion can be written as,

$$F_A = -\frac{\sigma^2 A_c}{2\varepsilon_0} - WA_c, \tag{16}$$

where WA_c represents a non-electrostatic (*i.e.*, surface-energy based) adhesion contribution. Literature estimates indicate contact charging can produce surface charge densities ranging from 0.5 to $5mC/m^2$ depending on the materials involved [Horn and Smith, 1992]. For $\sigma = 1mC/m^2$ and $Q = 8fC$, the electrostatic contribution to the adhesion force is ~$100nN$, which is comparable with measured values for toner particles [Hays, 1995].

Gady [1996] performed a series of AFM measurements on $3\mu m$ and $6\mu m$ polystyrene spheres (attached to an AFM cantilever and) brought toward an atomically flat, highly oriented pyrolytic graphite (HOPG) substrate. Polystyrene and HOPG lie at opposite ends of the tribocharging sequence (*i.e.*, they have large differences in their respective work functions) and thus can produce significant tribo-charging upon contact and separation. Gady used the change in frequency of a small driven oscillation of the cantilever to precisely determine the force and force gradient as functions of separation from the sub-

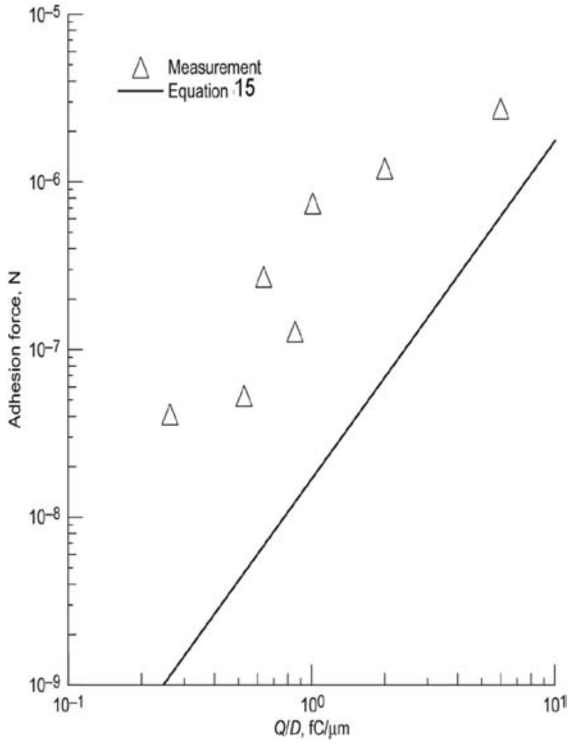

Fig. 2 Toner adhesion forces obtained from centrifuge measurements compared with image force model calculations (Eqn. 15 with $s \approx 0$, which assumes charge is distributed uniformly over the particle's surface) as a function of the average toner charge-to-diameter ratio [Hays, 1994].

strate. By first contacting the substrate, to establish a precise position for 'contact', and then separating the sphere from the substrate and operating in a non-contact mode, Gady was able to map the force-separation relation (until the snap-to-contact point when the sphere was a few nano-meters above the surface). Since local charge patches in the region of contact produced high local electric fields (~2.5×10^8 V/m), these measurements were conducted under a modest vacuum (10^{-2} Torr) in order to avoid discharge via breakdown in air. **Fig. 3** shows a representative force displacement curve for a $3\,\mu m$ polystyrene sphere. Also shown are theoretical curves for van der Waals force and an electrostatic force based on an assumed charge patch located within a sphere (inside the particle) collocated with the contact spot and having a radius equal to the JKR contact spot radius. The solid line on the **Fig. 3** is the sum of the two theoretical curves. The cross-over point where the van der Waals exceeded the charged-patch electrostatic force (for these highly-charged contacts) varied from $3nm$ to $10nm$ depending on the charge on the sphere. At separations closer than the crossover point van der Waals forces dominated the attractive force measured. (Not shown is a curve that would be appropriate for a charge uniformly distributed over the surface of the polystyrene sphere. Such a force-displacement curve would be lower in magnitude and much lower slope than the patch-charge curve at close separations).

Gady's small charged sphere analysis simplifies the mathematics somewhat over having the charge located only on a patch of the particle surface material; however, it still captures most of the physics of having the tribo-electric charge located near the contact region. Gady's approach is equivalent to modifying Eqn 15 to represent the image charge force due to a local charge patch of diameter $D_Q = 2a$, where a is the JKR contact spot radius,

$$F_{I_L} \approx -\beta \frac{Q_L^2}{4\pi\varepsilon_0 (D_Q + s)^2}. \tag{17}$$

A more complex mechanism than localized charge-patches, involving a non-uniform distribution of effective electron work-function values over the surface of particles, has also been proposed as an explanation of the high electrostatic attraction for small charged particles [Pollock, et al, 1994]; however, the simpler localized tribo-charged patches as described by Hays [1994] and/or Gady [1996; and Gady *et al*, 1996] appear to adequately describe the observed phenomena. In Gady's experiments with spherical particles near a smooth substrate, the van der Waals force did not dominate over image-charge forces until the gap spacing was on the order of $10nm$. Most irregularly shaped particles produced through comminution would have surface roughness at least as great as 10's of nanometers, lowering the effective attraction at contact by an order of magnitude or more.

4. Distance-dependence and Range-of-effect of Fine-particle Adhesive Forces

Range of effect – The electric field in the vicinity of a large charged surface (like the nearly uniformly charged lunar surface) decreases very slowly with distance away from the surface. The static-electric force on a charged particle in such a slowly varying electric field, likewise, varies slowly with distance. Because of their relatively long range nature, electrostatic forces have the potential to contribute both as long-range forces affecting *motion* of fine particles (especially for suspended particles) and as short-range forces affecting their *adhesion/cohesion*, depending on the net charge on a particle and on the surface charge-density near a contact point. While van der Waals forces, electrostatic forces between

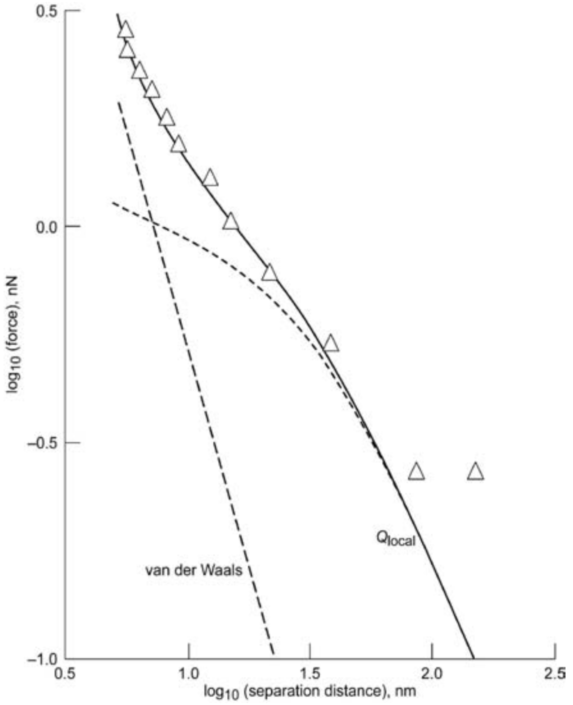

Fig. 3 AFM-measured force-displacement for a triboelectrically charged 3μm polystyrene sphere near an atomically flat HOPG substrate (symbols), van der Waals force (*i.e.*, Eqn. 5) (dashes), and a local charged-patch (of a JKR-contact-spot size, *i.e.*, Eqn 17) with Q_L adjusted to best fit the data (dotted line). Solid line is sum of van der Waals and charged-patch curves [Gady et al, 1997].

charges, and electrostatic image-forces, all vary as the inverse square of distance; the effective *distance* at closest approach (where the force has its maximum value) differs in each case. As described by Eqn 5, the net van der Waals force for a single spherical/planar contact (asperity or particle) depends on the distance between the centers of the surface atoms in the two bodies at their point of closest approach. This inverse square relation is not a fundamental property of the dipole forces which comprise the van der Waals interaction. Those forces all decay with the inverse seventh power of the distance on a molecular level. The inverse second power comes from the integrated effect of all (relatively near) atoms in a sphere and in the nearby plane. It should also be noted that at distances greater than approximately 10*nm*, retardation effects, of induced dipoles on the molecular level, begin to reduce the effective van der Waals interaction below that predicted by Eqn 5. Such effects are usually modeled as reductions in the Hamaker constant with distance beyond 10*nm* [Isrealachvili, 1991]. Thus, for a variety of reasons, surface-energy related adhesion forces are very short range and primarily affect fine particles when they are in contact with each other or touching surfaces. The electrostatic force on the other hand varies as the inverse second power of the distance between the two apparent centers of charge. If we consider the distance over which a force decreases by a fixed factor, say two orders of magnitude, below its maximum value at ‘closest approach,’ as one measure of the range-of-effect of that force, then we can see significant differences between the *effective ranges* of these three inverse-distance-squared forces (*i.e.*, Eqns 5b, 15b, and 17b),

$$F_{vdW} = \frac{K_{vdW}}{s^2}$$ van der Waals interaction (5b)

$$F_I \approx \frac{K_I}{(D_p + s)^2}$$ Image charge force − uniform charge on particle of diameter, D_p (15b)

$$F_{I_L} \approx \frac{K_{L_I}}{(D_Q + s)^2}$$ Image charge force − local charge patch, diameter ≈ D_Q (17b)

Xerography

(A technology utilizing tribo-charging and electrostatic transfer of fine particles)

Researchers and technologists developing and improving electrophotographic processes (Xerography) have been successfully charging, transporting, removing and precisely depositing 10 micron-scale toner particles onto and off of various surfaces for nearly 50 years. Since its introduction (late 1950’s) much of the development in xerographic technology has been by cut-and-try engineering methods. During the last two decades, our understanding of the underlying principles and forces involved in xerography have advanced dramatically, especially with the advent of various surface-force and scanning-probe measurement methods. Nonetheless, a cursory survey of current literature on particle adhesion, shows that, even today, several aspects of the process remain incompletely understood. [The following qualitative description, most closely fits the dry-powder xerographic technology of about a decade ago, when it was dominated by black-and-white dry-powder methods, but it still provides insight on methods that have been utilized to 'control' electrostatic- and tribo-charging of fine particles].

Xerography (continued)

The mechanics of the xerographic process require both electrostatic adhesion/cohesion and interparticle surface-energy-related forces to dominate at different stages. The average surface cohesive forces acting among the toner particles are usually 'adjusted' to a fixed (relatively low) value by blending the toner particles with nano-scale ($\sim 20nm - 40nm$) fumed-silica fines with a weight − fraction of fines in the range of 0.01% to 1%. These fines, deposited on the larger-particle surfaces, act as *props* to keep most of the potential surface area at contacts far enough apart that the short-range van der Waals surface forces are greatly reduced. The relatively small contact area of the few propping fines, and the remaining contacting asperities on the particles, provide an appropriate level of cohesion for the process to work.
In xerography the toner particles are triboelectrically charged by mixing with larger carrier beads. The charge on the toner particles enables the electrostatic transfer of these particles between surfaces, allowing the development of an electrostatic latent image and subsequent transfer of the developed image to paper. Because of the requirement for toner transfer, the cohesion and adhesion properties of toner particles are of considerable importance in optimizing the electrophotographic process [Hays, 1995; Pai and Springett, 1993].
In xerography tribocharging is controlled through selection of the material, for the carrier beads (with an appropriate value for its work-function) and toner particles, and by the intensity and duration of 'mixing'. The surface energy forces are controlled by adjusting the mass fraction of ultra-fine fumed silica blended with the toner; and, the electro-static force is controlled by the electric fields/potentials applied externally. Many of these quantities will be beyond the control of lunar explorers and in-situ resource utilization designers dealing with fine particles occurring on the moon's surface (and they may not be controllable in terrestrial powder processing operations).

where the K's and D's depend on material, size and/or charge but do not change with distance, s.

At 'contact' the distance between surface molecules centers, s_o, is approximately $4\mathring{A}$ (or $\sim 0.4nm$), and $D_p \gg D_Q \gg s_o$, so that the closest approach values of the denominators in these relations are usually much larger for electrostatic forces than the molecular-scales of van der Waals forces.

The van der Waals force which varies as the inverse second power of the *gap spacing* (e.g., Eqn 5b), is a very short-range force compared to typical particle dimensions − falling by two orders of magnitude by the time the surfaces are $40\mathring{A}$ ($\sim 4nm$) apart, and by four orders of magnitude by the time they are $40nm$ apart. In comparison, an image-charge force for a charged particle near a conducting surface, Eqn 15b, would decrease two orders of magnitude over a separation distance from touching (e.g. 1-diameter) to ten *particle* diameters (a distance of $10\mu m$ for a $1\mu m$ particle, or $100\mu m$ for a $10\mu m$ particle). The image-force from a small patch of concentrated charge on a particle's surface (Eqn 17b), say $100nm$ across, would also decrease more slowly than the van der Waals force (Eqn 5b). On a $10\mu m$ particle, a $100nm$ diameter patch-charge image-force would decreasing two orders of magnitude going from contact with a conductor to a separation distance of approximately $1\mu m$, according to Eqn 17b. This is 250 times the distance over which van der Waals force would decrease by two orders of magnitude. Thus it can be inferred that the image-force for a uniformly charged particle is, in effect, longer-range than the local charged-patch force, which is, in effect, longer-range than the van der Waals force.

Because their values change less rapidly with distance (near contact), the static-charge forces are less affected by surface asperities and roughness than are van der Waals forces. Thus, for small irregular particles coated with a light dusting of nano-scale fines (as is the case for xerographic toner particles) it is possible, with sufficient local charge deposition, for localized charge-patch forces to dominate over van der Waals surface forces even when the particles are 'contacting' the surface. Such may also be the case for small tribocharged lunar dust particles, or other fine irregular particles.

5. Effects of Particle Size on Fine-particle Adhesive Forces

One of the aims of this review is to determine under what conditions various forces are likely to domi-

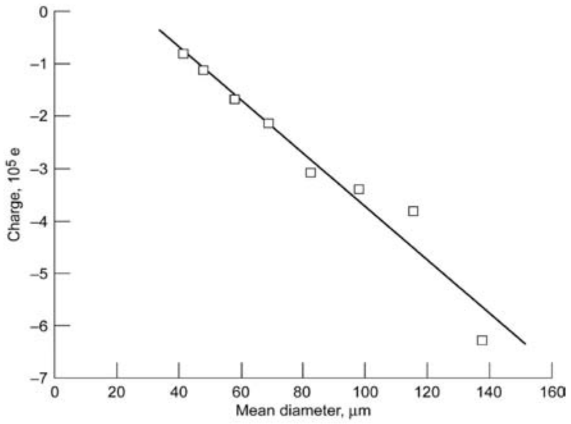

Fig. 4 The charge on JSC-Mars-1 from a contact with a Co surface for different dust sizes [Sternovsky *et al*, 2002].

nate in the adhesion of particles to surfaces. Because of the way surface forces scale relative to body forces and drag forces, surface phenomena are usually expected to dominate at small particle sizes. Gravity and inertial forces (*e.g.*, response to vibration, shaking or acceleration) scale with the mass of an object, $M = \rho V = \rho(4/3)\pi R^3$, where ρ is density (*e.g.*, kg/m^3), V is volume (*e.g.*, m^3) and R is the 'radius' of the object (assuming a spherical shape). Thus, as particles decrease in size the force of gravity, and that due to accelerations, would decrease with the cube of the particle size. The aerodynamic drag at high Reynolds numbers scales with the cross-sectional area of an object in the flow. As particle size decreases high-Reynolds-number drag forces decrease with the square of the particle size. Likewise, the surface area of a particle decreases with the square of its diameter. Thus, we might expect that most surface related phenomena will scale with the square of particle size (like the surface area). In fact, many phenomena, including some surface related ones, decrease more slowly with particle size than the square. Several important phenomena scale nearly linearly with particle size. As particle size decreases, phenomena which scale linearly with size will eventually dominate over phenomena that scale with higher powers of the size (like gravity, inertial forces, or high-Reynolds-number drag forces). Among phenomena that scale linearly with size, other controlling parameters need to be examined in order to determine which will have a greater influence on particle motion or behavior.

As previously described, the integrated effects of van der Waals interactions acting on a spherical particle near a surface (e.g., Eqn 5) depends linearly on the radius of curvature in the contact region (e.g., the van der Waals force varies linearly with particle size).

It is also well known that the electrical capacitance of an isolated conducting sphere depends linearly on the size of the sphere [Corson & Lorrain, 1962],

$$C = 4\pi\varepsilon_o R_p. \tag{18}$$

The charge carried by a particle with a uniform surface potential, Φ_s, is proportional to its capacitance,

$$Q = C\Phi_s = 4\pi\varepsilon_o \Phi_s R_p, \tag{19}$$

a quantity which varies linearly with particle size. In a uniform electric field, **E**, the force on a charged particle, also, would vary linearly with particle size,

$$\mathbf{F}_\mathbf{E} = Q\mathbf{E} = 4\pi\varepsilon_o \Phi_s \mathbf{E} R_p. \tag{20}$$

While the formula for capacitance (Eqn 18) is strictly valid only for conducting spheres, experimental evidence indicates that triboelectric charging of non-conducting particles, also, varies nearly linearly with particle size.

Fig. 4 shows the dependence of tribocharge with particle size for simulant JSC-1-Mars-1 particles, each experiencing the same type and duration of repeated contact with a Co surface [from Sternovsky *et al*, 2002].

It should be noted that, the static image-charge force, F_I, acting on a charged particle depends on the square of the charge on the particle, and if non-conducting particles carried uniformly distributed surface charges varying with size according to Eqn 19 and they were in contact with a conducting surface, they would experience an attractive image-charge force of,

$$F_I \approx \pi\varepsilon_o \Phi_s^2 \approx 0.05\ \Phi_s^2\ (nN/V^2), \tag{21}$$

independent of particle size! For particle sets comprised of particles with net charges proportional to their size, we would expect that below some threshold size, image-charge adhesion forces would dominate over surface-energy related forces.

Under certain circumstances, sets of particles are more likely to acquire charges that vary according to their effective cross-sections, and thus would be expected to have net charges that vary with the square of the particle size. For example, charging of micron-scale conductive aerosol water droplets via capture of like-charged ultra-fine particles in the upper reaches of thunderstorms results in a maximum charge per droplet that varies approximately with the square of the droplet size [Pruppacher & Klett, 1997, as cited in Tinsley et al, 1999]. For particle sets with charge distributions that scale with the square of particle size, the effective image-charge forces at contact would decrease in direct proportion with the particle size, and fine-particle adhesion would be dominated by surface-energy interactions.

Discussion

From the works of London, Hamaker, Feynman, Lifshitz, Keesom, Debye and others we have a reasonably good understanding of the molecular-scale sources of van der Waals forces; however, the integrated macroscopic effects of van der Waals forces as described above are only straightforward to calculate for idealized configurations. For most real contacts between macroscopic objects, the adhesive forces can differ substantially from what would appear to be a straightforward integration of a known intermolecular potential over all nearby molecular centers. It is the relatively short-range nature of van der Waals forces (from a macroscopic perspective) which give rise to much of the 'uncertainty' in calculating their effects for real macroscopic contacts. As pointed out by Isrealachvili [1991] one source of uncertainty in predicting adhesion forces from models of van der Waals interactions is uncertainty associated with the effective surface energy, since even monolayers of gas molecules adsorbed on a surface can affect the value of the adhesive force at contact. Two other factors which contribute significant uncertainty to making quantitative predictions of adhesion forces are *surface morphology* (or roughness), and *deformation* (elastic and plastic) in the contact region. Measurements of pull-off forces for small particles, can be substantially less than the values predicted a *prori* from known surface energies or Hamaker constants for the materials involved, with the over prediction by the theory increasing as the particle size decreases. Large soft spheres, on the other hand, adhere in almost exact agreement with the Johnson, Kendall, Roberts (JKR) theory [1971]. JKR theory accounts for elastic deformation in the contact region, but is still within 30% of the Derjagian approximation for undeformed spheres, e.g. Eqn (6), at contact. Surface roughness (e.g. detailed surface morphology) has been identified as one major contributor to the discrepancy between measured pull off forces for 'real' particles and theoretical predictions for smooth surfaces [Rabinovich, et al, 2000 and 2002; Rimai & Quesnel, 2001; Mizes, 1994; Schaefer et al, 1995]. Likewise as the particle size (or the radius of curvature in the contact region) decreases, it is possible for plastic deformations to occur at the contact, even with no external loads; however, plastic deformation are usually expected to cause less than a factor of two increase in effective adhesion forces (unless external loads are also applied to the contacting bodies).

Because of the short-range nature of adhesive surface forces, it can be said with some certainty that adhesive surface forces are likely to be a major concern *only* when attempting to remove particles from surfaces. Under most circumstances, surface forces will have *only a minimal contribution* as to whether or not particles make contact with surfaces. [This is contrary to the potential effects of surface forces on particles in a third media, like in aqueous suspensions, where net surface forces can have a strong influence on whether 'contact' occurs]. Static electric forces, and in particular, image-forces, can be a significant factor in adhesion. These forces have a much longer effective-range than surface energy interactions. Thus they can have a significant effect on both the *motion* and on the *adhesion* of fine particles on surfaces.

Rough estimates of distance ranges over which various force are likely to dominate (for 10-*micron*-scale particles under dry conditions) might be summarized as follows, where, s is the distance between a particle and a (conducting) surface:

- $s > 0.1$ micron, electrostatic forces due to the *net charge* on particles may dominate

- $100nm > s > 10nm$, electrostatic forces due to localized *charge patches* on particle surfaces may have a significant effect

- $s < 10nm$, van der Waals (surface energy related) forces may dominate (if surfaces are smooth enough and/or surface energies high enough).

Very rough, irregular particles or particles with a dusting of nano-scale fines may have very low effective van der Waals adhesion forces. For such cases, the electrostatic and image forces can exceed surface energy forces for particles considerably larger than 10 microns (and/or with lower charge densities than are typical in xerographic processes).

Acknowledgments

This work was supported by NASA under contract NNC06VC87P. The project manager for this work was Dr. Allen Wilkinson, Glenn Research Center. Dr. Wilkinson's encouragement and patience and NASA's support are gratefully acknowledged.

References

Corson, D.R., and Lorrain, P. (1962): "Introduction to Electromagnetic Fields and Waves", W.H. Freeman & Co. San Francisco and London.

Debye, P. (1920) : Phys Z., 21, p.178.

Derjaguin, B.V. (1934) : Kolloid Zeits, 69, pp.155-164.

Derjaguin, B.V, Muller, V.M. and Toporov, Y.P. (1975) : J. Colloid Interface Sci, 53, pp.314-326.

Feynman, R.P. (1939): Forces in Molecules, Phys. Rev. 56, pp.340 – 343.

Gady, Barrett, L. (1996): Measurement of Interaction Forces Between Micrometer-Sized Particles and Flat Surfaces Using an Atomic Force Microscope, PhD Thesis, Purdue University.

Gady, B, Reifenberger, R., Rimai, D.S. and DeMejo, L.P. (1997): Langmuir 13, pp.2533-2537.

Gady, B, Schleef, D., Reifenberger, R., DeMejo, L.P. and Rimai, D.S. (1996): Phys Rev B, 53, pp.8065-8070.

Hamaker, H.C. (1937): Physica 4, pp.1058-1072.

Hays, D.A. (1988) : in "Particles on Surfaces 1", Detection, Adhesion and Removal, K.L. Mittal (Ed.) pp.351-360, Plenum Press, NY.

Hays, D.A. (1994): Toner Adhesion, "Advances in Particle Adhesion", pp. 41-48, D.S. Rimai, and L.H. Sharpe (Eds).

Hays, D.A. (1995): Adhesion of Charged Particles, "Fundamentals of Adhesion and Interfaces", pp. 61-71 D.S. Rimai, L.P. DeMejo, and K.L.Mittal (Eds), VSP Utrecht, Netherlands.

Hertz, H. (1882): Über die Berührung fester elastische Körper (On the contact of elastic solids), J. reine und angewandte Mathematik, 92, pp.156-171. (for English translation see Miscellaneous Papers by H .Hertz, (Eds) Jones and Schott, London, Macmillan, 1896)

Horn, R.G., and D.T. Smith (1992): Science 256, pp.362-364.

Keesom, W.H. (1921): Phys Z., 22, p.643.

Krupp, H. (1967): Particle Adhesion, Theory and Experiment, Adv. Colloid Interface Sci., 1, pp.111-239.

Isrealachvili, J. (1991): "Intermolecular and Surface Force", 2nd Ed. Academic Press (Elsevier).

Johnson, K.L., Kendall, K. and Roberts, A.D. (1971): Surface energy and the contact of elastic solids, Proceedings, Royal Society, A324, pp.301-313.

Johnson, K.L. (1985): "Contact Mechanics", Cambridge Univ. Press, London.

Lian, G., Thornton, C., Adams, M.J. (1993): A theoretical study of the liquid bridge forces between two rigid spherical bodies, J. Coll. Int. Sc., 161, pp.138-147.

London, F. (1930): Z. Phys. Chem, B11, pp.222-251.

London, F. (1937): Trans. Faraday Soc, 33, pp.8-26.

Maugis, D., and H.M. Pollock, (1984): Acta Metall. 32, pp.1323-1334.

Mei, R., Shang, V, Walton, O.R. and Klausner, J.F. (2000): Concentration non-uniformity in simple shear flow of cohesive powders, Powder Technol., 112(1-2), pp.102-110.

Mizes, H.A. (1994): Surface Roughness and Particle Adhesion, "Advances in Particle Adhesion", D.S. Rimai & L.H. Sharpe (eds) Gordon & Breach Pub. pp.155-165.

Nagai, S.S.H. (2005): Multi-Scale Analysis and Simulation of Powder Blending in Pharmaceutical Manufacturing, Thesis, Massachusetts Institute of Technology, Chemical Engineering.

Pai, D.M., and Springett, B.E. (1993): Rev. Modern Phys. 65 (1), pp.163-211.

Pollock, H.M., Burnham, N.A. and Colton R.J. (1994): Attractive Forces Between Micron-Sized Particles: A Patch Charge model, D. S. Rimai and L.H. Sharpe (Eds.) , "Advances in Particle Adhesion", pp.71-86, Gordon & Breach Pubs.

Pruppacher, H.R., and Klett, J.D. (1997): "Microphysics of Clouds and Precipitation", 2nd ed. Kluwer, p.954.

Rabinowicz, E. (1965): "Friction and Wear of Materials", John Wiley and Sons, NY

Rabinovich, Y. J., Adler, J., Ata, A., Singh, R. and Moudgil, B. (2000): Colloid Interface Sci. 232, pp.10-16, and pp.17-24.

Rabinovich, Y., Adler, J., Esayanur, M., Ata, A., Singh, R. and Moudgil, B. (2002): Adv. Colloid Interface Sci. 96, pp.213-230.

Rimai, D.S., Demejo, L.P. and Bowen, R.C. (1994): The Adhesion of Particles to Polymer Coated Substrates, "Advances in Particle Adhesion", p139-154, D.S. Rimai and L.H. Sharp (eds) Gordon and Breach Pub, Amsterdam,.

Rimai, D.S., Demejo, L.P. and Bowen, R.C. (1995): Mechanics of Particle Adhesion, "Fundamentals of Adhesion and Interfaces", pp1-23, D.S. Rimai, L.P. DeMejo and K.L. Mittal (eds) VSP.

Rimai, D.S., and Quesnel, D.J. (2001): "Fundamentals of Particle Adhesion", Global Press.

Salisbury, J.W., Glaser, P.E., Stein, B.A. and Vonnegut, B. (1964): Adhesive Behavior of Silicate Powders in Ultrahigh Vacuum, J. Geophys. Res. 69, pp.235-242.

Schaefer, D.M., Carpender, M ., Gady, B., Reifenberger, R., Demejo, L.P. and Rimai, D.S. (1995): Surface roughness and its influence on particle adhesion using atomic force techniques, "Fundamentals of Adhesion and Interfaces", pp. 35-48.

Sternovsky, ?, Zoltán, ?, Robertson, S., Sickafoose, A., Colwell, J. and Horányi, M. (2002): Charging of lunar and Martian Dust Simulants, Journal of Geophysical Research, 107, No. E11, 5105, doi:10.1029/2002JE001897.

Thornton, C. and Ning, Z. (1998): A theoretical model for the stick/bounce behaviour of adhesive elastic-plastic spheres, Powder Technology, 99, pp.154-162.

Tinsley, B.A., Rohrbaugh, R.P., Hei, M. and Beard, K.V. (2000): Effects of image Charges on the Scavenging of Aerosol Particles by Cloud Droplets and on Droplet Charging and Possible Ice Nucleation Processes, J. Atmospheric Sci. 57, pp.2118-2134.

Walton, O.R. (2007): Adhesion of Lunar Dust, NASA/CR-2007-214685, NASA report available as pdf file at: http://gltrs.grc.nasa.gov/reports/2007/CR-2007-214685.pdf.

Xue, X. and Polycarpou, A.A. (2007): An improved meniscus surface model for contacting rough surfaces, Journal of Colloid and Interface Science、311-1, pp.203-211.

Nomenclature

A	Hamaker constant	[J]
A_t	Total surface area (of a charged particle)	[m^2]
A_c	Area of the charged portion of a particle's surface	[m^2]
$\AA$	Angstrom − length unit = 10^{-10} m, or 0.1nm	
α	Relative approach distance (after initial contact) between two spheres, also amount of overlap that would have occurred without surface deformation)	[m]
α_s	Surface displacement (negative) in tension at separation (JKR model)	[m]
C	Capacitance	[C/V]
C_f	Material dependant constant (for interatomic force relation)	[m^{7}kg^{-1}s^{-2}]
d	Distance between centers of atoms	[m]
D	Distance between charges	[m]
D_p	Diameter of a (charged) particle	[m]
D_Q	Diameter of a local charge patch	{m]
ε_0	Permittivity of free space	[8.8542×10^{-12} C^2 N^{-1} m^{-2}]
E	Youngs modulus	[GPa]
$\mathbf{E}$	Electric field (in Eqn 20 only)	[V/m]
F	Force	[N]
F_c	Cohesive (attractive) pull-off force	[N]
F_{cJKR}	Cohesive pull-off force JKR model	[N]
F_{cp}	Cohesive force per unit area for two planes in contact	[N/m^2]
$F_{c\text{-}plastic}$	Approximate cohesive force for plastically deformed spheres in contact	[N]
$\mathbf{F_E}$	Electrostatic portion of the force of adhesion	[N]
F_T	Total force of adhesion including both electrostatic and surface-energy terms	[N]
F_I	Electrostatic image-charge force acting on a charge near a conducting surface	[N]
F_{IL}	Electrostatic image-charge force due to a local charge patch near a conducting surface	[N]
F_{vdW}	van der Waals cohesive/adhesive force	[N]
F_s	Cohesive (attractive) force acting between (undeformed) contacting spheres	[N]
F_{ss}	Cohesive force acting between two equal size spheres	[N]
F_{sp}	Cohesive force acting between a sphere and a plane	[N]
F_Y	Applied load at which plastic yielding begins	[N]
$\Psi(d)$	Interatomic pair potential (as a function of distance, d).	[J]
Φ_s	Surface (electrical) potential	[V]
γ	Surface energy (per unit area)	[mJ/m^2]
h	Height above planar conducting surface (to where electric charge is located)	[m]
ν	Poisson's ratio	
M	Mass	[kg]
ρ	Density	[kg/m^3]
Q	Static electric charge	[C]
Q'	Image charge	[C]
Q_L	Charge located in a localized charge-patch (near the contact point)	[C]
R	Radius	[m]
R_p	Particle radius	{m]
R_{cY}	Particle radius below which plastic deformation expected with no applied load	[m]
R^*	Effective or reduced radius for two spheres of radii, R_1 and R_2; $R^*=R_1R_2/(R_1+R_2)$	
s	Gap spacing (distance between surfaces atom centers) for two near objects	[m]
s_0	Distance between surface atoms of contacting bodies at closest approach	[m]
σ	Surface charge density	[C/m^2]
V	Volume	[m^3]
$w_p(s)$	Energy per unit area as a function of separation distance, s, between two planar surfaces	[mJ/m^2]
Y	Yield strength	[GPa]

Author's short biography

Otis R. Walton

Otis Walton received his PhD in Engineering Applied Science from the University of California in 1980. While at Lawrence Livermore National Laboratory (30+ years) he specialized in modeling the properties of porous and granular materials, and developed discrete-element software to simulate the deformation and flow behavior of particulate assemblies. He spent 3 years at the University of Florida's Engineering Research Center for Particle Science, and 3 years in the pharmaceutical industry characterizing powders for pulmonary delivery of active pharmaceutical ingredients, before starting the engineering analysis and software development firm, Grainflow Dynamics, Inc. He is currently developing discrete-element simulation models for lunar regolith and also utilizing FEM codes to simulate explosions and hypervelocity impacts in geologic media. walton@grainflow.com

The Particle Design of Cellulose and the Other Excipients for a Directly Compressible Filler-Binder[†]

Hiroto Miyamoto
KNOWKATSU[1]

Abstract

Cellulose and saccharide are commonly used filler-binder. This summary refer to the technology for high performance filler-binder of direct compression, using these two materials. In case of saccharide filler-binder, spray dry technology and size controlling of primary particle were the key technology. In case of cellulose filler-binder, two different approaches were made. One was co-processing approach and the other was particle shape controlling approach. Some applications using high performance filler-binder were also introduced.

Keywords: filler-binder, direct compression, microcrystalline cellulose, compactibility, lactose, high performance

Introduction

It is well known that the majority of pharmaceuticals in the market are oral solid dosage form. It is said that the oral solid dosage form will continue to be the mainstream of the pharmaceutical formulations in the future and tablet is the major formulation within the oral solid dosage form. Tabletting seems grownup technology, but there still remain the unknown factors of the technology and there are many points which should be improved. Tablets consist of a lot of pharmaceutical excipients and active ingredients. Compactibility is one of the most important functions within the various functions of pharmaceutical excipients.

There are many substances which describe the function of high compactibility within the pharmaceutical excipients. These materials are divided into two categories: a saccharide group and a microcrystalline cellulose group. In this paper, I have summed up the technology for the high-compactibility excipients from the viewpoint of particle design, mainly focused on the microcrystalline cellulose which considered as the most efficient ingredient for compaction.

1.1 High-compactibility saccharide

1.1.1 High compactibility lactose

Lactose is one of the most commonly used pharmaceutical excipients. It is known that the compactibility of lactose highly depends on the process. **Fig. 1** shows the correlation between compactibility and the grade of lactose (offered by DMV Japan). Since beta anhydrous lactose (DCL-22) has different crystal form, we cannot compare it simply in the same system, but we can compare the other lactose which has the same crystal form: alpha lactose mono hydrate (DCL-14, DCL-11, DCL-15 and 100M). Within the alpha lactose mono hydrate group, crystalline lactose 100# (100M) shows the lowest hardness. Then pre-granulated lactose (DCL-15) gives higher hardness of the tablet. Next to the pre-granulated lactose comes the spray-dried lactose. It is well known that pre-granulation or spray drying make goods better compactibility. Both DCL-14 and DCL-11 are made by spray drying methods with the same crystalline form. But the lactose which carried out spray drying of the fine-ground alpha lactose (DCL-14) shows the highest compactibility in the chart. It means that the compactibility of lactose relates to the size of crystal in granules also. **Fig. 2** shows the scheme.

Beta anhydrous lactose is made by drum drying followed by grinding. It is said that the sharp particle shape of beta anhydrous lactose particle is the reason of the high-compactibility function. Correctly speaking, beta anhydrous lactose contains about 10% of alpha lactose. The content of alpha lactose depends on the production temperature. Because beta anhydrous lactose consists of a mixture of two crystal phase, and because it dry up before crystal grown up, it consists of small sized beta anhydrous crystal. The small sized crystal might be another possible reason for the high-compactibility of beta anhydrous lactose.

[†] Accepted: June 26, 2008

[1] 4-50-3706 Minamioizumi, Nerima-ku, Tokyo, 178-0064 Japan

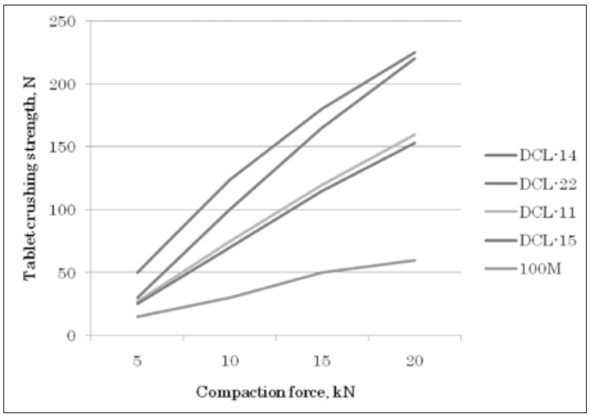

Fig. 1 Hardness of the tablet made from various lactose.

Lubricated with 0.5% mg stearate (5min. mixing), Kilian rotary press, 30,000 tab/hr,250mg tablet, 9mm flat punches.

(Offered by DMV –Fonterra Excipients)

1.1.2 The other high compactibility excipients

Fig. 3 shows high compactibility mannitol and **Fig. 4** shows high compactibility sorbitol respectively. Each product seems to be made by spray-drying method. It shows that the primary particle in each photo consists of fine crystal. It seems that the same concept as alpha lactose is also used to attain the high compactibility excipients for each saccharide system.

1.2 Comparison of saccharide system and microcrystalline cellulose system

The high compactibility saccharides, which considered to be made by spray drying, were studied through the brochure. Each of them uses granulated lactose as a comparative example to show the high compactibility of their products.

Since each company uses different unit systems and also they use the different evaluation systems in their brochure, we cannot compare each high compactibility product correctly form the presented data. I converted each unit and plotted it to a graph (**Fig. 5**) to see rough image of these systems, although unified comparison cannot be made. Even though we cannot compare in detail for each products in **Fig. 5**, it shows that there is big difference between the microcrystalline cellulose group and the saccharide group. It says that the microcrystalline cellulose group show much higher performance of compactibility compared with the saccharide group[1)].

1.3 Microcrystalline cellulose system

Microcrystalline cellulose is well known high compactibility products. In recent years, high-performance microcrystalline celluloses were lunched as research of the material progressed. I would like to focus on microcrystalline cellulose and to describe the history of invention, the feature of a material, development of the new material, and the characteristic of new materials.

1.3.1 Discovery of microcrystalline cellulose

Microcrystalline cellulose is reported by O.A.Battista and others of the American viscose Co., Ltd. in 1962[2)]. At that time, the authority of cel-

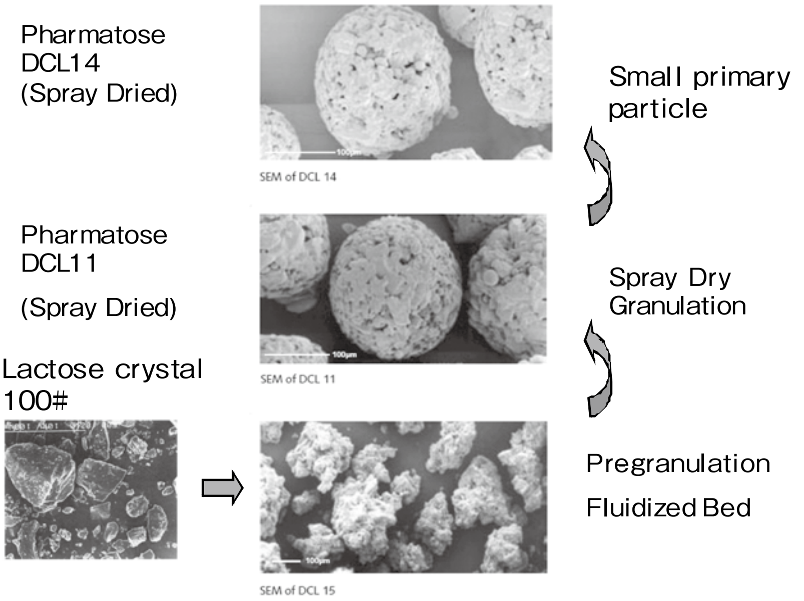

(Photos were offered by DM-V Fonterra Excipients)

Fig. 2 Development for better compactibility.

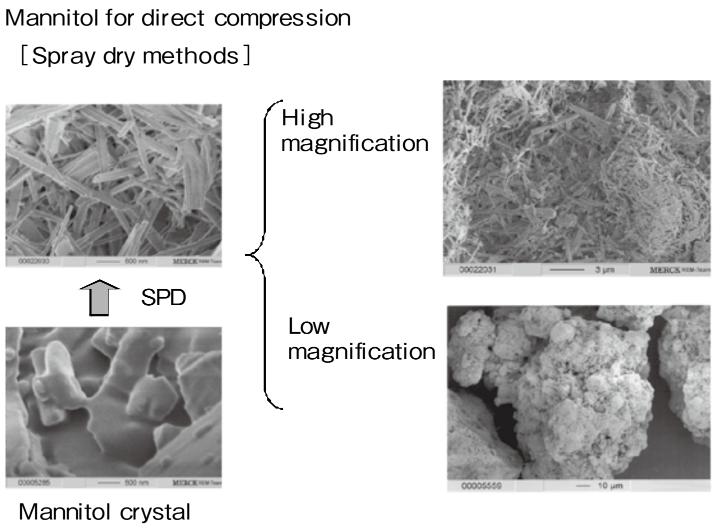

(Photos were offered by Merck Japan)

Fig.3 Mannitol for direct compression.

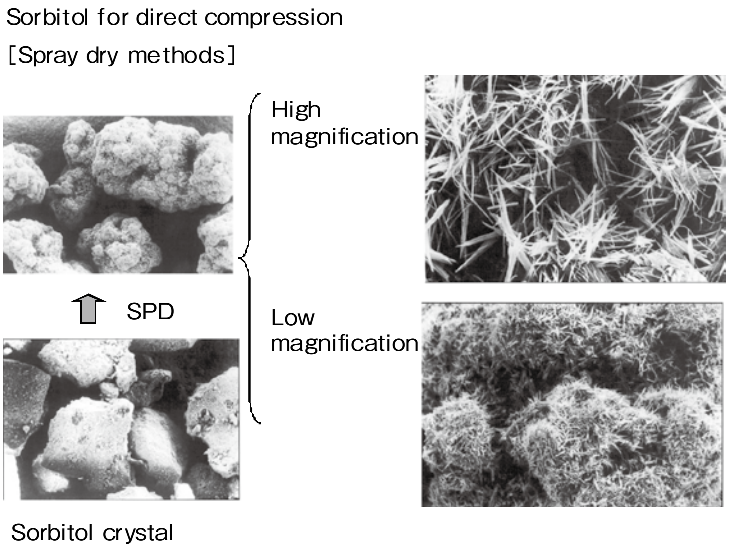

(Photos were offered by Merck Japan)

Fig. 4 Sorbitol for direct compression.

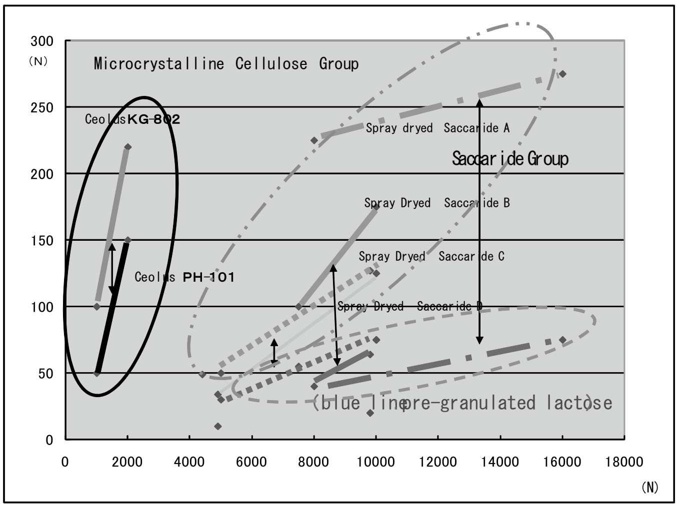

Fig. 5 Compactibility of cellulose and saccharide an overview.

lulose had gathered in the company of viscose rayon: American viscose. When cellulose was hydrolyzed and dried, white powder was made. But they did not know how to use it. They try to use it to diet food etc. Just then a researcher of SmithKline Corp. was studying direct compression technology. He heard of this new white powder and tried to use it to direct compression. It turned out to be the best matched material for direct compression.

As it was often heard in a success story, the microcrystalline cellulose was not aimed to develop for the direct compression.

1.3.2 Microcrystalline cellulose

I would like to explain microcrystalline cellulose a little more in detail. A cellulose molecule has the structure in which the glucose ring chained to make a straight line. Many glucose ring chain ran in parallel, formed the hydrogen bond between molecules into next chain, and became bunch-like structure. This is a crystal of microcrystalline cellulose. These cellulose crystal structures exist in natural cellulose, and make a repetition unit (micro crystalline) with constant size of bunch and length. Micro crystallines are connected to form the long fiber (micro fibril). Cotton is the common example of the cellulose fiber usually seen in which cellulose micro fibril gathered. Cellulose micro fibril looks the similar image as the train (micro crystallite portion) which was connected many cars. The connection part of micro crystallite and micro crystallite and the crevice between micro fibril and micro fibril are roughly combined by the polysaccharide such as free cellulose which is not making crystalline, and or mannose and or xylose. It is the so-called amorphous portion of cellulose. If acid hydrolysis of the cellulose is carried out, acid will penetrate into the amorphous portion, and then hydrolysis will take place in this portion. But as acid cannot penetrate into the inside of micro crystallite, it remains micro crystalline in the cellulose structure. This is microcrystalline cellulose. In the electron microscopic picture of microcrystalline cellulose, willow leave-like micro crystallite is observed on the surface (**photo. 1**). It is said that microcrystalline cellulose works as a dry binder of tablet that it will be easy to carry out plastic deformation if compression force is received for such a structure.

Photo. 1

⟷
500 nm
(Offered by Asahi-Kasei chemicals)

1.4 Development of the high compactibility tablet binder: SMCC (Silycated Microcrystalline Cellulose)

When we use the microcrystalline cellulose for wet granulation methods, we often experience the low activity of microcrystalline cellulose as a tablet binder. It is said that this phenomena is caused by the horning of the microcrystalline cellulose. If microcrystalline cellulose soaked water then dried, water between the micro crystallite of cellulose make liquid bridge construction between micro crystallite particles at the first stage of drying, and then the liquid bridge let the micro crystallite particles attach tightly each other, making the hydrogen bond between particles, along with drying. Finally a horn like hard cellulose block is produced. This is called horning. Once horning is occurred, the hard particles of cellulose will not carry out plastic deformation when it receives compression force: reduced compactibility. If we adjust the water content precisely or by adding ethanol during wet granulation to avoid hydrogen bond formation, horning does not take place[3)]. But the controlling method is very delicate and troublesome work. SMCC was developed to prevent the horning[4)].

When SMCC was used for the direct compression methods, it gave higher hardness of the tablet than the tablet from microcrystalline cellulose[4)]. SMCC is consists of about 2% of colloidal silica and 98% of microcrystalline cellulose. SMCC is made by mixing these two materials in process, so that silicon particulates are distributed over the surface of microcrystalline cellulose particle then dried. The function of SMCC depends on the way of in-process mixing. The function of high compactibility cannot be obtained only by mixing the two kinds of composing powder products. Such product as SMCC is called “co-processed products,” which gets the special function by the synergistic effect of in-process mixing. Sherwood said that by the in process mixing, the fine particulates of colloidal silica covered on the surface of microcrystalline cellulose, and this construction is fixed by drying. He said that this construction prevent the horning of microcrystalline cellulose, caused by liquid bridge formation[4].

The two types of microcrystalline cellulose mixture: a simple mixture of microcrystalline cellulose and colloidal silica, and a co-processed mixture of microcrystalline cellulose and colloidal silica (PROSOLV SMCC90: trade name of JRS Pharma) is compared in **Fig. 6**. The co-processed mixture of microcrystalline cellulose and a colloidal silica (PROSOLV SMCC90) shows the higher compactibility in this chart, which is not obtained in simple mixture. When microcrystalline cellulose(VVAPUR MCC102: trade name of JRS Pharma) and PRPSOLV SMCC90 are compared, it turns out that PROSOLV SMCC90 gives higher compactibility compared with the compactibility of microcrystalline cellulose (VVAPUR MCC102) . (**Fig. 6**)

SMCC is supplied by JRS Pharma under the trade name of "PROSOLV SMCC." There are three grades which has different particle size and bulk density.

1.5 High compactibility microcrystalline cellulose by particle shape control methods

As I mentioned above, composite is one resolution to get high compactibility microcrystalline cellulose. Asahi-kasei Chemicals Ltd. developed another method to get high compactibility microcrystalline cellulose. That is to control the particle shape of microcrystalline cellulose. Dr. Obae explains that the compactibility of microcrystalline cellulose is related to the aspect ratio of particles in the microcrystalline cellulose powder[5]. If the particles in microcrystalline cellulose powder excel in the direction of a long axis, it is supposed to make an oriented structure by compression force, causing the compression pressure transmits to an inside of the tablet effectively, together with tangling of fibrous particles to make hard tablet. The high compactibility microcrystalline cellulose product developed by this concept was named Ceolus KG-802(trade name of Asahi-kasei Chemicals). The performance of Ceolus KG-802 against Ceolus PH-101(trade name of Asahi-kasei Chemicals): the standard type of microcrystalline cellulose is given **Fig. 7**.

The particle shape of Ceolus PH-101 is given in **Photo. 2** and the particle shape of Ceolus KG-802; the high compactibility microcrystalline cellulose is given in **Photo. 3**. Ceolus KG-802 consists of longer particles than the particles of Ceolus PH-101. Dr. Obae studied the mechanism of Ceolus KG-802 by fractionating powder and studied the difference between Ceolus KG and Ceolus PH. It is showed in **Fig. 8**. It shows that Ceolus KG, which has long axis of particle, attained high hardness of tablet for each

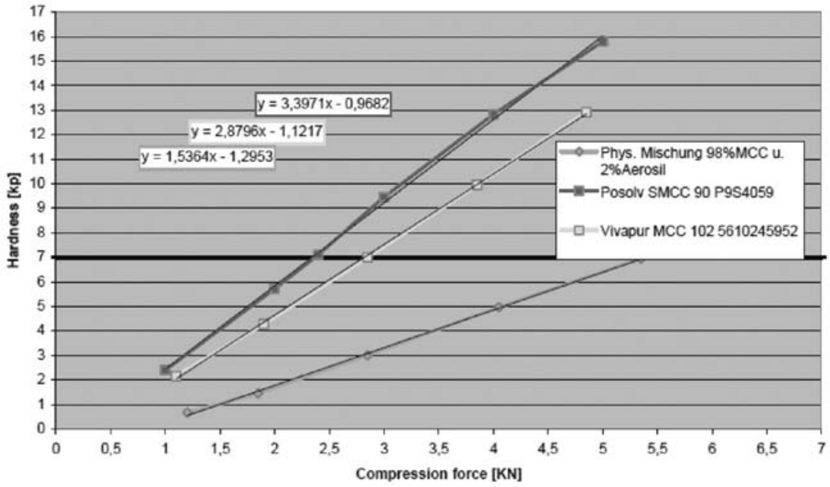

Fig. 6 Compactibility of 3types of dry binders (SMCC/physical Mixture/MCC).

Phys. Mischung (light green) was a mixture from 98 % MCC and 2 % Aerosil 200

VIVAPUR MCC 102 is regular microcrystalline cellulose type PH 102

PROSOLV SMCC 90 (dark green) is the compaction plot of PROSOLV

(Offerd by JRS Pharma)

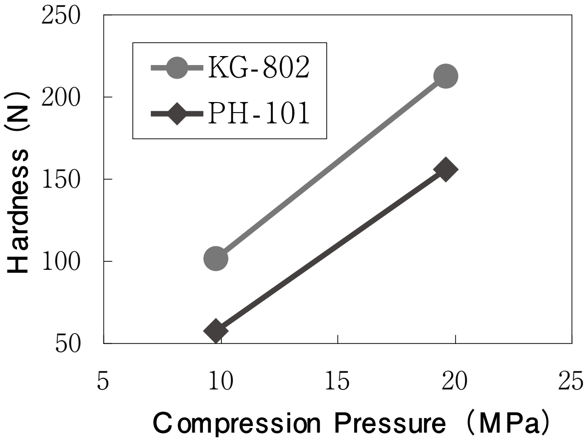

Fig. 7 Performance of Ceolus KG-802.

(Offered by Asahi-Kasei Chemicals)

compression force[5].

Fig. 9 shows an image diagram of each particle in die when KG-802 and PH-101 receives compression force. When compressed, the particles of KG-802, which has larger aspect ratio (L/D) than PH-101, oriented, tangled and make a hard tablet, but the particle of PH-101, which has smaller aspect ratio (L/D), little oriented, which prevent the transmittance of compression pressure, make medium hardness of tablet[5].

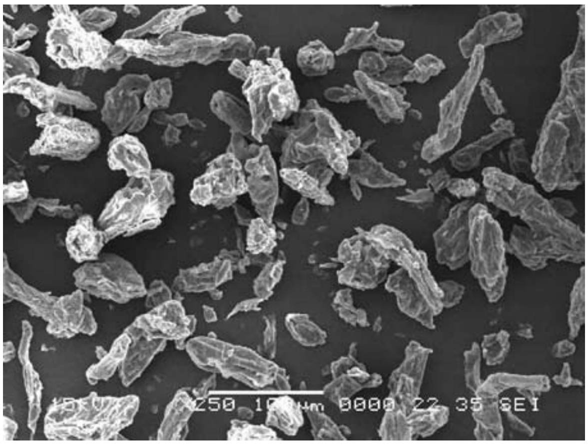

(Offered by Asahi-Kasei Chemicals)

Photo. 2 Ceolus PH-101: Standard Grade.

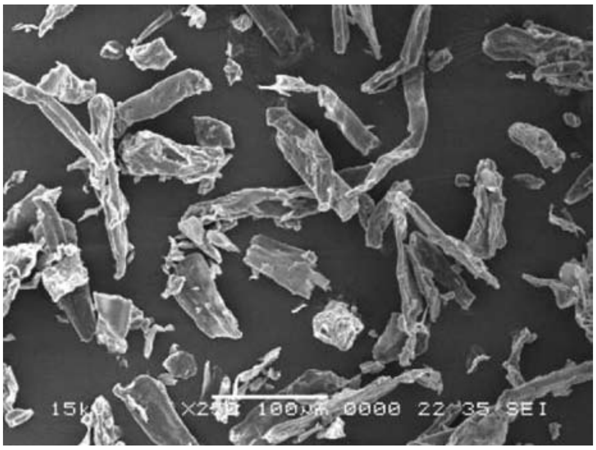

(Offered by Asahi-Kasei Chemicals)

Photo. 3 Ceolus KG-802: High Compactibility grade.

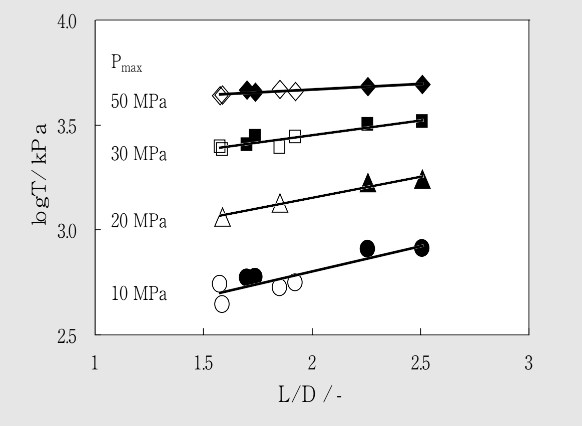

Fig. 8 Relationship between logT and L/D.

T; hardness of tablet, L/D; average length/diameter ratio of particles, PH grade: the standard grade, and KG grade: the high compactibility grade, were sieved to fractionated to four particle size. Compactibility of each fraction was studied for the average L/D of particles in each fraction. Where:

PH grade/ P1=0.41-0.43: open circle, P2=0.52-0.54: open triangle, P3=0.61-0.65: open square, P4=0.68-0.74: open diamond

KG grade/ P1=0.41-0.43: closed circle, P2=0.52-0.54: closed triangle, P3=0.61-0.65: closed square, P4=0.68-0.74: closed diamond

(Offered by Asahi-Kasei Chemicals)

Fig.10 shows the transmittance of compression force between upper punch and lower punch, and **Fig. 11** shows the relation between upper punch pressure and tablet thickness. It can be said from these data that Ceolus KG-802: the high compactibil-

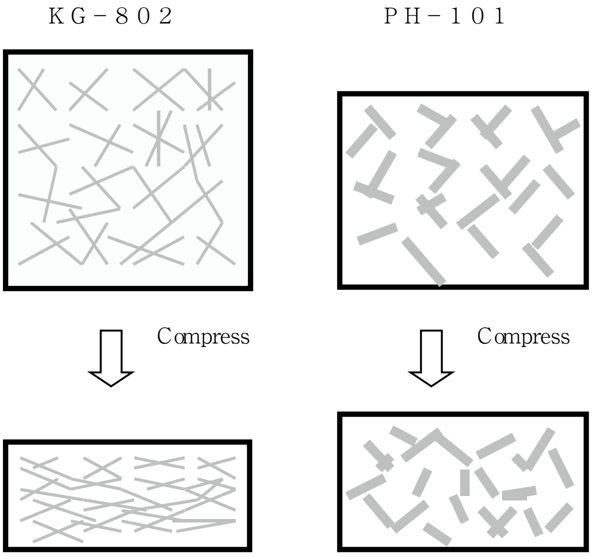

(Offered by Asahi-Kasei Chemicals)

Fig. 9 Image diagram of the compaction mechanism of Ceolus KG-802.

ity grade, transmit the compression force effectively to the tablet to make the tablet efficiently and precisely at compaction, compared with Ceolus PH-101.

In addition to the compatibility, particle shape of microcrystalline cellulose influences the other powder properties of microcrystalline cellulose. **Fig. 12** shows the relation between the compactibility and the powder properties for various microcrystalline celluloses. Ceolus KG-802 is bulkier than standard grade, and it is relatively poor flowability of powder. For this reason, Ceolus KG-802 seems to be rejected from the dry binders for high-speed tabletting, but in the case of the mixed powder of an actual formulation, it is not always true. Ozeki reported that a formulation with Ceolus KG 802 is suitable for high-speed tabletting rather than the formulation with standard grade[6]. It means that the powder suitable for high-speed tabletting depends not always on the properties of each component powder but on the properties of formulated powder mixture. **Fig. 13** shows the tablet weight variation under the tabletting condition of 8mm phi and 180mg tablet with the formulation 70% of the lactose (Super-Tab/ DMV International) and 30% of microcrystalline cellulose for direct compression. It says that the formulation with Ceolus KG 802 which has angles of repose 49 degree was stabilized at high speed tabletting from the formulation with PH-102 which has angles of repose 42 degree, and the formulation with PH-302 which has angles of repose 38 degree.

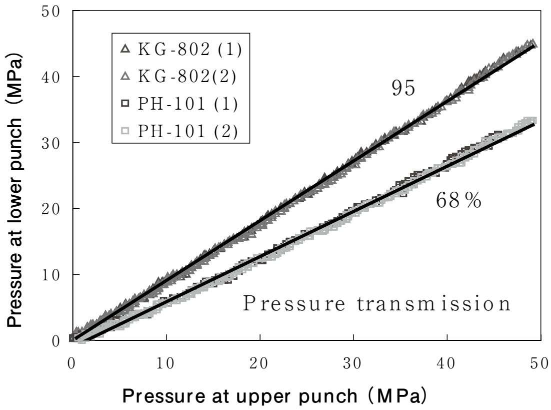

(Offered by Asahi-Kasei Chemicals)

Fig. 10 Pressure transmission between upper and lower punch.

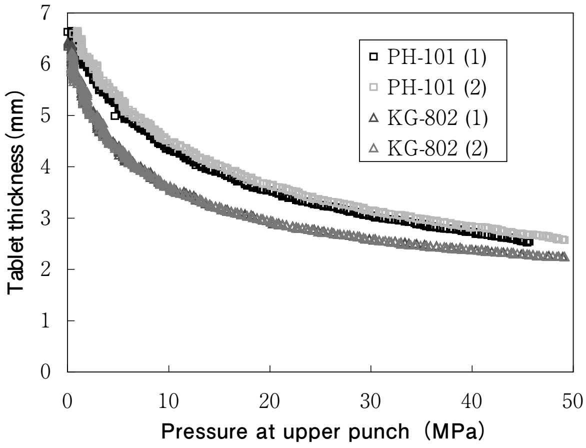

(Offered by Asahi-Kasei Chemicals)

Fig. 11 Pressure at upper punch and Tablet thickness.

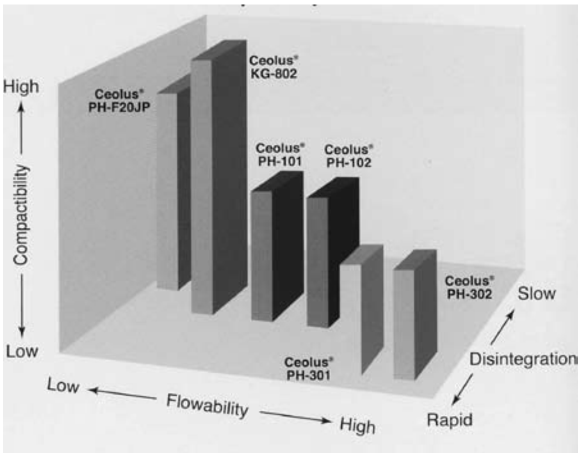

(Offered by Asahi-Kasei Chemicals)

Fig. 12 Powder properties of various microcrystalline cellulose grade.

1.6 A super-high compactibility microcrystalline cellulose

Ceolus KG-1000 which exceed Ceolus KG-802 are lunched from Asahi Chemical Chemicals in recent years. The concept of Ceolus KG-1000 is the same as that of KG-802, which controlled the aspect ratio of particles in the powder. **Photo. 4** shows the difference of particle shape between various microcrystalline cellulose and Ceolus KG-1000. It shows that the L/D value of particles in Ceolus KG is much larger than Ceolus KG-802.

Fig. 14 shows compatibility of various microcrystalline cellulose grades. The number in the figure shows the contents (%) of microcrystalline cellulose in each formulation. The remainder is the spray-dry-

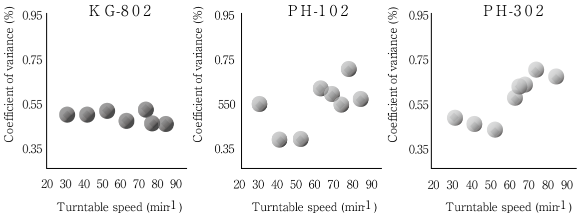

(Offered by Asahi-Kasei Chemicals)

Fig. 13 Formulation suitability for high speed tabletting.

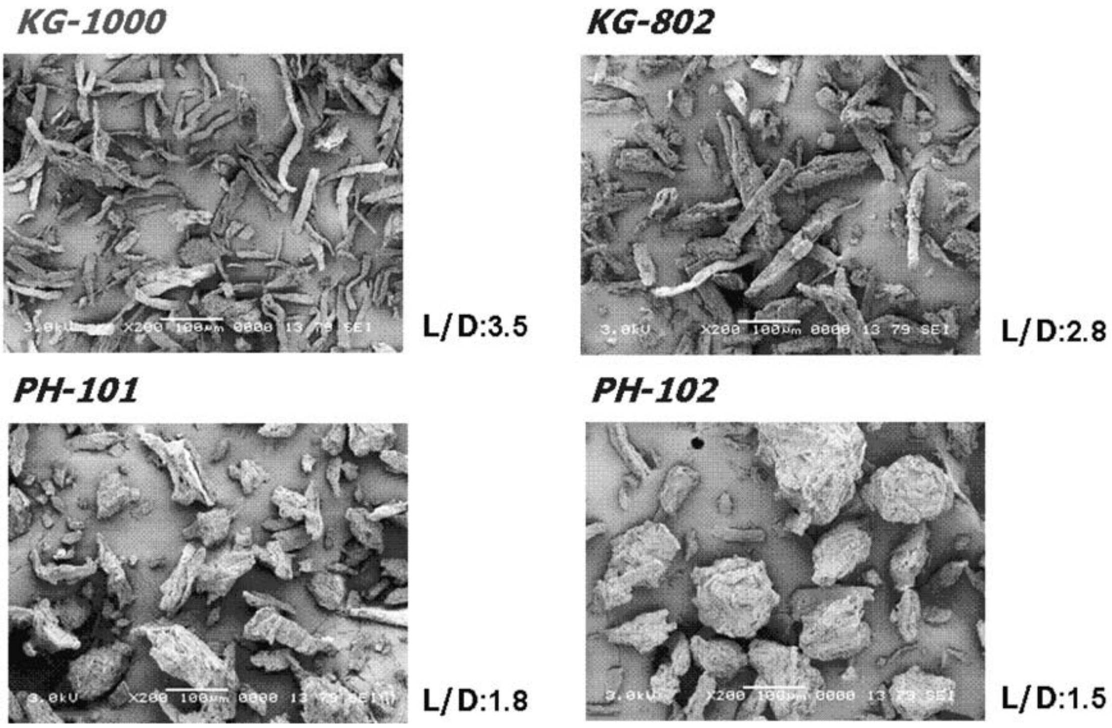

Photo.4 Ceolus KG-1000 and the other microcrystalline cellulose

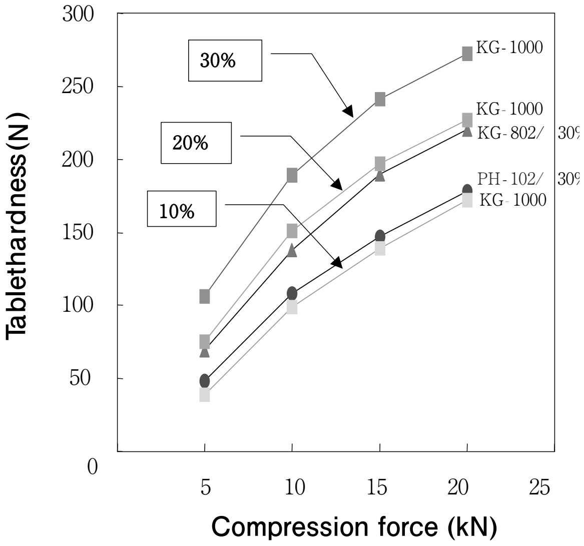

(Offered by Asahi-Kasei Chemicals)

Fig. 14 The performance of Ceolus KG-1000.

ing lactose (Super-Tab/DMV International). A rotary tabletting machine with 8mm phi punch at 53rpm to make 180mg tablet are used. Ceolus PH-102 is the standard grade which has same compactibility as Ceolus PH-101. In this chart, Ceolus KG-1000 of 10% gives the same tablet hardness as the Ceolus PH-102 of 30%. Ceolus KG-1000 of 20% gives the same effect as Ceolus KG-802 of 30% in this chart.

1.7 Applications for the high compactibility microcrystalline cellulose

The high compactibility microcrystalline cellulose sometimes makes the difficult application possible, which could not be attained in the past. Several examples of these applications are shown below.

1.7.1 Applications for the direct compression of enzyme

Enzyme is one of the delicate active pharmaceutical ingredients, which is easy to lose its enzymatic activity by handling. It is known if we make alpha amylase tablet by direct compression methods, alpha amylase lose enzymatic activity by the compression force during tabletting. Since Ceolus KG-802 require relatively lower tabletting force to get sufficient tablet hardness, when we applied Ceolus KG-802 to the formulation of enzyme, it will keep the enzymatic activity during direct compression. **Fig. 15** shows the enzymatic activity of alpha amylase which remained in the tablet. The experimental method of **Fig. 15** is shown in **Fig. 16**. The enzymatic activity of alpha-amylase in the formulation with PH-101 drop to 80% of the original activity, at tablet hardness of 50N, which is the limit hardness of tablet for practical use, on the other hand, in the formulation with Ceolus KG-802, enzymatic activity maintained to 95% of the original activity for the same tablet hardness.

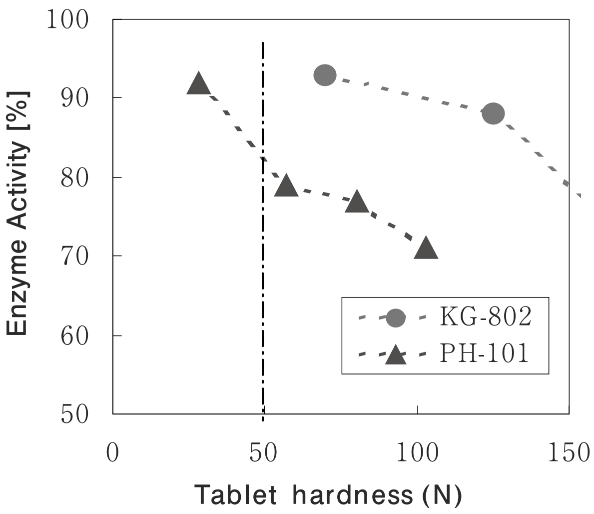

(Offered by Asahi-Kasei Chemicals)

Fig. 15 Alpha amylase activity remained in the tablet.

1.7.2 Direct compression of the tablet with high content of active ingredients

Generally speaking, the tablet including large amount of active ingredients is difficult to apply direct compression methods. Because of that wet granulation methods is often used for these formulation. By using high compactibility microcrystalline cellulose, people can chose direct compression methods even in the case of high content of active ingredient. **Fig. 18** shows the properties of the tablets obtained by direct compression including various microcrystalline celluloses in the model formulation with large amount of ascorbic acid. In the model formulation of 80% ascorbic acid contents, we could get enough hardness of the tablet for practical use by direct compression, by formulating Ceolus KG-802.

1.7.3 Direct compression of active ingredients with oily physical properties7)

The formulation which includes the active ingredients with oily physical properties is difficult to make the tablet with enough hardness by direct compression methods. When we make tablet using the powder with oily physical properties, we require the excipients in the formulation not only the function of compactibility but also the function of oozing out the oily ingredient. Since Ceolus KG-1000 is bulky powder, it can absorb the oily active ingredients oozing out during tabletting, and at the same time, it can bind the mixed powder as the highest performance tabletting agent. For this reason, Ceolus KG-1000 is one of the suitable excipients for the direct compression tablet with the oily active ingredients. The experimental method is shown in **Fig. 18** and the tablet hardness and the frying rate of the tablet for the oily active ingredient is shown in **Fig. 19**. In this formulation system, only the formulation with KG-1000 system attains the hardness of 50N and low frying rate, showing it can be used for the practical application in the market.

1.8 Final Comments

In this summery, I referred to the high compactibility tabletting agent, the mechanism of its function, and several applications of these materials, focusing on the microcrystalline cellulose, which is known to the highest compactibility excipients. As far as I

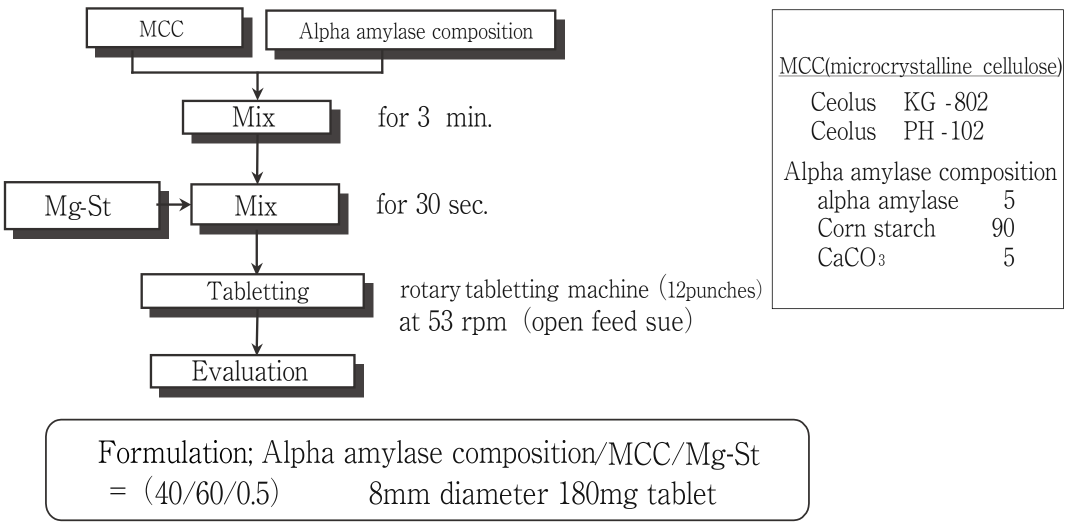

(Offered by Asahi-Kasei Chemicals)

Fig. 16 Experimental Methods.

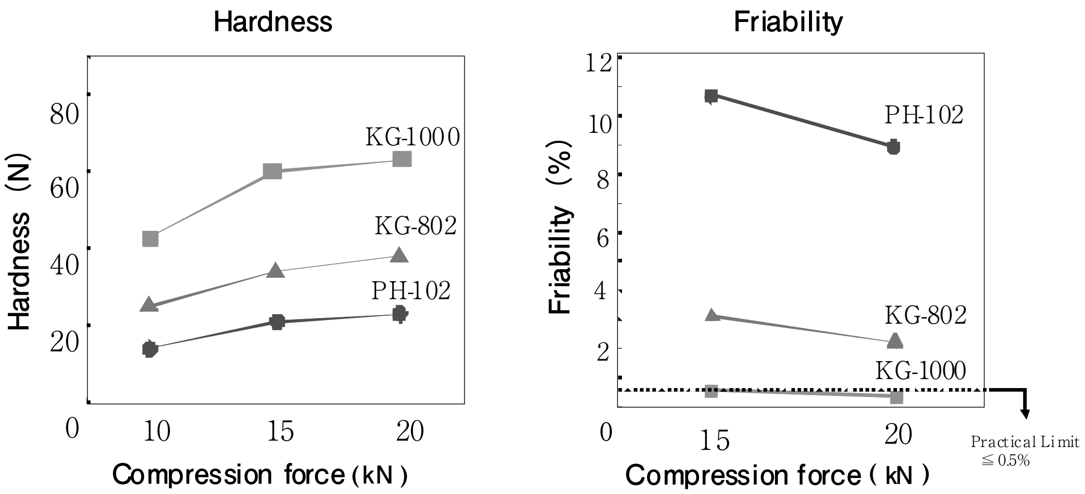

Fig. 17 Tablet with high Ascorbic acid contents by direct compression.

Formulation/ ascorbic acid: 80%, calcium silicate: 3%, MCC: 15%,croscarmellose:2%, Magnesium stearate 3 external%.
(MCC=microcrystalline cellulose)
Rotary tabletting machine at 50rpm with 12 punches. 12mm diameter, 600mg tablet. (Offered by Asahi-Kasei Chemicals)

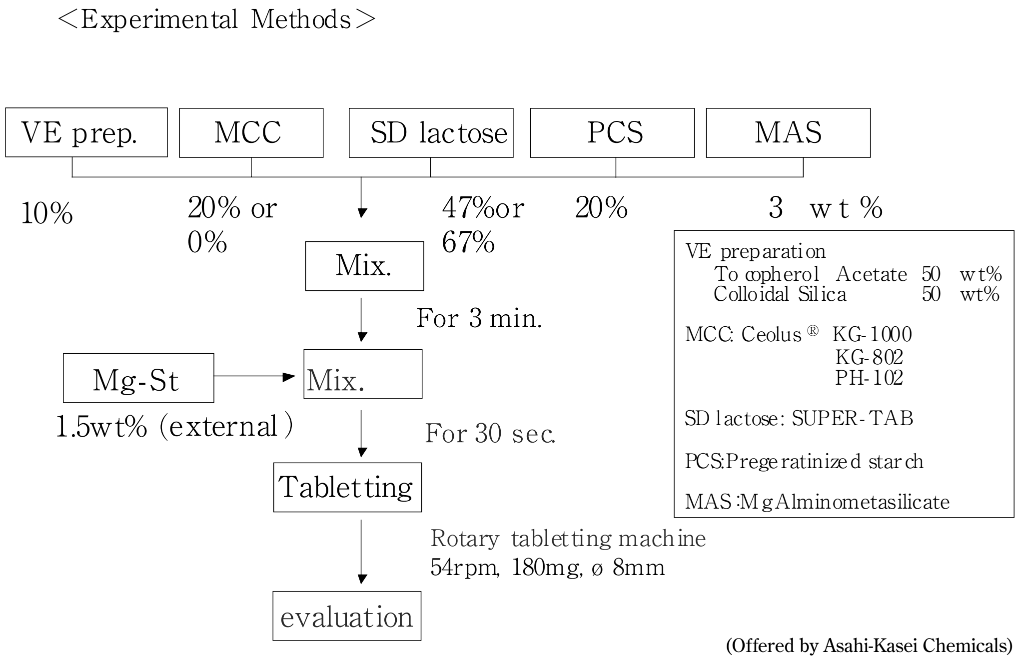

(Offered by Asahi-Kasei Chemicals)

Fig. 18 Tabletting methods for the formulation including oily API.

know, the excipients which show the highest compaction performance is Ceolus KG-1000 at present. In the tabletting formulation, the balance of mixed powder (a particle size, particle size distribution, particle shape, chemical properties of the particle, etc.) is critical. Therefore, a high compactibility tabletting agent is not simply evaluated by only compatibility. It is important to employ the characteristic of each material efficiently and it is important also to use properly according to the purpose of its use. In the actual formulation, it often raises difficult problems everywhere. I hope that the high performance tabletting agent introduced in this report may serve as effective solution in such a case. It is well-known that the high compactibility tabletting agent solved the film braking problem of the granule contain tablet. The high compactibility tabletting agent is also applicable for the sustained release drug, orally disintegrating

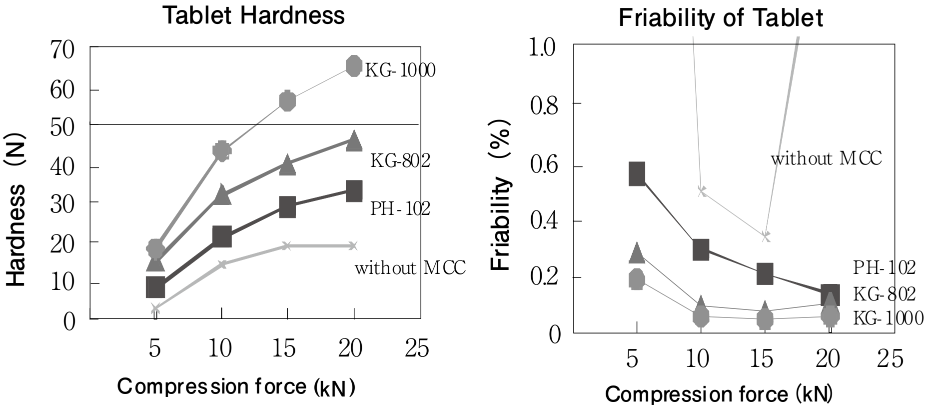

(Offered by Asahi-Kasei Chemicals)

Fig. 19 Direct compression tablet with oily API.

tablet in the mouth, etc. It seems that high compactibility excipients have wide range of applications. I am pleased if this summary stands on your work.

References

1) Hiroto Miyamoto, *Journal of Pharmaceutical Science and Technology Japan* **65** (2), 98-105 (2005).
2) O. A. Battista and P. A. Smith, *I & EC* **54** 20-29 (1962).
3) Yacoub S. Habib, et al., *Pharm. Dev and Tech.*,**4** (3), 431-437 (1999).
4) Bob E. Sherwood and John W. Becker, *Pharmaceutical Technology,* 78-88 (Oct.), (1998).
5) K. Obae, H. Iijima, and K. Imada, *Int. J. Pharm.*, vol. 182 p155-164 (1999).
6) Yuichi Ozeki et. al., *Executive Summary of The 2nd Seminar of Association for Innovative Formulation Technology* p83-97 (2005).
7) Masayuki Kakizawa et. al., *Ceolus Report*, 2-4, (2006).

Author's short biography

Hiroto Miyamoto

Graduated agricultural chemistry of Kyusyu University in 1971 and joined Asahi Chemical Industry Co., Ltd. Engaged to food and pharmaceutical excipient business, mainly microcrystalline cellulose, as business unit manager of R&D, plant manager and general manger of quality assurance. Also was experienced sales & marketing as regional director of South East Asia. Retired under the age clause.

As a member of Japan pharmaceutical Excipients Council (JPEC), was experienced the chairman of International Harmonization Committee of JPEC, the chairman of Guideline Committee of JPEC, the chairman of GMP Committee of JPEC. Also experienced a member of the Pharmaceutical Excipients Committee of PMDA: A branch committee of the Japanese Pharmacopoeia Investigation Committee of NHWL. Currently he is the director of "KNOWKATSU" and the consultant of "Inter-Pharma Express Inc."

Smart Particles as Foam and Liquid Marble Stabilizers[†]

Syuji FUJII*
Department of Applied Chemistry, Faculty of Engineering
Osaka Institute of Technology[1]
Ryo MURAKAMI
Department of Chemical Engineering, Polymer & Composite Engineering (PaCE) Group,
Imperial College London[2]

Abstract

Small particles adsorbed to gas-liquid interfaces are widely observed and utilized in many products and various industrial sections, such as flotation, washing, food, water treatment, treatment of radioactive wastes, and distillation in the petroleum industry. After a dormant period of nearly half a century, there is a revival of interests in studying their behaviour. Colloidal particles with a suitable wettability can strongly adsorb to gas-liquid interfaces, and can work as effective stabilizers for foams and liquid marbles (dry liquids). This article presents an overview of current research activities that center on foams and liquid marbles stabilized with well-defined colloidal particles. It is organized into three parts: i) brief discussions of small particles adsorbed to gas-liquid interfaces and their characterizations; ii) demonstrations of aqueous foams stabilized with inorganic or organic particles; and iii) demonstrations of liquid marbles (dry liquids) stabilized with colloidal particles.

Keywords: foams, bubbles, liquid marbles, dry liquids, colloidal particles, adsorption, gas-liquid interfaces, wettability

1. Introduction

A system in which a large number of gas bubbles are dispersed in a continuous liquid or solid is called a foam. The gas can be air, nitrogen, carbon dioxide and so on, that coexists with the liquid vapour. While the liquids can be water (aqueous solutions), oils (organic solvents), ionic liquids or molten metals, we consider, in particular, air bubbles dispersed in aqueous media in this paper. In general, ionic or non-ionic surfactants and surface-active polymers (including proteins) are used as the stabilizing agents for foams, because they can be adsorbed at the air-water interface and thereby reduce the interfacial energy of the interface. In addition to such molecular foam stabilizers, it has been also well known for over a century that particles can act as stabilizers for foams[1)]. There have been a relatively large number of systematic studies of particle-stabilized emulsions consisting of oil and water: oil-in-water emulsions are formed if the particles are more wetted by water than by oil (relatively hydrophilic particles), while water-in-oil emulsions are formed for relatively hydrophobic particles[2)]. Considering that air can be considered as an oil with an extremely low polarity and density, it is not surprising that solid particles stabilize foams by adsorbing to air-water interfaces. Such foams stabilized by the particles are observed and utilized in a wide range of industrial fields such as flotation, washing, food, water treatment, treatment of radioactive wastes, and distillation in the petroleum industry, *etc*[3)].

In recent years, after a dormant period of nearly half a century, there have been a resurgence of interests in the field of solid particles adsorbed at air-water interfaces. There are a large number of researches on foams using solid particles as foam stabilizers (or foam breaking agents) in the presence of molecular surfactants[2b,2d,4)]. In such surfactant-particle mixture

---

[†] Accepted: May 31, 2008
[1] 5-16-1 Ohmiya, Asahi-ku, Osaka, 535-8585, Japan
[2] South Kensington Campus, London, SW7 2AZ U.K.
[*] Corresponding author
E-mail: s.fujii@chem.oit.ac.jp

systems, as both surfactants and particles can adsorb at the air-water interface competitively and the surfactants can adsorb to the surface of particles, the mixture systems would be more complex to be analyzed than the independent systems. Therefore, it is thought to be important to carry out researches on foams stabilized solely with particles to obtain fundamental knowledge about the role of particles in foam stabilization. Moreover, sometimes it would be desirable not to add surfactants in some practical applications. Under such circumstances, recently, researches have been started on the foams solely stabilized with particles in the absence of any molecular surfactants[5]. These particle-stabilized foams are formed by using relatively hydrophilic particles. The question arises what will happen if relatively hydrophobic particles are mixed with water (or polar liquids). The materials prepared by aeration of the relatively hydrophobic particles and water have been shown to be water drops dispersed in air (water-in-air material), represented by dry water (liquids) and water (liquid) marbles[6,7]. The dry water consists of small water drops coated by the hydrophobic particles in air and behaves as a powder. This kind of water-rich powdery materials was first described in the 1960s[6] and the inversion between aqueous foams and water-in-air materials has been realized by controlling the stabilizing particle hydrophobicity and the air-water volume ratio[7]. This new class of methods of water (polar liquids) encapsulation in air would lead to promising applications in cosmetics, pharmaceuticals and food industry[8].

In this overview, we focus on the researches related to aqueous foams and liquid marbles (dry liquids) that are stabilized by particles. The particles presented in this article are inorganic particles and organic polymer particles. The inorganic particles such as silica and alumina can be commercially obtained in relatively large quantities from a number of companies[9] and are frequently used for fundamental studies on particle-stabilized foams and liquid marbles. In addition to the inorganic particles, the organic particles have recently been used as particulate foam and liquid marble stabilizers. Due to the development of technologies to design, synthesize and characterize the particles, the organic particles with precisely controlled surface/inner structures have found their applications in various industrial and academic sections[10]. Successful particle synthesis would inspire the construction of well-defined and functionalized particle-stabilized foams and dry liquid systems.

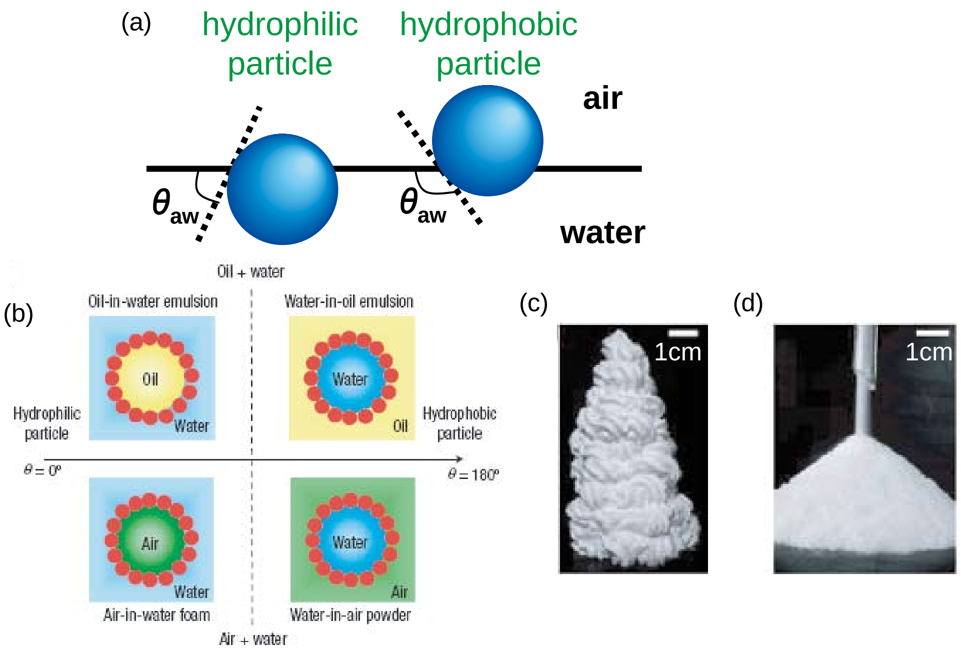

Fig. 1 (a) Small spherical particles adsorbed at an air-water surface; a relatively hydrophilic particle ($\theta_{aw} < 90°$, left) and relatively hydrophobic particle ($\theta_{aw} > 90°$, right). (b) Four quadrants of dispersed systems comprising of water, oil and air stabilized by particles. In mixtures of oil and water (upper quadrants), relatively hydrophilic particles stabilize oil-in-water type emulsions, while relatively hydrophobic particles stabilized water-in-oil emulsions. In mixtures of air and water (lower quadrants), air-in-water materials (bubble, foam) are formed by using relatively hydrophilic particles and water-in-air materials (water marbles, dry water) are formed by using relatively hydrophobic particles. (c) Whipped cream-like foams produced by aeration of water and relatively hydrophilic silica particles. (d) Dry water comprising water drops coated by hydrophobic particles in air, showing a free-flowing property. [Quoted from reference 7(a). Copyright, Nature publishing group.]

2. Particles Adsorbed at Air-Water Interfaces and Methods of Their Evaluation

2.1 Adsorption of particles at air-water interfaces

Based on the discussion regarding the effect of the particle wettability toward oil-water interface on a type of particle-stabilized emulsions[2b-2f], it is expected that relatively hydrophilic particles (contact angle which particles make at the air-water interface measured through the water phase, θ_{aw}, is less than 90°) are suitable to stabilize air bubbles dispersed in water and that relatively hydrophobic particles ($\theta_{\mathrm{aw}} > 90°$) are suitable to stabilize water droplets dispersed in air (see **Fig. 1**)[7]. Binks *et al.*[7] have demonstrated a phase transition between a system of air bubbles dispersed in water (foam) and that of water droplets dispersed in air (dry water: a free-flowing powder consisting of water drops coated by hydrophobic particles) by controlling the hydrophobicity of silica nanoparticles (see **Fig. 1**). Therefore, it is considered that even in particle-stabilized dispersed systems consisting of air and water, similar to those consisting of oil and water, the wettability of particles can be handled as one of very important factors that control the characteristics of the systems.

Assuming the particle is small enough (typically less than a few micrometers in diameter) so that the effect of gravity is negligible, the energy change when a spherical particle adsorbed at the air-water interface is removed from the interface (ΔG) is expressed by the following equation[11].

$$\Delta G = \gamma_{\mathrm{aw}} \pi a^2 (1 \pm \cos \theta_{\mathrm{aw}})^2$$

Here, γ_{aw} is the surface tension of the air-water interface, a is the radius of the particle and the sign inside the bracket is negative for removal into the water phase and positive for removal into the air phase. This equation indicates that ΔG is related not only to the contact angle but also to the air-water interfacial tension: the energy of adsorption becomes large as the particle diameter and the interfacial tension increase and the contact angle is close to 90°. Once the particles are adsorbed to the interface, it is difficult for them to desorb from the interface because of the high adsorption energy (relative to the thermal energy kT). This is in sharp contrast to surfactant molecules which adsorb and desorb on a relatively fast timescale. Hence it is expected that the stability of the foams stabilized by particles with a suitable wettability to air-water surfaces is higher compared to those stabilized with the molecular foam stabilizers.

2.2 Experimental evaluation of particles adsorbed at fluid interfaces

For many years, research has been conducted on the establishment of the method of measuring the contact angle of colloidal particles adsorbed at fluid-fluid interfaces. In the past several years, several types of new measurement methods have been proposed and have attracted attention. Paunov[12] has proposed a method called the gel trapping technique. After adsorbing particles at an air-aqueous solution of gelatine interface at 50°C, the aqueous phase is made into a gel by lowering the temperature to room temperature, and the particles are fixed at the interface. Next, poly(dimethylsiloxane) (PDMS) was slowly poured above the gelatine having the particles fixed at the surface and then PDMS was crosslinked. Then, by pulling apart this PDMS layer from the gelatine, the particles transferred onto the surface of PDMS, and this is observed by scanning electron microscopy. Butt *et al.*[13] have succeeded in measurement of the contact angle of the particles at an air-water interface using a colloidal probe atomic force microscope (AFM) (see **Fig. 2**). In this method, the single particle was attached to a cantilever of the AFM and a force curve obtained from the relationship between the particle and the air bubble using the cantilever was studied. It is worthy to note that the energy for the particle absorbed at the air-water interface to desorb particles from the interface to the water phase can be also measured by using this method.

Recently, a simple and rather direct method to measure contact angles of relatively hydrophilic particles ($\theta_{\mathrm{w}} < 90°$) adsorbed at an air-water interface *in situ* has been developed[14]. In this method, named film-calliper method (FCM), some particles adsorbed at an air-water thin film bridging both surfaces by sucking liquid out of the film meniscus are utilized (**Fig. 3a**). Once the particles bridge both two air-water interfaces, characteristic interference patterns of dark and bright fringes are observed. The patterns are recorded using a horizontal microscope in reflected monochromatic light (**Figs. 3b, 3c**). By analysing the interference pattern, the film thickness profile and the film thickness at the location of the bridging particle h_{e} at a different degree of shrinking of the film achieved by pumping water into the meniscus can be plotted against the radial distance from the center of the film (**Fig. 3d**). The bridging particle location is independent of the film profile as any deformation of the film surface associated with the particle immigration causes an increase in surface free energy. Hence, the contact angle of the bridg-

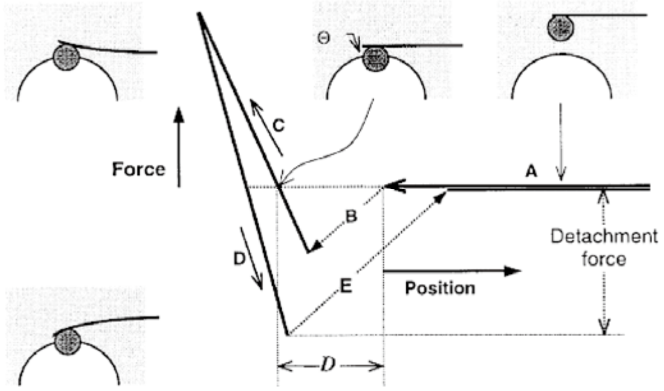

Fig. 2 Schematic of a force-versus-position curve between a spherical colloidal particle and a bubble. The position is the height position of the bubble. It was assumed that no long-range forces are active between the particle and bubble before contact and that the particle surface is not completely wetted by the liquid. At large distances the cantilever is not deflected (A). When the particle comes into contact with the air–water interface, it jumps into the bubble and a three-phase contact line is formed (B). The reason for the jump-in is the capillary force. Moving the particle further toward the bubble shifts the three-phase contact line over the particle surfaces (C). The important factor is the receding contact angle. When retracting the particle again (D) at some point the force is high enough to draw the particle off the air–water interface (E). [Quoted from reference 13(c). Copyright, Elsevier.]

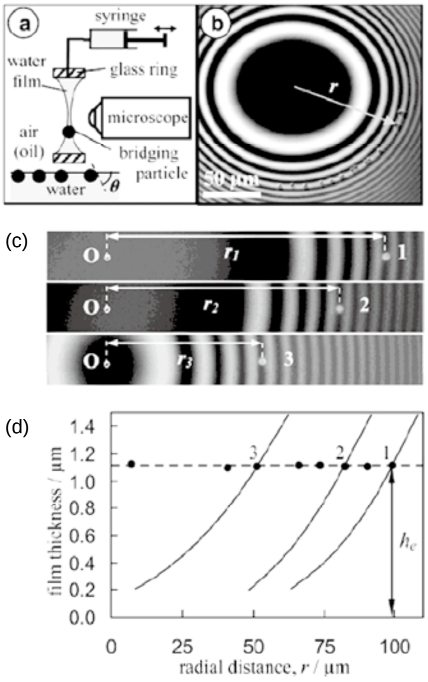

Fig. 3 Contact angle measurement by using film-calliper method. (a) Sketch of the experimental setup. (b) Image of a vertical water film in air with bridging 2 μm polystyrene latex particles in reflected light where the interference fringes are well seen. The arrow points toward one of the particles at a distance *r* from the film center. (c) Images of a water film in air with one bridging polystyrene latex particle of 2 μm diameter taken at different stages (1-3) during the shrinking of the film by pumping water into the meniscus. The particle moves closer to the film center O, so the radial distance, *r*, decreases ($r_1 > r_2 > r_3$). (d) Film thickness at the location of the bridging particle, h_e, versus radial distance from the film center during the shrinking of the film by pumping water into the meniscus (●). The dashed line shows the average he) 1.090 ± 0.008 μm. The solid lines are the thickness profiles of the meniscus corresponding to the images in part c. The other profiles are omitted for clarity. [Quoted from reference 14. Copyright, American Chemical Society.]

ing particles are simply determined by an equation. $\cos\theta_{\mathrm{aw}} = h_{\mathrm{e}}/d$, where *d* is the particle diameter. The contact angle values of micrometer-sized particles obtained by the FCM are in excellent agreement with those determined by previously developed other optical methods (side imaging and film trapping techniques)[15]. Moreover the FCM has an advantage of applicability to measurement of contact angles of particles with a diameter of submicrometer.

3. Foams Stabilized with Smart Particles

Foams stabilized with particles are observed and utilized as either intermediates or as end-products in various industrial sections, such as flotation, washing, food, water treatment, treatment of radioactive wastes, and distillation in the petroleum industry[3]. In many other unit operations, which frequently involve mixing of gas and liquids by pumping or stirring, the presence of solid particles can lead to undesirable foaming. For example, in the paper industry, detrimental foams are frequently generated which are stabilized by fibre, tars, and minerals such as clays. Such foaming can cause problems by blocking pipes and filters, and it makes monitoring of flow in pipes difficult. In the oil industry, obnoxious foams are produced in boilers and at various stages of distillation which are thought to be stabilized by asphaltene particles. In other cases, insoluble precipitates (partially hydrophobic particles from washing or hydrolyzed cationic precipitates such as iron oxide from steel mills) are adsorbed at air-water interfaces and can also cause foaming in effluent discharges feeding into rivers. However, in the fields of ore flotation and deinking flotation, foams are used effectively in order to make particles adsorbed at air-liquid interfaces and to recover the target materials. The particle-stabilized bubbles are also observed in space. Vanderhoff and Shaffer reported that nitrogen bubbles were stabilized with monodisperse polystyrene (PS) particles adsorbed at a nitrogen-water interface: the nitrogen bubbles would be formed by decomposition of azoinitiator during seeded emulsion polymerization experiment aboard the space shuttle orbiter Challenger (STS 7, June 1983). In space, the bubbles show no tendency to cream; therefore, the bubbles are stable against breakage caused by liquid drainage16).

3.1 Features of foam (air bubbles) stabilized by particles

3.1.1 Stabilities against coalescence and disproportionation

Foams, which are generally formed by stirring gas and liquids or by injection of gas into liquids, are thermodynamically unstable and eventually return to the initial separated two phases due to coalescence between bubbles and diffusion of gas from smaller bubbles to larger ones (disproportionation). However, it has been reported that foams stabilized by particles exhibit high stability against both coalescence and disproportionation2d, 17).

For emulsions, consisting of oil and water, stabilized with particles, two stabilization mechanisms have been proposed18). One is the mechanism of preventing the three-dimensional coalescence between liquid droplets and the diffusion of dispersed phases (oil, water) owing to densely packed adsorbed particle layers on the interface of the liquid droplets, i.e., formation of two-dimensional solid (steric stabilization mechanism: SSM). The other mechanism is formation of a single particle layer simultaneously wetted by two liquid droplet interfaces, preventing the coalescence between the liquid droplets (bridging stabilization mechanism: BSM). In foam systems, although any examples of the BSM have not yet been reported at this stage, stabilization by the SSM has been reported2d). Furthermore, it has been shown that air bubbles sufficiently covered with particles own enough surface elasticity to prevent disproportionation of bubbles17).

3.1.2 Non-spherical shapes and wrinkled skins of particle-stabilized foams

While bubbles stabilized by molecular surfactants take the spherical shape in order to minimize the interfacial area between air and liquid, in the case of air bubbles stabilized by particles, the bubbles can take not only the spherical shape but also the non-spherical shapes (elliptical, rod shape, *etc.*)19,20). This occurs because particles with a suitable wettability are irreversibly adsorbed to the air-water interface, and it is not practically possible for particles to be detached from the interface even if the area of the air-water interface decreases when two air bubbles covered (partially) with particles coalesce with each other. The inability of the particles to be expelled from the bubble surfaces also leads to the wrinkled bubble skins (see **Fig. 4**).

3.2 Foams stabilized with inorganic particles

Some typical inorganic particles used as a foam stabilizer are inorganic oxides such as silica, alumina and clays, and their surface characters are generally hydrophilic. As has been shown in the research on ore floatation, the adjustment of the hydrophobicity of particles is generally performed by addition of amphiphiles (surfactants) into the aqueous phase.4) By selecting appropriate combination of amphiphiles and particles, the synergistic effects (enhanced foam volumes and stability) can be induced21). In the amphiphile-particle mixture systems, however, both of them are adsorbed at air-water interfaces competitively, and their contribution to foam formation and stability may overlap. Therefore, it is expected that studies on foams stabilized by particles in the absence of amphiphiles enable us to obtain fundamental knowledge on the role of particles in the stabilization of foams. In this section, an outline is presented of research on foams stabilized by inorganic particles; (1) mixture systems of amphiphiles (surfactants)-inorganic particles where the wettability of particles is modified by adsorption of amphiphiles onto the particles, and (2) single systems of inorganic particles where the wettability of particles is controlled

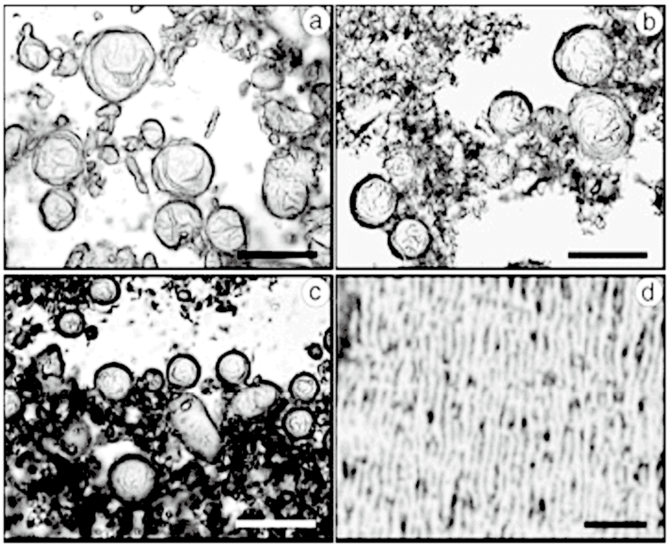

Fig. 4 **Fig. 3**. Optical microscopy images of aqueous foams stabilized by silica nanoparticles that contain 32% SiOH on their surfaces. Conditions and time after formation by homogenization: a) no salt, 3 wt/v% particles, 40 h, b) 8.5 mM NaCl, 0.86 wt/v% particles, 5 min, and c) 1 M NaCl, 0.37 wt/v% particles, 5 min. Also shown in d) is the image of a planar monolayer of silica nanoparticles (with 50% SiOH) at the air–water surface after compression to a surface pressure of 70 mN m^{-1}. The corrugations are parallel to the trough barriers. All scale bars: 50 μm. [Quoted from reference 18. Copyright, Wiley.]

by changes in particle surface chemistry and pH or salt concentration in water.

3.2.1 Foams stabilized by mixtures of amphiphiles (surfactants) and inorganic particles

Ionic surfactants with opposite charge against particle surface charge have been used to control hydrophobicity of the particles diversely. For example, silica particles are negatively charged in aqueous dispersions at pH > 2 due to dissociation of proton from the surface silanol groups. In the presence of cationic surfactants such as alkylammonium salts, it has been known that positively charged hydrophilic groups are bound to the negatively charged surface silanol groups, with the hydrophobic groups of the surfactant orientating to bulk water phase, due to the electrostatic interaction[21,22)]. The silica particle surfaces are covered by hydrophobic alkyl chains with increasing the surfactant concentration in water, and hence the hydrophobicity of the particles becomes increased. Further increase in the surfactant concentration, however, leads to the formation of bilayer of the surfactant at the silica particle surfaces, which render the silica particles back to hydrophilic[21)]. The maximum foam production occurs at the intermediate surfactant concentration, where the particles are barely charged and the most hydrophobized.

Recently the group in ETH-Zurich have adjusted the wettability of inorganic particles (Al_2O_3, ZrO_2, $Ca_3(PO_4)_2$, SiO_2), that are charged positively or negatively in aqueous media, by mixing with amphiphiles with short hydrocarbon chains (carboxylates, amines and gallates)[23)]. The amphiphilic substances adsorb and orient onto the particle surfaces with the hydrophilic groups towards the surface of the particle through the electrostatic interaction or ligand-exchange interactions, and the hydrophobicity of the particles increases with increasing the amphiphile concentration in the aqueous phase (see **Fig. 5**). Using a relatively large quantity of particles (35 wt % at maximum), the foams show significant stabilities against coalescence, disproportionation, and creaming.

3.2.2 Foams stabilized by inorganic particles alone

Among inorganic particles, silica particles are used frequently as the model particles as they are relatively easily available as high purity products. Furthermore, as reactive SiOH groups are present on the surface of silica particles, using suitable hydrophobilizing agents (for example, dimethyldichlorosilane: DCDMS), it is facile to adjust the hydrophobicity on the surface of particles chemically. The extent of hydrophilicity of the silica particles is quantified by the unreacted surface SiOH groups (100%SiOH: extremely hydrophilic, 20%SiOH or less: extremely hydrophobic). Binks and Horozov have shown that, the particles with a suitable hydrophilicity can form foams that are stable with respect to coalescence and disproportionation, although hydrophilic (≥70% SiOH) and extremely hydrophobic (14% SiOH) particles can not stabilize air bubbles[20]. The individual air bubbles obtained are not spherical in shape, and the surfaces of air bubbles are not smooth but wrinkled. In addition, from the fact that the silica particles developed at a plane air-water interface form such wrinkles at a high surface pressure, it is suggested that the air bubbles are covered with dense particle layers (see **Fig. 4**).

The silica particles wettability can be adjusted by controlling compositions in water[7b,20, 24]. By using nanometer sized fumed silica particles, the same type of particles as described above, the effects of pH and electrolyte concentration in water on the wettability of the particles and the foam stability have been investigated[7b]. For example, aeration of relatively hydrophilic silica particles (66% SiOH) and water results in an aqueous dispersion of the particles, however when the particles are aerated with aqueous solutions of NaCl[7b], foams are formed. The stability of the foams (referred by foam volumes after a period of preparation) increases with increasing the NaCl concentration (see **Fig. 6**). It has been suggested that the addition of electrolyte to the water phase induces not only shortening the Debye length, but also changing the hydration structure on the surface of the silica particles are responsible for the observed increase in the hydrophobicity of silica particles.

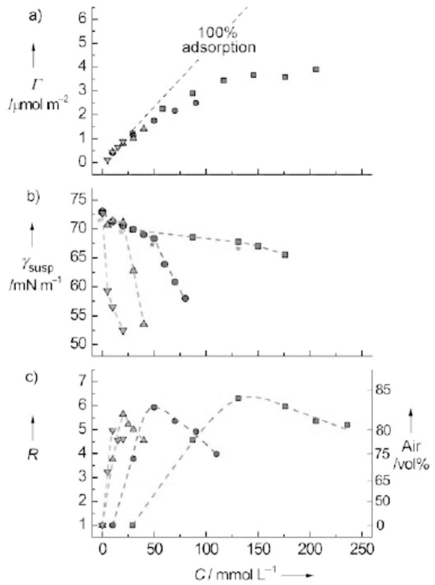

Fig. 5 Example of surface lyphobization and foaming behavior using alumina particles and short fatty acids as amphiphiles (■: propionic acid (C3), ●: butyric acid (C4); ▲: valeric acid (C5), ▼: enanthic acid (C7)). (a) The symbols Γ and C denote the amount of amphiphile adsorbed per unit surface area of alumina and the initial concentration of the amphiphile added to the suspension, respectively. (b) The ability of lyophobized particles to attach at air–water interfaces results in a significant decrease in the surface tension of colloidal suspensions (γ_{susp}). (c) The decrease in surface tension resulted in remarkably high foamability upon high mechanical shearing. *R* is the foam expansion ratio given by the volume of foam divided by the volume of the initial suspension. The volume percentage of air incorporated in the foams is also indicated on the right y-axis in (c). All data were obtained from 35 vol% alumina suspensions at pH 4.75. [Quoted from reference 23(a), Copyright, Wiley.]

3.3 Foams stabilized with organic particles alone

Organic polymer particles have mainly been used in the form of film in paint and adhesive industrial sections. In addition to the usage in the form of the film, there have been increasing interests in using the polymer particles in their particulate form[9,10]. The polymer particles have been used as absorbents, ion-exchangers, affinity bioseparators, drug and enzyme carriers, viscosity modifiers, support materials, calibration standards, and functional beads for medical diagnostics. The utilization of the organic polymer particles as a building block toward colloidal crystal is also attracting attention. The latex particles have also found their application as emulsion and foam stabilizers[2f,5]. Studies on the aqueous foams stabilized with polymer particles have recently been started, and advanced applications of these foams should be expected, considering the varieties of polymers. In aqueous dispersion of such organic particles, the particles themselves are electrostatically and/or sterically stabilized against flocculation. In this section, researches on aqueous foams stabilized by organic polymer particles with their respective stabilization mechanisms are described.

3.3.1 Charge-stabilized organic particles

Wilson[25] explored the foaming behavior of charge stabilized anionic PS latex particles with diameters ranging from 1.02 to 3.89 μm. Foaming could only be achieved after addition of either salt or cationic surfactant, or by making the latex highly acidic (pH < 1). Thus, the conditions required for generating stable foams either approached or exceeded those required for aggregation of the latex particles in bulk aqueous solution. Moreover, the foam quality decreased as the latex diameter was reduced, with the minimum particle diameter required to obtain stable foams being approximately 1.50 μm; stable foams could not be prepared using 1.02 μm PS latex. Wilson's observations appear to be closely related to the ‘surface coagulation’ phenomenon previously studied by Heller

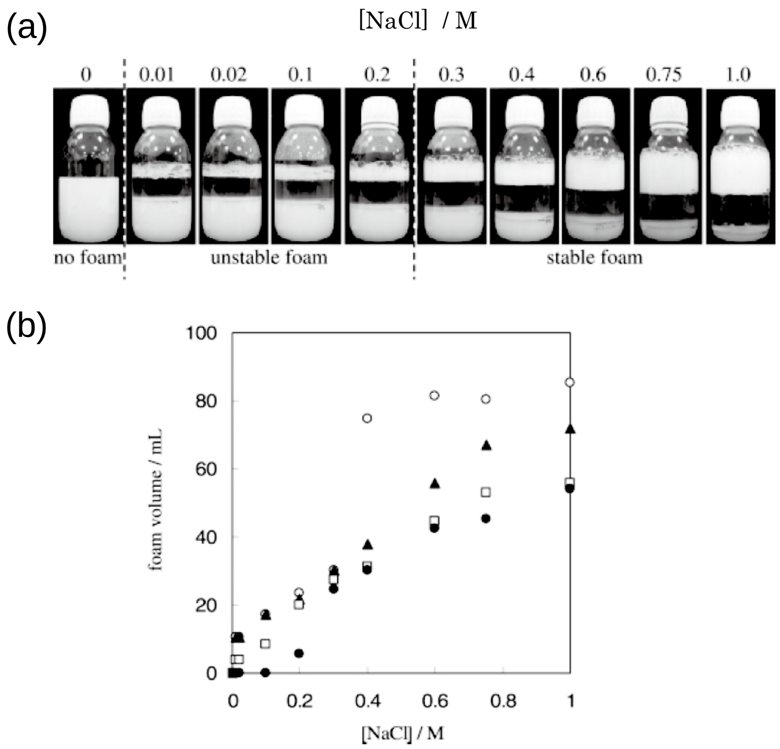

Fig. 6 Transitional phase inversion from aqueous dispersion to foam induced by an increase in the salt concentration at a fixed particle hydrophobicity (66% SiOH). (a) Photographs illustrating the formation of foam in the presence of salt 2 days after preparation. (b) Foam volume versus NaCl concentration at natural pH and different times after preparation (○ : 10 min; ▲ : 1 h; □ : 2 days; ●: 2 months). At high [NaCl], the foam volumes apparently decrease with time due to sedimentation of excess flocculated silica particles in the foams. [Quoted from reference 7(b). Copyright, American Chemical Society.]

and coworkers[26], in which colloidal dispersions of low charge density coagulated at an air-water interface after addition of salt. The critical salt concentration required to induce surface coagulation was just less than that required for coagulation in bulk solution[26].

Kettlewell *et al.*[27] have synthesized three types of micrometer-sized PS latexes by the precipitation or dispersion polymerization method using a cationic azo initiator, an anionic persulfate initiator, or the cationic azo initiator in combination with a non-ionic polymeric stabilizer, and the foam stabilization performance of each latex was examined in detail. Below pH 7, two of the three latexes had cationic character: under these conditions, latex concentrations as low as 3.0 wt % were sufficient to generate highly stable foams. The same latexes proved to be ineffective foam stabilizers above their isoelectric points (where they possessed net negative surface charge). In contrast, the permanently anionic PS latex did not produce stable foams under any conditions. Considering that the air-water interface is negatively charged [28], it can be considered that the electrostatic attractive force is the driving force for the particle to attach to the air-water interface, and the positively charged particles can be adsorbed to the air-water interface.

Velev and co-workers[29] described preparation of highly stable foams using polydisperse bisphenol A-based epoxy resin microrods with an average length of 23.5 μm and an average diameter of 0.6 μm, in the absence of any surfactant. Due to their rigid, entangled structure and resistance to mechanical perturbation, these microrod-stabilized foams were very stable, even after drying.

3.3.2 Sterically-stabilized organic particles

Fujii *et al.*[30] serendipitously discovered that PS latex particles with diameters ranging from submicrometer to micrometer, which were synthesized by emulsion and dispersion polymerizations using poly(*N*-vinylpyrrolidone) (PNVP) as a colloidal stabilizer, can stabilize air bubbles in water by adsorbing to the air-water interface (see **Fig. 7a**). Such foams can survive for more than two years in a wet state and remain intact even after drying. In contrast, foams stabilized with molecular surfactants such as sodium dodecyl sulphate and PNVP were destroyed after removal of the aqueous phase. Optical microscopy studies revealed hexagonally close-packed arrays of PS particles within the foam (**Fig. 7b**), which sug-

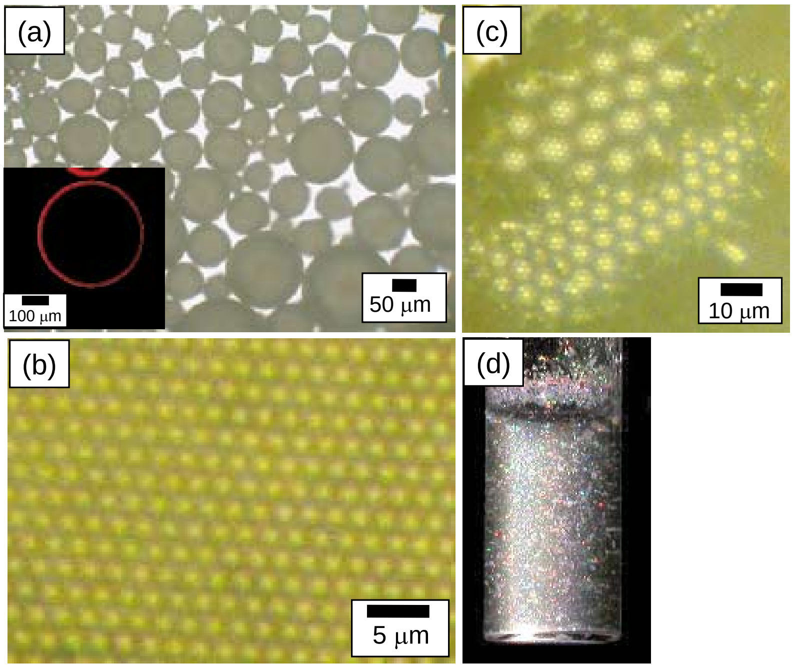

Fig. 7 Optical micrographs of the latex foam prepared using 1.57 μm sterically stabilized polystyrene latex particles. (b) Magnified image that shows hexagonally ordered latex particles at the surface of one of the air bubbles shown in (a). Confocal laser scanning microscopy studies on an individual bubble (see inset shown in **Fig. 7a**) revealed a red halo, which demonstrates that fluorescently labeled PNVP-stabilized PS particles were adsorbed at the air-water interface, which is a necessary and sufficient condition for stabilization of the air bubbles. (c) Moiré patterns produced by polystyrene latex bilayers as observed by optical microscopy. (d) Digital photographs of polystyrene latex-stabilized foam fragments redispersed in water viewed under transmitted sunlight after annealing at 105 °C for 10 min. Note the iridescence from the fragments. [Quoted from reference 30(a). Copyright, American Chemical Society.]

gests high colloidal stability for the PS particles prior to their adsorption at the air-water interface. This hexagonally close-packed latex arrays in the walls of the dried foam leads to localized moiré patterns (see **Fig. 7c**) being observed by optical microscopy. Moreover, the dried foams are highly iridescent in bright transmitted light (**Fig. 7d**), which may offer potential applications in security inks and coatings. Fujii *et al.* [30b,31] have also reported that poly(methyl methacrylate) particles, poly(4-bromostyrene) particles, and polyacrylonitrile (PAN) particles synthesized by dispersion polymerization using PNVP as the colloidal stabilizer can stabilize foams, but poly(2-hydroxypropyl methacrylate) particles do not stabilize a foam. These results have suggested that the polarity of particles should have an effect on the stabilization of foams.

In order to add smart functions to the foam stabilized with particles, researches have been started on a construction of stimuli-responsive foam system. In order to control the stability of the foam by external stimuli such as pH, temperature, etc. on demand, polymer particles containing stimuli-responsive component were used as the foam stabilizer. In such systems, control of the hydrophilicity and hydrophobicity of the particle surface (control of the wettability relative to the air-liquid interface) by some external stimuli leads to the adsorption of particles to the interface or the desorption from the interface, that is, foam stabilization or defoaming. Binks *et al.*[32)] have constructed a pH-responsive foam system using PS particles coated with poly(acrylic acid) (PAA) as a colloidal stabilizer on the particle surfaces (see **Fig. 8**). When the pH value of the aqueous media is below pK_a of PAA (< pH4.5), PAA colloidal stabilizer on the surface of the particles is protonated and the PS particles have affinity to air: the PS particles can absorb to the air-water interface, hence stable foam was prepared. On the other hand, at pH6 or more, PAA on the PS latex surface is de-protonated and the PS surface has highly anionic character: the PS particles can only disperse in the aqueous media due to the high hydrophilicity and no stable foam was stabilized. In addition, it has been clarified that, by adding alkali to the stable foam that is prepared at low pH, it is possible to destabilize the foam on demand (see **Fig. 8**). More recently, Dupin *et al.* have found out [33)] that the pH-responsive poly(2-vinylpyridine) (P2VP) microgel particles can work as an effective stimuli-responsive foam stabilizing agent and it is possible to destabilize

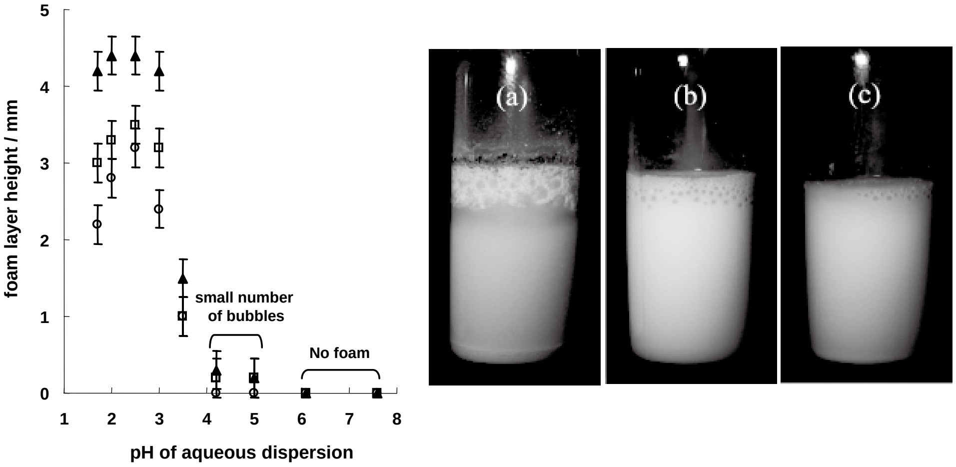

Fig. 8 Left Fig. pH-dependent behavior of foams prepared in batch mode using PAA-stabilized PS latex particles (2.6 wt %, 0.1 M aqueous NaCl),. Height of the foam layer versus pH of the aqueous dispersion recorded at different times: immediately after preparation (▲), after 1 week (□), and after 1 month (○). Right Figure: Photographs illustrating the pH-responsive behavior of foam prepared using PAA-stabilized PS latex particles (2.6 wt.%, 0.1 M aqueous NaCl). (a) At pH 2.5 after 24 h, (b) immediately after pH adjustment from 2.5 to 5 with gentle inversion, and (c) at pH 5 after 24 h. [Quoted from reference 32. Copyright, American Chemical Society.]

the foam by the addition of acid.

The particle-stabilized foams have also been exploited as a technology platform for the production of novel porous materials. Fujii *et al.*[31] have succeeded in creating porous carbon materials from the particulate foams. First, PAN latex particles were synthesized by dispersion polymerization as a precursor of carbon materials and prepared the particulate foam using the particles. After drying, the PAN-based particulate foam was heated up to 1000℃ in an N_2 atmosphere, which led to porous carbon materials with pore sizes dependent on the original air bubble diameters.

4. Method of Evaluating Foam Stabilized Using Particles

4.1 Microscope observation of air bubbles

Optical microscopy is suitable for observation of air bubbles with diameters ranging from micrometer to sub-millimeter in the wet and dry states, and is useful for obtaining the average diameter of the air bubbles. Sample preparation for the optical microscopy study is simple. Confocal laser scanning microscopy (CLSM) is also suitable for observation of air bubbles in the wet and dry states. CLSM studies on air bubbles stabilized with fluorescently labelled particles have revealed halos, which demonstrated that the particles were adsorbed at the air-water interface, which is a necessary and sufficient condition for stabilization of the air bubbles (**Fig. 7a** inset)[30].

4.2 Observation of bubble size and stability of foam

Generally, the foam was observed by the naked eye in order to evaluate the bubble size and their distribution or the stability. Foam columns equipped with glass frits are widely used to generate and characterize foams[34]. The foam columns were also used in the particulate foam system. Fujii and Armes *et al.*[30] have evaluated particulate foam generation, and stability of the foam against drying, and change in the volume using the foam column. Horozov and Binks[35] have developed an automated dispersion stability analyzer (DiStA 24) using a commercially available scanner, and have succeeded in evaluating coalescence and creaming of foams automatically well before it is possible by the naked eye at regular intervals of time.

4.3 Bubble preparation using microchannels

The use of microchannels makes possible not only preparation of bubbles with a uniform size, but also kinetic studies on adsorption of particles at air-water interfaces. Subramaniam *et al.*[36] have used a hydrodynamic focusing device with three channels (one channel for air, and the other two channels for aqueous medium), and have adjusted accurately the size and stability of air bubbles stabilized by particles (see **Fig. 9**). The air bubbles covered with the particles are formed with good reproducibility only at high flow speeds (10 cm s^{-1}), suggesting that the particles are adsorbed at the interface in a time scale on the order of several tens of microseconds. In addition, by loading particles differentially labelled with rhoda-

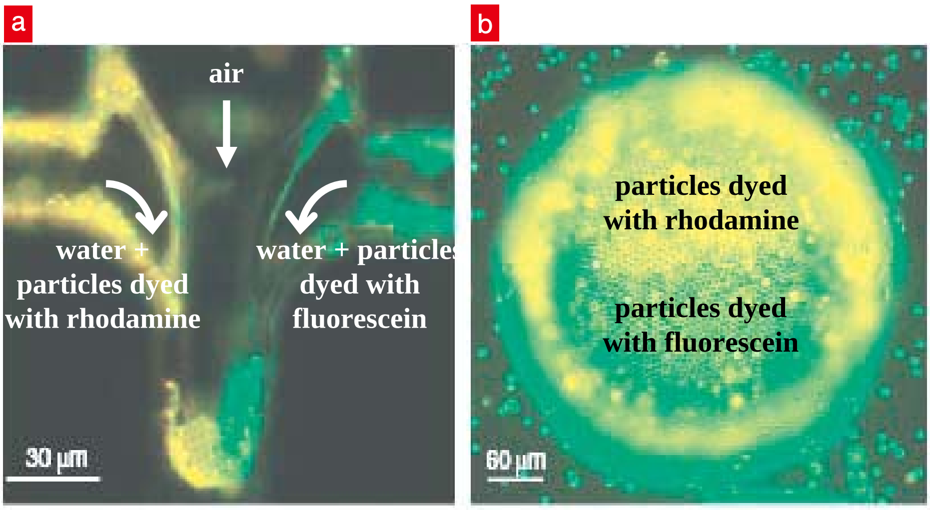

Fig. 9 Production of air bubbles covered with particles by using a three-channel hydrodynamic focusing device. (a) Delivery of 4.9-μm diameter polystyrene particles dyed with rhodamine (yellow) and 4.0 μm particles dyed with fluorescein (green) on an air/water surface. (b) An example of tailored production of an air bubble covered with approximately two hemispheres of different size particles (Janus shell). [Quoted from reference 36. Copyright, Nature Publishing Group.]

mine and fluorescein in the two outer channels of the microfluidic device, it was shown possible to produce hemi-shells, or Janus armour. The ability to assemble two or more types of particles on a single shell is the first step in producing chemically patterned shells that may be useful for targeting or sorting purposes.

5. Water Drops Stabilized by Particles in Air

As already shown in **Fig. 1**, preparation of water-in-air inverse foam systems has been demonstrated[7]. One example of these systems is liquid marbles. Droplets of polar liquids, such as water, glycerol, ionic liquids, coated by hydrophobic particles show non-sticking behaviour against substrates on which the liquids readily wet without the particle coating[6-8,37-42].

Aussillous and Quéré reported that liquid marbles could be obtained by making a small amount of liquid (typically between 1 and 10 mm^3) roll in a very hydrophobic powder (lycopodium grains of typical size 20 μm covered with fluorinated silanes)[37]. The grains spontaneously coat the drop, which can eventually be transferred onto other substrates. **Fig. 10a** shows a water marble of radius 1 mm, placed on a glass plate (which is wetted by water), where it is observed to adopt a spherical shape. Thanks to the adsorbed grain layers at the liquid-air interface, the wetting between the glass and the water is suppressed. These liquid marbles roll off an inclined plane rather than slide and also can be manipulated by applying external fields such as electric and magnetic fields[37,38]. Interestingly, these liquid marble can float on a water pool thanks to the hydrophobic particles on the marble surface (**Fig. 10b**). Bon and co-workers indicated that a water droplet with a diameter of *ca.* 5 mm in air could be stabilized with cross-linked poly(divinyl benzene) (PDVB) particles synthesized via precipitation polymerization[39]. The water droplet deviates from a spherical shape and appears oval on the glass plate, as the drop size is greater than the capillary length. Moreover, the evaporation process of the water droplet was investigated and deformation of the colloidal assembly on the air-water interface was observed. The PDVB particles are irreversibly adhered to the air-water interface and the total surface area of the droplet can no longer decrease. The only alternative for the droplet is to change its surface-to-volume ratio, which means it has to deform.

Much smaller water drops (tens to hundreds of micrometer) dispersed in air can be prepared by mixing hydrophobic particles and water at high shear speed by using a food blender or by using a planetary low shear mixer[7,40]. This water-in-air inverse foam system is termed dry water, as it shows free-flowing powder behaviour as shown in **Fig. 1d**, reflecting the powdery nature of the particles themselves. The water droplets in the dry water are armoured by the adsorbed hydrophobic particles (DCDMS-modified nano-sized silica particles), which prevent the droplet coalescence (**Fig. 10c**). Up to 98 wt.% of water can be incorporated into the powder. The dry water would potentially play a carrier of ingredients. By applying shear onto the dry water, for example, rubbing it on skin surfaces, small water drops are forced to coalesce. This leads to appearance of macroscopic

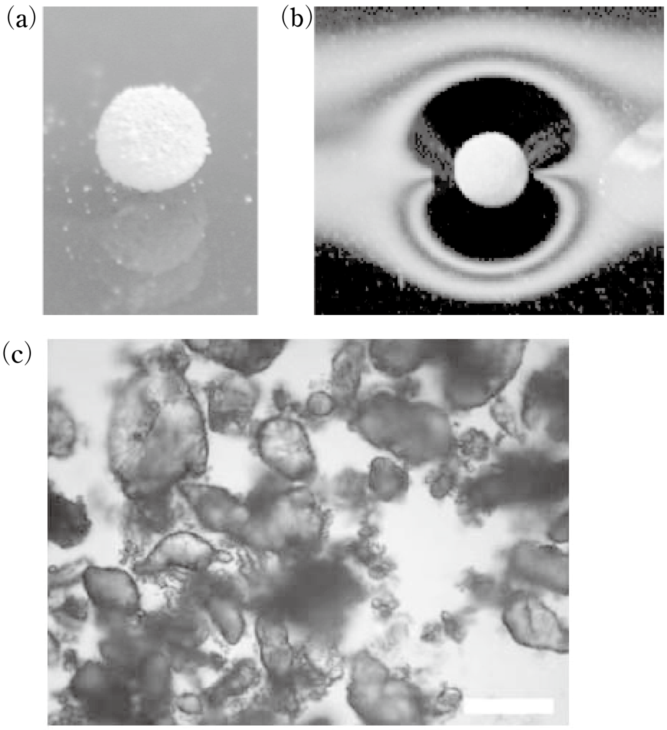

Fig. 10 Water marbles stabilized by hydrophobic particles placed on (a) a glass surface (side view) and (b) on a water pool (top view). [Quoted from reference 37(a). Copyright, The Royal Society.] (c) Optical micrograph of particle-stabilized water drops in air (dry water) prepared from 5wt% hydrophobic silica particles at a low volume fraction of water relative to the total volume of air and water (= 0.056). Non-spherical shapes are observed due to jamming of the adsorbed particles and their inability to be expelled after water drop coalescence during preparation. Excess particles contiguous with drop surfaces bind the drops together in a network. Scale bar = 200 μm. [Quoted from reference 7(a). Copyright, Nature Publishing Group.]

water and delivery of ingredients to the skin. In fact, skin whitening products consisting of toner lotion drops stabilized by particles have been already on the market (Benefiance luminizing powder-C essence poudre éclat C whitening, Shiseido). Recently, Cooper *et al.*[41] reported that the dry water stabilized with hydrophobic fumed silica nanoparticles is effective in methane storage application. They showed a great increase in the rate of methane uptake in methane gas hydrate by forming the hydrate in preformed dry water powders, comparing with bulk water.

Almost all the liquid marbles described in papers have been composed of either water or glycerol as the liquid and hydrophobized lycopodium, reactive polymer or silica as the stabilizing particles. These particles and liquid are potentially reactive and do not permit the use of organic chemistry; the liquids are volatile. Gao and McCarthy[42] reported the use of perfluoroalkyl particles (oligomeric and polymeric tetrafluoroethylene, which are unreactive) to stabilize a range of ionic liquid marbles. Ionic liquids are not volatile and have been demonstrated to be versatile solvents for chemical reactions.

6. Conclusion

An overview of foams and liquid marbles (dry liquids) stabilized by the colloidal particles was given. It is considered important to conduct researches on design, preparation, characterization of particulate foams and dry liquid systems using the particles whose surface characteristics are strictly controlled by utilizing particle surface engineering technology. The research for clarifying the correlation between the characteristics of the particles and the characteristics of foams and dry liquids should be also important. Further, it is required to develop foams and liquid marbles systems whose stability can be controlled by physical stimuli (temperature, light, electric fields, magnetic field, *etc.*), and/or by chemical stimuli (pH, ionic strength, solvent change). In addition, synthesis of functional materials using foams and dry liquids stabilized by particles as templates is also a field of research that will attract a lot of attentions.

Acknowledgement

The researches conducted and described by the authors in this paper were partially carried out with Prof. Steven P. Armes of Sheffield University (UK) and with Prof. Bernard P. Binks of University of Hull (UK). EPSRC is acknowledged for the postdoctoral grant for S.F. and R.M. S.F. thanks Professor Yoshinobu Nakamura of Osaka Institute of Technology. Further, the researches described here conducted by S.F. has received financial support from Japan Society for the Promotion of Science, grant-in-aid for young scientists (start-up) [No. 18850024], and grant-in-aid for young scientists (B) [No. 20750182]. Additional support for S.F. was provided by the Hosokawa Powder Engineering Foundation.

References

1) Ramsden, W. (1903): Proc. R. Soc. London, 72, p.156.
2) (a) Pickering, S. U. (1907): J. Chem. Soc., 91, p.2001. (b) Binks, B. P. (2002): Curr. Opin. Colloid Interf. Sci., 7, p.21. (c). Aveyard, R., Binks, B. P. and Clint, J. H. (2003): Adv. Colloid Interf. Sci., 503, pp.100-102. (d) Binks, B. P. and Horozov, T. S. (2006): "Colloidal Particles at Liquid Interfaces", Cambridge Univ. Press. (e) Nonomura, Y. (2005): Chem. Chem. Ind., 58, p.12. (f) Fujii, S. (2006): J. Adh. Soc. Jpn. 43, p.22.
3) (a) Bickermann, J. J. (1973): "Foams", Springer-Verlag, Berlin, (b) Garrett, P. R. (1993): "Defoaming; Theory and Industrial Applications", Surfactant Science Series 45, Marcel Dekker Inc., New York. (c) Prudhomme, R. K. and Khan, S. A. (1997): "Foams; Theory, Measurement and Applications", Surfactant Science Series 57, Marcel Dekker Inc., New York.
4) (a) Pugh, R. J. (1996): Adv. Colloid Interf. Sci., 64, p.67. (b) Aveyard, R., Binks, B. P., Fletcher, P. D. I., Peck, T. G. and Rutherford, C. E. (1994): Adv. Colloid Interf. Sci., 48, p.93.
5) Fujii, S. and Murakami, R. (2008): J. Surface Finish. Soc. Jpn. 59(1), p.33.
6) (a) Schutte, D., Schmitz, F.-T. and Brünner, H. (1968): US Patent 3393155. (b) Brünner, H., Schutte, D. and Schmitz, F.-T. (1969): Patent DE 1467023.
7) (a) Binks, B. P. and Murakami, R. (2006): Nat. Mater., 5, p.865. (b) Binks, B. P., Duncumb, B. and Murakami, R. (2007): Langmuir, 23, p.9143.
8) (a) Dampeirou, C. WO Patent (2005): 034917, (b) Lahanas, K.M. (2001): US Patent 6290941.
9) Xia, Y., Gates, B., Yin, Y. and Lu, Y. (2000): Adv. Mater., 12, p.693.
10) (a) Lovell, P. A. and El-Aasser, M. S., Eds. (1997): "Emulsion Polymerization and Emulsion Polymers" ; John Wiley & Sons, New York. (b) Kawaguchi, H. (2000): Polym. Sci., 25, p.1171. (c) Okubo M. Ed. (2005): "Polymer particles" Adv. Polym. Sci., Vol. 175, Springer.
11) Levine, S., Bowen, B. and Partridge, S. J. (1989): Colloids Surf., 38, p.325.
12) Paunov, V. N. (2003): Langmuir, 19, p.7970.
13) (a) Graeme, G. , Büscher, K., Preuss, M., Kappl, M., Butt, H.-J. and Graf, K. (2005): J. Phys., Condens. Matter, 17, S445. (b) Gillies, G., Kappl, M. and Butt, H.-J. (2005): Adv. Colloid Interf. Sci., 114–115, p.165.; (c) Preuss, M. and Butt, H.-J. (1998): J. Colloid Interf. Sci., 208, p.468.
14) Horozov, T.S., Braz, D.A., Fletcher, P.D. I., Binks, B.P. and Clint, J. H. (2008): Langmuir, 24, p.1678.
15) (a) Horvolgyiz, Z., Nemeth, S. and Fendler, J.H. (1993): Colloids Surf. A, 71, p.327. (b) Hadjiiski, A., Dimova, R., Denkov, N.D., Ivanov, I.B. and Borwankar, R. (1996): Langmuir, 12, p.6665.
16) (a) Vanderhoff, J.W. and Shaffer, O. EPI Lehigh University, Bethlehem, USA (STS 7, June 1983). (b) Vanderhoff, J. W., El-Aasser, M. S., Micale, F. J., Sudol, E. D., Tseng, C.-M., Sheu, H.-R. and Kornfeld, D. M. (1988) Document ID: 19890010947.
17) Martinez, A.C., Rio, E., Delon, G., Saint-Jalmes, A., Langevin, D. and Binks, B.P. (2008): Soft Matter, 4, p.1531.
18) Binks, B. P. and Horosov, T. S. (2006): Angew. Chem. Int. Ed. 45, p.773.
19) (a) Subramaniam, A. B., Abkarian, M., Mahadevan, L. and Stone, H. A. (2005): Nature, 438, p.930. (b) Subramaniam, A. B., Mejean, C., Abkarian, M. and Stone, H. A. (2006): Langmuir, 22, p.5986.
20) Binks, B. P. and Horosov, T. S. (2005): Angew. Chem. Int. Ed. 44, p.3722.
21) (a) Binks, B.P., Kirkland, M. and Rodrigues, J.A. (2008) Soft Matter 4, p.2373. (b) Zhang, S.Y., Lan, Q., Liu, Q., Xu, H. and Sun, D.J. (2008): Colloids Surf.: A, 317, p.406.
22) (a) Esumi, K,. Matoba, M. and Yamanaka, Y. (1996): Langmuir, 12, p.2130. (b) Koopal, L. K., Goloub, T., de Keizer, A. and Sidorova, M.P. (1999): Colloids Surf. A, 151, p15. (c) Velikov, K.P., Durst, F. and Velev, O.D. (1998): Langmuir, 14, p.1148.
23) (a) Gonzenbach, U. T., Studart, A. R., Tervoort, E. and Gauckler, L. J. (2006): Angew. Chem. Int. Ed. 45, p.3526. (b) Gonzenbach, U. T., Studart, A. R., Tervoort, E. and Gauckler, L. J. (2006): Langmuir, 23, p.1025.
24) (a) Dickinson, E., Ettelaie, R., Kostakis, T. and Murray, B. S. (2004): Langmuir, 20, p.8517. (b) Kostakis, T., Ettelaie, R. and Murray, B. S. (2006): Langmuir, 22, p.1273.
25) Wilson, J. C. (1980): "A Study of Particulate Foams", DPhil Thesis, University of Bristol, UK.
26) (a) Heller, W. and Delauder, W.B. (1971): J. Colloid Interface Sci., 35, p.60. (b) Delauder, W.B. and Heller, W. (1971): J. Colloid Interface Sci., 35, p.308.
27) Kettlewell, S. L., Schmid, A., Fujii, S., Dupin, D. and Armes, S. P. (2007): Langmuir, 23, p.11381.
28) (a) Takahashi, M. (2005): J. Phys. Chem. B, 109, p.21858. (b) Ciunel, K., Armélin, M., Findenegg, G. H., Klitzing, R. V. (2005): Langmuir, 21. p.4790 (c) Najafi, A. S., Drelich, J., Yeung, A., Xu, Z., Masliyah, J. (2007):

J., Colloid Interface Sci., 308, p344.
29) Alargova, R. G., Warhadpande, D. S., Paunov, V. N. and Velev, O. D. (2004): Langmuir, 20, p.10371.
30) (a) Fujii, S., Ryan, A. J. and Armes, S. P.: (2006): J. Am. Chem. Soc., 128, p.7882. (b) Fujii, S., Iddon, P. D., Ryan, A. J. and Armes, S. P.: (2006): Langmuir, 22, p.7512. (c) Armes, S. P., Fujii, S., Iddon, P. D. and Ryan, A. J.: (2005): GB Pat. 524186.4 .
31) Fujii, S. and Nakamura, Y., manuscript in preparation.
32) Binks, B. P., Murakami, R., Fujii, S., Schmid, A. and Armes, S. P. (2007): Langmuir, 23, p.8691.
33) Dupin, D., Howse, J. R., Armes, S. P. and Randall, D. P. (2008): J. Mater. Chem., 18, p.545.
34) (a) Foulk, C. W. and Miller, J. N. (1931): Ind. Eng. Chem., 23, p.1283. (b) Bikerman, J.J. (1938): Trans. Faraday Soc., 34, p.634. (c) Oh, S.-G., Klein, S.P. and Shah, D.O. (1991) Langmuir, 7, p.1316.
35) Horozov, T. S. and Binks, B. P. (2004): Langmuir, 20, p.9007.
36) Subramaniam, A. B., Abkarian, M. and Stone, H. A. (2006): Nat. Mater., 4, p.553.
37) (a) Aussillous, P. and Quéré, D. (2001): Nature, 411, p.924.; (b) Aussillous, P. and Quéré, D. (2006): Proc. R. Soc. A, 462, p.973.
38) (a) McHale, G., Herbertson, D. L., Elliott, S. J., Shirtcliffe, N. J. and Newton, M. I. (2007): Langmuir, 23, p.918. (b) Newton, M. I., Herbertson, D. L., Elliott, S. J., Shirtcliffe, N. J. and McHale, G. (2007): J. Phys. D: Appl. Phys. 40, p.20.
39) Colver, P. J., Chen, T. and Bon, S. A. F. (2006): Macromol. Symp. 34, p.245.
40) Forny, L., Pezron, I., Saleh, K., Guigon, P. and Komunjer, L. (2006): Powder Technology, 171 p.15.
41) Wang, W.X., Bray, C.L., Adams, D.J. and Cooper, A.I. (2008): J. Am. Chem. Soc., 130, p.11608.
42) Gao, L. and McCarthy, T. J. (2007): Langmuir, 23, p.10445.

Author's short biography

Dr. Syuji Fujii

Dr. Syuji Fujii is a lecturer at Osaka Institute of Technology (Japan). He received B.S. and M.S. degrees from Kobe University (Japan), where he also received a Ph.D. degree in polymer chemistry under the supervision of Prof. Masayoshi Okubo in 2003. His postdoctoral studies were carried out in Prof. Steven P. Armes group at University of Sussex (UK) from 2003 to 2004 and at University of Sheffield (UK) from 2004 to 2006. His major research interests focus on synthetic polymer chemistry, design and characterisation of polymer-based particles, and emulsions and foams stabilized with the particles.

Ryo Murakami

Ryo Murakami is a postdoctoral research associate of the Department of Chemical Engineering at the Imperial College London. He received a B.Sc., M.Sc. and Ph.D. from Kyushu University and then worked in Surfactant & Colloid Group at the University of Hull as a postdoctoral research associate. His research interests include adsorption of amphiphiles and particles at fluid-fluid interfaces and wetting phenomena, with emphasis on studies on particle-stabilized fluid-dispersed systems such as emulsions, foams.

Percolation Segregation and Flowability Measurement of Urea under Different Relative Humidity Conditions[†]

A. K. Jha, H. Yi, and V. M. Puri*
Materials Research Institute,
Department of Agricultural and Biological Engineering,
The Pennsylvania State University[1]

Abstract

Dry blended fertilizers are known to segregate. Furthermore, researchers have documented that the size of blended fertilizers is the most dominant physical property contributing towards segregation. Additionally, it is known that flowability is also affected by the size and moisture content of blended fertilizers. Therefore, segregation and flowability of binary size mixtures were studied at three different equilibrium relative humidity conditions 40%, 50%, and 60% with the goal to evaluate the feasibility to mitigate segregation using moisture content. To that end, binary size mixtures were prepared using coarse and fine size urea of size ratio 2.0 and 1.7 mixed in weight proportions 33:67 and 50:50, respectively (commonly found in 10-10-10 blends). Urea is the most hygroscopic and expensive component of the blended fertilizers. Percolation segregation was quantified using the Primary Segregation Shear Cell (PSSC-II). Based on experimental results using the PSSC-II, the segregated fines mass, normalized segregation rate (NSR), and segregation rate (SR) of fines for binary urea mixtures were higher at equilibrium relative humidity of 40% vs. 50% and 60%. The NSR is defined as the amount of fines percolated from the total initial fines in the binary mixture based on the total time of PSSC-II operation (kg/kg-h). For size ratios 2.0 and 1.7, only 2.8% and 7.0% decrease in NSRs were recorded for the increase in relative humidity by 10 points (from 40% to 50%), respectively, whereas 36.0% and 45.0% decrease in NSRs were recorded for increase in relative humidity by 20 points (from 40% to 60%), respectively ($P<0.5$). Additionally, the flowability of binary size mixtures was quantified using a true Cubical Triaxial Tester (CTT). For size ratios 2.0 and 1.7, angle of internal friction increased from 31.3° to 35.9° to 39.0° and 27.4° to 32.0° to 36.0° when relative humidity increased from 40% to 50% to 60%, respectively. The angle of internal friction values were significantly different ($P<0.05$) but cohesion values, at different relative humidity conditions were not significantly different ($P>0.05$). Based on experimental results, relative humidity, if implemented carefully, could be used as a tool to mitigate segregation in blended fertilizers.

Keywords: cubical triaxial tester, primary segregation shear cell, segregation rate, normalized segregation rate, angle of internal friction, and cohesion

Introduction

Particulate materials are handled in several industries such as agriculture, ceramic, construction, food, nutraceutical, pharmaceutical, power, and powder metallurgy. The physical and mechanical properties' difference during handling, mixing, conveying, and storage causes an unwanted phenomenon known as segregation. Segregation is defined as "demixing" or reverse mixing (Popplewell et al., 1989; and Rollins et al., 1995). Segregation causes uneven quality of fertilizers and tablets, fluctuating packet weights, low mechanical strength of compacts and abrasives, poor refractory materials, and low rates of contact and reaction (Shinohara, 1997). For example, different size granules in blended fertilizers separate from one another during conveying, transportation, and storage causing uneven distribution of fertilizer in the field

---

[†] Accepted on July 2, 2008

[1] 229 Ag Engineering Building, University Park, PA 16802, USA

* Corresponding author
TEL: 814-865-3559, FAX: 814-863-1031
E-mail: vmpuri@psu.edu

that leads to localized over- and under-supply. For blended materials, the uniformity of blend is highly dependent on physical attributes, such as, density, particle size and size distribution, shape, hardness, surface texture, and moisture content.

Several researchers have reported that size of granular materials is the most important parameter responsible for segregation (Tang and Puri, 2004; Bridle et al., 2004; and Bradley and Farnish, 2005). However, size segregation in conjunction with other physical parameters has greater detrimental effect than segregation by size alone. In addition, flowability of the blend is dependent on physical and mechanical properties of the constituents. Flowability of hygroscopic granular materials is one of the key mechanical properties for the quality of mixing and potential for segregation. High flowability of material has positive and negative effects: for mixing, high flowability is essential, whereas for segregation high flowability is detrimental. In the literature, relative humidity has been documented to reduce flowability and hence is expected to lower segregation. However, systematic and quantitative study correlating segregation with flowability of hygroscopic blended fertilizers could not be found in the literature. Therefore, percolation segregation and flowability were studied under different equilibrium relative humidities, with the objective to evaluate the use of relative humidity for mitigating segregation while maintaining flowability at acceptable level of blended fertilizers.

To know the flow properties at different equilibrium relative humidity conditions, quantifying their flowability is very important. Herein, a low pressure (<100 kPa) cubical triaxial tester (CTT) developed by Kamath and Puri (1997) was used to measure flowability using the Mohr-Coulomb model. The flexible-boundary of CTT allows unrestrained deformations in the samples and minimizes die-wall friction effect. The low pressure CTT is capable of measuring the three-dimensional response of cohesionless and cohesive particulate materials (Li and Puri, 1996).

The Mohr-Coulomb model, which states that the effective shear strength, τ, increases with effective normal stress, σ, on the failure plane, is the most commonly used yield criterion in bulk solids flow theory. It can be represented by equation 1.

$$\tau = c + \sigma \tan \phi \tag{1}$$

where, c, is the cohesion of the material, and ϕ is the angle of internal friction.

For both of the parameters, c and ϕ lower values indicate higher flowability and higher flowability leads to higher segregation (Duffy and Puri, 1997). Therefore, the specific objectives of the study were: 1) to quantify the percolation segregation under three equilibrium relative humidity conditions, and 2) to evaluate flowability of binary size mixtures for the same three equilibrium relative humidity conditions.

2. Materials and Methods

2.1 Test material selection, preparation, and parameter determination

Urea is a readily available but the most expensive constituent of dry blended fertilizers, which was selected for studying segregation and flowability at three equilibrium relative humidity conditions, i.e., 40%, 50%, and 60%, for two size ratios with differing mixing ratios (**Table 1**). The shape of urea particles was round with sphericity of 0.97 (SD = 0.02). For this study, different size ranges of urea were obtained using US standard sieves of $2^{1/4}$ series. The three equilibrium relative humidities (ERHs) were selected based on long-term weather data of University Park, PA, i.e., the stored fertilizer component urea is likely to be subjected to these types of conditions. All the samples were equilibrated at test ERHs by placing the material in microprocessor controlled humidity chamber (Model 9000L, VWR international, Sheldon Manufacturing Inc, Cornelius, Oregon) for 48 hours spread in a single layer on sieves. Samples were placed on sieves to allow air to circulate through sieve perforations all around the urea granules. All tests were performed after mixing coarse and fine urea granules (**Table 1**) to form binary size mixtures using lowest speed setting of a six-speed bench-top 225-W mixer (Model-106772N, Type-M27,

Table 1 Binary size mixtures of urea used for both segregation and flowability studies

Coarse Size	3350-4000 (d_{mean}= 3675 μm) and 2800-3350 (d_{mean} = 3075 μm)	
Fine Size*	1700-2000 (d_{mean}= 1850 μm)	
Size Ratio Coarse: Fine	3675:1850 = 2.0**, Mixing ratio = 33:67	3075:1850 = 1.7**, Mixing ratio = 50:50
Equilibrium Relative Hum idity	40%, 50%, and 60%	

* Based on segregation observed in dry blends that are normally stored in bagged fertilizers

** Rounded up

General Electric, Marketed by Wal-Mart Stores Inc., Bentonville, AR). The purpose of testing binary size mixtures was to lay the foundation for studying segregation potential of fines in multi-size mixtures leading to multi-size plus multi-component mixtures. The results from multi-size and multi-component mixtures will be presented in subsequent articles. Two size ratios 2.0 and 1.7, i.e., ratio of coarse:fines, were mixed by weight in the proportions 33:67 and 50:50, respectively. The two different size ratios and corresponding mixing proportions were selected based on size distributions of 10-10-10 and 10-20-20 fertilizer blend formulations collected from three blend plants in Pennsylvania. For flowability quantification, the binary size mixtures were tested at two confining pressures of 3.5 kPa and 7.0 kPa based on pressure in fertilizer bins under static storage conditions. All tests for segregation and flowability were conducted in an environment-controlled laboratory with average temperature of 22℃ ± 3℃ and relative humidity less than 40%. On the average, each test lasted for 40 minutes when urea was exposed to these environmental conditions, which is expected to have minimal influence on urea granules' moisture content.

2.2 Segregation

For segregation study, three parameters including material bed depth of 85 mm (comparable to depth of 22.7 kg bagged blended fertilizers), particle bed strain of 6% (corresponding to available head space in bags), and strain rate 0.5 Hz (similar to conveyors used to transport bagged fertilizers) were selected for operating PSSC-II as shown in **Table 2** (Tang and Puri, 2005; Vursavus and Ozguven, 2004). The dry blended formulation 10-10-10 (i.e., 10% total nitrogen-10% available phosphate-10% soluble potash) was selected for test parameter determination because of the high demand (inexpensive) and its higher susceptibility to segregation under handling and operating conditions. The higher amount of fillers in the low analysis (10-10-10 and others) bags is the primary reason for large head space that leads to non-uniformity. For each treatment, segregated fines mass was collected using the eight load cells (range ±0.001 g) installed at eight different locations and recorded using LabView (Version 6.0, National Instruments, Austin, TX). Based on published results (Duffy and Puri, 2002, and Tang and Puri, 2005), and preliminary testing with fertilizer blends, five replications were deemed sufficient for experimental data to be within the 95% confidence interval.

Table 2 Experimental design for segregation testing of binary size mixtures of urea

Parameter	Number
Size ratios 2:0 (Mixing Ratio-33:67) and 1.7 (Mixing Ratio-50:50)	2
Equilibrium relative humidities (40%, 50% and 60%)	3
Strain rate (0.5 Hz)	1
Strain (6%)	1
Bed depth (85 mm)	1
Replications (5 per treatment)	5
Number of tests	30

In this study, eight sampling points distributed in two rows (4 load cells in a row) were configured (**Fig. 1**). The rationale for the locations of the load cell was to collect maximum percolated fines. For ease of reference, these load cells are identified as BR (back right), FR (front right), BCR (back center right), FCR (front center right), BCL (back center left), FCL (front center left), BL (back left), and FL (front left) as shown in **Fig. 1(b)**. Sieve number 8 (opening size = 2,000 μm) was used throughout the tests so that the percolating fines could exit while coarse particles did not block sieve openings.

2.3 Flowability

The flexible-boundary CTT developed by Kamath and Puri (1997) was used for testing the flowability of binary size mixtures (**Tables 1** and **3**). The cubical

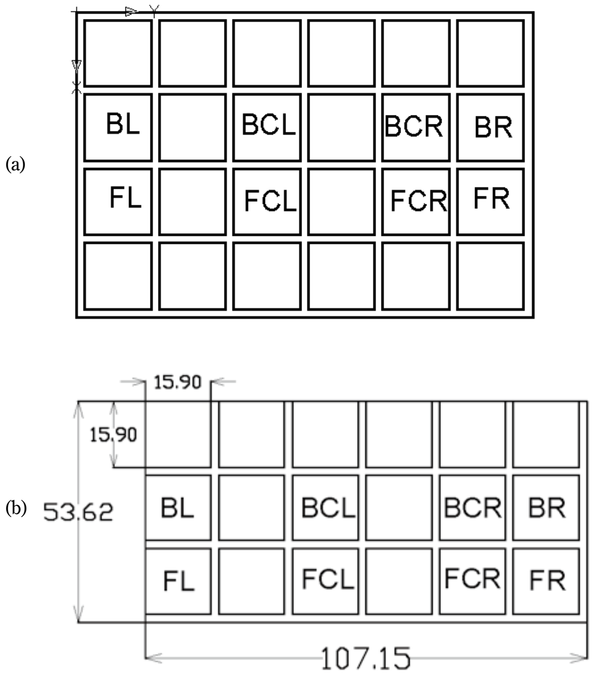

Fig. 1 Collection pan for fines showing eight load cell locations, (a) top view of shear box and eight load cell positions for data collection, (b) top view of collection pan (all dimensions in mm).

Table 3 Experimental design for flowability testing of binary size mixtures of urea

Parameter	Number
Size ratios 2:1 (mixing ratio − 33:67) and 1.7:1 (mixing ratio − 50:50)	2
Confining pressures (3.5 kPa and 7.0 kPa)	2
Equilibrium relative humidities (40%, 50% and 60%)	3
Replications (3 per treatment)	3
Number of tests	36

triaxial tester uses two individual pressure controllers (Proportion-Air Inc. QB1TFEE015), which can apply pressures from 0 to 100 kPa with ± 0.2% of accuracy over the entire range. Individual pressure controllers regulate horizontal and vertical pressures independently using software developed with LabView (Version 6.0, National Instruments, Austin, TX) by Kandala and Puri (2000). The flowability parameters were measured using the conventional triaxial compression (CTC) test. The CTC test begins with hydrostatic compression at pressure σ_c, or confining pressure. While this confining pressure is kept constant in horizontal directions, the pressure in the vertical direction (i.e., gravity directions) was increased until the sample failed. The failure stress was denoted as σ_f. These pressures (σ_c and σ_f) are the principal stresses that were plotted on the normal stress versus shear stress diagram to produce corresponding Mohr circles. Based on published results (Li and Puri, 1996; and Kandala and Puri, 2000), three replications were performed for each combination for testing flow behavior of samples using the CTT. A complete block design was selected for data analysis. One set of experiments was performed on binary size mixtures of urea equilibrated at relative humidity values of 40%, 50% and 60%. All the three data sets were analyzed separately and compared for determining flow properties corresponding to three different ERHs.

From the common tangent line of two Mohr circles, the angle of internal friction (ϕ) and the cohesion (c) of samples were determined. Before filling the cavity (50 mm × 50 mm × 50 mm), a low inflating pressure of 5 kPa was applied to ensure that membranes were in contact all around to prevent fertilizer from exiting or squeezing out. Then, well mixed binary size sample was placed into the cavity in three steps. In the first step, cavity was one-third filled and top surface was leveled off with a soft nylon brush; this was repeated for the next third and the final-one third. The amount of test material in the cavity was 59 g ± 1 g. After placing the sample into the cavity, a confining pressure was applied using a compressed air source. Subsequently, the pressure in the vertical direction was increased at 100 Pa/s until failure. The very low rate of pressure increase of 100 Pa/s was selected so that 1) particles have sufficient time for rearrangement, and 2) rate-dependent effects are minimized.

3. Results and Discussions

3.1 Physical properties determination

The characterization of physical properties of binary size mixtures such as bulk density, particle density, shape, and size of the test materials is essential before testing because of inherent variability of bulk solids (**Table 4**). The flow and segregation responses of bulk solids vary with variation in their physical properties.

In **Table 4**, for size ratios 2.0 and 1.7, both the particle density (PD) and bulk density (BD) increased with increase in RH from 40% to 60%. With increase in RH by 20% points (i.e., 40% to 60%), PD increased by 0.3% and 0.4%, respectively, whereas for increase in RH by 10% points (40% to 50%), PD increased by 0.1% and 0.1%, respectively. The small increase in PD with increase in equilibrium relative humidity was obtained because of surface air pores were filled by moisture (P>0.05). The same trend was observed for bulk density for both the size ratios 2.0 and 1.7 (P>0.05). No measurable change in porosity was noted when RH increased from 40% to 60%, which is beyond the detection capability of the multipyconometer used in this study.

3.2 Percolation segregation

The measured mass of segregated fines (g) for two binary size mixtures (2.0 and 1.7) conditioned at

Table 4 Physical property of binary size mixtures of urea (sphericity = 0.97) at three different equilibrium relative humidity conditions

Size Ratio	Mixing Ratio	Equilibrium Relative Humidity (%)	Particle density* (kg/m^3)	Bulk density* (kg/m^3)	Porosity**
2.0	33:67	40	1456 (2)	726 (2)	50
		50	1458 (3)	743 (3)	49
		60	1461 (5)	744 (4)	49
1.7	50:50	40	1455 (2)	727 (1)	50
		50	1458 (3)	732 (1)	50
		60	1461 (3)	733 (0)	50

* Measured values - Quantachrome multipyconometer (Model MVP-2) with ultra pure He- five replicates

** Calculated values

Table 5 Segregated fines, mean segregation rate and mean NSR for binary size mixtures of urea

Size ratio (Mixing Ratio)	ERH (%)	Average time for discharge (minutes)	Segregated fines (g)	Average segregation rate (kg/h)	NSR (kg/kg-h)
2 (33:37)	40	10.4 (0.1)	87.74 (1.15)	0.51 (0.01)	1.12 (0.02)
	50	10.4 (0.1)	85.69 (1.60)	0.49 (0.01)	1.09 (0.02)
	60	10.2 (0.2)	56.21 (1.52)	0.33 (0.01)	0.73 (0.02)
1.7 (50:50)	40	11.5 (0.0)	41.03 (1.19)	0.21 (0.01)	0.61 (0.02)
	50	11.4 (0.1)	38.40 (1.77)	0.20 (0.01)	0.58 (0.03)
	60	11.4 (0.2)	22.99 (1.29)	0.12 (0.01)	0.34 (0.02)

* Standard deviation values in parenthesis

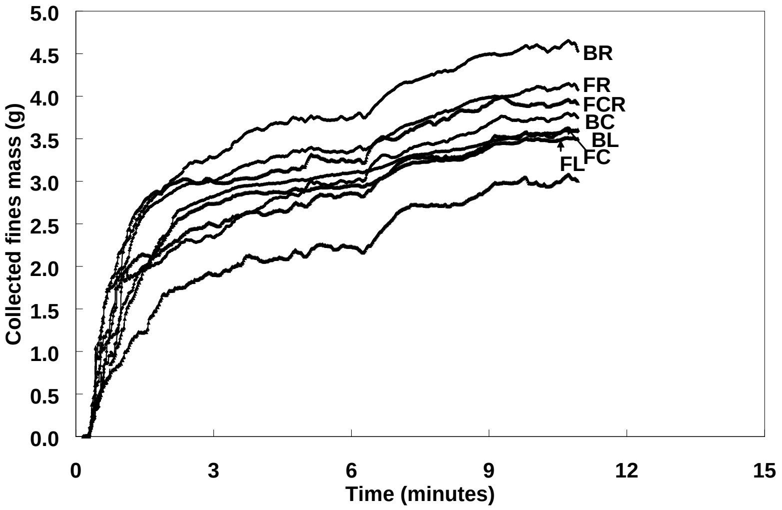

Fig. 2 Typical segregated fines mass of binary size urea mixture for size ratio 2.0 equilibrated at 50% relative humidity environment with bed depth of 85 mm. The curves are for different load cell locations shown in **Fig. 1**.

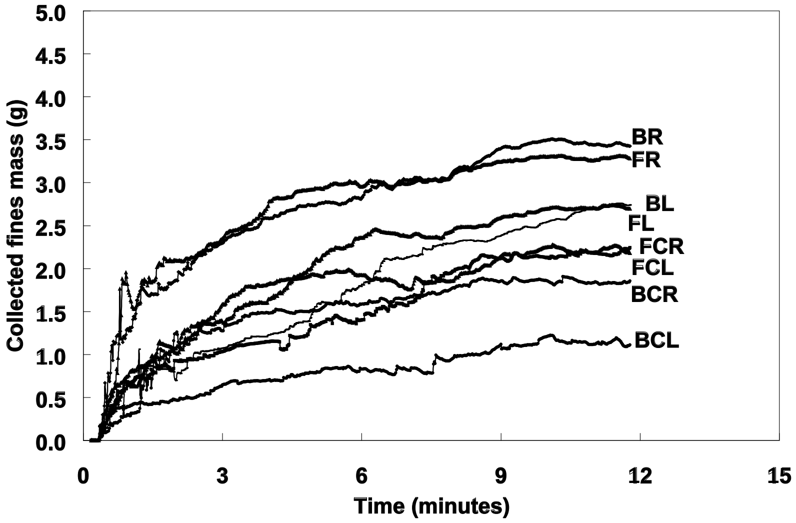

Fig. 3 Typical segregated fines mass of binary size urea mixture for size ratio 1.7 equilibrated at 50% relative humidity environment with bed depth of 85 mm. The curves are for different load cell locations shown in **Fig. 1**.

three different ERHs (40%, 50% and 60%) are summarized in **Table 5**. **Fig. 2** and **3** show typical profiles of cumulative fines mass collected by the eight load cells in real-time for size ratios 2.0 and 1.7, respectively. Similar profiles were obtained at other ERHs. Both of these figures show that most of the segregated fines were collected at the two ends, which is in agreement with the results reported for glass beads by Duffy and Puri (2002) and glass beads and mash feed by Tang and Puri (2005). Since the time evaluation of segregated fines was recorded using the PSSC-II, two rate metrics: segregation rate (kg/h) and normalized segregation rate (kg/kg-h) are introduced. Herein, segregation rate is defined as the mass of fines segregated from the binary size mixture of urea per unit total time of PSSC-II operation; whereas, NSR is defined as the ratio of collected fines mass to total mass of fines mixed with coarse divided by total time of PSSC-II operation.

In **Table 5**, for size ratio 2.0, when RH increased by 20% points (40% to 60%) and 10% points (40% to 50%), segregated fines decreased by 36.0% and 2.3%, respectively. For size ratio 1.7, when RH increased by 20% points (40% to 60%) and 10 points (40% to 50%) segregated fines decreased by 44.0% and 6.4%, respectively. As expected, segregation declined with increase of moisture content. These results suggest that relative humidity could be used as a tool to mitigate segregation.

Figs. 2 and 3 show typical profiles of segregated fines mass of binary mixture for size ratio 2.0 and 1.7, respectively, collected by the eight load cells configured four each in two rows (**Fig. 1**). The measured mass values are for binary mixtures of urea that were equilibrated at 50% relative humidity. Both of these figures show that fines masses collected by the eight load cells increased with time. Fines mass collected for size ratio 2.0 was higher compared with size ratio 1.7. Results confirmed that higher size ratio has higher segregation potential. Fines masses collected by eight load cells were different for both of these size ratios. For size ratio 2.0 (**Fig. 2**), fines mass collected by eight load cells were more uniform compared with mass collected for size ratio 1.7.

Fig. 4 shows iso-mass contours for segregated fines for size ratios 2.0 (**Fig. 4a**) and 1.7 (**Fig. 4b**) at the end of 10 minutes, which is the expected time duration of motion conditions for bagged fertilizer to experience between filling and transportation. Even though iso-mass contours are shown at the end of 10 minutes, these can be analyzed at any time from 0 to 10 minutes in the interval of 1 s. At the end of 10 minutes, the fines were collected more at both ends of the shear box such as BL, FL, BR and FR compared to the center zone such as BCL and FCL ($P>0.05$). Load cells in the center received less fines compared to other load cells because of diffusive percolation mechanism. This result is in agreement with previous results obtained for size ratio less than 4.0 (Duffy and Puri, 2002).

3.3 Normalized segregation rate (NSR)

For size ratio 2.0, NSR decreased from 1.12 kg/kg-h to 1.09 kg/kg-h to 0.73 kg/kg-h when urea

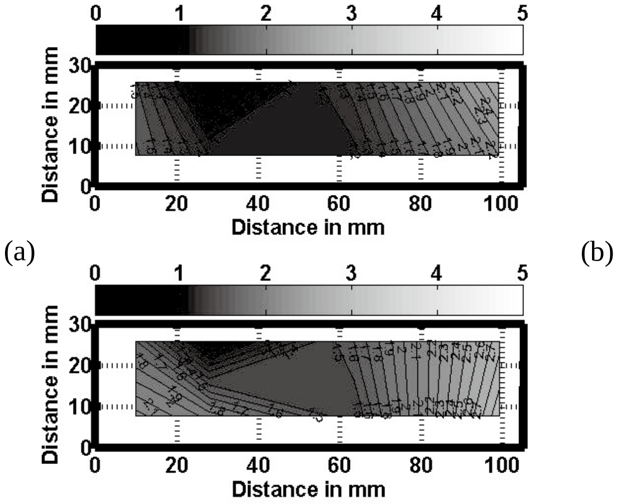

Fig. 4 Iso-mass contours of segregated fines for binary size urea mixtures equilibrated at 50% relative humidity at the end of 10 minutes for size ratios: (a) 2.0 and (b) 1.7; x and y axes dimensions denote the opening size available at the bottom of the shear box for fines to percolate.

binary size mixtures equilibrated relative humidity increased from 40% to 50% to 60%. Similarly, for size ratio 1.7, NSR decreased from 0.62 kg/kg-h to 0.58 kg/kg-h to 0.34 kg/kg-h urea binary size mixtures equilibrated relative humidity increased from 40% to 50% to 60%. Figure 5 shows a typical profile of NSR at 40% RH of binary mixture for size ratio 2.0. The NSR declined rapidly in the first few minutes (<3 minutes) of PSSC-II operation followed by an asymptotic approach to linear decline. The rapid initial decline can be attributed to the availability of fines due to their low coordination number, which increases with time, i.e., fines become more constrained. Similar profiles were obtained for other ERHs (50% and 60%) and for size ratio 1.7. The NSR profiles could be used to predict the amount of segregation in the mixture under given operating condition in real-time.

3.4 Distribution of segregation rate

Distribution of segregation rate (DSR) metric was used to evaluate the spatial distribution of segregation rate (SR) corresponding to the eight load cell locations. **Figs. 6 and 7** show typical SR of percolated fines along the eight load cells at 50% RH for the size ratios 2.0 and 1.7, respectively. Results were in agreement with the NSR result, i.e., NSR decreased with increasing relative humidity. **Fig. 6** for size ratio 2.0, shows that SR was higher at both ends of the shear box compared with the center region and decreased with time, i.e., 60 s (**Fig. 6a**) to 120 s (**Fig. 6b**) to 180 s (**Figs. 6c**) ($P>0.05$). At 60 s, SR was higher in the center and right of the shear box because of initial percolated fines present initially in the bottom of the mixture. **Fig. 7** for size ratio 1.7 shows fines mass were collected more at both ends of the shear box such as BL, FL, BR and FR compared to the center zone such as BCL and FCL ($P>0.05$) and SR decreased with time, i.e., 60 s (**Fig. 7a**), 120 s (**Fig. 7b**), and 180s (**Fig. 7c**). For both size ratios 2.0 and 1.7, load cells in the center received less fines compared to other load cells because of diffusive percolation mechanism. This result is in agreement with previous results obtained for size ratio less than 4.0 (Duffy and Puri, 2002).

3.5 Flowability

From the CTC tests, the failure stress values of binary mixtures were determined. **Fig. 8** illustrates the failure stress values of well-mixed binary size urea mixtures. For size ratio 2.0 at confining pressure σ_c = 3.5 kPa, the failure stress increased from 12.2 kPa to 15.5 kPa to 16.2 kPa when ERH increased from 40% to 50% to 60%. At relatively higher confining pressure σ_c = 7 kPa, the failure stress increased from 23.5 kPa to 29.3 kPa to 32.0 kPa for increase in ERH from 40% to 50% to 60%, respectively. For size ratio 1.7 at confining stress (σ_c= 3.5 kPa), the failure stress increased from 11.2 kPa to 14.5 kPa when ERH increased from 40% to 50% and plateaued thereafter, whereas the failure stress increased from 22.7 kPa to 28.0 kPa for increase in ERH from 40% to 60% at higher confining pressure σ_c= 7 kPa. A plausible explanation for the minimal to no effect of ERHs for size ratio of 1.7 at lower confining pressure (σ_c= 3.5 kPa) was a result of more tightly packed samples, i.e., 3.5 kPa of confining pressure was not sufficient to induce rearrangement of particles.

The results presented in this article demonstrated decreased segregation and flowability with the increase in relative humidity, as expected. Higher size

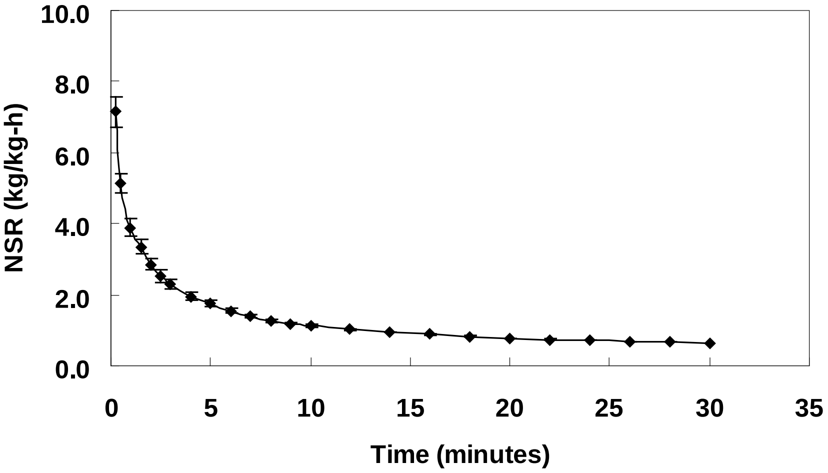

Fig. 5 Segregation rate at 40% ERH for size ratio 2.0.

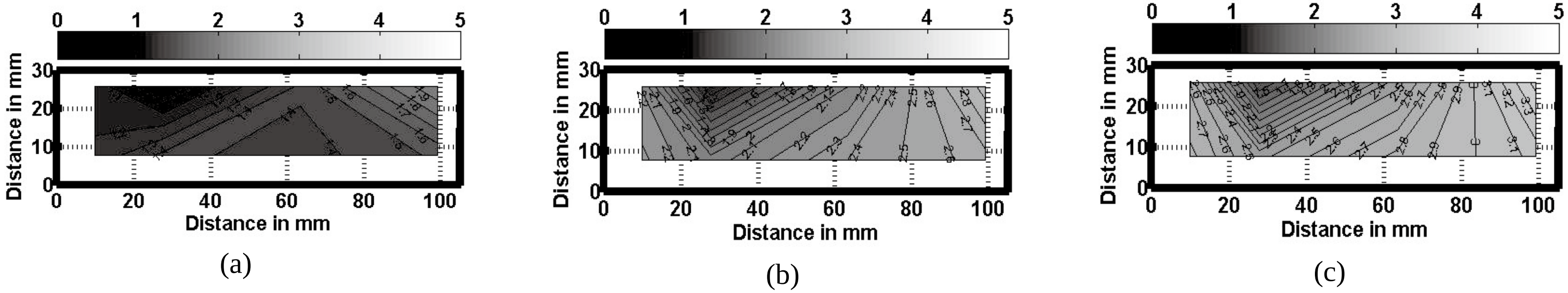

(a) (b) (c)

Fig.6 Iso-segregation rate of fines mass of binary urea mixtures for size ratio 2.0 and 50% ERH at, (a) 60 s, (b) 120 s, and (c) 180 s; x and y axes dimensions denote the opening size available at the bottom of the shear box for fines to percolate.

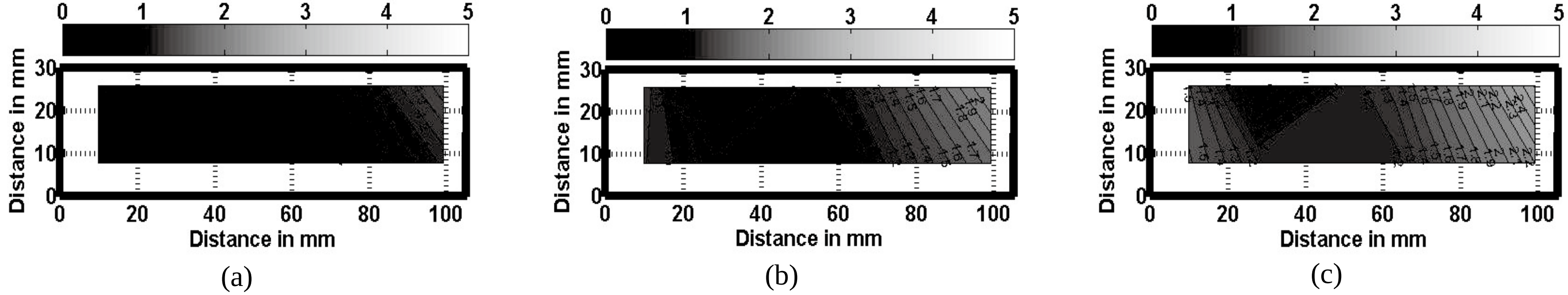

(a) (b) (c)

Fig. 7 Iso-segregation rate of fines mass of binary urea mixtures for size ratio 1.7 and 50% ERH at, (a) 60 s, (b) 120 s, and (c) 180 s; x and y axes dimensions denote the opening size available at the bottom of the shear box for fines to percolate.

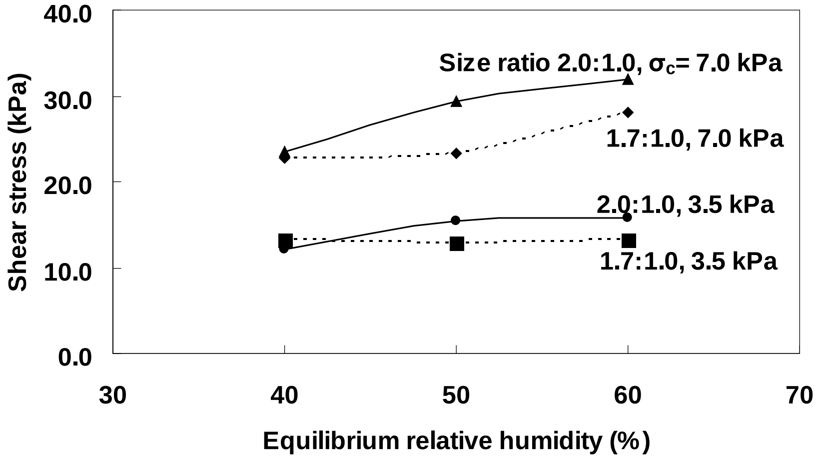

Fig. 8 Failure stress difference for binary mixtures of size ratios of 2.0 and 1.7 and confining pressures of 3.5 and 7.0 kPa.

Table 8 Flowability parameters for binary size mixtures at three equilibrium relative humidities*

Size Ratio (Mixing Ratio)	Equilibrium Relative Humidity (%)	Angle of Internal Friction (ϕ)	Cohesion (c, kPa)
2 (33:67)	40	31.3° (1.2)	0.3 (0.2)
	50	35.9° (1.7)	0.5 (0.3)
	60	39.0° (2.3)	0.3 (0.4)
1.7 (50:50)	40	27.4° (1.9)	0.5 (0.4)
	50	32.0° (3.4)	0.9 (0.9)
	60	36.0° (0.0)	0.3 (0.0)

* Standard deviation values in parenthesis

ratio and equilibrium relative humidity tend to induce higher failure stress, which implies tighter packing strength of the samples.

The flowability determining parameters, i.e., the angle of internal friction and cohesion are summarized in **Table 8**. For size ratio 2.0, the angle of internal friction increased from 31.3° to 35.9° to 39.0° for increase in ERH from 40% to 50% to 60%, respectively. For size ratio of 1.7, the angle of internal friction increased from 26.8° to 36.0° when relative humidity increased from 40% to 60%. In all cases, size ratio of 2.0 showed higher angle of internal friction than size ratio of 1.7 suggesting that size ratio of 2.0 mixture has lower flowability.

For both size ratios of 2.0 and 1.7, cohesion values remained constant and were not significantly different ($P>0.05$). Negligible cohesion values were consistent with visual observations.

Results showed that flowability of particles decreased with the increase in angle of internal friction while cohesion values were negligible. The lower flowability for size ratio of 2.0 compared to size ratio of 1.7 is because of the mixing and size ratios' differences; the large size ratio binary mixture had more fines compared to coarse (mixing ratio 33:67) and mixture's response was governed by the quantity of fines. For large size ratio, more pore spaces were available in the coarse particle bed vs. small size ratio. Furthermore, flowability parameter results also confirmed the segregation results. PSSC-II results also demonstrated that segregation in binary size mixtures of urea decreased with increasing ERHs from 40% to 60%. Results of flowability and segregation for binary size urea mixtures were in agreement with the results published by Duffy and Puri (1997) for food powders.

4. Conclusions

Percolation segregation was measured using the PSSC-II for binary size mixtures of urea prepared by blending fines (1700-2000 μm) with coarse (3350-4000 μm and 2800-3350 μm) equilibrated at three relative humidity values (40%, 50%, and 60%). All tests were conducted at bed depth of 85 mm, strain of 6%, and strain rate of 0.5 Hz. Results showed that the PSSC-

II is capable of quantifying segregation of binary size mixtures. For quantification of segregation, four metrics: 1) segregated fines mass, 2) segregation rate, 3) normalized segregation rate, and 4) distribution segregation rate of fines were used. The following conclusions were drawn from this study.

1. Size ratio 2.0
   - Segregated fines mass values decreased from 87.7 g to 85.7 g to 56.2 g when ERHs increased from 40% to 50% to 60%, respectively. Only 2.0% of decrease in collected fines mass was recorded for increase in ERH by 10 points (from 40% to 50%), whereas 36.0% decrease in fines mass was recorded for increase in ERH by 20 points (from 40% to 60%).
   - Segregation rate decreased from 0.141 kg/h to 0.137 kg/h to 0.091 kg/h when ERHs increased from 40% to 50% to 60%, respectively. Only 2.8% decrease in SR was recorded for increase in ERH by 10 points (from 40% to 50%), whereas 36.0% decrease in SR was recorded for increase in ERH by 20 points (from 40% to 60%).
   - NSR decreased from 0.332 kg/kg-h to 0.323 kg/kg-h to 0.215 kg/kg-h when relative humidity increased from 40% to 50% to 60%, respectively. Only 2.8% of decrease in NSR was recorded for increase in ERH by 10 points (from 40% to 50%), whereas 36.0% decrease in NSR was recorded for increase in ERH by 20 points (from 40% to 60%).

2. Size ratio 1.7
   - Segregated fines mass values decreased from 41.0 g to 38.4 g to 23.0 g when ERH increased from 40% to 50% to 60%, respectively. Only 6.0% of decrease in collected fines mass was recorded for increase in ERH by 10 points (from 40% to 50%), whereas 43.0% decrease in mass was recorded for increase in ERH by 20 points (from 40% to 60%).
   - SR decreased from 0.060 kg/h to 0.056 kg/h to 0.033 kg/h when ERH increased from 40% to 50% to 60%, respectively. Only 7.0% decrease in SR was recorded for increase in ERH by 10 points (from 40% to 50%), whereas 45.0% decrease in segregation rate was recorded for increase in relative humidity by 20 points (from 40% to 60%).
   - NSR decreased from 0.172 kg/kg-h to 0.161 kg/kg-h to 0.096 kg/kg-h when relative humidity increased from 40% to 50% to 60%, respectively. Only 7.0% decrease in NSR recorded for increase in ERH by 10 points (from 40% to 50%), whereas 45.0% decrease in NSR was recorded for increase in ERH by 20 points (from 40% to 60%).

With the two different mixture of fines (1700-2000 μm) and coarse (3350-4000 μm and 2800-3350 μm) at three different ERHs (40%, 50% and 60%), conventional triaxial tests were performed to evaluate flowability using the CTT. From those results, the following conclusions were drawn:

- For size ratio 2.0, angle of internal friction increased from 31.3° to 35.9°. to 39.0°. when ERH increased from 40% to 50% to 60%, respectively.
- For size ratio 1.7, angle of internal friction increased from 27.4° to 32.0°. to 36.0°. when ERH increased from 40% to 50% to 60%, respectively.
- The measured negligible cohesion values were not significantly different (P>0.05) for both size ratios 2.0 and 1.7 at all three ERHs.

In conclusion, addition of moisture could be used as a tool to mitigate segregation in granular materials by marginally reducing their flowability. Flowability should not be lowered below a critical value, otherwise flow issues may arise.

5. Acknowledgements

The authors would like to thank the Pennsylvania Department of Agriculture and Department of Agricultural and Biological Engineering, Pennsylvania State University for providing financial assistance for this project.

6. References

Bradley, M. S. A. and Farnish, R. J. (2005): Segregation of blended fertilizer during spreading. the effect of differences in ballistic properties, In Proc 554, The International Fertilizer Society, York, UK, 15p.

Bridle, I. A., Bradley, M. S. A. and Reed, A. R. (2004): Non-segregating blended fertilizer development- A new predictive test for optimising granulometry, In Proc 547. The International Fertilizer Society, York, UK, 27p.

Duffy, S. P. and Puri, V. M. (1997): Evaluation of computer controlled dynamic yield locus tester (DYLT), Powder Technology, 101, pp.257-265.

Duffy, S. P. and Puri, V. M. (2002): Primary segregation shear cell for size-segregation analysis of binary mixtures, KONA Powder and Particle Journal, 20, pp.196-207.

Li, F. and Puri, V. M. (1996): Measurement of anisotropic behavior of dry cohesive and cohesioless powders using a cubical triaxial tester, Powder Technology, 89,

pp.197-207.
Kamath and Puri, V. M. (1997): Measurement of powder flow constitutive model parameters using cubical triaxial tester, Powder Technology, 90, pp.59-90.
Kandala, R. N. and Puri, V. M. (2000): Measurement of cohesion and angle of internal friction using cubical triaxial tester and comparison with computer controlled shear cell, Particulate Science and Technology, An International Journal 18 (2), pp.71-88.
Popplewell, L.M., Campanella, O.H., Sapru, V. and Peleg, M. (1989): Theoretical comparison of two segregation indices for binary powder mixtures, Powder Technology, 58, pp.55-61.
Rollins, D.K., Faust, D.L. and Jabas. D. L. (1995): A superior approach to indices in determining mixture segregation, Powder Technology, 84, pp.277-282.
Shinohara, K. (1997): Segregation of particles, Powder Technology Handbook (2nd Ed. Ed.: Gotoh, K.H. Masuda, and K. Higashitani), Marcel Dekker Inc. New York. USA. pp.383-393.
Tang, P. and Puri, V. M. (2004): Methods for minimizing segregation, a review, Particulate Science and Technology, An International Journal 22 (4), pp.321-338.
Tang, P. and Puri, V. M. (2005): An innovative device for quantification of percolation and sieving segregation patterns – Single component and multiple size fractions, Particulate Science and Technology, An International Journal, 23 (4), pp.335-350.
Vursavus, K. and Ozguven, F. (2004): Determining the effects of vibration parameters and packaging method on mechanical damage in golden delicious apples, Turkey Journal of Agriculture, 28, pp.311-320.

Author’s short biography

Dr. Anjani Jha

Dr. Anjani Jha was a graduate research assistant in the Department of Agricultural and Biological Engineering at Pennsylvania State University from August 2004 to May 2008. He received B.S from Rajendra Agricultural University, Pusa, Bihar, and M.S. from at Indian Institute of Technology Kharagpur, both in India. The work reported in this paper is based on his Ph.D research work. His Ph.D research work has been widely published in several journals. Dr. Jha has received numerous research awards.

Dr. Hojae Yi

Dr. Hojae Yi has a B .A., M.S. from the Agricultural Engineering Department at Seoul National University (Republic of Korea). He joined the Pennsylvania State University as a visiting scholar in 2000 for one year where he started his researches on powder mechanics. He finished his Ph. D in Agricultural Engineering Department from Seoul National University in 2003. Dr. Hojae Yi has been a postdoctoral research fellow since 2006 at the Department of Agricultural and Biological Engineering Department of the Pennsylvania State University. Current research interests include experimental studies and mathematical modeling on compaction and flow behavior of particulate materials.

Virendra M. Puri

Virendra M. Puri, University Distinguished Professor, has been involved in research in the field of powder science, engineering, and technology for nearly three decades. He has served as the Acting Director of the NSF/IUCRC (Industry University Cooperative Research Center) – the Particulate Materials Center. Professor Puri has co-authored over 500 publications and co-inventor and holder of patents for four test devices in the area of powder flow, deposition and compaction. In addition, he has a Copyright for multi-purpose computational software dealing with powder processing applications. Professor Puri has been invited to serve on Editorial Boards, International Advisory Boards, and Chairpersons of several bulk solids-related publications and professional activities. He is Co-Editor-in-Chief of *Particulate Science and Technology, An International Journal*. Professor Puri regularly offers seminars, courses, and work shops in powder mechanics to industry and academia. He has received several teaching and research awards.

Comparison between a Uniaxial Compaction Tester and a Shear Tester for the Characterization of Powder Flowability[†]

Luca Parrella[1,3], Diego Barletta[1], Renee Boerefijn[2] and Massimo Poletto[1*]
Dipartimento di Ingegneria Chimica e Alimentare, Università degli Studi di Salerno[1]
Purac Biochem bv[2]

Abstract

The complete characterization of powder flow properties with shear cells is a long and time-consuming process that requires specially trained operators or costly automated instruments. For these reasons, in industrial practice, the use of simpler and less extensive measurement by uniaxial compaction testers is often preferred. However, previous studies in the literature indicate that the results of the two techniques are not directly comparable due to the different stress state conditions achieved in the two testers.

In this study, an experimental campaign to measure the flow function of five different powders with a ring shear tester (RST) and a uniaxial compaction tester (UCT) was performed. Different flowability results that arose for the more cohesive powders are explained by the wall friction effect in the UCT. Re-evaluation of the results accounting for the wall friction gave substantial agreement between the two experimental techniques for a calcium carbonate powder and only at low consolidation levels for the other four food powders. Phenomena other than wall friction seem to appear within these powders tested at high consolidation levels. The comparison between the results of the two techniques suggests that straightforward extrapolation of the UCT flow functions to a low consolidation condition can lead to an underestimation of powder cohesion.

Keywords: powder flowability, uniaxial compaction tester, ring shear tester, wall friction, cohesive powders

1. Introduction

The flow properties of bulk solids are key properties in the design and control for storage and handling operations in several industrial applications. Powder flowability is usually expressed in terms of flow functions which represent the unconfined yield strength, f_c, of the material as a function of the major principal stress at steady state, σ_1. The ratio between the two is referred to as the flow factor $ff_c = \sigma_1/f_c$ and is used as a flowability index according to the classification by Jenike (1961). This classification was extended by Tomas and Schubert (1979) and classifies the powder's behaviour as follows: $ff_c \leq 1$ hardened, $1 < ff_c \leq 2$ very cohesive, $2 < ff_c \leq 4$ cohesive, $4 < ff_c \leq 10$ easy flowing, $ff_c > 10$ free-flowing. After the pioneering work of Jenike (1961), a variety of different experimental techniques were developed over four decades to experimentally characterize the powder flow functions, as reported in recent comprehensive surveys by Schwedes (2003) and by Schulze (2008). All these testers are divided into two main categories: direct and indirect testers. In the first category, the shear region is directionally forced onto the powder sample, while in the second, this region is thought to develop independently of the tester geometry. Shear cells, from the first translational model developed by Jenike (1961) to the more recent rotational model developed by Schulze (1994), are so-called direct testers. In these testers, in fact, a shear force induces the formation of a shear region in the powder specimen consolidated by a normal force. Shear cells are widely used both for fundamental research and for industrial testing, e.g. in silo design. For this latter application, in particular, shear test methods different from shear cells are used, such as uniaxial compaction testers. In these testers, the bulk solids are com-

---

[†] Accepted: August 23, 2008

[1] Via Ponte Don Melillo, I-84084, Fisciano (SA), ITALY.
[2] P.O. Box 21, NL-4200 AA Gorinchem, THE NETHERLANDS
[*] Corresponding author:
Email: mpoletto@unisa.it
[3] Currently at "Processi Innovativi S. r. l." Viale Castello della Magliana, 68-00148 Roma, Italy

pacted in a cylindrical mould exerting some consolidation by means of a moving plunger or piston, then the mould is removed and the force necessary to break the sample, acting in the same direction of the compaction force, is measured. These are so-called indirect testers because shear regions are thought to develop along directions other than normal to the force. Several studies (Williams et al., 1971; Gerritsen, 1986; Maltby and Enstad, 1993) report that the main limitation of this technique is that a minimum consolidation stress on the powder sample is necessary to avoid its failure under gravity alone just after removing the mould. This minimum consolidation stress value is larger than the value that can be attained in shear cell tests and might be considerably larger than the stress acting within small process hoppers. In practice, this means that the powder compaction under its own weight is completely negligible, but cohesion forces may still cause flowability problems. Nevertheless, the uniaxial compression test is often preferred in industrial practice due to its simplicity and to the shorter time necessary to characterize the powder flowability, either in terms of a single unconfined yield strength for a single consolidation force, or in terms of a complete flow function. A recent example of this shear testing practice is given by Zhong et al. (2000), whose application to the classification of powder flowability was tested by Bell et al. (2007). Unfortunately, the comparison between the powder strength values measured by the two techniques is not straightforward. In fact, experimental results obtained with a biaxial tester by Schwedes and Schulze (1990) suggest that the powder specimen follows different stress histories in a shear tester and in a uniaxial tester during the consolidation step. In the first case, the powder sample finally attains steady state deformation, which means deformation without bulk density variation. In the second, it was not possible to achieve this condition due to the lateral confinement of the sample by the mould walls. As a result, the final consolidation states achievable by the two techniques could be different. A major difference between uniaxial compression tests and annular/linear shear tests is the role of friction exerted by the mould wall on the powder sample. This wall friction supports part of the external vertical force applied on the powder specimen for consolidation. By applying a simple balance of forces on a differential slice element of the powder under compression in the mould (in the style of Janssen as reported by Nedderman, 1992), we obtained the well-known equation for the effective normal stress σ in cylinders containing powders subject to their weight and to some external vertical load on the upper surface:

$$\sigma = \sigma_0 \exp\left(-\frac{4\mu_\mathrm{w} K z}{D}\right) + \frac{\rho_\mathrm{b} g D}{4\mu_\mathrm{w} K}\left[1 - \exp\left(-\frac{4\mu_\mathrm{w} K z}{D}\right)\right] \quad (1)$$

where σ_0 is the surcharge stress due to the external vertical force on the top surface, μ_w is the wall friction coefficient, K is the ratio between the radial and the vertical principal stresses, z is the vertical coordinate oriented downwards, D is the mould diameter, ρ_b is the powder bulk density and g is the acceleration due to gravity. Uniaxial compression tests are usually performed at high consolidation stresses, and the second term of equation (1) due to the powder weight can be neglected. Therefore, the resulting normal stress decreases exponentially over the powder sample depth.

Some effort to overcome the wall friction effect was pursued by Williams et al. (1971), who repeated the experiment by preparing powder samples obtained with the subsequent compaction of an increasing number of thin layers. They derived the unconfined yield strength from the measured values of sample yield strength extrapolated to an infinite number of layers. Maltby and Enstad (1993) tried to eliminate the wall friction problem by wrapping the powder sample in a flexible membrane and applying a lubricating oil between the membrane and the mould wall. Both the flow functions obtained by uniaxial compression tests by Williams et al. (1971) and by Maltby and Enstad (1993) are very close to those derived from Jenike shear cell experiments, suggesting that wall friction is perhaps the main cause of differences between rotational/translational shear testers and uniaxial compression test results. Unfortunately, the procedures proposed to avoid the wall friction effect with their complications risk annulment of the intrinsic simplicity of the uniaxial compression tests and are therefore not pursued in industrial practice.

The scope of this work is to compare uniaxial compression tests and shear cell tests for a number of food powders of different cohesion classes and for a reference calcium carbonate powder. In particular, going by experimental evidence reported in the literature, it is expected that uniaxial testing will provide apparent powder flowability that is higher than that evaluated with shear testing. An attempt will be made to account for the main causes of these discrepancies in order to reconcile the powder flowabilities obtained with the different techniques.

2. Experimental Set-Up

2.1 Apparatus

Three different testers for measuring the flow properties of bulk solids were used in this study: a uniaxial compaction tester and a Schulze ring shear tester (1994) to measure the powder flow functions, and a Peschl rotational shear tester (1989) to measure the angle of wall friction.

The uniaxial compaction tester (UCT) consists of a PVC cylindrical mould axially split into two halves. The cylinder (92.5 mm ID and 120 mm high) is secured by a chain-clamp to a thin disc fixed on to the horizontal base and a second disc is placed as the lid on the top surface of the powder sample in the mould. A piston moving downwards by means of an electrically driven motor applies a normal force to the lid over the specimen. This force is measured by a load cell.

The Schulze ring shear tester (RST) used in this study is the manually operated commercial version. Two different annular cells were used: the standard M cell with an internal volume of about 940 cm^3, and the smaller SV10 cell with an internal volume of about 96 cm^3. Normal loads were applied to the hanger hooked onto the lid of the cell. The shear force acting during the experiments was derived from the torque measured by the load cells connected to the cover through the tie rods. The powder sample volume was measured by a linear displacement transducer connected to the cell lid.

The rotational shear tester of Peschl was used to measure the wall yield loci of the powders. To this end, a wall sample was fixed to the cell base by three radial screws. A ring was centred on the wall sample and filled with the powder specimen. External loads were applied directly to the cylinder attached to the lid over the specimen top surface. The shear force was derived from the torque measured by a load cell connected to the lid through a rod.

2.2 Materials

Five different powders were tested. A calcium carbonate powder was used as a reference material. The other four powders, provided by PURAC Biochem, were used in this study to span the full range of flowability classes. For confidentiality reasons, we will refer to these as powders A, B, C and D. The volumetric particle size distribution of each powder was measured by a Malvern Mastersizer 2000 laser diffraction analyser on powder samples dispersed in a non-solvent liquid. The results in terms of median particle size d_{50}, Sauter mean size d_{32} and size range corresponding to 80% of the distribution are reported in **Table 1**. Scanning electron micrographs of materials shown in **Fig. 1** reveal that the calcium carbonate powder and powders A and B consist of irregular flaky particles while powders C and D show a more rounded shape. The aerated bulk density and tapped bulk density and therefore their ratio referred to as the Hausner ratio were measured by a Hosokawa tester. The angle of repose φ_r was also determined by a Hosokawa tester. All these results are reported in **Table 1**.

Under strict application of the Mohr-Coulomb analysis, the values of K appearing in Equation (1) can be calculated according to Rankine equation:

$$K = \frac{1-\sin\varphi_e}{1+\sin\varphi_e} \tag{2}$$

where φ_e is the effective angle of friction measured with the RST. Values of K calculated with equation (5) are reported in **Table 1**. These values fall in the range between 0.1 and 0.27. Instead, direct measurements of K reported by Kwade et al. (1994) show that K values are generally between 0.4 and 0.6 also for cohesive powders. Therefore, to avoid errors arising from an underestimation of K, its value was set to 0.4 for all the powders tested. The wall friction angle φ_w was derived from the wall yield loci measured with a Peschl shear tester on a wall sample of the same material which the UCT mould is made of.

2.3 Procedures

2.3.1 Uniaxial compression test procedure

Once the cylindrical mould is filled with the pow-

Table 1 Material properties

Material	d_{50} μm	80% range μm	d_{32} μm	aerated ρ_b kg m^{-3}	tapped ρ_b kg m^{-3}	CI %	ϕ_r deg	ϕ_e deg	ϕ_w deg	K eq (9)	Jenike (1961) flowability UCT corrected
CaCO$_3$	7	2-40	4	336	421	20.2	45	54	22	0.10	Cohesive
A	25	1-246	4	434	910	52.3	48	49	25	0.14	Cohesive
B	3	1-32	2	242	595	59.4	48	55	31	0.099	Very cohesive
C	267	149-467	221	610	667	8.6	37	47	26	0.16	Cohesive
D	198	82-386	117	688	706	2.6	32	35	12	0.27	Free flowing

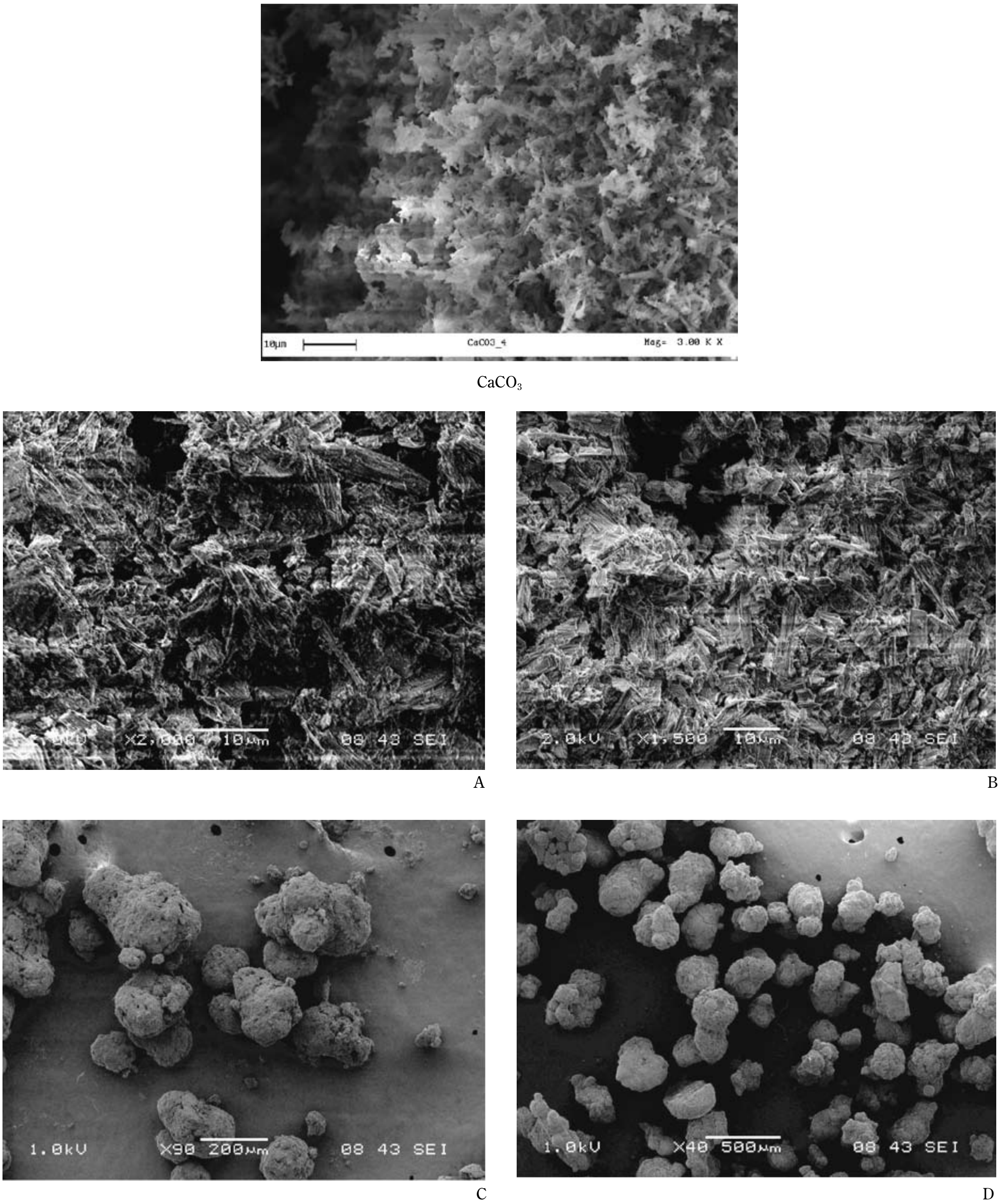

$CaCO_3$

A

B

C

D

Fig. 1 SEM micrographs of the materials used.

der specimen and the top lid is placed on its surface, the consolidation step is performed by moving the piston downwards and applying the desired normal load, N_c. Then the piston moves upwards, releasing the consolidation force. The mould is opened and removed carefully in order not to disturb the consolidated specimen. The compression step is carried out by moving the piston downwards onto the powder sample with increasing normal force until the specimen fails. From this test, a single f_c- σ_1 point of the flow function can be derived as follows:

$$\sigma_1 = \frac{N_c}{A_{UCT}} \tag{3}$$

$$f_c = \frac{N_f}{A_{UCT}} \tag{4}$$

where A_{UCT} is the cross-sectional area of the cylindrical mould and N_f is the normal force measured at failure. By repeating the whole procedure with different consolidation normal loads, a complete flow function is obtained.

A second procedure was used to account for wall friction. In particular, σ_1 was evaluated according to Equation (1), assuming z to be equal to the measured powder sample height after consolidation. The underlying hypothesis is that in the UCT, the compaction strength changes within the sample and, in particular, that the smaller consolidation, which determines the failure load, is attained at the sample bottom. In the same way, the unconfined yield strength f_c was also calculated by accounting for the contribution caused by the powder sample weight, M, as follows:

$$f_c = \frac{N_f + M}{A_{UCT}} \tag{5}$$

2.3.2 Ring shear test procedure

The standard measurement procedure was followed to measure a yield locus with a Schulze RST. According to this procedure, once the shear cell with the powder specimen has been prepared and the maximum normal load chosen, N_c, is applied to the cell lid. The pre-shearing step starts and is carried out up to attainment of a steady state value of the shear stress, τ. Then the shearing phase takes place under a normal load, N_1, lower than N_c, to reach a peak value of shear stress corresponding to the incipient flow of the material. The sequence of the two steps is repeated with the same N_c for each preshearing phase, but with decreasing normal loads for each shearing phase (i.e. $N_1 > N_2 > \cdots > N_n$). A qualitative sketch of a typical shear stress chart achievable during a shear test is reported in **Fig. 2**. In this work at least five failure points were measured for the construction of each yield locus and each complete test was repeated twice.

The normal stress σ acting on the shear plane in a failure test is calculated as follows:

$$\sigma = \frac{N}{A_{RST}} + \rho_b g \Delta z \tag{6}$$

where N is the external normal load applied, A_{RST} is the cell cross-sectional area and Δz is the powder height over the shear plane. The average shear stress τ acting on the shear plane is derived from the measured torque. The σ-τ points obtained at failure are reported in a plot to derive the powder static yield locus corresponding to the consolidation applied in the test as sketched in **Fig. 3**. In addition to these points, the average of the steady state σ-τ values

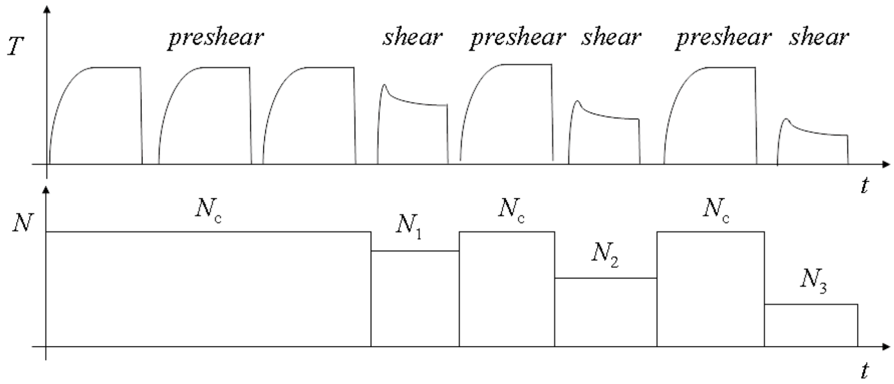

Fig. 2 Typical torque and normal load chart during a shear cell experiment.

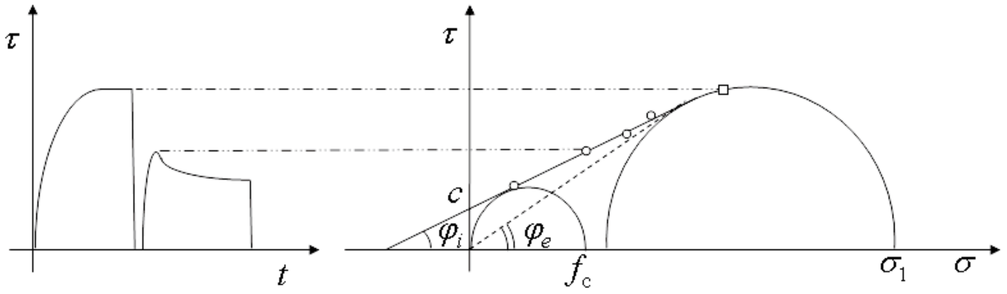

Fig. 3 Yield locus construction from shear experiment data.

obtained during the pre-shearing steps is reported on the same diagram. The Mohr circle drawn through the steady state point and tangent to the yield locus locates the major principle stress σ_1 corresponding to the consolidation applied. The unconfined yield strength of the powder f_c is given by the major principle stress of the Mohr circle through the origin and tangent to the yield locus. The angle φ_i between the static yield locus and the σ axis is the static angle of internal friction. The dashed line passing through the origin and tangent to the larger Mohr circle is the effective yield locus. Its angle of inclination with respect to the σ axis is the effective angle of friction, φ_e. By performing other complete shear tests at different N_c values, a complete flow function of the powder can be plotted.

2.3.3 Wall friction measurement procedure

The wall friction coefficient between the powder and the mould material was evaluated with the Peschl shear tester. The detailed procedure is as follows: after the ring placed on the wall sample has been filled with the powder, a normal load N_1 is applied to the cell lid and the shearing takes place until a steady state value of τ is measured; this step is repeated consecutively three times to be sure that critical consolidation of the powder has been reached under the applied load; this sequence is then repeated with the same sample by applying increasing normal loads (i.e. $N_1<N_2<\cdots<N_n$). Normal and shear stresses are calculated as in the Schulze RST, taking the different cell geometry into account. The σ-τ points are plotted to obtain the wall yield locus. The angle between the wall yield locus and the σ axis is the angle of wall friction φ_w. The wall friction coefficient, μ_w, is the tangent of this angle.

3. Results

The flow functions measured for all the materials are reported in **Figs. 4-8**. In these figures, solid black circles and hollow circles with thick contours refer to experiments carried out on the M cell of the RST, whereas hollow circles refer to experiments carried out on the SV10 cell of the RST and squares refer to experiments carried out on the UCT. As previously mentioned, all experiments were repeated twice and showed a good reproducibility of data, and therefore deviations from expected trends, as discussed in the following, can be attributed to inherent experimental conditions. A general inspection of the figures reveals that the five materials investigated cover a wide range of flow behaviours evaluated according to the Jenike classification. From the distribution of flow data in the Jenike classification regions and the analysis of **Table 1**, it appears clear that a good correlation exists between the flow behaviour of the powder measured with RST and the powder compressibility index in **Table 1**. This is in agreement with what was reported by Santomaso et al. (2003). The only exception to this agreement was found for powder C. This singularity might probably be attributed to the very irregular and complex shape of these particles shown in **Fig. 1**.

The flow function for calcium carbonate (**Fig. 4**) obtained with the RST lays within the cohesive region

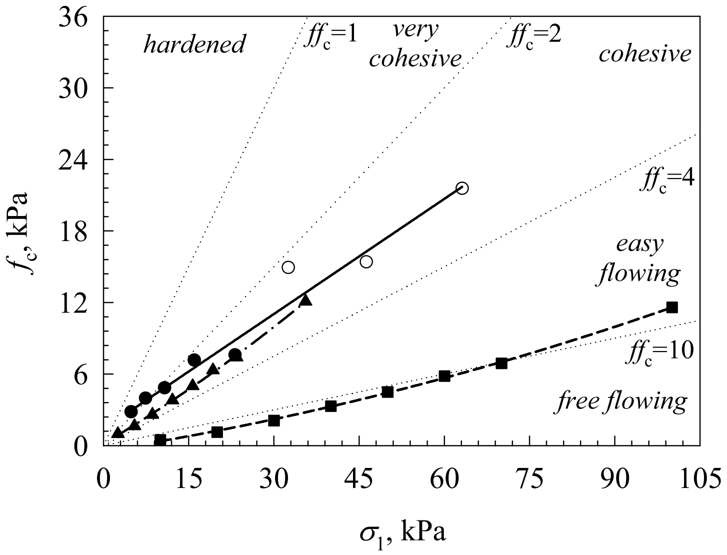

Fig. 4 Flow functions for calcium carbonate powder. ● RST M cell; ○, RST SV10 cell; ■, UCT; ▲, UCT corrected.

and tends to the very cohesive region at low consolidation. Both the M cell and the SV10 cell were used with the RST to cover a wider range of consolidation stresses. The UCT flow function is more linear and is located between the easy-flowing and free-flowing region.

The flow function for powder A (**Fig. 5**) obtained with the M cell of the RST crosses different regions of flow behaviour from very cohesive to easy flowing, showing an apparent better flowability as the major principal stress σ_1 increases. Significant time fluctuations typical of slip-stick behaviour were observed in shear stress charts of the experiments corresponding to $\sigma_1 > 5$ kPa. Since this phenomenon could lead to an incorrect estimation of the yield locus and consequently of the unconfined yield strength of the powder, this set of experiments was repeated with the smaller SV10 cell of the RST in which the slip-stick flow was not expected for the different elastic properties of the system due to the reduced height of the powder sample. As a result, the points derived from M cell tests, represented by hollow circles with thick contours, were discarded and, in the regression of the RST flow function (solid line), were substituted with the points obtained with the SV10 cell of the RST, which are reported as hollow circles. The RST flow function derived with this procedure shows a certain convexity and covers three different flowability regions. The flow function obtained with the UCT instead shows a linear increase of fc with increasing σ_1 and lies entirely in the easy-flowing region.

The flow function obtained for material B with the M cell RST (**Fig. 6**) follows a trend similar to that of powder A and extends over three different flowability regions (very cohesive, cohesive and easy flowing). Also in this case, the experiments for $\sigma_1 > 5$ kPa were repeated with the SV10 cell of the RST to better investigate the unexpected significant decrease of f_c values, which was not necessarily associated to slip-stick flow. The RST flow function curve resulting from the regression on filled circles and hollow circles with thin contours shows a high powder cohesion. Also in this case, the flow function derived from the UCT is a straight line and it falls in the region of cohesive powders. The corresponding f_c values are smaller than those measured with the RST for $\sigma_1 < 20$ kPa.

The flow function measurement for powder C with the M cell of the RST (**Fig. 7**) yielded a linear increase of f_c with increasing σ_1. All the flow function points belong to the cohesive region. Slip-stick flow was not observed for the whole range of investigated stress states, but additional experiments with the SV10 cell of RST were performed at high σ_1. Corresponding results confirmed the trend observed with the M cell. The flow function obtained with UCT is lower than the RST, suggesting an easy-flowing behaviour.

Powder D's flow function obtained with the M cell of RST (**Fig. 8**) is a straight line in the free-flowing region. Slip-stick behaviour was observed for $\sigma_1 > 10$ kPa, but the repeated tests with the SV10 cell RST gave identical f_c values. It was really difficult to perform the uniaxial compaction tests since the low cohesion of powder D allowed the preparation of stable powder specimens only at very high consolidation stresses. The resulting flow function coincides with that obtained with the RST.

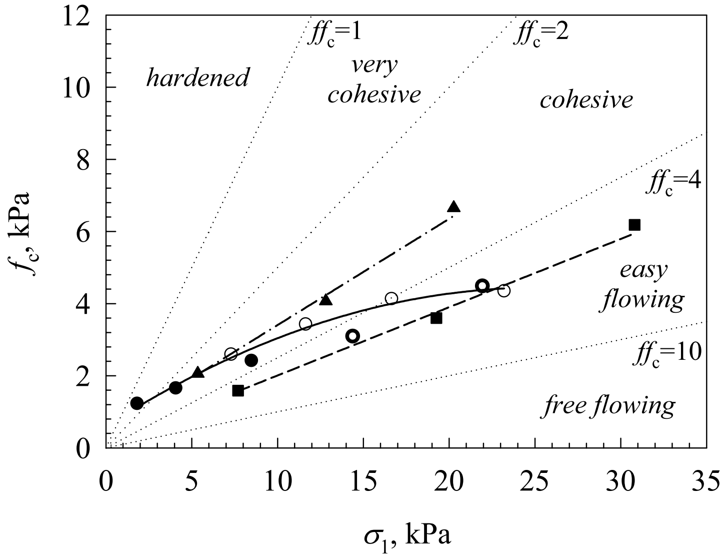

Fig. 5 Flow functions for powder A. ● ○ RST M cell; ○, RST SV10 cell; ■, UCT; ▲, UCT corrected.

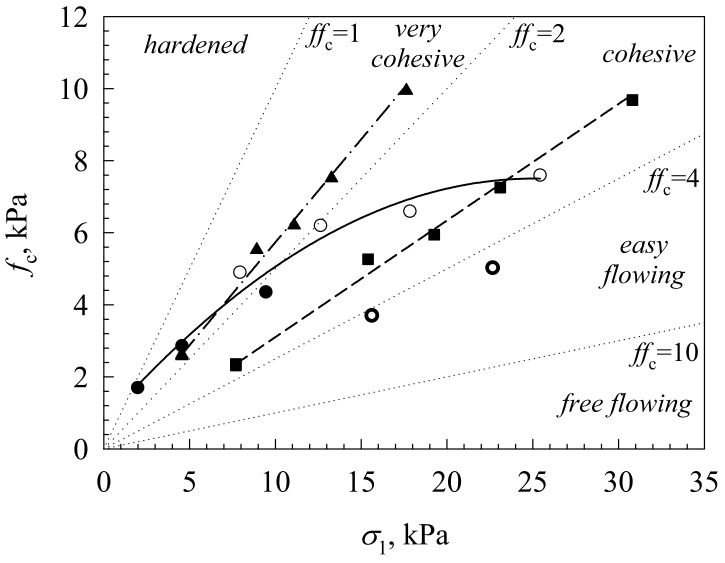

Fig. 6 Flow functions for powder B. ● ○RST M cell; ○, RST SV10 cell; ■, ideal UCT eqs. (1) and (2); ▲, UCT corrected.

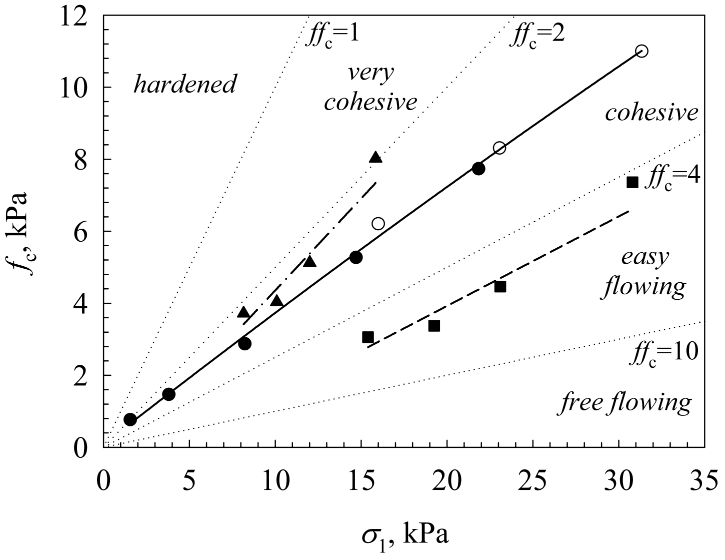

Fig. 7 Flow functions for powder C. ● ○ RST M cell; ○, RST SV10 cell; ■, ideal UCT eqs. (1) and (2); ▲, UCT corrected.

4. Discussion

Significant differences between the flow function results obtained with the RST and the UCT were observed for the more cohesive powders, calcium carbonate, A, B and C. In order to assess whether these discrepancies could be explained by different effective powder compaction values in the two experiments, the UCT results were recalculated taking into account the wall friction and the powder gravitational contribution to the stresses acting in the consolidation step. In support of the hypothesis that the lower consolidation value, which determines the failure load, is attained at the sample bottom, there is the visual observation that at sample failure, the fracture in the material started at the bottom and then propagated upwards. Resulting flow functions accounting for wall friction and calculated according to Equations (1) and (5) are reported as triangles in **Figs. 4-8**. The re-evaluated UCT flow function is close to the RST flow function for the calcium carbonate powder, suggesting the soundness of the approach followed for UCT flow function correction. Also for powders A, B and C, the re-evaluated UCT flow functions lie very close to those obtained by RST experiments, but only at low consolidation values. For these materials, the corrected UCT flow functions are steeper and more

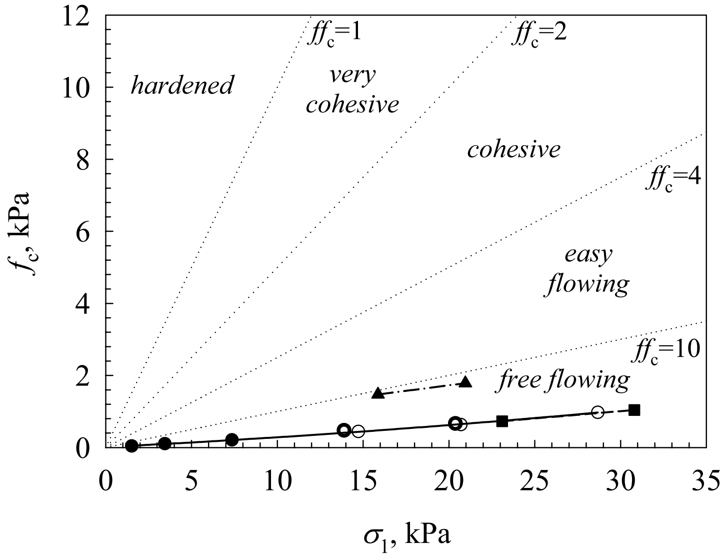

Fig. 8 Flow functions for powder D. ● ○ RST M cell; ○, RST SV10 cell; ■, ideal UCT eqs. (1) and (2); ▲, UCT corrected.

linear than the RST flow functions and, therefore, at the higher consolidation values, the RST flow functions provide lower values of the unconfined yield strength. For these powders, other phenomena have to be hypothesized to explain the observed differences at high consolidation levels.

It might be argued that the main reason for obtaining different results between UCT and RST experiments can be attributed to the different stress histories in the sample preparation during the compaction steps for the two testers. In fact, in the RST there is no limit on the maximum shear strain and it is always possible to reach a critical state of deformation in which the powder volume attains a steady value. In the RST procedure, this condition is required to conclude the pre-shearing phase in order to reach a bulk density for a certain compaction load which does not depend on the compaction history. In contrast, the compaction procedure in the UCT does not ensure that the internal deformation of the sample allows the bulk density proper of the critical state to be reached. As a result, it might be expected that under the same major principal stress during compaction, the unconfined yield strength measured with the UCT is somewhat lower than that derived from RST experiments. Nevertheless, as it was recalled in the introduction, experiments carried out by Williams et al. (1971) and by Maltby and Enstad (1993), in which the wall friction was minimized, produced a substantial overlapping of the flow functions obtained with uniaxial testers and the Jenike shear tester. This finding suggests that in these experiments, the internal shearing which occurs in the UCT sample during the compaction step was sufficient to determine a powder consolidation similar to that obtained with shear testing procedures.

As concerns the present experimental campaign, we have not minimized the wall friction effect in the UCT experiment, but we have accounted for it in the proposed correction of the UCT flow function. Therefore, the circumstance that for powders A, B and C at high consolidation levels, the corrected UCT flow function provides an unconfined yield strength larger than the RST flow function cannot be explained by the occurrence of any significant role of the different stress histories of powder samples in the two experiments. Another possibility is that the high shear induced in the RST might produce some change in the powder structure close to the shear plane such as particle fragmentation or orientation. This interpretation seems to be confirmed by the fact that calcium carbonate, a powder made of rigid particles and not subject to orientation phenomena during shear, does not show significant differences between the RST and the corrected UCT flow function at high consolidation levels. Further preliminary tests on the microscopic structure of the powder on the shear plane did not shed light on this point, and a more complex investigation, which exceeds the scope of this work, would be required.

As concerns the results obtained with powder D, it was observed that the original UCT and RST flow functions were almost identical at all the investigated consolidation levels and the UCT corrected flow function leads to greater unconfined yield strength values. An explanation of this difference with respect to the other powders tested might be found in the very low compressibility of powder D. This was observed in the consolidation step and was confirmed by the small values of the compressibility index. The consequence might be a reduced powder motion within the cell that might impair the hypothesis of full mobilization of the powder at the container wall during consolidation. This condition is at the base of the Mohr Coulomb approach used to obtain Equation (1) and, if not respected, might lead to an overestimation of the wall friction stress and its effects.

5. Conclusions

A comparison between the ring shear tester and the uniaxial compaction tester techniques for the measurement of powder flow functions was performed for five different powders. Deriving normal stresses simply from the applied external forces, the UCT flow functions gave unconfined yield strengths lower than those measured by the RST for the more cohesive powders, calcium carbonate, A, B and C. In particular, each of these powders resulted in belonging to different flowability regions according to the two techniques. A good agreement between the UCT and RST results was found only for the free-flowing powder D. Recalculation of the stress state of the powder sample in the UCT experiments, taking into account the mould wall friction and the powder weight, gave a flow function in close agreement with that obtained with the RST for the calcium carbonate powder, suggesting the soundness of the approach. For powders A, B and C, the agreement was satisfactory only at low consolidation values. This correction procedure requires knowledge of the K ratio and of the angle of wall friction measurable with shear cells or other testers. As a result, the use of an UCT alone could not be sufficient to measure reliable flow functions unless particular care was taken to eliminate the wall friction effect or at least a rough estimate of the K and wall friction angle of that material was available. **Table 1** suggests that the repose angle for these powders might be a sufficiently good estimate of the effective internal friction to apply equation (2) for estimating K. With cohesive materials, however, which give high angles of internal friction and therefore K values according to equation (2) lower than 0.4, K values equal to 0.4 may provide a fair estimate. For the materials tested, the wall friction angle is approximately half that of the effective internal friction.

It must be recognised, however, that some discrepancies between the RST and the UCT flow functions could not be solved simply taking account of wall friction. In fact at the highest consolidation stresses, the corrected UCT flow functions for cohesive powders (A and B) provide a significantly higher unconfined yield strength of powders. Further investigation is necessary for a better comprehension of this discrepancy.

The proposed correction procedure turns out to be effective to obtain more reliable powder flow functions from simple UCT measurements especially for industrial quality control purposes. Standard shear testers still appear the most reliable and conservative flowability characterization method if the results are to be used for the design of handling or storage equipment such as silos.

List of symbols

A_{RST}	shear cell cross-sectional area	[m^2]
A_{UCT}	UCT mould cross-sectional area	[m^2]
c	cohesion	[kPa]
CI	compressibility index	[-]
D	mould diameter	[m]
d_{32}	Sauter mean size	[μm]
d_{50}	median size	[μm]
f_c	unconfined yield strength	[kPa]
ff_c	flow factor	[-]
g	acceleration due to gravity	[m s^{-2}]
K	ratio between radial and vertical stresses	[-]
M	powder sample weight	[N]
N	external normal force	[N]
N_c	consolidation normal force	[N]
N_f	normal force at failure	[N]
t	time	[s]
z	vertical coordinate	[m]

Greek symbols

Δz	powder height over the shear plane	[m]
μ_w	wall friction coefficient	[-]
φ_e	effective angle of friction	[deg]
φ_i	static angle of friction	[deg]
φ_r	angle of repose	[deg]
φ_w	angle of wall friction	[deg]
ρ_b	powder bulk density	[kg m^{-3}]
σ	normal stress	[kPa]
σ_0	surcharge normal stress	[kPa]
σ_1	major principal stress	[kPa]
τ	shear stress	[kPa]

References

Bell, T.A., Catalano, E.J., Zhong, Z., Ooi, J.Y. and Rotter, J. M. (2007): Evaluation of the Edinburgh Powder Tester, Proc. of PARTEC 2007, Nuremberg (D), 27-29 March, pap S30_1.

Gerritsen, A.H. (1986): A simple method for measuring powder flow functions with a view to hopper design, Preprint of PARTEC Symposium, Nuremberg (D), 16-18 April 1986, pp.257-279.

Jenike, A.W., (1961): Gravity flow of bulk solids, University of Utah. Utah Engineering. Experiment Station, Bulletin 108.

Kwade, A., Schulze, D. and Schwedes, J. (1994): Determination of the stress ratio in uniaxial compression tests – Part 2, Powder Handling & Processing, 6, pp.199-203.

Maltby, L. P. and Enstad, G., (1993): Uniaxial tester for quality control and flow property characterization of powders, Bulk Solids Handling 13, pp.135-139.

Nedderman, R.M. (1992): "Statics and kinematics of granular materials", Cambridge University Press, Cambridge (UK).

Peschl, I. A. S. Z. (1989): Equipment for the measurement of mechanical properties of bulk materials, Powder Handling & Processing 1, pp.73-81.

Santomaso, A., Lazzaro, P. and Canu, P. (2003): Powder flowability and density ratios: the impact of granules packing, Chem. Eng. Sci., 58, pp.2857-2874.

Schulze, D., (1994): A new ring shear tester for flowability and time consolidation measurements, Proc. of 1st International Particle Technology Forum, Denver (USA), August, pp.11-16.

Schulze, D. (2008): "Powders and Bulk Solids", Springer, Berlin (D).

Schwedes, J. (2003): Review on testers for measuring flow properties of bulk solids, Granular Matter 5, pp.1–43.

Schwedes, J. and Schulze, D. (1990): Measurement of flow properties of bulk solids, Powder Technol. 61, pp.59-68.

Tomas, J. and Schubert, H. (1979): Particle characterisation, Proc. of Partec 79, Nuremberg, Germany, pp. 301-319.

Williams, J.C., Birks, A.H. and Bhattacharya, D. (1971): The direct measurement of the failure function of a cohesive powder, Powder Technol. 4, pp.328-337.

Zhong, Z., Ooi, J.Y. and Rotter, J.M. (2000): Nonlinear effects of blending on coal handling behaviour. Proc. of the 'From powder to bulk', IMechE Conference on Powder and Bulk Solids Handling, London (UK), 13-15 June, pp.17-26.

Author's short biography

Luca Parrella

Luca Parrella is presently design engineer at "Processi Innovativi S.r.l.". After a research stage at PURAC he graduated in Chemical Engineering at the University of Salerno in 2006 with a master level thesis on *"Validation of a simple test method for the rheological properties of food powders"*.

Diego Barletta

Diego Barletta is Assistant Professor of Chemical Engineering at the School of Engineering of the University of Salerno since 2005. He graduated cum laude in Chemical Engineering in 1999 at the University of Napoli Federico II. He obtained the Doctoral degree in Chemical Engineering in 2003 at the University of Salerno. His research activity concerns the use of aeration as a discharge aid of fine powders from storage equipment, the flow properties and the fluidisation behaviour of fine granular materials. In the past, he also worked on modelling combustion and desulphurisation in fluidised bed combustors. He is author of more than 40 papers on refereed international journals and conference proceedings.

Author’s short biography

Renee Boerefijn

Renee Boerefijn graduated in 1994 from Twente University in Mechanical Engineering, on the subject of Fluidised Bed Dynamics with Profs. J. J. H. Brouwers and P. Salatino (Naples), and completed a PhD in Chemical and Process Engineering from Surrey University in 1998 on Particle Breakage in Fluidised Bed Jets, under supervision of Prof. M. Ghadiri (Leeds). After this he worked at Unilever Laundry R&D in the roles of Skill Base Leader Granulation, Granulation Project Manager and Group Leader Added Benefit Compounds. Since 2005 with CSM subsidiary PURAC, he now heads the Competence Centre Powders and the Innovation Centre Food & Nutrition. Renee is vice-chair of the technical committee of the International Fine Particles Research Institute (IFPRI), board member of the foundation Ingredients for Food Innovators (IFFI), and member of the EFCE Working Party for Mechanics of Particulate Solids.

Massimo Poletto

Massimo Poletto is associate professor of Chemical Engineering since 2001 at the School of Engineering of the University of Salerno where he is a faculty member of the Department of Chemical and Food Engineering. Presently he is delegate of the Italian Association of Chemical Engineering (AIDIC) to the Working party of the European Federation of Chemical Engineering (EFCE) on “Mechanics of Particulate Solids” where is was elected chairman for the period 1/1/2008-31/12/2010. Massimo Poletto is author of more than 100 papers and conference presentations, more than 30 of which have been published on refereed international Journals in the field of fluidization powder mechanics and food technology applications of chemical engineering.

Scale-up of High-Shear Mixer Granulators[†]

N. Rahmanian, B.H. Ng, A. Hassanpour, Y.L. Ding,
S.J. Antony, X.D. Jia and M. Ghadiri[*]
Institute of Particle Science and Engineering, University of Leeds LS2 9JT

P.G.J. van der Wel and A. Krug-Polman
Hosokawa Micron BV, The Netherlands

D. York, A. Bayly and H.S. Tan
Procter and Gamble

Abstract

The mechanics of particle interactions and the prevailing level of compressive stresses and shear strains are affected by the scale of operation, which in turn affects the granule structure, strength and functional properties. This may be the main reason why the current scaling relationships are ineffective from a viewpoint of product engineering.

In a research programme supported by the EPSRC and four industrial organizations, i.e. Borax Europe, Hosokawa Micron BV, Pfizer Global Research and Development, and Procter and Gamble, we have addressed the following topics:

- *Development of methodologies for quantifying the structure of granules in terms of internal voidage and composition distributions, strength, shape, size and density.*
- *Identification of the parameters that affect the structure of granules by using fundamental theories of microscopic contact mechanics of particles using DEM, macroscopic granular flow dynamics and kinetics of wetting.*
- *Experimental work across several length scales (1 L, 5 L, 50 L and 250 L) to aid the analysis of the process.*

In this paper, an overview of findings and their implications for granulation practice is presented.

Keywords: granulation, high-shear granulator, scale-up, strength, Cyclomix, DEM modelling, PEPT

1. Introduction

Granulation is a key unit operation in many industrial sectors for manufacturing a wide range of intermediates and final products such as food, fertilizers, metalliferous ores, nuclear fuels, ceramics, carbon black, catalysts, pesticides, plastics, cement kiln feeds and detergents. The objective of the granulation process is essentially to improve material properties and behaviour such as flow, handling, dustiness, strength, appearance, structure and composition, rate of dissolution and resistance to segregation[1-4]. Granulators used in industry can be widely divided into two categories: low-shear mixer granulators (e.g. rotating drums and pans), and high-shear mixer granulators. High-shear mixer granulators are typically found in the pharmaceutical and detergent industries, and are capable of reducing the processing time and producing granules with high strength and density.

One of the most important challenges of granulation technology is process scale-up[5-8]. The ultimate goal in scale-up is to keep product properties constant. The scaling-up of granulation processes is often difficult, costly and problematic due to the complex dynamics of the process. Little effort has been made in the past to systematically study the scale-up of high-shear granulation processes and its effect on product characteristics and functionality. Most of the reports in the literature have focused on the mecha-

---

[†] Accepted: August 23, 2008

[*] Corresponding author:
TEL: (+44)113 34 32406
FAX: (+44)113 34 32405
E-mail: m.ghadiri@leeds.ac.uk

nisms of granulation at a single scale of operation and under specific operating conditions with the particle size distribution as the product attribute of interest[9-14]. Other product properties such as the strength and structure of the granules have not so far been widely addressed in the scale-up.

The literature survey shows that two scaling rules have been most frequently used, i.e. constant tip speed[15, 16] and constant Froude number[17], but more recently Tardos *et al.*[18-20] proposed a new rule based on constant shear stress. They considered the conditions for granule growth due to coalescence and granule breakage under shear deformation and related them to a critical level of prevailing shear stress, which was quantified by experimental work. They validated the proposed scaling rule with three scales of Fukae horizontal high-shear mixer granulator with capacities of 2, 7.5 and 25L[20].

The scaling rules have been mostly evaluated by comparing the granule size distribution. This is obviously incomplete, as granules of the same size can have very different structures hence different mechanical and physical properties. Although the characterisation of granule strength and structure has been reported by various authors[21-25], there is no work on the effect of scale-up on the strength and structure. The objective of this work is to investigate the effects of impeller speed at different scales of a high-shear granulator by following the three scale-up rules of constant tip speed, constant shear stress and constant Froude number on the mechanical strength of granules.

An overview of the current progress on the effect of scales of granulators on the properties of granules is presented here. The research work consists of experiments and modelling across the length scales as shown in the project flow chart in **Fig. 1**. In the experimental part, the granules are produced in four different high-shear mixer granulators (1, 5, 50, and 250 L Cyclomix, manufactured by Hosokawa Micron B.V.), and their properties are analysed as a function of scales in terms of strength and structure. The granule strength is determined by single granule compression and crushing between two platens known as the side crushing test. The macroscopic flow field of the granulators as a function of scale is also investigated using the Positron Emission Particle Tracking (PEPT) facility of the University of Birmingham[26-28] and high-speed video recording and image analysis to measure particle motion at the single particle level. In order to provide a mean to interpret the experimental observations, modelling work across the length scale is carried out at macroscopic and microscopic levels. The dynamics of the granulation process at the vessel scale (macroscopic level) is simulated by the Distinct Element Method (DEM) and also by computational fluid dynamics continuum (CFD) to analyse the velocity and stress

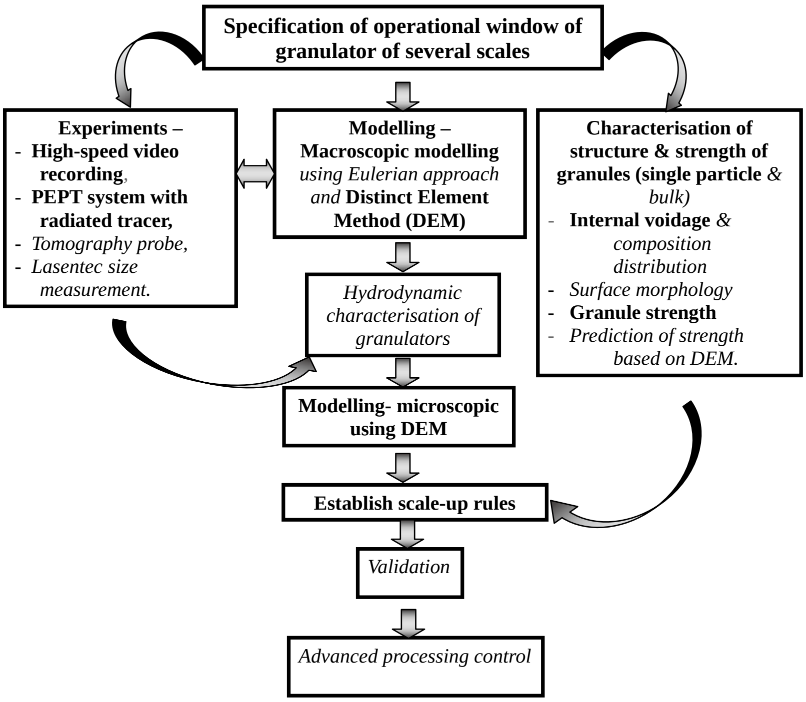

Fig. 1 Flow chart of the project.

field of the granulator at various scales. These methods were complemented by high-speed motion analysis of particles at the boundaries, and are particularly helpful where PEPT measurements cannot be used due to the scale of the granulator. DEM simulation is also conducted for the breakage of single granules at microscopic level in a shearing bed in order to analyse the microscopic interactions of the granule behaviour. The results obtained by the PEPT technique and macroscopic modelling are evaluated with DEM to investigate the effect of the velocity field of different scales of high-shear mixer granulators on the structure of the evolved granule. The interaction map of the project is shown in **Fig. 1**.

2. Methodologies

2.1 Experimental set-up

2.1.1 Materials, equipment and method

Calcium carbonate powder (Durcal 65 supplied by Omya UK, Ltd.) was used as primary particles. The particle size of Durcal 65 on the volume basis was d_{10}= 7 μm and d_{90}=225 μm. The geometric mean size of the powder was 60 μm[29]. A 65-wt% aqueous solution of polyethylene glycol (PEG 4000) was used as the binding agent. The liquid/solid ratio was 10 wt% and the density of primary particles was 2750 kg/m^3. The density of the PEG solution was 1165 kg/m^3 at 27 ℃ [30].

A type of high-shear mixer granulator, known as Cyclomix and manufactured by Hosokawa Micron B.V., was used for granulation. A schematic diagram of the granulator and its impellers is shown in **Fig. 2**. The granulator has an impeller consisting of a central shaft with four sets of blades and a pair of knives on the top. The impeller is enclosed in a bowl-shape in the frustum of a cone. The granulator has a blade (knife) at the top of the bowl to cut/break the loose large granules formed in the granulator. The experiments were conducted in four granulator sizes with nominal capacities of 1, 5, 50 and 250 litres. The liquid binder was added from the top to a bed of moving powder. The sample fill level was 60% of the granulator volume. Three scale-up rules were evaluated as summarised by Equation (1).

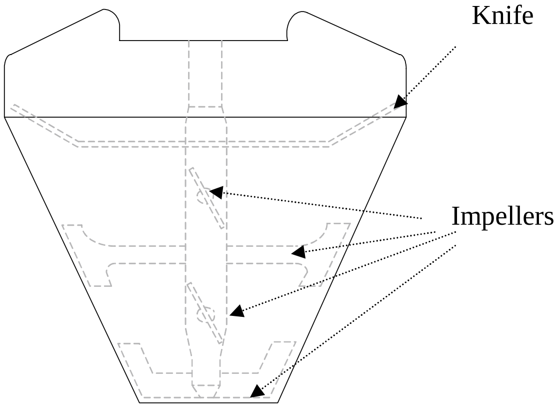

Fig. 2 Schematic diagram of Cyclomix granulator.

$$\frac{N_x}{N_y} = \left(\frac{D_y}{D_x}\right)^n \tag{1}$$

where N is the impeller revolution speed, D is the blade diameter, subscripts x and y represent different scales of granulators and n is a constant depending on the rule: (i) for constant tip speed, n = 1.0; (ii) for constant shear stress, n = 0.8; (iii) for constant Froude number, n = 0.5. The scale-up of the granulation time is based on the assumption that the granulation rate is proportional to the wall surface area of the granulator and inversely proportional to the volume of sample. During the granulation process, the wet mass is generally pushed to the periphery of the granulation bowl due to centrifugal effects when the Froude number exceeds a critical value. Granule growth and consolidation are postulated to take place at the high-impact and high-shear zones between the tips of the blades and the vicinity of the wall region of the granulator. Thus, the granulation rate increases (or processing time decreases) with increasing wall surface area. In contrast, the larger the quantity of material available for granulation, the longer the granulation processing time will be needed. Therefore, it is assumed that the granulation rate is inversely proportional to the volume of the sample. The recommended granulation time for different scales is given by Equation (2)

$$\frac{t_x}{t_y} \propto \left(\frac{S_y}{S_x}\right)\left(\frac{V_x}{V_y}\right) \tag{2}$$

The 50 L granulator is taken as the reference scale in this work. The impeller speed for the 1, 5 and 250 L granulators are established according to Equations (1) and (2) based on the conditions of the 50 L and are summarised in **Table 1**. As can be seen in **Table 1**, the granulation time increases as a function of scale. The impeller tip speed was calculated from the impeller rotation speed (N) in RPM and the impeller diameter (D). The Froude number, $Fr=N^2D/g$, where g is the gravitational acceleration, is also given in **Table 1** for each condition.

After the granulation process, the product was dried in an oven at 30℃ and then sieved to the size range of 125 – 1000 μm. The granules in the desired

Table 1 Operating condition of different scales of Cyclomix

Cyclomix	250 L			50 L	5 L			1 L		
Scale-up index (n)	1.0	0.8	0.5	Reference	1.0	0.8	0.5	1.0	0.8	0.5
Impeller tip speed (m/s)	4.13	4.60	5.39	4.13	4.13	3.52	2.76	4.13	3.17	2.12
Impeller speed (RPM)	90	100	118	155	346	295	232	584	448	300
Froude number	0.222	0.274	0.347	0.347	0.774	0.562	0.347	1.305	0.768	0.347
Granulation time(s)	884			517	240			140		

size range of 500-600 μm were then subjected to physical and mechanical properties analyses. More details of granulation methods have been reported previously[29, 31].

2.1.2 Strength measurement

The granule strength was characterised by the quasi-static side crushing test method[32]. Granules of the desired product size range of 500-600 μm were selected randomly. They were compressed individually between two rigid plates using an Instron 5566 mechanical testing machine. In order to obtain statistically reliable results, at least 100 granules were tested per sample. Details of strength measurement have already been reported[33].

2.1.3 Positron emission particle tracking (PEPT)

The positron emission particle tracking (PEPT) facility of the University of Birmingham (Birmingham, UK) was used to track particle motion. The principles of the PEPT technique and its capabilities can be found elsewhere[26-28]. In brief, the PEPT technique makes use of a single radioactive tracer that carries positrons. Positrons annihilate with local electrons, resulting in the emission of back-to-back 511 keV γ-rays. Detection of the pairs of γ-rays enables the tracer location to be found as a function of time by triangulation.

In this very initial attempt to study the scale-up of high-shear mixer granulators, the solids motion in two scales of 1 and 5 L were investigated and compared by using the positron emission particle tracking (PEPT) technique. The granular materials used were calcium carbonate (Durcal 65). While keeping all other operating conditions identical, the operating shaft speeds were set to follow the constant tip speed criterion, which corresponded to the top impeller tip speed of 4.1 ms-1 for both machines. In a typical experiment, calcium carbonate particles were loaded into the vessel of the mixer granulator, which was then started and run for a couple of minutes to ensure that the steady-state was reached before starting the data acquisition process. Resin beads of 60 μm diameter and 1050 kg/m^3 density were used as tracers, which were activated by an ion exchange method with radioactive water produced in a cyclotron[26-28]. The data acquisition was performed for 12 minutes for each run, which gave at least 20000 data points in the form of spatial locations in the Cartesian coordinate as a function of time.

2.1.4 Analysis of particle motion and granule breakage by distinct element method (DEM)

The distinct element method (DEM) models the interaction between constituent particles as a dynamic process, and the time evolution of the particles is advanced using an explicit finite difference scheme. The interactions between the constituent particles are based on theories of contact mechanics. More details on the methodology of DEM are given by Cundall[34]. For analysis of the macroscopic flow field of granulators, the PFC3D computer code developed by Itasca was used as it is capable of generating complicated geometries, i.e. vessel with knife and impellers. Particle motion in the granulator has been analysed to determine the granular dynamics, and in particular to identify the velocity gradient and stress field responsible for granule breakage in various scales. For granule simulation at a microscopic level, the TRUBAL code originally developed by Cundall and Strack[35] and further modified by Thornton and co-workers[36] was used. This code cannot easily handle complicated geometries, however, it used more realistic contact models for particle-particle interactions[36], which is more suitable for the microscopic modelling of granule behaviour within a shearing bed. The granule deformation and breakage under microscopic interactions within a shearing bed was analysed in order to quantify the effect of the velocity gradient on the breakage and deformation.

3. Results and Discussion

3.1 Single particle crushing

The mean crushing strength of granules produced in the different scales of Cyclomix granulators under the operating conditions specified in **Table 1** was reproduced by Rahmanian *et al.*[33] in **Fig. 3**. The error bars show one standard deviation. For the scales smaller than the reference scale, i.e. 1 and 5 L scales, granules with the highest mean crushing strength are those prepared at the constant tip speed, i.e. 4.13 m/s. The constant shear stress rule produces weaker granules than the constant tip speed rule. The Froude number rule produces the weakest granules in 1 and 5 L scales, but the opposite for the 250 L scale. For a given tip speed, the average crushing strength does not change much with the scale of the granulator. This is also the case, albeit to a lesser extent, for the constant shear stress rule. In contrast, the crushing strength clearly depends on the scale of manufacture for the constant Froude number case. For the given Froude number, i.e. Fr=0.347, the mean crushing strength of granules made in the 1 L scale is higher than that in the 5 L scale but less than those in the 50 and 250 L scales. It seems that the Froude number is not a suitable criterion for scaling-up high-shear granulators. This was also concluded by Hooijmajers *et al.*[37], who recently used a different methodology for scale-up and a different granulator, namely a Gral high-shear granulator using lactose as the primary powder and HPC solution as the liquid binder.

The trend of the variation of strength for different scales using the constant Froude number is surprising, as it is intuitively expected that the 5 L scale should produce stronger granules as compared to the 1 L scale. This point was investigated by identifying the velocity field in the Cyclomix [38-39]. It was found that under a constant Froude number, the velocity gradient in the 1 L is higher than the 5 L scale. This produces higher shear stresses and hence stronger granules. At constant shear stress conditions, the mean crushing strength gradually increases as the Cyclomix is scaled-up.

For all the samples tested, granules with the weakest and strongest crushing strengths are those produced by following the constant Froude number rule in the 5 and 250 L scale, respectively, as demonstrated in **Fig. 3**. The coefficient of variations, i.e. the ratio of the standard deviation to the mean crushing strength, has the lowest (0.21) and highest (0.54) values for granules made at constant tip speed and Froude number, respectively. This indicates that the constant Froude number criterion (n=0.5) produces a wider strength distribution of the granules as compared to the other two scale-up rules. The strength distribution and associated statistical analysis for these granules have already been reported[33]. It is shown that the Weibul statistical function is the best fit to the strength distribution of the granules produced under the constant tip speed rule.

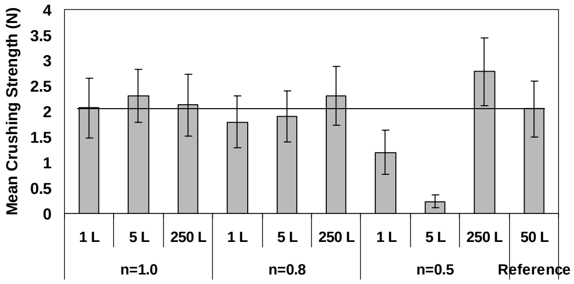

Fig. 3 Mean crushing strength of the granule as a function of scale-up for different scale-up criteria, after Rahmanian *et al.*[33].

3.2 Positron Emission Particle Tracking (PEPT)

The flow fields obtained by PEPT for both scales are shown in **Fig. 4**. The velocity fields obtained for the two scales are different. There are two clockwise swirl flows bounded at the top impeller in Cyclomix 5L, while there is one clockwise and one anti-clockwise swirl flow in Cyclomix 1L. Unlike the stagnant bed in Cyclomix 1L, the lower swirl in Cyclomix 5L involves the entire bed below the top impeller. The results imply that the scale of the toroidal flow structure is restricted by the limited space in the Cyclomix 1L. The overall velocity distributions in axial, radial and tangential directions are shown in **Fig. 5**. The difference in velocities can be seen clearly from **Fig. 5(a)**, which shows that Cyclomix 5L has a higher average magnitude in tangential direction. This is due to the larger area of highly agitated region around the top impeller (**Fig. 4(b)**). The maximum tangential velocities of both machine scales are close to each other (**Fig. 5(b)**) as a result of constant tip speed.

The axial, radial and tangential velocities are compared quantitatively at elevations of geometrical similarity (**Fig. 6**). The results are compared at 70 and 105 mm, which corresponds to the height of the third impeller in Cyclomix 1L and 5L, respectively. Generally, the radial and tangential velocities are greater while the axial velocity magnitude is less for Cyclomix 1L as compared to that of Cyclomix 5L. The trends of axial and tangential velocity are broadly similar. The correlation coefficients between the velocity distributions of different scales in **Figs. 7(a-c)** are 0.893, 0.6152 and -0.796, respectively. The results indicate that a similar flow field can be obtained at different machine scales by using the constant tip speed criterion while keeping other conditions identical.

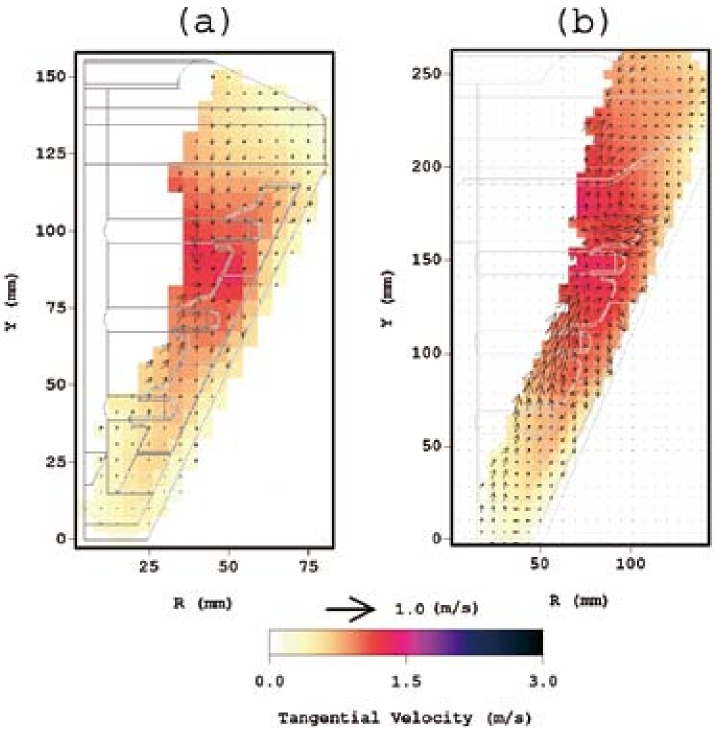

Fig. 4 Vector plots of the axial and radial velocities overlaid with the colour plot of the tangential velocity for (a) Cyclomix 1L and (b) Cyclomix 5L [Durcal 65; equal tip speed 4.1 ms^{-1}].

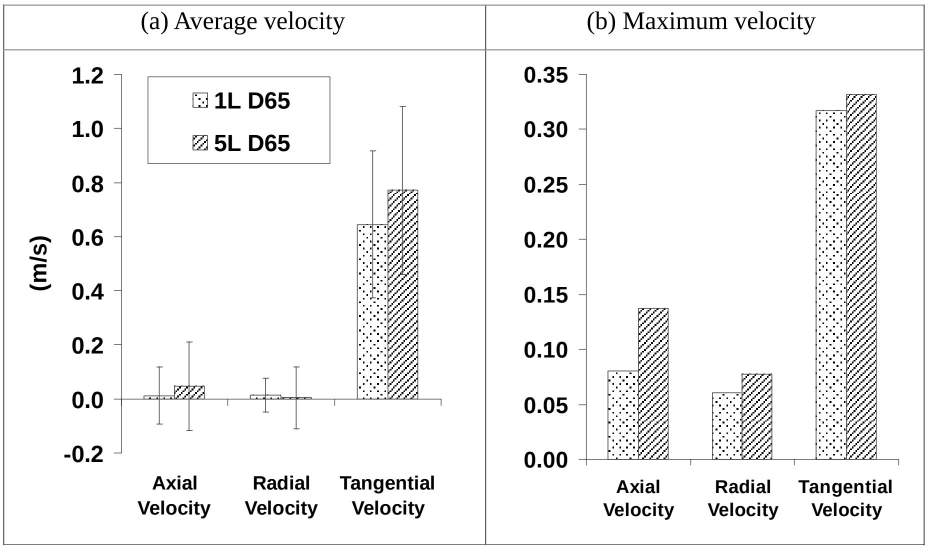
(a) Average velocity

(b) Maximum velocity

Fig. 5 (a) Average and (b) dimensionless maximum velocities in axial, radial and tangential directions for Cyclomix 1L and 5L normalised w.r.t. the tip speed [Durcal 65; equal tip speed 4.1 ms^{-1}].

In both scales, the granular material forms a thick layer attached to the vessel wall (**Fig. 7**). The normalised tracer occurrence for Cyclomix 1L and Cyclomix 5L is similar, indicating that both machine scales have similar dispersion characteristics with constant tip speed criterion.

In addition to the flow structure, the vertical circulation period and number of circulation are used to compare the vertical mixing power between the two scales. The upper boundary of Cyclomix 5L is about 10 mm above the top impellers, and the lower boundary is at the level of the second impellers. The selection of the boundaries of the Cyclomix 1L follows the geometrical similarity where the upper boundary is

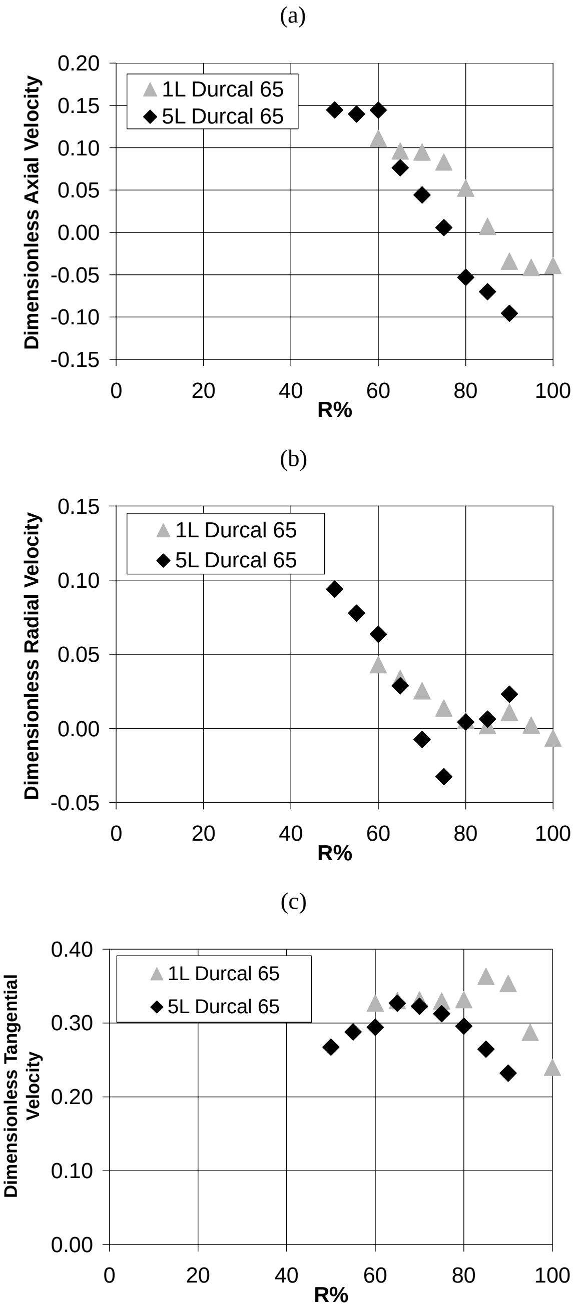

Fig. 6 Quantitative comparison of the (a) axial, (b) radial, (c) tangential velocities between Cyclomix 1L and 5L [Durcal 65; equal tip speed 4.1 ms^{-1}].

chosen to be 10 mm above the top impellers (Y120) and the lower boundary to be the level of the second impellers (Y43). There is no obvious difference between the Cyclomix 1L and 5L in the vertical circulation period and number of cycles (**Fig. 8**), although the number of cycles in Cyclomix 1L is slightly smaller than that of Cyclomix 5L. The results imply that, in so far as the mixing is concerned, geometrically similar mixer granulators can be scaled by applying the constant tip speed criterion. This is attributed to the finding that the constant tip speed criterion gives comparable vertical mixing, both in period and number of cycles.

3.3 DEM modelling

3.3.1 Macroscopic flow field of granulator

For simulation of the macroscopic flow field of the granulator, the vessel and the impeller were geometrically generated using the PFC3D DEM code (**Fig. 9**). Particles with the properties given in **Table 2** were generated randomly within the vessel. Gravity was then introduced to settle the assembly. The current computer power is unable to simulate the actual number of particles inside the granulator in reasonable computing time. Smaller numbers of particles, but of greater size, were therefore used for the simulation work. The approach here is to take the largest number of particles which can be simulated in a reasonable time and attribute to them a density (smaller than true density) such that the mass of the assembly is equal to the mass of fine powder (**Table 3**). More details on the method can be found in Hassanpour *et al.*[39].

After generating a stable assembly of particles in terms of contact and coordination number, the impeller was rotated at various rotational speeds according to the conditions of scale-up (n = 0.5, 0.8 and 1 as defined in **Table 1**. A snapshot of the velocity field of particles during agitation (7.47 Hz) is shown for 1 L granulator in **Fig. 10** as an example. The velocity field obtained from DEM analysis is qualitatively compared with PEPT measurements (**Fig. 7a**).

The shear stresses within the granulator in various regions were calculated for various granulator sizes and all scale-up rules. The results were compared to identify how the shear stress changes as a function of granulator size and scale-up rule. As an example, the results of variation of shear stress for 1 L granulators are shown in **Fig. 11**. In this figure, it can be seen that at the beginning of agitation, the highest shear stresses are in bottom part of the vessel (region 4). This is due to the stationary mass of powder sitting above region 4 which creates a high pressure. The stress in region 4 decreases rapidly as the bed of powder becomes dynamic. After a certain period of time (around 0.2 s) the shear stresses within all regions have peaks, corresponding to the times when the impellers pass through the stress calculation area. From **Fig. 11**, it can be seen that the highest level of shear stress exists in region 2, where the top impeller is placed.

The qualitative agreement between PEPT and

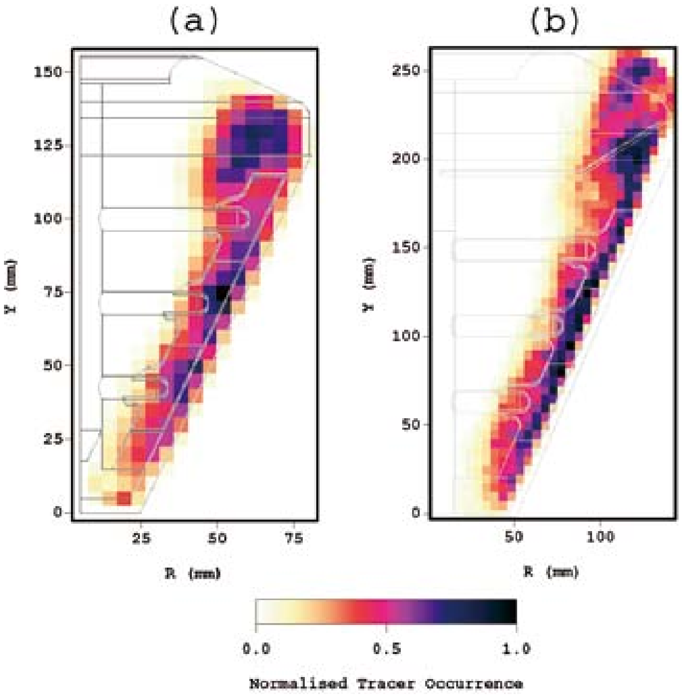

Fig. 7 Normalised tracer occurrence: (a) Cyclomix 1L and (b) Cyclomix 5L [Durcal 65; equal tip speed 4.1 ms^{-1}].

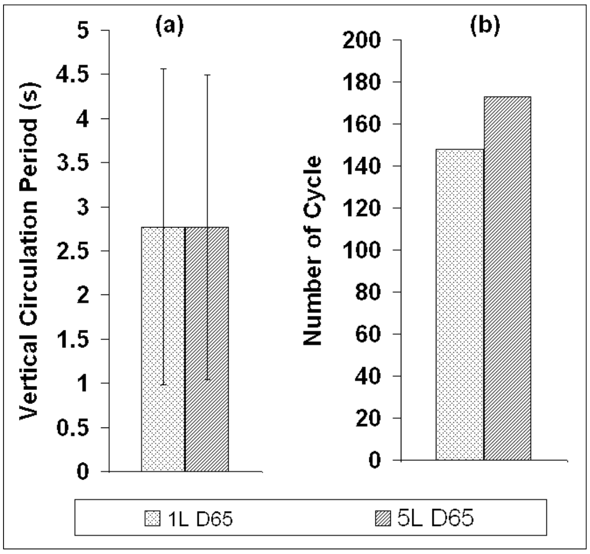

Fig. 8. Period of vertical circulations between upper boundary at Y=120 mm, Y=180 mm and the lower boundary at Y=43 mm, Y=60 mm for Cyclomix 1L and 5L, respectively [Durcal 65; equal tip speed 4.1 ms^{-1}].

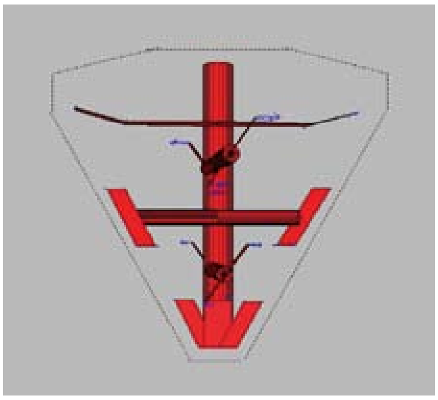

Fig. 9 Geometry of the Cyclomix granulator generated using DEM, after Hassanpour *et al.*, [39].

Table 2 The properties of particles and walls used in the simulation of the macroscopic flow field of a 1 L granulator

Material properties	Particles	Wall
Young's modulus (GPa)	35	215
Poisson's ratio	0.20	0.30
Density (kg m^{-3})	1550	7800
Coefficient of friction	0.35	0.15

Table 3 Number and size of particles used in the simulations of different granulator scales

Granulator	No of Particles	Size	Density
50 L	50,000	9.0-10.0 mm	1550
5 L	50,000	4.3-4.5 mm	1550
1 L	50,000	2.4-2.6 mm	1550

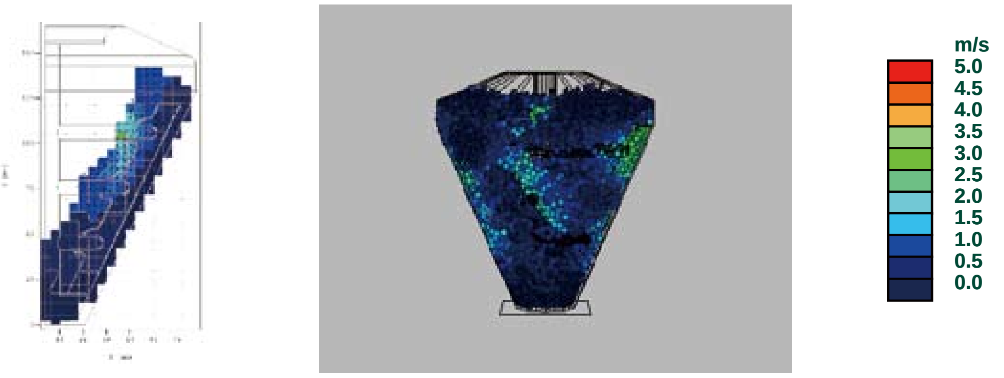

(a) PEPT **(b) DEM**

Fig. 10 A snapshot of DEM simulation of the velocity field within the 1 L granulator and comparison with PEPT analysis, after Hassanpour *et al.*,[39].

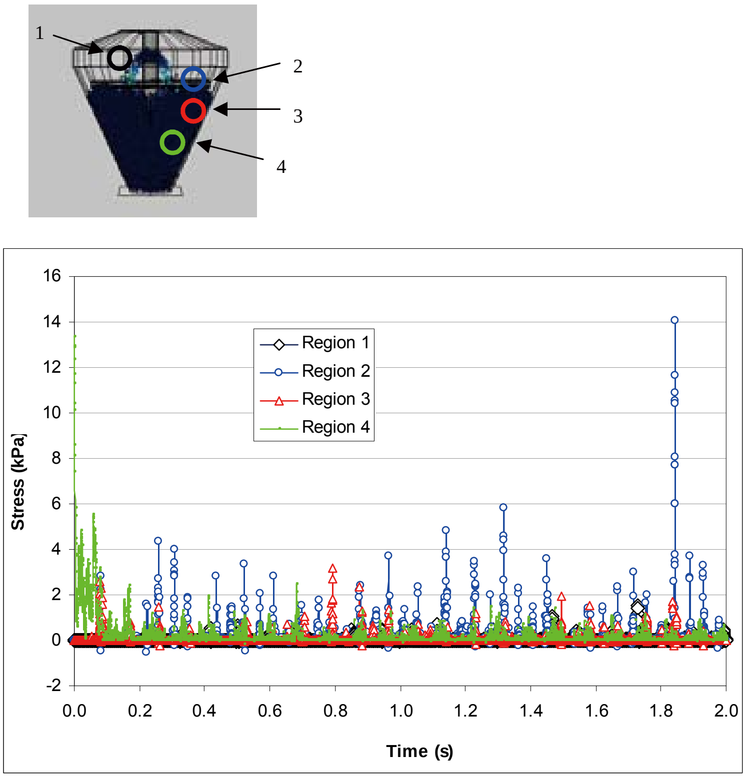

Fig. 11 DEM simulation of the shear stress evolution within specified regions during agitation, after Hassanpour *et al.*, [39].

DEM indicates that DEM analysis provides useful information on the macroscopic flow and shear stress field of the granulator. This approach can be used for analyses where PEPT measurement cannot be carried out due to the large scale of the granulator (larger than 5 L).

3.3.2 Microscopic interactions

In order to simulate the behaviour of granules at microscopic level during shearing, a small segment of the granulator is simulated. A granule of about 1 mm in diameter is embedded in a cubic assembly of primary particles (**Fig. 12**). The granule was made up of 500 primary particles with the properties given in **Table 4**. The assembly was then subjected to shear deformation by superimposing a velocity profile on the particles as shown schematically in **Fig. 12**. The results of the velocity gradient obtained from PEPT analysis (**Fig. 4**) are used as boundary conditions for superimposing a velocity profile on the particles

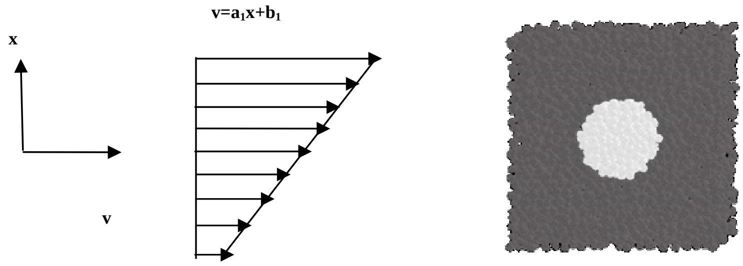

Fig. 12 The granule within an assembly of primary particles and the velocity profile superimposed on the surrounding particles for shearing of assembly.

Table 4 The properties of particles and walls used in the simulation of microscopic interaction

Material properties	Particles	Wall
Diameter (μm)	90-120	-
Young's modulus (GPa)	35	215
Poisson's ratio	0.20	0.30
Density (kg m^{-3})	2700	7800
Coefficient of friction	0.35	0.15

(**Fig. 12**). During shearing, the normal pressure was kept constant by allowing movement of the horizontal platen on the bed. The evolution of shear stress and behaviour of the granule is then monitored. More details on the method of creation of the granule and the assembly can be found in Hassanpour *et al.*, [25, 39].

In this simulation, the shear stress on the granule is calculated from the principal stresses on the granule. As an example, the results for the two velocity fields corresponding to 1 and 5 L granulator scales (scaled-up according to n=0.8) are shown in **Fig. 13**. It can be seen that for the case where the conditions of 1 L are used, the shear stresses are larger than

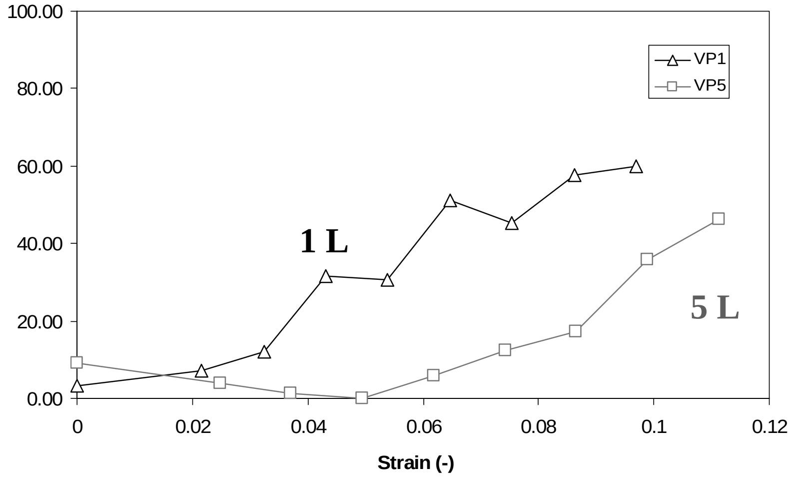

Fig. 13 Simulation of evolution of shear stress on the granule during shearing according to different conditions, after Hassanpour *et al.*, [39].

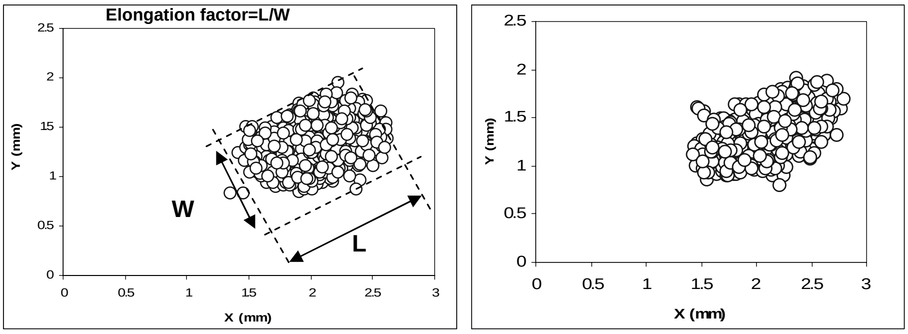

5 L **1 L**

Fig. 14. The granule within an assembly after shearing according to the conditions of the granulator, after Hassanpour *et al.*, [39].

those of 5 L. This means that the larger velocity gradient would create larger shear stress on the granule.

The granule behaviour for both cases of shearing conditions is shown in **Fig. 14**. It can be seen that the granules have two different shapes after shearing. The elongation factor expressed as the ratio between the maximum (L in **Fig. 14**) to the minimum dimensions of the granule (W in **Fig. 14**) and the packing fraction have been calculated for both granules and the results are shown in **Table 4**. It can be seen that for the case where the conditions of the 1 L granulator are used, the granule is more elongated and has a smaller packing fraction. According to the models of Rumpf [40] and Kendall [41], granules sheared with the conditions of 1 L would have a lower strength. This agrees well with the experimental results obtained in **Fig. 2**, where granules produced in 1 L have a lower strength if the granulator is scaled up using the condition of constant shear stress (n=0.8).

4. Conclusions

The granulation process operated in several scales of Cyclomix high-shear granulators is influenced by different scale-up rules. Three different scale-up rules of constant tip speed, constant shear stress and constant Froude number have been evaluated. The effect of scale of operation on the granules' strength distribution, characterised by side crushing tests, was investigated.

The constant tip speed rule produces agglomerates of comparable strength. The difference in agglomerate strength distribution produced in different scales becomes progressively larger for the constant shear stress and constant Froude number rules, respectively. Hence, it can be concluded that the constant Froude number rule is unsuitable for the scale-up of high-shear granulators in so far as the interest is on keeping the crushing strength constant. However, when the conditions of constant shear stress are used to scale up the granulator, the granules produced in 1 L are weaker than those of 5 L. This behaviour has been examined by detailed work to characterise the velocity field and stress fields of granules in the granulator by DEM and PEPT to provide a better insight into the flow and stress profiles as a function of equipment scale. PEPT analysis shows that the macroscopic flow fields of 1 L and 5 L granulators are different, which could affect the final strength of the granules. PEPT results were used in DEM for modelling the microscopic interactions of granules within a shearing bed. The simulation results confirm that the flow conditions of the 1 L granulator make the granule more elongated and with a lower packing fraction, indicating that the granule in 1 L is weaker, a trend corroborated by experimental data.

Table 5 Properties of granules after shearing according to the conditions of the granulators

Shearing conditions	Elongation factor	Packing fraction
1 L	1.99	0.48
5 L	1.41	0.55

Acknowledgements

The work reported here is part of a project supported financially by the EPSRC (Grant No. GR/S25029/01), Borax Europe Ltd., Hosokawa Micron B.V., Pfizer Global R&D, and P&G. The authors are grateful for the support and project coordination provided by the representatives of the industrial sponsors, in particular Dr I. Hayati (Borax Europe Ltd.), and Drs A.C. Bentham and D. Golchert (Pfizer).

References

1) Capes, C.E.(1980): Particle size enlargement, In Handbook of Powder Technology. Vol. 1. Elsevier, Amsterdam.
2) Pietsch, W.(1991): “Size enlargement by agglomeration”, Wiley; Aarau; Salle and Sauerländer, Chichester.
3) Ennis, B. J., Litster, J. D.(1997): Principles of size enlargement. In Green D, Perry R. eds. Perry's Chemical Engineers Handbook 7th Edition. New York: Mc Graw Hill.
4) Litster, J. and Ennis, B.(2004): “The science and engineering of granulation process”, Dordrecht, The Netherlands, Kluwer academic publishers.
5) Faure, P. York, R.C. and Rowe, (2001): Process control and scale-up of pharmaceutical wet granulation processes: A Review, European Journal of Pharmaceutics and Biopharmaceutics 52, pp.269-277.
6) Knight P.(2004): Challenges in granulation technology, Powder Technol. 140, pp.156-162.
7) Timothy A. B.(2005): Challenges in the scale-up of particulate processes - an industrial perspective, Powder Technol. 150, pp.60-71.
8) Mort, P. R.(2005): Scale-up of binder agglomeration processes, Powder Technol. 150, pp.86-103.
9) Newitt, D.M. and Conway-Jones, J. M.(1958): A contribution to the theory and practice of granulation, Trans. Inst. Chem Eng. 36, pp.422-441.
10) Kapur, P.C. and Fuerstenau, D.W.(1969): A coalescence model for granulation, Ind. Eng. Chem. Process Des. Dev. 8, pp.56-62.
11) Iveson, S. M., Litster, J.D. and Ennis, J.D.(1996): Fundamental studies of granule consolidation: Part 1. Effects of binder viscosity and binder content, Powder

Technol. 88, pp.15-20.
12) Knight, P.C., Instone, T., Peason, J.M.K. and Hounslow, M.J.(1998): An investigation into kinetics of liquid distribution and growth in high shear mixer agglomeration, Powder Technol. 97, pp.246-257.
13) Knight, P.C., Johansen, A., Kristensen, P.C., Schaefer, P.C. and Seville, J.P.K. (2000): An investigation of the effects on agglomeration of changing the speed of a mechanical mixer, Powder Technol. 110, pp.204-209.
14) Scott, A., Hounslow, M.J. and Instone, T.(2000): Direct evidence of heterogeneity during high shear granulation, Powder Technol. 113, pp.205-213.
15) Johansen, A. and Schaefer, T.(2001): Effects of interactions between powder particle size and binder viscosity on agglomerate growth mechanisms in a high shear mixer, Eur. J. Pharm. Sci. 12, pp.297-309.
16) Faure, A., Grimsey, I. M, Rowe, R.C., York, P. and Cliff, M.J.(1998): A methodology for the optimization of wet granulation in a model planetary mixer, Pharm. Dev. Technology 3, pp.413-422.
17) Bock, T K. and Kraas (2001): Experience with the Diosna mini-granulator and assessment of process scalability, European Journal of Pharmaceutics and Biopharmaceutics 52, pp.97-303.
18) Horsthuis G.J.B., van Larrhoven J. A. H, van Rooij R. C. B. M. and Vormans H. (1993): Studies on up scaling parameters of the Gral high-shear granulation process, Int. J. Pharm. 92, pp.143-150.
19) Tardos G.I, Irfan Khan, M. and Mort, P.M.(1997): Critical parameters and limiting conditions in binder granulation of fine powders, Powder Technol. 94, pp.245-258.
20) Tardos, G.I., Hapgood, K.P., Ipadeola, O.O. and Michaels, J.N.(2004): Stress measurements in high-shear granulators using calibrated "test" particles: application to scale-up, Powder Technol. 140, pp.217-227.
21) Subero, J. And Ghadiri, M.(2001): Breakage patterns of agglomerates, Powder Technol. 120 (3), pp.232-243.
22) Salman, A.D., Fu, J., Gorham, A. D. and Hounslow, M.J.(2003): Impact breakage of fertiliser granules. Powder Technol. 130 (1-3), pp.359-366.
23) Golchert, D., Moreno, R., Ghadiri, M. and Litster, J.(2004): Effect of granule morphology on breakage behaviour during compression, Powder Technol.143-144, pp.84-96.
24) Antonyuk, S., Khanal, M., Tomas, J., Heinrich, S. and Mörl, L.(2006): Impact breakage of spherical granules: experimental study and DEM simulation, Chemical Engineering and Processing 45 (10), pp.838-856.
25) Hassanpour, A., Antony, S.J. and Ghadiri, M.(2007): Effect of size ratio on the behaviour of agglomerates embedded in a bed of particles subjected to shearing - DEM analysis, Chem. Eng. Sci. 62, pp.935-942.
26) Parker, J., Hawkesworth, M.R., Broadbent, C.J., Fowles, P., Fryer, T. D. and McNeil, P. (1994): Industrial positron-based imaging: principles and applications, Nuclear Instruments and Methods in Physics Research A, 348, pp.583-592.
27) Parker, D. J., Dijkstra, A.E., Martin, I.T.W and Seville, J. P. K. (1997): Positron emission particle tracking studies of spherical particle motion in rotating drums, Chemical Engineering Science, 52(13), pp.2011-2022.
28) Parker, D. J., Forster, R.N, Fowles, P. and Takhar, P.S.(2002): Positron emission particle tracking using the new Birmingham positron camera, Nuclear Instruments and Methods in Physics Research A, 477, 540-545.
29) Kwan, C. C., Hare, C., Ding, Y., Williams, R.A. and Ghadiri, M.(2006): How granule characteristics change when high shear mixer granulator are scale-up, Fifth World Congress on Particle Technology, 23-27 April, Florida, USA.
30) Eliassi, A., Modarres, H. and Mansoori, G.A.(1998): Densities of Polyethyleneglycol and water mixtures in the 298.15-328.15K temperature range, J. Chem. Eng. Data, 43, pp.719-721.
31) Kwan, C.C., Ding, Y., Williams, R. A. and Ghadiri, M.(2005): Effects of operating parameters of high shear granulator on the evolved properties and structure of calcium carbonate granules, in Particular Systems Analysis Stratford-upon-Avon, UK.
32) Rahmanian, N., Ghadiri, M., Ding, Y. and Jia X.(2007): Influence of scale-up of high shear mixer granulators on the strength and properties of granules, PARTEC 2007, P06_03 27-29 March, Nuremberg, Germany.
33) Rahmanian, N., Ghadiri, M. and Ding, Y. (2008): Effect of scale of operation on granule strength in high shear granulators, Chem. Eng. Sci., 63 (4), pp.915-923.
34) Cundall, P. A.(1971): A computer model for simulating progressive, large-scale movements in blocky rock systems, Proc. Symp. Int. Soc. Rock Mech., Nancy 2, 8.
35) Cundall, P.A. and Strack, O.D.L.(1979): A discrete numerical model for granular assemblies, Geotechnique 29, pp.47-65.
36) Thornton, C., and Yin, K.K.(1991): Impact of elastic sphere with and without adhesion, Powder Technol. 65, pp.153-166.
37) Hooijmaijers, R., Oostra, W. and van den Dries, K. (2007): An investigation of upscaling factors in high shear granulation, International Congress on Particle Technology, PARTEC 2007, S05_1 27-29 March 2007, Nuremberg, Germnay.
38) Ng, B. H., Kwan, C.C., Ding, Y. L. Ghadiri, M. and Fan, X.F.(2007): Solids motion in a conical frustum-shaped high shear mixer granulator, Chem. Eng. Sci. 62, pp.756-765.
39) Hassanpour, A., Kwan, C.C., Ng, B.H., Rahmanian, N., Ding, Y.L., Antony, Y.L., Jia, Y.L. and Ghadiri, M. (2008): Effect of granulation scale-up on the structure and strength of granules, in print, Powder Technol., doi: 10.1016.
40) Rumpf, H.(1962): The strength of granules and agglomerates, In Agglomeration (ed. W.A. Knepper), Proceedings of the First International Symposium on Agglomeration, Philadelphia. John Wiley and Sons,

New York/London, pp.379-418.
41) Kendall, K. (1988): Agglomerate strength, Powder Metallurgy, 31 (1), pp.28-31.

Author’s short biography

Nejatollah Rahmanian

Mr Nejatollah Rahmanian BSc (Petroleum University of Technology, Iran), MSc (Shiraz University, Iran) worked previously for about 8 years for Petropars Ltd., Iran, as a process engineer on the development of the South Pars gas field reservoir. He is currently working as a PhD student on the granulation project. His research interests are on the granulation processes and application of particle technology in the gas and oil industries.

Boon Ho Ng

Dr Boonho Ng obtained his PhD from the University of Leeds in 2008. At present he is working on a research programme sponsored by Proctor and Gamble. Boonho's research interests focus on multiphase flow, in particular on the flow of granular materials in agitated mixers and spray dryers. His current research includes the effect of the machine scale, type of granular material and size, and operation speed on the granular flow in an agitated mixer as well as drying phenomena in a spray tower.

Ali Hassanpour

Dr Ali Hassanpour BSc (Sharif University, Tehran) PhD (Leeds University) is currently a postdoctoral research fellow at the Institute of Particle Science and Engineering at the University of Leeds. His research activities include the use of the distinct element method (DEM) for the simulation of granular media, mechanical characterisation of particles, size reduction (breakage and attrition of the particles) and size enlargement (granulation of powders), scale-up of particulate processes and flowability and dispersion behaviour of cohesive powders.

Yulong Ding

Professor Yulong Ding BEng MSc PhD became a professor of Nanoparticle Engineering with the Institute of Particle Science and Engineering and Chemical Engineering Discipline at the University of Leeds after previous employment with the Imperial College London, University of Birmingham and University of Science and Technology (Beijing). He has been working on both the experimental aspects and mathematical modelling of particulate and multiphase reacting systems on both small (nano and micro) and large (meso and macro) scales over the past decade. Professor Ding’s recent research has focused on two areas of nanofluids for thermal management and multiphase transport phenomena associated with particle classification and characterisation and separation enhanced reaction processes. His research has led to over 180 technical papers, 8 book chapters and 9 patents.

Author's short biography

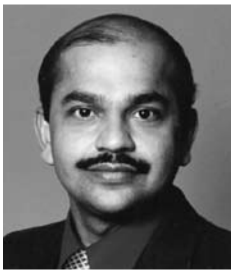

Joseph Antony

Dr Joseph Antony is a lecturer at the Department of Chemical Engineering, University of Leeds. His primary research interest is in the area of particulate science and engineering; especially on the computational modelling of particulate materials using advanced numerical methods such as DEM, FEM and BEM. He obtained the prestigious *MIT Young Researcher Fellowship Award (2001) for Exemplary Research in Computational Mechanics.*

Xiaodong Jia

Dr Xiaodong Jia obtained his BSc in engineering physics from Tsinghua University, China, in 1986 and a PhD in chemical engineering from the now University of Manchester in 1992. He is a senior research fellow at the Institute of Particle Science and Engineering, University of Leeds. His interests are particle and powder characterisation and modelling.

Mojtaba Ghadiri

Professor Mojtaba Ghadiri is director of the Institute of Particle Science and Engineering, University of Leeds. His research area is in engineering science of processes involving particulate matter such as attrition, comminution, agglomeration, dispersion, compaction, nanopowder processing, electrical effects, mechanics of particle motion and super-critical fluid processing. The focal point of his work is the development of relationships between microscopic and macroscopic properties and phenomena; i.e. the way in which the microstructure of particulate solids and the micromechanics of their behaviour in process equipment influence the performance of the process and the characteristics of the product.

Peter G.J. van der Wel

Dr Peter van der Wel works as the research & development manager at Hosokawa Micron BV in Doetinchem, the Netherlands. His main responsibility is the development and improvement of powder processing equipment in the field of mixing, drying and agglomeration. In 1987, he graduated from the Delft University of Technology in the field of chemical engineering – powder technology. At the same university, he obtained his Ph.D. in 1993 on the subject of dust explosions.

Allet Krug-Polman

Ing. Allet Krug-Polman works as an application engineer at Hosokawa Micron BV in Doetinchem, the Netherlands. Hosokawa Micron BV sells industrial machines and processes for the powder processing industry. Her main responsibility is support in and sale of machines and processes used in the powder processing industry in the field of mixing, drying and agglomeration. In 1996 she graduated from the Hoge Technische School Groningen in the field of chemical technologies. She started working at Hosokawa Micron BV in 1998 and became the Cyclomix product specialist.

Author's short biography

David York

Prof. David York is a process engineer at Procter and Gamble with over 30 years of experience in the area of powder processing, from upstream research and plant design and start-up to plant process optimisation and trouble shooting, including some time as a product designer. He is very active on the research side of the business, and supports especially academic research and has set up the strategic partnership with the EPSRC. He has a wide range of patents from spray drying to agglomeration, encapsulation to plasma coating, nano particles to highly impact-resistant particles as well as water-soluble units to dose products. He is a visiting professor at the Institute of Particle Science and Engineering at the University of Leeds and was recently elected a fellow of the Royal Academy of Engineering.

Andrew Bayly

Dr. Andrew Bayly BA, MEng, MA, PhD is process modelling and simulation group leader at Procter & Gamble's Technical Centre at Newcastle Upon Tyne in the U.K., where he has been researching and developing granular laundry detergents and their production processes since 1995. Prior to this, he received a Masters degree in chemical engineering from the University of Cambridge (Pembroke College) and studied for a PhD in dispersed bubbly flows at the same institution. In the past 10 years, his research has involved the experimental and numerical investigation of particulate systems across all scales, from process system modelling to micro-structure investigation. Much of this work has involved the spray drying process, where he has led significant developments in the understanding and simulation of the process and its products. His research interests remain broad and cross the boundaries between fluid dynamics, heat and mass transfer, particle technology and surfactant science.

Hong Sing Tan

Dr Hong Sing Tan works as a process development engineer at Procter and Gamble in Newcastle, United Kingdom. His responsibility is in the development of modelling and simulation tools to support the dry laundry business in the area of agglomeration and powder flow processes. He graduated from the University of Sheffield in mechanical engineering. At the same university, he obtained his PhD in 2004 on the subject of the kinetics of fluidised bed granulation.

Single Particle Mass Spectrometry – Bioaerosol Analysis by MALDI MS[†]

W.A. Kleefsman[1,*], M.A. Stowers[1], P.J.T. Verheijen[2] and J.C.M. Marijnissen[1]

Delft University of Technology, Faculty of Applied Sciences, Nanostructured Materials[1]
Delft University of Technology, Faculty of Applied Sciences, Bioprocess Technology[2],

Abstract

The development of an aerosol mass spectrometer for the analysis of biological aerosols is described. The working principles of the aerosol mass spectrometer are particle sizing, particle selection and particle analysis by matrix-assisted laser desorption/ionization mass spectrometry (MALDI). The instrument has the capability of selecting only those aerosol particles that emit fluorescence when excited with 266 nm laser light, which differentiates the biological particles from virtually all other particles likely to be present in an aerosol.

The implementation of a new ion source and delayed extraction has resulted in the capability of obtaining high-quality mass spectra of single bioaerosol particles. Isotopic resolution was obtained for a low-mass peptide. The sensitivity limit of the instrument was determined to be 1 zeptomole. The suitability of the aerosol mass spectrometer for the analysis of bacterial aerosol particles is demonstrated with an aerosol containing vegetative cells of the bacterium Escherichia coli when prepared off-line. The mass spectrum obtained has good resolution and covers a mass range up to 15 kDalton.

Keywords: bioaerosols, aerosol mass spectrometry, single particle analysis,MALDI MS, on-line analysis

Introduction

The on-line chemical characterization of atmospheric (bio)aerosol particles has been investigated by researchers for many years[1,2] and has resulted in several (commercial) instruments. In 1988, Marijnissen et al.[3] proposed an instrument for on-line aerosol analysis in which size determination, laser-induced fragmentation and time-of-flight mass spectroscopy were combined. The novelty in the proposed apparatus of Marijnissen et al.[3] was the combination of particle sizing and laser fragmentation for time-of-flight mass spectrometry.

Throughout the following years a substantial amount of research was carried out to optimize the performance of this aerosol mass spectrometer. For instance, Kievit[4,5] investigated the particle introduction into the instrument and designed and characterized the aerosol beam generator. The aerosol beam generator is the interface which transports the aerosol particles from atmospheric pressure to the working pressure (10^{-6} mbar) of the mass spectrometer. Weiss[6,7] implemented the aerodynamic sizing principle for the instrument. The aerodynamic sizing principle was adapted from Prather et al.[8] who were the first to implement such a sizing system in an aerosol mass spectrometer. Weiss[6,7] replaced the flash-lamp pumped Nd:YAG laser by an Excimer laser. Excimer lasers can be triggered much faster due to the shorter delay time between trigger and radiation output, and are therefore better suited for the application. In addition, with an Excimer laser, multiple wavelengths can be applied. Weiss[7] also implemented a new triggering circuit based on the design of Nordmeyer and Prather[9], who were the first to implement such a triggering circuitry in an aerosol mass spectrometer. Software to acquire and process the data of the instrument was also developed by Weiss[7].

Stowers et al.[10] and Van Wuijckhuijse[11] implemented MALDI mass spectrometry, a technique that al-

---

[†] Accepted: August 23, 2008

[1] Julianalaan 136, 2628 BL, Delft, The Netherlands
[2] Julianalaan 67, 2628 BC, Delft, The Netherlands
[*] Corresponding author:
TEL: +31 15 278 4372 FAX: +31 15 278 4945
Email: w.a.kleefsman@tudelft.nl

lows the ionization of high-molecular-mass molecules and which is widely used for the analysis of complex compounds, including the analysis of bacteria[12-14].

A fraction of the atmospheric aerosol particles are biological aerosol particles. A biological aerosol particle is defined as: an airborne solid particle (dead or alive) that is or was derived from living organisms, including microorganisms and fragments of all varieties of living things[15]. The microorganisms under consideration are viruses, bacteria, fungi, protozoa or algae. To reserve the instrument only for the analysis of the biological fraction of the total aerosol, Stowers et al.[16] implemented the collection of fluorescence emitted by biological particles, which was inspired by the work reported by, e.g. Pinnick et al.[17,18], Hairston et al.[19] and Pan et al.[20] The amino acid tryptophan present in bacteria particles emits strong fluorescence when irradiated with 266 nm laser light. The emission of fluorescence is used as a selection criterion in the aerosol mass spectrometer.

All the above-mentioned developments have led to an efficient instrument which is able to generate (single particle) mass spectra of reasonable quality in terms of mass range and mass resolution of proteinaceous aerosol particles.[21] The performance indicates the suitability of the instrument for the analysis of bacterial aerosol particles.

Instruments capable of the on-line measurement and classification of airborne bacterial aerosol particles could be used for monitoring the atmospheric bioaerosol concentrations or in the defense against bioterrorism, but could also be used in hospitals or in hygienic production processes.

A few research groups are working on mass spectrometric instruments for the on-line analysis of bacterial aerosol particles. At the Lawrence Livermore National Laboratory, an on-line bioaerosol mass spectrometer (BAMS) is being developed. The applied mass spectrometric technique is LDI (Laser Desorption/Ionization) time-of-flight mass spectrometry. This technique requires no reagents, and mass spectral signatures of individual spores are reported.[22,23] Fergenson et al.[24] were able to discriminate individual spore particles of either *Bacillus thuringiensis and Bacillus atrophaeus*, based on the presence or absence of only one peak.

A more powerful approach for on-line bioaerosol analysis is aerosol MALDI mass spectrometry, as employed by Murray and coworkers.[25,26] Jackson et al.[25] reported the on-line MALDI TOF MS analysis of proteinaceous material, whereby the particles were coated in-flight with the matrix nitrobenzyl alcohol. Good results were obtained from an aerosol containing *Escherichia coli* with a semi on-line method. In this method, the bacteria particles were impacted on a MALDI target plate, which was precoated with matrix. This MALDI target plate was subsequently analyzed in a standard MALDI mass spectrometer.[26]

Researchers at Oak Ridge National Laboratory use an ion trap mass spectrometer and have reported the on-line detection of proteins and peptides, applying the matrix by evaporation and condensation onto the aerosol particles.[27, 28] So far, no on-line analysis of bacteria containing aerosol particles has been reported by the researchers from Oak Ridge National Laboratory.

On-line analysis of bacteria containing aerosols by aerosol MALDI has only been reported from the aerosol mass spectrometer in Delft.[10,11, 21] Stowers et al.[10] reported the on-line aerosol MALDI MS analysis of *Bacillus atrophaeus* spores and found a reproducible peak at a mass of 1224 Dalton, which was attributed to a part of peptidoglycan. The work done by Van Wuijckhuijse[11,21] included the on-line aerosol MALDI analysis of spores of *Bacillus atrophaeus* and of vegetative cells of *Escherichia coli*. The obtained mass spectra covered a mass range up to 10 kDa. However, the S/R-ratio of the spectra was low and the spectra were hard to reproduce.

This paper describes the working principle of the aerosol mass spectrometer and further improvements of the aerosol mass spectrometer to improve the performance of the instrument in the analysis of bacteria-containing aerosol particles. The improvements include the implementation of a new ion-source and delayed extraction. The effect of the improvements on the performance of the aerosol mass spectrometer is discussed. The paper concludes with a description of analyses performed on off-line-prepared aerosol particles containing the bacterium *Escherichia coli*, to prove the suitability of the aerosol mass spectrometer for bacterial analysis.

Experimental

The aerosol mass spectrometer

In **Fig. 1**, a schematic diagram of the aerosol mass spectrometer is given and is described as follows. Aerosol is sucked into the instrument at a flow rate of 0.6 l/min through four differentially pumped chambers by a network of vacuum pumps. The pressure in the first section can be regulated and holds aerodynamic lenses which, together with the subsequent nozzle and two skimmers, act to generate a focused particle beam. The width of the beam was measured by Van Wuijckhuijse[11)] at the location of the ionization laser focus (approximately 50 mm below the second skimmer) to be around 100 μm. The pressure in the ionization chamber is maintained at approximately 10^{-6} mbar. The aerodynamic size of individual particles is obtained by measuring the transit time between two continuous laser beams, realized by splitting a randomly polarized, continuous-wave (cw) laser beam (532 nm) (MBD-266 laser Coherent Inc., Santa Clara, USA) into two beams with a beam displacement prism. The resulting 532-nm laser beams, focused to 75-μm spots, are 2.8 mm apart in a direction perpendicular to the particle trajectory.

In and at the exit of the nozzle-skimmer system, the particles are accelerated as a function of their aerodynamic diameter up to velocities as high as 250 m/s. A photomultiplier tube (PMT, Thorn EMI, Middlesex, UK; Type 9202B), located 45° relative to forward scattering, records elastic scattering from particles intersecting the detection laser beams. The transit time is a measure for the aerodynamic size of the particle. The aerodynamic particle sizing is calibrated with monodisperse aerosol particles of polystyrene latex (Duke Scientific Corp, Palo Alto, CA, USA) in the size range of 0.24 to 5 μm. The density difference between natural aerosol particles and latex particles can be corrected by using eq. 1:

$$d_a = d_p\sqrt{\frac{\rho_p}{\rho_0}} \qquad \text{(eq. 1)}$$

In which d_a is the aerodynamic diameter, d_p the particle diameter, ρ_p the particle density and ρ_0 the standard particle density of 1 g/ml. The density of latex particles is 1.05 g/ml.

The alignment of the detection laser beams can be monitored using a digital camera (Canon Powershot A95) mounted at 90° relative to forward scattering.

Preselection of the biological fraction out of the total aerosol is accomplished by collecting the fluorescence emitted from the biological particles. A part of the 532-nm cw-beam of the MBD-266 laser is deflected and goes into an external doubler, where a 266-nm laser beam is generated. The 266-nm cw laser beam intercepts the particle beam at the same spot as the top 532-nm laser beam. The emitted fluorescence is recorded on a gated UV-sensitive photomultiplier tube (Electron Tubes Ltd., Ruislip, UK; Model 9235QB) at 135° relative to forward scattering. A wave pass filter allowing light between 290 and 500 nm is placed in front of the photomultiplier tube. The collection time of the fluorescence by the PMT equals the residence time of the particles in the UV laser beam, which is approximately 1 μs[11,16,21)].

The time between the PMT output pulses is also used to trigger the Excimer ionization laser (ATL Lasertechnics, Friedrichstal, Germany; Model EC50), which is focused at 0.5 mm below the second detection beam.

The 308-nm Excimer laser, with a nearly flat top-beam profile and pulse width of 3 ns, establishes desorption and ionization of the particles. The UV laser spot area is approximately 300 × 500 μm and the laser fluence is adjusted for MALDI analysis, typically to values of approximately 1.5 J/cm^2. As a result of the particle-size-dependent triggering and proper alignment, over 95% of all particles intersecting both cw beams are intercepted by the ionization laser beam to generate ions. This particle detection efficiency of the instrument was measured by comparing the particle concentration outside the instrument (using a particle counter) with the number of particles detected by the aerosol mass spectrometer during a certain time period at a fixed suction flow rate. The overall efficiency of the instrument is 1-5% for aerosol particles within the size range of 0.5 to 2 μm.

Positive ions produced in the ionization process are accelerated in a two-stage ion source toward a microchannel plate (MCP) detector that records the mass-dependent arrival time of the ions; this is called time-of-flight mass spectrometry. The two-stage ion source consists of a repeller plate, an extractor plate and a ground plate. The ions are formed in between the repeller and extractor plate and are accelerated due to the presence of an electric field. Further acceleration of the ions is caused due to the electric field between the extractor and ground plate. The length of the flight tube is 1.5 m. The voltages of the repeller, extractor, ion lens (to focus the ions), the deflector plates (to steer the ion beam) and detector are adjusted to obtain maximum response on the detector. In the ion source, the ions formed are accelerated to the same final kinetic energy due to the presence of the electric field:

$$\frac{1}{2}mv^2 = eV \qquad \text{(eq. 2)}$$

where m is the mass of the ions (kg), v the velocity of the ions (m/s), e the elementary charge ($1.6\ 10^{-19}$ C) and V the acceleration voltage. In the drift region (the flight tube), no electric field is present and the ions formed cross the drift region with a velocity proportional to the square root of the mass of the ions:

$$v = \sqrt{\frac{2eV}{m}} \qquad \text{(eq. 3)}$$

The flight time (t) of the ions through the drift region of length L is then:

$$t = \sqrt{\frac{m}{2eV}}L \qquad \text{(eq. 4)}$$

Thus, singly charged ions of high molecular mass will have a lower velocity (eq. 3) and a longer flight time (eq. 4) than singly charged low-mass ions.

The resolution of time-of-flight mass spectrometers is a result of three factors: the initial kinetic energy distribution, the spatial and the temporal distribution of the ions[29]. Each of these factors is discussed in the following.

Initial kinetic energy distribution is a result of the initial velocity of the ions. Ions with an initial velocity component along the time-of-flight axis will arrive earlier at the detector than same-mass ions with no initial velocity. Generally, the initial kinetic energy distribution is minimized by operating the source at high acceleration voltages. The relative difference between the smallest and the largest initial velocities decreases with respect to the final velocity due to the acceleration. The ion source in the aerosol mass spectrometer has been optimized to allow the use of high acceleration voltages, typically 35 kV.

Spatial ion distributions are due to different positions of ion formation within the source, resulting in different travel distances in the source region and thus in ions with a kinetic energy distribution. Ions formed at the detector side in the source will enter the drift region sooner, but have a low velocity and will reach the detector later than ions formed higher up in the source region (further away from the detector). At a certain distance in the drift region the two above-mentioned ions catch up with each other. This distance is called the space-focus plane and is independent of the ion mass. Ideally, the detector should be located at the space-focus plane. A way to minimize the effect of spatial distribution is the use of a dual extraction source. The aerosol mass spectrometer is equipped with such a dual extraction source. A dual extraction source consists of two extraction regions, of which the second extraction field is much higher than the first extraction field, where the ions are formed.

The temporal distribution includes the difference in time of ion formation and the device-dependent spread in ion detection due to the length of the flight tube for instance. Ions with the same mass, formed with a time difference δt, will enter the drift region with a time difference of δt and arrive at the detector with the same time difference δt. This time difference causes a lower resolution (R), which is determined by:

$$R = \frac{t}{2\Delta t} \qquad \text{(eq. 5)}$$

and for ions formed at time δt:

$$R = \frac{t + \delta t}{2\Delta(t + \delta t)} \qquad \text{(eq. 5a)}$$

with Δt at full width at half maximum (FWHM) of the peak. The FWHM (i.e. Δt) is the width of a peak at the intensity, which is half of the maximum intensity of that peak.

Increasing the length of the flight tube, thus increasing the flight time, will increase the resolution. Another way to minimize the temporal ion distribution is to change the way the ions are extracted. In the aerosol mass spectrometer 'delayed extraction' is implemented. In delayed ion extraction, the voltages of the repeller and extractor plate are set to 35 kV. After a delay of typically 450 ns after ionization, the voltage potential on the first extractor plate is pulsed down to voltages of 30-25 kV to accelerate the ions. During the delay time there is a field-free region in the ion source and the formed ions distribute themselves according to their initial kinetic energy, as a result of the ion formation.

When the extraction field is applied, i.e. when the voltage of the first extractor plate is pulsed down, ions with high initial kinetic energy will arrive at the detector at the same time as the same-mass ions with low initial kinetic energy. When the initial kinetic energy of two ions is in opposite direction, the ion drifting away from the detector will receive more energy when the extraction field is applied than the ion drifting toward the detector. This results in a high resolution.

A 500-MHz digital oscilloscope (LeCroy, Chestnut Ridge, NY, USA; Model 9354CL) is used to sample the signals from the PMT and the detector and to send the spectrum output to a personal computer via a GPIB interface; the data are then further processed by a data system developed in-house. The instrument thus provides the aerodynamic size, fluorescence characteristics and a mass spectrum for all particles. Particles in the size range 0.2 to 10 micrometers can be analyzed with this system, however, the triggering circuitry can be adjusted to select a range of aerodynamic particle sizes or can be set to detect suitably sized particles with a fluorescence emission in the specified wavelength range.

Sample preparation

All chemicals, unless noted otherwise, were obtained from Sigma-Aldrich Chemie BV, Zwijndrecht,

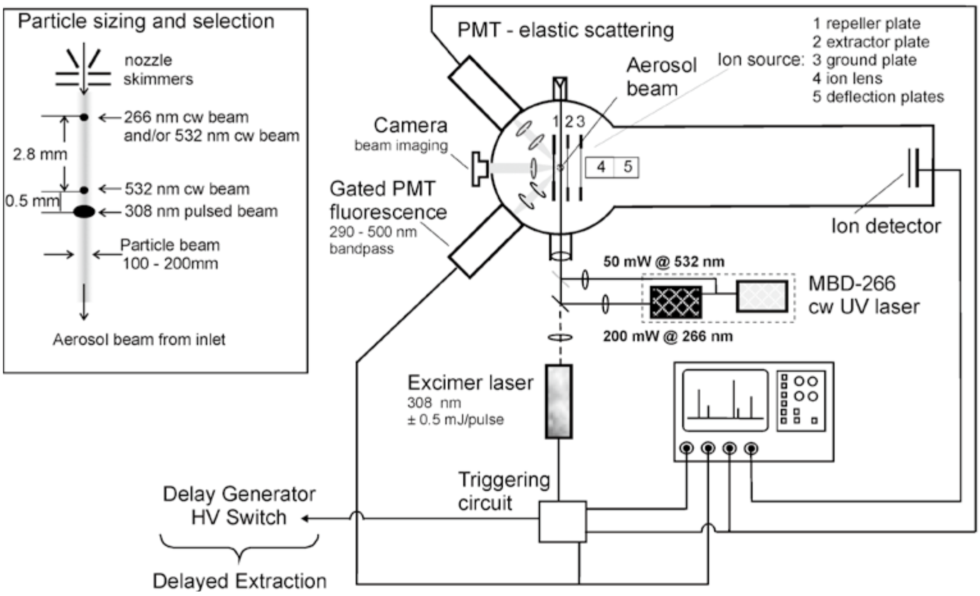

Fig. 1 Schematic diagram of the aerosol mass spectrometer and a cross-section of the particle sizing and detection region.

The Netherlands, and were used without further purification.

Protein particles were generated from solutions of analyte compounds pre-mixed with matrix using a Collison 6-jet nebulizer (BGI, Inc, Waltham, MA, USA). The flow rate through the nebulizer was set at 5 l/min, with approximately 0.6 l/min pulled into the instrument; the carrier gas was filtered air. The aerosol was dried in a diffusion drier packed with silica gel. Ten milligrams of the protein insulin or the neuropeptide substance P were dissolved in 5 ml of deionized water and the matrix materials 2,5-dihydroxy benzoic acid (DHB) or PMC, a proprietary-made compound kindly provided by TNO Defence, Security and Safety, Rijswijk, The Netherlands, were dissolved in 3.3 ml of acetonitrile. Subsequently 1.7 ml of deionized water was added to the matrix solutions to dissolve the matrix compound. Just before aerosolization, the analyte and matrix solution were mixed so that the final solution had an analyte concentration of 1 mg/ml in deionized water/acetonitrile (2:1). The matrix/analyte molar ratio used was in the range of 400:1. Trifluoroacetic acid (TFA) was added to the insulin solution at 0.1 volume percent, to dissolve the insulin.

Also, vegetative cells of the bacterium *Escherichia coli* K12 XL1 blue (cultured and harvested at TNO Defence, Security and Safety, Rijswijk, the Netherlands) were analyzed. Prior to nebulization, the bacterial samples containing 10^9 cfu/ml (determined by optical density at 260 nm), were washed three times by centrifuging the solution at 4000 rpm for 5 minutes; each time the supernatant was removed and the bacteria pellets were then re-suspended in deionized water to approximately 10^9 cfu/ml. The solution was mixed with the same volume of a 20-mg/ml sinapinic acid matrix solution (SA) containing 0.1 % of TFA in a Petri dish. This mixture was vacuum-dried overnight and the resulting solids were ground. The produced powder was nebulized with a DeVilbiss powder blower (Model 175).

Results and Discussion

Improved resolution

An example of the increased mass resolution due to the implementation of delayed extraction is given in **Fig. 2**. The experiments were performed with aerosol particles consisting of insulin and the matrix PMC. First, continuous ion extraction was applied. In continuous extraction there is a continuous field between the repeller (35 kV) and extractor plate (typically 28 kV). This experiment was immediately followed by an experiment in which the ion extraction was delayed. Thus, the experimental conditions were the same, except for the different ion extraction methods.

The resolution is calculated according to eq. 5 for the main protonated insulin peak, at 5734 Dalton. As can be seen, the resolution of 900, obtained with delayed extraction (**Fig. 2b**), is higher than the resolution with continuous extraction, which is 350 (**Fig. 2a**).

The insets in **Fig. 2** show the appearance of the main protonated insulin peak at 5734 Dalton. The resolution in continuous extraction mode is too low to separate the sodium adduct. In single-particle spectra obtained in continuous extraction mode (data not shown), the sodium adduct can be distinguished. The inset in delayed extraction mode shows a peak attributed to the sodium adduct next to the main protonated peak.

The higher resolution in delayed extraction mode is due to the smaller difference in the flight times of the insulin ions. Note that the intensity of the peak is lower in the delayed extraction mode. The cause of this decrease in intensity is not clear. The implementation of delayed extraction has improved the performance of the mass spectrometer. A good resolution is required to make the instrument suitable for the analysis of high-mass molecules.

Isotopic resolution

Another way to examine the effect of the increased mass resolution due to the implementation of delayed extraction and the new high-voltage ion source is to investigate the presence of isotopes. For this purpose, an aerosol was produced from a solution containing the neuropeptide substance P (1347 Dalton) and the matrix PMC. In **Fig. 3**, a mass spectrum of a single particle (**Fig. 3a**) and a mass spectrum of a summation of 50 particles (**Fig. 3b**) is given. The inset in **Fig. 3a** shows the appearance of the main protonated peak, in which different peaks, with a mass difference of 1 Dalton, can easily be discriminated. The peaks are attributed to the isotopes, since the pattern corresponds to the isotope distribution observed in nature from this protein. The isotope distribution was obtained from http://prospector.ucsf.edu/prospector\newline/4.27.1/cgi-bin/msForm.cgi?form=msisotope.

The mass spectrum in **Fig. 3b** is a summation of the mass spectra of 50 single aerosol particles. Again, the inset shows the resolution of the main protonated peak. The different isotopes, as obtained for a single aerosol particle, are not clearly separated. Note that the single-particle resolution and the summed resolution are different. The resolution for a single particle is optimized by a high acceleration voltage and by delayed extraction, but due to the width of the particle beam, the place of ionization is not the same for each particle (spatial distribution), resulting in a

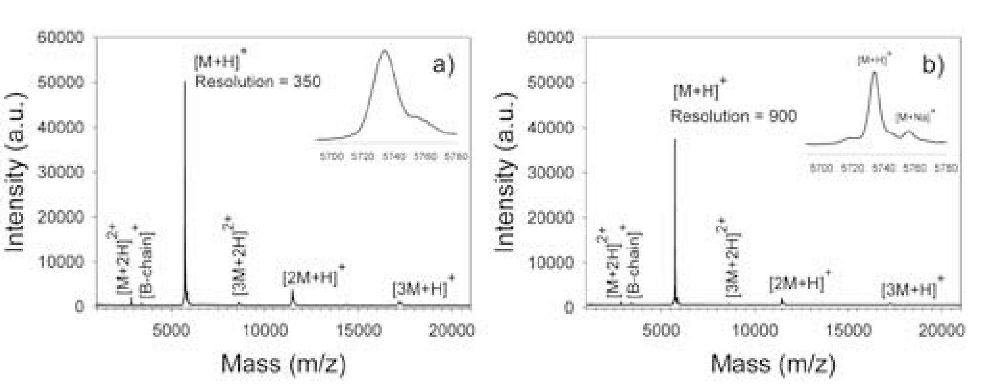

Fig. 2 MALDI mass spectra (summation of 1000 insulin particles premixed with the matrix PMC) obtained with a) continuous extraction and b) delayed extraction. The insets show the main protonated peak.

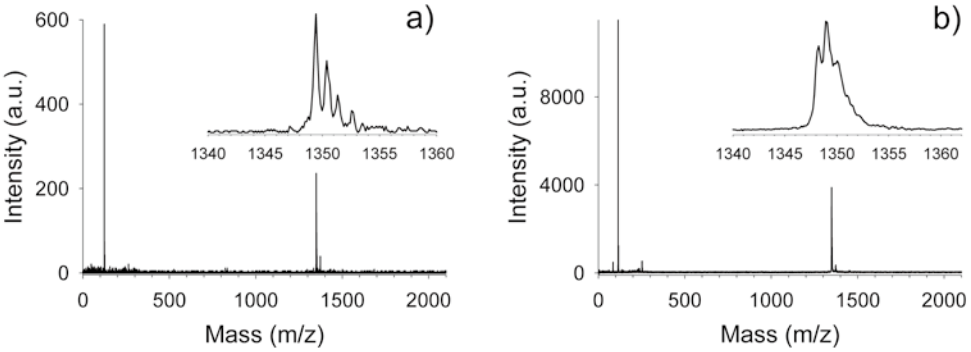

Fig. 3 MALDI mass spectra of aerosol particles consisting of the protein substance P premixed with the matrix PMC; a) single-particle spectrum and b) summation of 50 aerosol particles. The insets show the protonated peak.

lower summed resolution. The spread in ionization locations could be decreased by reducing the particle beam width or by decreasing the diameter of the detection laser beams. However, this will result in a lower efficiency of the instrument.

The detection of isotopes in single-particle mass spectra indicates the applicability of the aerosol mass spectrometer for the analysis of bacteria-containing particles, since the resolution is so good that the individual components of more complex mixtures can be distinguished.

Sensitivity limit of the aerosol mass spectrometer

Identification of bacteria based on their MALDI spectra requires a very sensitive instrument. Madigan et al.[30)] estimated the protein content of vegetative bacterial cells. The total number of protein molecules per cell is estimated to be 2.4 million and the number of different proteins is estimated to be around 1900. Therefore, the average amount of molecules per protein per cell will be in the order of 10^3. Based on the above-mentioned numbers, a sensitivity requirement of 1 zeptomole (10^{-21} mole) can be derived.

The sensitivity of the aerosol MALDI mass spectrometer is determined with an aerosol produced from a solution containing the protein insulin (5733 Dalton) and the matrix 2,5-dihydroxy benzoic acid (DHB). The molar ratio of matrix to analyte in the solution was gradually increased from 500:1 to 50,000:1, by serial dilution. The solutions were aerosolized and the resulting aerosol particles are assumed to have the same matrix-to-analyte ratio as the original solution, assuming a homogeneously mixed solution. Up to a matrix-to-analyte ratio of 50,000:1, peaks caused by insulin ions were appearing in the mass spectra.

For this matrix-to-analyte ratio, the size range of the detected particles was changed from the whole detection range to the size range with an average aerodynamic diameter of 0.26 µm. In **Fig. 4**, an average spectrum of 30 0.26-µm insulin-containing particles at a matrix-to-analyte ratio of 50,000:1 is given.

Russel et al.[31)] determined the sensitivity limit of their BAMS system (bioaerosol mass spectrometer) and used eq. 6 to calculate the number of analyte molecules per particle, assuming spherical, homogeneously mixed particles:

$$N_{analyte} = \frac{4}{3}\pi r^3 \left(\frac{\rho}{MW_{matrix}}\right)\left(\frac{moles_{analyte}}{moles_{matrix}}\right) N_A \qquad \text{(eq. 6)}$$

in which:

$$r = \frac{d_a}{2\sqrt{\rho}} \qquad \text{(eq. 7)}$$

and in which $N_{analyte}$ is the number of analyte molecules per particle, r the particle radius (cm), ρ the particle density (assumed to be the density of the matrix, which is 1.44 g/ml for DHB), MW_{matrix} the molecular weight of the matrix (which is 154 g/mole for DHB), N_A Avogadro's number and d_a the aerodynamic diameter. Note that eq. 7 is not correct. The aerodynamic particle size is defined as the diameter of a spherical particle with a density of 1 g/ml that has the same settling velocity as the particle. Formally therefore, the ratio of the densities should be used (see also eq. 1)[32)]:

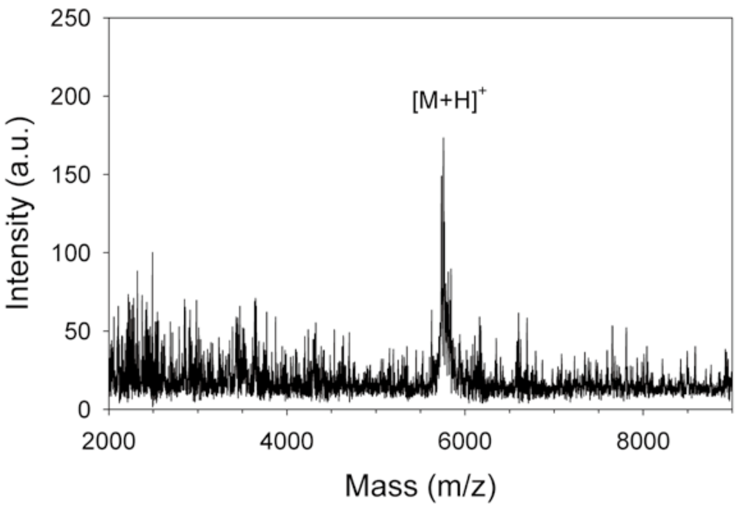

Fig.4 Average MALDI mass spectrum of 0.26-µm aerosol particles of the protein insulin premixed with the matrix 2,5-dihydroxy benzoic acid in a matrix-to-analyte ratio of 50,000:1.

$$r = \frac{d_a}{2\sqrt{\frac{\rho}{\rho_0}}} \qquad \text{(eq. 8)}$$

in which ρ_0 is the standard particle density of 1 g/ml. Since the ratio of the densities has the same value as the density of the matrix only, the calculated values of Russell et al.[31] are correct.

Russell et al.[31] report a sensitivity limit of 14 zeptomole for their instrument. The obtained sensitivity of 14 zeptomole equals approximately 8400 molecules. If their BAMS system were to be applied for the analysis of bacteria particles, only a few ubiquitous types of proteins would be detected, covering a very small fraction of the protein content of a cell.

The sensitivity limit of the aerosol mass spectrometer is calculated by applying eq. 6 and 8 for these experiments and gives a number of 600 molecules per particle, corresponding to 1 zeptomole. Although this value is lower than the sensitivity criterion defined above, it should be noted that this value is based on single-component aerosol particles. In a bacterium, many more types of molecules (biomarkers) are present, and it is highly likely that only a very few molecules of each biomarker will be detected by means of aerosol MALDI mass spectrometry.

Bacterial analysis by aerosol MALDI mass spectrometry

The implementation of a new ion source and delayed extraction were inspired by the idea to optimize the aerosol mass spectrometer for the analysis of bacteria-containing aerosol particles. To investigate the suitability of the aerosol mass spectrometer for bacterial analysis, aerosol particles containing the bacterium *Escherichia coli* K12 XL1 blue and the matrix sinapinic acid were produced and analyzed. For comparison, the same culture of *Escherichia* was analyzed with a standard MALDI mass spectrometer (Biflex III, Bruker Daltonics, Bremen, Germany, located at TNO Defence, Security and Safety, Rijswijk, The Netherlands). The matrix material used was also sinapinic acid in water/acetonitrile 7:3 (v/v) 0.1% TFA. The sample was prepared according to the so-called dried droplet method. The obtained mass spectra are given in **Fig. 5**. Generally, the standard mass spectrum (**Fig. 5a**) is rather similar to the aerosol mass spectrum (**Fig. 5b**), with the remark that the resolution for the aerosol mass spectrum is better compared to the resolution obtained from the standard spectrum. However, more peaks at a mass-to-charge ratio higher than 17 kDalton are observed

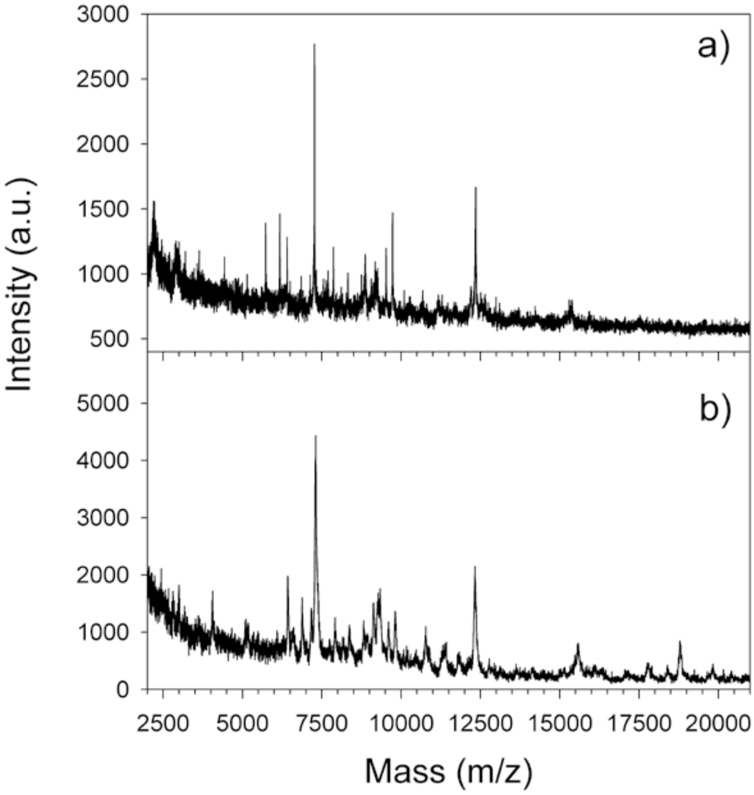

Fig.5 Mass spectra of *Escherichia coli* K12 XL1 blue with the matrix sinapinic acid; a) summed aerosol mass spectrum of 2000 aerosol particles (prepared off-line) and b) mass spectrum obtained with a standard MALDI mass spectrometer.

in the standard MALDI mass spectrum. Note that for standard MALDI analysis, resolutions are reported in the range of 10,000-25,000.

It can be concluded from this experiment with *Escherichia coli* that the mass spectrum from complex aerosol particles analyzed using the aerosol mass spectrometer covers a wide mass range and has good resolution. The highest mass peak appears at a mass-to-charge ratio of approximately 15 kDalton. This mass falls within the mass range (4-20 kDalton) proposed by Fenselau and Demirev[13)] to contain the so-called biomarkers, which could be used for the classification of bacteria. However, since the highest mass detected by the aerosol mass spectrometer is lower than the proposed upper limit of 20 kDa, there is a chance that biomarkers are not detected by the aerosol mass spectrometer, making classification more difficult. Specially designed software to identify the peaks as well as matching the peaks with existing protein databases could be used for the classification of the samples analyzed by aerosol MALDI mass spectrometry. It can also be concluded from this experiment that the performance of the aerosol mass spectrometer for bioaerosol particles up to a mass of 15 kDalton is as good as the performance of the standard MALDI mass spectrometer which is used in this experiment, despite the differences in hardware of both systems.

Conclusions

The aerosol mass spectrometer as initially proposed by Marijnissen et al.[3)] has been further developed and optimized to make the instrument suitable for the analysis of bacteria-containing aerosol particles. The implementation of a new ion source and delayed extraction has resulted in the capability of obtaining high-quality mass spectra of single bioaerosol particles. Isotopic resolution was obtained for a low-mass peptide on a single-particle level. The sensitivity limit of the instrument was determined to be 1 zeptomole for an aerosol of insulin.

The capability of the aerosol mass spectrometer for bacterial analysis has been demonstrated with an off-line-prepared aerosol containing the bacterium *Escherichia coli*. The obtained mass spectrum has good resolution and a mass range up to 15 kDalton is covered. However, more research is required to improve the sensitivity of the aerosol mass spectrometer to obtain good (on-line) single-particle mass spectra to allow discrimination on a single-particle level.

Acknowledgements

The authors would like to thank TNO Defense, Security and Safety; Bruker Daltonics (Germany) and the Dutch Ministry of Defense for funding and assistance in experiments.

Nomenclature

d_a	aerodynamic diameter	m
d_p	particle diameter	m
e	elementary charge	$1.6\ 10^{-19}$ C
L	length	m
N_A	Avogadro's number	$6.02\ 10^{23}$
$N_{analyte}$	number of analyte molecules	-
m	mass	kg
MW_{matrix}	molecular weight of the matrix	g/mole
t	flight time	s
r	particle radius	m
R	resolution	-
v	velocity	m/s
V	acceleration voltage	V
ρ	particle density	kg/m^3(g/ml)
ρ_0	standard particle density	1000 kg/m^3 (1 g/ml)

References

1) Stowers, M. A. and Marijnissen, J. C. M. (2005) in: "History & Reviews of Aerosol Science". American Association for Aerosol Research, USA.
2) Noble, C. A. and Prather, K. A. (2000): Mass Spectrom. Rev., Vol. 19, pp.248-274.
3) Marijnissen, J. C. M., Scarlett, B. and Verheijen, P. J. T. (1988): J. Aerosol Sci. Vol. 19, pp.1307-1310.
4) Kievit, O. (1995): Ph.D. Dissertation, Delft University of Technology, The Netherlands.
5) Kievit, O., Weiss, M., Verheijen, P. J. T., Marijnissen, J. C. M. and Scarlett, B. (1996): Chem. Eng. Comm., Vol. 151, pp.79-100.
6) Weiss, M., Verheijen, P. J. T., Marijnissen, J. C. M. and Scarlett, B. (1997): J. Aerosol Sci., Vol. 28, pp.159-171.
7) Weiss, M. (1997): Ph.D. Dissertation, Delft University of Technology, The Netherlands.
8) Prather, K.A., Nordmeyer, T. and Salt, K. (1994): Anal. Chem., Vol. 66, pp.1403-1407.
9) Nordmeyer, T. and Prather, K.A. (1994): Anal. Chem., Vol. 66, pp.3540-3544.
10) Stowers, M. A., van Wuijckhuijse, A. L., Marijnissen, J. C. M., Scarlett, B., van Baar, B. L. M. and Kientz, Ch. E. (2000): Rapid Comm. Mass Spectrom., Vol. 14, pp.829-833.
11) Van Wuijckhuijse, A. L. (2003): Ph.D. Dissertation, Delft University of Technology, The Netherlands.
12) Lay, J. O. (2001): Mass Spectrom. Rev., Vol. 20, pp.172-194.
13) Fenselau, C. and Demirev, P. A. (2001): Mass Spectrom. Rev., Vol. 20, pp.157-171.

14) Van Baar, B. L. M. (2001): FEMS Microbiol. Rev., Vol. 24, pp.193-219.
15) Matthias-Maser S. and Jaenicke, R. (1995): Atm. Res., Vol. 39, pp.279-286.
16) Stowers, M. A., van Wuijckhuijse, A. L., Marijnissen, J. C. M., Kientz, Ch. E. and Chiach. T. (2006): Appl. Optics, Vol. 45, pp.8531-8536.
17) Pinnick, R.G., Hill, S.C., Nachman, P., Pendleton, J.D., Fernandez, G.L, Mayo, M.W. and Bruno, J.G. (1995): Aerosol Sci. Technol., Vol. 23, pp.653-664.
18) Pinnick, R.G., Hill, S.C., Nachman, P., Videen, G., Chen, G. and Chang, R.K. (1998): Aerosol Sci. Technol., Vol. 28, pp.95-104.
19) Hairston, P.P., Ho, J. and Quant, F.R. (1997): J. Aerosol Sci., Vol. 28, pp.471-482.
20) Pan, Y.L.,Holler, S., Cheng, R.K., Hill, S.C., Pinnick, R.G., Niles, S. and Bottiger, J.R. (1999): Opt. Lett., Vol. 24, pp.116-118.
21) Van Wuijckhuijse, A. L., Stowers, M. A., Kleefsman, W. A., van Baar, B. L. M., Kientz, Ch. E. and Marijnissen, J. C. M. (2005): J. Aerosol Sci., Vol. 36, pp.677-687.
22) Steele, P.T., Tobias, H.J., Fergenson, D.P., Pitesky, M.E., Horn, J.M., Czerwieniec, G.A., Russell, S.C., Lebrilla, C.B., Gard, E.E. and Frank (2003): Anal. Chem., Vol. 75, pp.5480-5487.
23) Srivastava, A., Pitesky, M.E,. Steele, P.T., Tobias, H.J., Fergenson, D.P., Horn, J.M., Russell, S.C., Czerwieniec, G.A., Lebrilla, C.B., Gard, E.E. and Frank, M. (2005): Anal. Chem., Vol. 77, pp.3315-3323.
24) Fergenson, D.P., Pitesky, M.E., Tobias, H.J., Steele, P.T., Czerwieniec, G.A., Russell, S.C., Lebrilla, C.B., Horn, J.M., Coffee, K.R., Srivastava, A.. Pillai, S.P., Shih, M-T.P., Hall, H.L., Ramponi, A.J., Chang, J.T., Langlois, R.G., Estacio, P.L., Hadley, R.T., Frank, M. and Gard, E.E. (2004): Anal. Chem., Vol. 76, pp.373-378.
25) Jackson, S. N., Mishra, S., Murray, K. K. (2004): Rapid Comm. Mass Spectrom., Vol. 18, pp.2041-2045.
26) Kim, J.K, Jackson, S.N. and Murray, K.K. (2005): Rapid Comm. Mass Spectrom., Vol. 19, pp.1725-1729.
27) Harris, W. A., Reilly, P. T. A., Whitten, W. B. (2005): Anal. Chem., Vol. 77, pp.4042-4050.
28) Harris, W.A., Reilly, P.T.A. and Whitten, W.B. (2006): Int. J. Mass Spectrom., Vol. 258, pp.113-119.
29) Cotter, R. J. (1997): "Time of Flight Mass Spectrometry; Instrumentation and Application in Biological Research" Chemical Society, Washington, DC, USA.
30) Madigan, M.T., Martinko, J.M. and Parker, J. (2000): "Brock Biology of Microorganisms" , 9th ed., Prentice Hall, Upper Saddle River, USA.
31) Russell, S. C., Czerwieniec, G., Lebrilla, C., Steele, P., Riot, V., Coffee, K., Frank, M. and Gard, E. E. (2005): Anal. Chem., Vol. 77, pp.4734-4741.
32) Hinds, W.C. (1999): "Aerosol Technology: Properties, Behaviour and Measurement of Airborne Particles" , 2nd ed., John Wiley and Sons, Ltd, Chichester, New England.

Author's short biography

W. A. Kleefsman

W.A. (Ineke) Kleefsman (1979) received her master of science degree in pharmacy and in pharmaceutical engineering in 2002 at the University of Groningen (The Netherlands). After that she did her Ph.D. research at Delft University of Technology (The Netherlands): Aerosol MALDI mass spectrometry for bioaerosol analysis (2003-2007). Since 2008, she has been working as a development scientist at Schering-Plough Oss, The Netherlands.

Formulation of Highly Concentrated Suspensions for Spray Drying in a Fluidized Bed[†]

Anne DUSANTER, Khashayar SALEH* and Pierre GUIGON
UMR 6067, Laboratoire Technologie des Poudres et Suspensions,
Département Génie des Procédés Industriels,
Université de Technologie de Compiègne, Centre de Recherches de Royallieu[1]

Abstract

Spray drying of suspensions leads most often to free-flowing powder products of good quality. However, this process is energy-consuming, especially because of the high amounts of liquid to be evaporated from the sprayed suspension. Indeed, in order to ensure a good quality and stability of spraying, the amount of solvent must be determined so as to avoid excessive suspension viscosities. For a given amount of solvent, it is also possible to improve the viscosity of concentrated suspensions by deflocculation using appropriate dispersants.

Through the use of an adequate dispersant, we showed that it is possible to obtain fully dispersed suspensions and to optimize their dryness in order to reduce the moisture content to be evaporated. The effect of different salts and the molecular weight of polyacrylic acid is investigated to improve the formulation of concentrated calcite suspensions with the focus on spray drying.

A new continuous process, developed to enable the drying of highly concentrated slurries at low temperature, is also described. This process is based on the coupling of coating/attrition of a suspension in a fluidized bed of inert particles, and it strongly increases the surface area available for heat and mass transfers.

Further analysis of this process has been carried out addressing the drying kinetics in a drying pipe. It shows a strong influence of the support wettability as well as the surface tension of suspension on the drying kinetics of suspension films. The surface tension of the suspension and humidity were found to be crucial parameters to optimize the powder recovery.

Keywords: spray drying, inert particles, suspension, drying kinetics, attrition

1. Introduction

The drying of bulk materials plays an important role in a lot of industrial processes. Most of the processes of manufacturing mineral powders use a thermal dehydration of the initial suspension followed by a mechanical milling step.

The spray drying process can also be used, but it is a high-cost drying technology especially if the initial suspensions have a low solid content. Spray drying involves the evaporation of moisture from an atomised feed by mixing the spray and the drying medium – typically air. The drying proceeds until the desired moisture content is reached in the sprayed particles and the product is then separated from the air. Low viscosity is essential to the ease of pumping and to a homogeneous spray of the suspension (Tsetsekou et al., 2001).

Sometimes, mechanical filtration can be a partial alternative to the thermal dehydration process in order to obtain a concentrated suspension. This step can be followed by spray drying if the filtration cake can be pulverized. Unfortunately, it is not always possible because of the high viscosity of suspensions. New drying processes for these types of highly concentrated suspensions have to be developed to enable a lower production cost of the dried powder.

Moreover it is well known that in order to decrease the viscosity of concentrated suspensions and in order to improve their stability, it is necessary to avoid the agglomeration of particles and to enhance their

---

† Accepted: August 23, 2008

[1] BP 20529, 60205 Compiègne Cedex, France
* Corresponding author
TEL :+33 (0)3 44 23 44 23 FAX : +33 (0)3 44 23 19 80
E-mail: khashayar.saleh@utc.fr

deflocculation. For this purpose, dispersants can be used as deflocculation agents. Several studies have shown the effect of dispersants on the rheological properties of slurries (Tari and Ferreira, 1998, Kugge and Daicic, 2004). Polyelectrolyte dispersants such as the salts of polyacrylic acid can be used to prepare concentrated suspensions of mineral powder (Garcia, 2001, Tobori and Amari, 2003) and can improve the rheological properties of concentrated calcite suspensions.

Recent work carried out in the chemical engineering department of the Compiègne University of Technology led to development of a new filtration process of mineral suspensions (Husson et al., 2002). This process uses dispersing agents in order to obtain a highly concentrated and easily fluidifying final cake (Mouroko-Mitoulou, 2002). With this process, the mechanical dehydration can lead to pulverizable concentrated suspensions which can be dried by thermal dehydration, e.g. atomization. Hence, this process is important from an energetic point of view.

Furthermore, fluidized beds are well known for their high heat transfer capacity. Conventional fluidized bed dryers are not efficient enough to dry concentrated slurries. Recent works have developed new techniques for slurry spray drying which ultimately enables low drying temperatures for temperature-sensitive products.

These emerging processes are based on the coating followed by the attrition of a suspension sprayed onto fluidized inert particles. The drying mechanism of this process relies on several concomitant steps as showed in **Fig. 1**. First, the sprayed suspension sticks to the heated particle surface. This deposited coating then dehydrates and peels off from the inert bodies because of the interparticle friction. The crushing of the coated layer occurs due to intensive interparticle collisions induced by the fluidized bed flow, allowing removal of the dried product by elutriation. The dried powder is then conveyed by the fluidizing air to a cyclone or a filter for collection (Grbavcic et al., 2004).

Various geometries and configurations for these types of processes have been developed and patented, for example by Zedlets and Bogdanov (1977), Lukach et al. (1978), Dobronogov et al. (1981), Shmaryan (1981), Chevikov (1981), Dvortsin et al. (1982), Kozachek and Shikunov (2003).

Several researchers have shown that the turbulent mixing induced by the flow of inert particles enables slurries to be dried in fluidized bed dryers containing inert particles such as sand (Mousa, 1979), glass spheres (Grbavcic et al., 1998) or Teflon cubes (Benali and Amazouz, 2006). These inert particles – used as heat conveyors – strongly increase the surface area available for heat and mass transfers.

More recently, Marques et al. (2006) studied the influence of the surface energy – of the inert particles – on the drying effectiveness. This study revealed that highly hydrophilic particles lead to a difficult recovery of the dried powder because the coating phenomenon becomes predominant compared to the peeling/drying mechanism. However, highly hydrophobic materials can prevent adequate coating of the liquid to be dried on the inert particles and consequently reduce heat transfers due to a smaller surface available for the transfers. The choice of materials also seems to depend on the surface tension of the liquid to be dried.

However, there is a lack of information in the literature regarding the understanding of these phenomena on a small scale to better understand the processes of drying in a fluidized bed of inert particles.

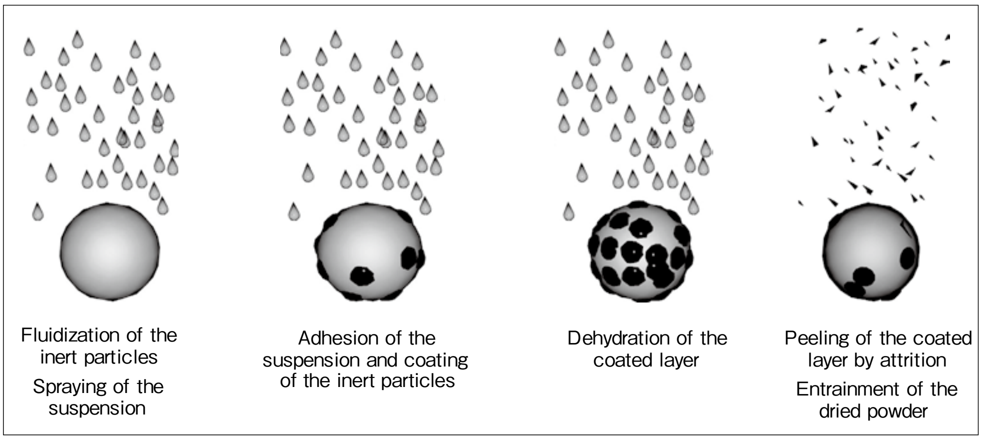

Fig. 1 Drying mechanism on fluidized inert particles.

2. Experimental

2.1 Materials

Suspensions were manufactured by introducing dried powder into an aqueous solution of dispersant.

Calcium carbonate, supplied by Verbiese (France), was chosen as the raw material for its high commercial interest. The median diameter of CaCO$_3$ particles was 3 μm with a density of 2.74 g/cm^3. The size and morphology of the CaCO$_3$ used can be seen on the SEM photographs in **Fig. 2**. Previous researchers (Dusanter et al., 2007) showed that the optimized solid content of the suspension – leading to the best agreement between a high CaCO$_3$ content and sufficient sprayability on the apparatus – was 60% of CaCO$_3$ w/w. Dispersing agents were four aqueous solutions of polyacrylate salts. They differ by the type of their counter-ion (sodium or ammonium) and the medium molecular weight of polymers (approximately 2500 and 5000 g/mol). Characteristics of these dispersants are summarized in **Table 1.** The dispersant concentration was fixed as a percentage of the mass of active polymer per mass of dry calcium carbonate powder for all suspensions.

2.2 Suspension drying

Conventional spray drying tests were carried out using a BÜCHI mini spray dryer B-190 (**Fig. 3**). This dryer works in co-current flow, *i.e.* the sprayed product and preheated drying air stream flow in the same direction. The suspension is sprayed by means of a two-fluid nozzle. The particles are then separated by a cyclone. The finest particles are collected in a filter bag. For the experiments, the air inlet temperature was kept constant at 175℃.

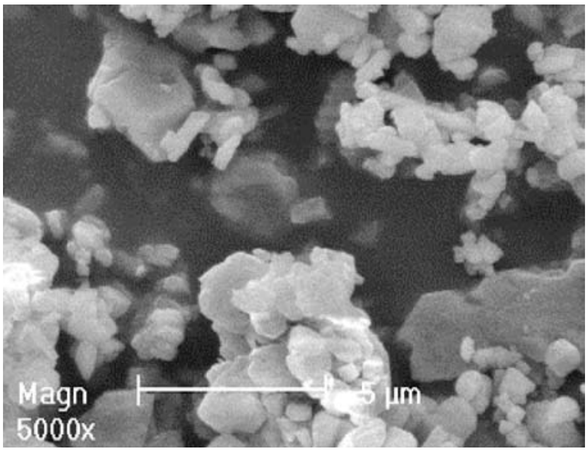

Fig. 2 SEM photograph of CaCO$_3$ as-received.

Table 1 Dispersing agent properties

Identification	Counter-ion	Medium molecular weight of polymers	Content of active ingredient
PNH4_5000	Ammonium	5188 g/mol	42.2
PNa_5000	Sodium	5733 g/mol	43.6
PNH4_2500	Ammonium	2545 g/mol	38.8
PNa_2500	Sodium	2551 g/mol	43.3

The process of spray drying fluidized inert particles relies on the atomization of the highly concentrated suspension in a fluidized bed of inert particles. The experimental apparatus is shown in **Fig. 4**. It consists of a cylindrical column in which inert particles (glass spheres 630-800 μm) are fluidized. An electric heater located upstream of the fluidization column supplies the air at the desired temperature by the use of a PID regulator. The spraying system is a two-fluid nozzle located in the middle of the fluidized bed. The suspension is supplied by means of a piston pump and sprayed downwards within the fluidized bed of heated particles. In order to provide a vigorous fluidization, the excess air velocity (U-U_{mf}) was fixed at 0.11 m.s-1. This velocity ensured an appropriate fluidization of inert particles (U_{mf}= 0.33$m.s^{-1}$) and the elutriation of dried peeled particles. At the column outlet, the air passes through a box containing a filter cartridge where the particles are collected.

The inlet air temperature was fixed at 80℃ in the wind box. As soon as the temperature in the fluidized bed became stable (71.5 ± 0.2℃), the suspension was sprayed within the fluidized bed (feeding flow: 5 ml/min). It could thus be observed that the glass spheres gradually became less opalescent (coating). This step is quickly followed by the appearance of white dust ascending to the top of the column due to abrasion of the coated layer. Due to the large surface area of the glass spheres and the fineness of the deposited coating layer by spraying, the drying occurred in a very short time. During the feeding and after a stabilization period, the bed temperature remained stable at 52 ± 3℃.

2.3 Analysis apparatus

Several methods were used to characterize initial suspensions and powders obtained by standard spray drying or the spray drying of fluidized inert particles.

A rotation coaxial rheometer VT 550 (HAAKE) was used to study the viscosity, η, of initial suspensions, by measuring the strain at different shear rates ($\dot{\gamma}$ = 0 to 500 s^{-1}, 500 s^{-1}, and 500 to 0 s^{-1}). The temperature was fixed at 20℃.

An environmental scanning electron microscope (Philips XL30 ESEM-FEG) was used to observe the

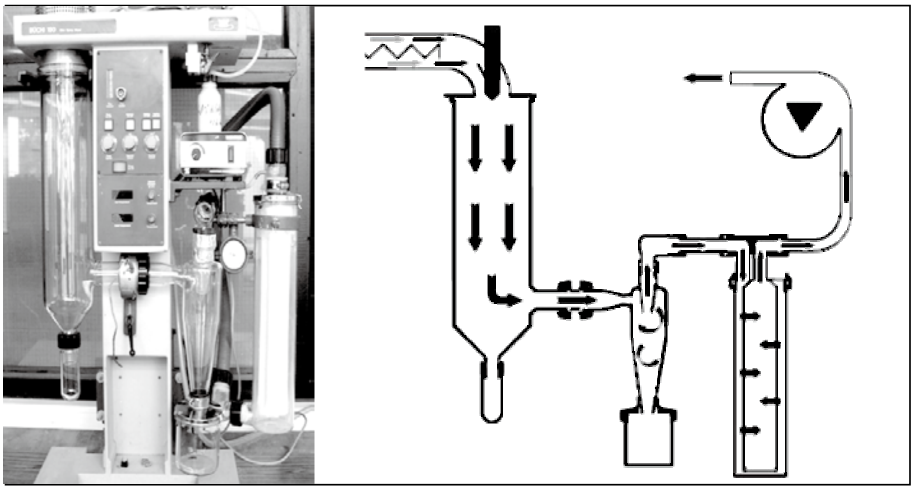

Fig. 3 Laboratory spray dryer BÜCHI-190 and flow of the drying air.
(extract from BÜCHI documentation)

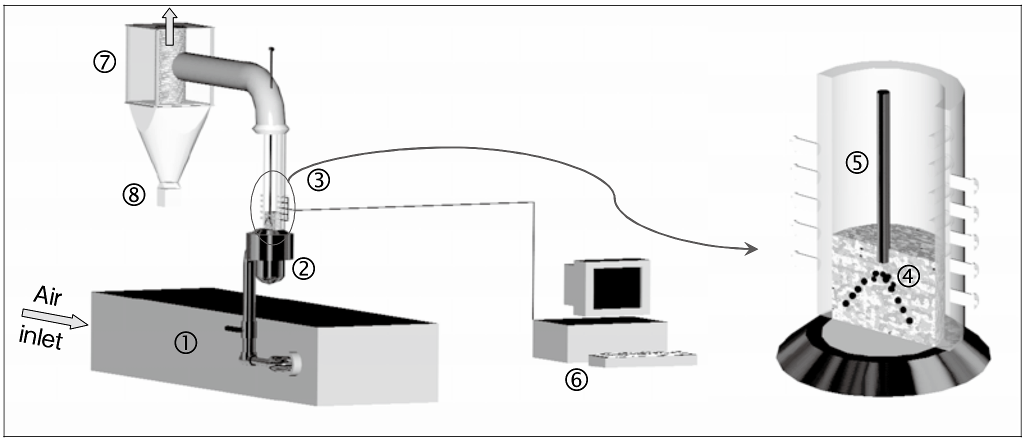

Fig. 4 General view of the experimental drying apparatus:
①air heater, ② wind box, ③ fluidization column, ④ fluidized inert particles,
⑤ spray drying apparatus, ⑥ acquisition, ⑦ filter cartridge, ⑧ dried powder collector

shape and size of the $CaCO_3$ particles.

A Blaine permeameter was used to estimate the fineness and the specific area of dried powder. The basic principle of this test consists in measurement of the time necessary for a given amount of the air to flow through a packed bed of powder of a known volume. The Blaine specific surface B (cm^2/g) is thus calculated using the following equation:

$$B = \frac{K}{\rho} \cdot \frac{\sqrt{e^3}}{1-e} \cdot \frac{\sqrt{t}}{\sqrt{0,1 \cdot \eta}}$$

where K stands for the Blaine apparatus constant,
e is the porosity of the packed bed,
t is the time taken by the fixed quantity of air to flow through the powder bed,
ρ is the powder density, and
η is the viscosity of air at the temperature of experiment.

2.4 Device for determination of the drying kinetics

In this section, the study of the drying kinetics of thin layers of calcium carbonate suspensions by convection on microscope glass plates is described. The experiments were carried out in a drying pipe where microscope glass plates coated with suspensions are positioned in parallel to the drying air flow (**Fig. 5**). The device is inspired by previous works of Camisard (1997). The drying kinetics were studied by applying a film of suspension onto microscope glass plates previously subjected or not to a hydrophobic treatment by silanisation.

Drying occurred by means of air coming from the system of compressed air. The air flow rate was

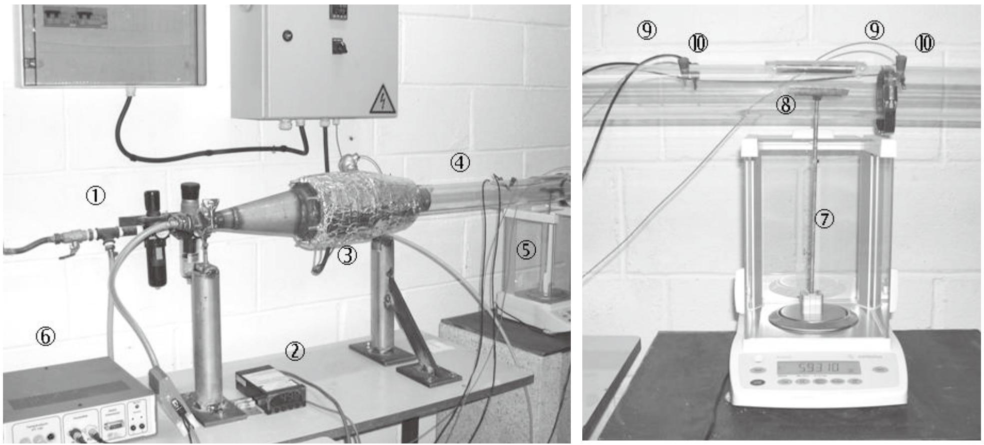

(a) (b)

Fig. 5 General view of the drying device (a) and measurement device (b)
① compressed air, ② flowmeter, ③ heating of the drying air, ④ drying pipe, ⑤ balance, ⑥ acquisition device, ⑦ sample carrier, ⑧ coated glass plate, ⑨ temperature probes, ⑩ humidity probes

controlled using a mass flowmeter placed upstream of the heating zone. This air was pre-heated by a heating ring surrounding the drain in which the air circulates. The temperature of the drying air was controlled by a PID regulator based on a Pt100 probe placed downstream of the heating zone.

The drying pipe was made of a polymethyl methacrylate tube in which the sample to be dried was positioned on a sample carrier, itself positioned on a balance. The acquisition device recorded the temperature and relative humidity evolution of the inlet and outlet air as well as the mass variation of the sample.

The film of suspension was applied to the glass plate –heated to the temperature of the test beforehand – using a coating bar "K Hand Coater" enabling the application of a 100-μm-thick film.

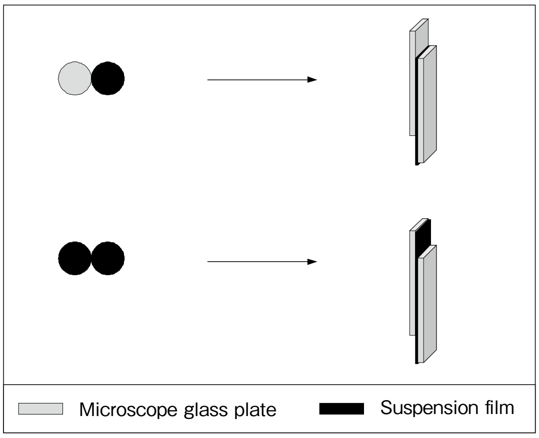

Fig. 6 Study of the properties of adhesion: extrapolation on glass plates.

2.5 Device for estimation of the adhesion/attrition mechanism

Shear tests (block shear) were carried out, taking the ASTM C-273 standard as a starting point. The assembly must enable a relative displacement of two surfaces (*i.e.* microscope glass plates) of the sample, the joint (suspension film) being then solicited parallel to the surfaces of joining (Bretton and Villoutreix, 2005). Either one – for simulating the adhesion between a coated glass bead and an uncoated one – or both – for simulating the sticking together of two coated glass beads – microscope plates were coated with suspension (see **Fig. 6**) using the same coating bar as previously (2.4). The sample was then dried over a period of at least 14 hours at 60℃ and then conditioned at the temperature and relative humidity of the test room for at least half a day before testing. The shear test was performed using an Instron 4464 compression machine with a 2 kN load cell (**Fig. 7**) chosen according to the range of the experimental measurements (from about 10 to 520 N). The compression test enabled the shear modulus of suspension films to be calculated by the following equation:

$$G = \frac{\sigma_c}{\varepsilon_c} = \frac{F_{\max}}{S} \cdot \frac{E}{d_{\max}}$$

with $$S = l \cdot L \cdot \left(1 - \frac{S_{uncoated}}{S_{total}}\right)$$

where $S_{uncoated}$ stands for the uncoated part of the specimen – due to the introduction of air bubbles during the sticking step, l and L are the specimen length and width, respectively.

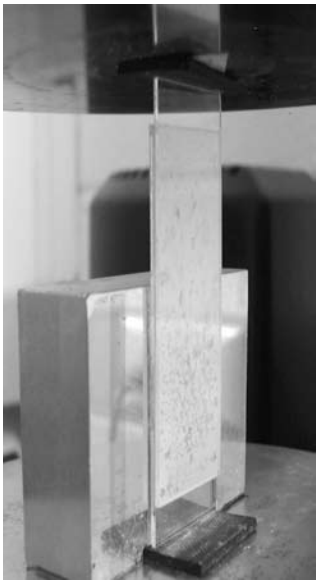

Fig. 7 Experimental device for the estimation of the adhesion/attrition mechanism. (specimen before testing)

3. Results and Discussion

3.1 Characterization of initial calcium carbonate suspensions

It is important to control the rheological properties of suspensions so as to attain a high solid content with sufficient fluidity to be pulverized. Preliminary experiments (Dusanter et al., 2006) were carried out to assess the influence of shearing time on stress σ of dispersed $CaCO_3$ suspensions containing 1% of dispersant ($CaCO_3$ content varied from 30 to 70%). The shear thinning behaviour indicated a linear behaviour up to a critical rate and was associated to a Bingham behaviour fluid, showing that a minimum stress is necessary to break the residual agglomerates in the suspension (Vorobiev et al., 2004).

By applying the Bingham model ($\sigma = \sigma_y + \eta_p \dot{\gamma}$) for each rheogram, it was then possible to study the effect of dispersant content on plastic viscosity for different counter-ions and different molecular weights of the dispersants used.

Fig. 8 and **Fig. 9** show that plastic viscosity evolves in various ways as a function of the dispersant content in the suspension: - a first decreasing part for which the viscosity depends on the concentration of dispersant, highlighting the progressive deflocculation of calcium carbonate agglomerates, - a second zone - where the plastic viscosity remains stable - probably representative of the optimum concentration of dispersant, - a last part with a strong increase of the plastic viscosity of suspensions when the concentration of dispersant grows. This phenomenon probably corresponds to a destabilization of the suspension by reduction of the zone of interparticle depletion. Indeed the surplus molecules of dispersant which could not be adsorbed on the surface of the particles tend to become organized in the form of polymeric balls. These balls behave like additional particles and decrease the available space in the dispersing solution. Thus they reduce the effect of steric repulsion. If these forces become higher than the repulsion forces between the particles, they can induce a destabilization of the suspension promoting an increase of the plastic viscosity. So when the polymer concentration is higher than necessary to recover the particles, an aggregation by depletion is observed. In our case, the minimum concentration of dispersant to recover the totality of the calcium carbonate particles

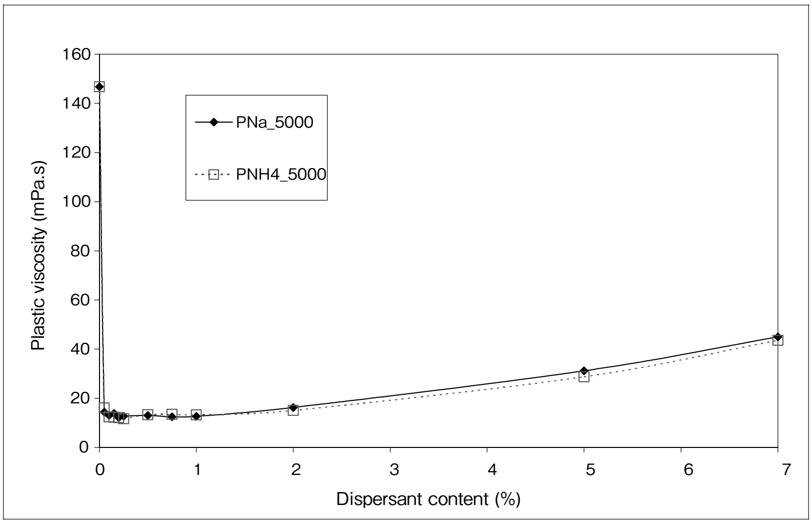

Fig. 8 Influence of the dispersant quantity and the type of polyacrylate counter-ion on the plastic viscosity of calcium carbonate suspensions.

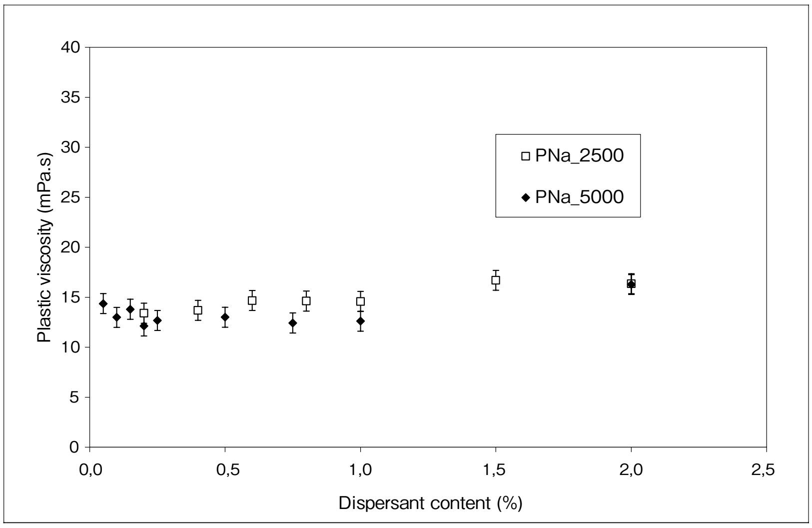

Fig. 9 Influence of the dispersant quantity and the medium molecular weight of polymers on the plastic viscosity of calcium carbonate suspensions.

was about 1%.

The type of concentration – sodium or ammonium – (**Fig. 8**) seems to have no influence on the plastic viscosity of suspensions. This point is confirmed in some work by Geffroy et al. (1997), showing that only the anionic part – *i.e.* the polyacrylic part – plays a role in the dispersion of calcium carbonate particles.

Concerning the effect of the molecular weight of the polymer (**Fig. 9**), the viscosity of suspensions is slightly higher for the dispersant with the lower molecular weight. Geffroy et al. (2000) showed that for polymers with a low molecular weight, the fractions with a molar mass lower than 1500 g/mol are not adsorbed. We can thus suggest that the quantity of dispersant adsorbed is less important for the dispersant PNa_2500, which explains why the corresponding suspensions have a higher viscosity, since the agglomerates are less dispersed.

3.2 Powders obtained by suspension drying

In this work, we investigate the drying of the concentrated suspensions by two spray drying methods: the conventional one in a laboratory dryer and an emerging one which consists of spraying the suspension in a fluidized bed of glass spheres.

The parameters of drying for both processes are summarized in **Table 2**. One can first notice that the process of drying in a fluidized bed of inert particles makes it possible to significantly decrease the drying temperature.

- **Morphology**

An example of a typical powder obtained by conventional spray drying of a suspension – containing 1% dispersant and 60% $CaCO_3$ – is shown in **Fig. 10 (a)**. First of all, essentially all the granules are rounded. The structure of such a granule at high magnification shows that each granule is composed of a particle agglomerate arrangement of the rhombohedrical calcium carbonate particles which constituted the initial raw material – used to prepare the suspension – presented in **Fig. 2**.

Table 2 Operational parameters of the drying processes

	Conventionnal spray drying (Büchi-190)	Drying in a fluidized bed of inert particles
Inlet temperature*	175℃	80℃
Inside temperature before pulverization	100 to 110℃	71.3 to 71.7℃
Drying temperature	90 to 95℃	49 to 55℃

*minimum temperature required for the drying with the apparatus used.

An SEM image of the calcium carbonate powder obtained by spray drying on fluidized bed of inert particles is shown in **Fig. 10 (b)**. The fragmented agglomerates observed on this figure are very different from the ones obtained by conventional spray drying. No spherical agglomerates were observed in the powder, which implies that the drying by coating is predominant with regard to the drying of $CaCO_3$ on fluidized inert particles.

Moreover as one can see, the particle size of the powder particles is close to that of the initial raw material (**Fig. 2**). This can be explained by the breaking of aggregates which were previously formed by the dried coating on the surface of glass beads. Indeed, fluidization of the glass spheres creates a lot of collisions and thus leads to attrition of the aggregates. As

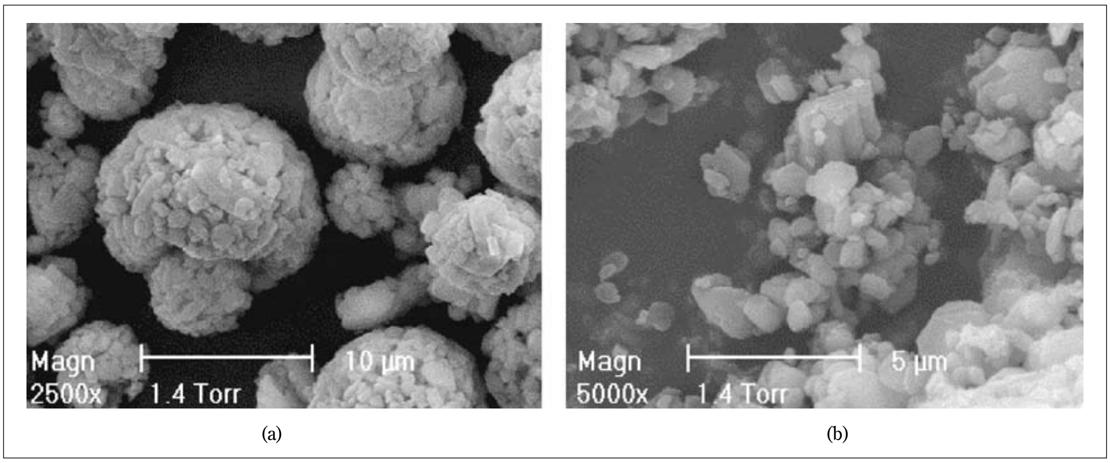

(a) (b)

Fig. 10 Scanning electron micrographs of powders produced from a suspension containing 60% $CaCO_3$ and 1% sodium polyacrylate with conventional spray drying (a) and with drying in a fluidized bed of glass spheres (b)

a consequence, this drying process could avoid an ulterior grinding. Although the fineness of the product can lead to a worse flowability, this process remains more interesting from an energetic point of view because of better heat transfer coefficients.

- **Blaine surface area**

The morphological observation of powders is confirmed by a Blaine surface area of 12317 cm^2/g for the product dried on inert particles which is close to the raw material value (13470 cm^2/g), whereas the powder obtained by conventional spray drying has a specific surface of 5972 cm^2/g. However, by decreasing the concentration of dispersant in the suspension pulverized by the laboratory spray dryer (*i.e.* 0.1% instead of 1% w/w) or by lowering its solid content (*i.e.* 30% instead of 60% w/w), it is possible to increase the specific surface. Indeed, in these cases, the granules formed during drying are more friable so the specific surface of the powder obtained increases. Thus one can obtain a Blaine surface area which is close to 10000 cm^2/g – depending on the drying conditions – but this value still remains lower than the one obtained by the drying process in the fluidized bed of glass spheres. Moreover the process would be more difficult to control or would require more energy to evaporate the solvent due to more diluted suspension.

3.3 Determination of the drying kinetics

Parameters which are studied in the drying pipe are the temperature and flow rate of the drying air, the initial dispersant content of the film, and the wettability of the support.

Typical recorded curves of the tests (**Fig. 11**) present the variation of the mass sample (LOD, in g of loss on drying per g of solid) and the evolution of the inlet (Ti) and outlet (To) air temperature and relative humidity (RHi and RHo in **Fig. 11**) versus time. Trials were done with either 0 or 1% of dispersant

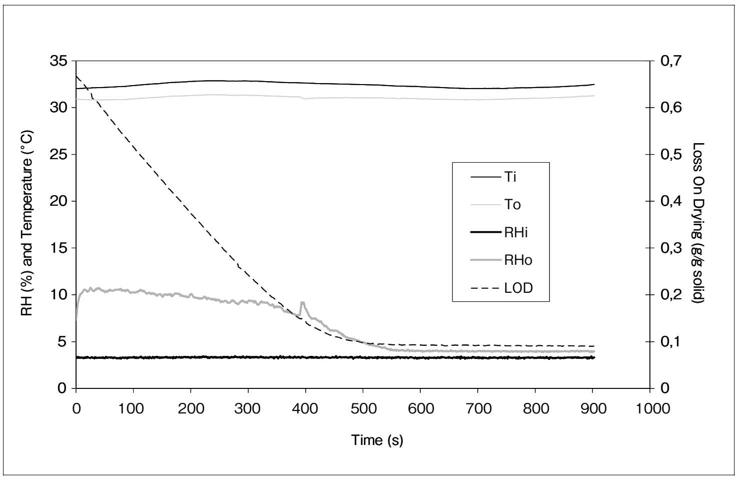

Fig. 11 Typical experimental curves obtained in the drying pipe (Q_{air}=50 L/h, T=40℃)

related to the mass of calcium carbonate. The loss on drying in the suspension film results in a decrease of the drying air humidity after the sample. Taking into account the small quantities of evaporated water, the outlet temperature of the air does not vary.

It appears (see **Fig. 12**) that the increase of the drying temperature slightly increases the kinetic rate of dehydration, but also especially reduces the quantity of remaining water (which drops by 9% to 3% for an increase of 10℃).

Concerning the influence of the hydrophobicity level of the plate (**Fig. 13**), it seems that the use of a hydrophobic support reduces the kinetic rate of water evaporation. However, the film application on this kind of plate is more difficult than the application on untreated supports (hydrophilic) because of their poor wettability. In this case, the film thickness is thus less homogeneous and locally higher, which leads to a reduction in the thermal heat-transferring surface.

In the same way, in the absence of dispersant and for hydrophobic supports (**Fig. 14**), the quantity of remaining water is higher than that remaining in the presence of dispersant. Indeed, in this case the suspension has less affinity for the support than when it contains dispersant due to the light modification of the surface tension.

3.4 Estimation of the adhesion/attrition mechanism

The adhesion represents the tendency of the powder particles to stick to each other or to the inert particles. The performance of the drying process in a fluidized bed of inert particles can then be estimated by the propensity of dried coating to peel off from inert particles and by avoiding the formation of

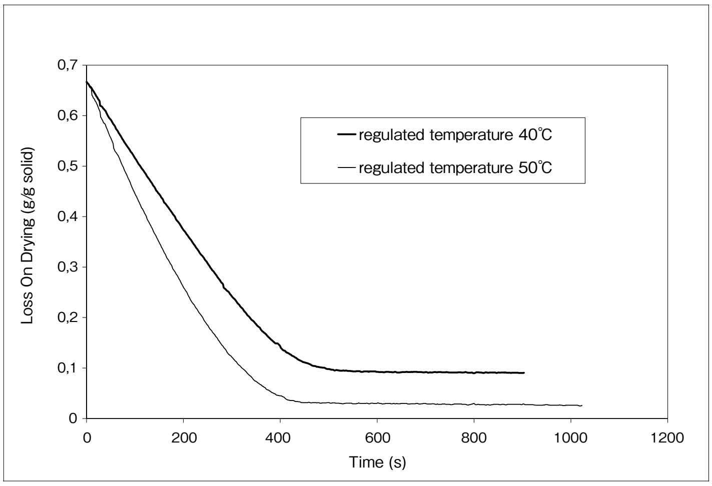

Fig. 12 Influence of the drying temperature on the drying kinetics. (Q_{air}=50 L/h, 1% PNa_5000, untreated plates)

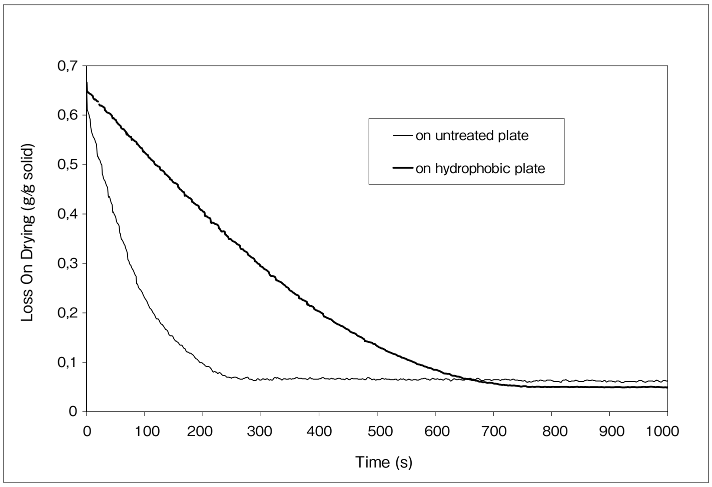

Fig. 13 Influence of the plate hydrophobicity on the drying kinetics. (T=65℃, Q_{air}=75 L/h, 1% PNa_5000)

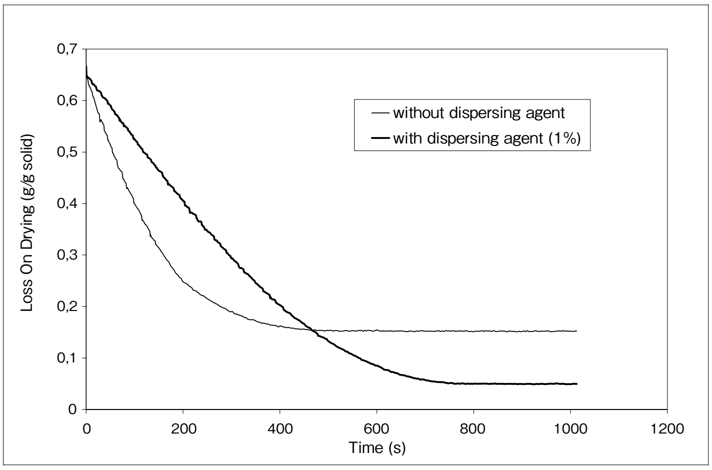

Fig. 14 Influence of the dispersant quantity on the drying kinetics. (T=65℃, Q_{air}=75 L/h, hydrophobic plates)

agglomerates. This phenomenon depends on the attrition of the glass spheres related to the fluidization movement, but also to the adhesion forces between the dried coating and the inert support.

The shearing tests show the same tendency for the specimens made by only one or two coated plates (**Fig. 15**). The shear modulus is maximum for highest concentrations of dispersant and for lowest humidity. Indeed, dispersant addition tends to decrease the size of the calcium carbonate particles by deflocculation of the agglomerates. This makes it possible to increase the surface energy and thus the energy of adhesion. The influence of the dispersant content can also be related to the surface-active character of sodium polyacrylate. It improves the wettability of glass and thus the adhesion of the suspension on the support.

In addition, when the humidity increases, the powder flow, *i.e.* the displacement of dried film, is increasingly difficult because the increase in the water content of the powder involves the creation of interparticle liquid bridges (Teunou, 2003).

To decrease the shear stress and to limit the agglomeration and the sticking of glass particles in the process of drying in a fluidized bed of inert particles, it is necessary to increase the relative humidity. However, the process being continuous, a high humidity always remains in the fluidized layer.

Moreover, to improve the peeling of the dried powder and its recovery, it is necessary to optimize the quantity of dispersant: sufficiently high to make the suspension sprayable, but sufficiently low to reduce the affinity of the film for the coated surface.

4. Conclusions

The present work involved the preparation and spray drying of highly concentrated suspensions of calcium carbonate. The effectiveness of polyacrylate salts on the reduction of the viscosity was confirmed for the suspensions of calcium carbonate.

Drying of these concentrated suspensions by two spray drying methods showed that it is possible to form particles of different shape and size depending on the method used. It was also shown that the drying in a fluidized bed of glass spheres can be applied to concentrated slurries with a low viscosity. Conventional spray drying of such suspensions leads to

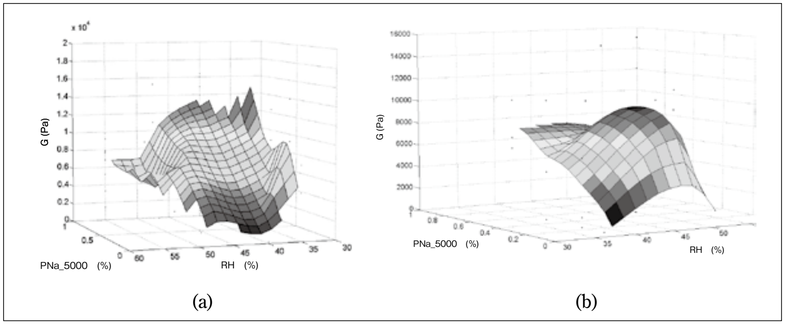

(a) (b)

Fig. 15 Influence of the humidity and the dispersant quantity on the shear modulus: specimens coated on one side (left) and on both sides (right).

granules, whereas drying on fluidized inert particles enables a fine powder close to the elementary particles to be obtained.

From the study of the drying kinetics, we were able to highlight the influential parameters on the kinetics of drying. It appeared that the use of a hydrophobic support could be beneficial provided that the suspension is finely sprayed at the surface of inert particles (*i.e.* by using a pneumatic nozzle).

In addition, surface tension of the suspension and ambient humidity seem to be crucial parameters to optimize the powder recovery after drying the coated layer.

These results extrapolated on the level of the coating of glass spheres make it possible to better understand and optimize the process of drying in a fluidized bed of inert particles.

Acknowledgements

The financial support of ADEME – Agence de l'Environnement et de la Maîtrise de l'Energie – is acknowledged.

Nomenclature

B	Blaine specific surface	$[cm^2/g]$
d	displacement	[m]
e	porosity	
E	thickness	[m]
F	load	[N]
G	shear modulus	[Pa]
K	Blaine apparatus constant	
l	specimen length	[m]
L	specimen width	[m]
LOD	Loss On Drying	
Q	flow rate	$[m^3/h]$
RH	relative humidity	[%]
S	specimen surface	$[m^2]$
t	time	[s]
T	temperature	[℃]
U	air velocity	$[m \cdot s^{-1}]$

Greek letters

ε	strain	[–] or [%]
$\dot{\gamma}$	shear rate	$[s^{-1}]$
η	viscosity	$[Pa \cdot s]$
ρ	density	$[cm^3/g]$
σ	stress	[Pa]

Subscripts

c	shear
f	fluidization
i	inlet
m	minimum
max	maximum value (corresponding to a complete shear of the suspension film)
o	outlet
p	plastic
y	yield

References

Benali, M. and Amazouz, M. (2006): Journal of Food Engineering, Vol.74, pp.484-489.

Bretton, C. and Villoutreix, G. (2005): Techniques de l'Ingénieur, N1650.

Camisard, V. (1997): Ph.D. Dissertation, Institut National Polytechnique de Toulouse, France.

Chevikov, S.A. (1981): URSS patent, 861905.

Dobronogov, V.G., Lukach, Y.E., Marchevskij, V.N., Petrov, V.T., Tarasova, L.D and Khodatenko, G.A. (1981): URSS patent, 879207.

Dusanter, A., Saleh., K. and Guigon, P. (2006): 5th World Congress on Particle Technology, Orlando, Florida, U.S.A.

Dusanter, A., Saleh., K. and Guigon, P. (2007): Science et Technologie des Poudres & Poudres et Matériaux Frittés, Albi, France.

Dvortsin, R.D., Ilnitskij, I.I., Norenko, A.N. and Shmaryan, E.M. (1982): URSS patent, 985647.

Garcia, F. (2001), Ph.D. Dissertation, Institut National Polytechnique de Toulouse, France.

Geffroy, C., Persello, J., Foissy, A., Cabane, B., Tournilhac, F. (1997): Revue de l'Institut Français du Pétrole, Vol.52 (2), pp.183-190.

Geffroy, C., Persello, J., Foissy, A., Lixon, B., Tournilhac, F. and Cabane, B. (2000): Colloids and Surfaces A, Vol.162, pp.107-121.

Grbavcic, Z.B., Arsenijevic, Z. L. and Garic-Grulovic, R.V. (2004): Drying Technology, Vol.22, pp.1793-1812.

Grbavcic, Z.B., Arsenijevic, Z. L. and Zdanski, F.K. (1998): Proceedings of the 11th International Drying Symposium, Vol.C, pp.2090-2097, Halkidiki, Greece.

Husson, M., Jacquemet, C. and Vorobiev, E. (2002): French Patent, 0209015.

Kozachek, A.V. and Shikunov, A.N. (2003): Russian patent, 2208476.

Kugge, C. and Daicic, J. (2004): Journal of Colloid and Interface Science, Vol.271, pp.241-248.

Lukach, Y.E., Marchevskij, V.N., Dobronogov, V.N., Konnov, V. A. and Petrov, V.T. (1978): URSS patent, 606065.

Marques, A., Donida, M., Rocha, S. (2006): 15th International Drying Symposium, Budapest, Hungary, pp.177-182.

Mouroko-Mitoulou, T. (2002): Ph. D. Dissertation, Université de Technologie de Compiègne, France.

Mousa, A. (1979): International Journal of Mineral Processing, Vol.6, pp.155-163.

Shmaryan, E.M. (1981): URSS patent, 879221.

Tari, G. and Ferreira, J. (1998): Ceramics International, Vol.24, pp.527-532.

Teunou, E. (2003): Technologie des pulvérulents dans les IAA, Sciences & Techniques Agroalimentaires, Ch.4, pp.93-118.

Tsetsekou, A., Agrafiotis, C., Leon, I. and Milias A. (2001): Journal of the European Ceramic Society, Part II: Spray-drying, Vol.21, pp.493-506.

Tobori, N. and Amari, T. (2003): Colloids and Surfaces A : Physicochemical and Engineering Aspects, Vol.215, pp. 163-171.

Vorobiev, E., Mouroko-Mitoulou, T. and Soua, Z. (2004): Colloids and Surfaces A: Physicochemical and Engineering Aspects, Vol.251, pp.5-17.

Zedlets, I. and Bogdanov, V.M. (1977): URSS patent, 580426.

Author’s short biography

Anne Dusanter

Anne DUSANTER is a Chemistry Engineer from the Ecole Nationale Supérieure de Chimie de Lille (France) with a specialization in formulation processes. She obtained a research Master's degree in the field of Industrial Processes from the Université de Technologie de Compiègne (France) in 2003. The research project of the Master was focused on the characterisation of filtration cakes obtained by mechanical filtration implementing a prelayer and in the presence of chemical dispersants. She prepared a PhD thesis on the study of interactions between formulation and rheology of high concentrated suspensions and their spray drying and obtained her doctor's degree in 2007. She worked as Project Unit Coordinator in the Galenic Developpement Department of Ethypharm company (Houdan, France) on the improvement of drug delivery of pharmaceutical solid oral forms.

Khashayar Saleh

Khashayar SALEH received a B.S. degree in Chemical Engineering from Sharif (Aryamehr) university of technology (Tehran/Iran) in 1992. He prepared a PhD thesis on the coating of fine powders in the Chemical Engineering Laboratory of Toulouse and obtained his doctor's degree in 1998 from Institut National Polytechnique de Toulouse (France). Dr Saleh is currently associate professor in the chemical engineering department of the Compiègne University of Technology. His work is focused on powder technology including size enlargement technology and powder's characterisation methods.

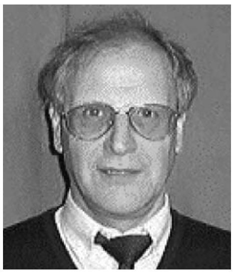

Pierre Guigon

Pierre Guigon is a Chemical Engineer from ENSIGC Toulouse (France 1971). Master of Engineering Science, UWO London Ontario, (Canada 1974), Docteur Ingénieur UTC Compiègne (France 1976), Docteur es Science UTC Compiègne (France 1978), Fellow of the Institution of Chemical Engineers. He is head of the chemical engineering department of Compiègne University of Technology. His research is in the field of particle suspensions (fluidization, pneumatic transport) and particle technology (communition and agglomeration).

Control of Apparent Specific Gravity in Binary Particle Systems of Gas-Solid Fluidized Bed[†]

Mikio Yoshida, Jun Oshitani*, Keiko Ono, Miki Ishizashi and Kuniaki Gotoh
Department of Applied Chemistry,
Graduate School of Natural Science and Technology, Okayama University[1]

Abstract

Fluidized bed medium separation (FBMS) was applied to separate objects with a small specific gravity difference by precisely controlling the apparent specific gravity of gas-solid fluidized bed with binary particle systems. The binary systems of particles with various specific gravities and diameters were employed, and the apparent specific gravity of fluidized bed, g_{fb}, and fluctuation, Δg_{fb}, were measured by changing the volume mixing rati of heavier particle, V_{hp}, and the superficial air velocity, u_0. It was found that g_{fb} can be controlled by V_{hp} and u_0 because g_{fb} varies with the total mass of particles and bed expansion. On the other hand, since Δg_{fb} is determined by the extent of segregation of fluidized particles and fluidization intensity, Δg_{fb} decreases with reducing the extent of the segregation and the vertical fluctuation of fluidized bed surface. The experimental results showed that practical fluidized conditions for FBMS are in the wide range of $g_{fb} \approx 0.5$~3.8 and $\Delta g_{fb} \leq$ about 0.1. Under these fluidized conditions, plastics with a small difference in specific gravity (0.04~0.24) were almost completely separated at the top and bottom of the fluidized bed.

Keywords: fluidized bed, dry gravity separation, binary particle systems, segregation, floating and sinking

1. Introduction

If a gas is fed vertically upwards from below a particle bed, the floating force of the gas on the particle bed overcomes the gravitational force. At this time, the particle bed goes into the floating and fluidized state. Because of this, the particle bed has an apparent specific gravity and apparent viscosity which are properties similar to a liquid[1-4]. This is called a gas-solid fluidized bed. If an object is inserted inside this bed, an object having a smaller specific gravity than the apparent specific gravity of the fluidized bed floats, and an object with a higher specific gravity sinks. Therefore, while being a dry method, it becomes possible to separate objects based on the difference in their specific gravities. Compared to the wet type specific gravity separation method of using a specific gravity adjusted liquid instead of a particle bed, in this dry type specific gravity separation method, it is possible to separate objects that are weak against wetting, and has superior features such as it is not necessary to have a waste liquid treatment process or a drying process after separation, etc. Because of this, this dry method is being used for the separation of various objects. Fraser et al.[5] used this in the 1920's for the first time as a coal cleaning technology. In the 1970's Joy et al.[6] used this as an ore processing technology for separating fluorspar, pallasite, and galena. In the 1980's, Zaltzman et al [7-9] succeeded in separating agricultural products such as potatoes from mud or pebbles. The authors too have used this method so far and have succeeded in a) coal cleaning[10,11], b) material separation in automobile shredder reside[12-14], c) separation of plastics containing chlorine from home electrical appliance shredder reside[15], and d) ore refining[16,17]. Particularly in ore refining, it was shown that it is possible to separate silica stone and pyrophyllite with a specific gravity difference of a mere 0.25. However, even though this much utility has been confirmed, at present, this dry method has not yet replaced the wet

---

[†] This paper, appeared originally in Japanese in J. Soc. Powder Technology, Japan 43, 567-576(2006), is published in KONA Powder and Particle Journal with the permission of the editorial committee of the Soc. Powder Technology, Japan.

* Corresponding author
TEL & FAX: +81-86-251-8086
E-mail: oshitani◎cc.okayama-u.ac.jp

[1] 3-1-1 Tsushima-naka Okayama 700-8530 Japan

method. This is considered to be due to the following two reasons. The first reason is that, it takes an extremely long time to determine the fluidized bed conditions for obtaining an apparent specific gravity suitable for separating an arbitrary object. This is because, in order to obtain the desired specific gravity, it is necessary to adjust by trial and error the fluidized bed conditions such as the type of fluidized particles, the superficial air velocity from below the particle bed, etc. The second reason is that, in this dry method, in general, it is difficult to separate objects with relatively small difference in specific gravity. This is because, unlike in the wet method, in this dry method, there are flow of particles and flow of air bubbles within the gas-solid fluidized bed, and it is difficult to suppress fluctuations in the apparent specific gravity.

In order to solve these problems, it should be possible to determine the fluidized bed conditions easily, and also, it is necessary that it should be possible to separate even objects with small difference in specific gravity under those fluidized bed conditions. When it is not possible to obtain the desired apparent specific gravity with a single component fluidized particle bed, it is considered to be possible to adjust the apparent specific gravity by varying the ratio of mixing of two types of particles with different true specific gravities. However, in general, if particles with different specific gravities are mixed, a segregation phenomenon occurs in which the composition of the particle bed becomes spatially non-uniform. The segregation phenomenon is known to be affected largely by not only the true specific gravities of the particles but also by the ratio of particle diameters. In view of this, in this research, we mixed various types of particles with true specific gravity in the range of 1.02 to 7.50 and particle diameters in the range of 75 to 710 μm, and prepared a binary fluidized particle bed with different true specific gravity ratios and different particle diameter ratios. These were fluidized with a prescribed superficial air velocity. Spheres with the specific gravity adjusted to 0.30 to 1.40 were inserted into those beds, the floating and sinking behaviour of the spheres was observed, and an attempt was made to obtain the apparent specific gravity of the fluidized bed and the fluctuations in the apparent specific gravity. Further, in order to evaluate the fluidization state at this time, the extent of segregation of particles and the bed height variations that become an indication of the strength of fluidization were measured. From these results, we investigated the effect of the state of fluidization on the apparent specific gravity and on the fluctuations in the apparent specific gravity. Based on these findings, we attempted the realization of a gas-solid fluidized bed that makes fluctuations in the apparent specific gravity small over a wide range of apparent specific gravities. Further, we tried to prepare an "apparent specific gravity map" summarizing these results. It becomes easy to determine the fluidized bed conditions if this map is used. In addition, in order to investigate the appropriateness of the apparent specific gravity map, we conducted experiments of floating and sinking separation of five types of plastic spheres with extremely small gravity difference.

2. Experiments

2.1 Fluidized particles and target objects of separation

Polystyrene particles (P.S.), granulated sugar particles (G.S.), glass beads (G.B.), Unibeads (U.B.), and steel shots (S.S.) were used as the fluidized particles. The respective particle diameters, true specific gravities, bulk specific gravities, and particle shapes are shown in **Table 1**. Two components were selected from these particles, mixed in different volume ratios, and attempts were made to adjust the apparent specific gravity.

Five types of plastic spheres (with 1.91cm diameters) of polypropylene (PP), polyethylene (PE), 6-Nylon, polyoxymethylene (POM), and polyvinyl chloride (PVC) were used as the target objects of

Table 1 Characteristics of fluidized particle employed

Particle	Diameter D_p (μm)	True specific gravity g_t (−)	Bulk specific gravity g_b (−)	Particle shape
Polystyrene (P.S.)	355 ~ 425 425 ~ 500 500 ~ 600 600 ~ 710	1.02 ~ 1.04	0.63 ~ 0.67	Sphere
Granulated Sugar (G.S.)	355 ~ 425 425 ~ 500	1.59 ~ 1.61	0.99 ~ 1.00	Nonsphere
Glass Beads (G.B.)	90 ~ 106 106 ~ 125 125 ~ 150 150 ~ 180 180 ~ 212 212 ~ 250 250 ~ 300 300 ~ 355 355 ~ 425 425 ~ 500	2.48 ~ 2.52	1.50 ~ 1.65	Sphere
Uni Beads (U.B.)	180 ~ 212	4.11	2.54	Sphere
Steel Shot (S.S.)	75 ~ 90	7.50	4.00	Sphere

separation. Their true specific gravities are shown in **Table 2**. The specific gravity difference among the different plastic spheres is very small, being in the range of 0.04 to 0.24. Because of this, it is expected that these are objects which are difficult to separate by their specific gravities.

2.2 Experimental apparatus

Explanations of the experimental apparatus and the method of operation are omitted as they are similar to those given in other reports[13,16]. An acrylic cylindrical tube of internal diameter of 15cm, height 40cm, and thickness 0.6cm was used as the body of the fluidized bed column. An air dispersion plate was placed at the bottom of the bed. The structure of this air dispersion plate is such that one sheet of cloth is clasped between two stainless steel plates having holes of diameter 0.2cm, pitch 0.3cm, and open ratio 40.3%. The particles to be fluidized were put in the fluidized bed column so that the height is 10cm. After that, the bed was fluidized by feeding air from a blower. The control of the superficial air velocity u_0 was done by a motor valve. The minimum fluidization velocity of each fluidized particle u_{mf} was obtained using the following procedure. Firstly, a particle bed with a setting of about u_0=15 cm/s was completely fluidized. After that, the pressure drop ΔP of the particle bed was measured in the process of gradually reducing u_0. The value of u_0 at which ΔP starts decreasing from a fixed value in association with the reduction in u_0 is taken as u_{mf}.

2.3 Measurement of apparent specific gravity of fluidized bed and its fluctuations

In order to measure the apparent specific gravity g_{fb} of the fluidized bed and its fluctuation Δg_{fb}, we prepared specific gravity adjusted spheres with specific gravities g_{sp} in the range of 0.30 to 1.40 with specific gravity spacing of 0.01. The adjustment of g_{sp} was done by filling prescribed quantities of S.S. inside spherical shells of a diameter of 3.75cm. Firstly, the particle bed was fluidized with a superficial air velocity ratio of u_0/u_{mf} = 1.1 to 4.0. The maximum and minimum values of the bed surface height were read out visually, and the average bed height h_{ave} of these two and the difference between the two heights Δh_{surf} were calculated. Next, the specific gravity adjusted sphere was placed at the center of the topmost bed and fluidized for one minute, and the floating or sinking behaviour was stabilized sufficiently. After that, the height of the position h of the bottom end of the sphere from the bottom of the bed was measured. The value obtained by deducting the radius from h_{ave} was divided into h, thereby obtaining the normalized height h_{sp}. However, it is not possible to measure h visually from outside the fluidized bed. Therefore, h was calculated from the depth of penetration of a string attached beforehand to the sphere. The sphere is floating if $g_{sp}<g_{fb}$, and h_{sp} becomes 1 if the sphere has floated completely. If $g_{sp}\approx g_{fb}$, there is no floating or sinking but the sphere is positioned at middle within the fluidized bed. The sphere has sunk if $g_{sp}>g_{fb}$, and h_{sp} becomes 0 if it has sunk completely. h_{sp} was obtained for each g_{sp} sphere, the maximum g_{sp} for which h_{sp}=1 is taken as g_1, the minimum g_{sp} for which h_{sp}=0 is taken as g_2, and the average value of the two is taken as g_{fb}. Further, the range Δg_{fb} in which there is no complete floating or sinking is obtained by the difference between g_1 and g_2. Δg_{fb} indicates the fluctuation in the apparent specific gravity. Therefore, in order to separate the separation target object completely into top and bottom bed, it is necessary that Δg_{fb} must be smaller than the specific gravity of the separation target object. The measurements were made five times under each measurement condition.

Table 2 Specific gravity of plastic sphere employed

Plastic sphere	Specific gravity of sphere (−)
Polypropylene (PP)	0.86
Polyethylene (PE)	0.90
6-Nylon	1.12
Polyoxymethylene (POM)	1.36
Polyvinyl Chloride (PVC)	1.46

2.4 Measurement of segregation coefficient

The segregation coefficient which is considered to reflect the segregation state of the fluidized state was measured using the following method. To begin with, the two component fluidization particles were mixed with a prescribed volume ratio. Here, the volume mixing ratio of the larger particles to the particles with smaller true specific gravity is taken as V_{hp}. This mixture is put into the fluidization column so that the height of the bed becomes 10cm, and fluidization was made with a surperficial air velocity ratio u_0/u_{mf} of 1.1 to 4.0. The air flow was stopped after fluidizing until the segregation state became completely stable for a maximum of 120 minutes. After that, the fluidized particles were sucked gradually from the top using a vacuum cleaner, and were sampled. The height of the binary fluidized bed after fluidization varies slightly depending on the fluidization conditions such as the types of the particles, the volume mixing ratio, and u_0/u_{mf}, etc. Therefore, at the time of sucking the fluidized particles from the top bed using a vacuum cleaner, only the height range from 8cm to 10cm is sucked together, and the remaining height range is sucked by dividing it into 8 layers of 1cm height each. After sampling, the fluidized particles in each layer i are classified into the different components and the respective masses were measured. From the result of mass measurement, the volume ratio x_i of the particles with larger true specific gravity in each layer i was calculated. Here, i indicates the height position in 1cm units from the bottom of the layer, and only the layer that is 8cm to 10cm from the bottom of the layer is taken as i=9. The segregation coefficient C_s defined by Eq. (1) including the Mixing Index[18] was calculated as a parameter indicating the segregation state.

$$C_s = 1 - \frac{\sum_{i=1}^{9} |x_i^* - x_i|}{\sum_{i=1}^{9} |x_i^* - x_{\mathrm{ave}}|} \quad (1)$$

Here, x_i^* indicates the ratio of the particles with larger true specific gravity in each layer i when completely segregated. Since the particles with large true specific gravity segregate at the bottom part of the layer, as an example, in the case of V_{hp}=0.6, x_1^*~x_6^* become 1.0 and x_7^*~x_9^* become 0.0. Also, x_{ave} is the average value of the volume ratio of the particles with large true specific gravity in all the layers when mixed completely, and hence x_{ave} becomes equal to V_{hp}. C_s has been defined so that it becomes closer to 1.0 as the segregation state becomes nearer, and becomes closer to 0.0 as the uniformly mixed state becomes closer.

2.5 Plastic floating and sinking experiment

The particle bed was fluidized similar to Section 2.3, and the average bed height h_{ave} was obtained. After that, (one each of) the five types of plastic spheres shown in **Table 2** were placed at the center of the top bed and were left like that for 1 minute. The position of the bottom of each plastic sphere from the bottom of the bed was measured. These values were divided into a value obtained by subtracting the radius of each plastic sphere from h_{ave} thereby calculating the normalized height h_{p}. The measurements were made five times under each measurement condition.

3. Results and Discussion

3.1 Apparent specific gravity and its fluctuation in binary particle system of P.S. and G.B.

The two types of particles of P.S.(355~425 μm) and G.B.(150~180 μm) were used as the binary fluidization particle system. The effects of the superficial air velocity ratio u_0/u_{mf} and the volume mixing ratio $V_{\mathrm{G.B.}}$ of G.B. on the apparent specific gravity g_{fb} and on its fluctuation Δg_{fb} were investigated. **Fig. 1** shows the normalized height h_{sp} with respect to the specific gravity g_{sp} at each u_0/u_{mf} when $V_{\mathrm{G.B.}}$ is varied. At any u_0/u_{mf}, spheres with small specific gravity float, and as the specific gravity of the sphere increases, the sphere does not float or sink but is positioned at the middle bed. The sphere sank completely when the specific gravity increased further. However, the details of the floating and sinking behaviour changed depending on the value of u_0/u_{mf} or $V_{\mathrm{G.B.}}$. The number of spheres remaining in the middle bed without floating or sinking was small at $V_{\mathrm{G.B.}}$=0.1 or 0.9 for u_0/u_{mf}=1.1, and the floating and sinking of spheres is clear. On the other hand, the number of spheres remaining in the middle bed was large at $V_{\mathrm{G.B.}}$=0.3 ~

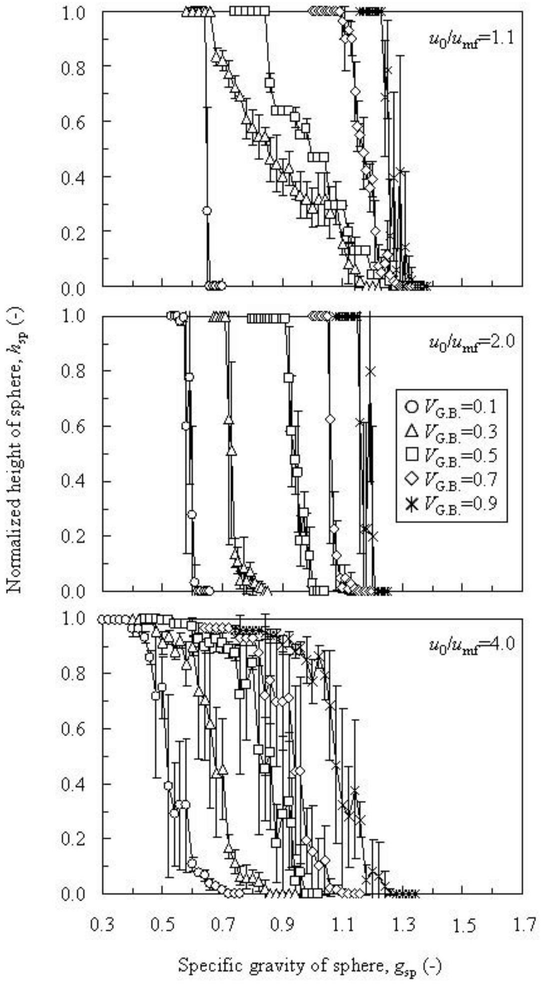

Fig.1 Dependences of normalized height on specific gravity of sphere for various bulk volume fractions of G.B.
(Mixture of P.S.(355~425 μm, u_{mf}=4.7 ± 0.4 cm/s) and G.B.(150~180 μm, u_{mf}=2.9 ± 0.1 cm/s)).

0.7 for u_0/u_{mf}=1.1, and the result showed that there is a wide range of specific gravity of spheres that do not sink or float completely. When increased from u_0/u_{mf}=1.1 to u_0/u_{mf}=2.0, at any $V_{G.B.}$, the floating and sinking of spheres was clear. However, when increased up to u_0/u_{mf}=4.0, the result changed, and the number of spheres remaining in the middle bed increased at any $V_{G.B.}$. Further, along with the increase in u_0/u_{mf}, it was confirmed that the apparent specific gravity g_{fb} of the fluidized bed had decreased (that the g_{sp} at which the floating and sinking interchange has shifted to the left). The values of g_{fb} and average bed height h_{ave} calculated from these results of sphere floating and sinking are shown with respect to u_0/u_{mf} in **Fig. 2**. As shown in the results in **Fig. 1**, at any value of $V_{G.B.}$, g_{fb} decreased gradually along with increases in u_0/u_{mf}. At this time, it can be confirmed that h_{ave} is increasing along with u_0/u_{mf}. Therefore, the entire fluidized bed expands along with increases in u_0/u_{mf}, and hence g_{fb} is considered to have decreased. Further, when compared at each u_0/u_{mf}, the decrease in $V_{G.B.}$, that is, along with increases in light P.S., g_{fb} decreases at almost equal intervals. At this time, it can be confirmed that h_{ave} is almost constant and does not depend on changes in $V_{G.B.}$. Hence it is considered that the total mass of the binary particles filled in the column decreased due to the decrease in $V_{G.B.}$, and even g_{fb} decreased. Therefore, it can be said that it is possible to control g_{fb} by varying u_0/u_{mf} and the volume mixing ratio of particles with different specific gravities.

The values of Δg_{fb}, the bed height difference Δh_{surf}, and the segregation coefficient C_s are shown in **Fig. 3** at each $V_{G.B.}$ with respect to changes in u_0/u_{mf}. The relationship with respect to u_0/u_{mf} of Δg_{fb}, dividing roughly, shows two different trends in the cases of $V_{G.B.}$=0.1 and 0.9, and $V_{G.B.}$=0.3~0.7. Firstly, when the composition of a binary particle system is close to a single component of P.S. and G.B. such as $V_{G.B.}$=0.1 and 0.9, along with increase in u_0/u_{mf} even Δg_{fb} also increased. On the other hand, when $V_{G.B.}$=0.3~0.7, Δg_{fb} showed a minimum value at about u_0/u_{mf}=2.0~2.5. The reason for this different trend depending on $V_{G.B.}$ is studied later. There are no big

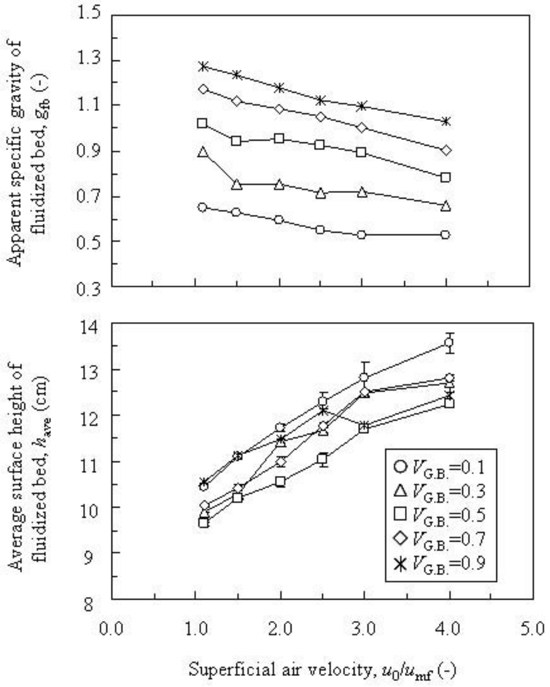

Fig.2 Dependences of apparent specific gravity and average surface height of fluidized bed on u_0/u_{mf} for various bulk volume fractions of G.B.
(Mixture of P.S.(355~425 μm, u_{mf}=4.7 ± 0.4 cm/s) and G.B.(150~180 μm, u_{mf}=2.9 ± 0.1 cm/s)).

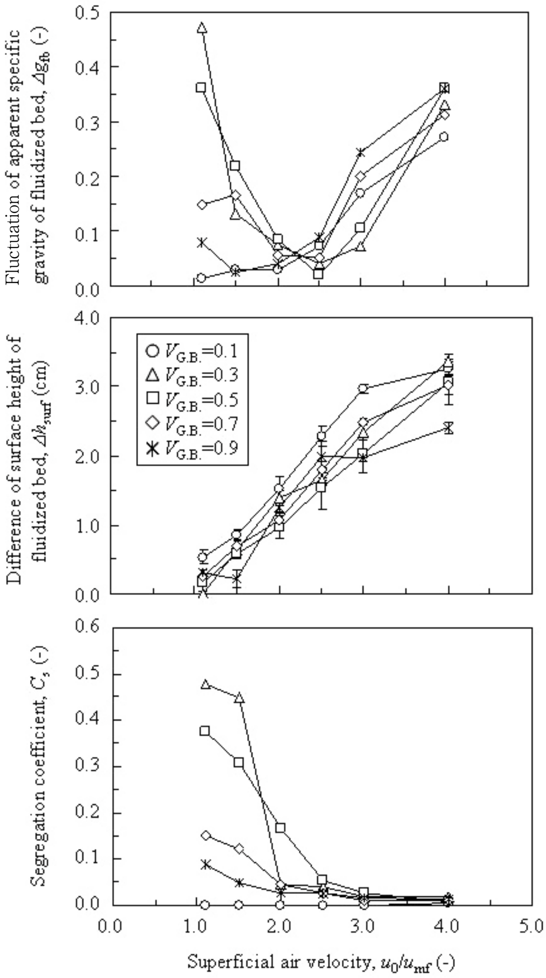

Fig.3 Dependences of the fluctuation of g_{fb}, difference of surface height of fluidized bed and segregation coefficient on u_0/u_{mf} for various volume mixing ratio of G.B.
(Mixture of P.S.(355~425 μm, u_{mf}=4.7 ± 0.4 cm/s) and G.B.(150~180 μm, u_{mf}=2.9 ± 0.1 cm/s)).

differences in value of Δh_{surf} at each u_0/u_{mf} for any $V_{G.B.}$. However, Δh_{surf} increased along with increases in u_0/u_{mf}. This is considered to be because the fluidization became stronger with the increase in u_0/u_{mf} The segregation coefficient C_s in the large superficial air velocity region of $u_0/u_{mf} \geq 2.5$ in not dependent on $V_{G.B.}$ but $C_s < 0.1$, and there is almost no segregation. This is considered to be because both P.S. and G.B. are fluidized strongly and a uniformly mixed state has been reached. On the other hand, in the small superficial air velocity region of $u_0/u_{mf} < 2.5$, C_s exhibits small values in the cases of $V_{G.B.}=0.1$ and 0.9, and large values in the cases of $V_{G.B.}=0.3$ and 0.5, and hence the result was different depending on $V_{G.B.}$. When two types of particles with different true specific gravities are mixed as in this case, along with the reduction in u_0/u_{mf}, it becomes difficult for G.B. having a larger specific gravity to become fluidized compared to P.S. with a smaller specific gravity, and hence segregation is expected to occur. However, in the cases of $V_{G.B.}=0.1$ and 0.9 which are almost single component, the number of particles with different states of fluidization is small, and hence it is thought that segregation did not occur.

Now we discuss the reason why the relationship of Δg_{fb} with respect to u_0/u_{mf} described above was widely different for different $V_{G.B.}$ **Fig. 4** shows Δg_{fb}, Δh_{surf}, and C_s at $V_{G.B.}=0.4$ with respect to u_0/u_{mf}. The reason why $V_{G.B.}$ was made equal to 0.4 is because at this value, although not shown in the results in **Fig. 3**, the average value of C_s for each value of u_0/u_{mf} showed the highest value. Similar to the result in **Fig. 3** for $V_{G.B.}=0.3$~0.7, with respect to u_0/u_{mf}, Δg_{fb} showed the smallest value at $u_0/u_{mf}=2.5$. Further, along with increases in u_0/u_{mf}, Δh_{surf} increased and C_s decreased. From this, it is possible to explain as follows the relationship of Δg_{fb} with u_0/u_{mf}. When u_0/u_{mf} is small, C_s is large, and P.S. with smaller specific gravity is present close to the top bed and G.B. with larger specific gravity is present close to the bottom bed. Because of this, there will be a difference in g_{fb} between the top and bottom beds of the fluidized bed, and hence Δg_{fb} increased. When u_0/u_{mf} increases, gradually segregation is suppressed, and at about $u_0/u_{mf}=2.0$~2.5, Δg_{fb} decreased. On the other hand, since Δh_{surf} increased along with increases in u_0/u_{mf}, that is, since fluidization has become stronger, the floating and sinking of spheres became gradually unstable. As a result, it is considered that Δg_{fb} increased again at $u_0/u_{mf} > 2.5$. Further, the fact that Δg_{fb} is determined by increases or decreases in C_s and Δh_{surf} in this manner can also be applied to the cases of $V_{G.B.}=0.1$ and 0.9 when Δg_{fb} showed a trend of almost simple increase with respect to increases in u_0/u_{mf}. In this case, it is considered because C_s is almost constant and is low at any value of u_0/u_{mf}, since the particle composition is close to a single component system, and Δh_{surf} increased along with u_0/u_{mf}. Therefore, in order to obtain a fluidized bed that can separate objects with small difference in the specific gravity, it can be said necessary that (1) the segregation of particles is suppressed, and also (2) it is necessary to operate at an appropriate superficial air velocity ratio at which the fluidization state is rather gentle.

3.2 Particle diameter ratio and true specific gravity ratio of fluidized particles

As is shown in **Table 3**, the average particle diameter ratio $D_{G.B.}/D_{P.S.}$ was varied using P.S. and G.B. with different particle diameters, and the effect of

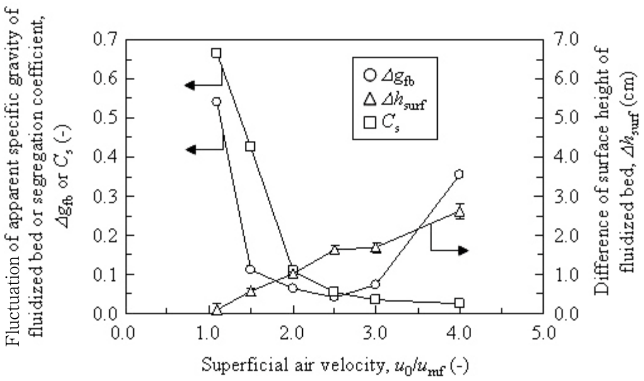

Fig.4 Dependences of the fluctuation of g_{fb}, segregation coefficient and difference of surface height of fluidization on u_0/u_{mf} at $V_{G.B.}=0.4$. (Mixture of P.S. (355~425 μm, $u_{mf}=4.7 \pm 0.4$ cm/s) and G.B. (150~180 μm, $u_{mf}=2.9 \pm 0.1$ cm/s)).

$D_{G.B.}/D_{P.S.}$ on g_{fb}, Δg_{fb}, C_s, and Δh_{surf} was studied. Here, the conditions were u_0/u_{mf}=1.1 and $V_{G.B.}$=0.4 at which the largest segregation coefficient was obtained for u_0/u_{mf} and $V_{G.B.}$ in the binary particle system of the last section. The segregation in the fluidized bed can be density segregation (specific gravity segregation) in which particles with smaller specific gravity are present in large numbers in the top bed and the particles with larger specific gravity are present in large numbers in the bottom bed, or can be particle size segregation in which the particles with smaller particle diameter segregate to the top bed and the particles with larger particle diameter segregate to the bottom bed. This is because the particles with larger specific gravity or diameter are harder to fluidize, and the more easily fluidized particles with smaller specific gravity or particle diameter pass through the air gap between the larger particles and reach the top bed. Therefore, in order to suppress segregation in the fluidized bed, it is necessary to combine small particles with a large specific gravity (G.B.) and large particles with a smaller specific gravity (P.S.) (particle diameter ratio $D_{G.B.}/D_{P.S.} \leq 1.0$). **Fig. 5** shows g_{fb}, Δg_{fb}, Δh_{surf}, and C_s with respect to $D_{G.B.}/D_{P.S.}$. Firstly, it became clear that g_{fb} is almost constant at any $D_{G.B.}/D_{P.S.}$ This is considered to be because, as is shown in the results in **Fig. 2**, g_{fb} is dependent on the total mass of the binary particles poured inside the column (volume mixing ratio $V_{G.B.}$=0.4). Therefore, it became clear that it is not necessary to consider the particle diameters and their ratio regarding the control of g_{fb}. In contrast, the result showed that Δg_{fb} decreases with decrease in $D_{G.B.}/D_{P.S.}$. Similar to the above, it is expected that even Δg_{fb} with respect to $D_{G.B.}/D_{P.S.}$ is determined by Δh_{surf} and C_s. To begin with, the results showed that Δh_{surf} is almost constant and does not depend on changes in $D_{G.B.}/D_{P.S.}$. This is considered to be because there is no large difference in the intensity of fluidization since u_0/u_{mf} is constant. Next,

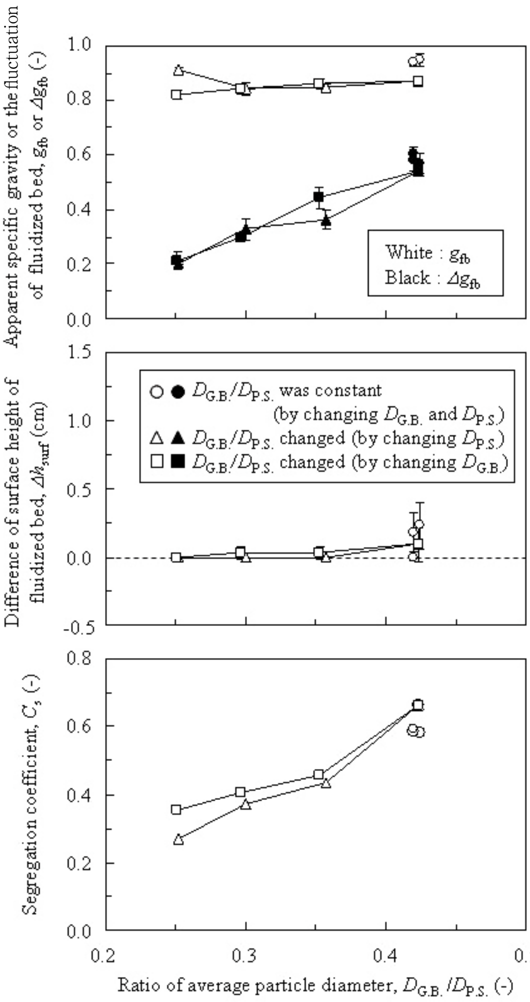

Fig.5 Apparent specific gravity, the fluctuation, surface height of fluidized bed and segregation coefficient plotted against ratio of average particle diameter.

even C_s decreased with the decrease in $D_{G.B.}/D_{P.S.}$. This can be considered to be an appropriate result when considered along with necessary conditions for suppressing segregation as described above (large specific gravity = small particle diameter, small spe-

Table 3 Characteristics of fluidized particles for various $D_{G.B.}/D_{P.S.}$ experiments

P.S. diameter, $D_{P.S.}$ (μm)	G.B. diameter, $D_{G.B.}$ (μm)	$D_{G.B.}/D_{P.S.}$ (−)	u_{mf} (cm/s)
355 ~ 425	150 ~ 180	0.42	2.9 ± 0.2
425 ~ 500	180 ~ 212		3.4 ± 0.2
500 ~ 600	212 ~ 250		4.3 ± 0.0
600 ~ 710	250 ~ 300		7.2 ± 0.2
600 ~ 710	150 ~ 180	0.25	3.2 ± 0.5
500 ~ 600		0.30	3.0 ± 0.3
425 ~ 500		0.36	3.0 ± 0.3
355 ~ 425		0.42	2.9 ± 0.2
355 ~ 425	90 ~ 106	0.25	1.0 ± 0.0
	106 ~ 125	0.30	1.2 ± 0.0
	125 ~ 150	0.35	1.9 ± 0.1
	150 ~ 180	0.42	2.9 ± 0.2

cific gravity = large particle diameter). Therefore, in order to control Δg_{fb} to become a small value, it is considered very important to avoid segregation by making $D_{G.B.}/D_{P.S.}$ small (making the particle diameter difference large).

Next, as is shown in **Table 4**, we varied the true specific gravity ratio g_{hp}/g_{lp} ($\geq$1.0), and studied the effect on Δg_{fb}, C_s, and Δh_{surf}. Here, the volume mixing ratio of large particles with respect to particles with small true specific gravity V_{hp} and the particle diameter ratio D_{hp}/D_{lp} were respectively set the same as in the combination so far of G.B. and P.S., that is, V_{hp}=0.4 and D_{hp}/D_{lp}=0.42. The values of Δg_{fb}, Δh_{surf}, and C_s with respect to g_{hp}/g_{lp} for each superficial air velocity ratio u_0/u_{mf} are shown in **Fig. 6**. At u_0/u_{mf}=1.1, Δg_{fb} decreased along with decreases in g_{hp}/g_{lp}. Further, Δh_{surf} did not depend on changes in g_{hp}/g_{lp}, but was almost a constant value. In addition, C_s decreased along with g_{hp}/g_{lp}. Therefore, it became clear that segregation is suppressed due to the decrease in g_{hp}/g_{lp}, and it is possible to control Δg_{fb} to a small value. This is considered to be due to the fact that density segregation (specific gravity segregation) can be suppressed as a binary particle system when the combination of small g_{hp}/g_{lp} is used, based on the above described necessary conditions for suppressing segregation. In contrast with this, at u_0/u_{mf}=2.0, Δg_{fb} was suppressed to a small value at any value of g_{hp}/g_{lp}. The values of Δh_{surf} and C_s with respect to g_{hp}/g_{lp} at u_0/u_{mf}=2.0, are similar to the trend at u_0/u_{mf}=1.1, and Δh_{surf} does not depend on changes in g_{hp}/g_{lp} but is almost constant, and C_s has a trend of decreasing with g_{hp}/g_{lp}. However, when the absolute values of Δh_{surf} and C_s at each g_{hp}/g_{lp} is compared with the case for u_0/u_{mf}=1.1, since the fluidization is stronger in the case of u_0/u_{mf}=2.0, it can be confirmed that Δh_{surf} has increased and C_s has decreased. From these results, it is considered that at u_0/u_{mf}=2.0, the effect of the decrease in C_s is more than the effect on Δg_{fb} of an increase in Δh_{surf}, and hence a small value of Δg_{fb} has been obtained. Therefore, when it is inevitable to mix particles with large true specific gravity ratio in order to obtain a value of g_{fb} suitable for separation, by setting $u_0/u_{mf} \approx 2.0$, it is possible to control Δg_{fb} to a small value.

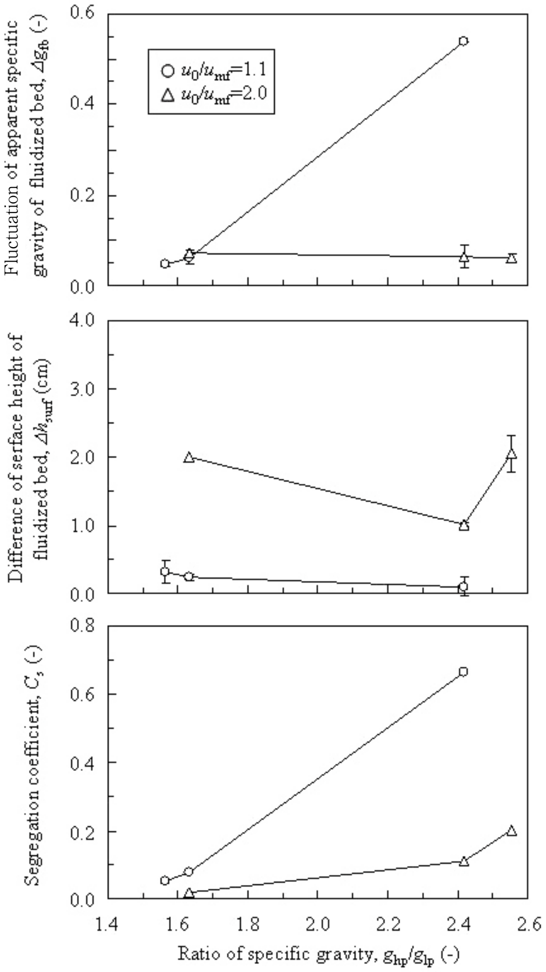

Fig.6 Fluctuation of apparent specific gravity, surface height of fluidized bed and segregation coefficient plotted against ratio of specific gravity.

3.3 Apparent specific gravity map for specific gravity separation

We carried out experiments of floating and sinking of specific gravity adjusted spheres by mixing various binary fluidized particles at different volume mixing ratios. From the results of the studies of varying g_{hp}/g_{lp} in the last section, u_0/u_{mf} was set at 1.1 when

Table 4 Characteristics of fluidized particles for various g_{hp}/g_{lp} experiments

Lighter particle			Heavier particle				
	Diameter, D_{lp} (μm)	Specific gravity, g_{lp} (−)		Diameter, D_{hp} (μm)	Specific gravity, g_{hp} (−)	g_{hp}/g_{lp} (−)	u_{mf} (cm/s)
G.S.	355 ~ 425	1.59	G.B.	150 ~ 180	2.49	1.57	4.0 ± 0.2
G.B.	425 ~ 500	2.52	U.B.	180 ~ 212	4.11	1.63	7.0 ± 0.6
P.S.	355 ~ 425	1.03	G.B.	150 ~ 180	2.49	2.42	2.9 ± 0.2
G.S.	425 ~ 500	1.61	U.B.	180 ~ 212	4.11	2.55	7.4 ± 0.2

g_{hp}/g_{lp} is small, and set to 2.0 when g_{hp}/g_{lp} is large. The results of g_{fb} and Δg_{gf} for different fluidized particles are shown in **Fig. 7**. Here, in these results, Δg_{fb} is indicated by an error bar (white diamonds), and in all cases D_{hp}/D_{lp} was taken as 0.42. From these results, a fluidized bed having continuous variations was obtained in the range of g_{fb}=0.5~3.8. In addition, in any combination of binary particles, Δg_{fb} could be controlled to be extremely small, being about 0.1. Because this apparent specific gravity map is obtained, it has become possible to know at one look the fluidized bed conditions such as the types of fluidized particles, their volume mixing ratios, the superficial air velocity ratio, etc., suitable for any separated objects. In addition, it can be said that it has become possible to solve the two problematic aspects of the dry method, which are, 1) taking a long time to determine the fluidized bed conditions, and 2) it being difficult to separate objects with small specific gravity difference.

3.4 Floating and sinking of plastics

Using the fluidized bed of **Fig. 7** which suggested that it is possible to separate objects with a small specific gravity difference, floating and sinking experiments were made of the five types of plastics shown in **Table 2** with specific gravity differences of 0.04~0.24. The results of plastic floating and sinking when V_{hp} is varied in a fluidized bed of G.S. and G.B., G.S. and U.B. are shown in **Fig. 8**. Firstly, in the fluidized bed of G.S. and G.B., the trend was confirmed of the plastics floating starting from the smaller specific gravities with increase in V_{hp}. This is because g_{fb} increases with increases in V_{hp}. In the range $V_{hp} \leq 0.10$, PP and PE were almost completely separated to the top and bottom beds. Also, PE and 6-Nylon were completely separated in the range $0.30 \leq V_{hp} \leq 0.40$, and 6-Nylon and POM were separated completely in the range $0.70 \leq V_{hp}$. Regarding the separation of PP and PE, it should be noted that they were almost completely separated in spite of the fact that the specific gravity difference is extremely small being 0.04. Because of this, it was proved that it is possible to separate objects with small specific gravity differences in this fluidized bed. In addition, although it was impossible to separate POM and PVC, clearly the reason for this is that the specific gravities of these two plastics (POM=1.36, PVC=1.46) are larger than the range of g_{fb} (g_{fb}=0.87~1.33). Therefore, if the apparent specific gravity of the fluidized bed is selected appropriately, it is considered possible to separate POM and PVC. Further, in the results for the fluidized bed of G.S. and U.B. (g_{fb}=0.73~2.09), the results of separation of only POM and PVC are shown. POM floats in the condition of V_{hp}=0.5, and PVC sinks to the bottom of the fluidized bed indicating that they can almost be separated. From this, it was indicated that it is possible to separate almost completely the five types of plastics with specific gravity differences of 0.04~0.24

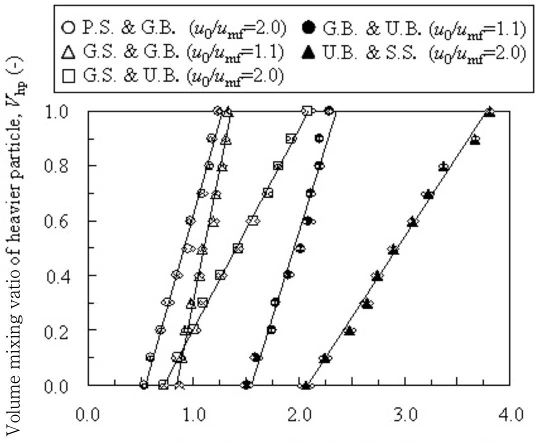

Fig.7 Apparent specific gravity of fluidized bed and the fluctuation plotted against volume mixing ratio of heavier particle.
(P.S. (355~425 μm, u_{mf}=4.7 ± 0.4 cm/s), G.B. (150~180 and 425~500 μm, u_{mf}=2.9 ± 0.1 and 15.3 ± 0.9 cm/s), G.S. (355~425 and 425~500 μm, u_{mf}=8.1 ± 0.3and11.6 ± 0.3cm/s), U.B. (180~212 μm, u_{mf}=5.9 ± 0.1 cm/s), S.S. (75~90 μm, u_{mf}=2.3 ± 0.0 cm/s))

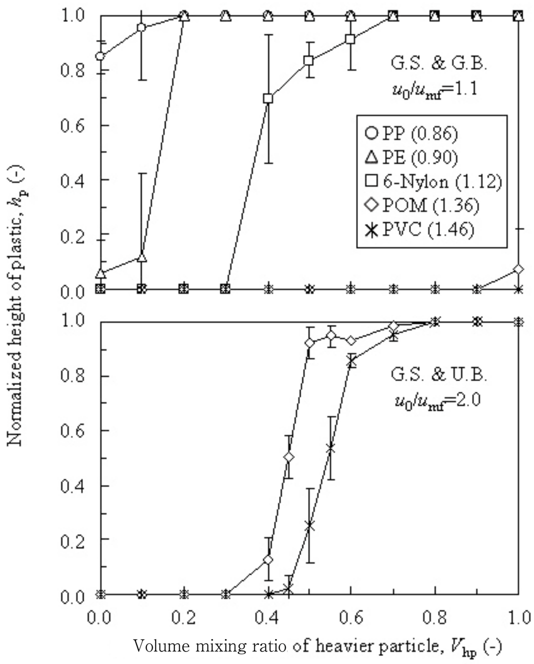

Fig.8 Dependences of normalized height of plastic on volume mixing ratio of heavier particle.
(G.B. (150~180 μm, u_{mf}=2.9 ± 0.1 cm/s), G.S. (355~425 and 425~500 μm, u_{mf}=8.1 ± 0.3 and 11.6 ± 0.3 cm/s), U.B. (180~212 μm, u_{mf}=5.9 ± 0.1 cm/s)).

to the top and bottom beds by adopting the fluidized bed conditions shown in the apparent specific gravity map.

4. Conclusions

In the dry specific gravity separation method using a gas-solid fluidized bed, an attempt was made to obtain an “apparent specific gravity map” with which it is possible to determine easily the fluidized bed conditions that make possible the separation of any objects with small specific gravity differences. Binary particle systems were used as the fluidized particles with different true specific gravity ratios and different particle diameter ratios. Studies were made of the effect of the superficial air velocity ratio u_0/u_{mf} and the volume mixing ratio of fluidized particles V_{hp} on the apparent specific gravity g_{fb} of the fluidized bed and its fluctuations Δg_{fb}. From these results, it was found that g_{fb} is dependent on the expansion of the bed and on the total mass of the two particles poured into the fluidized column. Therefore, it became clear that g_{fb} can be controlled by u_0/u_{mf} and V_{hp}. On the other hand, Δg_{fb} has a close relationship with both the extent of segregation and the intensity of fluidization, and it became clear that it is possible to suppress Δg_{fb} to a small value as the extent of segregation becomes small and the fluidization becomes gentle. Based on this knowledge, a gas-solid fluidized bed with continuous variation is achieved when g_{fb} is in the range of 0.5-3.8, and Δg_{fb} is almost 0.1 or less in all cases. By summarizing these, we obtained the desired “apparent specific gravity map”. From this map, it became possible to know at one look the fluidized bed conditions suitable for separating any objects. Because of completing this map, it has become possible to solve the two problematic aspects of the dry method, i.e., taking a long time to determine the fluidized bed conditions, and it being difficult to separate objects with small specific gravity difference. In addition, using a fluidized bed indicated in the apparent specific gravity map, we attempted separation of five types of plastics with extremely small specific gravity differences of 0.04~0.24. From these results, it was found that it is possible to almost completely separate all the plastics to the top and bottom beds.

Acknowledgment

This research was pursued with aid from Fiscal 2004 Industrial Technology Research Aid Program of the New Energy and Industrial Technology Development Organization, and assistance from the Japan Foundation for the Promotion of Science (young researcher (A) 17686067, young researcher (B) 15760614) for which we wish to express our gratitude here.

Nomenclature

C_s : segregation coefficient [−]
$D_{G.B.}$: diameter of glass beads [μm]
D_{hp} : diameter of heavier fluidized particle [μm]
D_{lp} : diameter of lighter fluidized particle [μm]
D_p : diameter of fluidized particle [μm]
$D_{P.S.}$: diameter of polystyrene particle [μm]
g_b : bulk specific gravity of fluidized particle [−]
g_{fb} : apparent specific gravity of fluidized bed [−]
g_{hp} : true specific gravity of heavier fluidized particle [−]
g_{lp} : true specific gravity of lighter fluidized particle [−]
g_{sp} : specific gravity of sphere [−]
g_t : true specific gravity of fluidized particle [−]
h : lowest height of sphere in fluidized bed [cm]
h_{ave} : average surface height of fluidized bed [cm]
h_p : normalized height of plastic [−]
h_{sp} : normalized height of sphere [−]
i : layer number in fluidized bed [−]
u_0 : superficial air velocity [cm/s]
u_{mf} : minimum fluidization velocity [cm/s]
$V_{G.B.}$: volume mixing ratio of glass beads [−]
V_{hp} : volume mixing ratio of heavier fluidized particle [−]
x_{ave} : average of volume ratio of heavier fluidized particle for all layer numbers with the completely mixed state [−]
x_i : volume ratio of heavier fluidized particle at layer number i [−]
x_i^* : volume ratio of heavier fluidized particle at layer number i with the completely segregated state [−]
Δh_{surf} : difference of surface height of fluidized bed [cm]
Δg_{fb} : fluctuation of apparent specific gravity of fluidized bed [−]
ΔP : pressure drop of bed [Pa]

References

1) Kunii, D. and O. Levenspiel (1991): “Fluidization Engi-

neering 2nd ed.", p.4, Butterworth- Heinemann.
2) Schmilovitch, Z., A. Zaltzman, D. Wolf and B.P. Verma (1992): Transactions of the ASAE, 35, pp.11-16.
3) Bakhtiyarov, S.I. and R.A. Overfelt (1998): Powder Technol., 99, pp.53-59.
4) Horio, M. and S. Mori (1999): "Fluidization Handbook", p.57, Baifuhkan.
5) Fraser, T. and H.F.Yancey (1926):, Coal Age, 29, pp.325-327.
6) Joy, A. S., E. Douglas, T. Walsh and A. Whitehead (1972): Filtration and Separation, 9, pp.532-538 and p.544.
7) Zaltzman, A., R. Feller, A. Mizrach and Z. Schmilovitch (1983):, Transactions of the ASAE, 26, pp.987-990 and p.995.
8) Zaltzman, A. and Z. Schmilovitch (1986) : Transactions of the ASAE, 29, pp.1462-1469.
9) Zaltzman, A., B. P. Verna and Z. Schmilovitch (1987) : Transactions of the ASAE, 30, pp.823-831.
10) Oshitani, J., K. Tani, K. Takase and Z. Tanaka (2004): J. Soc. Powder Technol., Japan, 41, pp.334-341.
11) Tanaka, Z., J. Oshitani, T. Nakamura, T. Syouji and A. Horiuchi (2000): Kagaku Kogaku Ronbunshu, 26, pp.327-331.
12) Oshitani, J., K. Kiyoshima and Z. Tanaka (2001): J. Soc. Powder Technol., Japan, 38, pp.487-492.
13) Oshitani, J., T. Kajiwara, K. Kiyoshima and Z. Tanaka (2001): J. Soc. Powder Technol., Japan, 38, pp.702-709.
14) Oshitani, J., K. Kiyoshima and Z. Tanaka (2003): Kagaku Kogaku Ronbunshu, 29, pp.8-14.
15) Yoshida, M., J. Oshitani, K. Kaname and K. Gotoh (2006): Kagaku Kogaku Ronbunshu, 32, pp.115-121.
16) Oshitani, J., M. Kondo, H. Nishi and Z. Tanaka (2001): J. Soc. Powder Technol., Japan, 38, pp.4-10.
17) Oshitani, J., K. Tani and Z. Tanaka (2003): J. Chem. Eng. Japan, 36, pp.1376-1383.
18) Marzocchella, A., P. Salatino, V. Di Pastena and L. Lirer (2000): AIChE Journal, 46, pp.2175-2182.

Author's short biography

Mikio Yoshida

Dr. Mikio Yoshida graduated from Doshisha University in 2000, and from the graduate school of Doshisha University in 2002. He obtained the Doctor degree of Engineering from Doshisha University in 2005. He was Post-Doctoral researcher of Graduate School of Natural Science and Technology at Okayama University from 2005 to 2007. He has been Assistant Professor of Graduate School of Natural Science and Technology of Okayama University since 2007.

Jun Oshitani

Dr. Jun Oshitani graduated from Kyoto University in 1994, and from the graduate school of Kyoto University in 1996. He obtained the Doctor degree of Engineering from Kyoto University in 1998. He was appointed Research Associate of Applied Chemistry Department of Okayama University in 1998. Presently he is Associate Professor of Graduate School of Natural Science and Technology of Okayama University since 2004.

Kuniaki Gotoh

Dr. Kuniaki Gotoh graduated from Hiroshima University in 1986, and from the graduate school of Hiroshima University in 1988. He obtained the Doctor degree of Engineering from Kyoto University in 1995. He was appointed Associate Professor of Mechanical Engineering Department of Yamaguchi University in 1997. Presently he is Professor of Graduate School of Natural Science and Technology of Okayama University since 2003.

Measurement of Force Curve due to Electrostatic Charge on a Single Particle using Atomic Force Microscope[†]

Tatsushi MATSUYAMA[*], Masa-aki OHTSUKA and Hideo YAMAMOTO
Department of Environmental Engineering for Symbiosis
Faculty of Engineering
Soka University[1]

Abstract

A single particle is brought into contact with a metal target, and the force acting on the particle is measured by using atomic force microscope (AFM). By focusing on measuring the force 'curve', rather than looking only at the maximum adhesive force, electrostatic interaction was successfully observed by separating other interactions such as liquid bridge and intermolecular forces. To evaluate the force curve, the force curve with an approximation of disk-to-disk interaction based on image force was numerically calculated and a good analytical approximation was developed. The fact of successful agreement between the observed force curve and the theory revealed that the force curve observed can be surely attributed to the electrostatic interaction, and that the amount of charge on the particle and the radius of the charged (contact) area can be estimated from the analysis. The order of magnitude of the measured charge density was 10^{-2} *C/m*^{2}*, which is much greater than that obtained with impact charging experiment as* 10^{-4} *C/m*^{2}*. From this it was concluded that the force curve measurement with AFM can capture the net amount of the charge generated before charge relaxation due to gas discharge taking place. In the experiment using 8 kinds of metal (Al, Au, Cr, Ni, Pt, Ti, Zn, and Zr) and polystyrene particle, the net charge generated was shown to be compared fairly well with the conventional simple condenser model based on metal-to-metal contact model in terms of contact potential difference in its order of magnitude. Although a clear correlation was not obtained between the measured charge density and the work functions of metal targets because of a large scatter in the data, a strong relationship between the charge density and contact area was found. The underlying mechanisms for the relationship is not known at this moment; however the finding gives a good hint for the next attempt.*

Keywords: contact electrification, tribo-charging, tribo-electrification, adhesive force measurement, electrostatic adhesion, Coulomb's law

1. Introduction

The first establishment of so-called reversed square law of the electrostatic interaction is credited to Coulomb's direct measurement (1785) by using torsion balance[1)] (although there might be some arguments in the context of science history, but it is beyond the subject of this technical paper). 200 yeas after Coulomb, the first attempt of the direct measurement of the electrostatic interaction working on small single particles, like powders, was demonstrated by Arakawa et al.[2)] by using precise balance modified from adsorption balance system. Their study was conducted in the context of direct evaluation of powder adhesion, after which they applied such direct measurement of force between single particles to small particle size region, down to 100 μm. With regard to the electrostatic interaction, they successfully measured force curves satisfying the reversed square law. Note here that the Coulomb's law had been one of the most established and essential laws in physics; therefore, they did not 're-discover' it. The

---

[†] This paper, appeared originally in Japanese in J. Soc. Powder Technology Japan 43, 174-180(2006), is Published in KONA Powder and Particle Journal with the permission of the editorial committee of the Soc. Powder Technology, Japan.

[1] 1-236 Tangi-cho, Hachioji Tokyo, 192-8577 JAPAN

[*] Conesponding authe
TEL & FAX: +81-(0)42-691-8169
E-mail: tatsushi@t.soka.ac.jp

force curve measurement means that the amount of charge on the particle can be evaluated from it. In their work, e.g., charge of 2.5 pC was measured on a 200 μm glass bead; thereby, the order of magnitude of the results was reasonable.

When the adhesive force of dry powder is discussed, any textbook on powder technology describes that there are three kinds of forces as liquid bridge force, intermolecular force and electrostatic force, in which the order of magnitude of the forces decreases in the order. It is generally understood that electrostatic force can be negligible. On the other hand, however, there are a lot of technologies to control powder by electrostatic force. It is found not exclusive only on the technology of electrophotograpy. There are more than few discussions attributing unexpected kinetic behaviors of powder to electrostatic force in industrial processes (or in lab-scaled experiments) of dry powder handling. Again these situations are incompatible to the discussions that the electrostatic force is negligible.

One of the major reasons of this kind of controversial situation where whether the electrostatic interaction is negligible or not in actual dry powder processes is due to the difficulty of evaluation or prediction of the amount of charge on powder. If the amount of charge on particles is estimated, the force acting on the particle can be determined by the Coulomb's law. The reverese is true that if the adhesive force acting on a particle can be measured precisely, the amount of charge on the particle can be reversely calculated and determined. Additionally the measurement can give new information on electrostatic charge generation on a single particle if the contact and separation of the particle against a target are well controlled.

As mentioned above, there are three mechanisms for the adhesive force working on a particle. On the other hand, however, the capillary force works only after the liquid bridge is generated when the contact of a particle is accomplished, i.e., this interaction has hysteresis before and after the contact. The intermolecular force is very sensitive to the surface distance; therefore, it decays rapidly with an increase of contact distance comparing to the electrostatic interaction. With considering these characteristics of three kinds of interactions, the information of the electrostatic interaction can be separated from a measurement of a force curve working on a single particle. Note here that it is important to record 'force curve,' i.e., it is necessary to evaluate not only the maximum adhesive force but also the force with the surface distance simultaneously and precisely.

A candidate of an instrument realizing such measurement may be atomic force microscope (AFM), which is now widely used in various applications. Though it is a kind of a ultra precise stylus method in which a microscopic bending of a small cantilever is measured with a principle of light lever. It was originally a microscope to observe surface morphology, the use of its 'force curve mode' makes it possible to measure the force working between a particle, which is fixed on the tip of a cantilever, and a flat target with precise control or measurement of the surface distance. It may be also noted that such measurements can be performed in both liquid phase and gas phase with the system.

In this work, 'force curve' of a single particle in dry system was measured using AFM. Based on the results of the measurements, evaluations on electrostatic interaction and charge generation on a single particle due to contacts to metal flat target will be discussed in details.

2. Experimental Method

The AFM used is JSPM-4210, JEOL. On the tip of a cantilever, a single spherical particle was fixed by epoxy adhesion as normal way. Sample particles were glass beads of around 30 μm in diameter, polystyrene spheres of around 30 and 100 μm in diameter. Before use, they were cleaned with ethanol and dried. As targets, a sample stage of the AFM, coated by gold on the surface, was used as a flat gold target. Additionally, 8 different metal plates (Al, Au, Cr, Ni, Pt, Ti, Zn, Zr), mirror finished by buffing, were used. **Table 1** summarizes work function values cited3) for these metals and the results of the measurement of their surface roughness (Surfcom, Tokyo Seimitsu). The force curve measurements were performed in an ambient air. The humidity for the measurement was not controlled but monitored, which was in the range of 25 to 45 %R.H.

Table 1 Surface roughness and work functions3) of 8 kinds of metal plate samples

metal	Al	Au	Cr	Ni	Pt	Ti	Zn	Zr
Roughness (Ra) [μm]	0.14	0.02	0.12	0.01	0.09	0.11	0.02	0.04
Work function [eV]	4.17	5.38	4.5	5.2	5.64	4.33	3.63	4.05

3. Results and Discussion

Fig. 1 shows an example of the measured force curve with a 35 μm glass bead. This is the result of the force curve reached to a stable condition after repeated contacts of tens of times. Although the actual

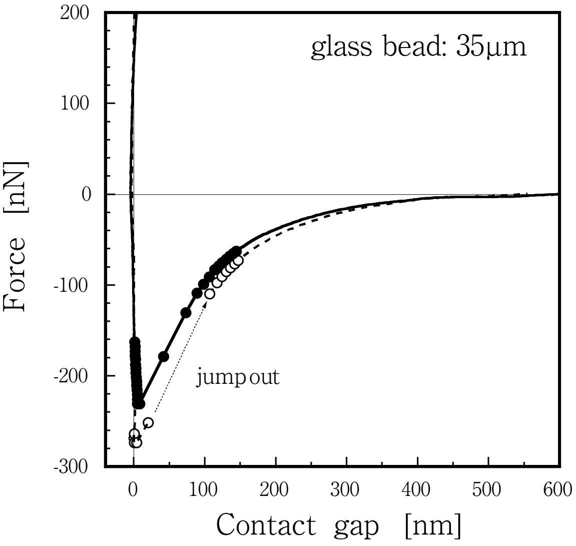

Fig. 1 An example of the obtained force curve against AFM stage as a target made of gold (glass bead, 35 μm).

data were recorded discretely or digitally, the number was more than 2000 for each way of approach or separation, thus the curves are drawn with only lines: only several important points just around jump-in and jump-out are plotted with markers. The curves in approach and separation are the same; therefore, no liquid bridge force is obtained in the measurement. The estimated intermolecular force for the separation distance range was negligible to the order of the measured force; therefore, it is concluded that the obtained force curve shows only the electrostatic interaction due to electrostatic charge generated on the tip of the particle by contact with the target.

Discussed in the next step is how the force curve can be evaluated. If a sphere is charged on its surface uniformly, the electric field around the particle is equivalent to that generated by a point charge of the total amount located on the center of the sphere. In this case the image force working between the center charge and its 'image' located inside of the metal target can be calculated as the electrostatic interaction working on the particle. Still, it should be noted that the polarization effect is neglected in the calculation[4].

Such a calculation with a center charge is only for a uniformly charged sphere. In the case of the force curve to be evaluated here, the charge after repeated contacts between the particle and the target is localized only on the contact area. Therefore the use of reversed square law for the center charge and its image is not reasonable. On the other hand, an approximation with a point charge localized on the tip of a particle gives force divergent with gap zero, which is also unreasonable.

If the contact area on the tip of a particle is sufficiently small, comparing to the curvature of the particle, the contact area can be approximated with a flat disk. With an assumption of uniform charge on the flat disk, the interaction between the disk charge and its image is calculated. A schematic illustration of this approximation is shown in **Fig. 2**.

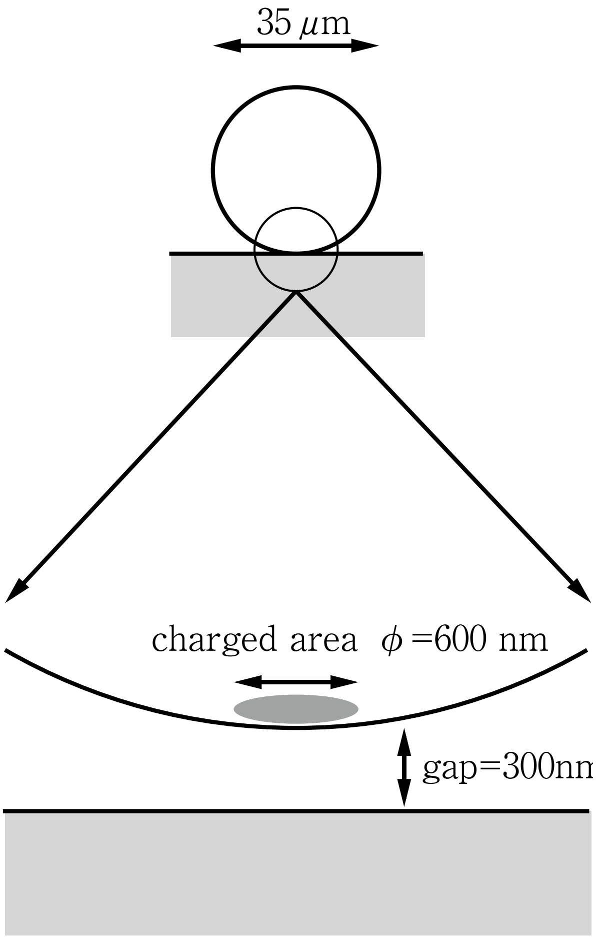

Fig. 2-a

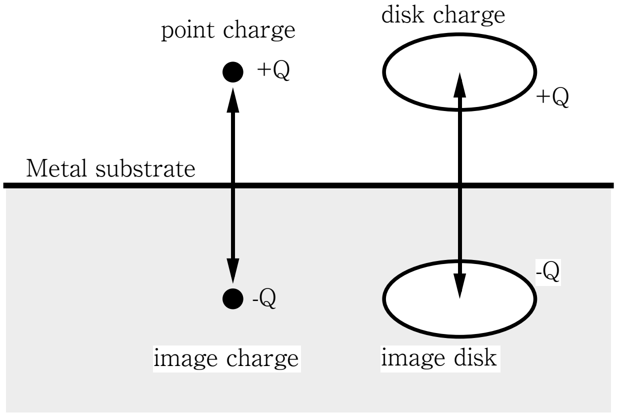

Fig. 2-b

Fig. 2 Schematic illustration of (a) contact area, and of (b) a comparison of point-to-point charge interaction and disk-to-disk interaction.

The force working between the disks of radius a and surface charge densities σ and $-\sigma$, which are separated coaxially with a distance h, is calculated as follows.

$$F = \frac{\sigma^2}{4\varepsilon_0}\int_0^a\int_0^a\int_0^{2\pi}\int_0^{2\pi}\frac{hr_1r_2}{R^3}dr_1dr_2d\varphi d\theta \tag{1}$$

$$R = \sqrt{h^2+r_1^2+r_2^2-2r_1r_2\cos(\theta-\varphi)} \tag{2}$$

The force is normalized by eq.(3) with the total charge on the disk q= $\sigma\pi a^2$ as,

$$F_N = F/\left(\frac{q^2}{4\pi\varepsilon_0 a^2}\right) \tag{3}$$

Then the normalized force is given as,

$$F_N = \frac{1}{\pi^2a^2}\int_0^a\int_0^a\int_0^{2\pi}\int_0^{2\pi}\frac{hr_1r_2}{R^3}dr_1dr_2d\varphi d\theta \tag{4}$$

This cannot be integrated analytically. Thus, after evaluating this numerically, an analytical approximation applicable for parameter-fitting afterward is found by a trial-and-error.

$$F_N = \frac{2}{2(h/a)^2+(h/a)+1} \tag{5}$$

Fig. 3 shows the comparison between the result of numerical integration of eq.(4) and the approximation of eq.(5). A good approximation is shown for the entire range, although an error goes up to 20% only with a very short gap. For comparison, the result of the approximation with a point charge, located on the tip of the particle, is also shown. Because the force increases rapidly and goes to infinity for the short gap naturally, this calculation is useless to evaluate the obtained force curve.

Let d be the distance between a particle and a flat metal target. Because the distance between the disk charge and its image is h=2d, from eq.(5) the force working on the disk charge is given as,

$$F = \frac{q^2}{4\pi\varepsilon_0 a^2}\cdot\frac{2}{8(d/a)^2+2(d/a)+1} \tag{6}$$

Note that the force goes to $F=\pi\sigma^2\sigma^2/2\varepsilon_0$ with the limit of $d\rightarrow 0$. This corresponds to the force between sufficiently large disks, comparing to the gap.

As discussed above, the point charge approximation gives the interaction divergent with the short gap. To avoid this difficulty, sometimes another approximation is used with a point charge located inside of the sphere with a small distance a, implied to the size of the contact area, from the tip of the sphere. For this case, however, the equivalent surface charge distribution on the particle corresponding to the point charge cannot be given simply. With this approximation, the force is evaluated with the following equation, which can be compared with eq.(6).

$$F = \frac{q^2}{4\pi\varepsilon_0 a^2}\cdot\frac{1}{4(d/a)^2+8(d/a)+4} \tag{7}$$

Fig. 4 shows an example of the evaluation of an obtained force curve, shown in **Fig. 1**. With using eq.(6), the regression analysis was applied to the data with parameters as the radius of charge area (disk) and the total amount of charge (on the disk). For comparison, a result of data fitting with the approximation of the point charge located on the tip of the particle is also shown. The point charge approximation obviously gives the force going to the infinity. On contrary, the disk charge approximation fits to the data for the entire range. From the results, it was concluded that the force curve obtained corresponds to the electrostatic interaction and the charge area on the particle can be expressed as a disk.

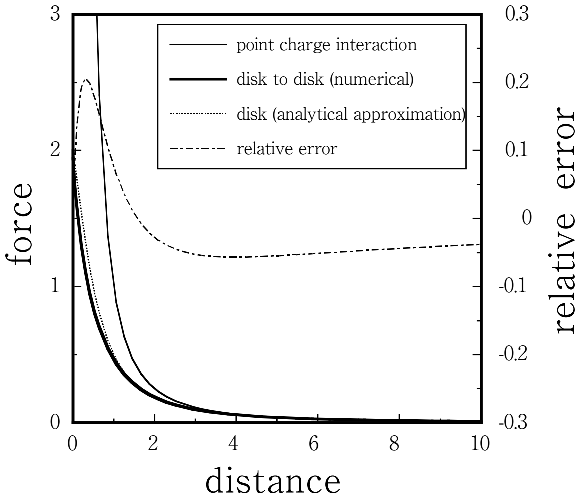

Fig. 3 Numerically calculated disk-to-disk charge interaction, compared with point-to-point interaction as well as the analytical approximation. Also the relative error of the approximation is shown.

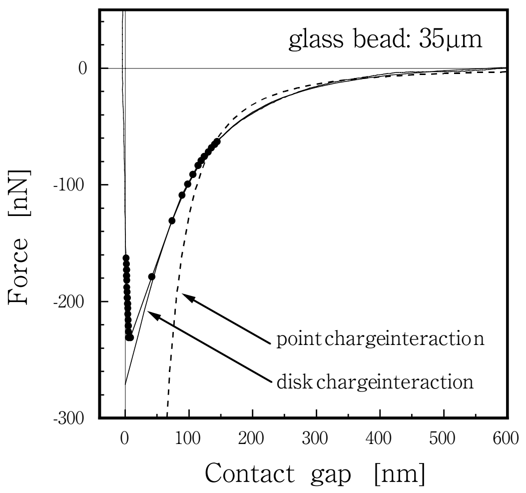

Fig. 4 Data from **Fig. 1** with fitted line of disk-to-disk charge interaction. The case of point charge interaction is also shown, which doses not explain the data.

Fig. 5 shows an example of the obtained data with polystyrene particle of 27.5 μm in diameter. The result is similar to the case of the 35 μm glass bead.

Next, **Fig.6** shows a result of polystyrene particle of 100 μm in diameter. The result was completely different from other results of smaller particles shown above, i.e., the force curves in approach and separation were different to each other. Note that the results were obtained after repeated contacts, as was the case of the smaller particles, in which the force curves were measured stably. The big force in the separation was lost in the next approach, but appeared again in the next separation. This bigger force in the separation appeared after 'jump-out,' this is not due to the capillary force.

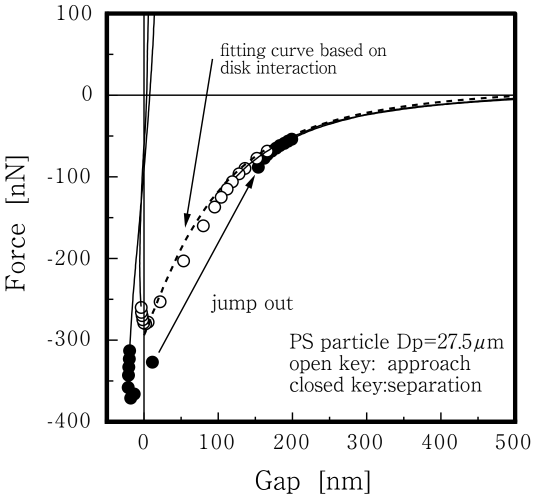

Fig. 5 Force curve of PS particle of 27.5 μm against AFM stage with curve fitted.

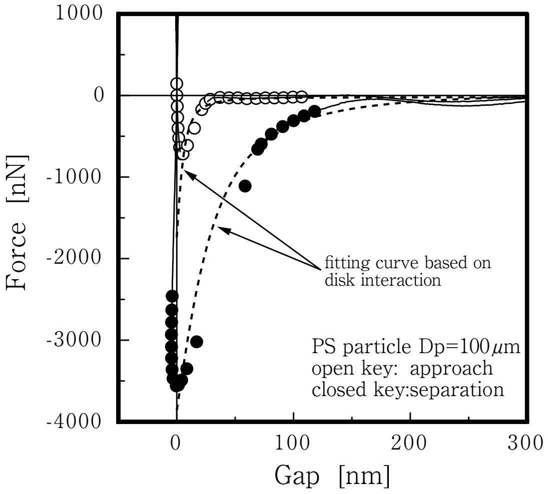

Fig. 6 Force curve of glass bead of 100 μm against AFM stage. The curves for approach and separation are completely different to each other. The force in separation is significantly bigger than that in approach, although the data are taken after repeated contact, and it is repeatable.

If these forces were of electrostatic interaction due to the charge on a particle, this result means that there is a process as follows: (1) in approach, the particle has a certain amount of charge, (2) in contact, the contact charge is generated on the particle, (3) as its result, the bigger force curve is obtained in the separation process, (4) however, in the separation process, somehow and somewhat the particle loses its charge, (5) and this process is repeatable.

On the other hand, however, this process does not correspond directly to our model of 'charge relaxation due to gas discharge' [5,6] because of the model based on Paschen's law of gas discharge where the specific gap of it is in μm range. This is far bigger than the range in the present measurement of the force curve. This point should be studied in more detail in the future.

Fig. 7 shows the results of the experiments with 8 kinds of metal target and polystyrene particle of 100 μm in diameter. The relationship between the work functions of the metal targets and the charge density is shown, where the generated charge on the particle was estimated by the data regression as discussed above from the force curve measurement. In the evaluation, the data in the separation process were used because they were considered to correspond to the amount of charge which is just generated by the contact event, as discussed above.

First of all, the data scattered considerably. We repeated experiments to improve this situation; however the reason is not known at this moment. Therefore, the correlations of charge density to metal work function are not considered here. However, it should

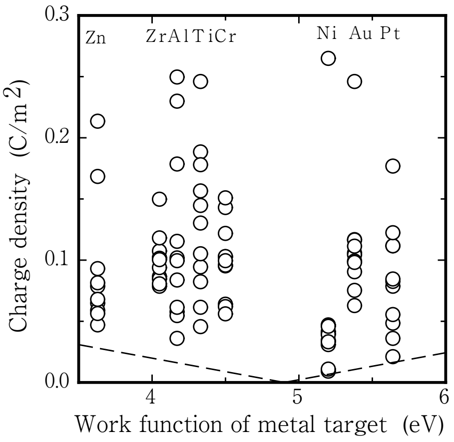

Fig. 7 Relationship of obtained charge density and work function of metal targets for 100 μm PS particle. Dashed line shows the charge density expected from the condenser model with an assumption of 4.9 eV for the effective work function of PS.

be noted that the evaluated charge densities were extraordinary high as 10^{-2} to 10^{-1} C/m^2 in its order of magnitude. In our previous work of 'impact charging experiments[7],' the obtained charge density with the same polystyrene particle of 100 μm in diameter was in the order of 10^{-4} C/m^2. In comparison the former is extremely high. From this discussion, it is suggested that the net charge transfer due to contact is obtained in the force curve measurement with AFM, whereas the charge after the charge relaxation due to gas discharge is obtained in the impact charging experiment. However, the order obtained in the present work is even higher than that estimated by the standard or conventional condenser charging model (or metal-to-metal contact model, or high-density-limit model[8,9]), which is drawn for comparison in **Fig.7** with an assumption of 4.9 eV as the effective work function of polystyrene. At this moment we can offer no theory to explain this. Therefore, possibilities of experimental errors or failures in the procedure of the force curve evaluation are still necessary to be studied.

Furthermore, we continued to repeat the measurements and accumulated more data. **Fig. 8** shows the relationship between the evaluated surface charge density and the contact area. This figure shows only the result of Zn target case. In **Fig.7**, the charge density looked only as scattered, but in **Fig.8**, it was found that the charge density follows a certain function or a correlation to the contact area. **Fig. 9** shows the similar result for polystyrene particle of 30 μm in diameter. In the data of **Fig.9**, the force curves, obtained with 30 μm polystyrene particle and Zn target, were similar to the result shown in **Fig.6**, which showed a bigger interaction in separation than that in approach. Also they were different from the result shown in **Fig. 5**, even though the particle size was similar to the case of **Fig.5.** Again it is not known at present that whether these kinds of different 'modes' in the force curve are resulted only from the difference in targets. This is an interesting point to be explored in the future in more detail.

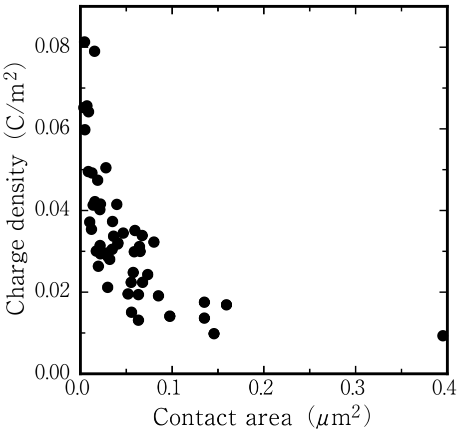

Fig. 8 The relationship between charge density and contact area (PS 100 μm particle, Zn target.)

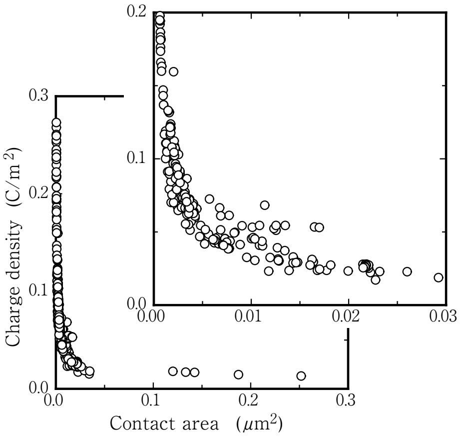

Fig. 9 The relationship between charge density and contact area (PS 30 μm particle, Zn target.)

With regard to **Figs. 8** and **9**, it was also interesting that the relationship or correlation between the charge density and the contact area was found although the charge density data seemed just as scattered as **Fig.7**. In the future study, the detailed studies are necessary to explore whether the relationship has any significant physical meaning or there still are any errors or artifacts in the measurements or evaluation procedures. It would be interesting if this kind of investigation could be a new key to open the new door to understand the contact charging of a single particle.

4. Conclusions

The electrostatic interaction due to charge generated by repeated contacts between a single spherical particle glued on the tip of the cantilever of AFM and flat metal targets were measured with the force curve measuring mode of AFM. It was shown that the electrostatic force working on the particle can be evaluated independently and separately from the capillary force and the intermolecular force by evaluating the obtained force curve, not only the maximum contact force. To evaluate the force curve by electrostatic interaction, a disk charge approximation, in which the contact area on the tip of a particle is evaluated as a small and flat disk, was studied. The force between a disk and its image was numerically calculated, and a good analytical approximation was found to express the force as a function of the contact gap. By comparing the data and the obtained theoretical force curve, it was shown that the measured force curve corresponds the electrostatic interaction and that the surface charge density and the size of the contact area (radius of the disk) can be estimated by the data fitting. The obtained or evaluated surface charge density was in the order of 10^{-2}C/m^2, which was significantly bigger than 10^{-4}C/m^2 obtained in our previous work with impact charging experiments with the same particles. This fact suggested that the charge obtained in the AFM-force curve measurement is corresponding to the net charge which is just generated by the contact before the charge relaxation due to gas discharge takes place. With the detailed experiments using 8 kinds of metal target, any clear correlation between the generated charge (density) and the metal work function could not be found. The obtained charge density was bigger than that predicted by the standard condenser charging model. The reason why such kinds of results were obtained is not known at this moment. The obtained charge density scatted significantly with many measurements. Afterwards, however, it was found that the data did not simply scattered but there was a certain relationship between the charge density and the contact area. However, the significance of this relationship is unclear at this point. We hope that the clarification of this point would become the clue to the detailed study on the contact charging of a particle in the future.

Acknowledgements:

This work was supported by IFPRI (International Fine Particle Research Institute). The authors appreciate Mr.T.Sueyoshi, JEOL, for his helpful suggestions on the force curve measurement by AFM. The authors also appreciate Nihon Micro Coating for their help in finishing the surface of the flat metal plates as the target.

Nomenclature

a: radius of charged disk	[m]
d: distance between particle and target	[m]
F: force	[N]
F_N: normalized force	[-]
h: distance	[m]
q: charge	[C]
R: distance	[m]
r: radius	[m]
ε_0: dielectric constant of space	[F/m]
ϕ : angle	[rad]
σ : surface charge density	[C/m^2]
θ : angle	[rad]

References

1) e.g., Roller, D., DHD. Roller: "The development of the concept of elctric charge", In: J. B.Contant ed. Harvard Case Histories in Experimental Science vol.2, Cambrige, USA: Harvard University Press, pp.541-633 (1970).
2) Arakawa, M., S. Yasuda S: "The measurement of interaction force on microparticles", Zairyo, 26, pp.858-562 (1977).
3) Inst. Electros. Jap. ed.: "Seidenki Handbook", Ohmusha, Tokyo (1981).
4) e.g., Matsuyam, T., H. Yamamoto: "The electrostatic force between a charged dielectric particle and a conducting plane", J. Soc. Pow. Tech., Jap., 34, pp.154-159 (1997).
5) Matsuyama, T., H. Yamamoto: "Charge relaxation process dominates contact charging of a particle in atmospheric conditions", J. Phys. D: Appl. Phys., 28, pp.2418-2423 (1995).
6) Matsuyama, T., H. Yamamoto: "Charge relaxation process dominates contact charging of a particle in atmospheric conditions II. general model", J. Phys. D: Appl. Phys., 30, pp.2170-2175 (1996).
7) Matsuyama, T., M. Ogu, H. Yamamoto, JCM. Marijnissen, B. Scarlett: "Impact charging experiments with single particles of hundred micrometre size", Pow. Tech., 135/136, pp.14-22 (2003).
8) Schein, LB., M. LaHa, G. Marshall: "Electrostatic charging of two insulating powders", J. Appl. Phys., 69, pp.6817-6826 (1991).
9) Schein, LB.: "Recent advances in our understanding of toner charging", J. Electros., 46, pp.29-36 (1999).

Author's short biography

Tatsushi Matsuyama

Dr.Tatsushi MATSUYAMA is Professor of Department of Environmental Engineering for Symbiosis, Faculty of Engineering, Soka University. He graduated from Department of Chemical Engineering, the University of Tokyo, in 1987. He received the PhD degree in chemical engineering from the University of Tokyo in 1995, with the thesis on the mechanism of impact charging of single particles. Since then, he has been contributing in the field of powder technology, and his major research interests have been still in the areas of powder and electrostatics. He spent his sabbatical leaves as visiting researcher at the Delft University of Technology, the Netherlands, with Prof.B.Scarelett's group in 1998, and at the Institute of Particle Science and Engineering, Leeds University, UK, with Prof.M.Ghadiri's group in 2007. He is currently the editor-in-chief of Journal of the Institute of Electrostatics Japan.

Masaaki Ohtsuka

Masa-aki OHTSUKA obtained his BSc (2005) and MSc (2007) from Faculty of Engineering, Soka University and its Graduate School of Engineering.

Hideo Yamamoto

Dr.Hideo YAMAMOTO is Professor of Department of Environmental Engineering for Symbiosis, Faculty of Engineering, Soka University. He graduated from the Department of Chemical Engineering, the University of Tokyo, in 1967. He received the Dr.Eng. degree from the University of Tokyo in 1979. He joined Department of Chemical Engineering, the University of Tokyo in 1976, and in 1989 to become an Ass.Prof. at the Institute of Industrial Science, the University of Tokyo. He was a visiting researcher at the Delft University of Tecunology, in the Netherlands from 1984 to 1986. He joined the Department of Bioengineering at Soka University, as a Professor in 1991. His field and interesting is in particle technology and applied electrostatics. His current researches are particle separation from gases, particle size analysis, production and application of nano-particles, chemical reaction in surface corona plasma and its application for pollution control.

Selective Immobilization of Aceticlastic Methanogens to Support Material[†]

Toshiyuki Nomura*, Takanori Nagao, Akinori Yoshihara,
Hayato Tokumoto, Yasuhiro Konishi
Department of Chemical Engineering
Osaka Prefecture University[1]

Abstract

The effect of electrostatic and hydrophobic properties of microbes in anaerobic sludge on immobilization to support materials was examined. The most popular aceticlastic methanogen, Methanosaeta concilii, was uncharged and hydrophobic. Methanosarcina barkeri of a methyltrophic methanogen, and acidogens cultivated selectively from anaerobic sludge, were negatively charged and hydrophobic. Immobilized microbes on support materials were incubated with sodium acetate. Methanogens were dramatically immobilized to bamboo charcoal, in contact with hydrophilic alumina. Methanosaeta-like microbes were immobilized to bamboo charcoal. These results indicate that the hydrophobic and negatively-charged support material that can suppress the immobilization of microbes except for Methanosaeta species is suitable for selective immobilization of Methanosaeta species, which is the most important microbe in methane fermentation.

Keywords: biocolloid, immobilization, methanogen, electrophoretic mobility, hydrophobicity

1. Introduction

The establishment of a "recycling society" in Japan is rapidly advanced due to improvement in various recycling laws (e.g., "Fundamental Law for Establishing a Sound Material-Cycle Society"). Methane fermentation has received renewed attention as a technology for producing energy from organic waste with high water content. Conventional methane fermentation has various problems: (i) fermentation efficiency is low, and the treatment of undigested residues is necessary because the growth rate of the methanogens is extremely low; and (ii) wash-out of methanogens in the fermenter is carried out. High concentrations of methanogens must be immobilized in a fermenter to realize highly efficient methane fermentation.

Immobilization of methanogens as a method to maintain a high concentration in the fermenter has been investigated. Support materials such as glass, slag, resin, foam stones, and zeolites have been used for methanogen immobilization. It was reported that suitable support material has a hydrophobic surface, or a shape to which microbial cells can easily adhere. Contrary reports have also been published; the mechanism of cell immobilization is incompletely understood [1]. The reason is that bacterial strains immobilized on support materials were different because the type of treated waste water was different; or the composition of waste water was different because of the season, even if the same type of waste water was used. Many researchers have examined the surface properties of the support material used to immobilize microbial cells, but few scholars have focused on the surface properties of various microbes in the methane fermenter.

If a microbe is considered to be a living particle, a fine-particle technology approach aids elucidation of the microbial adhesion phenomenon. When microbes adhere to solid surfaces, an electrostatic, hydrophobic, or specific interaction between the surfaces of the solid and the microbial cells are related. In this study, the electrostatic and hydrophobic interactions were noted as the first step to clarify the mechanism of immobilization of various microbes in the liquid phase to a solid surface. Selective immobilization of aceticlastic methanogens (a rate-limiting step in the

---

[†] This paper, appeared originally in Japanese in J. Soc. Powder Technology, Japan, 43, 653-659 (2006), is published in KONA Powder and Particle Journal with the permission of the editorial committee of the Soc. Powder Technology, Japan

[1] 1-1 Gakuen-cho, Sakai, Naka-ku, Osaka, 599-8531, Japan
* Corresponding author
TEL: 072-254-9300 FAX: 072-254-9911
E-mail: nomura@chemeng.osakafu-u.ac.jp

methane fermentation process) to support materials was investigated using anaerobic sludge collected from an anaerobic treatment plant.

2. Process of Methane Fermentation

The methane fermentation process is an artificial ecosystem in which many types of microbes exist at high density. Anaerobic digestion of complex organic materials to produce methane comprises a cascade of biochemical conversions catalyzed by different physiological groups of interacting microbes (**Fig. 1**) [2]. Complex organic compounds are first hydrolyzed to simpler organic compounds before being fermented to volatile acids by acidogens. Volatile acids are subsequently converted to acetate and hydrogen gas by hydrogen-producing acetogens. Finally, acetate or hydrogen is converted to methane and carbon dioxide by methanogens [3]. In this process, acetate is the precursor for about 70% of the methane produced during the anaerobic digestion of complex organic materials [4]. Decarboxylation of acetate is the rate-limiting step in anaerobic digestion [1]. *Methanosaeta* and *Methanosarcina* species are the only methanogens capable of acetate catabolism [5]. High concentrations of acetate-utilizing methanogens must be immobilized in the anaerobic digester to achieve highly efficient anaerobic digestion.

3. Materials and Methods

3.1 Microbial cells and support materials

Five typical microbe species were selected to investigate the surface characteristics of microbes living in an anaerobic digester. Because the complex organic materials mainly comprised proteins, carbohydrates, and lipids, three acidogens that decompose these materials were enriched from anaerobic sludge. Pure cultures of *Methanosarcina barkeri* JCM 10043 and *Methanosaeta concilii* DSM 3671 were the acetate-utilizing methanogens. *Methanosarcina barkeri* isolated by Bryant et al. [6] was purchased from the Japan Collection of Microorganisms (Wako, Japan). *Methanosaeta concilii* isolated by Patel [7] was purchased from the Deutsche Sammlung von Mikroorganismen und Zellkulturen (Braunschweig, Germany). Anaerobic sludge was collected from the anaerobic treatment plant at the Yagi Bio-Ecology Center, Kyoto, Japan.

Three acidogens (proteolytic bacteria, amylolytic bacteria, lipolytic bacteria) were enriched at 37℃ and neutral pH in a specific medium supplemented with a specific substrate per 1 L of PGY medium (peptone 2 g/L, yeast extract 1 g/L, glucose 0.5 g/L). The specific substrate for proteolytic bacteria was skimmed milk (10 g/L), it was amylogen (2 g/l) for amylolytic bacteria, and it was tributyrin (5 g/L) for lipolytic bacteria. *Methanosarcina barkeri* and *Methanosaeta concilii* were grown under anaerobic condtions without shaking at 37℃ and neutral pH in pressure culture

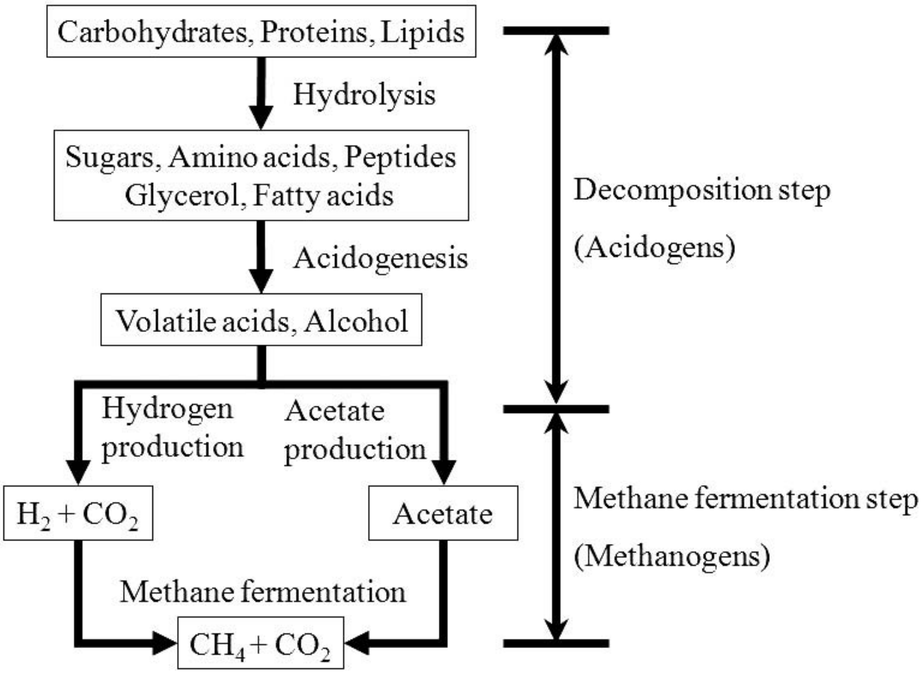

Fig. 1 Process of methane fermentation (schematic).

bottles sealed with a butyl rubber stopper and aluminum crimp seal [8]. A pure culture of *Escherichia coli* JM 109 was the control microbe.

Precultured microbes were filtered through ADVANTEC No.2 Toyo paper filter to remove residues. Cells were harvested by centrifugation at 10,000 rpm for 10 min, and washed thrice using 0.9% (w/v) sterile NaCl aqueous solution. Washed cells were resuspended in sterile solution to evaluate the physicochemical properties of microbial cells.

Two support materials were used. Bamboo charcoal is a hydrophobic and negatively-charged particle; alumina is a hydrophilic and positively-charged particle. The size of these support materials was about 5 mm in diameter.

3.2 Methane fermentation

Methane fermentation was done as follows. Four milliliters of anaerobic sludge and 1 mL of substrate solution were placed into serum bottles of capacity 21 mL (20-CV, Perkin Elmer). Bottles were capped with butyl rubber stoppers and crimped with aluminum seals. After sealing, headspaces of the bottles were purged using a deoxygenized gas pressure injector (IP-8, Sanshin) with an oxygen-free 80% N_2/20% CO_2 gas mixture at 120 kPa. Serum bottles were subsequently incubated at 37℃ under the N_2/CO_2 atmosphere. The initial concentration of the substrate was 20 mol/m^3 of the sodium acetate or methanol. Biogas production was determined by thermal conductivity (TCD) gas chromatography (GC-8APT, Shimadzu). Control cultures were prepared in the same way, but without dissolving substrates in the content of the bottle. Each experiment was done in triplicate.

3.3 Measurements of electrophoretic mobility (EPM)

The EPM of microbial cells was measured using an electrophoretic light-scattering spectrophotometer (ELS-800, Otsuka Electronics). Washed microbial cells were resuspended in phosphate buffer (pH 7.0; ionic strength, 100 mol/m^3).

3.4 Hydrophobicity measurements

Surface hydrophobicity of microbial cells was determined by microbial adhesion to hydrocarbon (MATH) assay [9]. Washed cells were resuspended in PUM buffer (pH 7.1, $K_2HPO_4 \bullet 3H_2O$ 22.2 g/L, KH_2PO_4 7.26g/L, Urea 1.8 g/L, $MgSO_4 \bullet 7H_2O$ 0.2 g/L). Subsequently, 0.4 mL of hydrocarbon (n-hexadecane) was added to a test tube containing 2.4 mL of washed cell suspension. Mixtures were vortexed uniformly for 2 min. The solution was allowed to stand for 15 min to ensure complete separation of the two phases. Absorbance of the aqueous cell suspension was measured at 400 nm using a spectrophotometer (UVmini-1240, Shimadzu). Hydrophobicity of microbial cells and support materials was calculated using the following equation:

$$F = (1 - A_t/A_0) \times 100 \qquad (1)$$

where A_0 is the initial absorbance of the microbial suspension before mixing, and A_t is the absorbance after mixing. Surface hydrophobicity of support materials was evaluated using the crushed ones by the same method.

3.5 Immobilization tests of microbes

Immobilization of microbes in anaerobic sludge on support material was carried out using the experimental design shown in **Fig. 2**. The immobilization test comprised three steps: immobilization of microbes, washing of support materials, and incubation using immobilized methanogens. Four milliliters of DSM 120 medium inoculated with 5.0% (v/v) of anaerobic sludge and 1.0 g of support material were placed into each of the 21-mL serum bottles. Bottles were subsequently capped with butyl rubber stoppers and crimped with aluminum seals. After sealing, headspaces of the bottles were purged with

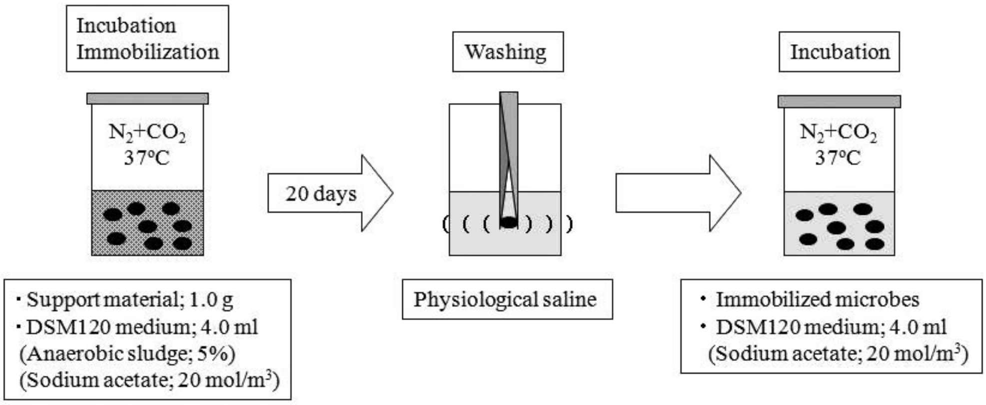

Fig. 2 Immobilization of microbes in anaerobic sludge and methane fermentation using immobilized microbes on support material.

oxygen-free N_2/CO_2 gas. Sodium acetate was used as substrate at an initial concentration of 20 mol/m^3. Serum bottles were incubated at 37℃ under anaerobic conditions. Biogas production was measured to check the activity in each of the three cultures. After saturation of biogas production (20 days' later), support materials were removed from the bottles. Support materials were washed with 0.9% (w/v) sterile NaCl aqueous solution to remove the residues on the support materials. Washed support materials were put into new 21-mL serum bottles filled with 4.0 mL of DSM 120 medium dissolved in 20 mol/m^3 of substrate. Cultures were grown at 37℃ in an atmosphere of N_2/CO_2. The substrates used were the same at the first and final steps. Biogas production was determined by TCD gas chromatography

3.6 Direct observation of microbes

Microbes immobilized onto support materials were observed directly using a field emission scanning electron microscope (JSM-6700F, JEOL). Samples were fixed with glutaraldehyde solution, and dehydrated in a graded series of acetone. Samples were washed in *tert*-butyl alcohol to remove acetone and frozen in a refrigerator. The frozen sample was freeze-dried using a vacuum freeze drier (ES-2020, Hitachi).

4. Results and Discussion

4.1 Methane fermentation

Fig. 3 shows methane production using different substrates with incubation time. Methane gas was generated from the start of incubation when sodium acetate was the substrate. Generation of methane gas was observed two days after the culture was started when methanol was used. *Methanosaeta* and *Methanosarcina* species are the only methanogens capable of acetate catabolism. *Methanosaeta* species can use acetate as sole growth substrate; *Methanosarcina* species can use acetate, H_2/CO_2, methanol, and methylamines as growth substrates [5]. When acetate and methanol are in the culture simultaneously, *Methanosarcina* species suppress the metabolizing of acetate, and use methanol preferentially [10]. *Methanosaeta* species were the dominant species in the anaerobic sludge used in our study.

Methane conversion ratio using different substrates with incubation time is shown in **Fig. 4**. The final ratio of methane conversion of acetate and methanol was 55% and 75%, respectively. The stoichiometric equations and free energy change $\Delta G^{0'}$ for standard conditions of substrates converted to methane are [11]:

$$CH_3COO^- + H_2O \rightarrow CH_4 + HCO_3^- \qquad (\Delta G^{0'} = -30\ \mathrm{kJ/mol}) \qquad (2)$$

$$4CH_3OH \rightarrow 3CH_4 + HCO_3^- + H^+ + H_2O \qquad (\Delta G^{0'} = -314\ \mathrm{kJ/mol}) \qquad (3)$$

The substrates of sodium acetate and methanol in the bottles were almost fully converted to methane gas because the theoretical methane conversion ratio based on carbon balance was 50% and 75%, respectively.

4.2 Electrostatic interaction

Table 1 shows the EPM of five typical microbes living in an anaerobic digester. EPM measurement was conducted in 100 mol/m^3 phosphate buffer at pH

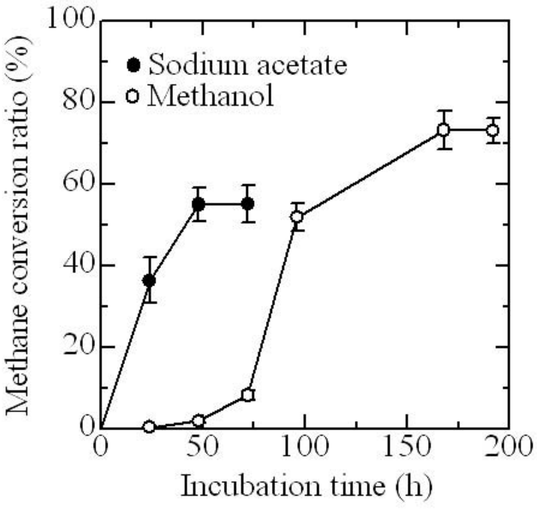

Fig. 3 Methane production using different substrates with incubation time.

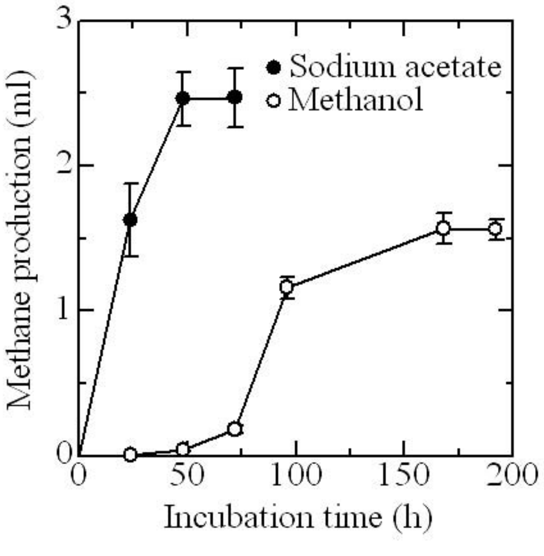

Fig. 4 Methane conversion ratio using different substrates with incubation time.

Table 1 Electrophoretic mobility of microbes measured by Laser Doppler method (pH 7.0; ionic strength, 100 mol/m^3)

	Sample	Electrophoretic mobility $\times 10^{-8}$ (m^2/V/s)	Zeta-potential (mV)
Methanogen	*Methanosaeta concilii*	0.09	1.2
	Methanosarcina barkeri	-1.60	-20.7
Acidogen	*Proteolytic bacteria*	-2.19	-28.3
	Amylolytic bacteria	-1.35	-17.5
	Lipolytic bacteria	-1.32	-17.2
Control	*Escherichia coli*	-1.45	-18.8
Support material	Bamboo charcoal	Negatively-charged	
	Alumina	Positively-charged	

7.0. Zeta potentials calculated by the Smoluchowski equation are shown in **Table 1**. Polymer chains grew on the surface of microbial cells like seaweed. Solution flow in this polymer layer cannot be disregarded, so the zeta potential calculated from the Smoluchowski equation is a reference value [12–14]. Proteolytic bacteria, amylolytic bacteria, and lipolytic bacteria enriched from the anaerobic sludge were found to be negatively charged. *Methanosarcina barkeri* was also negatively charged. In general, most microbial cells are negatively charged at neutral pH (e.g., *Escherichia coli*). The EPM of *Methanosaeta concilii* was significantly smaller than that of the three acidogens, as well as *Methanosarcina barkeri*. It was shown that *Methanosaeta concilii* was uncharged. This is a unique result compared with that from general microbes. There are only few kinds of microbes reported to be uncharged at neutral pH [15].

Based on EPM measurements, we can postulate the following. The acidogens and *Methanosarcina barkeri* easily adhere to alumina by electrostatic attractive forces, but not to bamboo charcoal. *Methanosaeta concilii* easily adheres to bamboo charcoal and alumina by van der Waals interaction because *Methanosaeta concilii* is uncharged.

4.3 Hydrophobic interaction

Table 2 shows the hydrophobicity of microbes and support materials measured by MATH method. The percentage of hydrophilic *Escherichia coli* adhering to hydrocarbon was 6.4%. The adherence of *Methanosaeta concilii*, *Methanosarcina barkeri* and the three acidogens was >50%. These five typical microbes were hydrophobic. The adherence of bamboo charcoal to n-hexadecane was 86.6%, and to alumina was 7.3%. It was confirmed that bamboo charcoal was hydrophobic, and alumina was hydrophilic.

Based on hydrophobicity measurements, we can postulate the following. The acidogens and *Methanosarcina barkeri* easily adhere to bamboo charcoal by hydrophobic interaction, but not to alumina. Taking EPM measurements into consideration, we can speculate that *Methanosaeta* species (the most important microbes in the anaerobic sludge) selectively adhere onto bamboo charcoal.

Table 2 Hydrophobicity of microbes and support materials measured by MATH method

	Sample	MATH *F* (%)
Methanogen	*Methanosaeta concilii*	66.7
	Methanosarcina barkeri	56.0
Acidogen	*Proteolytic bacteria*	49.7
	Amylolytic bacteria	73.7
	Lipolytic bacteria	67.1
Control	*Escherichia coli*	6.4
Support material	Bamboo charcoal	86.6
	Alumina	7.3

4.4 Immobilizing of acetate-utilizing methanogens

Fig. 5 shows methane production using immobilized microbes with incubation time. Methane production increased gradually when bamboo charcoal was used as a support material. Methane production was barely observed when alumina was used. These results indicated that acetate-utilizing methanogen adhered to the surfaces of bamboo charcoal, but not to alumina. This agreed well with the prediction led by the measurements of EPM and hydrophobicity of five typical microbes.

Fig. 6 shows scanning electron microscope images of microbes and immobilized microbes on support material. Many rod-shaped bacteria were in the culture solution (**Fig. 6a**), but the rod-shaped Methanosaeta-like species adhered to bamboo charcoal (**Fig. 6b**), and microbes barely adhered to alumina (**Fig. 6c**). *Methanosaeta* species were found to selectively adhere to bamboo charcoal because the proportion of *Methanosaeta* species on bamboo charcoal was obviously higher than that in the culture solution.

Microbial adhesion will be energetically more

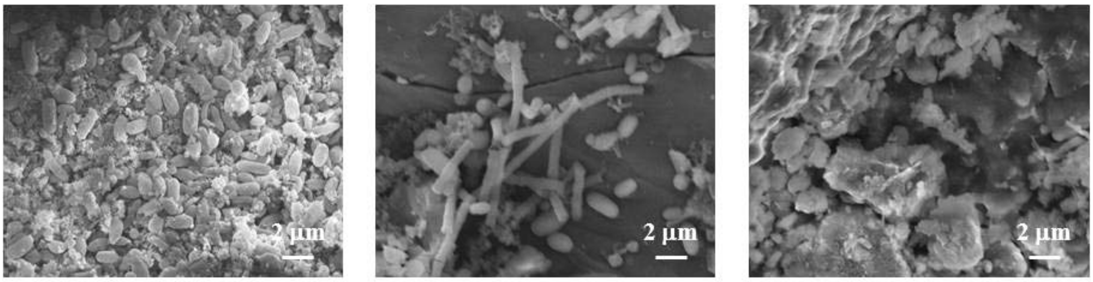

(a) Microbes existed in anaerobic sludge

(b) Immobilized microbes on bamboo charcoal

(c) Immobilized microbes on alumina

Fig. 5 Methane production using immobilized microbes with incubation time.

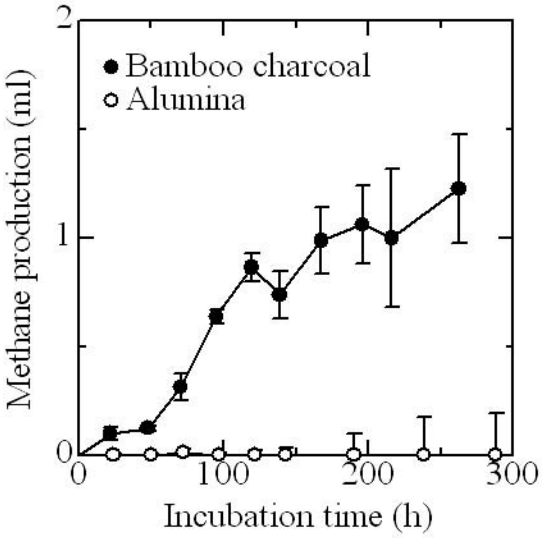

Fig. 6 Scanning electron microscope images of microbes and immobilized microbes on support material.

favorable because the surface tension of the solid increases if the surface tension of the liquid is larger than that of the bacterium [16]. Based on the above reports and the immobilization test, we can postulate the following. The electrostatic repulsive force between *Methanosaeta* species and bamboo charcoal is barely present. *Methanosaeta* species approach bamboo charcoal by van der Waals force and adhere to bamboo charcoal by hydrophobic attractive force. Because the microbes except for *Methanosaeta* species are negatively charged and hydrophobic, adhesion to bamboo charcoal can be suppressed by the electrostatic repulsive force, but a part of the microbes adhered by the hydrophobic attractive force. The reason why microbes hardly adhered to alumina is thought to be because microbes can approach alumina by the electrostatic attractive force, but cannot stably immobilize onto the surface due to the difference in their hydrophobicity. *Methanosaeta* species is the most important microbe in the methane fermentation, and is uncharged and hydrophobic. Microbes except for *Methanosaeta* species in the fermenter are negatively charged and hydrophobic. The hydrophobic and negatively charged support material that can suppress immobilization of microbes except for *Methanosaeta* species is suitable for selective immobilization of *Methanosaeta* species.

5. Conclusions

Selective immobilization of aceticlastic methanogens, which was a rate-limiting step in the methane fermentation process, onto support materials was investigated using anaerobic sludge. Acidogens cultivated selectively from the anaerobic sludge and *Methanosarcina barkeri* JCM 10043 were negatively charged and hydrophobic. *Methanosaeta concilii* DSM 3671 was uncharged and hydrophobic. This is a unique result compared with that seen in general microbes. Immobilized microbes on support materials (bamboo charcoal or alumina) were incubated with sodium acetate. Methanogens were dramatically immobilized to bamboo charcoal (negatively charged and hydrophobic) in contract to alumina (positively charged and hydrophilic). It was also proven that *Methanosaeta*-like microbes were immobilized to bamboo charcoal. These results indicate that the hydrophobic and negatively charged support material that can suppress the immobilization of microbes except for *Methanosaeta* species is suitable for selective immobilization of *Methanosaeta* species, which is the most important microbe in methane fermentation.

Acknowledgment

This work was supported by a Grant-in-Aid for

21st Century, COE program, 24403, E-1 (Science and Engineering for Water-Assisted Evolution of Valuable Resources and Energy from Organic Wastes).

References

1) Speece, R. E. (1996): “Anaerobic Biotechnology for Industrial Wastewaters”, p.25, p.127, Archae Press.
2) McCarty, P. L., and Smith, D. P. (1986): “Anaerobic Wastewater Treatment”, Environ. Sci. Technol., **20**, pp.1200-1206.
3) Murata, T. (2000): “Haikibutsu no Shigenka Gijutsu”, p.32, Ohmsha.
4) Jeris, J. S., and McCarty, P. L. (1965): Biochemistry of Methane Fermentation Using C14 Tracers, J. Wat. Poll. Control Fed., **37**, p.178-192.
5) Koga, Y. (1988): “Kosaikin”, p.17, Tokyo Daigaku Shuppan.
6) Bryant, M. P., and Boone, D. R. (1987): Emended Description of Strain MST (DSM800T)-The Type Strain of Methanosarcina-barkeri, Int. J. Syst. Bacteriol., **37**, pp.169-170.
7) Patel, G. B. (1984): Characterization and Nutritional Properties of Methanothrix-concilii sp-nov-A Mesophilic, Aceticlastic methanogen, Can. J. Microbiol., **30**, pp.1383-1396.
8) Sowers, K. R., and Schreier, H. J. (1995): “Archaea A Laboratory Manual methanogens”, p.15, Cold Spring Harbor Laboratory Press.
9) Bellon-Fontaine, M. N., Rault, J. and vanOss, C. J. (1996): Microbial Adhesion to Solvents-A Novel Method to Determine the Electron-Donor/Electron-Acceptor or Lewis Acid-Base Properties of Microbial Cells, Colloids and Surface B, **7**, pp.47-53.
10) Ueki, K., and Nagai, S. (1993): “Kenki Biseibutsugaku”, p.95, Yokendo.
11) McCarty, P. L. (1972): “Water Pollution Microbiology”, p.91, Wiley.
12) Ohshima, H., and Kondo, T. (1989): Approximate Analytic-expression for the Electrophretic Mobility of Colloidal Particles with Surface-charge Layers, J. Colloid Interface Sci., **130**, pp.281-282.
13) Ohshima, H., and Kondo, T. (1991): On the Electrophoretic Mobility of Biological Cells, Biophys. Chem., **39**, pp.191-198.
14) Ohshima, H., Nakamura, M. and Kondo, T. (1992): Electrophretic Mobility of Colloidal Particles Coated with a Layer of Adsorbed Polymers, Colloid Polym. Sci., **270**, pp.873-877.
15) Sharma, P. K., Das, A., Rao, K. H. and Forssberg, K. S. E. (2003): Surface Characterization of Acidithiobacillis ferrooxidans Cells Grown under Different Conditions, Hydrometallurgy, **71**, pp.285-292.
16) Busscher, H. J., Weerkamp, A. H., van der Mei, H. C., van Pelt, A. W., de Jong, H. P. and Arends, J. (1984): Measurement of the Surface Free Energy of Bacterial Cell Surfaces and its Relevance for Adhesion, Appl. Environ. Microbiol., **48**, pp.980-983.

Nomenclature

A_o	Initial absorbance of cell suspension (400 nm)	[–]
A_t	Absorbance of cell suspension after vortex mixing (400 nm)	[–]
F	Adhesion ratio of cell to organic solvent	[%]
$\Delta G^{0'}$	Standard change of free energy	[kJ/mol]

Author's short biography

Toshiyuki Nomura

Dr. Toshiyuki Nomura is an Associate Professor of the Department of Chemical Engineering at Osaka Prefecture University. He received his B.S. in 1993 and M.S. in 1995 degrees from the Department of Chemical Engineering at Kyoto University. He obtained the Doctor degree of Engineering at Osaka Prefecture University in 1999. Currently, he is an editor of Journal of the Society of Powder Technology, Japan and Journal of Advanced Powder Technology. His major research interests are microbial adhesion and its application, shape and size control of nanoparticles, and microcapsule preparation.

Takanori Nagao

Mr. Takanori Nagao received his B.S. in 2004 and M.S. in 2006 from the Department of Chemical Engineering at Osaka Prefecture University. Since 2006, he has been working at Aica Kogyo Co., Ltd.

Akinori Yoshihara

Mr. Akinori Yoshihara received his B.S. in 2006 and M.S. in 2008 degrees from the Department of Chemical Engineering at Osaka Prefecture University. Since 2008, he has been working at Sumitomo Bakelite Co., Ltd.

Hayato Tokumoto

Dr. Hayato Tokumoto was appointed in 2005 to a Research Associate in the Department of Chemical Engineering at the Osaka Prefecture University. He received his Doctor degree in Division of Biology & Geosciences, Faculty of Sciences at Osaka City University in 2002. He has as a background in biology, physiology, biological organic chemistry and biochemistry.

Yasuhiro Konishi

Yasuhiro Konishi is a professor of chemical engineering at Osaka Prefecture University, where he earned his doctor's degree in 1983. Konishi joined the faculty of the Department of Chemical Engineering at Osaka Prefecture University in 1983, and he has spent 25 years in research and lecturing. Also, he was a postdoctoral scholar in the Department of Materials Science and Mineral Engineering at the University of California at Berkeley from 1988 to 1989. Konishi's research focuses on biochemical engineering in the processing and behavior of materials, natural minerals, wastes and effluents.

Differential Mobility Analysis of Aerosols: A Tutorial[†]

Richard C. Flagan
Division of Chemistry and Chemical Engineering 210-41
California Institute of Technology[1]

Abstract

Differential mobility analysis enables particle size distribution measurements of submicron aerosols with resolution well beyond that attainable in other size regimes of aerosols or other particulate media. The pages that follow present a tutorial introduction to differential mobility analysis, describing the underlying physics, the differential mobility classifiers and associated detectors, data analysis, data presentation, and some of the challenges in using this powerful measurement method.

Keywords: aerosol, mobility, size distribution, differential mobility analyzer, instrumentation

Introduction

Suspensions of fine particles in gases, known as aerosols, arise in many contexts. Aerosol reaction technologies produce millions of tons of particulate products each year; these include major commodity chemicals such as carbon black, titanium dioxide, fume silica, and a wide range of more specialized products. Aerosol synthesis is central to a number of developments in the burgeoning arena of nanotechnology, providing an efficient route for the synthesis of nanoparticles with control over size, composition, structure, and morphology.

Fine particles are also released into the air inadvertently or form as a result of atmospheric physical and chemical transformations. Epidemiological studies reveal profound adverse health effects of exposures to particles small enough to penetrate into the lower airways, i.e., those smaller than about 2.5 μm aerodynamic diameter - so-called PM2.5 (Pope, 1996; Dockery et al., 1993; Donaldson et al., 2000; Donaldson et al., 2002). Perhaps surprisingly, the most serious of those outcomes are not direct respiratory effects, but rather an increased incidence of a range of cardiovascular disease exacerbations that have been related to reactive oxidative stress induced by the fine particles. Neurological problems have also been linked to ultrafine particle exposures. For example, some welders exhibit manganism, a neurological disease with symptoms similar to Parkinson's disease, at a relatively young age. Nanoparticles have been observed to translocate across the olfactory mucosa, and subsequent migration along the olfactory neurons and into the olfactory cortex (Oberdorsteret et al., 2004). Nanoparticles may, thus, enter the brain without having to cross the blood-brain barrier, where they may contribute to such health outcomes.

To understand both the processes by which commercial fine particles are produced, and the adverse effects that may result in the workplace or in the environment, the nature of the particles must be known. The distribution of particles with respect to size is one of the most basic measurements. The primary method for determining the particle size distribution of particles smaller than 1mm diameter is differential mobility analysis, a technique that had its beginnings in the late nineteenth century (Flagan, 1998), but that developed into a robust measurement technology in the last quarter of the twentieth century, due in large part to the introduction of commercial instruments. A number of additional manufacturers have introduced differential mobility analyzers to the marketplace in the last few years. Moreover, differential mobility analyzers continue to undergo rapid development in the research community so the term "differential mobility analyzer" no longer refers to a specific instrument, but rather to a broad class of related devices.

[†] Accepted : July 2, 2008

[1] 1200 East California Blvd, Pasadena, CA 91125, USA
TEL: (626) 395-4383, FAX: 1-626-568-8743
E-mail: flagan@cheme.caltech.edu

It should be noted that the device that is commonly labeled a “differential mobility analyzer” is not a stand-alone instrument; instead, it is actually a classifier. Differential mobility analysis requires that the classifier be interfaced to a detector, a flow control system, and a data acquisition system to enable a measurement to be made. Following traditional nomenclature, in the discussion that follows the abbreviation “DMA” will be taken to refer to the classification component of a differential mobility analysis system.

Differential mobility analysis combines a particle classifier that transmits particles within a narrow interval of sizes from an initially polydisperse aerosol, and a detector that counts the particles within that differential size interval. With computer control of flows and voltages within the classifier, and sensitive, continuous-flow particle detection, differential mobility analysis systems can be made sufficiently robust to enable unattended operation for extended periods of time and even in the challenging measurement environments encountered in airborne measurements.

To date, differential mobility analysis has been used primarily to study atmospheric particles and in laboratory studies. Due to its cost, complexity, and some challenges in its application, it has seen relatively little use in aerosol process technology, even though it affords an opportunity to monitor the quality of product particles in real time with size resolution that is unattainable in most other particle characterization technologies. The pages that follow will present a tutorial introduction to this powerful measurement technology. This tutorial will not attempt an exhaustive review; the interested reader may find that in a historical survey by the author (Flagan, 1998), and numerous other review papers (e.g., McMurry, 2000). Instead, this tutorial will introduce the underlying principals, details of operation, data analysis techniques, and challenges in measurement.

Aerosol Particle Size Classification: Fundamentals

Separation of aerosol particles into size classes is accomplished by introducing forces that balance or counteract the forces that are inherent to the particle, inertia and aerodynamic drag. The inertial force is simply the mass times the acceleration,

$$\vec{F_i} = m\frac{d\vec{v}}{dt} \tag{1}$$

The drag force is a function of particle size and shape. For a spherical particle that is much larger than the mean free path of the gas molecules, and that is moving at a low velocity relative to the surrounding gas, the drag force is given by Stokes Law:

$$\vec{F_d} = 3\pi\mu d_p(\vec{u} - \vec{v}) \tag{2}$$

where μ is the viscosity of the gas, and d_p is the particle diameter. Stokes law holds so long as the Reynolds number describing the motion of the particle relative to the gas (velocity u), $\text{Re}=|r\ (u\text{-}v)\ d_p\,/\,\mu\,|$, is much smaller than unity. For particles that are sufficiently small relative to the mean free path of the gas, λ, the gas no longer behaves as a continuum fluid. A slip correction factor is introduced to account for particle slip; the drag force then becomes

$$\vec{F_d} = \frac{3\pi\mu d_p}{C(\text{Kn})}(\vec{u} - \vec{v}) \tag{3}$$

where $\text{Kn}=2\,\lambda/d_p$ is the Knudsen number of the particle. The slip correction is given by an empirical equation of the form

$$C_c = 1 + \text{Kn}(\alpha + \beta e^{-\gamma/\text{Kn}}) \tag{4}$$

where $\alpha=1.257$, $\beta=0.4$, and $\gamma=1.1$.

A convenient short-hand for the evaluation of the drag force is to define the mechanical mobility of the particle, $B = C(\text{Kn})/3\rho\mu d_p$, as the drag force per unit of relative velocity between the gas and the particle. Equating the inertial and drag forces, and dividing by the particle mass, we find the particle equation of motion,

$$\frac{d\vec{v}}{dt} = \frac{\vec{u} - \vec{v}}{mB} = \frac{\vec{u} - \vec{v}}{\tau_a} \tag{5}$$

The product mB has units of time, and can be identified as an aerodynamic relaxation time, τ_a. This is the characteristic time for a particle's motion to relax to equilibrium with that of the gas following a disturbance. It provides the fundamental property that can be used to separate particles that are large enough, when subjected to disturbances that are brief enough that inertial effects are important. Under normal ambient atmospheric conditions, the aerodynamic relaxation time for a 1μm diameter particle with unity specific gravity is about 3.6×10^{-6}s, and the aerodynamic relaxation time decreases rapidly with decreasing particle size below this value.

Although inertial separations of small particles are possible by deflecting high velocity flows over very small dimensions, imposition of electrostatic forces provides a more convenient method for high resolution separations of such small particles. This forms the basis for differential mobility analysis. A particle that carries charge q exposed to an electric field experiences a force

$$\vec{F}_e = q\,\vec{E} \tag{6}$$

Equating that force to the drag force yields the terminal electrophoretic migration velocity

$$\vec{v}_e = q\,B\vec{E} = Z\vec{E} \tag{7}$$

where Z is the electrical mobility of the particle (migration velocity per unit of electric field; units: $m^2V^{-1}s^{-1}$). Because the aerodynamic relaxation time for submicron particles is so short and the terminal migration velocities are relatively small for the conditions of differential mobility analysis, it is not usually necessary to consider the transient inertial in mobility analysis.

Thus, we see that electrophoretic migration of charged aerosol particles does not depend upon the particle mass. Only the drag force and electrostatic forces influence the measurement. A very special case arises when the charge on the particle is one elementary charge, i.e., $q = \pm e$. Then the electrostatic force acting on the particle is known exactly, so measurement of the migration velocity directly reveals the mechanical mobility B. This in turn reveals the particle diffusivity since, by the Stokes-Cunningham-Einstein relation, the particle diffusivity is

$$D = BkT \tag{8}$$

The primary mechanism of respiratory tract deposition of inhaled particles smaller than a few tenths of a micron in diameter is diffusion, so determination of the electrical mobility directly measures a key parameter that governs their potential health effects. Mobility analysis does not directly measure particle size; instead, it measures a very important transport property, B. If one knows, or assumes the particle shape, the particle size can be calculated from the mobility.

Differential Mobility Analysis

We seek to use a measurement of how fast particles migrate in a well-defined electric field to determine the electrical mobilities of those particles. This is accomplished using an classifier that is commonly called a differential mobility analyzer (DMA). The DMA consists of a flow channel between two electrodes. A small aerosol flow is introduced near one of those electrodes; a larger sheath flow fills the remainder of the channel. As the combined gas flows carry the particles through the channel, a voltage difference between the electrodes drives particles of appropriate polarity across the channel. In differential mobility analyzers, a small flow that exits through a downstream port in the counter electrode extracts particles that have mobilities in a narrow range. In an alternate configuration, the counter electrode is divided into a number of segments, each of which is connected to an electrometer that monitors the charge that accumulates as particles deposit, thereby again determining the numbers of particles within a narrow size interval.

DMAs have been built with a number of different geometries. By far the most common geometry is the cylindrical DMA (cDMA) in which the classification takes place in the flow between concentric cylinders (Knutson and Whitby, 1975a; Winklmayr et al., 1991; Chen et al., 1998; Heim et al., 2005; Rosell-Llompart, et al., 1996). Classification is also performed using radial flow between parallel disk electrodes in the so-called radial DMA (rDMA) (Zhang et al., 1995; Fissan et al., 1996). Although rectangular channels appear in the early literature, edge effects reduce the resolution of such DMAs. Nonetheless, the ability to miniaturize such devices has led to recent developments with this geometry (Zhang and Wexler, 2006; Kulkarni and Wang, 2006).

To illustrate the fundamental operation of the DMA, we consider the classical Knutson and Whitby (1975a) cylindrical DMA design (KW-cDMA), long the only commercially available DMA and still the most common instrument. Other DMAs differ in their design details, and somewhat in performance, but the basic operation is the same for all of designs.

Fig. 1 illustrates the DMA schematically. Aerosol enters the classification region through a slot in one electrode. For the DMA to achieve the theoretical performance described below, some mechanism must ensure that the aerosol flow is uniform over the entire length of the slot. In the KW-cDMA, a narrow annulus provides the pressure drop required to ensure uniform flow. Other instruments use a tangential inlet into an entrance channel to achieve uniform flow with low diffusional losses of fine particles, following the approach of Winklmayr et al., (1991). The sheath flow fills the space between the two electrodes. Again, some form of flow distributor is needed to ensure uniform, laminar flow; this is often a screen. A converging flow entrance region may be used to further improve flow uniformity. This can be taken to extreme limits in efforts to maximize resolution in the classification of particles of sizes approaching the molecular regime.

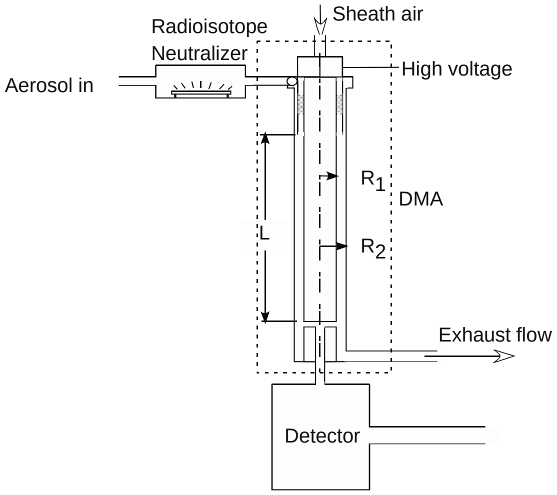

Fig. 1 Schematic illustration of a cylindrical differential mobility analyzer measurement system. The aerosol first passes through a charging system, typically a so-called neutralizer using a radioisotope source to produce gas ions that attach to the particles. The aerosol then enters the differential mobility analyzer that transmits particles within a narrow range of mobilities across a sheath flow to a classified sample outlet port; the remaining flow is exhausted. The classified particles are then counted using a condensation particle counter or electrometer.

Differential Mobility Analysis: Theory

Two flows enter the DMA classification region, and two exit from it. The entering flows are the aerosol flow, with a volumetric flow rate of Q_a, and the sheath flow, Q_{sh}. The exiting flows are the classified sample flow, Q_c, and the exhaust flow, Q_e. Two flow rate ratios characterize the instrument,

$$\beta = \frac{Q_a + Q_c}{Q_{sh} + Q_e} \text{and } \delta = \frac{Q_c - Q_a}{Q_c + Q_a}. \tag{9}$$

β denotes the aerosol flows to that of the larger sheath and exhaust flow. The resolving power of the DMA will be shown to vary inversely with β. δ reveals imbalance between the two aerosol flows. In typical DMA operation, β^{-1} is between about 4 and 20, although some instruments and measurement scenarios favor more extreme values. For many measurements, β^{-1}=10 has traditionally been used.

The reasons for describing the performance in terms of β^{-1}can be seen by examining the trajectories of particles through the DMA in the kinematic (nondiffusive) limit. The DMA is set to classify particles with a nominal mobility, Z^*, corresponding to a particle that enters at the centroid of the incoming aerosol flow, and exits at the centroid of the outgoing classified aerosol flow. Such a particle must traverse one-half of the aerosol and classified flows and the entire sheath flow as it is carried through the classifier from the aerosol entrance port to the classified aerosol outlet port, i.e., it must cross a region through which a volumetric flow rate of Q_{sh} + $(Q_a + Q_c)/2$ passes. The corresponding mobility is

$$\text{cDMA: } Z^*_{cDMA} = \frac{Q_{sh} + Q_e}{r\pi LV} \ln \frac{R_2}{R_1}$$

$$\text{rDMA: } Z^*_{rDMA} = \frac{(Q_{sh} + Q_c)b}{2\pi(R_2^2 - R_1^2)V} \tag{10}$$

where V is the voltage difference between the two electrodes; dimensions for the cDMA are illustrated in **Fig. 1**; for the rDMA, R_2 and R_1 denote the radii of the aerosol entrance slot and the classified sample extraction port, respectively ($R_2 > R_1$), and b is the separation distance between the parallel disk electrodes.

Particles of slightly higher and lower mobilities will also be transmitted from the aerosol flow to the classified aerosol flow. In the kinematic limit, upper and lower bounds on transmitted particle mobility are determined by, $Z_{min}=Z^*(1-\beta)$, and $Z_{max}=Z^*(1+\beta)$ if the flows are balanced (δ=0). The probability that a particle of mobility Z will be transmitted from the aerosol flow to the classified aerosol flow when the instrument is set to classify particles of mobility Z^* is called the transfer function of the classifier and denoted $\Omega(Z, Z^*)$. The kinematic limit transfer function assumes a discontinuous form, that is triangular if the flows are balanced, but that may assumes a trapezoidal form when flows are imbalanced (Knutson and Whitby, 1975a), i.e.,

$$\Omega_K(Z, Z^*) = \max\left\{0, \min\left[1, \frac{\frac{Z}{Z^*} + \beta - 1}{\beta - \beta\delta}, \frac{1 + \beta - \frac{Z}{Z^*}}{\beta - \beta\delta}\right]\right\} \tag{11}$$

The triangular transfer function that is found when the flows are balanced has special significance: the ratio of the mobility at the peak of that transfer function to the full width at one half of that maximum value is equal to β^{-1}. Thus, the flow rate ratio serves as a figure of merit for the ideal DMA against which real classifiers can be compared. Using terminology analogous to a range of spectroscopies, this figure of merit has been called resolving power or resolution in the kinematic limit, i.e., $R_k = \beta^{-1}$.(Flagan, 1999).

The kinematic limit is an approximation that is only approached when an ideal DMA is operated at the highest possible voltages. As the voltage is reduced, Brownian diffusion broadens the transfer function, and reduces the peak transmission efficiency. During classification, a particle must migrate the across the gap between the electrodes. The particle migrates at a velocity $v_e=ZE$ where $E=V/r\ln(R_2/R_1)$ for a cylindrical DMA with inner and outer radii of R_1 and R_2, respectively. For a radial DMA with a spacing between electrodes of b, $E=V/b$. To examine the extent to which diffusion allows particles to deviate from their kinematic trajectories through the classification region, we examine the ratio of transport by electrophoretic migration to that by diffusion. This ratio forms a migration Peclet number,

$$\mathrm{Pe}_{mig} = \frac{bv_e}{D} = \frac{vZE}{D}. \tag{12}$$

Recalling that the electrical mobility, $Z=qB$, and particle diffusivity, D, are related through the Stokes/Cunningham/Einstein relationship, Eq. (8), and using the appropriate form for the electric field, we find

$$\mathrm{Pe}_{mig,cDMA} = \frac{|n_e|V}{kT}\frac{1-\frac{R_1}{R_2}}{\ln\frac{R_2}{R_1}}$$

$$\text{and} \tag{13}$$

$$\mathrm{Pe}_{mig,rDMA} = \frac{|n_e|eV}{kT}$$

where we have restated the charge on the particle in terms of the number of elementary charges, $q=|n_e|e$. For singly charged particles, $|n_e| =1$. Then, the relative importance of Brownian diffusion in transport of charged particles through the classification region of the a DMA is determined by

$$\frac{eV}{kT}f(\text{geometry}).$$

eV is simply the electrostatic potential energy of the particle in the electric field of the DMA; kT is the thermal energy of the particle. The geometry factor is of order unity, and varies only slightly from one DMA design to another, although there do exist a few ways to achieve modest improvements in DMA performance through design optimization.

Thus, the operating voltage of a DMA is the primary factor that determines whether diffusion will influence the classification. Turbulence, misalignment of key components, nonuniform distribution of the aerosol flow around the entrance port, or other factors may cause additional degradation. For any DMA and flow rate ratio, β, there exists a minimum voltage below which diffusion will degrade the classification quality.

An exact derivation of the transfer function that includes the effects of diffusion is not possible. Some authors have reported the effects of diffusional broadening of the transfer function in terms of a fictional, broadened triangular transfer function. While expedient, this approach hides the physical factors that influence the broadening, and that can be understood through more rigorous modeling. (Stolzenburg, 1988; see also Flagan, 1999 or Hagwood et al., 1999) provides an elegant semi-analytical derivation of the diffusion-broadened DMA transfer function that can readily be evaluated in terms of parameters that are readily interpreted physically. The Stolzenburg diffusion-broadened transfer function is

$$\begin{aligned}\Omega_d &= \frac{\tilde{\sigma}}{\sqrt{2}\beta(1-\delta)}\left[\mathcal{E}\left(\frac{\tilde{Z}-(1+\beta)}{\sqrt{2}\tilde{\sigma}}\right)+\mathcal{E}\left(\frac{\tilde{Z}-(1-\beta)}{\sqrt{2}\tilde{\sigma}}\right)\right.\\ &- \left.\mathcal{E}\left(\frac{\tilde{Z}-(1+\beta\delta)}{\sqrt{2}\tilde{\sigma}}\right)-\mathcal{E}\left(\frac{\tilde{Z}-(1-\beta\delta)}{\sqrt{2}\tilde{\sigma}}\right)\right]\end{aligned}$$

where

$$\mathcal{E}(x) = \int_0^x \operatorname{erf}(u)du = x\operatorname{erf}(x) + \frac{1}{\sqrt{\pi}}e^{-x^2}. \tag{15}$$

and $\tilde{\sigma}$ is a dimensionless broadening parameter that is evaluated as an integral along the particle migration path, i.e.,

$$\tilde{\sigma} = \left(\frac{4\pi}{Q_{sh}+Q_e}\right)^2\int_{entrance}^{exit} 2\mathcal{D}r^2v^2dt = \frac{G}{\mathrm{Pe}_{mig}}\frac{Z}{Z^*} \tag{16}$$

By assuming either a uniform velocity over the gap between the electrodes (plug flow), or fully developed laminar flow with a parabolic (rDMA) or nearly parabolic (cDMA) velocity profile, one can analytically derive the broadening parameter. Generally, the laminar flow version best matches observed DMA performance since DMAs are operated in the laminar flow regime. For a number of years, only a few DMA designs were available, and a simple table would suffice to summarize DMA performance (see Flagan, 1999). Several new DMA designs have been introduced recently, and designs continue to evolve; **Fig. 2** shows the variation of G with the key dimensionless parameters that describe cylindrical DMA performance, along with the parameters characteristic of a number of existing DMA designs. Most of the DMAs lie within a narrow range of G values.
Fig. 3 shows the transfer function for several different values of Pe_{mig} (and V for the traditional KW-cDMA), and compares the result with the kinematic transfer functions. Equation (14) asymptotically ap-

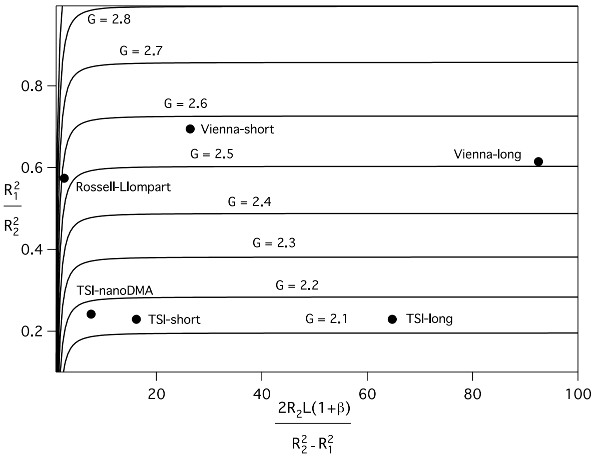

Fig. 2 Contour plot of the variation of G with dimensionless design parameters for the cylindrical DMA operated in the laminar flow regime at a flow rate ratio of β =0.1.

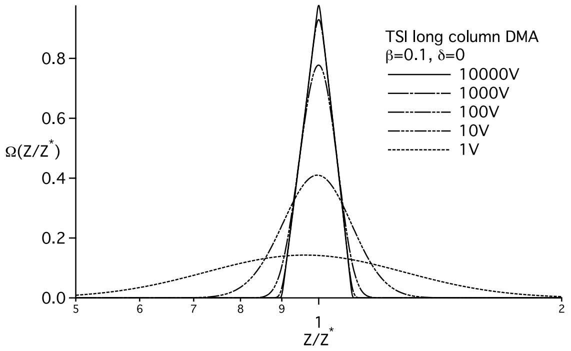

Fig. 3 Stolzenburg (1988) transfer function for the TSI-long column DMA operated at a flow rate ratio of β =0.1.

proaches the triangular transfer function predicted in the kinematic limit at high voltages, as expected, but approaches a Gaussian distribution as expected for diffusion dominated migration in the low voltage limit.

A more convenient way to illustrate the performance of the DMA is to define a figure of merit for its classification efficacy. Following approaches used in a wide range of spectroscopies, we define the resolving power or resolution of the DMA for particle classification as the ratio of the mobility at the peak of the transfer function, to the full-width of the transfer function where the transmission efficiency is one-half of the peak value. As previously noted, this definition of the DMA mobility resolution implies that, in the kinematic limit, $R_K= \beta^{-1}$. The DMA resolution is plotted as a function of voltage for a number of DMA designs in **Fig. 3**. Little difference is seen between the performance of different DMA geometries. Note also that, for different flow rate ratios, the resolution closely approximates the kinematic limit, so long as the voltage is greater than a critical value, and that for all flow rate ratios, the resolution approaches a single diffusional limit for low voltages. That limit can be approximated as

$$\mathcal{R}_D \approx 0.425\left[\frac{\mathrm{Pe}_{mig}}{G}\right]^{\frac{1}{2}} \tag{17}$$

Equating the resolution at the kinematic limit with that in the diffusive limit provides an estimate of the voltage below which diffusional effects dominate, i.e., for balanced flows,

$$V_{\text{diff}} = \frac{0.14G}{\beta^2 f} \tag{18}$$

where f is a factor that accounts for nonuniformities in the electric field. For the rDMA, f=1, while, for the cDMA, $f=(1-R_1/R_2)/\ln(R_2/R_1)$.

For most DMA designs, electric fields greater than about 10 kV/cm lead to electrostatic breakdown. The resulting arcs produce ions and particles that confound measurements and that may damage expensive components of the DMA. If the DMA is operated at altitude, at reduced pressure, or at high relative humidity, the field strengths that can be tolerated diminish further. Most DMAs employ electrode spacings of about 1 cm, so voltages are typically limited to less than 10 kV. The resolution of the DMA is, therefore, limited by electrostatic breakdown. Moreover, as one attempts to increase the resolution of the DMA, the measurement size range decreases rapidly. While one might achieve a resolution of slightly greater than 100, particles of different mobilities could only be measured with that high resolution by varying the flow rates through the classifier, either in discrete steps for different size ranges, or by continuously scanning flow through flow DMA as proposed by Collins et al. (2000).

Particle Charging

Differential mobility analysis is commonly used to measure particle size distributions, but this requires knowledge of the probability distribution of charge states as a function of particle size, i.e., $P(n_e,d_p)$ denotes that a particle of size d_p carries n_e charges. The simplest model of aerosol particle charging is that of the Boltzmann equilibrium charge distribution. Unfortunately, that model is not applicable for particles in low-pressure gases. For particles in aqueous solution, the charge state is a well-defined state of charge equilibrium that is achieved as a result of rapid, reversible reactions between solute ions and the particle surfaces. Low temperature gases do not contain sufficient ion concentrations to enable such rapid charge transfer reactions; nor are the charge transfer "reactions" reversible. A particle that carries n_e charges can increase or decrease charge only by attachment of a gas ion of appropriate polarity. The charge state of an aerosol is, therefore, a function of its history (initial charge distribution) and its exposure to gas ions.

Because the charge state or history is not generally known at the point where the aerosol is sampled, quantitative determination of the fraction of particles that exist in a given charge state can only be achieved by altering the charge state to produce a known charge distribution. This is most commonly accomplished by exposing the aerosol to an ion cloud that is overall electrically neutral, but that contains a large balanced concentration of positive and negative ions. This charge state is achieved by passing the aerosol through a bipolar (or ambipolar) diffusion charger that is, somewhat confusingly, called an *aerosol neutralizer*. Within this device, an electrically neutral ion cloud is usually produced by exposure of the gas to ionizing radiation from a radioactive source, although alternatives to the use of the radioactive source are under development. With adequate time of exposure to this ion cloud, and for a number concentration of particles that is not too large, a steady-state charge distribution is asymptotically approached. This distribution is not truly electrically neutral; because the positive and negative ions have different mobilities and diffusivities, a slight charge imbalance results. The precise balance depends on the composition of the gas in which ionization performed. Most studies involve charging in air, wherein negative ions have higher mobility than do positive ones. For this reason, the "neutralized" aerosol has a slight excess of negatively charged particles, as illustrated in **Fig. 4**. Below about 100 nm diameter, few particles carry more than one charge, and only a small fraction carry any charge. As particle size increases above this threshold, the probability that a particle will acquire more than one charge increases to the point that, at 1 μm diameter, approximately 13% of the particles carry two charges. This imposes an important limit on the use of differential mobility analysis. The method is generally applied only to particles smaller than about 1 μm diameter.

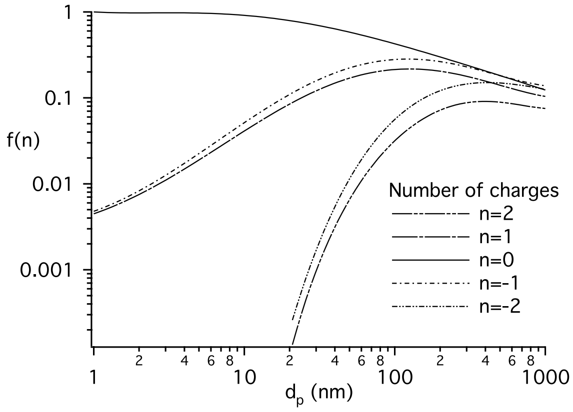

Fig. 4 Charge distribution for bipolar charging in ambient pressure air calculated using the Wiedensohler (1988) approximation to the Fuchs charge distribution.

The detailed theory of aerosol charging was developed by Fuchs (1963), and extended by Hoppel and Frick (1990). While the full theory is beyond the scope of this tutorial, Wiedensohler (1988) provides a readily evaluated expression for the fraction of particles that carry k charges in the steady-state charge distribution, i.e.,

$$f(k) = 10^{\left[\sum_{i=0}^{i=5} a_i(k)(\log_{10} D_{nm})^i\right]}, \qquad (19)$$

where the coefficients $a_{i,k}$ were empirically fitted to the Fuchs solution. Those coefficients are summarized in **Table 1**. **Fig. 4** displays the resulting charging probabilities.

Table 1 Coefficients $a_{i,k}$ for Wiedensohler's (1988) approximation to the corrected Fuchs charge distribution. (*Note that coefficients* $a_{4,1}$ *and* $a_{5,2}$ *differ from those originally published to correct a typographical error.*)

k	-2	-1	0	1	2
$a_{0,k}$	-26.3328	-2.3197	-0.0003	-2.3484	-44.4756
$a_{1,k}$	35.9044	0.6175	-0.1014	0.6044	79.3772
$a_{2,k}$	-21.4608	0.6201	0.3073	0.4800	-62.8900
$a_{3,k}$	7.0867	-0.1105	-0.3372	0.0013	26.4492
$a_{4,k}$	-1.3088	-0.1260	0.1023	-0.1553	-5.7480
$a_{5,k}$	0.1051	0.0297	-0.0105	0.0320	0.5049

Increasing interest in particles in the low nanometer size regime has heightened interest in overcoming the measurement inefficiency that the decreasing charging probability imposes. Unipolar diffusion charging, wherein the particles are exposed to gas ions of only one polarity, can dramatically increase the probability that particles are charged, although the charging probability no longer approaches a well-defined steady state, but, rather, depends on the product of the ion concentration and the exposure time, $N_i t$. High charging probabilities for nanoparticles have been reported from such studies. In contrast to bipolar diffusion chargers that yield a charge state that is largely independent of charger design, unipolar charger performance is a strong function of charger design. For that reason, we will not attempt to describe the details of their performance in this tutorial.

The highly variable charging probability leads to another problem in particle charging: any uncertainty in the charging probability can lead to a large uncertainty in estimated concentration variations with particle size. This uncertainty in concentration determination is, perhaps, the weakest link in differential mobility analysis.

Particle Detection

In order to use the DMA to make size distribution measurements, the classifier must be coupled to a particle detector. DMA measurements typically extend well below 1μm diameter; many instruments probe the low nanometer size range. Direct detection by light scattering is impractical for such small particles due to their small scattering cross sections. Two types of detectors are used to detect mobility classified particles: (*i*) the condensation particle counter (CPC); or (*ii*) the aerosol electrometer (AE). The former method is most common due to its high counting efficiency. The latter is used when particle concentrations are high, or when particles are too small to be detected by the CPC. We will briefly discuss the two methods below.

Condensation Particle Counter

The condensation particle counter is an instrument that condenses a vapor on small particles to grow them to sufficiently large size that they can be detected optically. The CPCs that enable DMAs to be used for size distribution measurements count particles in a continuous aerosol flow. A vapor (typically butanol or water) is mixed with the aerosol under conditions that produce supersaturation of the vapor. Particles larger than the so-called *Kelvin equivalent size* activate and grow. That size is

$$d_{Kelvin} = \frac{2\sigma v_l}{kT \ln S}. \tag{20}$$

σ is the surface tension, v_l is the molecular volume, k is the Boltzmann constant, T is temperature, and $S=p_v/p_{sat}$ is the saturation ratio, the ratio of the vapor pressure to the saturation vapor pressure. For water vapor, and, to a lesser extent for other vapors used in CPCs, the minimum size of particles that will be activated may also depend on the composition of the particle. Vapor condensation grows particles to supermicron sizes (d_p>1μm). Counting efficiencies can be nearly 100% for particles ranging from a few microns down to minimum sizes that are typically in the range of 15nm to 2.5nm, although some prototype CPCs detect even smaller particles. The performance of a CPC is generally characterized in terms of the minimum size that is counted with 50% efficiency.

High quality size distribution measurements require sufficient counts in each channel (or at least in those channels that dominate the size distribution) to minimize uncertainties due to counting statistics. For large particles, number concentrations are often low enough that counting statistics are an issue unless long counting times are employed; for small particles, the low charging probability reduces the number of counts, and the mechanisms employed to produce sheath flows that reduce particle losses within some ultrafine CPCs result in counting particles in only a small fraction of the flow entering the CPC – flows as small as 0.5 $\mathrm{cm^3s^{-1}}$ are employed in some instruments. Size distributions measured under some circumstances will appear quantized as a result of counting only a few particles in each channel, a clear indication that Poisson statistics are degrading the measurement. High flow rate CPCs that can measure the ultrafine particles (Russell et al., 1996; Hering and Stolzenburg, 2005) overcome this weakness in ultrafine particle measurements.

Although CPCs may count particles within very short time intervals, the responses of some of these detectors can be quite slow. Most of the simpler commercial detectors (TSI Models 3010, 3022; MSP; Grimm) have response times of order 2-3 seconds. The TSI Model 3025 and the TSI Model 3785 water based CPC have response times of 0.18s and 0.35s, respectively. These response times become important as one attempts to reduce the time required to make size distribution measurements.

Aerosol Electrometer

Since the DMA classifies charged aerosol particles, that charge can be used to detect the transmitted particles. This is performed using an aerosol electrometer (AE). For typical classified aerosol flow rates, $O(1\ \mathrm{L/min})$, measurable currents (greater than a lower detection limit of 10^{-17}-10^{-15} A) are obtained only when aerosol concentrations are high. Moreover, the charging probability decreases with decreasing particle size, so the particle-concentration sensitivity of the electrometer detector decreases with particle size. Nonetheless, aerosol electrometers have proven very useful in measurements of fine particles emitted by engines and other sources, and for characterizing particles produced by aerosol synthesis reactors. Because aerosol electrometers are based upon a fundamental physical measurement, charge, they are also used in the calibration condensation particle counters and other detectors using mobility classified, and therefore charged, particles.

Differential Mobility Analysis for Size Distribution Measurements

When the DMA was first introduced, it was used primarily as a source of classified aerosol particles for calibration of other instruments (Knutson and Whitby, 1975a), although, even in the earliest papers, the potential to use the DMA to measure particle size distributions was recognized. The introduction of the continuous-flow condensation particle counter (CPC), which will be discussed in greater detail later, and the availability of computer data acquisition and instrument control provided the tools necessary to transform an elegant calibration instrument into the premier particle size distribution measurement technique. The DMA produces an aerosol flow that contains a representative sample of particles with mobilities in the narrow range of the DMA transfer function. By making measurements at voltages that span the operating range of the DMA, one acquires *differential* measurements of the concentrations of particles in narrow mobility bins. Since the relationship between mobility and particle size is well known (at least for spherical particles), the mobility bin data can readily be translated to determine the particle size distribution. There are three basic approaches to differential mobility analysis of aerosol particles.

Stepping mode size distribution analysis

The simplest mode of DMA operation for size distribution analysis is so-called stepping mode in which the classifier is stepped through a sequence of voltages to enable measurement of particle concentrations in each corresponding mobility bin. The first commercial version of a DMA system for size distribution measurements employed this mode in the so-called differential mobility particle sizer (DMPS, TSI) A more recent instrument that employs this mode of operation is the Grimm sequential mobility particle sizer + counter (SMPS+C), which should not be confused with the scanning mobility particle sizer (SMPS) that is described in the next section.

To determine the size distribution from a sequence of measurements, one must "invert" the data. Consider first a single voltage channel in which the concentration of transmitted particles is measured using a detector that produces an average signal $s(d_p,n_e)$ for each particle of size d_p and charge n_e. The total signal for that channel is the sum of contributions from all transmitted particles, i.e.,

$$\begin{aligned} S_j &= \int_0^\infty \sum_{n_e} n(d_p,n_e)s(d_p,n_e)\eta(d_p,n_e) \\ &\quad \times \Omega(Z(d_p,n_e),Z^*)dd_p, \qquad j=1,2,....,J \end{aligned} \tag{21}$$

where $\eta\ (d_p,n_e)$ is the overall transmission efficiency for the target particles. Each voltage channel nominally corresponds to a different size for singly charged particles. From a sequence of measurements, we seek to determine $n(d_p,n_e)$. Unfortunately, the solution of the set of J Fredholm integral equations (Eq. 21) is a mathematically ill-posed problem for which no unique solution exists.

We can reduce these integral equations to a set of linear equations by noting that the DMA transfer function, signal generated, and transmission efficiency are generally narrow enough that they change little over the range of sizes for which transmission is significant for any given operating voltage. Those functions can then be taken outside the integral to produce:

$$\begin{aligned} S_j &= \sum_{n_e} n(d_{p,j},n_e)s(d_{p,j},n_e)\eta(d_{p,j},n_e)\Omega_J, \\ &\quad j=1,2,...,J \end{aligned} \tag{22}$$

where

$$\Omega_j = \int_0^\infty \Omega(Z(d_p, n_e), Z^*(V_j)dd_p,$$

$$j = 1, 2, ..., J \qquad (23)$$

is a transfer function weighting parameter. The set of linear equations represented by Eq. (22) can be solved to estimate values of the size distribution function corresponding to each of the voltage. Measurement errors and uncertainty make direct solution risky. Instead, constrained statistical solutions are generally preferred, e.g., least squares fits to the set of channel measurements that are constrained to only allow positive values of $n(d_{p,j}, n_e)$.

The solution is further simplified if the particle charge can be tuned to allow only single charge, e.g., $n_e = \pm 1$. Methods to approach this ideal will be discussed when we examine approaches to particle charging.

Scanning mode size distribution analysis

Stepping mode DMA size distribution measurements are simple, but, due to the long times required for particles to pass through the DMA and associated plumbing to reach the point at which particles are counted (or otherwise measured) in the detector, more time is spent waiting for the signal to reach steady-state than is spent counting particles. Wang and Flagan (1990) provided a simple way to eliminate this long waiting time. The key to differential mobility analysis is separation of particles in terms of their electrophoretic mobilities. Rather than performing this separation with the DMA voltage held at a constant value, they continuously scanned the voltage, and continuously counted particles. Inference of the particle mobility required that all delays between the time that a particle exits the classification column and the time that it is detected be taken into account. The transfer function of the DMA operated in scanning mode was shown to be identical to that of one operated at the average voltage during the particle transit time. An additional subtlety was identified by Collins et al. (2004); the changing voltage during the particle transit time can alter how long a particle spends in different regions within the velocity profile of the classifier. This is reflected in a difference in the size distribution measured during a scan of increasing voltage (*an up-scan*) and that measured with decreasing voltage (*a down-scan*).

Ideally, all transmitted particles should follow the same trajectories through the DMA during any scan. This can be accomplished if the ratio of the voltage applied at any point in its transit through the classifier to that when it first enters the classifier is kept constant for all particles, a condition that is only achieved for constant or exponentially ramped voltage, i.e., $V = V_0 e^{\pm t/\tau_{scan}}$ so this was the voltage schedule used in the original, and most, if not all, implementations of scanning mode DMA operation. The instrument based upon scanning mode operation was originally labeled the scanning electrical mobility spectrometer (SEMS). The first commercial version was the scanning mobility particle sizer (SMPS) produced by TSI. This is not to be confused with the GRIMM sequential mobility particle sizer and counter (SMPS +C) that is a stepping mode instrument. The scanning mode technology is not patented and has been implemented in other instruments.

Detector Response Time Issues

Scanning mode DMA operation promises tremendous enhancements in measurement speed. Unfortunately, present detectors prevent that full potential from being realized because of limitations in the detector time response. This effect was first identified using commercially available condensation particle counters (Russell et al., 1995). Mixing within the internal volume of the CPC produces a distribution of residence times within the mixing region for particles that enter the CPC within a single counting time interval. The probability that a particle reaches the detection point within a differential time interval between t and $t+dt$ can be expressed as $dP=E(\mathrm{t})dt$. For most of the CPCs for which response time distributions, that residence time distribution can be approximated as

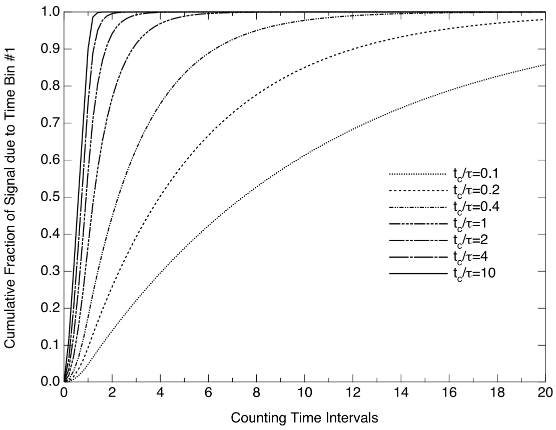

Fig. 5 CPC response time smearing.

$$E(t) = e^{-\frac{t}{\tau_r}} \tag{24}$$

Only if the counting time interval t_c is long compared to the mean residence time, t_r, will the counts be recorded within the expected time interval. If the ratio t_c/t_r approaches unity, the counts will be distributed over about 6 channels, as illustrated in **Fig. 5**. Decreasing t_c/t_r to 0.4 smears the signal such particles that first order data analysis would attribute to a single mobility channel actually span more than 10 channels of the measurement.

Electrometers may enable faster measurements, but they are also subject to smearing due to the inherent electronics time constant, $\tau_E = RC$, where R and C are the effective resistance and capacitance of the electrometer, respectively. Efforts to increase the sensitivity of aerosol electrometers are generally accompanied by an increase in τ_E, although this parameter is rarely reported.

This smearing of the transfer function was first reported in studies of the scanning mode of DMA size distribution analysis (Russell et al., 1995), *but it affects all DMA size distribution measurements, regardless of whether scanning mode or stepping mode operation is employed!* An examination of the reported mean residence times demonstrates that the effect must be taken into account to accurately deduce size distributions from DMA measurements. Some of the reports in the literature fit data to a more complex double-exponential residence time distribution, i.e.,

$$E(t) = \alpha e^{-\frac{t}{\tau_1}} + (1-\alpha)e^{-\frac{t}{\tau_2}}. \tag{25}$$

One must count for $t \sim 10\,\tau_R$ for 90% of the counts to attributed to the proper time bin, so the time required per channel to make smearing unimportant varies from about 0.1 s for the fastest developmental CPCs to as long as 10 s or more for some of the commercial instruments. When one measures tens of mobility channels, the time required to complete a measurement add up rapidly. Most measurement protocols have been designed with limited attention to this smearing effect, and operate much more rapidly than the idealized protocol that the above discussion suggests.

Russell et al. (1995) derived an analytical solution for the smeared transfer function, but that result is far too complex to be practical. Collins et al. (2002) developed a much simpler deconvolution procedure for redistributing accumulated counts into the "proper" time bins (channels). For a continuously operating CPC, the number of particles that entered the CPC during the k^{th} time interval can be estimated using a simple recursion relationship. Assuming a simple, single exponential residence time distribution, the number of particle counts that would ideally have been recorded during that interval is

$$R_k = \frac{C_k - F_k}{1 - \frac{u-1}{u \ln u}} \tag{26}$$

where C_k is the recorded counts in the counting time interval, $u=\exp(t/tR)$, and F_k is a history function that is defined such that

$$F_k = R_{k-1}\frac{(u^2-1)^2}{u \ln u} + F_{k-1} \tag{27}$$

$$F_{k-1} = \sum_{i=-\infty}^{k-2} R_i \frac{u^2-1}{u \ln u}\frac{1}{u^{k-i}} \tag{28}$$

Although subject to statistical uncertainties, especially when particle counts are low, this deconvolution is fast enough to be computed as data are acquired to enable presentation of data that are de-smeared to a

Table 2 Reported CPC response time characteristics

CPC	τ_1 (s)	α	τ_2 (s)	t_{90} s	Reference
Commercial Instruments					
TSI Model 3010	0.95	1	-	2.19	Quant *et al.* (1992)
	0.83	1	-	1.92	Buzorius (2001)
	1.35±0.05	1	-	3.11	Wang *et al.* (2002)
	0.76	0.929	2.61	2.00	Heim *et al.* (2004)
TSI Model 3022	0.71	0.859	7.32	3.22	Heim *et al.* (2004)
TSI Model 3025	0.174±0.005	1	-	0.400	Wang *et al.* (2002)
	0.14	1	-	0.329	Buzorius (2001)
	0.10	1	-	0.241	Quant *et al.* (1992)
TSI Model 3785 Water CPC	0.35	1	-	0.806	Hering *et al.* (2005)
Grimm 5.403	0.97	0.861	5.72	3.47	Heim *et al.* (2004)
Developmental Instruments					
Caltech fast mixing CPC	0.055	1	-	0.146	Wang *et al.* (2002)
UCRiverside fast mixing CPC	0.0104	1	-	0.090	Shah & Cocker (2005)

first degree. Of course, the raw data should always be recorded so that any problems encountered in the deconvolution can be addressed in post-processing of the measurements.

Data Presentation

Once one has inverted the data, it is usually plotted. The approaches to data representation used in much of the powder and particle technology are often inappropriate for DMA measurements. Because the measurement is a true, differential measurement, and, with modern detectors, can provide absolute concentration data (number per unit volume of sampled gas), representation of the results of DMA measurements as count fractions or cumulative dis-

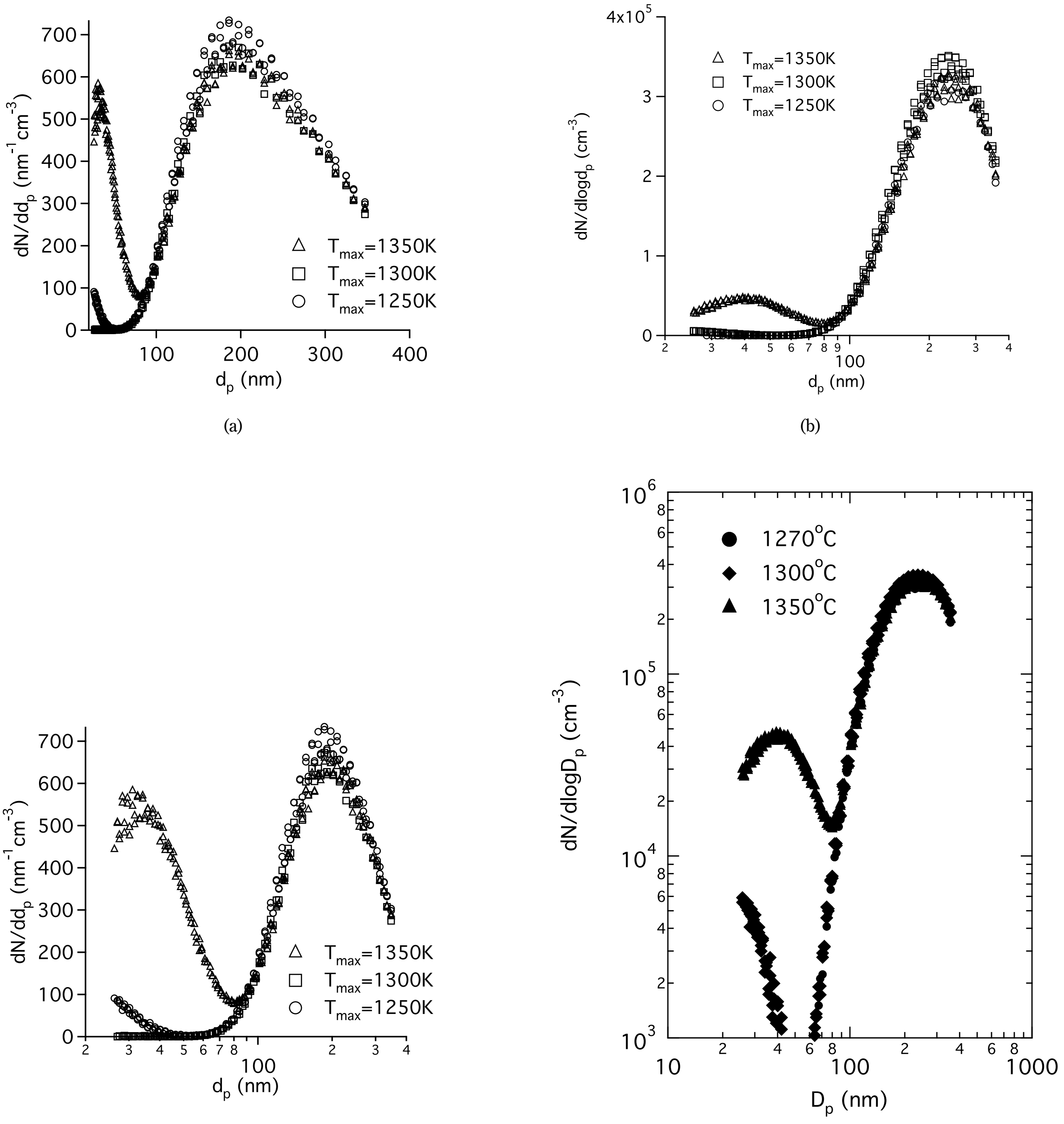

(a)

(b)

(c)

(d)

Fig. 6 Size distributions obtained using a scanning mode DMA system probing a silicon aerosol produced by a multistage silane pyrolysis reactor (Lunden, 1995). The aerosol consists of coarse mode particles, with a number median diameter of ~ 200 nm. A second, fine mode is produced when silicon that vaporizes in a high-temperature sintering reactor nucleates; the amount in that mode increases with temperature. (a) Linear plot of the size distribution. (b) A properly drawn size distribution in which the particle size is represented on a linear scale. Note that the fraction of the total area in the fine mode is comparable for plots (a) and (b). (c) An incorrectly drawn size distribution in which d_N/dd_p is plotted with a logarithmic diameter scale. Note that this misrepresentation suggests that the fine mode particles are much more abundant that the properly drawn figures show. (d) A log-log plot of the size distribution that shows the consistency of the form of the self-preserving particle size distribution for both the coarse and fine mode particles.

tributions is undesirable. First, the cumulative representation ignores the particles that are not counted at either end of the size range sampled. Furthermore, if measurements are normalized to produce fractional distributions, that omission of the uncounted particles makes the cumulative measurement meaningless. Instead, size distributions should be represented as differential distributions.

Plotting $\Delta N/\Delta d_p$ versus d_p on a linear scale, as in **Fig. 6** (a) enables one to visually integrate the size distribution to see how particles are distributed with respect to size. Because particles are often distributed over a wide range of sizes, a logarithmic size axis is often more convenient; in that case, the size distribution should be plotted as $\Delta N/\Delta \log d_p$ versus $\log d_p$, as illustrated in **Fig. 6** (b). Again, this enables one to visually integrate the size distribution and properly interpret the relative importance of different portions of the size range. Plotting $\Delta N/\Delta d_p$ versus $\log d_p$ produces a misleading plot and should be avoided. This is clearly demonstrated in **Fig. 6** (c) that suggests that the fine mode of particles contribute much more to the total number than either of the earlier figures do. Finally, the shape of the size distribution often contains useful information about the processes that govern particle formation. Plotting $\log(\Delta N/\Delta \log d_p)$ versus $\log d_p$ (**Fig. 6** d) is an effective way to visualize that information, particularly if one is systematic about the relative scales of a decade on the size and concentration axes. My personal preference is to ensure that the lengths corresponding to one decade are the same on both axes, even though this sometimes leads to tall, narrow plots. By routinely doing so, one quickly learns to recognize the so-called *self-preserving particle size distribution* in which the shape stays the same as particles grow and decrease in number due to Brownian coagulation (Lai et al., 1972), such as that shown by the large particle mode in **Fig. 6** (d). The data in these plots come from an experiment involving the synthesis of silicon particles by silane pyrolysis, followed by processing at high temperature to densify the agglomerate particles (Lunden, 1995); as the peak temperature in the sintering region increases, some of the silicon vaporizes; when this later condenses, the nuclei coagulate to produce a second self-preserving particle size distribution. The similarities in the two shapes are readily apparent. Narrower distributions generally result from growth by condensation or other vapor deposition mechanisms.

Closing Comments

This tutorial has introduced the method of differential mobility analysis for measurement of particle size distributions of submicron particles entrained in a gas. The method is powerful and enables rapid, high resolution differential size distribution measurements. Like all particle measurements, there exist limits to the range of particle sizes that can be measured: a lower bound on particle size due to limits of the particle detection technology employed, and to low charging probability and high diffusional losses of extremely small particles. It should be noted, however, that subnanometer particles (or gas ions) have been successfully classified with high resolution, high flow rate DMAs (de Juan and de la Mora, 1998). Size resolution diminishes for particles larger than about 1 μm diameter due to ambiguity in the charge state as the particles acquire multiple charges. The maximum attainable resolution of the method is determined by the ratio of the sheath to aerosol flow rates - the higher the ratio, the higher the size resolution. As one attempts to increase the resolution, however, the available measurement range at the high resolution narrows. In theory, an ideal DMA could achieve a resolving power of 300, but only for one particle size at any volumetric flow rate through the instrument since lower voltages would allow diffusional broadening of the transfer function, and higher voltages would induce arcing within the DMA.

Size resolution can be degraded by a number of factors: low voltage operation enables Brownian diffusion to compete with electrophoretic migration; design defects may distort the azimuthal symmetry in the electric or flow fields; turbulence or flow instabilities can also distort the flow fields; too-rapid stepping or scanning of the classifier voltage can result in particles being counted in the wrong size bins due to the finite response time of the detector.

To evaluate the performance of a DMA relative to the theoretical ideal, one should examine the classification of large particles at high voltage where diffusion is not significant; what is “large” is determined by the size range that is targeted, i.e., one should test at the upper end of the available size range for a particular instrument. Comparisons of different DMA designs at the same particle size, as has frequently been reported in the literature, says little about how good the DMA design is; however, it may reveal how well suited a particular instrument is for a specific measurement scenario.

References

Buzorius, G. (2001): Cut-off sizes and time constants of the cpc tsi 3010 operating at 1-3 lpm flow rates. Aerosol Sci. Technol., 35, pp.577–585.

Chen, D.R., Pui, D.Y.H., Hummes, D., Fissan, H., Quant, F. R., & Sem, G. J. (1998): Design and evaluation of a nanometer aerosol differential mobility analyzer (nano-dma). J. Aerosol. Sci., 29(5-6), pp.497–509.

Collins, D. R., Nenes, A., Flagan, R.C., & Seinfeld, J. H. (2000): The scanning flow DMA. J. Aerosol. Sci., 31(10), pp.1129 – 1144.

Collins, D.R., Flagan, R.C., & Seinfeld, J.H. (2002): Improved inversion of scanning DMA data. Aerosol Sci. Technol., 36(1), pp.1–9.

Collins, D. R., Cocker, D.R., Flagan, R.C., & Seinfeld, J.H. (2004): The scanning DMA transfer function. Aerosol Sci. Technol., 38(8), pp.833 – 850.

de Juan, L. & de la Mora, J.F. (1998): High resolution size analysis of nanoparticles and ions: Running a Vienna DMA of near optimal length at Reynolds numbers up to 5000. J. Aerosol. Sci., 29(5-6), pp.617 – 626.

Dockery, D. W., Pope, C.A., Xu, X.P., Spengler, J.D., Ware, J.H., Fay, M.E., Ferris, B.G., & Speizer, F.E. (1993): An association between air-pollution and mortality in six U. S. cities. New Engl. J. Med., 329(24), pp.1753–1759.

Donaldson, K., Stone, V., Gilmour, P.S., Brown, D.M., & MacNee, W. (2000): Ultrafine particles: mechanisms of lung injury. Philos. T. Roy. Soc. A, 358(1775), pp.2741–2748.

Donaldson, K., Brown, D., Clouter, A., Duffin, R., MacNee, W., Renwick, L., Tran, L., & Stone, V. (2002): The pulmonary toxicology of ultrafine particles. J. Aerosol Med., 15(2), pp.213–220.

Fissan, H., Hummes, D., Stratmann, F., Buscher, P., Neumann, S., Pui, D. Y. H., & Chen, D. (1996): Experimental comparison of four differential mobility analyzers for nanometer aerosol measurements. Aerosol Sci. Technol., 24, pp.1–13.

Flagan, R. C. (1998): History of electrical aerosol measurements. Aerosol Sci. Technol., 28(4), pp.301–380.

Flagan, RC. (1999): On differential mobility analyzer resolution. Aerosol Sci. Technol., 30(6), pp.556 – 570.

Fuchs, N. A. (1963): On the stationary charge distribution on aerosol particles in a bipolar ionic atmosphere. Geofis. pura appl., 56, pp.185–193.

Hagwood, C., Sivathanu, Y., & Mulholland, G. (1999): The DMA transfer function with Brownian motion a trajectory/Monte-Carlo approach. Aerosol Sci. Technol., 30, pp.40–61.

Heim, M., Kasper, G., Reischl, G. P., & Gerhart, C. (2004): Performance of a new commercial electrical mobility spectrometer. Aerosol Sci. Technol., 38, 3–14, Suppl.2..

Hering, S.V., Stolzenburg, M.R., Quant, F. R., Oberreit, D.R., & Keady, P. B. (2005): A laminar-flow, water-based condensation particle counter (WCPC). Aerosol Sci. Technol., 39, pp.659–672.

Hoppel, W. A., & Frick, G. M. (1990): The nonequilibrium character of the aerosol charge distributions produced by neutralizers. Aerosol Sci. Technol., 12, pp.471–496.

Knutson, E. O., & Whitby, K. T. (1975): Aerosol classification by electric mobility: apparatus, theory, and applications. J. Aerosol Sci., 6, pp.443–451.

Kulkarni, P., & Wang, J. (2006): New fast integrated mobility spectrometer for real-time measurement of aerosol size distribution - I: Concept and theory. J. Aerosol Sci., 37, pp.1303–1325.

Lai, F.S., Hidy, G.M., Friedlander, S.K., & Pich, J. (1972): Self-preserving particle size distribution for Brownian coagulation in the free molecule regime. J. Colloid Interf. Sci., 39, p.395.

Lunden, M. M. (1992): "Sintering of aerosol agglomerates". Ph.D. thesis, California Institute of Technology.

McMurry, P.H. (2000): A review of atmospheric aerosol measurements. Atmos. Environ., 34(12-14), pp.1959–1999.

Oberdorster, G, Sharp, Z, Atudorei, V, Elder, A, Gelein, R, Kreyling, W, & Cox, C. (2004): Translocation of inhaled ultrafine particles to the brain. Inhal. Toxicol., 16(6-7), pp.437 – 445.

Pope, C. A. (1996): Particulate pollution and health: A review of the Utah Valley experience. J. Expo. Anal. Env. Epid., 6(1), pp.23–34.

Quant, F. R., Caldow, R., Sem, G. J., , & Addison, T. J. (1992): Performance of condensation particle counters with three continuous-flow designs. J. Aerosol Sci., 23, S1251S1264.

Rossell-Llompart, J., Loscertales, I. G., Bingham, D., & d. l. Mora, J. F. (1996): Sizing nanoparticles and ions with a short differential mobility analyzer. J. Aerosol Sci., 27, pp.695–719.

Russell, L. M., Flagan, R. C., & Seinfeld, J. H. (1995): Assymetric instrument response resulting from mixing effects in accelerated DMA-CPC measurements. Aerosol Sci. Technol., 23, pp.491–509.

Russell, L. M., Stolzenburg, M. R., Zhang, S. H., Caldow, R., Flagan, R. C., & Seinfeld, J. H. (1996): Radially classified aerosol detector for aircraft based submicron aerosol measurements. J. Atmos. Ocean. Tech., 13, pp.598–609.

Shah, S. D., & Cocker, D.R. (2005): A fast scanning mobility particle spectrometer for monitoring transient particle size distributions. Aerosol Sci. Technol., 39, pp.519–526.

Stolzenburg, M. R. (1998): "An ultrafine aerosol size distribution measuring system" , Ph.D. thesis, University of Minnesota,.

Wang, J., McNeill, V. F., Collins, D. R., & Flagan, R. C. (2002): Fast mixing condensation nucleus counter: Application to rapid scanning differential mobility analyzer measurements. Aerosol Sci. Technol., 36(6), pp.678 – 689.

Wang, S. C., & Flagan, R. C. (1990): Scanning electrical mobility spectrometer. Aerosol Sci. Technol., 13, pp.230–240.

Wiedensohler, A. (1988): An approximation of the bipolar charge distribution for particles in the submicron size range. J. Aerosol Sci., 19, pp.387–389.

Winklmayr, W., Reischl, G. P., Lindner, A. O., & Berner, A. (1991): A new electromobility spectrometer for the measurement of aerosol size distributions in the size range from 1 to 1000nm. J. Aerosol Sci., 22, pp.289–296.

Zhang, M., & Wexler, A.S. (2006): Cross flow ion mobility spectrometry: Theory and initial prototype testing. Int. J. Mass Spectrom., 258, pp.13–20.

Zhang, S. H., Akutsu, Y., Russell, L.M., Flagan, R.C., & Seinfeld, J.H. (1995): Radial differential mobility analyzer. Aerosol Sci. Technol., 23(3), pp.357–372.

Author’s short biography

Richard C. Flagan

Richard Flagan is the McCollum/Corcoran Professor of Chemical Engineering, Professor of Environmental Science and Engineering, and Executive Officer of Chemical Engineering at the California Institute of Technology. His research spans the field of aerosol science and technology, including aerosol instrumentation, aerosol technologies for engineered nanoparticle synthesis, and atmospheric aerosols. He is past president of the American Association for Aerosol Research and has served as the Editor-in-Chief for its journal, *Aerosol Science and Technology*. He has received numerous awards including the Fuchs Memorial Award that is given jointly by the American Association for Aerosol Research, the Gesellschaft für Aerosolforschung, and the Japan Association for Aerosol Science and Technology, the American Chemical Society Award for Creative Advances in Environmental Science and Technology, and the Thomas Baron Award in Fluid Particle Systems of the American Institute of Chemical Engineers.

Information Articles

The 42th Symposium on Powder Technology

The 42nd Symposium on Powder Technology was held on September 1, 2008 at Hotel Tokyo Garden Palace in Tokyo under the sponsorship of the Hosokawa Powder technology Foundation and with the support of Hosokawa Micron Corporation. The symposium was very successful as usual with the attendance of 127 including 28 academic people. The main subject was “Nanoparticle Technology: New Development for Its Application and Commercialization”.

The 42th Symposium on Powder Technology

Subject: Nanoparticle Technology: New Development for Its Application and Commercialization

• Opening Address	Prof. Hiroaki Masuda (professor emeritus of Kyoto Univ.)

Session 1 Chairperson: Prof. Kikuo Okuyama (Hiroshima Univ.)

• Nano-tech-challenge by Mechanochemistry	Prof. Fumio Saito (Tohoku Univ.)
• Synthesize of $LiCoO_2$ by Excess Li Method and Application for Li Secondary Cells	Prof. Jun-ichi Yamaki (Kyushu Univ.)

Session 2 Chairperson: Prof. Kiyoshi Nogi (Osaka Univ.)

• Synthesis of Ceramic Hollow Nano-Particle and Development of Material for Low Environmental Impact	Prof. Masayoshi Fuji (Nagoya Institute of Technology)
• Development of a Novel Medical Instrument Using Nanoparticles	Prof. Ryuichi Morishita (Osaka Univ.)

Session 3 Chairperson: Prof. Makio Naito (Osaka Univ.)

• Development of “Paper Like –Electronic Display” by Designing Nano-Scale Functionarized Powders	Dr. Koji Takagi (Bridgestone Co.)
• Mass Production Technology of Composite Oxide Nanoparticles and its Application for Industrial Materials	Dr. Akira Watanabe (Hosokawa Powder Technology Research Inst.)
• Closing Address	Mr. Masuo Hosokawa (Hosokawa Micron Corporation)

The 16th KONA Award

Dr. Fumio Saito, Professor of Tohoku University, was selected as the winner of the 16th KONA Award, which is sponsored by Hosokawa Powder Technology Foundation and given to the scientist(s) or group(s) who have achieved distinguished research works in the field of particle science and technology.

Dr. Saito is the director of the Institute of Multidisciplinary Research of Advanced Materials of Tohoku University since 2005. He received BS (1970) and MS (1972) degrees in chemical engineering from Yamagata University, and he received Doctor of Engineering (1982) in Tohoku University. He started his research career from the work of single particle crushing in Yamagata University. After moving to Tohoku University, he developed his research to the field of mechano-chemistry. His current work is classified into two subjects. The one is the development of new mechanical refining processes and synthesis of useful powder materials with an aid of mechanochemical effects and reactions. The other is the production and characterization of nanoparticles of ceramics materials and its application to the separation and purification of materials. Besides research in the university, he contributes much to several academic societies and associations as a leader of research groups, an editor of journals and an organizer of conferences and symposiums.

On January 24, 2008, Mr. Masuo Hosokawa, President of the Foundation, handed the 16th KONA Award to Dr. Saito at the presentation ceremony held at Hosokawa Micron Corporation in Hirakata.

Academic publication concerning powder technology in Japan (2008)

Content Extract: Journal of the Society of Powder Technology, Japan, Vol. 45 (2008)

No.1

ORIGINAL PAPERS

REVIEW

LECTURE SERIES

- Powder Nanotechnology
  3. Measurement and Analysis for Nanoparticles

DOCTORAL THESIS INTRODUCTIONS

No. 2

ORIGINAL PAPERS

REVIEW

DOCTORAL THESIS INTRODUCTIONS

No. 3

Special Issue of 43rd Summer Symposium
"Self- assembly and Array Structure of Fine Particles : Exploring the Feasibility of Bottom – up Technology"

REVIEWS

ORIGINAL PAPERS

- DNA Mediated Sequential SelF assembly of Au Nano- particles
  Tatsuya Kusakabe, Tomoki Tanemura, Yuichi Higuchi, Koji Sugano

DOCTORAL THESIS INTRODUCTIONS

No. 4

ORIGINAL PAPERS

REVIEW

REVIEW : FRONTIER RESEARCH SERIES

LECTURE SERIES

DOCTORAL THESIS INTRODUCTION

No. 5

ORIGINAL PAPERS

REVIEW

REVIEW : FRONTIER RESEARCH SERIES

LECTURE SERIES

DOCTORAL THESIS INTRODUCTIONS

No. 6

Special Issue of 43rd Particle Technology Meeting
"Recent Development of Particle Technology using Electrostatic Phenomena
– Electrostatic Charging and Discharging of Particles/ Characterization, Measurement and Control of Charged Particles –"

0RIGINAL PAPERS

REVIEIVS

DOCTORAL THESIS INTRODUCTIONS

No. 7

ORIGNAL PAPERS

REVIEW

REVIEW: FRONTIER RESEARCH SERIES

LECTURE SERIES

● Powder Nanotechnology

DOCTORAL THESIS INTRODUCTIONS

No. 8

ORIGINAL PAPERS

REVIEW

REVIEW: FRONTIER RESEARCH SERIES

LECTURE SERIES

DOCTORAL THESIS INTRODUCTIONS

No. 9

Special Issue of 45th Symposium on Powder Science Technology

REVIEWS

ORIGINAL PAPERS

DOCTORAL THESIS INTRODUCTIONS

No. 10

0RIGINAL PAPERS

REVIEW

REVIEW:PRACTICAL ENVIRONMENTAL TECHNOLOGY SERIES

LECTURE SERIES

DOCTORAL THESIS INTRODUCTIONS

No. 11

ORIGINAL PAPERS

REVIEW

LECTURE SERIES

DOCTORAL THESIS INTRODUCTIONS

No. 12

ORIGINAL PAPERS

REVIEW

REVIEW : FRONTIER RESEARCH SERIES

LECTURE SERIES

DOCTORAL THESIS INTRODIJCTIONS

Content Extract: Kagaku Kogaku Ronbunshu Vol. 34 (2008)

No.1

Special Issue [Phenomenological Analysis and Process Intensification]

Particle Engineering

Thermal Engineering

Process Systems Engineering and Safety

Micro and Nano Systems

Materials Engineering and Interfacial Phenomena

Environment

General Research and Others

No.2

Physical Properties and Physical Chemistry

Transport Phenomena and Fluid Engineering

Separation Engineering

Chemical Reaction Engineering

Process Systems Engineering and Safety

Materials Engineering and Interfacial Phenomena

Energy

Environment

No.3

Transport Phenomena and Fluid Engineering

Particle Engineering

Separation Engineering

Thermal Engineering

Chemical Reaction Engineering

Process Systems Engineering and Safety

Materials Engineering and Interfacial Phenomena

Energy

Environment

No.4

Transport Phenomena and Fluid Engineering

Separation Engineering

Thermal Engineering

Process Systems Engineering and Safety

Biochemical, Food and Medical Engineering

Materials Engineering and Interfacial Phenomena

Energy

Environment

No.5

Separation Engineering

Thermal Engineering

Environment

No.6

Transport Phenomena and Fluid Engineering

Thermal Engineering

Chemical Reaction Engineering

Materials Engineering and Interfacial Phenomena

Environment

GENERAL INFORMATION

HISTORY OF THE JOURNAL

In the history of KONA Powder and Particle Journal, two organizations have been playing an important role. The one is the Council of Powder Technology, Japan (CPT) and the other is the Hosokawa Powder Technology Foundation (Hosokawa Foundation). The CPT was established in 1969 by Hosokawa Micron Corporation as a nonprofit organization to enhance the activities of research and development on powder science and technology. The Hosokawa Foundation was established in 1991 as a public-service corporation approued by the Ministry of Education, Culture, Sport, Science and Technology of Japan. The issues from No.1 (1983) to No.12 (1994) of KONA were published by CPT and the issues from No.13 (1995) by the Hosokawa Foundation.

The aim of KONA in the early days was to introduce excellent Japanese papers to the world and thus KONA consisted of papers recommended by some Japanese academic societies and translated from Japanese to English. From the issue of No.8, the CPT changed its editorial policy to internationalize the KONA and to incorporate papers by authors throughout the world in addition to translated papers. In response to this change, three editorial blocks have been organized in the world; Asian-Oceania, American and European. The policy and system have not changed after the Hosokawa Foundation has taken over from the CPT. The CPT is active still today and collaborates with the Hosokawa Foundation.

AIMS AND SCOPE

KONA publishes papers in a broad field of powder science and technology, ranging from fundamental principles to practical applications. The papers discussing technological experiences and critical reviews of existing knowledge in special areas are also welcome.

The submitted papers are published only when they are judged by the Editor to contribute to the progress of powder science and technology, and approved by any of the three Editorial Committees. The paper submitted to the Editorial Secretariat should not have been previously published except the translated papers which are selected by the Editorial Committees.

CATEGORY OF PAPERS

- Invited papers
  Original research and review papers invited by the KONA Editorial Committees.
- Contributed papers
  Original research and review papers submitted to the KONA Editorial Committees, and refereed by the Editors.
- Translated papers
  Papers translated into English, which were previously published in other languages, selected by the KONA Editorial Committees with the permission of the authors and / or the copyright holder.

SUBMISSON OF PAPERS

Papers should be sent to each KONA Editorial Secretariat.

- Asia/Oceania Editorial Secretariat
  Mr. T. Kawamura
  Hosokawa Powder Technology Foundation
  1-9 Shodai-Tajika Hirakata, 573-1132 JAPAN
- Europe/Africa Editorial Secretariat
  Dr. J. Stein or Mrs. P. Krubeck
  Hosokawa Micron
  Division of Hosokawa Alpine AG.
  Welserstr. 9-11, 51149 Koeln, GERMANY
- Americas Editorial Secretariat
  Dr. C.C. Huang
  Hosokawa Micron Powder Systems
  10 Chatham Road, Summit NJ 07901 USA

PUBLICATION SCHEDULE

KONA is published annually. The publication date is December 25th.

SUBSCRIPTION

KONA Powder and Particle Journal is distributed free of charge to senior researchers at universities and laboratories as well as to institutions and libraries in the field throughout the world. The publisher is always glad to consider the addition of names of those who wish to obtain this journal regularly to the mailing list. Distribution of KONA is made by each Secretariat.

Free electronic publication of KONA Powder and Particle Journal is available in
http://www.kona.or.jp

INSTRUCTIONS TO AUTHORS

(1) Manuscript format

- Two copies should be submitted to the Editorial Secretariat, in double-space typing on pages of uniform size. The final accepted version should be submitted electronically by CD or by online. Authors' short biography and photograph should be attached to the final version.
- The structure of manuscripts should follow the following order; title, authors, affiliations, abstract, main text, (acknowledgements), (appendix), nomenclature, references, figures, tables and captions of figures and tables. The items with parentheses are not mandatory. Place of figure and table insertion is to be indicated in the margin of the manuscript. For electronic submission, all figures should be in digital form with 350 dpi at least.
- Full postal addresses must be given for all the authors. Indicate the corresponding author by the mark“*” after the name. Telephone and fax numbers and e-mail address should be provided for the corresponding author.
- Abstract should not exceed 200 words.
- The appropriate number of keywords is 5 or 6.
- Symbols and units should be listed in alphabetical order with their definition and dimensions in SI units in a separate nomenclature section.
- Concerning references, either the numbering system or the alphabetical system should be adopted. In the numbering system, references should be numbered in sequence starting at the beginning of the paper. References should be given in the following form:
  1) Carslaw, H. C. and Jaeger, J. C.(1960): “Conduction of Heat in Solids” , 2nd ed., Clarendon Press, Oxford, England.
  2) Howell, P. A. (1963):US Patent, 3, 334,603
  3) Seborg, D. E. (1969): Ph.D. Dissertation, Princeton Univ., N.J., U.S.A.
  4) Zhang, N. and Rosato, A. D. (2006): KONA Powder and Particle Journal, No.24, Experiments and Simulations on Vibration Induced Densification of Bulk Solids, pp.93-103.
  In the alphabetical system, all publications cited in the text should be presented in alphabetical order of the authors. In the text make references by name and year, e.g. Zhang and Rosato (2006).

(2) Reprint

- The authors shall receive 50 free reprints. Additional reprints will be furnished when ordered with return of galley proof.

(3) Copyright and permission

- Original papers submitted for publication become immediately the property of the Hosokawa Powder Technology Foundation and remain so unless withdrawn by the author prior to acceptance for publication or unless released by the Editor. The original papers in KONA should not be reproduced nor published in any form without the written permission of the Hosokawa Foundation. The Hosokawa Foundation does not claim the copyright for translated papers. Authors are responsible for obtaining permission from the copyright holder to reproduce any figures and photos for which copyright exists.

HOSOKAWA MICRON

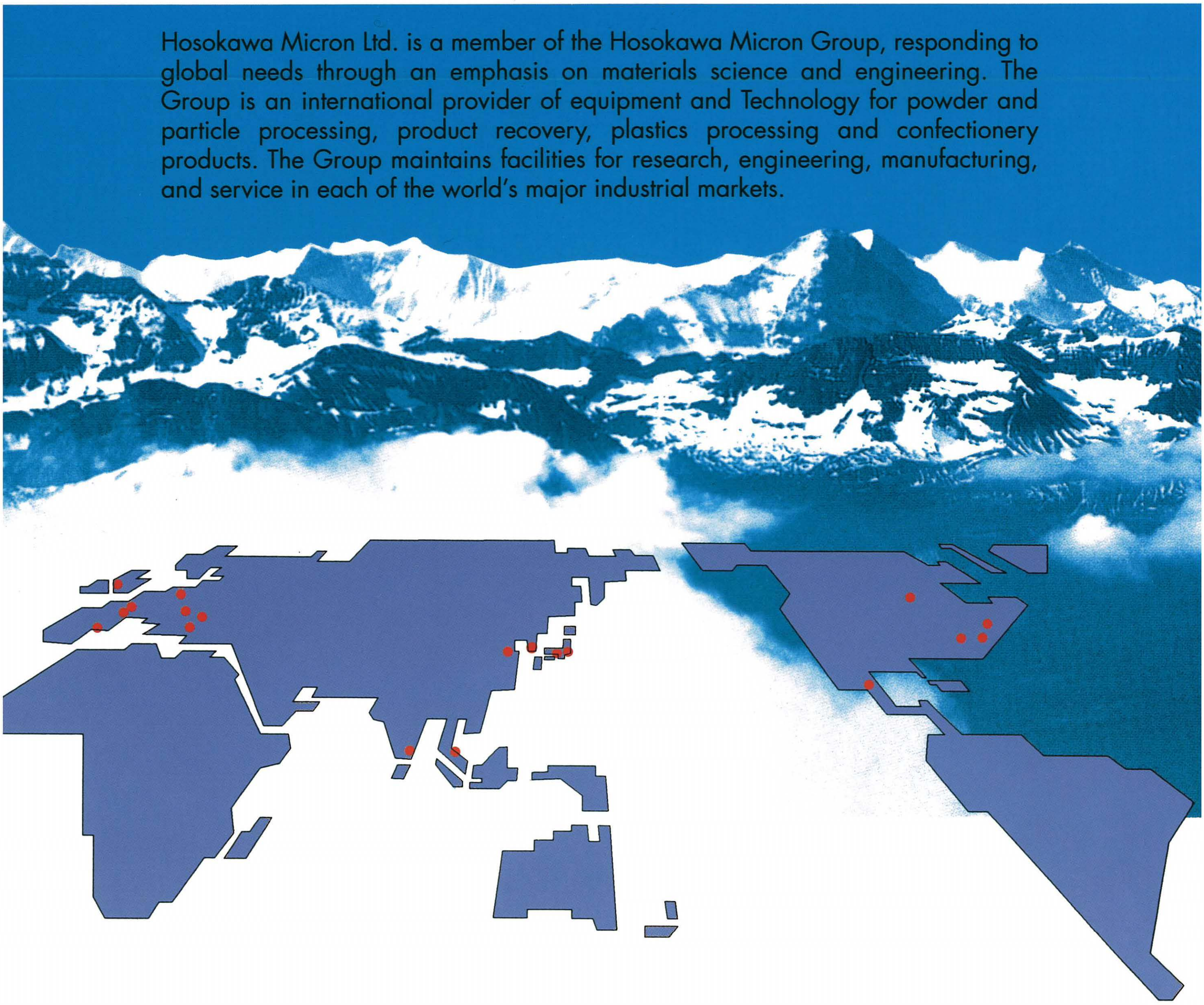

Hosokawa Micron Ltd. is a member of the Hosokawa Micron Group, responding to global needs through an emphasis on materials science and engineering. The Group is an international provider of equipment and Technology for powder and particle processing, product recovery, plastics processing and confectionery products. The Group maintains facilities for research, engineering, manufacturing, and service in each of the world's major industrial markets.

Process Technologies for Tomorrow

HOSOKAWA MICRON

Headquarter Locations;
HOSOKAWA MICRON CORPORATION
http://www.hosokawamicron.co.jp